Mohamed Farhat O. Hameed
Salah Obayya *Editors*

Computational Photonic Sensors

Springer

Computational Photonic Sensors

Mohamed Farhat O. Hameed
Salah Obayya
Editors

Computational Photonic Sensors

Springer

Editors
Mohamed Farhat O. Hameed
Center for Photonics and Smart Materials and Nanotechnology Engineering Program
Zewail City of Science and Technology
Giza
Egypt

and

Mathematics and Engineering Physics Department, Faculty of Engineering
Mansoura University
Mansoura
Egypt

Salah Obayya
Center for Photonics and Smart Materials
Zewail City of Science and Technology
Giza
Egypt

and

Electronics and Communication Engineering Department, Faculty of Engineering
Mansoura University
Mansoura
Egypt

ISBN 978-3-319-76555-6 ISBN 978-3-319-76556-3 (eBook)
https://doi.org/10.1007/978-3-319-76556-3

Library of Congress Control Number: 2018933458

© Springer International Publishing AG, part of Springer Nature 2019
This work is subject to copyright. All rights are reserved by the Publisher, whether the whole or part of the material is concerned, specifically the rights of translation, reprinting, reuse of illustrations, recitation, broadcasting, reproduction on microfilms or in any other physical way, and transmission or information storage and retrieval, electronic adaptation, computer software, or by similar or dissimilar methodology now known or hereafter developed.
The use of general descriptive names, registered names, trademarks, service marks, etc. in this publication does not imply, even in the absence of a specific statement, that such names are exempt from the relevant protective laws and regulations and therefore free for general use.
The publisher, the authors and the editors are safe to assume that the advice and information in this book are believed to be true and accurate at the date of publication. Neither the publisher nor the authors or the editors give a warranty, express or implied, with respect to the material contained herein or for any errors or omissions that may have been made. The publisher remains neutral with regard to jurisdictional claims in published maps and institutional affiliations.

Printed on acid-free paper

This Springer imprint is published by the registered company Springer International Publishing AG part of Springer Nature
The registered company address is: Gewerbestrasse 11, 6330 Cham, Switzerland

Acknowledgement

All Praise is due to Allah, and peace and blessings be upon Prophet Muhammad and upon his family and his Companions.

The editors would like to dedicate this book to the soul of Prof. Ahmed Zewail for his continuous encouragement, support, and the opportunity to contribute to the Egypt National project of renaissance: Zewail City of Science and Technology.

The editors would also like to dedicate the book to their families, whose love, support, patience, and understanding are beyond any scope.

Contents

Part I
Fundamentals

Chapter 1
Introduction to Optical Waveguides

Essam M. A. Elkaramany, Mohamed Farhat O. Hameed and S. S. A. Obayya

Abstract This chapter presents an introduction to the optical waveguides including planar and nonplanar structures. Additionally, an analysis of planner waveguides based on ray-optical approach and Maxwell's equations approach is investigated. In this context, types of modes, dispersion, cutoff frequency, and effective thickness of the optical waveguides are discussed thoroughly. Further, the different numerical techniques and their based mode solvers which are used to analyze optical waveguides are summarized in brief. Finally, the coupling mechanisms to the optical waveguide are introduced including transversal coupling techniques and the longitudinal coupling techniques.

Keywords Optical waveguides · Dispersion curves · Coupling techniques Numerical techniques

E. M. A. Elkaramany
Engineering Mathematics and Physics Department, Faculty of Engineering, Cairo University, Giza, Egypt
e-mail: ekramani@zewailcity.edu.eg

M. F. O. Hameed (✉)
Center for Photonics and Smart Materials and Nanotechnology Engineering Program, Zewail City of Science and Technology, October Gardens, 6th of October City, Giza, Egypt
e-mail: mfarahat@zewailcity.edu.eg

M. F. O. Hameed
Mathematics and Engineering Physics Department, Faculty of Engineering, Mansoura University, Mansoura, Egypt

S. S. A. Obayya
Centre for Photonics and Smart Materials, Zewail City of Science and Technology, October Gardens, 6th of October City, Giza, Egypt
e-mail: sobayya@zewailcity.edu.eg

S. S. A. Obayya
Electronics and Communication Engineering Department, Faculty of Engineering, Mansoura University, Mansoura, Egypt

© Springer International Publishing AG, part of Springer Nature 2019

M. F. O. Hameed and S. Obayya (eds.), *Computational Photonic Sensors*, https://doi.org/10.1007/978-3-319-76556-3_1

1.1 Introduction—Historical Review

The concept of optical waveguides is mainly based on the electromagnetic theory of light and its interaction with the matter. The first attempt to use light waves for communication was in 1880, when Alexander Graham Bell invented his "photophone" shortly after his invention of the telephone in 1876. He used modulated sunlight to transmit speech through air to the receiver at 200 m apart. In 1899, David D. Smith of Indianapolis has used a bent glass rod as a surgical lamp [1]. In 1926, Clarence W. Hansell in a laboratory at RCA proposed the fundamentals of optical fiber communications system and patented a design for transmission of images over bundles of glass fibers from remote locations. The concept of transmitting multiple wavelengths in optic fibers originated in the 1930s. At that time, no suitable light source was available that could reliably be used as an information carrier. In 1952, Prof. H. H. Hopkins began his research to develop bundles of glass fibers as an endoscope [2], which was produced and marketed in 1966.

Since the discovery of the laser in 1960, enormous steps of waveguiding phenomena with carrier waves at optical frequencies began. Kao and Hockham in 1966 suggested that optical fibers based on silica glass could provide the necessary transmission medium if metallic and other impurities could be removed [3]. Their paper triggered serious research in developing low-loss optical fibers, and the first low-loss single-mode optical fibers were fabricated in 1970 by Kapron, Keck, and Maurer in USA [4]. They managed to get silica fibers with a loss of about 17 dB/km at a wavelength of 633 nm. By 1985, extremely low-loss glass fibers (<0.2 dB/km) were routinely produced where the distance between two consecutive repeaters (used for amplifying and reshaping the attenuated signals) could be as large as 250 km.

In recent times, the idea of the confined propagation of light in optical waveguides goes far beyond the telecommunications area. Biomedical applications include imaging and sensing in many medical specialties that are developed where optical waveguides in integrated photonics are used to confine and transmit light along tens or hundreds of micrometers. Additionally, optical waveguides can be used as passive and active devices such as fibers [5], waveguide couplers [6], optical routers [7], polarization rotators [8–10], polarization splitters [11], polarizers [12], multiplexer-demultiplexer [13, 14], sensors [15, 16], and modulators. This is due to the developments of rapid and efficient numerical methods for computational simulations and the related advancements in optical technologies in laser science and material fabrication.

In this chapter, the fundamentals of optical waveguides are discussed including waveguides structure, properties of guided modes, Maxwell's field equations, wave equation and its solutions, boundary conditions, operation, coupling and numerical methods.

1.2 Optical Waveguides Structures

Optical waveguides are basically dielectric waveguides which guide the light beam from one place to another. They are fundamental parts of optical communications systems and optical integrated circuits. The basic structure of a dielectric waveguide consists of a *core* which is longitudinally extended high-index optical medium and is transversely surrounded by the cladding low-index media. The guided optical wave propagates through the high-index material along the longitudinal direction of the waveguide. Generally, the dimensions of a waveguide should have the same order of magnitude as the wavelength used.

Optical waveguides can be classified according to their geometry, mode profile, refractive index distribution, materials, and the number of dimensions where the light is confined [17]. Generally, the characteristics of a waveguide are determined by the transverse profile of its dielectric constant $\varepsilon_r(x, y)$, which is independent on the longitudinal direction. The optically isotropic waveguide can be categorized with a single spatially dependent transverse profile of the index of refraction $n(x, y)$.

According to their geometry, the optical waveguides can be categorized by three basic structures: planar, rectangular channel, and cylindrical channel. Common optical waveguides can also be classified based on mode structure as single mode and multiple modes.

In a *planar waveguide*, Fig. 1.1a, the core is sandwiched between cladding layers in only one direction, say the x-direction, with an index profile $n_1(x) > n_2(x), n_3(x)$, while the upper and lower cladding layers are called the cover and the substrate, respectively. The core should have a refractive index higher than the refractive indices of the cover and the substrate. As a result, light beam is trapped within the core by total internal reflection.

In *cylindrical channel*, Fig. 1.1b, a central core region is surrounded by the cladding material. Of course, to confine the light within the core, the core must have a higher refractive index than that of the cladding.

In a *nonplanar waveguide*, Fig. 1.1c, a rectangular channel is sandwiched between an underlying planar substrate and the upper medium, which is usually air. Again, it is necessary for the channel to have a refractive index greater than that of

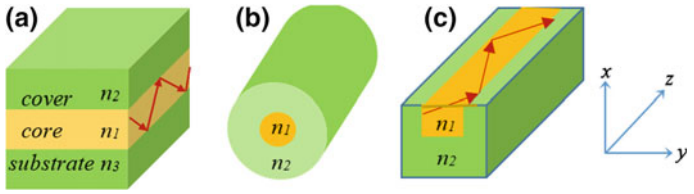

Fig. 1.1 Schematics of optical waveguides: **a** planar waveguide, **b** cylindrical channel, and **c** nonplanar waveguide

the substrate to trap the light within the channel. In this case, the refractive index *n (x, y)* is a function of both x- and y-coordinates. The rectangular channel represents the best choice for fabricating integrated photonic devices.

Optical waveguides can be classified based on the number of dimensions where the light rays are confined. In planar waveguides, the confinement of light takes place in a single direction and so the propagating light will diffract in the plane of the core. In contrast, in the case of nonplanar waveguides, shown in Fig. 1.1c, the confinement of light takes place in two directions and thus diffraction is avoided, forcing the light propagation to occur only along the main axis of the structure. Further, photonic crystal structure can confine the light in three dimensions. In this case, the light confinement is based on Bragg reflection. Photonic crystals have very interesting properties and have been proposed in several devices, such as waveguide bends, drop filters, couplers, and resonators [18].

Classification of optical waveguides according to the materials and refractive index distributions results in various optical waveguide structures. A waveguide where the index profile has abrupt changes between the core and the cladding, as shown in Fig. 1.2a, is called a step-index waveguide. However, the index profile of graded-index waveguide varies gradually, as shown in Fig. 1.2b, where the refractive index of the core varies as a function of the radial distance [19].

Most of the waveguides of the different applications are *nonplanar* waveguides where the index profile *n(x, y)* is a function of both transverse coordinates *x* and *y*. The main difference between the common types of channel waveguides is in the shape and the size of the film deposited onto the substrate. The most common types of channel waveguide structures include:

(i) *The strip-loaded waveguide*, Fig. 1.3a, is formed by loading a planar waveguide with a dielectric strip of index $n_2 < n_1$ or a metal strip to facilitate optical confinement in the *y*-direction. In this case, the core of the waveguide is the n_1 region under the loading strip.

(ii) *The rib waveguide*, Fig. 1.3b, has a structure similar to that of a strip waveguide, but the strip has the same index n_1 as the high-index planar layer beneath it and is part of the waveguiding core.

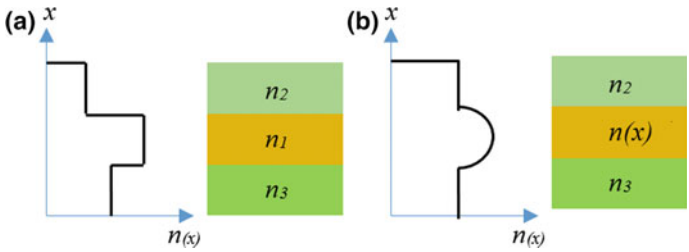

Fig. 1.2 **a** Step-index waveguide and **b** graded-index waveguide

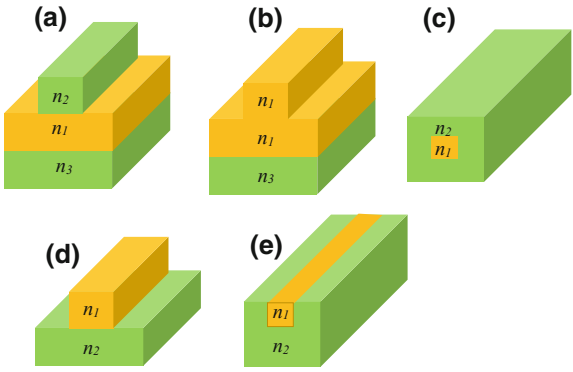

Fig. 1.3 Common types of nonplanar waveguides, **a** the strip-loaded waveguides, **b** the rib waveguides, **c** the buried channel waveguides, **d** the ridge waveguides, and **e** the diffused waveguides

(iii) *The buried channel waveguide*, Fig. 1.3c, can be produced by increasing the refractive index of a certain zone of the substrate by the diffusion methods [2]. The waveguiding core can have any cross-sectional geometry especially the preferred rectangular shape.

(iv) *The ridge waveguide*, Fig. 1.3d, has a structure that looks like a strip waveguide, but the strip, or the ridge, on top of its planar structure has a high index and is actually the waveguiding core. A ridge waveguide has strong optical confinement because it is surrounded on three sides by low-index air region (or cladding material).

(v) *The diffused waveguide*, Fig. 1.3e, is formed by creating a high-index region in a substrate through diffusion of dopants, such as $LiNbO_3$ waveguide with a core formed by *Ti* diffusion. Because of the diffusion process, the core boundaries in the substrate are not sharply defined.

Generally, optical waveguides can be analyzed by solving Maxwell's equations or their reduced wave equation, with appropriate boundary conditions determined by their geometry and the materials properties. The main issue is to analyze the supported modes of the waveguide which is an eigenvalue problem. Analytical solutions of waveguides modes are only available in few simple cases such as planner waveguide which is invariant along the waveguide axis. The optical waveguides are in general open structures with a transverse plane cross section; therefore, propagating, radiation, and evanescent modes exist. The most practical waveguides have usually complex geometries with non-uniform structure in the direction of wave propagation such as waveguide tapers, gratings, photonic crystal waveguides, Y-splitters, S-bends, and helical waveguides. Another examples are the waveguides with structures composed of nonlinear, anisotropic, or metamaterials. In these cases, numerical methods are needed for computing complex modes and to simulate the light wave propagation.

1.3 Analysis of Planner Waveguides

In this section, the analysis of planar, step-index, waveguides will be introduced. Firstly, a simple ray-optical picture based on total internal reflection (TIR) will be used to describe the optical confinement of light in a waveguide and introduce the concept of guided modes. Next, Maxwell's equations are used to derive the discrete nature of these guided modes. At the end of the section, the analysis of the graded-index planner waveguides is discussed.

1.3.1 Ray-Optical Approach

Consider the case of the guided mode propagating along an optical waveguide via series of total internal reflections at the core–substrate and core–cladding interfaces, as shown in Fig. 1.4a. The critical angle at the core–substrate interface is $\theta_{c1} = sin^{-1}\frac{n_s}{n_{co}}$ and that at the core–cladding interface is $\theta_{c2} = sin^{-1}\frac{n_c}{n_{co}}$. Then, the angle $\boldsymbol{\theta}$ must be greater than the critical angles at both interfaces ($\boldsymbol{\theta > \theta_{c1}, \theta_{c2}}$) to have total internal reflection. In this case, light is confined in the waveguide corresponding to a guided mode which propagates along the waveguide in a zigzag path.

The important parameter to be considered in this analysis is the propagation constant, which is used to characterize waveguide modes. As shown in Fig. 1.4b, the orthogonal components of the propagation constant, k_x in x-direction and $k_z = \beta$, in z-direction are related by the "k-vector triangle". The plane wave propagation constant in the wave-normal direction is defined as $k = k_o n_{co} = \frac{2\pi}{\lambda_o} n_{co}$, where λ_o is the free space wavelength of light. From the figure, the propagation constants along the x- and z-directions are:

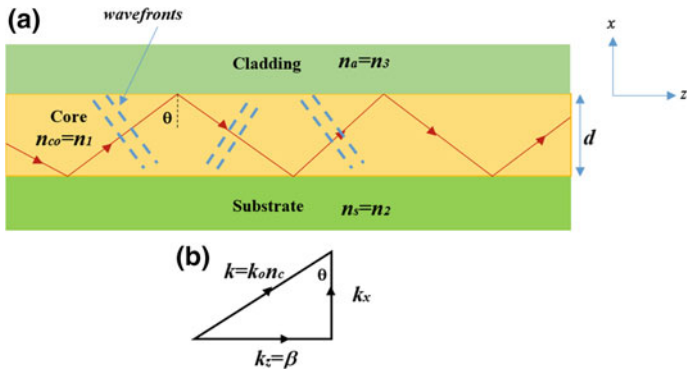

Fig. 1.4 **a** Guided mode propagating along an optical waveguide and **b** the k-vector triangle

$$k_x = k_o n_{co} \cos\theta \tag{1.1}$$

$$k_z = \beta = k_o n_{co} \sin\theta \tag{1.2}$$

For lossless waveguides, k_z is equivalent to the mode propagation constant in an infinite medium with an index of $n_{co} \sin\theta$. Hence, the effective indices of modes, N, is defined as:

$$N = \frac{k_z}{k_o} = n_{co} \sin\theta \tag{1.3}$$

which specifies the ratio of the wave velocity in a vacuum to that in the direction of propagation (z). Hence, the guided propagating mode along the z-direction sees the effective index N.

Since θ can only have values greater than the critical angles at the core–substrate and core–substrate interfaces, then, in the practical case where $n_s > n_a$, the guided modes can be only supported in the range,

$$n_{co} > N > n_s \tag{1.4}$$

Now, considering the "zigzag" wave in the waveguide, as shown in Fig. 1.5, where (sb) is parallel to the wave fronts of rays (oa) and (bc), the optical path difference in the optical field due to a complete round-trip passage is $\delta = n_{co}$ $(sa + ab)$. If the thickness of the core is d, it may be seen from the geometry of the figure that

$$\delta = 2\, n_{co}\, d \cos\theta \tag{1.5}$$

which is equivalent to a phase shift = $2k_o\, n_{co}\, d\, \cos\theta$.

An additional phase shifts ϕ_1 and ϕ_2 are associated with the internal reflections in the lower and upper interfaces. These phase shifts depend on the angle θ and on the polarization of the propagated wave. Figure 1.6a shows the transverse magnetic (TM) wave in which the magnetic field is confined in the transverse plane,

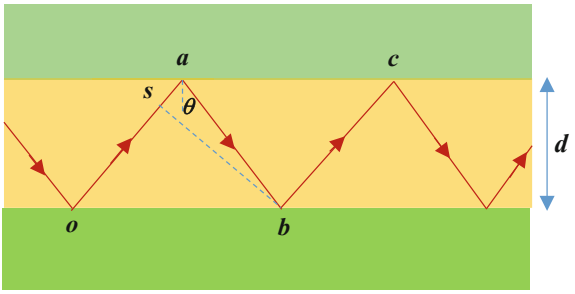

Fig. 1.5 Diagram to calculate the optical path difference due to a complete round-trip passage

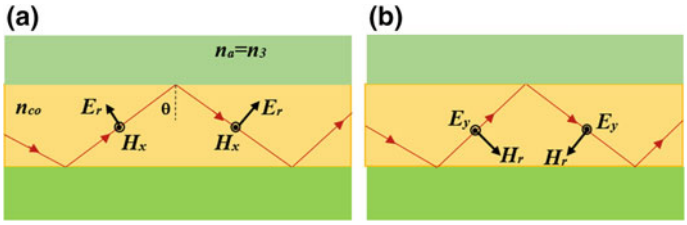

Fig. 1.6 Types of the polarization of the propagated wave **a** TM waves and **b** TE waves

while Fig. 1.6b presents the transverse electric (TE) wave where the electric field is confined in the transverse plane.

By applying the boundary conditions at the two interfaces, the reflection coefficients of the fields at the interfaces can be obtained [20]. The reflection coefficient $\boldsymbol{r}(= |\boldsymbol{r}|e^{j\phi})$ at the interface between two media n_1 and n_2 ($n_1 > n_2$) is given by:

$$r_{TE} = \frac{\cos\theta - \sqrt{\left(\frac{n_2}{n_1}\right)^2 - \sin^2\theta}}{\cos\theta + \sqrt{\left(\frac{n_2}{n_1}\right)^2 - \sin^2\theta}} \tag{1.6a}$$

$$r_{TM} = \frac{\left(\frac{n_2}{n_1}\right)^2 \cos\theta - \sqrt{\left(\frac{n_2}{n_1}\right)^2 - \sin^2\theta}}{\left(\frac{n_2}{n_1}\right)^2 \cos\theta + \sqrt{\left(\frac{n_2}{n_1}\right)^2 - \sin^2\theta}} \tag{1.6b}$$

And the phase change due to the reflection ϕ is given by:

$$\phi_{(n_1,n_2)} = 2\tan^{-1}\left[\left(\frac{n_2}{n_1}\right)^{2\nu}\sqrt{\left\{\frac{N^2 - n_2^2}{n_1^2 - N^2}\right\}}\right] \tag{1.7}$$

where

$$\begin{aligned} \nu &= 0 \quad \text{for TE polarization} \\ &= 1 \quad \text{for TM polarization} \end{aligned}$$

$N = n_1 \sin\theta$ is the effective index (see Eq. 1.3).

The reflection coefficient $\boldsymbol{r}$ has the following properties:

- If $\left(\theta < \theta_c = \sin^{-1}\frac{n_2}{n_1}\right)$, $\boldsymbol{r}$ is real and $0 < |\boldsymbol{r}| < 1$
- If $\left(\theta > \theta_c = \sin^{-1}\frac{n_2}{n_1}\right)$, $|\boldsymbol{r}| = 1$, case of *total internal reflection* (there is no propagation in medium n_2).

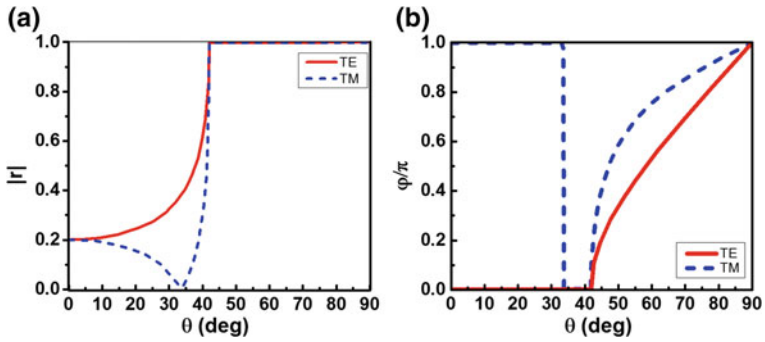

Fig. 1.7 Variation of reflection coefficient r with the incident angle θ, **a** magnitude of r and **b** phase of $\boldsymbol{r}$

Figure 1.7a shows the variation of the magnitude of the reflection coefficient $|\boldsymbol{r}|$ with the incident angle θ for $n_1 = 1.5$ and $n_2 = 1.0$, while Fig. 1.7b shows the variation of the phase of the reflection coefficient ϕ with the incident angle θ. Accordingly, the phase shifts ϕ_1 (at core–substrate interface) and ϕ_2 (at core–cladding interface) are given by,

$$\phi_{1(n_{co},n_s)} = 2\ \tan^{-1}\left[\left(\frac{n_s}{n_{co}}\right)^{2\nu}\sqrt{\left\{\frac{N^2-n_s^2}{n_{co}^2-N^2}\right\}}\right] \tag{1.8}$$

$$\phi_{2(n_{co},n_c)} = 2\ \tan^{-1}\left[\left(\frac{n_c}{n_{co}}\right)^{2\nu}\sqrt{\left\{\frac{N^2-n_c^2}{n_{co}^2-N^2}\right\}}\right] \tag{1.9}$$

In order to maintain light propagation within the core, it is important that the light undergoes constructive interference and the total phase difference should be a multiple of 2π. Therefore, the condition for constructive interference is given by,

$$2kd\cos\theta - \phi_1 - \phi_2 = 2m\pi \tag{1.10}$$

where m is an integer ≥ 0. Equation 1.10 can be written as,

$$2k_o\ d\sqrt{(n_{co}^2 - N_m^2)} = \phi_1 + \phi_2 + 2m\pi \tag{1.11}$$

where $N_m = n_{co}\ sin\ \theta_m$, which depends on the mode order m.

Equation 1.11 indicates that light propagates within a medium as discrete modes of effective indices N_m that depend on the mode order m. Such guided mode dispersion equation reveals that only a discrete number of guiding modes can exist for fixed values of $n_{s,}$ $n_{co,}$ n_a, d, and k_o. Therefore, only rays with certain bounce angles, θ_m, related to certain values of m, can propagate as guided modes. The zeroth-order mode corresponds to a ray propagating with an angle, $\theta_{(m\ =\ 0)}$

closest to 90° with the highest effective index. For higher-order modes, θ_m decreases until it approaches the critical angle at the core/cladding interface so that N tends to n_a and the condition of total internal reflection is no longer satisfied. This is known as *cutoff* condition where the light is no longer confined in the guiding layer but leaks into the cladding region. This limits the number of higher-order modes that may propagate in the core region. In summary,

- The number of modes that can be supported depends on the thickness d of the core, $n_{s,}$ n_{co}, n_a, and $k_{o.}$
- For given $n_{s,}$ n_{co}, n_a, and d, there is a cutoff frequency ω_c below which waveguiding cannot occur. This frequency corresponds to a long wavelength cutoff $\lambda_c \left(= \frac{2\pi}{k_{oc}} \right)$.
- The waveguide condition (1.11) describes discrete values of the propagation constant β_m for guided modes corresponding to the mode number m, where $\beta_m = k_o n_{co} \cos\theta_m$.
- The critical angles at the lower and upper interfaces do not depend on the polarization of the wave, while the phase shifts, $\phi_1(\theta)$ and $\phi_2(\theta)$, caused by the internal reflection at a given angle θ rely on the polarization. So, TE and TM waves have different solutions for condition (1.11), resulting in different propagation constant β_m and different mode characteristics for a given mode number m.
- For a given polarization, solution of the waveguide condition yields a smaller value of θ with a corresponding smaller value of β for a larger value of m. Therefore, $\beta_0 > \beta_1 > \beta_2 > \ldots$
- The guided mode with $m = 0$ is called the fundamental mode while those with $m \neq 0$ are called higher-order modes.

The optic-ray approach cannot be used to determine the guided mode electric field distribution, and hence, it is necessary to consider the Maxwell's equations approach.

1.3.2 TE and TM Field Distribution—Maxwell's Equations Approach

The analysis of the planar waveguides can be driven from Maxwell's equation. For a source free, homogeneous, linear, isotropic, and lossless dielectric medium, Maxwell's equations can be written as follows:

$$\nabla x E = -\frac{\partial B}{\partial t} \tag{1.12a}$$

$$\nabla x H = -\frac{\partial E}{\partial t} \tag{1.12b}$$

$$\nabla \cdot E = 0 \tag{1.12c}$$

$$\nabla \cdot D = 0 \tag{1.12d}$$

where $D = \varepsilon E$ and $B = \mu H$. For the planner geometry shown in Fig. 1.5, it implies that no variation in y-direction $\left(\frac{\partial}{\partial y} = 0\right)$. Recalling that $\frac{\partial}{\partial t} = j\omega$ for harmonic variations and $\frac{\partial}{\partial z} = j\beta$ for mode propagation in z-direction, the traveling fields in the waveguide can be expressed as,

$$E(x, z, t) = E(x)e^{j(\omega t - \beta z)} \tag{1.13a}$$

$$H(x, z, t) = H(x)e^{j(\omega t - \beta z)} \tag{1.13b}$$

Substitution of Eqs. 1.13a and 1.13b into Maxwell's equations, these equations are separated into two different modes with orthogonal polarization. The first is the ***TE*** mode where the electric field is polarized in y-direction (normal to the propagation direction) and consists of the field components (H_z, E_y, H_x). The second is the ***TM*** mode where the magnetic field is polarized in y-direction and consists of the field components (E_z, H_y, E_x). Each of these fields components obeys the wave equation which can be expressed as,

$$\frac{\partial F(x)}{\partial x^2} + \left(k_o^2 n^2 - \beta^2\right) E_y(x) = 0 \tag{1.14}$$

where $F = E(x)$ or $H(x)$ and $n = \sqrt{\varepsilon_r}$.

The guiding condition in the core layer for both guiding modes depends on the field distributions functions $E(x)$ and $H(x)$ that have an exponential decay outside the core (as x approaches $\pm\infty$, and a standing wave inside the core in the range $0 < x < d$, where d is the thickness of the guide).

Considering the guiding ***TE*** mode, Eq. 1.14 for the field component $E_y(x)$ for the three layers can be expressed as,

$$\frac{\partial E_y(x)}{\partial x^2} + \gamma_1^2 E_y(x) = 0 \quad \text{in the core layer } n_{co} \tag{1.15a}$$

$$\frac{\partial E_y(x)}{\partial x^2} - \gamma_2^2 E_y(x) = 0 \quad \text{in the substrate layer } n_s \tag{1.15b}$$

$$\frac{\partial E_y(x)}{\partial x^2} - \gamma_3^2 E_y(x) = 0 \quad \text{in the cladding layer } n_c \tag{1.15c}$$

where

$$\gamma_1^2 = k_o^2 n_{co}^2 - \beta^2 \tag{1.16a}$$

$$\gamma_2^2 = \beta^2 - k_o^2 n_s^2 \tag{1.16b}$$

$$\gamma_3^2 = \beta^2 - k_o^2 n_c^2 \tag{1.16c}$$

Since $k_o n_{co} \geq \beta \geq k_o n_s \geq k_o n_c$, $\beta = k_o n_{co} \sin\theta$, the last choices ensure the guiding condition in the core $\left(\gamma_1^2 \geq 0\right)$ and evanescent waves into substrate and cladding layers $\left(\gamma_2^2 \geq 0,\ \gamma_3^2 \geq 0\right)$.

Using Eqs. 1.15a, 1.15b, 1.15c, the electric field E_y can be expressed as,

$$E_y(x) = A\ \sin\gamma_1 x + B\cos\gamma_1 x \quad -d < x < 0 \tag{1.17a}$$

$$= Ce^{\gamma_2(x+d)} \quad -\infty < x < -d \tag{1.17b}$$

$$= De^{-\gamma_3 x} \quad 0 < x < \infty \tag{1.17c}$$

where A, B, C, and D are constants that can be determined by matching the boundary conditions at the two interfaces. The boundary conditions require the continuity of E_y and its derivative $\frac{\partial E_y}{\partial x}$ (or the component H_z) across the interfaces. Using these conditions, the constants are given by [21]:

$$A = -\frac{\gamma_3}{\gamma_1} \tag{1.18a}$$

$$B = D \tag{1.18b}$$

$$C = D\left(\cos\gamma_1 d + \frac{\gamma_3}{\gamma_1}\sin\gamma_1 d\right) \tag{1.18c}$$

and

$$\gamma_1 d = tan^{-1}\left(\frac{\gamma_2 + \gamma_3}{\gamma_1 - \frac{\gamma_2\gamma_3}{\gamma_1}}\right) = tan^{-1}\left(\frac{\gamma_3}{\gamma_1}\right) + tan^{-1}\left(\frac{\gamma_2}{\gamma_1}\right) + m\pi \tag{1.19}$$

where m is an integer ≥ 0 that defines the mode order.

The constant D can be determined by using the normalization condition [22, 23] and is given by,

$$D_m = 2\gamma_{1,m}\left(\frac{\omega\mu_o}{\beta_m\left(d + \frac{1}{\gamma_{3,m}} + \frac{1}{\gamma_{2,m}}\right)\left(\gamma_{1,m}^2 + \gamma_{3,m}^2\right)}\right)^{\frac{1}{2}} \tag{1.20}$$

Figure 1.8 shows the field distributions for the first two orders well guiding modes TE_0 and TE_1, where $k_o n_{co} \geq \beta \geq k_o n_s \geq k_o n_c$.

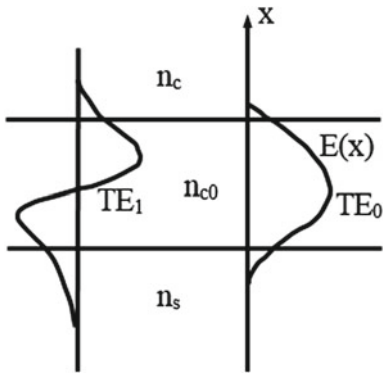

Fig. 1.8 Field distributions for the first two orders modes TE_0 and TE_1

The propagation constant of a waveguide mode β_m, (and therefore N_m,where $\beta_m = k_o N_m$), can be obtained from Eq. 1.16a, 1.16b, 1.16c with known values of n_c, n_{co}, n_s, and d. If $k_o n_{co} \geq k_o n_s \geq \beta \geq k_o n_a$ in which $\gamma_2^2 < 0$, the field varies sinusoidally in the substrate and the optical energy is confined at the core–cladding interface. In this case, light propagates in the substrate as shown in Fig. 1.9a as a substrate mode. If $k_o n_{co} \geq k_o n_s \geq k_o n_a \geq \beta$ where γ_2^2 and $\gamma_3^2 < 0$, the field varies sinusoidally in both the substrate and the cladding regions and the optical energy radiates in the three mediums as shown in Fig. 1.9b.

Similar analysis can be done for the TM mode case (H_y, E_x, E_z). The boundary conditions at the interfaces lead to the following dispersion equation,

$$\gamma_1 d = tan^{-1}\left(\frac{\gamma_1\left(\frac{n_{co}^2}{n_s^2}\gamma_2 + \frac{n_{co}^2}{n_c^2}\gamma_3\right)}{\gamma_1^2 - \frac{n_{co}^2}{n_s^2}\frac{n_{co}^2}{n_c^2}\gamma_2\gamma_3}\right) = tan^{-1}\left(\frac{n_{co}}{n_c}\frac{\gamma_3}{\gamma_1}\right) + tan^{-1}\left(\frac{n_{co}}{n_s}\frac{\gamma_2}{\gamma_1}\right) + m\pi \tag{1.21}$$

And by using the normalization condition [10, 11], one can get,

$$D_m = 2\left(\frac{\omega\varepsilon_o}{\beta_m d_e}\right)^{\frac{1}{2}} \tag{1.22}$$

where d_e is given by,

$$d_e = \left(\frac{\left(\frac{n_{co}^2}{n_c^2}\gamma_3\right)^2 + \gamma_1^2}{\left(\frac{n_{co}^2}{n_c^2}\gamma_3\right)^2}\right)\left[\frac{d}{n_{co}^2} + \frac{1}{n_c^2\gamma_3}\left(\frac{\gamma_3^2+\gamma_1^2}{\left(\frac{n_{co}^2}{n_c^2}\gamma_3\right)^2 + \gamma_1^2}\right) + \frac{1}{n_s^2\gamma_2}\left(\frac{\gamma_2^2+\gamma_1^2}{\left(\frac{n_{co}^2}{n_s^2}\gamma_2\right)^2 + \gamma_1^2}\right)\right] \tag{1.23}$$

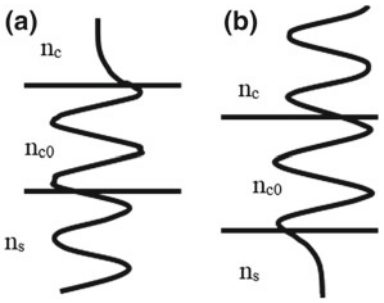

Fig. 1.9 **a** Field distribution of substrate mode and **b** field distribution of cladding mode

1.3.3 Dispersion Curves

Equations 1.19 and 1.21 are referred as the dispersion relation for *TE* and *TM* modes, respectively. When the refractive indices of the substrate and cladding regions are constant, Fig. 1.10a shows the variation of the effective index *N* as a function of the core thickness for different *TE* guided modes of order *m* with $n_{co} = 2.224$, $n_s = 2.19$, *and* $n_c = 1$ at $\lambda = 632$ nm [21]. Figure 1.10b shows the dispersion relation for TM guided modes.

It can be noted from Fig. 1.10 that for a certain guided mode *m*, the effective index increases by increasing the thickness toward a maximum value. Also, for a certain mode *m,* there exists a minimal thickness, corresponds to a minimal value for *N* below which the mode *m* cannot by supported. This thickness is known as the cutoff thickness. Using the dispersion relations, the cutoff thickness can be expressed as follows,

$$d_{cut-off}(TE_m) = \frac{m\pi + tan^{-1}\left(\frac{n_s^2 - n_c^2}{n_{co}^2 - n_s^2}\right)^{\frac{1}{2}}}{k_o\left(n_{co}^2 - n_s^2\right)^{\frac{1}{2}}} \tag{1.24}$$

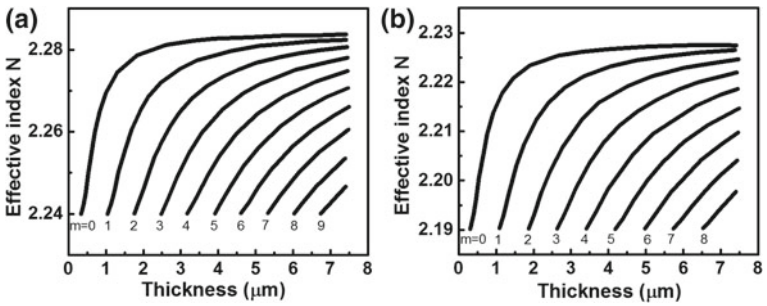

Fig. 1.10 Variation of the effective index *N* as a function of the core thickness for the **a** TE modes, and **b** TM modes

$$d_{cut-off}(TM_m) = \frac{m\pi + tan^{-1}\left[\left(\frac{n_{co}}{n_c}\right)^2\left(\frac{n_s^2 - n_c^2}{n_{co}^2 - n_s^2}\right)^{\frac{1}{2}}\right]}{k_o\left(n_{co}^2 - n_s^2\right)^{\frac{1}{2}}} \tag{1.25}$$

Note that the cutoff thickness for the TM_m mode is always $\geq$ that of the TE_m mode. For the symmetric waveguide ($n_s = n_c = n$), the cutoff thickness for both *TE* and *TM* modes is equal to,

$$d_{cut-off} = \frac{m\pi}{k_o\left(n_{co}^2 - n^2\right)^{\frac{1}{2}}} \tag{1.26}$$

For the fundamental mode ($m = 0$), the cutoff thickness is equal to zero, so, this mode always exists. Equations 1.24 and 1.25 can be used to calculate the maximum number of the guided modes supported by a certain waveguide structure. In this regard, it is necessary to find the guided mode order which corresponds to a guide cutoff thickness similar to the guide thickness considered. Complete analysis can be found in [21]. The maximum number of modes M is given by,

$$M = nearst\ integer\ to\left[\left(\frac{1}{\pi}\right)dk_o\left(n_{co}^2 - n_s^2\right)^{\frac{1}{2}} - \tan^{-1}\left(\left(\frac{n_2}{n_1}\right)^{2\nu}\sqrt{\left\{\frac{n_s^2 - n_c^2}{n_{co}^2 - n_s^2}\right\}}\right)\right] \tag{1.27a}$$

For symmetric waveguide $n_s = n_c$, it leads to,

$$M = nearst\ integer\ to\left[\frac{dk_o}{\pi}\left(n_{co}^2 - n_s^2\right)^{\frac{1}{2}}\right] \tag{1.27b}$$

Therefore, to fabricate single-mode waveguides for a fixed wavelength, the values of d, $n_{co,}$ and n_s need to be carefully chosen such that $1 < M < 2$.

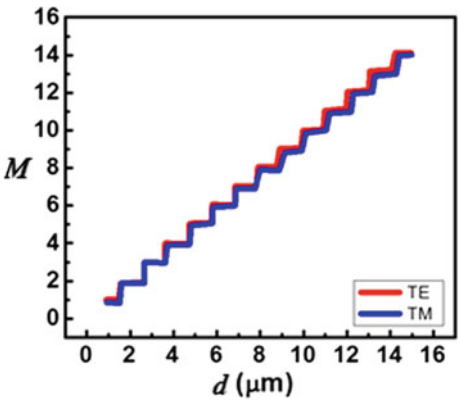

Fig. 1.11 Effect of the thickness d on the number of modes M

Figure 1.11 shows the effect of the thickness d on the number of modes M for both *TE* and *TM* guided modes at index difference $n = 0.02$.

1.3.4 Effective Thickness

The optic-ray undergoing total internal reflection penetrates into the substrate and the cladding, as evanescent waves as indicated in Fig. 1.12. From that point of view, we can consider that light travels within a core with a different thickness called the guide effective thickness [24].

The guide effective thickness can be written as:

$$d_{eff} = d + \delta_{12} + \delta_{13} \tag{1.28}$$

where δ_{12} and δ_{13} are given by [24],

$$\delta_{1i} = \frac{1}{k_o \sqrt{\left(N_m^2 - n_i^2\right)}} \quad i = 2,\ 3 \quad \text{for TE modes} \tag{1.29}$$

$$= \frac{1}{k_o \sqrt{\left(N_m^2 - n_i^2\right)} \left[\frac{N_m^2}{n_i^2} + \frac{N_m^2}{n_{co}^2} - 1\right]} \quad \text{for TM modes} \tag{1.30}$$

which depends on the mode order m.

It may be seen from Fig. 1.12 that there exists a lateral displacement of $2d_s$ and $2d_c$ on the two interfaces core–substrate and core–cladding, respectively. These displacements are known as the Goos–Hänchen effect and are given by,

$$d_i = \frac{N_m}{\delta_{1i} \sqrt{\left(n_{co}^2 - N_m^2\right)}} \quad i = 2\ (\text{for substrate}),\ 3\ (\text{for cladding}) \tag{1.31}$$

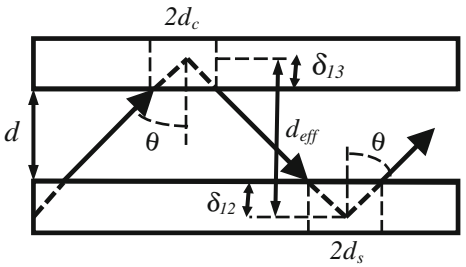

Fig. 1.12 Effective thickness of the guide d_{eff}

1.4 Numerical Methods

Analytical solution for modes and corresponding propagation constants are available for a limited number of ideal, simple waveguide constrictions. In general, waveguides with complex structures that are non-uniform in the direction of propagation are now basic parts of integrated optical circuits, for example a bent waveguide to turn the direction of propagation, a Y-branch to split one waveguide into two parts, S-bend waveguide to introduce a lateral displacement, and a taper to excite a waveguide or to connect two waveguides of different geometries. To simulate the light wave propagation in these structures, accurate and efficient numerical methods are needed. Many commercial CAD software based on different approaches are now available to analyze different complex waveguides. In this section, many mode solvers which are used to analyze optical waveguides are classified according to the used numerical technique.

1.4.1 Finite Element Technique (FEM) [25–27]

The finite element method (FEM) is used to find an approximate solution of partial differential equations (PDE) for structures with complex geometries or boundary conditions. The computational domain is divided into small elements such as triangles and rectangles of various shapes which allow the use of an efficient irregular grid. The FEM can be used for mode solving and propagation problems. The FEM uses two approaches to solve waveguide problems: the variational method and the weighted residual method. Both approaches lead to the same eigenvalue equation that should be solved to get the resonance modes. Many software based on the FEM are available. For more details about the software packages, see optical waveguides: numerical modeling Web site (http://optical-waveguides-modeling.net/index.jsp). Examples of software packages are:

- FEMLAB (sold by COMSOL Multiphysics).
- EMFlex (by Weidlinger Associates).
- FemSIM (sold by RSoft).
- FIMMWAVE-FEM-Solver (sold by Photon Design).
- JCMwave (sold by JCMwave).
- PDE2D (sold by Visual Numerics).
- EMAP (free software developed by Lawrence Livermore National Laboratory).
- EMSolve (free software developed by Lawrence Livermore National Laboratory).
- FlexPDE (sold by PDE Solutions).
- FreeFem++ (developed by O. Pironneau, F. Hecht, and A. Le Hyaric at Université Pierre et Marie Curie Laboratoire Jacques-Louis Lions).
- PdnMesh (Free software).
- HFSS (sold by Ansoft).

- Concerto-Opera-Soprano (sold by Vector Fields), used for microwave waveguides.
- WaveSim (sold by Field Precision).Used for microwave waveguides.

1.4.2 Plane Wave Expansion (PWE) Method [28]

The plane wave expansion (PWE) is based on the expansion of the fields in terms of complete basis of definite-frequency states (for example, plane waves with a finite cutoff) to solve the resultant linear eigenvalue problem. Examples of software packages which are based on PWE include:

- Band SOLVE software (sold by RSoft).
- Waveguide Mode Solver (Free software).

1.4.3 Transfer Matrix Method (TMM) [29]

TMM is used efficiently when the waveguide structure consists of a few more easily solvable components. The waveguide is divided into a number of layers. Then, at certain frequency, we can use analytical, finite difference, or any other methods to compute the transfer matrix, relating field parameters at one end of a layer, with those at the other end. The mode vectors are obtained from the eigenvalues of the resulting matrix. Examples of software packages based on the TMM are:

- GratingMOD™ (sold by RSoft).
- TMM Mode Solver and Anisotropic TMM Mode Solver (Free codes developed by Henri Uranus—University of Twente).
- WAVEGUIDE (Free software developed by the Southern Methodist University group).

1.4.4 Beam Propagation Method BPM [30]

BPM is used in the practical waveguides where the relative variation in refractive index is small enough to approximate scalar wave equation to form the Helmholtz equation. The BPMs include different approaches such as the fast Fourier transform (FFT-BPM) [31, 32], finite difference BPM, [33, 34], finite element BPM [35], etc.

Examples of software packages based on BPM include:

- Beam PROPTM software (sold by RSoft Inc.).
- OlympIOs BPM (sold by C2 V).

- OptiBPM (sold by Optiwave).
- OptoDesigner (sold by PhoeniX).

Many other software packages with different approximation approaches which can be used to analyze the optical waveguides are also available. Examples of these software packages that are based on finite difference time domain (FDTD) technique [36] are,

- FDTD Solutions (sold by Lumerical).
- XFdtd (sold by Remcom).
- EMPLab2D/EMPLab3D (sold by EM Photonics).
- GMES (Free software. Python package developed at GIST to model photonic systems).

1.5 Coupling Techniques

The coupling techniques that can be employed to excite a guided mode into an optical waveguide are discussed in this section. This is important to study and evaluate optical properties and propagation characteristics of the waveguide and also for the practical use of this component in integrated optical circuits. These techniques can be divided into two categories: the transversal coupling techniques and the longitudinal coupling techniques.

1.5.1 The Transversal Coupling Techniques

The aim of these techniques is to couple the incident light directly into waveguides through its cross section. Two main transversal coupling techniques are discussed here: end coupling and taper coupling.

1.5.1.1 End Coupling

This method is probably the easiest method of coupling light into a waveguide. As shown in Fig. 1.13, a laser source is used to generate a light beam which is focused into the cross section of the waveguide through a microscope objective lens. For its simplicity, this method is suitable for practical use in optical integrated circuits. Although this technique is simple and practical, it has some drawbacks. In this regard, the end coupling configuration does not allow excitation with a selective guided mode. Besides, very accurate alignment is needed to avoid instability problems. So, an optical fiber or another waveguide may be used. Additionally,

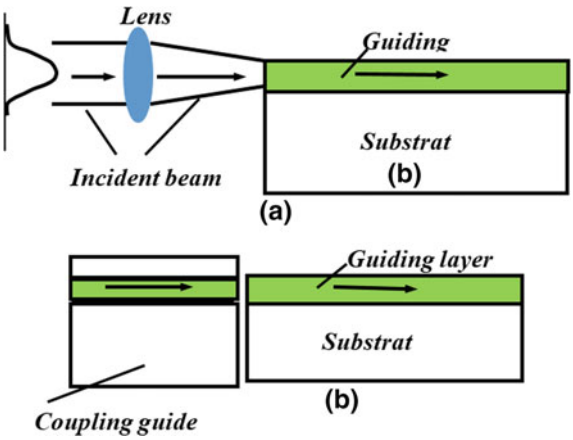

Fig. 1.13 End coupling technique using **a** a direct coupling and **b** a coupling guide

a very high optical polishing of the guide cross section is needed to avoid optical diffusion losses. This reduces the coupling efficiency [21, 37].

1.5.1.2 Taper Coupling

In this configuration, the concept of cutoff thickness is used [38], where a tapered structure is created on the waveguide surface over a distance of 10 to 100 times the wavelength as shown in Fig. 1.14. The incident light can be progressively coupled into or out from the waveguide throughout the tapered structure, while the cutoff thickness of the guided mode is reached. The taper allows a continuous variation of the reflection angle around the critical angle. This technique is of great interest with high-index thin films where it is difficult to find a high-index transparent prism [38]. However, the taper coupling has some drawbacks [21]: it is a destructive method due to the created tapered structure on the surface of the guide; low coupling efficiency; and it is difficult to excite selective guided modes.

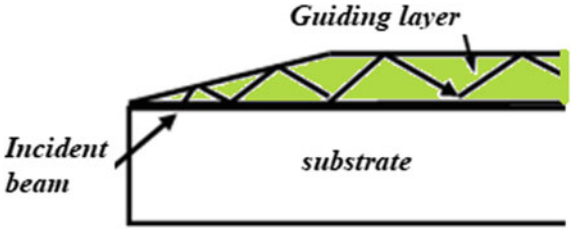

Fig. 1.14 Taper coupling technique

1.5.2 The Longitudinal Coupling Techniques

In these methods, coupling device as prism or grating is used to couple the light across the surface of the waveguide. These techniques require that the longitudinal component of the wave vector should be equal to the guided mode propagation constant.

1.5.2.1 Prism Coupling

This method is the most frequently technique for optical waveguide characterization. As mentioned before in Sect. 1.3.1, for light confinement within the guide, the following condition should be satisfied,

$$n_{co} > N > n_s \geq n_c$$

thus,

$$\beta_m = k_o n_{co} \sin\theta_m \geq k_o n_s \geq k_o n_c \tag{1.32}$$

where cladding index n_c is usually air. This condition cannot be satisfied if the beam is directly incident on the surface of the waveguide. In order to excite guided modes, it is necessary to use a high-index incident medium. As shown in Fig. 1.15, a high-index prism is used to couple the laser beam into the waveguide. To maintain a very small air gap, (of order of half a wavelength) between the prism and the guide surface, spring-loaded clamps are used to press the prism onto the surface of the waveguide [39].

When the angle between the incident light and normal to the prism base exceeds the critical angle at the prism–air interface, total internal reflection occurs at the base of the prism and a stationary wave is formed inside the prism. In the air gap, an evanescent wave exists. If the phase matching condition is satisfied such that the propagation constant of the light passing through the prism is equal to the

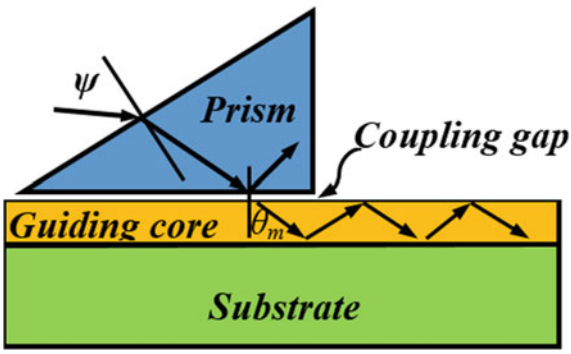

Fig. 1.15 Prism coupling technique

propagation constant of the guided mode, the coupling of the incident light into the guided mode is obtained. This can only occur when

$$n_p \sin \psi = n_{co} \sin \theta_m \tag{1.33}$$

where n_p is the prism refractive index. Figure 1.16 shows the excitation of guided modes throughout the evanescent waves created in the air gap between the prism and the guiding layer.

The coupling efficiency mainly depends on [21]:

- The thickness of air gap which can be controlled by the pressure applied to the prism by the clamps.
- The incident beam profile and the incident beam section at the base of the prism, which are related to the optical setup and the used laser source.

The main attractive feature of the prism coupling technique is the ability to select and alter individual modes by altering the angle ψ. Also, such configuration can be used to characterize the waveguide by coupling the propagating light out of the guide in order to image it onto a screen. Usually, the prisms used in this technique were made from rutile ($Ti0_2$), which has refractive indices, $n_o = 2.584$ and $n_e = 2.872$ at wavelength of 633 nm.

1.5.2.2 Grating Coupler

In this technique, a periodic grating structure of period Ω is fabricated on the surface of the waveguide as shown in Fig. 1.17. This technique was first developed by Dakss et al. [40]. When a light laser beam with propagation vector β_o is incident on the grating region, the light is diffracted and components of a period 2π/Ω appear

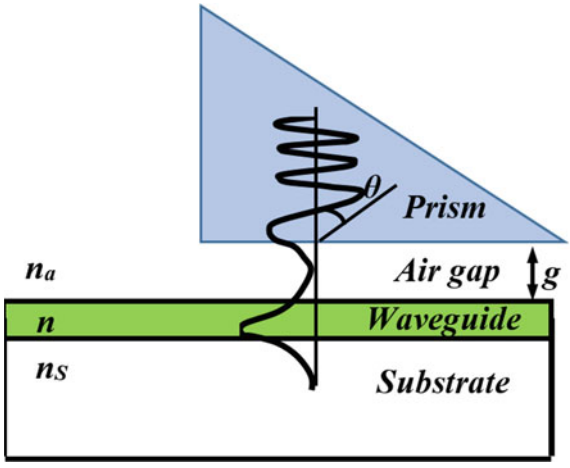

Fig. 1.16 Excitation of guided modes using prism coupling technique

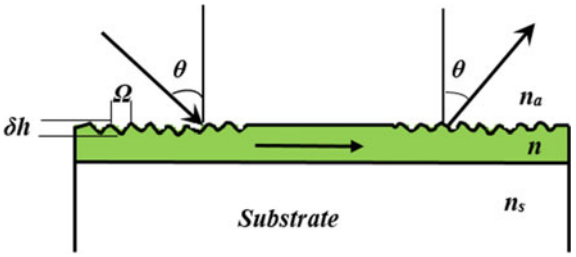

Fig. 1.17 Excitation of guided modes using grating coupler

in the longitudinal component of the wave vector [41, 42]. These wave components have propagation constant,

$$\beta = \beta_o + 2\pi \frac{\gamma}{\Omega} \tag{1.34}$$

where γ is the diffraction order, integer: 0, ± 1, ± 2, ± 3, …

Thus, light can be coupled to guided modes m when the propagation vector of the guided mode β_m fulfills the phase matching condition in relation (1.34).

The coupling efficiency is optimal for specific values of the incident angle θ that are solutions of the phase matching relation. It depends on many factors: the grating structure (the grating period Ω and the grating depth h), the form of the incidental beam, and the zone of coupling [21]. Coupling coefficient of 75% has already been reported [41].

References

1. Publication number: US624392A, Publication type: Grant, Publication date: May 2, 1899, Filing date: Apr 25, 1898, Inventors: David D. Smith
2. H.H. Hopkins, N.S. Kapany, A flexible fiberscope using static scanning. Nature **1954**(173), 39–41 (1954)
3. K.C. Kao, G.A. Hockham, Dielectric-fibre surface waveguides for optical frequencies. Proc. IEE. **113**(7), 1151–1158 (1966)
4. F.P. Kapron, D.B. Keck, R.D. Maurer, Radiation losses in glass optical waveguides. Appl. Phys. Lett. **17,** 423–425 (1970)
5. M.F.O. Hameed, S.S.A. Obayya, K. Al-Begain, M.I. Abo el Maaty, A.M. Nasr, Modal properties of an index guiding nematic liquid crystal based photonic crystal fiber. IEEE J. Lightwave Technol. **27**(21), 4754–4762 (2009)
6. M.F.O. Hameed, S.S.A. Obayya, Coupling characteristics of dual liquid crystal core soft glass photonic crystal fiber. IEEE J. Quant. Electron. **47**(10), 1283–1290 (2011)
7. S.S.A. Obayya, M.F.O. Hameed, N.F.F. Areed, *Computational Liquid Crystal Photonics: Fundamentals, Modelling and Applications*, Wiley, April 2016
8. M.F.O. Hameed, A.M. Heikal, S.S.A. Obayya, Novel passive polarization rotator based on spiral photonic crystal fiber. IEEE Photon. Technol. Lett. **25**(16), 1578, 1581 (2013)
9. M.F.O. Hameed, S.S.A. Obayya, H.A. El-Mikati, Passive polarization converters based on photonic crystal fiber with L-shaped core region. IEEE J. Lightwave Technol. **30**(3), 283–289 (2012)

10. M.F.O. Hameed, Maher Abdelrazzak, S.S.A. Obayya, Novel design of ultra-compact triangular lattice silica photonic crystal polarization converter. IEEE J. Lightwave Technol. **31** (1), 81–86 (2013). January 1
11. Rasha A. H. Ali, M.F.O. Hameed, S.S.A. Obayya, Ultra-compact polarization splitter based on silica photonic liquid crystal fiber. J. Appl. Computat. Electromagnet. Soc. **30**(6), 599–607 (2015)
12. S. Azzam, M.F.O. Hameed, N. Fayez, S.S.A. Obayya, H. Elmikati, M. Abd-Elrazzak, Proposal of ultracompact CMOS compatible TE-/TM- Pass polarizer based on SOI platform. IEEE Photon. Technol. Lett. **26**(16), 1633–1636 (2014)
13. M. El-Azab, M.F.O. Hameed, S.M. El-Hefnawy, S.S.A. Obayya, Ultra-compact liquid crystal dual core photonic crystal fibre multiplexer–demultiplexer. IET J. Optoelectron. **10**(1), 21–27 (2016). https://doi.org/10.1049/iet-opt.2015.0009
14. M.F.O. Hameed, R.T. Balat, A.M. Heikal, M.M. Abo-Elkhier, M.I. Abo el Maaty, S.S.A. Obayya, Polarization-independent surface plasmon liquid crystal photonic crystal multiplexer-demultiplexer. Photon. J. IEEE **7**(5), 1–10 (2015)
15. M.F.O. Hameed, M. El-Azab, A.M. Heikal, S.M. El-Hefnawy, S.S.A. Obayya, Highly sensitive plasmonic photonic crystal temperature sensor filled with liquid crystal. IEEE Photon. Technol. Lett. http://ieeexplore.ieee.org/xpl/RecentIssue.jsp?punumber=68**28**(1), pp. 59–62 (2015)
16. Shaimaa I. Azzam, Rania Eid A. Shehata, Mohamed Farhat O. Hameed, A.M. Heikal, S.S.A. Obayya, Multichannel photonic crystal fiber surface plasmon resonance based sensor. J. Optic. Quant. Electron. **48**, 142 (2016)
17. G. Lifante, *Integrated Photonics Fundamentals* (Wiley, Hoboken, 2003)
18. J.D. Joannopoulos, R.D. Meade, J.N. Winn, *Photonic Crystals: Molding the Flow of Light* (Princeton University Press, Princeton, 2001)
19. A. Ghatak, K. Thyagarajan, *Introduction to Fiber Optics* (Cambridge University Press, Cambridge, 1998)
20. M. Born, E. Wolf, *Principles of Optics* 7th edn. (Cambridge University Press, 1999)
21. A. Boudrioua, *Photonic Waveguides: Theory and Applications*, ISTE Ltd and Wiley (2009)
22. A. Yariv, Coupled-mode theory for guided wave optics. IEEE J. Quant. Electron. **9**(9), 919–933 (1973)
23. B. Vincent, Conversion de frequencies dans les guides d'ondesfabriqués par implantation ioniquedans les cristauxpériodiquementpolarises, PhD Thesis, University of Metz (2003)
24. R.G. Hunsperger, *Integrated Optic: Theory and Technology*, 2nd ed. (Springer, 1985)
25. M. Koshiba, H. Saitoh, M. Eguchi, K. Hirayama, Simple scalar finite element approach to optical waveguides. lEE Proc. 1 **139**, 166–171 (1992)
26. M. Koshiba, *Optical Waveguide Theory by the Finite Element Method* (KTK Scientific Publishers and Kluwer Academic Publishers, Dordrecht, Holland, 1992)
27. F.A. Fernandez, Y. Lu, Microwave and optical waveguide analysis by the finite element method, in *Electronic and Electrical Engineering Research Studies Optoelectronics Series* (Wiley 1996)
28. S. Johnson, J. Joannopoulos, Block-iterative frequency-domain methods for Maxwell's equations in a plane wave basis. Opt. Expr. **8**, 173 (2001)
29. A. Ghatak et al., Numerical analysis of planar optical waveguides using matrix approach. J. Lightwave Technol. **5**, 660 (1987)
30. L. Thyelen, The beam propagation method: an analysis of its applicability. Opt. Quant. Electron. **15**, 433 (1983)
31. D. Yevick, B. Hermansson, Efficient beam propagation techniques. IEEE J. Quant. Elect. **26**, 109 (1990)
32. D. Yevick, B. Hermansson, Efficient beam propagation techniques. IEEE J. Quant. Electron. **26**, 109 (1990)
33. Y. Chung, N. Dagle, Assessment of finite difference beam propagation. IEEE J. Quant. Elect. **26**, 1335 (1990)

34. T. Koch, J. Davies, D. Wickramasinghe, Finite element/finite difference propagation algorithm for integrated optical devices. Electr. Lett. **25**, 514 (1989)
35. M. Koshiba, Y. Tsuji, Design and modeling of microwave photonic devices. Opt. Quant. Electron. **30**, 995 (1998)
36. A. Taflove, S. Hagness, Computational electrodynamics, in *The Finite-Difference Time-Domain Method*, 3rd edn. (Artech House, 2005)
37. G.Y. Wang, E. Garmire, Efficient coupling into tapered proton-exchanged LiNbO3 waveguides fabricated by vertically controlled immersion. Opt. Lett. **21**, 42–45 (1996)
38. P.K. Tien, R.J. Martin, Experiments in light waves in a thin, tapered film and a new light wave coupler. Appl. Phys. Lett. **18**, 398–401 (1971)
39. P.K. Tien, R. Ulrich, R.J. Martin, Modes of propagating light waves in thin deposited semiconductor films. Appl. Phys. Lett. **14**, 291–294 (1969)
40. M.L. Dakss, L. Kuhn, P.F. Heidrich, B.A. Scott, Grating couplers for efficient excitation of optical guided waves in thin films. Appl. Phys. Lett. **16**, 523–525 (1970)
41. R. Petit, *Electromagnetic Theory of Gratings*, Springer (1980)
42. Planar Waveguides of Y2O3, Y2O3: Tb3+ and YAG Prepared by sol-gel: Analysis, Structure and Optical. PhD dissertation, Claude Bernard University, Lyon

Chapter 2
Fundamentals of Photonic Crystals

Essam M. A. Elkaramany, Mohamed Farhat O. Hameed and S. S. A. Obayya

Abstract In this chapter, the basic principles of photonic crystal (PhC) structures and their possible applications are presented. In this context, one-dimensional photonic crystals, Bloch's theorem including Maxwell's equations in periodic media, are discussed thoroughly. Additionally, the different types of defects, bandgap size, and the relation between the Brillouin zone and the reciprocal lattice are introduced. Further, the different types of PhCs such as one-dimensional, two-dimensional, and three-dimensional structures are presented in detail.

Keywords Photonic crystal · Bandgap · Defects · Bloch's theorem Photonic crystal fibers

E. M. A. Elkaramany
Faculty of Engineering, Engineering Mathematics and Physics Department, Cairo University, Giza, Egypt

M. F. O. Hameed (✉)
Center for Photonics and Smart Materials and Nanotechnology Engineering Program, Zewail City of Science and Technology, October Gardens, 6th of October City, Giza, Egypt
e-mail: mfarahat@zewailcity.edu.eg

M. F. O. Hameed
Mathematics and Engineering Physics Department, Faculty of Engineering, Mansoura University, Mansoura, Egypt

S. S. A. Obayya
Centre for Photonics and Smart Materials, Zewail City of Science and Technology, October Gardens, 6th of October City, Giza, Egypt
e-mail: sobayya@zewailcity.edu.eg

S. S. A. Obayya
Electronics and Communication Engineering Department, Faculty of Engineering, Mansoura University, Mansoura, Egypt

© Springer International Publishing AG, part of Springer Nature 2019

M. F. O. Hameed and S. Obayya (eds.), *Computational Photonic Sensors*, https://doi.org/10.1007/978-3-319-76556-3_2

2.1 Introduction

Photonic crystals (PhCs) are inhomogeneous materials with periodic structure where dielectric properties vary periodically in space on the order of the light wavelength [1–4]. Perhaps, Lord Rayleigh was the first scientist who studied this structure in 1887 when he formulated a precise theory for the reflective properties of a crystalline mineral with periodic twinning planes and identified its bandgap property. Although multilayer structures as films received intensive study over the last century, the term photonic crystal was first used by Yablonovitch [5] and John [6], in 1987. In this context, they proposed PhCs as materials that could localize light and inhibit spontaneous emission of atoms if a light source is embedded in such a crystal. They demonstrated the analogy between the electronic and the photonic crystals and explained that PhCs with periodic dielectric constants deal with photons in a similar way as semiconductor crystal structures behave with electrons. Both electronic and photonic crystals are governed by the Bloch–Floquet theorem. However, for PhCs, Maxwell's equations are used to describe their behavior, while the Schrödinger equation is used to describe the behavior of electronic crystal. Although this fundamental difference does exist, electronic and photonic crystals share many properties due to the periodic nature of both materials. In this regard, the semiconductor crystal structure has periodic potential which results in a "forbidden gap" for electrons, while PhCs' periodic structures result in a forbidden bandgap for photons.

After 1987, the number of research papers concerning photonic crystals began to grow exponentially. However, due to the fabrication difficulty of these structures at optical scales, early studies were either theoretical or in the microwave centimeter scale. This fact is due to a property of the electromagnetic fields known as scale invariance. Additionally, solutions for centimeter-scale structure at microwave frequencies are the same as for nanometer-scale structures at optical frequencies. By 1991, Yablonovitch has demonstrated the first three-dimensional photonic bandgap in the microwave regime [7]. In 1996, Thomas Krauss made the first demonstration of a two-dimensional photonic crystal at optical wavelengths [8]. This opened up the way for semiconductor photonic crystals' fabrication in the same manner of the semiconductor industry.

The main concept of the PhCs is the periodic reflections and refractions at the boundaries of the alternating dielectric materials. Since the periodicity is in order of the light wavelength, the phase difference of the interfered waves is an important factor that determines the optical response of such a structure. This can be used to establish destructive interference where light cannot propagate through the structure at certain frequency bands and specific incident angles. The frequency bands at which the waves cannot propagate are referred as photonic bandgap (PBG).

2.2 One-Dimensional Photonic Crystals—Bloch's Theorem

One-dimensional photonic crystal structures are easy to construct by stacking alternating layers of different refractive indices on top of each other. Such periodic structures were discovered and used in many applications many years ago before people thought about photonic crystals.

The basic concepts of photonics can be best understood from a study of the simple one-dimensional crystal model shown in Fig. 2.1. It consists of alternating layers of dielectrics, ε_1 and ε_2, with thickness of a_1 and a_2, respectively. In this study, the effect of normal incident plane electromagnetic wave (E_x, H_y) of wavelength λ, from the left is investigated. As in the case of thin films, there are reflections and transmissions from each interface. At particular frequencies, the reflections and transmissions in the propagation direction can destructively interfere in such a way that there is no forward traveling wave and all the energy is reflected back. The crystal behaves as a mirror at this frequency. In order to analyze the fields in the crystal, we must solve Maxwell's equations in periodic media.

2.2.1 Maxwell's Equations in Periodic Media—Bloch–Floquet Theorem

Assuming time-harmonic fields with time dependence $e^{i\omega t}$, and using the two Maxwell's curl equations, the electric field is governed by the wave equation

$$\frac{\partial^2}{\partial z^2}E_x(z) - \left(\frac{\omega}{c}\right)^2 \varepsilon(z)E_x(z) = 0 \tag{2.1}$$

with the periodic dielectric constant given by

$$\begin{aligned} \varepsilon(z) &= \varepsilon_1 \quad \text{in the first medium 1} \\ &= \varepsilon_2 \quad \text{in the second medium 2} \end{aligned} \tag{2.2}$$

With a period, $a = a_1 + a_2$.

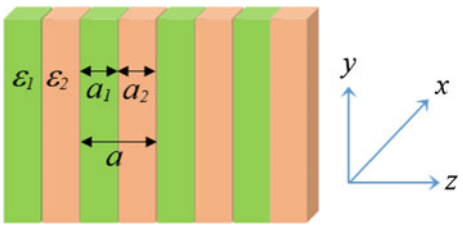

Fig. 2.1 One-dimensional photonic crystal

Equation (2.1) is a single Hermitian generalized eigenproblem where the eigenvalues $\left(\frac{\omega}{c}\right)^2$ are real and the eigenstates $E_x(z)$ are complete and orthogonal.

Since the eigenoperator is periodic (due to the periodicity of $\varepsilon(z) = \varepsilon(z + a)$), then we can apply Bloch–Floquet theorem. In this context, the solutions of the eigenstates of a Hermitian eigen-problem whose operator is a periodic function of position z, can be chosen of the form:

$$e^{ikz} \cdot E_x^{(k)} \tag{2.3}$$

where $E_x^{(k)}$ is a periodic function of k. So, the solutions of the electric field can be expressed as

$$E_x^{(k)}(z) = \sum_{r=-\infty}^{r=\infty} A_r e^{i\left(k+\frac{2\pi r}{a}\right)z}, \quad r = 0, \pm 1, \pm 2, \ldots. \tag{2.4}$$

Note that the basic functions $e^{i\frac{2\pi r}{a}z}, r = 0, \pm 1, \pm 2, \ldots.$, are complete and orthogonal.

Using Fourier series expansion, periodic function $\varepsilon(z)$ may be expanded as follows:

$$\varepsilon(z) = \sum_{r=-\infty}^{r=\infty} B_r e^{i\frac{2\pi r}{a}z} \tag{2.5}$$

The Fourier coefficients B_r can be obtained from the orthogonality relation as follows:

$$B_r = \frac{1}{a} \int_{z=0}^{a} \varepsilon(z) e^{-i\frac{2\pi r}{a}z} dz \tag{2.6}$$

Using Eq. (2.2), the coefficients B_r are given by

$$\begin{aligned} B_r &= \varepsilon_1 \frac{a_1}{a} + \varepsilon_2 \frac{a_2}{a} \quad \text{for } r = 0 \\ &= \frac{i}{2\pi r}(\varepsilon_1 - \varepsilon_2)\left(e^{-i\frac{2\pi r}{a}a_1} - 1\right) \quad \text{for } r \neq 0 \end{aligned} \tag{2.7}$$

Substituting the expansions for $E_x(z)$ and $\varepsilon(z)$ into the wave Eq. (2.1) with a prefactor of $e^{i\left(k+\frac{2\pi r}{a}\right)z}$ zero, we get:

$$\left(k + \frac{2\pi r}{a}\right)^2 A_r - \sum_{r=-\infty}^{\infty} \left(\frac{\omega}{c}\right)^2 B_{r-r'} A_{r'} = 0, \quad r' = 0, \pm 1, \pm 2, \ldots. \tag{2.8}$$

From which we obtain a system of linear coupled equations for the coefficients A_r for different values of r. To get non-trivial solutions, the values of ω must satisfy the characteristic equation given by

$$det\begin{vmatrix} \cdots & \cdots & \cdots & \cdots & \cdots & \cdots \\ \cdots & (k-\frac{2\pi}{a})^2-(\frac{\omega}{c})^2\beta_0 & -(\frac{\omega}{c})^2\beta_{-1} & -(\frac{\omega}{c})^2\beta_{-2} & \cdots & \cdots \\ \cdots & -(\frac{\omega}{c})^2\beta_1 & (k)^2-(\frac{\omega}{c})^2\beta_0 & -(\frac{\omega}{c})^2\beta_{-1} & \cdots & \cdots \\ \cdots & -(\frac{\omega}{c})^2\beta_2 & -(\frac{\omega}{c})^2\beta_1 & (k+\frac{2\pi}{a})^2-(\frac{\omega}{c})^2\beta_0 & \cdots & \cdots \\ \cdots & \cdots & \cdots & \cdots & \cdots & \cdots \end{vmatrix}=0 \tag{2.9}$$

According to the Bloch theorem, the solution is assumed as periodic and satisfies the relation $E_x(z+a)=e^{ika}E_x(z)$ of a periodic system. The wave number k specifies the eigensolutions $E_x^{(k)}$, which is periodic with respect to k. Also, the solutions of Eqs. (2.7) and (2.8) for k and for $\left(k+\frac{2\pi r}{a}\right)$ at an integer r are identical with the same values of ω. This is because the two values for k lead to the same form in Eq. (2.4), which may be seen by renumbering the coefficient A_r. Since the set of wave numbers $\left(k+\frac{2\pi r}{a}\right), r=0,\pm1,\pm2,\ldots,$ give identical solutions, all possible solutions of Eq. (2.9) are covered by running k over the first Brillouin zone (BZ), which is given by

$$-\frac{\pi}{a}\le k\le\frac{\pi}{a} \tag{2.10}$$

In summary:

- Since $E_x^{(k)}$ is periodic, we only need to consider this eigenvalue problem over a finite domain (the unit cell of periodicity). Mathematically, eigenvalue problems with finite domains result in discrete eigenvalues and eigenvectors [9].
- Accordingly, there are only a discrete set of eigenvalues, ω_p, $p = 1, 2, \ldots$, and periodic functions $E_x^{(k)}(z)$, for each k. This can be seen if we consider the eigenstates for the wave vector $\left(k+\frac{2\pi}{a}\right)$ in the form of Eq. (2.3). In this case, the complex exponential will have a term $e^{i\left(\frac{2\pi}{a}\right)z}$ which is periodic and can be absorbed into $E_x^{(k)}(z)$. But since $E_x^{(k)}(z)$ for each k is distinct, this implies that the solutions for $\left(k+\frac{2\pi}{a}\right)$ are the same as those for k.
- As a result, we do not need to use the entire range of k, and it is sufficient to solve the eigenproblem for a finite range of k. In our case, this is the first ***Brillouin zone*** of the crystal $\left(-\frac{\pi}{a}\le k\le\frac{\pi}{a}\right)$.
- For any given value of k in the first BZ, Eq. (2.9) gives a set of eigenvalues $\omega_1(k)$, $\omega_2(k)$, …, $\omega_p(k)$, …, which are continuous functions of k.
- The number of eigenvalues is fixed by the size of the matrix truncated by Eq. (2.9).
- As k varies, each of the eigenvalues changes gradually.

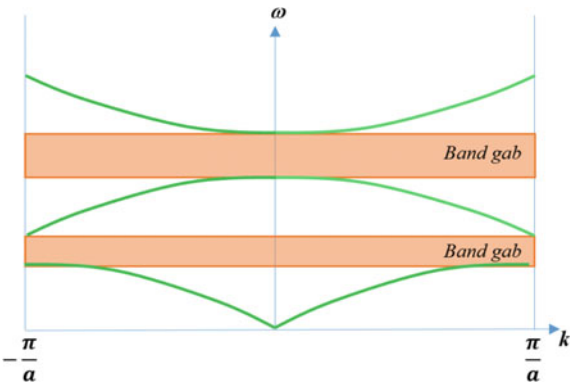

Fig. 2.2 Bandgaps for one-dimensional photonic crystal

- When plotted for all k, $\omega_p(k)$ forms the so-called band structure of the photonic crystal.
- These are the dispersion curves of the photonic bands of the one-dimensional system.
- The subscript p of $w_p(k)$ is called the band index.

Figure 2.2 shows the band diagram that plots $\omega_p(k)$ as a function of k in the Brillouin zone. The bandgaps are the regions of frequencies where there is no associated k in the crystal. This is the photonic bandgap. The width of the normalized bandgap $\frac{\Delta\omega}{\omega}$ increases as the ratio between the two dielectrics $\frac{\varepsilon_1}{\varepsilon_2}$ gets larger [1]. Note that k is imaginary for ω in the bandgap and the wave at this frequency is evanescent. Thus, plane waves with frequency in the bandgap cannot enter the crystal and all of the energy is reflected back [1, 9]. This is similar to metallic waveguide where frequencies below a certain value (cutoff) cannot enter the guide. In the case of photonic crystals, these ranges are discrete bands.

Whenever the photonic crystal has a rotation, mirror reflection, or inversion symmetry, then $w_p(k)$ functions have that symmetry as well [1]. Consequently, we do not need to consider them at every k point in the Brillouin zone. The smallest region within the Brillouin zone where the functions $w_p(k)$ are not related by the symmetry is called the ***irreducible Brillouin zone*** (region $0 \leq k \leq \frac{\pi}{a}$) as shown in Fig. 2.2.

2.2.2 Bandgap Size

The useful parameter that can be used to describe the bandgap is the (***gap–midgap***) ratio which is independent of the scale of the crystal. If ω_m is the frequency at the middle of the gap, the gap–midgap ratio is defined as $(\frac{\Delta\omega}{\omega_m})$, expressed as a percentage. In one-dimensional crystal with normal incidence, the gap–midgap ratio

depends on the dielectric contrast $\left(\frac{\Delta\varepsilon}{\varepsilon}\right)$ and relative width of structure $\left(\frac{a_1}{a}\right)$. The dependence of the gap–midgap ratio can be summarized as follows:

- For weak periodicity $\left(\frac{\Delta\varepsilon}{\varepsilon} \ll 1\right)$ or small relative width $\left(\frac{a_1}{a}\right)$, the gap–midgap ratio can be approximated by [1]

$$\frac{\Delta\omega}{\omega_m} \approx \frac{\Delta\varepsilon}{\varepsilon}\frac{\sin\left(\frac{\pi a_1}{a}\right)}{\pi}. \tag{2.11}$$

- More generally, the gap is maximized if $a_1\, n_1 = a_2\, n_2$ [10], where n_1 and n_2 are the refractive indices of the structure, where $n = \sqrt{\varepsilon}$. In this case, it may be shown that the midgap frequency is given by,

$$\omega_m = \frac{n_1 + n_2}{4n_1 n_2}\frac{2\pi c}{a} \tag{2.12}$$

which corresponds to the vacuum wavelength $\lambda_m = \frac{2\pi c}{\omega_m}$, and the thicknesses of the layers in this case are exactly quarter wavelength $a_1 = \frac{\lambda_m}{4n_1}$, $a_2 = \frac{\lambda_m}{4n_2}$. For the gap between the first two bands of this structure, the gap–midgap ratio is given by

$$\frac{\Delta\omega}{\omega_m} = \frac{4}{\pi}\sin^{-1}\left(\frac{|\Delta n|}{n_1 + n_2}\right) \tag{2.13}$$

If the one-dimensional crystal is excited with white light at normal incidence, it reflects colors corresponding to the bandgap frequencies. If we change the angle of the incoming light, it sees larger crystal spacing due to the inclined path, so the bandgaps are shifted, and different colors are reflected. This is a natural phenomenon called iridescence.

2.2.3 The Relation Between the Brillouin Zone and the Reciprocal Lattice

In crystallography, a Bravais lattice is an infinite array of discrete points (that may be atoms, molecules, group of atoms or molecules) which can be generated in the three-dimensional case by three primitive vectors $\vec{A}_1$, $\vec{A}_2$, and $\vec{A}_3$, so that every lattice point can be written as

$$\vec{R} = r\vec{A}_1 + q\vec{A}_2 + s\vec{A}_3, \quad r, q, s = 0, \pm 1, \pm 2, \ldots. \tag{2.14}$$

So, for any choice of position vector $\vec{R}$, the lattice looks exactly the same.

The primitive unit cell of the crystal is defined as the volume of space that, when translated through all the vectors of a Bravais lattice, just fills all of space without either overlapping itself or leaving voids [11].

A vector $\vec{V}$ belonging to the primitive cell can be expressed as

$$\vec{V} = \alpha\vec{A}_1 + \beta\vec{A}_2 + \gamma\vec{A}_3, 0 \le \alpha, \beta, \gamma \le 1 \tag{2.15}$$

where a periodic function can be expressed as

$$f\left(\vec{V}\right) = f\left(\vec{V} + \vec{R}\right) \tag{2.16}$$

The reciprocal lattice is defined as the set of vectors $\vec{k}$ generated by its three reciprocal primitive vectors, defined by,

$$\vec{k}_1 = 2\pi \frac{\vec{A}_2 x \vec{A}_3}{\vec{A}_1 . \left(\vec{A}_2 x \vec{A}_3\right)} \tag{2.17a}$$

$$\vec{k}_2 = 2\pi \frac{\vec{A}_3 x \vec{A}_1}{\vec{A}_2 . \left(\vec{A}_3 x \vec{A}_1\right)} \tag{2.17b}$$

$$\vec{k}_3 = 2\pi \frac{\vec{A}_1 x \vec{A}_2}{\vec{A}_3 . \left(\vec{A}_1 x \vec{A}_2\right)} \tag{2.17c}$$

In two-dimensional case in the *xy* plane, the reciprocal primitive vectors can be obtained by letting $\vec{A}_3 = \vec{a}_z$ where $\vec{a}_z$ is the unit vector perpendicular to the xy plane of the primitive set vectors $\vec{A}_1$ and $\vec{A}_2$, since both lie in the xy plane. The vector $\vec{k}_3$ is perpendicular to the xy plane and thus can be safely neglected.

It can be proved that the Brillouin zone for a Bravais lattice is the primitive unit cell of the reciprocal lattice. Consequently, band diagrams for a given lattice are periodic functions over its reciprocal lattice. This can be easily seen in the one-dimensional crystal with periodicity *a* shown in Fig. 2.1. It should be noted that the primitive vector is $\vec{a} = a\vec{a}_z$ and every lattice point can be written as

$$\vec{R} = r\vec{a}, \quad r = 0, \pm 1, \pm 2, \ldots. \tag{2.18}$$

Further, the primitive cell of the reciprocal lattice shown in Fig. 2.3 is defined by the vector

$$\vec{k} = \frac{2\pi}{a}\vec{a} \tag{2.19}$$

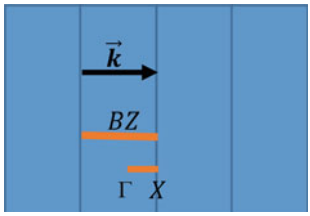

Fig. 2.3 Reciprocal lattice for one-dimensional photonic crystal

which defines the width of the Brillouin zone $\left(\frac{2\pi}{a}\right)$ in this case. Also from the symmetry, the reduced Brillouin zone is determined by the two points Γ (center of the Brillouin zone) and X (edge of Brillouin zone) that correspond to $\vec{k}_z = 0$ and $\vec{k}_z = \frac{\pi}{a}\vec{a}_z$, respectively.

2.3 Two-Dimensional Photonic Crystals

Recently, attention is given in making materials with a periodic variation in refractive index in two and three dimensions for different reasons. This leads to many subsequent developments in theory, techniques of fabrication, and their applications. Nowadays, the goal of such devices is to make integrated circuits that combine both electronic and optical functions.

Yablanovitch, in 1987 [5], suggested that an omnidirectional bandgap could be created with photonic crystals that were periodic in more than one dimension. Two-dimensional photonic crystals have a periodic geometry in two directions and are homogeneous in the third. Two examples may be realized by fabricating regular arrays of cylindrical pillars in a substrate as shown in Fig. 2.4a, or by drilling a regular pattern of air holes as shown in Fig. 2.4b. Many two-dimensional patterns are realized for many applications in integrated optics.

The two-dimensional photonic crystals can be analyzed by a similar way to the one-dimensional case. The differences between 1D and 2D photonic crystals can be summarized as follows:

- Two vectors in the two directions of the crystal are used to determine the Bloch state.
- The reciprocal lattice is also two-dimensional lattice; consequently, the Brillouin zones are areas. For example, the square lattice with periodicity a in both directions, shown in Fig. 2.5a, has a reciprocal lattice shown in Fig. 2.5b.
- The Brillouin zone is a two-dimensional region of wave vectors, so the bands $\omega(k)$ are actually surfaces, but practically the band extrema always occur at the high-symmetry directions (along the boundaries of the irreducible zone).

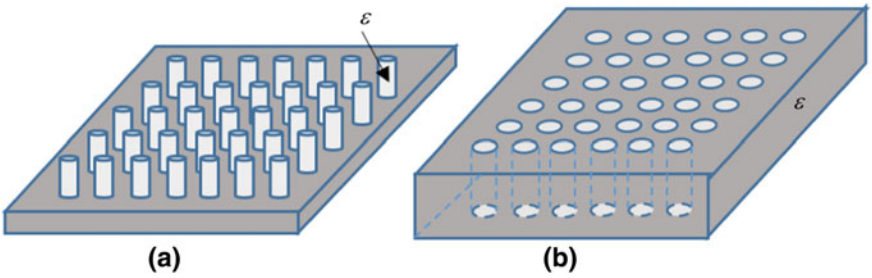

Fig. 2.4 **a** Cylindrical pillars lattice and **b** cylindrical veins lattice

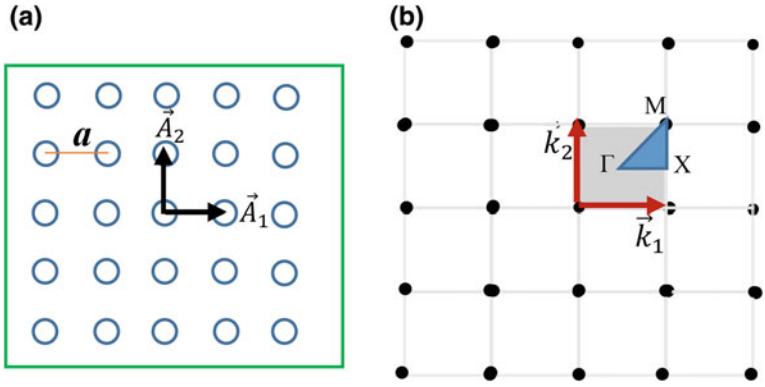

Fig. 2.5 **a** Square lattice with primitive vectors and **b** its reciprocal lattice

Therefore, to identify the bandgap, it is conventional to only plot the bands along these boundaries.

The reciprocal lattice vectors in this case are given by

$$\vec{k}_1 = \frac{2\pi}{a}\vec{a}_x \tag{2.20a}$$

$$\vec{k}_2 = \frac{2\pi}{a}\vec{a}_y \tag{2.20b}$$

where the Brillouin zone is the shaded square with sides of length 2π/a. Consequently, due to the three types of symmetries: up/down symmetry, left/right symmetry, and 90° rotation symmetry, the irreducible Brillouin zone is a right triangle of base and height π/a determined by the three points Γ (center of the Brillouin zone), X (center of a side), and M (center of an edge) that correspond to $\vec{k}_{x,y} = 0$, $\vec{k}_{x,y} = \frac{\pi}{a}\vec{a}_x$, and $\vec{k}_{x,y} = \frac{\pi}{a}\vec{a}_x + \frac{\pi}{a}\vec{a}_y$, respectively.

Polarization of light must be taken into account in the two-dimensional case. The beam can be decomposed into two different polarizations: transverse electric (TE),

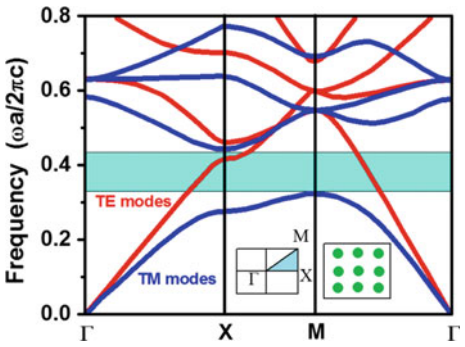

Fig. 2.6 Bandgaps for square lattice of isolated ε rods—TM bandgaps are favored

in which the beam is polarized perpendicular to the plane of periodicity, and transverse magnetic (TM), where the beam is polarized in the plane of periodicity. In one-dimensional photonic crystal, polarization is not taken into consideration because the crystal is isotropic in the plane normal to the direction of propagation.

The photonic bandgap diagram can be constructed by plotting the eigenvalues along the vertical axis as the Bloch wave vector is varied. Figure 2.6 shows the photonic bandgap diagram for TE and TM polarization defined on the path around the irreducible Brillouin zone ΓXMΓ [1], of a square lattice of isolated ε rods. In this case, the TM bandgaps are favored. Since the Brillouin zone in two-dimensional case is area, the complete bandgap diagram consists actually from sheets as shown in Fig. 2.7. There is an infinite set of eigenfrequencies associated with each point in the Brillouin zone.

Figure 2.8a shows another example of a photonic crystal of air holes arranged in a hexagonal lattice [1]. In this case, the primitive vectors of the unit cell are

$$\vec{A}_1 = a\vec{a}_x, \quad \vec{A}_2 = \frac{a}{2}\left(-\vec{a}_x + \sqrt{3}\vec{a}_y\right) \tag{2.21}$$

and the reciprocal lattice vectors in this case are given by

$$\vec{k}_1 = \frac{2\pi}{a}(\vec{a}_x + \frac{1}{\sqrt{3}}\vec{a}_y), \quad \vec{k}_2 = \frac{4\pi}{a\sqrt{3}}\vec{a}_y \tag{2.22}$$

where

$$\left|\vec{k}_1\right| = \left|\vec{k}_2\right| = \frac{4\pi}{a\sqrt{3}}$$

The Brillouin zone for this crystal is the Wigner–Seitz cell for the unit cell of the reciprocal lattice [11]. The Wigner–Seitz cell is the space volume surrounding a point in the lattice that is closer to that point than any other point. This is indicated by the shaded hexagonal shown in Fig. 2.8b.

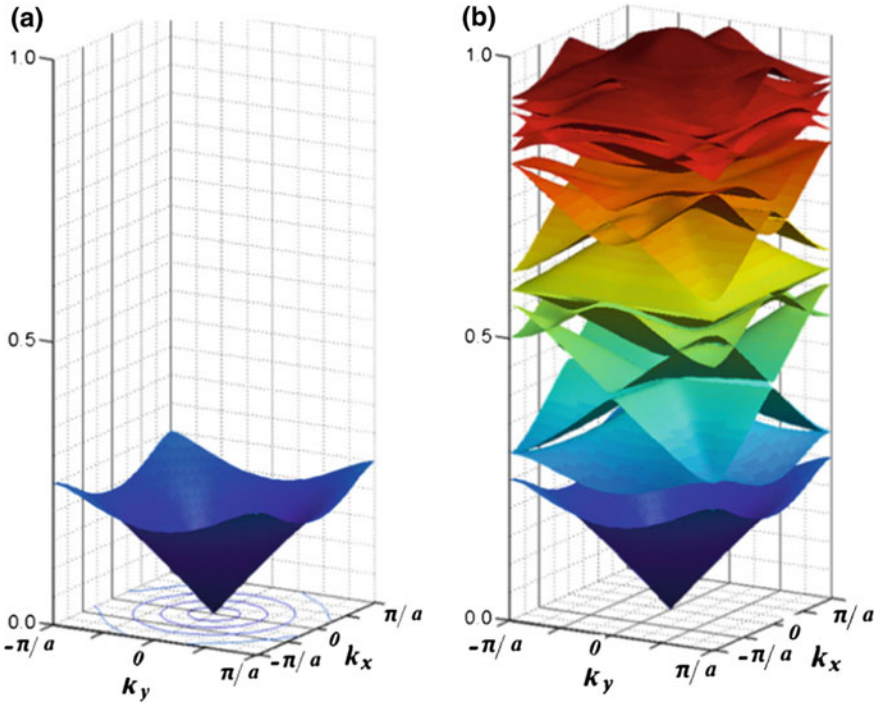

Fig. 2.7 **a** First-order band diagram and **b** complete bandgap diagram for the square crystal

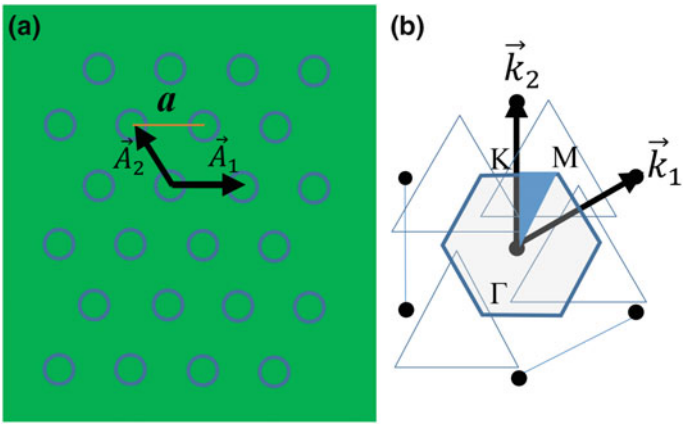

Fig. 2.8 **a** Crystal and its primitive vectors and **b** reciprocal cell and Brillouin zone

The irreducible Brillouin zone is the triangle ΓMK which is constructed by using symmetry considerations. The three corners of the irreducible Brillouin zone are

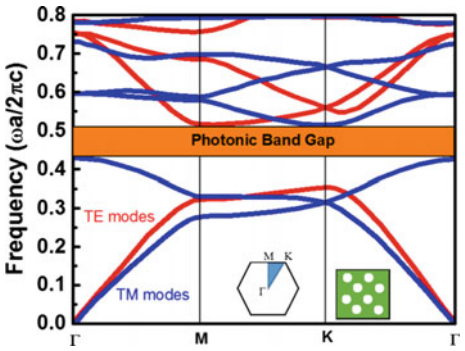

Fig. 2.9 Band diagram of hexagonal crystal in Fig. 2.8a

$$\Gamma: \vec{k}_{x,y} = 0, \quad K: \vec{k}_{x,y} = \frac{2\pi}{3a}\vec{a}_y \text{ and } \mathrm{M}: \vec{k}_{x,y} = \frac{2\pi}{3a}\vec{a}_x + \frac{2\pi}{\sqrt{3}a}\vec{a}_y \tag{2.23}$$

The band diagram is plotted along the edges of the irreducible Brillouin zone. The frequency axis is normalized by the lattice spacing a. As shown in Fig. 2.9, the crystal exhibits a complete bandgap for which both TM and TE polarized light cannot propagate through the photonic crystal structure.

2.4 Three-Dimensional Photonic Crystals

The three-dimensional photonic crystal is a dielectric structure which is periodic along three different axes in space. Practically, the three-dimensional photonic crystals are the most interesting objects to study. If the right crystal structure is chosen with sufficient index contrast, the crystal can be designed so that light cannot propagate within a certain frequency range.

The possibility of the three-dimensional photonic bandgaps was early suggested by Yablonovitch [5] and John [6]. Beginning from 1989, many realistic designs with a complete photonic bandgap have been suggested [12–16]. Recently, huge number of three-dimensional photonic bandgap structures was developed and fabricated. One of the early microstructures for infrared light is the woodpile crystal [13, 15] shown in Fig. 2.10 [17]. It is constructed by stacking alternating layers of dielectric silicon logs (usually rectangular) with alternating orthogonal orientations. Therefore, the third and fourth layers will have the same orientation as the first and second layers but are offset by half of the horizontal spacing. In this manner, the dielectric logs form a face-centered cubic lattice stacked in the [001] direction. The photonic bandgap of the woodpile crystal with $\varepsilon = 13$ logs in air is shown in Fig. 2.11.

Three-dimensional photonic crystals can be constructed by stacking a sequence of two-dimensional different layers. An example is shown in Fig. 2.12, where a hexagonal lattice of dielectric rods in air is stacked on another dielectric layer with holes. Figure 2.13 shows the photonic band diagram for this structure with $\varepsilon = 12$. More details are given by Johnson and Joannopoulos [18].

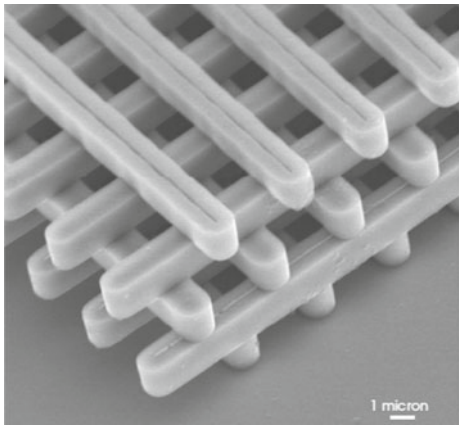

Fig. 2.10 Woodpile photonic crystal image by electron microscope [17]

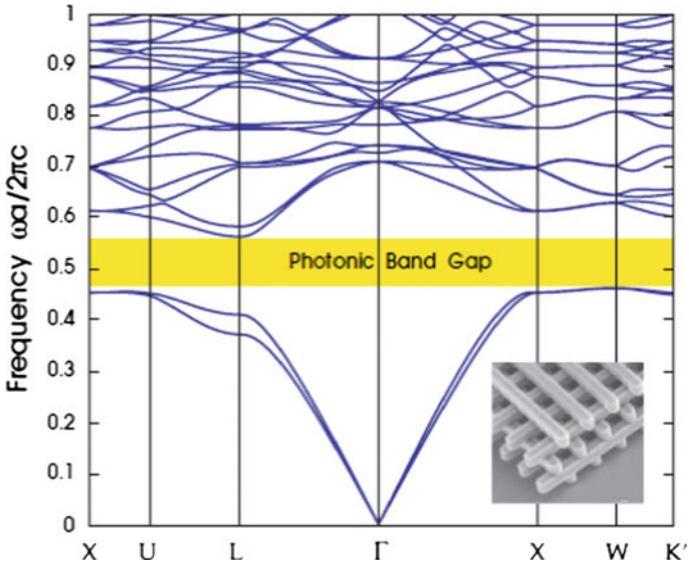

Fig. 2.11 Photonic bandgap diagram for the woodpile photonic crystal [17]

2.5 Defects in Photonic Crystals

In the previous sections, we were interested in finding bandgaps of photonic crystal structures. For the frequencies inside the gap, no modes are allowed to propagate. If the periodicity of the lattice is perturbed due to a predesigned defect, we can permit a localized defect mode or set of modes that have frequencies within the gap. At these frequencies, light may be trapped or allowed to propagate at the position of the defect in the lattice. At the same time, this light cannot leak into the crystal because it is in the bandgap.

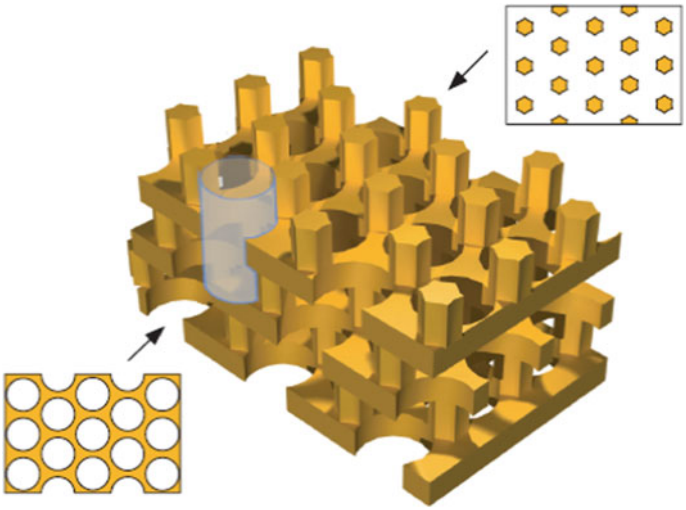

Fig. 2.12 Three-dimensional photonic crystal formed by stacking of two different layers [18]

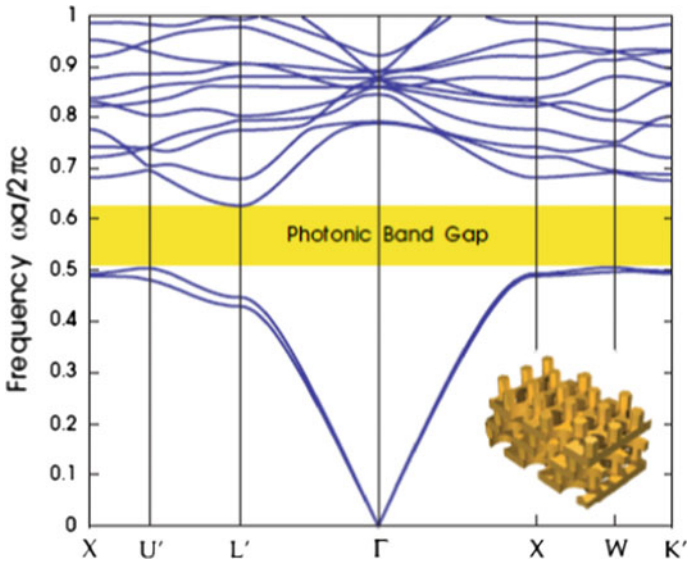

Fig. 2.13 Photonic bandgap of the dimensional photonic crystal formed by stacking of two different layers in Fig. 2.12 [18]

Considering the gap of the one-dimensional photonic crystal, the wave number is imaginary inside the gap and the states decay exponentially. As we traverse the gap, the decay constant grows toward the gap center, then decreases again, and disappears at the lower edge of the gap [1]. However, if a defect is introduced in the

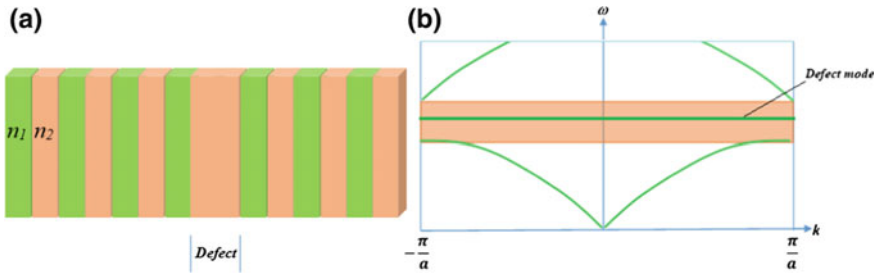

Fig. 2.14 **a** One-dimensional lattice with defect and **b** bandgap with defect mode

lattice by adding a layer of material 2, as shown in Fig. 2.14a, the structure is no longer periodic and it is found that the defect can terminate the exponential growth and permits an evanescent mode as shown in Fig. 2.14b. Figure 2.15a, b shows the transmittance curve as a function of frequency for a crystal without defect and that with defect, respectively.

In two-dimensional case, we have many options to introduce defects within the crystal. A point defect (Fig. 2.16a) or a line defect (Fig. 2.16b) can be introduced by removing rods or replacing them with another rod of different sizes, shapes, or refractive indexes. In this case, a localized defect-induced state is trapped at the location of the defect but it cannot penetrate into the rest of the crystal, since it has a frequency in its bandgap [19, 20]. This can be physically explained as follows: The crystal reflects the light of certain frequencies due to its bandgap. By introducing a defect within it, we create a cavity surrounded by reflecting walls. If this cavity has the proper dimensions to support a mode in the bandgap of the crystal, then the light cannot escape and a localized mode can be created [21].

Nowadays, the techniques of introducing defects in the photonic crystal open the door to the future of "*optical semiconductors*" which can be used in many applications: photonic crystal fibers, lasers, waveguides, optical logic circuit, add–drop filters, all-optical transistors, amplifiers, biological sensors, routers, photonic integrated circuits, optical computing. We are going to discuss some of these applications in the rest of this chapter.

2.5.1 Photonic Crystal Fibers

The simplest design of the photonic crystal fibers (PCFs) [22, 23] is shown in Fig. 2.17 where tiny cylindrical air holes arranged in triangular lattice are patterned into a fiber. With proper dimensions of the holes and core (which acts as defect), light cannot propagate in the cladding region due to the photonic bandgap. In this case, light can be confined in a solid or hollow core with a lower refractive index. In comparison with conventional optical fibers, photonic crystal fiber depends on bandgap effect, and the core may be of low index or air. However, optical fiber

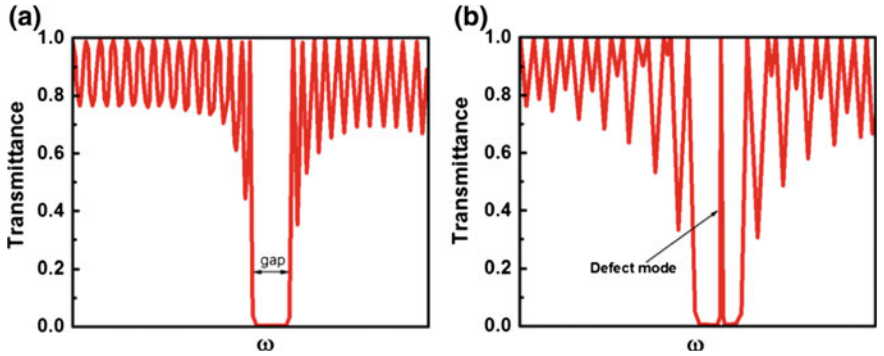

Fig. 2.15 Transmittance curve as a function of frequency of the **a** lattice without defect and of the **b** lattice with defect

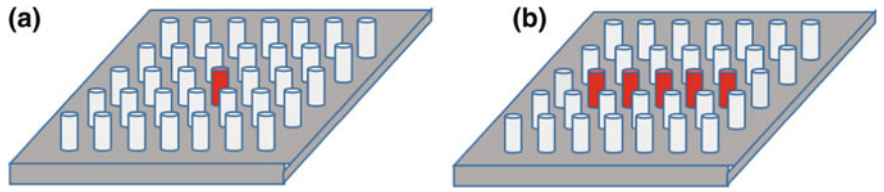

Fig. 2.16 2D photonic crystal **a** with a point defect and **b** with a line defect

Fig. 2.17 Photonic crystal fiber

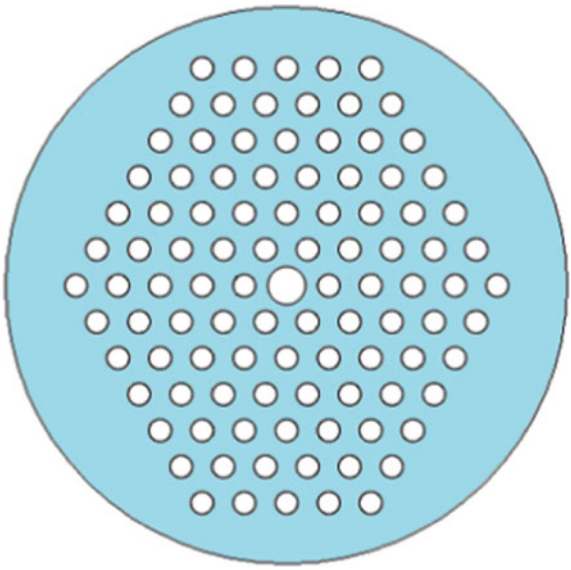

contains high index core and is based on total internal reflection (TIR) principle. In this manner, extremely low loss photonic crystal fibers with air or vacuum core can be created [24].

2.5.2 Photonic Crystal Planar Waveguides

Photonic crystal waveguides can be fabricated by introducing a line defect in the crystal which supports a mode that is in the bandgap. This mode is forbidden from propagating in the bulk of the crystal because it falls in the bandgap, as shown in Fig. 2.18, which shows the electric field (E_z) pattern in a line defect formed by removing a row of rods from a square lattice of dielectric rods in air.

When a bend occurs in the waveguide, a line defect of the same shape is introduced as shown in Fig. 2.19. It is impossible for light to escape since it cannot propagate in the bulk crystal. Therefore, the mode is forced to propagate through the line defect which takes the shape of a sharp bend, leading to lossless

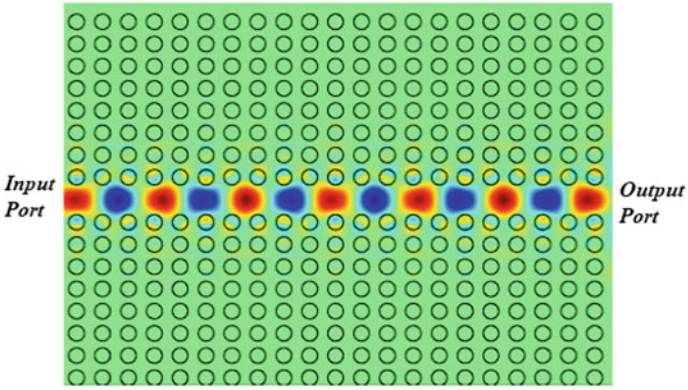

Fig. 2.18 Optical line-defect waveguide

Fig. 2.19 Optical waveguide bend

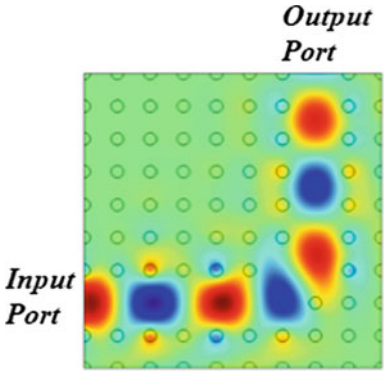

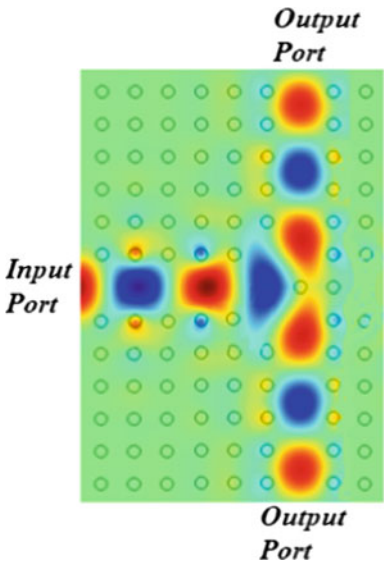

Fig. 2.20 Optical waveguide T-splitter

propagation. In conventional fibers, it is impossible to bend the fiber with radius of order of light wavelength because the TIR conditions will fail leading to leaky modes. The calculations show that guiding of light around such a sharp 90° corner is possible with high efficiency (up to 98%) [25, 26].

Optical waveguide splitter which divides the power equally in an input waveguide between two output waveguides can be realized as shown in Fig. 2.20. In this case, obstructions are made between the junction and the outputs (by adding a single rod before each of the output waveguide) to weaken the coupling between the two outputs in order to increase the transmission [27].

A channel drop filter based on photonic crystal structure can be designed to transfer a narrow bandwidth from one waveguide to another waveguide by creating two different cavity modes between the two line waveguides (simply by removing two rods), as shown in Fig. 2.21. The filter redirects a very narrow bandwidth around a single mode to the output port, while other frequencies propagate directly along the top waveguide. By carful design of the two cavity modes, it is possible to get 100% dropping in one direction of the output waveguide [28, 29].

2.5.3 Optical Logic Circuits

Optical logic gates are considered as key elements in optical processing and communication systems which make the important functions at the nodes of network such as data encoding and decoding, pattern matching, recognition, and various switching operations. Most of conventional designs suffer from certain

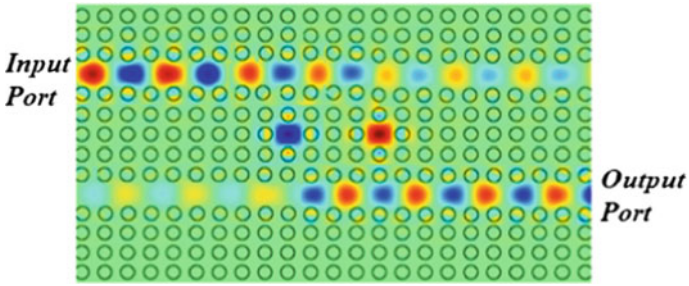

Fig. 2.21 Optical channel drop filter

limitations such as big size, difficult to perform chip-scale integration, high power consumption, low speed, and the spontaneous emission noise. Nowadays, photonic crystal technology is applicable to optical logic gates because of their compact size, high speed, low power consumption, and versatile functions [30]. Recently, many design techniques were reported to build the optical logic gates [31, 32]: photonic crystal based on nonlinear materials [33, 34], self-collimated beams [35, 36], graphene photonic crystals [37], photonic crystal with liquid crystal materials [38], and multi-mode interference [39–42].

2.5.4 Optical Transistors

The aim of optical transistor is to switch or amplify optical signals. If we can control the incident light signal on an optical transistor, then the intensity of light beam emitted from the transistor's output can be changed. Such a device is the optical analog of the electronic transistor that forms the basis of modern electronic devices. Output power is supplied by an additional optical source. Optical transistors have applications in optical computing and fiber optic communication networks. Recently, many design techniques for optical transistors were reported [43–46]. With optical logic integrated circuits and optical transistor technology, the road toward optical integrated circuits and optical computing is possible. Unlimited speeds, huge storage density, minimal cross talk, and interference are some of the advantages that we expect in the future.

2.5.5 Photonic Crystal Polarization Handling Devices

The optical properties of integrated photonic circuits are usually polarization-dependent. Polarization rotators (PRs) [47–49] and polarization splitters [50–52] can simply remove this dependence, which makes any optical element

polarization independent. Therefore, PR is a key element of integrated photonic circuits that can control the polarization of the propagating wave. In this context, high tunable nematic liquid crystal (NLC) PCF PR has been proposed with a strong polarization conversion ratio of 99.81% and a device length of 1072 μm [47]. Further, single- and multiple-sectioned passive PRs based on silica PCF with L-shaped core region have been presented in [48]. The single- and multiple-sectioned PCF PRs offer nearly 100% polarization conversion ratio with device lengths of 1743 m and 1265 m, respectively [48]. Furthermore, a silica PCF PR with a slanted rectangular core region has been reported with a nearly 100% polarization conversion ratio with a device length of 2839 μm at wavelength of 1.55 μm [49].

Recently, PCF couplers have attracted much interest in recent years due to their different applications in communication systems. The PCF couplers [50–52] can be obtained by making two adjacent defects in the photonic crystal structure. In addition, they have short coupling length with more flexibility design. The PCF couplers can be used as a polarization splitter [52–54], broadband directional coupler [55], wavelength division multiplex components [50, 56–58], and filters [59]. This can increase the bandwidth of the communication systems by increasing the amount of sent data using different wavelengths or different polarizations.

2.5.6 Photonic Crystal Biosensors

Recently, surface plasmon resonance (SPR) PCF-based biosensors have attracted immense research interest worldwide [60–64]. The PCF biosensors depend on the coupling between the leaky core mode and the SPR mode along the metal layers inside the PCF structure. The SPR PCF sensors are widely used due to their high sensitivity with molecular labels free [65]. Further, they overcome the miniaturization and integration problems associated with the commercial SPR sensors based on the conventional prism-coupled configuration [66]. Furthermore, 2D photonic crystal structures [67, 68] can be effectively used for refractive index monitoring which has great applications in biomedical sectors.

References

1. J.D. Joannopoulos, R.D. Meade, J.N. Winn, *Photonic Crystals: Molding the Flow of Light* (Princeton University Press, Princeton, NJ, 1995)
2. M.F.O. Hameed, S.S.A. Obayya, K. Al-Begain, M.I. Abo el Maaty, A.M. Nasr, Modal properties of an index guiding nematic liquid crystal based photonic crystal fiber. IEEE J. Lightwave Technol. **27**(21), 4754–4762 (2009)
3. K. Sakoda, *Optical Properties of Photonic Crystals* (Springer, Berlin, 2001)
4. S.G. Johnson, J.D. Joannopoulos, *Photonic Crystals: The Road from Theory to Practice* (Kluwer Academic Publishers, Boston, 2002)

5. E. Yablonovitch, Inhibited spontaneous emission in solid state physics and electronics. Phys. Rev. Lett. **58**, 2059 (1987)
6. S. John, Strong localization of photons in certain disordered dielectric super lattices. Phys. Rev. Lett. **58**, 2486 (1987)
7. E. Yablonovitch, T.J. Gmitter, K.M. Leung, Photonic band structure: the face-centered-cubic case employing nonspherical atoms. Phys. Rev. Lett. **67**(17) (1991)
8. T.F. Krauss, R.M. De La Rue, S. Brand, Two-dimensional photonic-bandgap structures operating at near-infrared wavelengths. Nature **383**(6602) (1996)
9. S.G. Johnson, J.D. Joannopoulos, Introduction to Photonic Crystals: Bloch's Theorem, Band Diagrams, and Gaps (But no Defects), Pamphlet. Feb 2003
10. P. Yeh, *Optical Waves in Layered Media* (Wiley, New York, 1988)
11. N. Ashcroft, N. Mermin, *Solid State Physics* (Harcourt College Publishers, 1976)
12. S. Satpathy, Ze Zhang, M. R, Theory of photonic bands in three—dimensional periodic dielectric structures. Phys. Rev. Lett. **64**, 1239–1242 (1990)
13. K.M.C. Ho, T. Chan, C.M. Soukoulis, Existence of a photonic gap in periodic dielectric structures. Phys. Rev. Lett. **65**, 3152–3155 (1990)
14. C.T. Chan, K.M. Ho, C.M. Soukoulis, Photonic band gaps in experimentally realizable periodic dielectric structures. Europhys. Lett. **16**, 563–568
15. H.S. Sozuer, J.P. Dowling, Photonic band calculations for woodpile structures. J. Mod. Opt. **41**(2), 231–239 (1994)
16. H.S. Sozuer, J.W. Haus, Photonic bands: Simple-cubis lattice. J. Opt. Soc. Am. B **10**(2), 296–302 (1993)
17. S.-Y. Lin, J.G. Fleming, D.L. Hetherington, B.K. Smith, R. Biswas, K.M. Ho, M.M. Sigalas, W. Zubrzychi, S.R. Kurtz, J. Bur, A three-dimensional photonic crystal operating at infrared wavelengths. Nature **394**, 251–253 (1998)
18. S.G. Johnson, J.D. Joannopoulos, Three dimensionally periodic dielectric layered structure with omnidirectional photonic band gap. Appl. Phys. Lett. **77**, 3490–3492 (2000)
19. S.L. McCall, P.M. Platzman, R. Dalichaouch, D. Smith, S. Schultz, Microwave propagation in two dimensional dielectric lattices, Phys. Rev. Lett. **67,** 2017–2020 (1991)
20. R.D. Meade, A.M. Rape, K.D. Brommer, J.D. Joannopoulos, O.L. Alerhand, Accurate theoretical analysis of photonic band-gap materials. Phys. Rev. B **48**, 8434–8437 (1993)
21. E. Istrate, E.H. Sargent, Photonic crystal Heterostructures and interfaces. Rev. Mod. Phys. **78**, 455–481 (2006)
22. M.F.O. Hameed, S.S.A. Obayya, H.A. El-Mikati, Highly nonlinear birefringent soft glass photonic crystal fiber with liquid crystal core. IEEE Photonics Technol. Lett. **23**(20), 1478–1480 (2011)
23. M.F.O. Hameed, A.M. Heikal, S.S.A. Obayya, Novel passive polarization rotator based on spiral photonic crystal fiber. IEEE Photonics Technol. Lett. **25**(16), 1578–1581 (2013)
24. P. Russell, Photonic crystal fibres. Science **299**, 358–362 (2003)
25. A. Mekis, J.C. Chin, I. Kurland, S. Fan, P.R. Villeneuve, J.D. Joannopoulos, Experimental demonstration of guiding and bending of electromagnetic waves in a photonic crystal. Science **282**, 274–276 (1998)
26. S.-Y. Lin, E. Chow, V. Hietala, P.R. Villeneuve, J.D. Joannopoulos, High transmission throuth sharp bends in photonic crystal waveguide. Phys. Rev. Lett. **77**(81), 3787–3790 (1996)
27. S. Fan, G. Steven, J.D. Joannopoulos, C. Manolatou, H.A. Haus, Waveguide branches in photonic crystal. J. Opt. Soc. Am. B **18**(2), 162–165 (2001)
28. S. Fan, G. Steven, P.R. Villeneuve, J.D. Joannopoulos, H.A. Haus, Channel drop tunneling throught localized states. Phys. Rev. Lett. **80**(5), 960–963 (1998)
29. C. Manolatou, M.J. Khan, S. Fan, P.R. Villeneuve, H.A. Haus, J.D. Joannopoulos, Coupling of modes analysis of resonant channel add-drop filters. IEEE J. Quantun Electron. **35**(9), 1322–1331 (1999)
30. F. Parandin, M.M. Karkhanehchi, Tetrahertz all-optical nor and lgic gates based on 2d photonic crystal. Superlattices Microstruct. **101**, 253–260 (2016)

31. S.S.A. Obayya, M.F.O. Hameed, N.F.F. Areed, *Computational Liquid Crystal Photonics: Fundamentals, Modelling and Applications* (John, Apr 2016)
32. A. Salmanpour, S.M. Nejad, A. Bahrami, Photonic crystal logic gates: an overview. Opt. Quantum Electron. **47**(7), 2249–2275 (2015)
33. H. Alipour-Banaei, S. Serajmohammadi, F. Mehdizadeh, All optical nor and nand gate based on nonlinear photonic crystal ring resonator. Opt. Int. J. Light Electron Opt. **125**(19), 5701–5704 (2014)
34. P. Chanalia, A. Gupta, Realization of high speed all-optical logic gates based on the nonlinear characteristics of a SOA. Indian J. Sci. Technol. **9**(36) (2016)
35. R. Fan, X. Yang, X. Meng, X. Sun, 2d photonic crystal logic gates based on self- collimated effect. J. Phys. D Appl. Phys. **49**(32), 325104 (2016)
36. S.C. Xavier, B.E. Carolin, A.P. Kabilan, W. Johnson, Compact photonic crystal integrated circuit for all- optical logic operations. IET Optoelectron. **10**(4), 142–147 (2016)
37. Z.H. Chen, Q.L. Tan, J. Lao, Y. Liang, X.G. Huang, Reconfigurable and tunable flat graphene photonic crystal circuits. Nanoscale, **7**(25), 10912–10917 (2015)
38. N.F.F. Areed, A. El Fakharany, M.F.O. Hameed, S.S.A. Obayya, Controlled optical photonic crystal AND gate using nematic liquid crystal layers. Opt. Quantum Electron. **49**(1), 1–12 (2017)
39. Y. Ishizaka, Y. Kawaguchi, K. Saitoh, M. Koshiba, Design of ultra compact all-optical XOR and AND logic gates with low power consumption. Opt. Commun. **284**(14), 3528–3533 (2011)
40. C. Tang, X. Dou, Y. Lin, B. Wu, Q. Zhao, Design of all-optical logic gates avoiding external shifters in a two-dimensional photonic crystal based on multi-mode interference for bpsk signals. Opt. Commun. **316**, 49–55 (2014)
41. E. hak Shaik, N Rangaswamy, Multi-mode interference- based photonic crystal logic gates with simple structure and improved contrast ratio. Photonic Netw. Commun. **34**, 140–148 (2017)
42. N.M. D'souza, V. Mathew, Interference based square lattice photonic crystal logic gates working with different wavelengths. Opt. Laser Technol. **80**, 214–219 (2016)
43. B.D. Clader, S.M. Hendrickson, Microresonator-based all-optical transistor. J. Opt. Soc. Am. B **30**(5), 1329 (2013)
44. V.G. Arkhipkin, S.A. Myslivets, All-optical transistor using a photonic-crystal cavity with an active Raman gain medium. Phys. Rev. A. **88**(3) (2013)
45. P. Andreakou, S.V. Poltavtsev, J.R. Leonard, E.V. Calman, M. Remeika, Y.Y. Kuznetsova, L.V. Butov, J. Wilkes, M. Hanson, A.C. Gossard, Optically controlled excitonic transistor. Appl. Phys. Lett. **104**(9), 091101 (2014)
46. C.Y. Hu, Photonic transistor and router using a single quantum-dot-confined spin in a single-sided optical microcavity. Sci. Rep. **7**, Article number: 45582 (2017)
47. M.F.O. Hameed, S.S.A. Obayya, R.J. Wiltshire, Beam propagation analysis of polarization rotation in soft glass nematic liquid crystal photonic crystal fibers. IEEE Photon. Technol. Lett. **22**(3), 188–190 (2010)
48. M.F.O. Hameed, S.S.A. Obayya, H.A. El-Mikati, Passive polarization converters based on photonic crystal fiber with L-shaped core region. IEEE J. Lightwave Technol. **30**(3), 283–289 (2012)
49. M.F.O. Hameed, S.S.A. Obayya, design consideration of polarization converter based on silica photonic crystal fiber. IEEE J. Quantum Electron. **48**(8) (2012)
50. K. Saitoh, Y. Sato, M. Koshiba, Coupling characteristics of dualcore photonic crystal fiber couplers. Opt. Exp. **11**(24), 3188–3195 (2003)
51. M.F.O. Hameed, S.S.A. Obayya, K. Al-Begain, A.M. Nasr, M.I. Abo el Maaty, Coupling characteristics of a soft glass nematic liquid crystal photonic crystal fibre coupler. IET Optoelectron. **3**(6), 264–273 (2009)
52. N. Florous, K. Saitoh, M. Koshiba, A novel approach for designing photonic crystal fiber splitters with polarization-independent propagation characteristics. Opt. Express **13**(19), 7365–7373 (2005)

53. R.A.H. Ali, M.F.O. Hameed, S.S.A. Obayya, Ultra-compact polarization splitter based on silica photonic liquid crystal fiber. J. Appl. Comput. Electromagnet. Soc. (ACES) **30**(6), 599–607 (2015)
54. M.Y. Chen, J. Zhou, Polarization-independent splitter based on all solid silica-based photonic-crystal fibers. J. Lightw. Technol. **24**(12), 5082–5086 (2006)
55. J. Lægsgaard, O. Bang, A. Bjarklev, Photonic crystal fiber design for broadband directional coupling. Opt. Lett. **29**(21), 2473–2475 (2004)
56. N.J. Florous, K. Saitoh, M. Koshiba, Synthesis of polarizationin dependent splitters based on highly birefringent dual-core photonic crystal fiber platforms. IEEE Photonics Technol. Lett. **18**(11), 1231–1233 (2006)
57. M.F.O. Hameed, S.S.A. Obayya, R.J. Wiltshire, Multiplexer-demultiplexer based on nematic liquid crystal photonic crystal fiber coupler. J. Opt. Quantum Electron. **41**(4), 315–326 (2009)
58. M.F.O. Hameed, R.T. Balat, A.M. Heikal, M.M. Abo-Elkhier, M.I. Abo el Maaty, S.S.A. Obayya, Polarization-independent surface plasmon liquid crystal photonic crystal multiplexer-demultiplexer. Photonics J. IEEE **7**(5), 1–10 (2015)
59. K. Saitoh, J.N. Florous, M. Koshiba, M. Skorobogatiy, Design of narrow band-pass filters based on the resonant-tunneling phenomenon in multi-core photonic crystal fibers. Opt. Express **13**(25), 10327–10335 (2005)
60. J.N. Dash, R. Jha, Graphene-based birefringent photonic crystal fiber sensor using surface plasmon resonance. IEEE Photonics Technol. Lett. **26**(11), 1092–1095 (2014)
61. M.F.O. Hameed, Y.K.A. Alrayk, S.S.A. Obayya, Self-calibration highly sensitive photonic crystal fiber biosensor. IEEE Photonics **8**(3), 6802912–6802912 (2016)
62. M.F.O. Hameed, M. El-Azab, A.M. Heikal, S.M. El-Hefnawy, S.S.A. Obayya, Highly sensitive plasmonic photonic crystal temperature sensor filled with liquid crystal. IEEE Photonics Technol. Lett. **28**(1), 59–62 (2015). http://ieeexplore.ieee.org/xpl/RecentIssue.jsp?punumber=68Vol
63. E.K. Akowuah et al., Numerical analysis of a photonic crystal fiber for biosensing applications. IEEE J. Quantum Electron. **48**(11), 1403–1410 (2012)
64. S.I. Azzam, R.E.A. Shehata, M.F.O. Hameed, A.M. Heikal, S.S.A. Obayya, Multichannel photonic crystal fiber surface plasmon resonance based sensor. J. Opt. Quantum Electron. **48**, 142, (2016)
65. J. Homola, S.S. Yee, G. Gauglitz, Surface plasmon resonance sensors: review. Sens. Actuators B Chem. **54**(1/2), 3–15 (1999)
66. R. Jha, A.K. Sharma, High-performance sensor based on surface plasmon resonance with chalcogenide prism and aluminum for detection in infrared. Opt. Lett. **34**(6), 749 (2009)
67. M.S. Mohamed, M.F.O. Hameed, N.F.F. Areed, M.M. El-Okr, S.S.A. Obayya, Analysis of highly sensitive photonic crystal biosensor for glucose monitoring. J. Appl. Comput. Electromagnet. Soc. (ACES) **31**(7), 836–842 (2016)
68. N.F.F. Areed, M.F.O. Hameed, S.S.A. Obayya, Highly sensitive face-shaped label-free photonic crystal refractometer for glucose concentration monitoring. J. Opt. Quantum Electron. **49**(5), 1–12 (2017)

Chapter 3
Basic Principles of Surface Plasmon Resonance

A. M. Heikal, Mohamed Farhat O. Hameed and S. S. A. Obayya

Abstract In this chapter, the basic concept concerning the surface plasmon phenomena is presented. Different types of surface plasmon wave (localized and propagating) are reviewed. Moreover, the thin metallic film surface plasmon waveguide is analyzed in order to show the symmetric and asymmetric modes. Finally, other types of surface plasmon waveguides are discussed to show the trade-off between the confinement of the field profile and the attenuation loss.

Keywords Plasmon · Plasmonic · Slab waveguide · Symmetric mode
Asymmetric mode · Surface plasmon mode · Attenuation loss
Diffraction limit

3.1 Introduction

'Plasmonics' is a relatively new term in photonics which refers to applications or phenomena where the surface plasmon (SP) is introduced [1]. The SPs can be defined as the interaction of surface electrons of metals with electromagnetic waves.

A. M. Heikal · S. S. A. Obayya
Center for Photonics and Smart Materials, Zewail City of Science and Technology, October Gardens, 6th of October City, Giza, Egypt
e-mail: aheikal@zewailcity.edu.eg

S. S. A. Obayya
e-mail: sobayya@zewailcity.edu.eg

M. F. O. Hameed (✉)
Center for Photonics and Smart Materials and Nanotechnology Engineering Program, Zewail City of Science and Technology, October Gardens, 6th of October City, Giza, Egypt
e-mail: mfarahat@zewailcity.edu.eg

A. M. Heikal · S. S. A. Obayya
Electronics and Communication Engineering Department, Faculty of Engineering, Mansoura University, Mansoura, Egypt

M. F. O. Hameed
Mathematics and Engineering Physics Department, Faculty of Engineering, Mansoura University, Mansoura, Egypt

© Springer International Publishing AG, part of Springer Nature 2019

M. F. O. Hameed and S. Obayya (eds.), *Computational Photonic Sensors*, https://doi.org/10.1007/978-3-319-76556-3_3

However, the difference between the characteristics of surface electrons and those in the bulk of metals has been known for a long time, only recently have the surface plasmons phenomena attracted the attention of scientist and engineers from varying disciplines. The great development in technology enables the fabrication and implementation of nanometallic structures. Therefore, the surface plasmon has many applications in photonics communication devices [2–4], sensing [5–8], and materials science; thanks to its ability to confine the electromagnetic fields at the interface between metal and dielectric [9–11]. Generally, plasmonic sensing devices are categorized into two types: propagating surface plasmon resonance (SPR) sensors and localized surface plasmon resonance (LSPR) sensors. Moreover, over the past several years, there has been remarkable progress in the design, fabrication, and application development of plasmonic PCF devices.

3.1.1 Propagating Surface Plasmons (PSPs)

While the optical field is confined in higher refractive index region in dielectric waveguides. Surface plasmons travel along dielectric and metal interfaces. For a planar interface of a metal and a dielectric, the electromagnetic field is confined at the interface [12]. The field decays exponentially in both metal and dielectric in the direction perpendicular to the interface. The interfaces can be complicated geometries or even be periodic (grating). For certain geometries, the electromagnetic field of surface plasmon waveguides can be confined in a few nanometres. An example is a very thin dielectric film embedded between metal claddings metal–insulator–metal (MIM) structure [13]. Since electromagnetic field components decay in metal much faster than in dielectric, the effective thickness of this type of waveguide is just a few nanometres. Moreover, dielectric waveguides have a fundamental limit for the mode size, the diffraction limit. The diffraction limit principle states that the dimensions of optical mode of a dielectric waveguide cannot be smaller than half the wavelength in the core [14]. However, SP waveguides led to more compact optical systems instead of the conventional dielectric waveguides.

3.1.2 Localized Surface Plasmons (LSPs)

If light is incident on a metallic nanoparticle, free electrons of the nanoparticle respond to the electromagnetic field. When the diameter of the particle is much smaller than the wavelength of field, the free electrons move in phase and oscillate with a certain frequency. This frequency depends on the shape, size, and material of the particle. Moreover, the properties of the surrounding cladding and the wavelength of the exciting light have a great effect on the oscillation of these free electrons. The electric dipole model can be used to implement theoretically,

the electron oscillation over a very small localized distance. Energy builds up in the dipole field to a level that the near field of the dipole could be enhanced by several orders of magnitude compared to the exciting field. The confinement of free electrons to a very small volume leads to electromagnetic field enhancement. This phenomenon is the main idea for a number of applications including single molecule detection [15], microscopy [16], and small particle manipulation [17]. The nanoparticle strong near field encourages nonlinear effects that can be used for novel applications such as all-optical switching. When metallic nanoparticles are arranged close enough to interact with each other, each particle can be modelled by an electric dipole that couples to the next one. A single-dimensional array of particles has been used as a waveguide [18] with a very small cross section. Sharp bends have also been presented [19]. Two-dimensional arrays of particles can be adjusted to form gratings with different capabilities [20].

3.2 Single-Interface Surface Plasmon Waveguide (SPWG)

Consider the interface between a dielectric and a metal as shown in Fig. 3.1. Using Maxwell equations, by assuming a harmonic time variation ($\partial/\partial t = j\omega$) with no charge ($\rho = 0$), no current ($J = 0$) and $\partial/\partial y = 0$

$$\nabla \times E = -j\omega\mu H \tag{3.1}$$

$$\nabla \times H = j\omega\varepsilon E \tag{3.2}$$

Equations (3.1) and (3.2) can be decoupled into two sets of equations for transverse electric (TE) and transverse magnetic (TM) modes:

The TE mode (no z component for the electric field):

$$\frac{\partial E_y}{\partial z} = j\omega\mu H_x \tag{3.3}$$

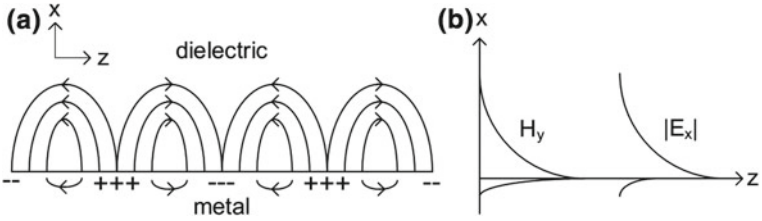

Fig. 3.1 **a** Single-interface SPWG schematic showing the electric field lines. **b** Amplitudes of magnetic and normal electric fields above and below the interface indicating the penetration depth in each region

$$\frac{\partial E_y}{\partial x} = -j\omega\mu H_z \tag{3.4}$$

$$\frac{\partial H_x}{\partial z} - \frac{\partial H_z}{\partial x} = j\omega\varepsilon E_y \tag{3.5}$$

The TM mode (no z component for the magnetic field):

$$\frac{\partial H_y}{\partial z} = -j\omega\varepsilon E_x \tag{3.6}$$

$$\frac{\partial H_y}{\partial x} = j\omega\varepsilon E_z \tag{3.7}$$

$$\frac{\partial E_x}{\partial z} - \frac{\partial E_z}{\partial x} = -j\omega\mu H_y \tag{3.8}$$

In the TE case for a guided mode with propagation constant β in z direction we can separate the z coordinate dependence as

$$\mathrm{E}_y(x, z) = E_y(x)e^{-j\beta z} \tag{3.9}$$

Equations (3.3)–(3.5) result in the wave equation

$$\frac{d^2E_y}{dx^2} + \left(\omega^2\mu\varepsilon - \beta^2\right)E_y = 0 \tag{3.10}$$

The solutions to the wave equation are exponential functions. Considering that a physical solution cannot contain unbounded growth as distance increases from the interface [12] then,

$$E_y = \begin{cases} A_1 e^{-k_{x1}x}, & x > 0 \\ A_2 e^{k_{x2}x}, & x < 0 \end{cases} \tag{3.11}$$

where A_1 and A_2 are constants and k_x is the x component of the wave vector given by

$$\beta^2 - k_{x1,2}^2 = \omega^2\mu\varepsilon_0\varepsilon_{1,2} \tag{3.12}$$

The interface conditions rule that E_y and H_z (or equivalently $\frac{\partial E_y}{\partial x}$) must be continuous at $x = 0$. The first condition leads to $A_1 = A_2$ which makes the second condition unsatisfiable. This means that a single planar interface between two media cannot support TE modes. For the case of TM waves, however, things turn out to be different. Here, we have

$$\frac{d^2H_y}{dx^2} + \left(\omega^2\mu\varepsilon - \beta^2\right)H_y = 0 \tag{3.13}$$

with the solution

$$H_y = \begin{cases} A_1 e^{-k_{x1}x}, & x > 0 \\ A_2 e^{k_{x2}x}, & x < 0 \end{cases} \tag{3.14}$$

with $k_{x\ 1,2}$ given by (3.12). Interface conditions demand H_y and $\frac{1}{\varepsilon}\frac{\partial H_y}{\partial x}$ be continuous across the interface leading to $A_1 = A_2$ and

$$\frac{k_{x1}}{\varepsilon_1} = -\frac{k_{x2}}{\varepsilon_2} \tag{3.15}$$

First, we notice that (3.15) requires ε_1 and ε_2 have different signs (if they are real). Using (3.12) in (3.15), the dispersion equation can be found as

$$\beta = k_0\left(\frac{\varepsilon_1\varepsilon_2}{\varepsilon_1 + \varepsilon_2}\right)^{\frac{1}{2}} \tag{3.16}$$

where $k_0 = \omega\sqrt{\mu\varepsilon_0}$ wave number of vacuum is used. In practice, ε_1 is commonly a dielectric material with small or negligible loss and $\varepsilon_2 = \varepsilon_2^{'} - j\varepsilon_2^{''}$ is a metal with $\varepsilon_2^{'} < 0$ and $\left|\varepsilon_2^{'}\right| > \varepsilon_2^{''}$. In this case, real and imaginary parts of the propagation constant in (3.16) can be written as [12]

$$\beta^{'} = k_0\left(\frac{\varepsilon_1\varepsilon_2^{'}}{\varepsilon_1 + \varepsilon_2^{'}}\right)^{\frac{1}{2}} \tag{3.17}$$

$$\beta^{''} = k_0\left(\frac{\varepsilon_1\varepsilon_2^{'}}{\varepsilon_1 + \varepsilon_2^{'}}\right)^{\frac{3}{2}}\frac{\varepsilon_2^{''}}{2\left(\varepsilon_2^{'}\right)^2} \tag{3.18}$$

For $\beta^{'}$ to be real, we must have $\left|\varepsilon_1^{'}\right| > \varepsilon_1^{''}$. Additionally, $\beta^{''}$ is defined as the decay of the guided mode due to the loss of metal represented by $\varepsilon_2^{''}$. In a metal and dielectric interface, oscillation of free electrons of metal at the surface (surface plasmons) is the main reason of the guided SP mode. Electric field lines at the surface are shown in Fig. 3.1. Maximum of the field occurs at the interface and decays exponentially. If metal has no damping loss, the decay constant in the dielectric $k_{x1} < \beta$, but in the metal $k_{x2} > \beta$. This means that the fields decay faster in metal than they do in dielectric.

The dispersion of single-interface surface plasmon waveguide for an interface between air and a metal is shown in Fig. 3.2. The dielectric permittivity of the lossless metal can be obtained from Drude model:

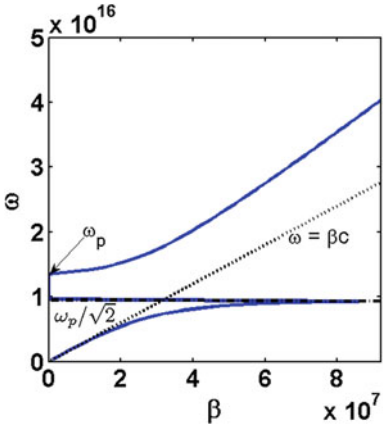

Fig. 3.2 Dispersion curve for single-interface surface plasmon waveguide

$$\varepsilon_2 = 1 - \left(\frac{\omega_p}{\omega}\right)^2 \tag{3.19}$$

where ω_p is the plasma frequency for silver ($\omega_p = 2\pi \times 2.18 \times 1\,0^{15}$ rad/s). In the dielectric, the light line can be calculated by $\omega = \frac{kc}{n_d}$ where c is the speed of light in free space, k is the wavenumber in the dielectric, and n_d is the dielectric refractive index. This line is represented by a dotted line in Fig. 3.2. Due to momentum (k) mismatch, any field whose dispersion curve comes below the dotted line cannot propagate in that dielectric and is called nonradiative field. However, fields whose dispersion curves fall in the left side of light line can propagate into the dielectric region ('radiative' fields). The dispersion curve of single-interface surface plasmon waveguide has two regions, the nonradiative zone and the radiative zone.

It may be seen from Fig. 3.2 that there is a discontinuity at $\omega = \frac{\omega_p}{\sqrt{2}}$ where $|\varepsilon_2| = \varepsilon_1 = 1$. In the ideal case (lossless) when frequency increases and reaches the discontinuity, the frequency propagation constant becomes very large, and phase and group velocities approach zero. In the practical case (losses are included), the propagation constant is bounded and it reaches a maximum which depends on the loss value. As mentioned before, the maximum of fields of the surface plasmon mode occurs at the interface and decays exponentially into the surrounding zone. Skin depth (x_d) can be defined as the distance at which the dominant field component approaches 1/e times its maximum value.

$$x_d = \begin{cases} \frac{1}{k_{x1}} = \frac{1}{k_0}\left(\frac{\varepsilon_1 + \varepsilon_2'}{-\varepsilon_1^2}\right)^{\frac{1}{2}}, & x > 0 \\ \frac{1}{k_{x2}} = \frac{1}{k_0}\left(\frac{\varepsilon_1 + \varepsilon_2'}{-\varepsilon_2^2}\right)^{\frac{1}{2}}, & x < 0 \end{cases} \tag{3.20}$$

where $k_0 = \frac{2\pi}{\lambda}$ and ε_1, ε_2 can be obtained using the Drude model [12]. At $\lambda = 1.55$ μm, the skin depth in air (silver/air interface is considered) is $x_{d_1} = 2.66$ μm

while $x_{d_2} = 22.82$ nm in the silver layer. Therefore, the field expansion into the dielectric is over hundred times that in metal.

The main disadvantage of the single-interface surface plasmon waveguide is the very short propagation length due to metal loss. The imaginary part of the metal permittivity leads to a complex propagation constant and fields decrease exponentially by $\exp(-|\beta''|z)$. The propagation length can be defined as the distance by which the intensity of electromagnetic field attenuates to 1/e from its maximum value. However, intensity is proportional to $\exp(-2|\beta''|z)$, the propagation length is $L = \frac{1}{2|\beta''|}$ where β'' is imaginary part of complex propagation constant. Also, $\alpha = 2|\beta''|$ is called the attenuation constant. For silver/air interface at the wavelength of 1.55 μm the propagation length is about 299 μm and the attenuation constant is 32 cm^{-1}. The very small propagation of field into the metal is enough to cause a large attenuation value that limits the application of single-interface surface plasmon waveguide at visible and near-infrared wavelengths.

3.3 Thin Metallic Film Surface Plasmon Waveguide

Now, consider the existence of guided modes for insulator–metallic–insulator (MIM) structure as shown in Fig. 3.3. The film of thickness h is embedded between two dielectrics and z is the direction of propagation. Dielectrics in zones 1 and 3 have refractive indices n_1 and n_3, respectively. For the TE mode, the solution to the eigenvalue Eq. (3.10) can be obtained by applying the radiation boundary condition for regions 1 and 3 [21]:

$$E_y = \begin{cases} A_1 e^{k_{x1}x} & x \le -\frac{h}{2} \\ A_2 \cosh(k_{x2}x) + A_3 \sinh(k_{x2}x) & \frac{-h}{2} \le x \le \frac{h}{2} \\ A_4 e^{-k_{x3}x} & x \ge \frac{h}{2} \end{cases} \tag{3.21}$$

where A_1 to A_4 are constants and wavenumbers k_{x1}, k_{x2}, and k_{x3} in the x-direction are calculated, as before, from

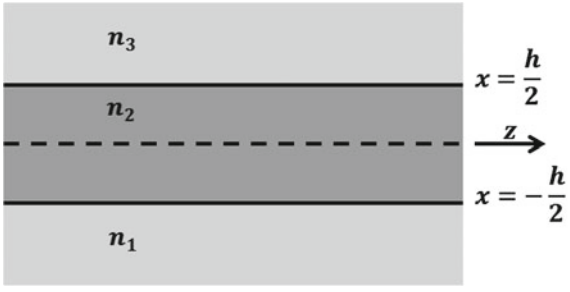

Fig. 3.3 Thin film surface plasmon waveguide

$$\beta^2 - k_{xi}^2 = \omega^2 \mu \varepsilon_0 \varepsilon_i, \quad i = 1, 2, 3 \tag{3.22}$$

At the two interfaces, the electric field component E_y and its derivative must be continuous. Therefore, four algebraic equations with four unknown constants A_1 to A_4 are obtained:

$$\begin{aligned}
&A_1\, e^{-k_{x1}\frac{h}{2}} - A_2\, cosh\left(-k_{x2}\frac{h}{2}\right) - A_3\, sinh\left(-k_{x2}\frac{h}{2}\right) = 0 \\
&A_1\, k_{x1} e^{-k_{x1}\frac{h}{2}} - A_2\, k_{x2}\, sinh\left(-k_{x2}\frac{h}{2}\right) - A_3\, k_{x2}\, cosh\left(-k_{x2}\frac{h}{2}\right) = 0 \\
&-A_4\, e^{-k_{x3}\frac{h}{2}} + A_2\, cosh\left(k_{x2}\frac{h}{2}\right) + A_3\, sinh\left(k_{x2}\frac{h}{2}\right) = 0 \\
&A_4\, k_{x1} e^{-k_{x3}\frac{h}{2}} + A_2\, k_{x2}\, sinh\left(k_{x2}\frac{h}{2}\right) + A_3\, k_{x2}\, cosh\left(k_{x2}\frac{h}{2}\right) = 0
\end{aligned} \tag{3.23}$$

Since the equations are homogenous, in order to have nontrivial solutions for the constants, the determinant of the system of equations must be zero:

$$D = \begin{vmatrix}
e^{-k_{x1}\frac{h}{2}} & -cosh\left(-k_{x2}\frac{h}{2}\right) & -sinh\left(-k_{x2}\frac{h}{2}\right) & 0 \\
k_{x1} e^{-k_{x1}\frac{h}{2}} & -k_{x2}\, sinh\left(-k_{x2}\frac{h}{2}\right) & -k_{x2}\, cosh\left(-k_{x2}\frac{h}{2}\right) & 0 \\
0 & cosh\left(k_{x2}\frac{h}{2}\right) & sinh\left(k_{x2}\frac{h}{2}\right) & -e^{-k_{x3}\frac{h}{2}} \\
0 & k_{x2}\, sinh\left(k_{x2}\frac{h}{2}\right) & k_{x2}\, cosh\left(k_{x2}\frac{h}{2}\right) & k_{x1} e^{-k_{x1}\frac{h}{2}}
\end{vmatrix} = 0 \tag{3.24}$$

After simplification, one can obtain

$$tanh(k_{x2}h)\left(1 + \frac{k_{x1}k_{x3}}{k_{x2}^2}\right) + \left(\frac{k_{x1}}{k_{x2}} + \frac{k_{x3}}{k_{x2}}\right) = 0 \tag{3.25}$$

or

$$tanh(k_{x2}h)(1 + s_1 s_3) + (s_1 + s_3) = 0 \tag{3.26}$$

where

$$s_1 = \frac{k_{x1}}{k_{x2}}, \quad s_3 = \frac{k_{x3}}{k_{x2}} \tag{3.27}$$

For lossless waveguides (neither metallic nor dielectric loss), where β is real and positive, there is no solution for Eq. (3.26) for β. Therefore, TE guided modes cannot exist in a thin film surface plasmon waveguide.

Now, consider TM guided modes supported by the thin film structure. Here,

$$H_y = \begin{cases} A_1\, e^{k_{x1}x} & x \le -\frac{h}{2} \\ A_2\, cosh(k_{x2}x) + A_3\, sinh(k_{x2}x) & \frac{-h}{2} \le x \le \frac{h}{2} \\ A_4\, e^{-k_{x3}x} & x \ge \frac{h}{2} \end{cases} \tag{3.28}$$

with the x-direction wavenumbers given by

$$\beta^2 - k_{xi}^2 = \omega^2 \mu \varepsilon_0 \varepsilon_i, \quad i = 1, 2, 3 \tag{3.29}$$

Applying the boundary conditions at the two interfaces. These are the continuity of H_y and $\frac{1}{\varepsilon}\frac{dH_y}{dy}$ which generate four equations:

$$\begin{aligned} &A_1 e^{-k_{x1}\frac{h}{2}} - A_2\, cosh\left(-k_{x2}\frac{h}{2}\right) - A_3\, sinh\left(-k_{x2}\frac{h}{2}\right) = 0 \\ &A_1 \frac{k_{x1}}{\varepsilon_1} e^{-k_{x1}\frac{h}{2}} - A_2 \frac{k_{x2}}{\varepsilon_2}\, sinh\left(-k_{x2}\frac{h}{2}\right) - A_3 \frac{k_{x2}}{\varepsilon_2}\, cosh\left(-k_{x2}\frac{h}{2}\right) = 0 \\ &-A_4 e^{-k_{x3}\frac{h}{2}} + A_2\, cosh\left(k_{x2}\frac{h}{2}\right) + A_3\, sinh\left(k_{x2}\frac{h}{2}\right) = 0 \\ &A_4 \frac{k_{x3}}{\varepsilon_3} e^{-k_{x3}\frac{h}{2}} + A_2 \frac{k_{x2}}{\varepsilon_2}\, sinh\left(k_{x2}\frac{h}{2}\right) + A_3 \frac{k_{x2}}{\varepsilon_2}\, cosh\left(k_{x2}\frac{h}{2}\right) = 0 \end{aligned} \tag{3.30}$$

Setting the determinant of the above equations to zero brings us to the same dispersion equation given by (3.26) [21]:

$$tanh(k_{x2}h)(1 + s_1 s_3) + (s_1 + s_3) = 0 \tag{3.31}$$

But with the following definition

$$s_1 = \frac{\varepsilon_2}{\varepsilon_1}\frac{k_{x1}}{k_{x2}}, \quad s_3 = \frac{\varepsilon_2}{\varepsilon_3}\frac{k_{x3}}{k_{x2}} \tag{3.32}$$

From this equation, s_1 and s_3 are negative real numbers. Therefore, the first term of (3.31) is positive, while the second term is negative and hence there are solutions to that equation. Specifically, there are one or two solutions which rely on the structure parameters. Before considering the general case, we take a look at two special cases,

Case 1: Very thick film ($h \to \infty$)
From (3.31) as $k_{x2}h$ is very large, $tanh(k_{x2}h)$ is replaced with unity. As a result, the equation becomes

$$(1 + s_1)(1 + s_3) = 0 \tag{3.33}$$

with the solution $s_1 = -1$ or $s_3 = -1$. Using (3.29) and (3.32), the dispersion relations for a single MI interface given in (3.16) can be obtained:

$$\beta = k_0 \left(\frac{\varepsilon_1 \varepsilon_2}{\varepsilon_1 + \varepsilon_2} \right)^{\frac{1}{2}} \tag{3.34}$$

Or

$$\beta = k_0 \left(\frac{\varepsilon_3 \varepsilon_2}{\varepsilon_3 + \varepsilon_2} \right)^{\frac{1}{2}} \tag{3.35}$$

Therefore, for a very thick metal film there are two independent surface plasmon modes at each interface. Each mode decays exponentially into the film, therefore, for very thick films; the two modes cannot be coupled. When the film becomes thinner coupling occurs and give rise to two 'super modes' as shown in Fig. 3.4.

Case 2: Symmetric structure, $(\varepsilon_1 = \varepsilon_3)$
The dispersion Eq. (3.31) becomes

$$tanh(k_{x2}h) = \frac{-2s_1}{1+s_1^2} \tag{3.36}$$

which after some algebraic manipulation changes to

$$\left(tanh\left(\frac{k_{x2}h}{2} \right) + s_1 \right) \left(s_1 tanh\left(\frac{k_{x2}h}{2} \right) + 1 \right) = 0 \tag{3.37}$$

giving two equations

$$tanh\left(\frac{k_{x2}h}{2} \right) = -s_1 \tag{3.38}$$

$$tanh\left(\frac{k_{x2}h}{2} \right) = -\frac{1}{s_1} \tag{3.39}$$

Figure 3.4 shows symmetric and asymmetric modes in thin film surface plasmon waveguide formed by coupling of SPP modes. It is clear that by putting $A_3 = 0$ in

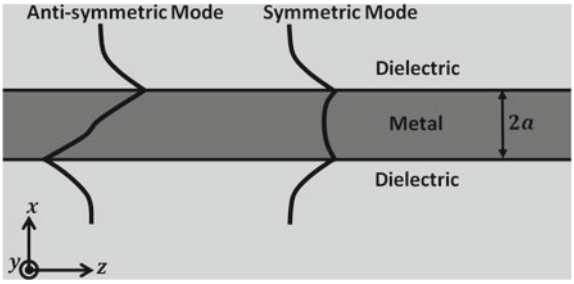

Fig. 3.4 Symmetric and asymmetric modes in thin film surface plasmon waveguide

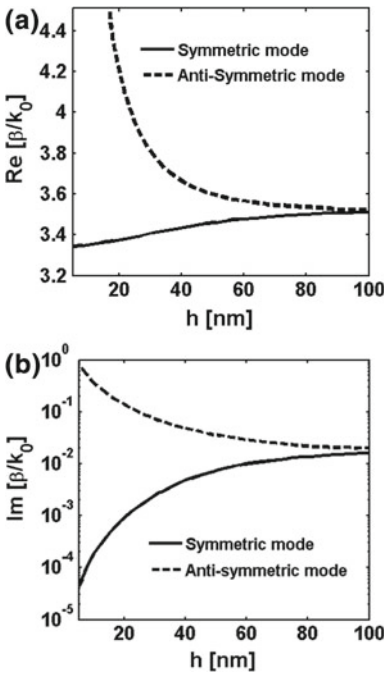

Fig. 3.5 Variation of the **a** real part and **b** imaginary part of the propagation constant of the symmetric and asymmetric modes of thin surface plasmon waveguide with film thickness h

the Eqs. (3.30), (3.38) is obtained, which is the dispersion equation of a mode at $A_3 = 0$. This mode is a symmetric mode. However, Eq. (3.39) is the dispersion relation of asymmetric mode at $A_2 = 0$.

Figure 3.5 shows the effect of the film thickness on real and imaginary parts of the propagation constants of symmetric and asymmetric mode. In this study, the values shown are the normalized to the free space wavenumber (the effective indices of guided modes). Further, it is assumed that $\varepsilon_1 = \varepsilon_3 = 10.23$ and $\varepsilon_2 = -115.37 - j11.14$ (dielectric constant of silver at $\lambda = 1550$ nm [21]). At small metal thicknesses h, the real part of effective index of the symmetric mode converges to the refractive index of dielectric claddings. It is evident from the symmetric mode profile in Fig. 3.5 that as the film thickness reaches zero, the symmetric mode becomes similar to a plane wave propagating in the dielectric medium surrounding the film. Moreover, the symmetric mode loss which is proportional to the imaginary part of the effective index reaches zero. However, in asymmetric mode case, the real effective index increases unboundedly as film thickness decreases to zero. Therefore, the mode becomes more and more confined inside the film. The asymmetric mode cannot be supported by the dielectric region when film thickness approaches zero as the sign of H_y field component should be changed suddenly. Therefore, the asymmetric mode is compressed inside the film. Additionally, the asymmetric mode loss is larger than that of the symmetric mode. The symmetric and asymmetric modes are also called long-range and short-range surface plasmon modes (LRSP and SRSP), respectively. When the film thickness

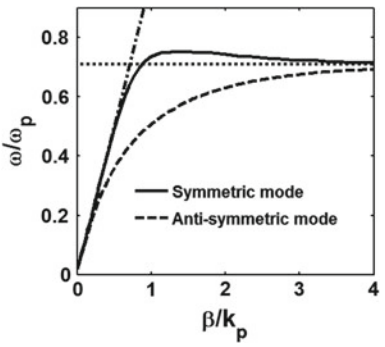

Fig. 3.6 Dispersion curves for symmetric and asymmetric modes of thin film SP waveguide

increases, propagation constants of the modes get closer and in the limit of thick film they degenerate, as previously explained. Figure 3.6 shows the frequency dispersion of the LRSP and SRSP modes for a 20 nm thick film embedded in dielectric materials of $\varepsilon_1 = \varepsilon_3 = 1$. The Drude model is used for calculating the dielectric constant of metal with a plasma frequency $\omega_p = 2\pi \times 2.19 \times 10^{15}$ rad/s. Additionally, the frequencies are normalized to the plasma frequency while the propagation constants are normalized to the free space wavenumber at the plasma frequency (k_p). As the two modes are below the light line, they cannot travel in the dielectric zones and are bound to the metal interface. At large propagation constants, the normalized frequencies of the two modes become constant and reach a frequency called the surface plasmon frequency. It is clear from the dispersion Eqs. (3.38) and (3.39) that when $\beta \to \infty, tanh\left(\frac{k_{x2}h}{2}\right) \to 1, s_1 \to \frac{\varepsilon_2}{\varepsilon_1}$ and both dispersion equations give $\omega_\infty = \frac{\omega_p}{\sqrt{1+\varepsilon_1}}$ which is the surface plasmon frequency of single-interface surface plasmon waveguide. This is because at very large propagation constants, the guided wavelength is very small and the film appears as a very thick to the modes.

In the general case, where $\varepsilon_1 \neq \varepsilon_3$ the two modes are quasi-symmetric and quasi-asymmetric. Figure 3.7 shows the mode profiles for an asymmetric structure with $\varepsilon_1 < \varepsilon_3$. The major difference between symmetric and asymmetric thin film surface plasmon waveguides is the existence of a cut-off film thickness for the symmetric mode in an asymmetric structure [21]. For metal films thinner than the cut-off value, the symmetric mode stops propagating. Similarly, there is a cut-off wavelength above which the symmetric mode stops propagating. Figure 3.8 shows the real and imaginary parts of the propagation constant of an asymmetric surface plasmon waveguide. The parameters of the surface plasmon waveguide are similar to those used for Fig. 3.5 except that $\varepsilon_3 = 11$. At cut-off, if $\varepsilon_1 < \varepsilon_3$ and the lateral wavenumber (k_x) in region 3 is zero, by applying (3.29) one can obtain:

$$\beta = k_0\sqrt{\varepsilon_3} \tag{3.40}$$

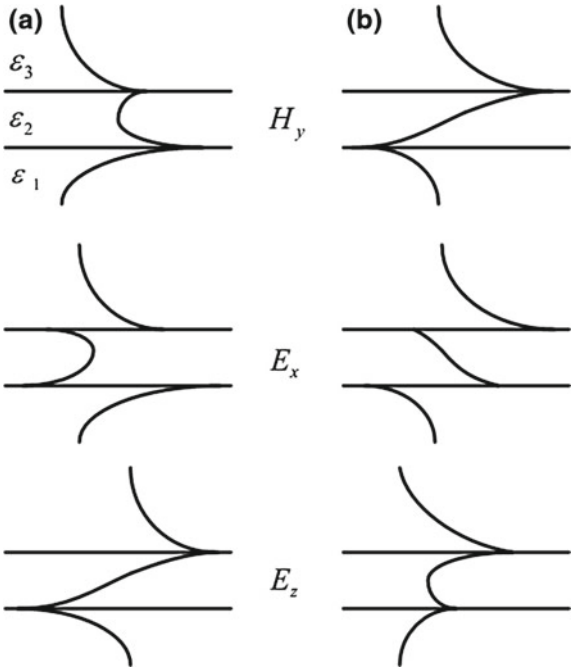

Fig. 3.7 **a** Quasi-symmetric mode and **b** quasi-asymmetric mode for asymmetric thin film surface plasmon waveguide

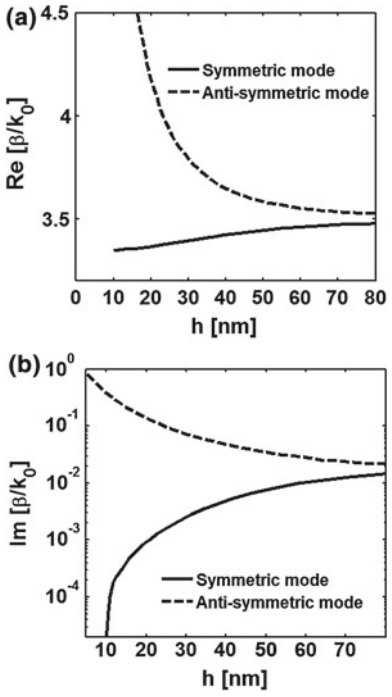

Fig. 3.8 Variation of the **a** real part and **b** imaginary part of the propagation constant with thickness h for asymmetric film

Therefore, the propagation constant for lossless dielectrics at cut-off is real. This is confirmed by Fig. 3.8, as waveguide loss drops dramatically near cut-off. Other lateral wavenumbers are obtained as follow:

$$k_{x1} = k_0(\varepsilon_3 - \varepsilon_1)^{\frac{1}{2}} \tag{3.41}$$

$$k_{x2} = k_0(\varepsilon_3 - \varepsilon_2)^{\frac{1}{2}} \tag{3.42}$$

Using these relations in the dispersion Eq. (3.31), an analytical formula is obtained for the cut-off film thickness where metal loss is neglected [21]

$$h_c = \frac{1}{2k_0(\varepsilon_3 - \varepsilon_2)^{\frac{1}{2}}} ln\left(\frac{\varepsilon_1(\varepsilon_3 - \varepsilon_2)^{\frac{1}{2}} - \varepsilon_2(\varepsilon_3 - \varepsilon_1)^{\frac{1}{2}}}{\varepsilon_1(\varepsilon_3 - \varepsilon_2)^{\frac{1}{2}} + \varepsilon_2(\varepsilon_3 - \varepsilon_1)^{\frac{1}{2}}}\right) \tag{3.43}$$

which is valid when

$$\frac{|\varepsilon_2|}{\varepsilon_1}\left(\frac{\varepsilon_3 - \varepsilon_1}{\varepsilon_3 - \varepsilon_2}\right)^{\frac{1}{2}} < 1 \tag{3.44}$$

Symmetric modes of thin film tolerate only a small amount of structural asymmetry, especially, at longer wavelengths. For a surface plasmon waveguide with $\varepsilon_3 = 11$ and a Drude metal with plasma frequency of $\omega_p = 1.36 \times 10^{16}$ rad/s, Fig. 3.9 shows the cut-off film thickness as a function of ε_1. The plotted curves 1, 2, and 3 are corresponding to wavelengths of 1 μm, 1.3 μm, and 1.55 μm, respectively.

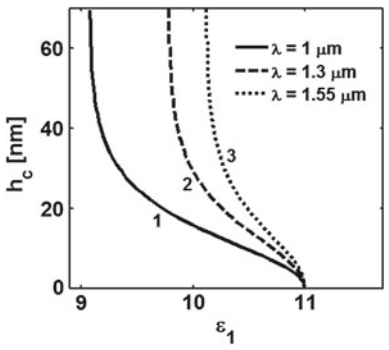

Fig. 3.9 Variation of the cut-off thickness h_c with the permittivity of the dielectric in region 1 for asymmetric thin film

3.4 Metal–Insulator–Metal (MIM) Surface Plasmon Waveguide

The planer MIM structure similar to the IMI structure does not support TE mode. However, it supports two TM SP modes; one symmetric and one asymmetric. Moreover, there are ordinary TE/TM modes of the conventional type considered in the introductory waveguide theory (where the structure is usually called the parallel plate waveguide). Unlike surface modes, the ordinary modes do not decay away from metal interfaces into the dielectric region and metal claddings act merely as reflectors. The energy carried by the ordinary modes is concentrated in the dielectric region rather than metal surfaces. As a result, the dielectric layer should be reasonably thick where these type of modes depends on the geometry of the metallic grooves. The supported modes are called channel plasmon polariton (CPPs) modes. Now consider surface modes, for a symmetric structure with $\varepsilon_1 = \varepsilon_3 = -116.37 - j11.12$ and $\varepsilon_2 = 11.3$ at $\lambda = 1.55$ μm, Fig. 3.10 shows the variation of propagation constant with dielectric film thickness. It is clear that from Figs. 3.5 and 3.10 there are a number of differences between MIM and IMI surface plasmon waveguides. A lower cut-off thickness for the asymmetric mode of MIM structure exists even for a symmetric structure. Second, the symmetric mode loss is huge and increases as the dielectric layer thickness decreases. This makes the structure impractical for many applications. For a very thick dielectric layer, the propagation constants and losses of the two modes reach their corresponding values of a single-interface structure. Therefore, the propagation losses of both modes are always larger than the losses of a single-interface surface plasmon waveguide. Since the electromagnetic field decays much faster in metal than it does in dielectric, the spatial extent of the surface plasmon modes in the MIM configuration can be dramatically less compared to mode sizes in the IMI counterpart. This makes the MIM structure attractive for subwavelength and nanophotonic applications. But as a waveguide, its use is restricted to very short distances.

3.5 Other Types of Surface Plasmon Waveguide

Other than the three simple geometries considered in the previous sections, numerous types of surface plasmon waveguides with more complex geometries shown in Fig. 3.11 are discussed in this section. The main purpose of these structures is to achieve low loss and well-confined long-range surface plasmon modes. Such structures are the backbone of the implementation of a high density optical and optoelectronic integrated systems. Ease of in- and out-coupling of SPP modes to free space, optical fibres, or other waveguides is another important design consideration.

The first three surface plasmon waveguides shown in Fig. 3.11a–c are called nanowires. The cylindrical shell nanowire shown in Fig. 3.11b with large radius has lower losses than the solid cylinder in Fig. 3.11a [22, 23]. Further, the shell

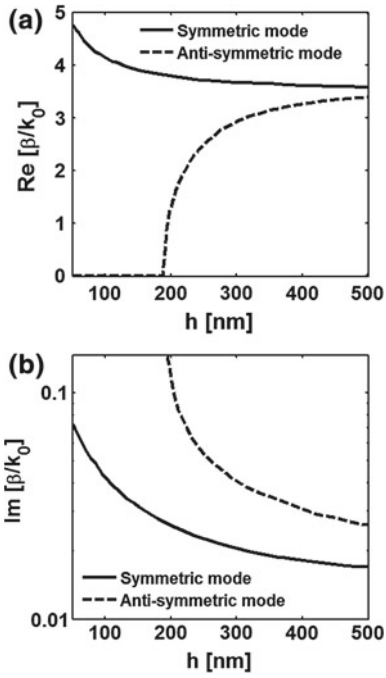

Fig. 3.10 Variations of the **a** real and **b** imaginary parts of the propagation constant of the MIM structure modes with dielectric thickness h

waveguide supports one LRSP mode and when the radius is large it becomes similar to the LRSP mode of an IMI structure. Additionally, the square cross section SPWG presented in Fig. 3.11c not only supports low loss LRSP modes, but also can be coupled favourably to optical fibre. Such planar feature makes the fabrication easier compared to Fig. 3.11a, b. Because of its symmetry, the square cross section waveguide supports two degenerate TE and TM modes polarized perpendicularly. Modal power loss as low as 0.14 dB/mm with a coupling loss of 3 dB to a single mode fibre is expected computationally [21]. The square waveguide is also a limiting case of Fig. 3.11g with equal metal width and thickness. Therefore, the supported modes by the square metallic structure are the evolved versions of those obtained by the design in Fig. 3.11g.

The waveguides in Fig. 3.11d–f are 1D geometries which support LRSP modes [21–23]. Further, these waveguides contain high index dielectric slabs close to the metal slab. Individually, these dielectric slabs have their well-known conventional modes and therefore, when they get closer to the metal slab their conventional modes couple to SPP modes of metal slab to form hybrid modes. Since part of the field is guided outside the metal slab, its LRSP modal loss is lower than that of metal slab LRSP mode with carefully selected structural parameters. The low index gaps adjacent to the metal slab in Fig. 3.11e, f push the LRSP of those structures toward cut-off where the loss decreases dramatically. The structural parameters, therefore, should be selected to operate near the cut-off case. The problem, however, is the sensitivity to layer thicknesses as a slight offset leaves the LRSP mode

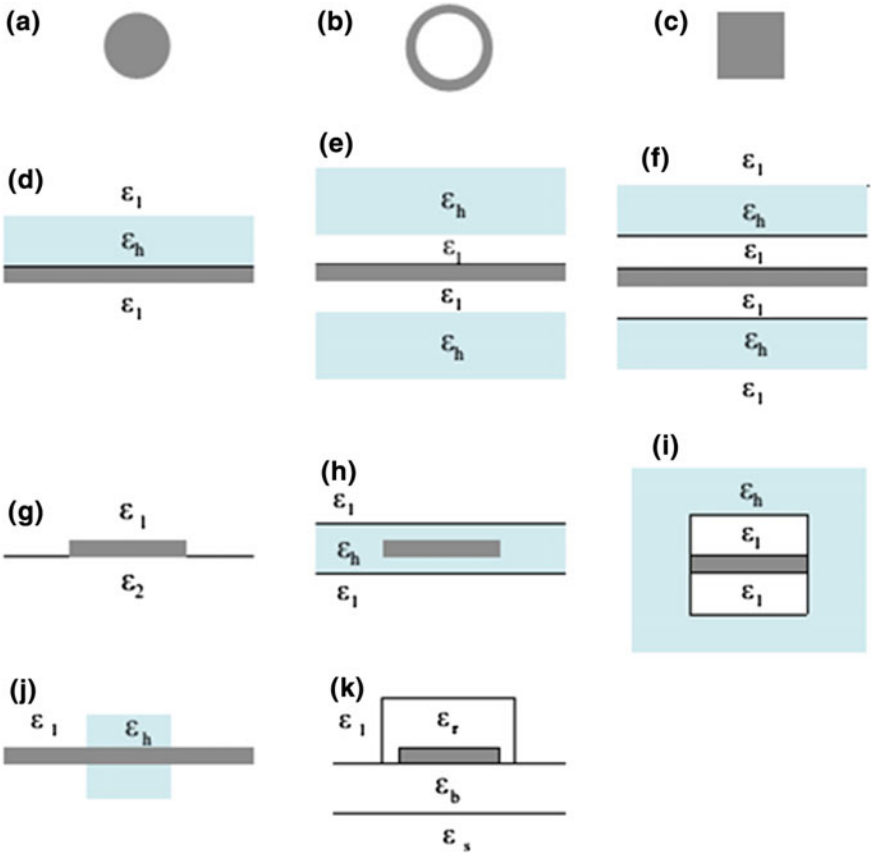

Fig. 3.11 Various types of surface plasmon waveguides

in the cut-off region. If the low index slabs in Fig. 3.11e are filled with a high index material while the high index claddings are replaced with a low index material, the loss will be increased compared to the IMI system with enhanced modal confinement which indicates the loss-confinement trade-off.

In order to achieve good confinement in both transverse directions, structures shown in Fig. 3.11g–k have been introduced.

The thin metal stripe SPWG in Fig. 3.11g is the most extensively studied one among the two-dimensional SPWGs. Reducing the width of a metal slab to a finite value makes the modal loss smaller with a dramatic change in the mode spectrum. Unlike its metal slab counterpart, the propagation characteristics of metal stripe SPWG cannot be calculated analytically and the computational effort involved is considerably greater. The metal stripe SPWG supports four fundamental bounded modes [24, 25] as opposed to only two bounded modes of the IMI structure. Further, higher order modes can exist depending on the structural parameters. One of the fundamental modes referred to as ss_b^0 acquires a large propagation length with

asymmetric structure ($\varepsilon_1 = \varepsilon_2$) and a reasonable small film thickness. The mode is, accordingly, named LRSP mode. Similar to the metal slab structure, there is a loss-confinement trade-off as the film thickness varies. However, the loss in the finite width stripe can be orders of magnitude lower than that of the metal slab waveguide. Additionally, the LRSP mode can be efficiently excited using end-recoupling to dielectric waveguides and optical fibre [24, 25]. Reference [26] demonstrated the propagation of the LRSP in SPWG with a gold stripe of 8 μm wide, and 20 nm thick embedded in SiO_2 at the communications wavelength of 1550 nm with a modal loss of 0.9 dB/mm. Modal losses of smaller than 0.1 dB/mm at the same wavelength have been theoretically predicted.

The structure of Fig. 3.11h is obtained by embedding a metal stripe in a dielectric slab waveguide. In this case, the modes are hybrid SPP-dielectric modes. Such a structure can alleviate the attenuation-confinement trade-off compared to design of Fig. 3.11g [27]. The propagation length of a 6 μm wide and 10 nm thick gold stripe in BCB material was equal to several millimetres at the 1550 nm wavelength [28].

The SPWG in Fig. 3.11j comprises a metal slab passing through a buried rectangular dielectric waveguide. The modes are similar to the modes of IMI waveguide [29], except they are laterally confined due to the higher index of the buried channel. If the slab is thin enough, the waveguide will support an LRSP mode [25]. The waveguide of Fig. 3.11i can be considered as the 2D generalization of waveguide presented in Fig. 3.11e which adds lateral confinement to the benefits of the former [25, 26]. Reference [25] reports the simulation results of a structure with a gold stripe of 1 μm × 20 nm cross section, $\varepsilon_l = (1.45)^2$, $\varepsilon_h = (1.6)^2$ operating at $\lambda = 850$ nm. Without the low index nanolayers, the LRSP mode size was 1.76 μm and the 1/e propagation length was 935 μm. With 25 nm thick nanolayers, the mode swelled to a size of 7.18 μm while the propagation range reached 2.65 cm. Further increasing the nanolayers thickness pushes the mode toward cut-off. At a critical thickness, the mode stops being bounded to the film and the mode size is infinitely large similar to the waveguide of Fig. 3.11e.

Finally, the asymmetric structure shown in Fig. 3.11k can be designed in such a way to support a tightly confined long-range SPP mode. Reference [28] shows that at $\lambda = 1.55$ μm, a propagation length of over 3 mm with a mode size of 1.6 μm can be achieved. Most of structures shown in Fig. 3.11 are very complicated to get an accurate analytical solution for the guided mode. Therefore, a numerical model for those structures is needed in order to investigate their characteristics.

3.6 Summary

In this chapter, the definition of surface plasmons has been presented. It is the interaction between surface electrons at metal/dielectric interface and the electromagnetic wave of light. Plasmonic waveguide can be considered as a metal-insulator-metal (MIM) or insulator-metal-insulator (IMI) waveguide. Plasmonic

waveguides enable the propagation of light behind the diffraction limit. However, plasmonic waveguides suffer from metal damping losses. The traditional planer MIM and IMI waveguides have been studied. Both of them can support symmetric and asymmetric plasmonic modes. However, MIM waveguide has a high confinement; it has also a high metal damping losses compared to IMI waveguide. Also, different geometries of plasmonic waveguides have been presented. Such waveguides are designed for different proposes depending on the application.

References

1. E. Economou, Surface plasmons in thin films. Phys. Rev. **182**(2), 539–554 (1969)
2. A.M. Heikal, F.F.K. Hussain, M.F.O. Hameed, S.S.A. Obayya, Efficient polarization filter design based on plasmonic photonic crystal fiber. J. Lightwave Technol. **33**(13), 2868–2875 (2015)
3. M.F.O. Hameed, R.T. Balat, A.M. Heikal, M.M. Abo-Elkhier, M.I. Abo el Maaty, S.S.A. Obayya, Polarization-independent surface plasmon liquid crystal photonic crystal multiplexer demultiplexer. IEEE Photon. J. **7**(5), 1–10 (2015)
4. B.M. Younis, A.M. Heikal, M.F.O. Hameed, S.S.A. Obayya, Coupling enhancement of plasmonic liquid photonic crystal fiber. Plasmonics **12**(5), 1529–1535 (2016)
5. M.F.O. Hameed, Y.K.A. Alrayk, S.S.A. Obayya, Self-calibration highly sensitive photonic crystal fiber biosensor. IEEE Photon. J. **8**(3), 1–12 (2016)
6. M.F.O. Hameed, Y.K.A. Alrayk, A.A. Shaalan, W.S. El Deeb, S.S.A. Obayya, Design of highly sensitive multichannel bimetallic photonic crystal fiber biosensor. J. Nanophoton. **10**(4), 046016 (2016)
7. A.M. Heikal, F.F.K. Hussain, M.F.O. Hameed, S.S.A. Obayya, Efficient polarization filter design based on plasmonic photonic crystal fiber. J. Lightwave Technol. **33**(13), 2868–2875 (2015)
8. S.I. Azzam, M.F.O. Hameed, R.E.A. Shehata, A.M. Heikal, S.S.A. Obayya, Multichannel photonic crystal fiber surface plasmon resonance based sensor, Optic. Quant. Electron. **48**(2) (2016)
9. F.F.K. Hussain, A.M. Heikal, M.F.O. Hameed, J. El-Azab, W.S. Abdelaziz, S.S.A. Obayya, Dispersion characteristics of asymmetric channel plasmon polariton waveguides. IEEE J. Quant. Electron. **50**(6), 474–482 (2014)
10. A.M. Heikal, M.F.O. Hameed, S.S.A. Obayya, Coupling characteristic of a novel hybrid long-range plasmonic waveguide including bends. IEEE J. Quant. Electron. **49**(8), 621–627 (2013)
11. A.M. Heikal, M.F.O. Hameed, S.S.A. Obayya, Improved trenched channel plasmonic waveguide. J. Lightwave Technol. **31**(13), 2184–2191 (2013)
12. S. Maier, Plasmonics: metal nanostructures for subwavelength photonic devices. IEEE J. Sel. Top. Quant. Electron. **12**(6), 1214–1220 (2006)
13. R. Zia, M. Selker, P. Catrysse, M. Brongersma, Geometries and materials for subwavelength surface plasmon modes. J. Opt. Soc. Am. A **21**(12), 2442 (2004)
14. J. Takahara, S. Yamagishi, H. Taki, A. Morimoto, T. Kobayashi, Guiding of a one-dimensional optical beam with nanometer diameter. Opt. Lett. **22**(7), 475 (1997)
15. T. Koo, S. Chan, A. Berlin, Single-molecule detection of biomolecules by surface-enhanced coherent anti-Stokes Raman scattering. Opt. Lett. **30**(9), 1024 (2005)
16. B. Rothenhäusler, W. Knoll, Surface–plasmon microscopy. Nature **332**(6165), 615–617 (1988)

17. M. Quinten, A. Leitner, J. Krenn, F. Aussenegg, Electromagnetic energy transport via linear chains of silver nanoparticles. Opt. Lett. **23**(17), 1331 (1998)
18. Z. Liu, Y. Wang, J. Yao, H. Lee, W. Srituravanich, X. Zhang, Broad band two-dimensional manipulation of surface plasmons. Nano Lett. **9**(1), 462–466 (2009)
19. S. Maier, M. Brongersma, P. Kik, S. Meltzer, A. Requicha, H. Atwater, Plasmonics-A route to nanoscale optical devices. Adv. Mater. **13**(19), 1501–1505 (2001)
20. M.H. Muhammad, M.F.O. Hameed, S.S.A. Obayya, Broadband absorption enhancement in periodic structure plasmonic solar cell. Opt. Quant. Electron. **47**(6), 1487–1494 (2015)
21. J. Burke, G. Stegeman, T. Tamir, Surface-polariton-like waves guided by thin, lossy metal films. Phys. Rev. B **33**(8), 5186–5201 (1986)
22. S. Al-Bader, M. Imtaar, Azimuthally uniform surface-plasma modes in thin metallic cylindrical shells. IEEE J. Quant. Electron. **28**(2), 525–533 (1992)
23. S. Al-Bader, M. Imtaar, Optical fiber hybrid-surface plasmon polaritons. J. Opt. Soc. Am. B **10**(1), 83 (1993)
24. P. Berini, Plasmon-polariton modes guided by a metal film of finite width bounded by different dielectrics. Opt. Express **7**(10), 329 (2000)
25. P. Berini, Plasmon-polariton waves guided by thin lossy metal films of finite width: Bound modes of asymmetric structures. Phys. Rev. B, **63**(12) (2001)
26. R. Charbonneau, P. Berini, E. Berolo, E. Lisicka-Shrzek, Experimental observation of plasmon–polariton waves supported by a thin metal film of finite width. Opt. Lett. **25**(11), 844 (2000)
27. A. Degiron, C. Dellagiacoma, J. McIlhargey, G. Shvets, O. Martin, D. Smith, Simulations of hybrid long-range plasmon modes with application to 90° bends. Opt. Lett. **32**(16), 2354 (2007)
28. T. Holmgaard, J. Gosciniak, S. Bozhevolnyi, Long-range dielectric-loaded surface plasmon-polariton waveguides. Opt. Express **18**(22), 23009 (2010)
29. J. Guo, R. Adato, Control of 2D plasmon-polariton mode with dielectric nanolayers. Opt. Express **16**(2), 1232 (2008)

Chapter 4
Introduction to Silicon Photonics

Mohamed Farhat O. Hameed, A. Samy Saadeldin, Essam M. A. Elkaramany and S. S. A. Obayya

Abstract This chapter reviews the fundamentals of the silicon on insulator (SOI) technology due to its advantages. The chapter starts with an introduction to the SOI followed by the different waveguides based on the SOI technology and their advantages. Further, the novel platforms that have been recently emerging beside the SOI are also presented. Finally, various fabrication processes for performing the SOI wafer are introduced in more detail.

Keywords Silicon on insulator · SOI · Slot waveguides · Silicon on sapphire Silicon on nitride · Silicon on calcium fluoride

M. F. O. Hameed (✉)
Center for Photonics and Smart Materials and Nanotechnology Engineering Program, Zewail City of Science and Technology, October Gardens, 6th of October City, Giza, Egypt
e-mail: mfarahat@zewailcity.edu.eg

M. F. O. Hameed
Mathematics and Engineering Physics Department, Faculty of Engineering, Mansoura University, Mansoura, Egypt

A. S. Saadeldin
Electronics and Communication Engineering Department, Akhbar Elyom Academy, 6th of October City, Egypt

A. S. Saadeldin · E. M. A. Elkaramany
Faculty of Engineering, Engineering Mathematics and Physics Department, Cairo University, Giza, Egypt

S. S. A. Obayya
Centre for Photonics and Smart Materials, Zewail City of Science and Technology, October Gardens, 6th of October City, Giza, Egypt
e-mail: sobayya@zewailcity.edu.eg

S. S. A. Obayya
Electronics and Communication Engineering Department, Faculty of Engineering, Mansoura University, Mansoura, Egypt

© Springer International Publishing AG, part of Springer Nature 2019

M. F. O. Hameed and S. Obayya (eds.), *Computational Photonic Sensors*, https://doi.org/10.1007/978-3-319-76556-3_4

4.1 Silicon on Insulator (SOI): Introduction

Silicon (Si) is the greatest semiconductor material due to its advantages such as high-quality native oxide, stable under high temperature, easy to form a single crystal with high purity, available in abundance, and superior electrical and thermal characteristics. Additionally, the SiO_2 can be successfully grown on a silicon layer. Further, the Si is the most predominant semiconductor material for electronic applications. Additionally, for the telecommunication wavelengths, the silicon leads to a very high optical confinement when combined into waveguiding structures.

SOI wafers consist of multilayer semiconductor/dielectric structures that enhance the performance of the advanced Si devices. The SOI wafers usually comprise of a top layer of single crystalline silicon separated by an insulating layer (usually SiO_2), from the bulk substrate as shown in Fig. 4.1 or directly supported by an insulating substrate. The thickness of the crystalline silicon thin layer ranges from 10 nm to a few micrometers, depending on the required application. However, the SiO_2 layer which is usually called buried oxide (BOX) has a thickness range from 50 nm to several hundreds of nm.

SOI devices and circuits have many advantages compared to their equivalent of bulk silicon. Almost the factor that leads to these advantages is the complete dielectric isolation of the devices from one another. This will prevent the penetration of the optical modes to the below silicon substrate. Further, the SOI is compatible with CMOS integrated circuit (IC). Therefore, the integration of photonic devices into CMOS IC can be fabricated. In this regard, low propagation loss single-mode waveguides have been reported in SiO_2 and Si/SiO_2 structures. Currently, many integrated circuit companies use SOI wafers for their advanced performance. Digital logic circuits, such as microprocessors, run faster in SOI than in bulk Si for the same supply voltage. Alternatively, power consumption of SOI chips can be reduced by lowering their operating voltage, while still keeping the clock rate. The SOI literature is very extensive, and it includes many books and review articles including materials, technology, and applications [1–6]. In this context, the SOI technology is widely used in many applications such as large volume integrated circuit (LVIC), power integrated circuits, microelectromechanical systems

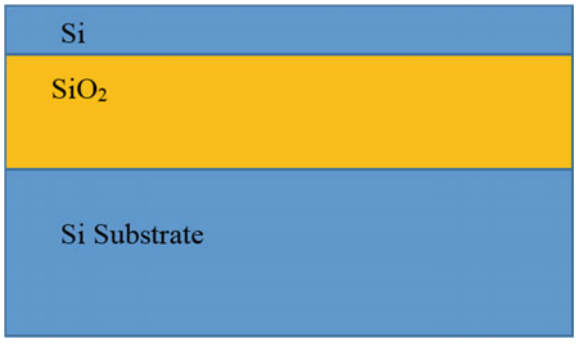

Fig. 4.1 Silicon on insulator (SOI) structure

(MEMS), integrated optics, high-temperature applications, and the high-performance applications including microprocessors, digital signal processors (DSPs). Recently, SOI technology is widely used in nanophotonic applications where optical devices such as optical waveguides, optical transistors, and optical logic circuits are now available. With optical devices technology, the road toward optical integrated circuits and optical computing is possible. Unlimited speeds, huge storage density, minimal crosstalk, and interference are some of the advantages that we expect in the future.

The optical circuits have been designed in 1969 by Stewart Miller who investigated a miniature form of laser beam circuitry [7]. The proposed super chip has a set of integrated optical components, which have the ability to transfer us to the light generation. This includes guiding, modulation, manipulation, detection, and amplification. Starting from mid-1980, the research effort increased rapidly toward the design and fabrication of optical IC components [8–10]. The following section includes the main features of optical waveguide, which is the most important elements of integrated optical system.

4.2 Optical Waveguide Development

The optical waveguide is one of the main elements of any integrated optical system. Starting from the latest years in 1960s, and over 1970s and 1980s, a large number of researches have been reported on the planar optical waveguides [11–18]. Soref et al. proposed a single crystal silicon waveguide [19, 20]. However, these devices were fabricated using highly doped silicon substrates, while other substrate configurations such as Silicon on Sapphire (SOS) [21] and SOI [22, 23] were employed subsequently. In the late 1980s and early 1990s, the silicon waveguide started to make use of the fabrication methods in the semiconductor industry. In this context, separation by implantation of oxygen (SIMOX) substrates and bond and etch-back SOI (BSOI and BESOI) [24, 25] have been used where different early optical waveguide designs were produced [22, 26–29]. In [28], Davies et al. have presented an optical waveguide by SIMOX technology with 4 dB/cm measured loss. Further, multiple layer waveguide has been reported using SIMOX technique in [23, 29]. Although some of the initial work yielded very large losses, the loss was rapidly decreased to respectable levels. Weiss et al. [30] reported a 2 μm thick planar waveguide with 30 dB/cm losses in SIMOX structure. In order to reduce the loss, many attempts were done by Rickman et al. [31] based on the BOX thickness.

In [32], a planar waveguide of thickness 0.2 μm with a 0.5 μm BOX layer thickness was reported with losses less than 1 dB/cm. The coupling loss for Si layer of few microns can be decreased by increasing the BOX layer thickness greater than 0.4 μm. Starting from the early 1990s, the optical loss was decreased rapidly. In 1991 [33], a silicon rib waveguide with 0.4 dB/cm loss was presented. Further, by 1994 [34], the loss was decreased to a similar level of pure Si for transverse electric (TE) polarized light at a wavelength of 1.5 μm. Consequently, the Si is a practicable

waveguiding material with low propagation loss. In these early investigations, most of the work was carried out on relatively large waveguides with several microns in cross-sectional dimensions [35, 36]. However, such very small waveguides have very high losses. The high loss is due to the weak confinement through the waveguides and/or highly surface roughness. Starting from 2000s, the researchers aimed to design micro- and nanophotonics circuits. The coupling of the light to these small waveguides is still a problem, particularly for very small, submicron, waveguides [37–43]. Most of the applications require a single-mode optical waveguide. In order to obtain a single-mode planar SOI-based waveguides, the thickness of the over layer should equal to several hundred nanometers. The geometrical constraints for implementing a large cross-sectional single-mode rib waveguides were determined by Petermann et al. [44]. Additionally, Soref et al. [45] have reported the cross-sectional dimensions of a single-mode rib waveguide as follows,

$$\frac{a}{b} \leq 0.3 + \frac{r}{\sqrt{1-r^2}} \left(assuming\, 2b\sqrt{n_1^2 - n_2^2} \geq 1 \right) \tag{4.1}$$

where a, b, r, n_1, and n_2 are defined in Fig. 4.2. Further, λ is the light wavelength in free space. This work was realized based on SOI by Rickman et al. [34, 35]. The geometrical constraints for single-mode waveguides have attracted the attention of researchers again as reported in [46–48]. Additionally, the polarization dependence of submicron waveguides is investigated [49].

Recently, the silicon photonics offers a very inexpensive strongly integrated electronic-photonic platform, based on the advanced silicon technology [50–52]. This platform can collect an ultra-compact photonic devices and electronic circuits. The required optical waveguide should have properties that can combine photonic devices together like wavelength filters and modulators. In addition, the propagation loss is another important parameter that should be as low as possible to construct and integrate these photonic functions. The following requirements must be

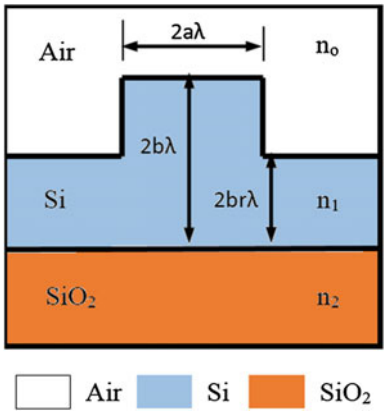

Fig. 4.2 Single-mode SOI rib waveguide

obtained for the electronic–photonic integration, which is the most important merit of silicon photonics:

- Waveguides should be implemented with Si electronic devices on the same platform or on Si substrate.
- The fabrication processes of the waveguide should not be harm for electronic devices and vice versa.
- Waveguide materials must be compatible with Si electronics.
- The interference of the geometrical criteria should be isolated between photonic layout and electronic layout.

4.3 Slot Waveguide Based on Silicon on Insulator

The slot waveguide is one of the most usable waveguides in the last decade due to the strong confinement of the light in the low index region [53]. The slot waveguide consists [54] of two strips waveguides separated by a distance called slot region. The two strips have refractive index higher than that of the slot region as shown in Fig. 4.3. It is evident from this figure that the slot region is vertically aligned between the two strips waveguide. Therefore, it is also called vertical slot waveguide, where n_1 refers to the high index region while n_2 indicates the low index region (slot region) and n_3 depicts the cladding region, which surrounds the slot waveguide.

The basic working principle of the slot waveguide is based on the boundary condition of the electric field at materials interface with high index contrast. The boundary condition of the normal component of the electric field at material interface is given by:

$$D_{n1} = D_{n2} \tag{4.2}$$

$$\frac{E_{n1}}{E_{n2}} = \frac{\varepsilon_2}{\varepsilon_1} \tag{4.3}$$

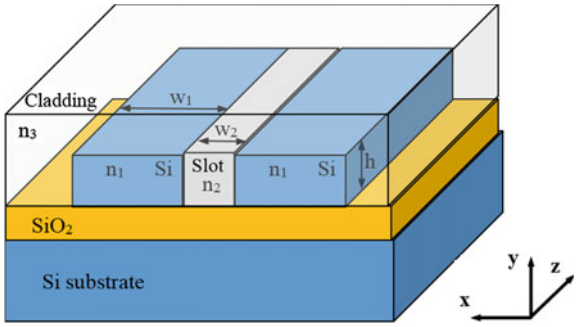

Fig. 4.3 Slot waveguide based on SOI

where D is the electric displacement field, E is the electric field, ε is the dielectric constant, n indicates the normal component, and 1 and 2 refer to high index region and low index region, respectively.

Since $\varepsilon = n^2$, and due to the high index contrast ($n_1 \gg n_2$), the E_{n2} will be much larger than E_{n1}, i.e., $E_{n2} \gg E_{n1}$. Given that the slot dimension is comparable to the exponential decay length of the dominant mode of the guided-wave structure, the resulting E-field normal to the high index contrast interfaces is enhanced in the slot and remains high across it. The slot waveguide offers much higher power density than that in the high index regions. Since wave propagation is due to total internal reflection, there is no interference effect involved and the slot structure exhibits very low wavelength sensitivity [50]. Figure 4.4 shows the norm of the electric field distribution of a SOI slot waveguide with a SiO_2 filled 50 nm wide slot region for (a) TE and (b) TM mode, respectively, at an operating wavelength $\lambda = 1550$ nm. The Comsol Multiphysics software [55] based on full vectorial finite element method is used for calculating the modes shown in Fig. 4.4. It is evident from this figure that the TE mode has stronger confinement in the slot region than TM mode due to the discontinuity of the normal component (x-component in this case) of the electric field at the high index contrast interface. Figure 4.5 shows the norm of the electric field plot of the TE mode along the x-axis at the center of the waveguide.

Multiple slot regions in the same guided-wave structure have also been proposed in order to increase the optical field in the low refractive index regions [56]. The horizontal slot waveguide shown in Fig. 4.6 can be also used to obtain a strong confinement in the slot region for TM mode [57]. In this regard, the strong light confinement mode is the TM mode because the normal component of the electric field now becomes the y-component. Figure 4.7 depicts the norm of the electric field distribution of the TM mode for the SOI horizontal slot waveguide at $\lambda = 1550$ nm.

The slot waveguides have many advantages over conventional waveguides such as high E-field amplitude, high optical power, and high optical intensity in low index materials which leads to strong interaction between fields and surrounding

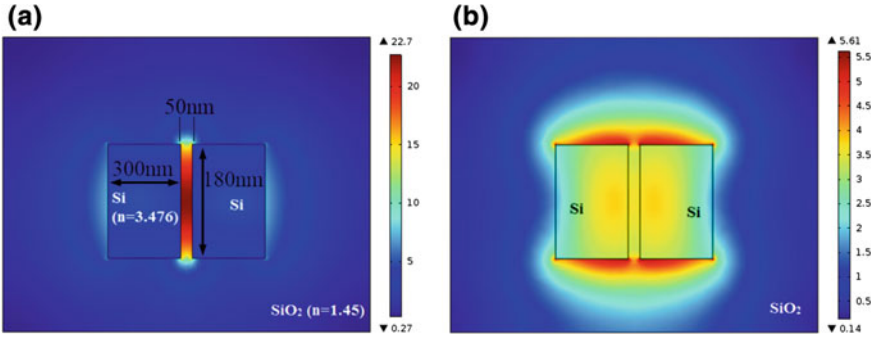

Fig. 4.4 Norm of the E-field distribution at wavelength 1550 nm for **a** TE mode and **b** TM mode

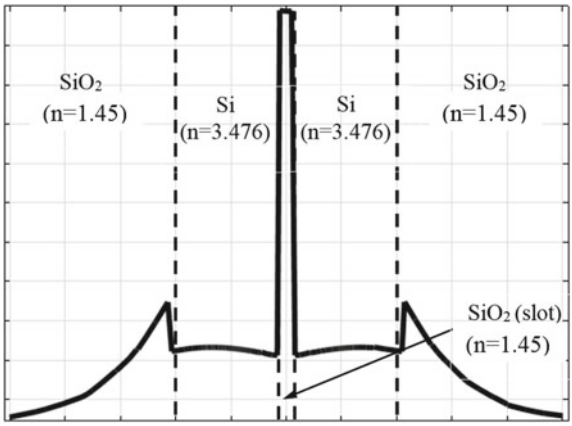

Fig. 4.5 Norm of the electric field of the TE mode along x-axis

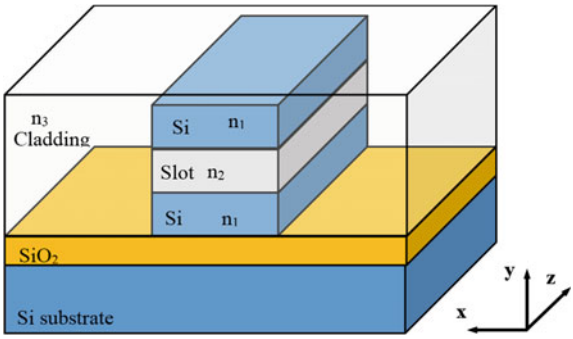

Fig. 4.6 Horizontal slot waveguide based on SOI

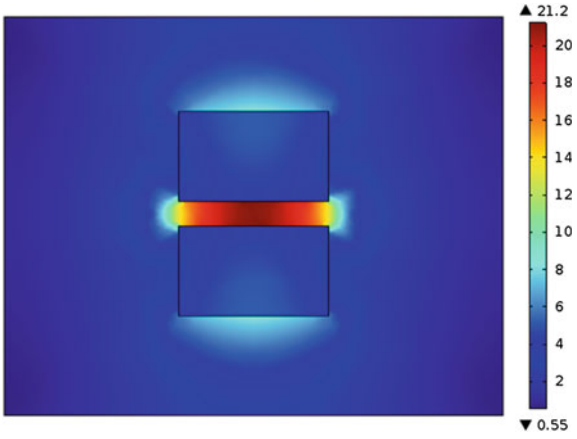

Fig. 4.7 Norm of the E-field distribution at wavelength 1550 nm for TM mode

materials. Therefore, the slot waveguide can be used in many applications with high efficiency such as all-optical switching [58], optical amplification [59], and polarization handling devices [60] on integrated photonics. Further, the slot waveguide can be used to produce highly sensitive optical sensing devices [61] or to enhance the efficiency of near-field optics probes.

4.4 Recent Technologies in Photonic Platforms

Novel platforms have been newly reported due to different imperfections of SOI photonics [62]. These shortcomings are due to the use of:

- Si top layer as a waveguide core.
- SiO_2 lower cladding layer.

To overcome the first group of imperfections, many heterogeneous platforms such as chalcogenide glass, silicon nitride, and semiconductors have been proposed to replace the Si top layer of SOI [63–66]. However, silicon has several key advantages, which collectively set it apart from other materials. Namely, it allows high index contrast, high stability as a monocrystalline material with excellent thermal and mechanical properties; offers a transparency window bridging the near-to-mid-IR with no absorption peaks interrupting it; and it can be easily integrated with electronics.

The BOX layer can produce high optical loss in the mid-IR range at $\lambda = 3$ μm and above 4 μm [67], so, it is not an ideal platform for the integrated photonics in mid-IR range. Such high loss can be reduced by increasing the top Si device layer at the expense of increasing the system size. Therefore, the solution of the shortcomings due to the SiO_2 BOX layer and alternative platforms such as silicon nitride, sapphire, and lithium niobate has been investigated for Si photonics. The Si core can be grown on the top of the alternative substrate which acts as a mechanical support and lower cladding layer. Additionally, these alternative platforms have low optical loss in mid-IR range, high thermal conductivity, enhanced dispersion engineering, may have single polarization behavior, and they are easy for fabrication. Another SOI platform for mid-IR applications is silicon on silicon [68]. In the fact, before the SOI platform, the doped silicon on silicon was used as Si photonics platform [69]. However, this platform was unattractive due to the very low index contrast with free-carrier loss. The following subsections present various encouraging high contrast platforms.

4.4.1 Silicon on Sapphire (SOS)

Silicon on Sapphire (SOS) is one of SOI semiconductor technologies. It is formed by depositing a thin layer of silicon onto a sapphire wafer at high temperature. At first, the sapphire wafers of the SOS are grown as a large crystal in a controlled environment to get an extremely pure single crystal of sapphire, which is cut at an angle of about 60° along the "R-plane" which is the (1102) plane. This plane has a remarkable compatibility with the plane (100) in the silicon crystal, so that a thin layer of silicon can be easily deposited onto sapphire wafer at high temperature.

Practical applications of SOS started in 1960 when researchers at the RCA Laboratories in Princeton, New Jersey, worked on its fabrication. The researchers also realized the speed and low-power benefits of SOS which can be used for commercial applications. Perhaps, the first published report about SOS is by Harold Manasevit and William Simpson at 1964 [70].

The Si-based electronics usually uses sapphire (Al_2O_3) substrate due to its insulating properties and its inherent resistance to radiation [68]. Therefore, it was first used in aerospace and military applications. Also, sapphire offers transparency up to roughly 5 μm, so it can be used for applications in mid-IR range and high-performance radio frequency (RF) applications [71–79].

Further, SOS substrates are obtainable at relatively inexpensive cost for large or small amount and can be bought in small amount even in a single-unit quantity. Consequently, the SOS will be most attractive substrate for laboratory research to investigate more advanced applications. Additionally, the processing of the SOS substrate is strongly similar to that of the SOI, and hence, the same tools and process can be used.

There are some other Si-based platforms available with several merits over SOS, as may be seen later. However, these other Si-based platforms require important post-processing or preparation for the substrate. Thus, SOS will likely stand on its own for some time in the domain of shorter-wavelength studies in the mid-IR. The following subsections will review some of the new substrates for Si photonics in mid-IR range, which permit propagation at longer wavelengths than that with SOS substrates.

4.4.2 Silicon on Nitride (SON)

The BOX layer (SiO_2) here will be replaced with the silicon nitride which offers transparency up to $\lambda = 6.7$ μm. This new platform is called silicon on nitride (SON) which has been reported and investigated theoretically in [80, 81]. The silicon nitride has a relatively low refractive index (~ 2) which offers a strong confinement which is necessary for practical operation at longer wavelengths. However, the higher refractive index of cladding silicon nitride ($n > 2$, depending on silicon fraction) compared with sapphire ($n \sim 1.7$) also reduces the available

photonic band gap in photonic crystal structures. Furthermore, at $\sim\lambda = 3.4$ μm, SON waveguides are also more lossy (5.2 dB/cm) compared to SOS ridge waveguides (2.1 dB/cm) [82]. The fabrication steps of the SON can be summarized as follows: silicon nitride (SiN_x) is deposited on SOI wafer, and then, a spin on glass assisted bonding is used between SiO_2 and the SiN_x followed by splitting the backside. Finally, the Si device is placed on the top of SiN_x layer (buried layer).

4.4.3 Silicon on Calcium Fluoride

Calcium fluoride (CaF_2) is another substrate for mid-IR range that has been investigated (transparent up to $\lambda = 8$ μm wavelength). Chen et al. [83], in 2014, reported the first experimentally study for silicon on calcium fluoride. The paring and compressing with a flexible temporary substrate are the methodology to transfer the silicon layer into a final CaF_2 substrate, with an area of 1.5×0.8 cm^2. This shows encouraging elementary performance for crystalline silicon on CaF_2 as a platform.

4.5 Fabrication Methods

This section quickly addresses the most common technologies of fabrication of the SOI wafers. Several novel techniques for fabricating SOI wafers have been developed starting from 1970 [84]. The most common methods are separation by implantation of oxygen (SIMOX), bonded silicon on insulator (BSOI), epitaxial layer transfer (Eltran®), and Smart Cut™ technologies. This section also summarizes the fabrication steps for each method.

4.5.1 Separation by IMplantation of OXygen (SIMOX) Technology

The SIMOX technology is based on using the oxygen ion beam and very high-temperature annealing (T > 1300 °C) to implant a (SiO_2) buried oxide layer (BOX) [85–90]. The manufacturing steps are illustrated in Fig. 4.8.

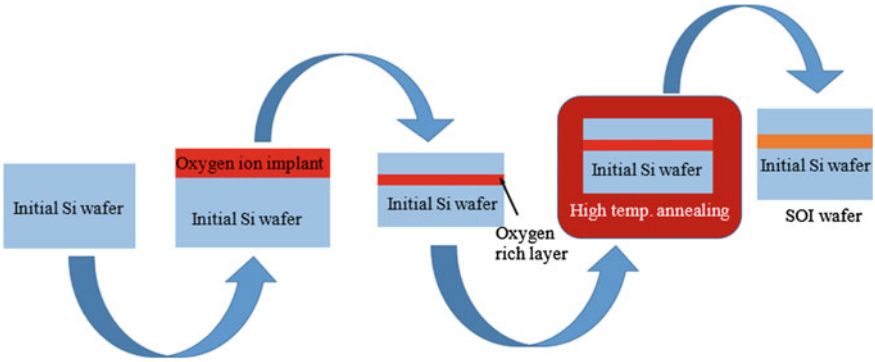

Fig. 4.8 Typical steps used in SIMOX process

4.5.2 *Bonded Silicon on Insulator (BSOI) and Bond and Etch-Back Silicon on Insulator (BESOI) Processes*

These technologies depend on the direct bonding of silicon wafers prepared with hydrophilic oxide surfaces (native, chemical deposited, or thermally grown oxides) [91–94]. High-temperature annealing processes were tuned to strengthen adhesion after the direct bonding.

Figure 4.9 shows the steps for SOI fabrication by BSOI method. The steps can be summarized as follows:

- Cleaning and conditioning the two initial wafers surfaces (wafer A and wafer B).
- Growing (thermally) or depositing an oxide layer on the surface of wafer A and/or wafer B.
- Preparing the surfaces for direct bonding by smoothing and cleaning.
- Direct bonding and annealing to strengthen adhesion.
- Thinning by grinding, or chemical processes (wet or dry etching), or lift-off techniques.

4.5.3 *Eltran® Process*

The development of the epitaxial layer transfer technique (Eltran®) was done by Canon for SOI fabrication [95]. It uses the porous Si layer and their mechanical and structural properties besides epitaxy and direct wafer bonding technologies. The improvement of the growth and surface preparation of bulk Si wafer for

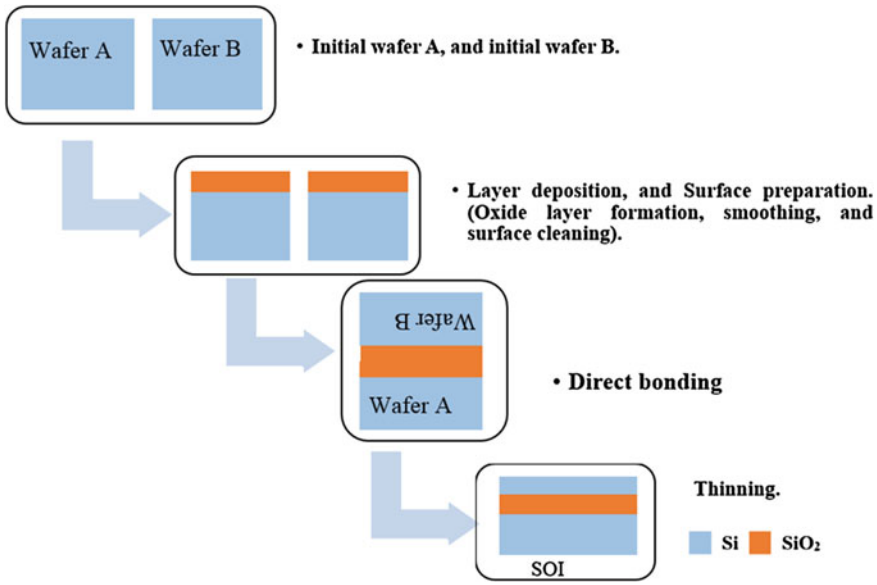

Fig. 4.9 Typical steps used in BSOI process

microelectronics applications has attracted the researchers' attention for several decades. So it is applicable now to perform very high goodness wafers in large diameters.

The use of the epitaxial layers is a way to manufacture SOI wafer with low threading defects densities. The Eltran® technique to perform a SOI wafer as shown in Fig. 4.10 can be summarized in the following steps:

- The porous Si layers are formed on the initial wafer surface.
- Growing high-quality epitaxial layers on top of these porous layers.

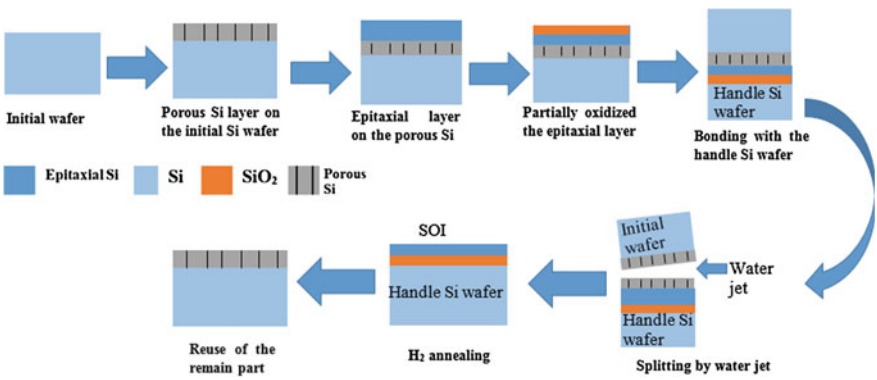

Fig. 4.10 Eltran® process as described to produce SOI wafers

- Partially oxidizing the epitaxial layers thermally.
- Bonding the initial wafer to the final handling Si wafer.
- Splitting the porous Si layer by water jet.
- Smoothing the SOI wafer by H_2 annealing. (the rest part of the initial wafer can be reused).

One of the advantages of the Eltran® SOI wafers is the highly controllable of the epitaxial layer thickness with a few nanometers to several micrometers. This controllable thickness depends on the changing of the conditions of the growth. Also, the buried oxide layer thickness can be controlled independently on the SOI thickness. Another advantage of the Eltran® is using the H_2 annealing process which makes the SOI layer surface thin and smooth. This process has thickness uniformity greater than the conventional chemical mechanical polishing (CMP) which produces unacceptable variation in the thickness.

4.5.4 *Smart Cut™ Technology*

The principle of this technique is the direct bonding between two wafers. Figure 4.11 shows the manufacturing steps of a SOI wafer by Smart Cut™, which can be summarized as follows [96, 97]:

- Oxidizing the first Si wafer (wafer A) thermally.
- Inducing a buried weak zone by ion implantation (hydrogen or helium) in the oxidized wafer A.
- Bonding the implanted wafer A to the second wafer (wafer B) after cleaning. The second wafer is preferred to be a thick layer hard enough to allow splitting.

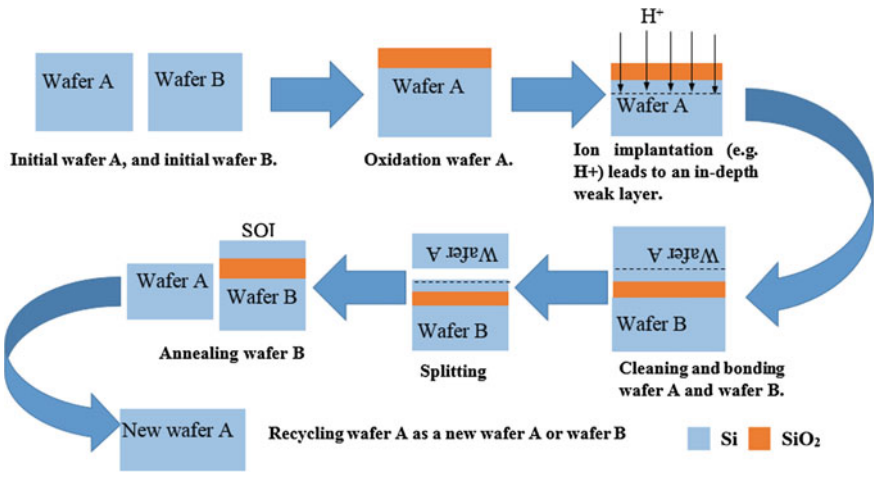

Fig. 4.11 Smart Cut™ process for producing SOI wafers

- Splitting the weakened zone in the wafer A, in order to grow a thin layer onto the wafer B.
- Cleaning the surfaces after splitting. (the rest part of the wafer A (the separated part) can be reused).

The smart Cut^{TM} technique has many merits, such as perfect similarity in thickness and the high quality of the grown layer. Additionally, the rest of the first wafer can be recycled as a new wafer. Besides, Smart Cut^{TM} is a highly generic and flexible technique because it can be used to perform a broad set of single crystal layer on top of many various supports.

References

1. G.K. Celler, Silicon-on-insulator structures: fabrication. Encycl. Adv. Mater. (1994)
2. J.P. Colinge, Soi materials, in *Silicon-on-Insulator Technology: Materials to VLSI*, 2nd edn. (Springer, US, 1997)
3. B. Aspar, A.J. Auberton-Hervé, Silicon wafer bonding technology for VLSI and MEMS applications, in *Inspec, Emis processing*, vol. 1 (2002)
4. A. Marshall, S. Natarajan, *SOI Design* (Springer Science & Business Media, 2002)
5. M. Alexe, U. Gösele (eds.), *Wafer Bonding: Applications and Technology*, vol. 75. (Springer Science & Business Media, 2013)
6. O. Kononchuk, B.Y. Nguyen, *Silicon-on-Insulator (SOI) Technology: Manufacture and Applications* (Elsevier, 2014)
7. S.E. Miller, Integrated optics: an introduction. Bell Labs Tech. J. **48**(7), 2059–2069 (1969)
8. G.T. Reed, A.P. Knights, *Silicon Photonics: An Introduction* (Wiley, 2004)
9. R. Soref, The past, present, and future of silicon photonics. IEEE J. Sel. Top. Quant. Electron. **12**(6), 1678–1687 (2006)
10. L. Pavesi, D.J. Lockwood (eds.), *Silicon Photonics III: Systems and Applications*, vol. 122, (Springer Science & Business Media, 2016)
11. J.N. Polky, G.L. Mitchell, Metal-clad planar dielectric waveguide for integrated optics. JOSA **64**(3), 274–279 (1974)
12. J. Nezval, WKB approximation for optical modes in a periodic planar waveguide. Opt. Commun. **42**(5), 320–322 (1982)
13. H.M. De Ruiter, Limits on the propagation constants of planar optical waveguide modes. Appl. Opt. **20**(5), 731–732 (1981)
14. T. Tamir, Leaky waves in planar optical waveguides. Nouvelle Revue d'Optique **6**(5), 273 (1975)
15. F. Payne, Generalized transverse resonance model for planar optical waveguides, in *Tenth European Conference* on *Optical Communications, ECOC '84* (1984)
16. M. Kawachi, M. Yasu, T. Edahiro, Fabrication of SiO_2-TiO_2 glass planar optical waveguides by flame hydrolysis deposition. Electron. Lett. **19**(15), 583–584 (1983)
17. O. Hanaizumi, M. Miyagi, S. Kawakami, Low radiation loss Y-junctions in planar dielectric optical waveguides. Opt. Commun. **51**(4), 236–238 (1984)
18. H. Jerominek, Z. Opilski, J. Kadziela, Some elements of integrated-optics circuits based on planar gradient glass waveguides. Opt. Appl. **13**(2), 159–168 (1983)
19. R. Soref, J. Larenzo, All-silicon active and passive guided-wave components for $\lambda = 1.3$ and 1.6 μm. IEEE J. Quant. Electron. **22**(6), 873–879 (1986)
20. R.A. Soref, J.P. Lorenzo, Single-crystal silicon: a new material for 1.3 and 1.6 μm integrated-optical components. Electron. Lett. **21**(21), 953–954 (1985)

21. D.J. Albares, R.A. Soref, Silicon-on-Sapphire waveguides, in *Proceedings of SPIE: Integrated Optical Circuit Engineering IV*, vol. 704 (1987), pp. 24–25
22. E. Cortesi, F. Namavar, R.A. Soref, Novel silicon-on-insulator structures for silicon waveguides, in SOS/*SOI Technology Conference* (IEEE, Oct 1989), p. 109
23. F. Namavar, E. Cortesi, R.A. Soref, P. Sioshansi, On the formation of thick and multiple layer SIMOX structures and their applications, in *Ion Beam Processing of Advanced Electronic Materials Symposium* (1989), p. 147
24. G.T. Reed, L. Jinhua, C.K. Tang, L. Chenglu, P.L.F. Hemment, A.G. Rickman, Silicon on insulator optical waveguides formed by direct wafer bonding. Mater. Sci. Eng., B **15**(2), 156–159 (1992)
25. A.F. Evans, D.G. Hall, W.P. Maszara, Propagation loss measurements in silicon-on-insulator optical waveguides formed by the bond-and-etchback process. Appl. Phys. Lett. **59**(14), 1667–1669 (1991)
26. N.M. Kassim, H.P. Ho, T.M. Benson, D.E. Daveias, Assessment of SIMOX material by optical waveguide losses, in *ESSDERC '90 on 20th European Solid State Device Research Conference* (IEEE, Oct 1990), pp. 5–8
27. B.L. Weiss, G.T. Reed, The transmission properties of optical waveguides in SIMOX structures. Opt. Quant. Electron. **23**(8), 1061–1065 (1991)
28. D.E. Davies, M. Burnham, T.M. Benson, N.M. Kassim, M. Seifouri, Optical waveguides and SIMOX characterisation, in *SOS/SOI Technology Conference* (IEEE, Oct 1989), pp. 160–161
29. R.A. Soref, E. Cortesi, F. Namavar, L. Friedman, Vertically integrated silicon-on-insulator waveguides. IEEE Photonics Technol. Lett. **3**(1), 22–24 (1991)
30. B. Weiss, G. Reed, S. Toh, R. Soref, F. Namavar, Optical waveguides in SIMOX structures. IEEE Photon. Technol. Lett. **3**(1), 19–21 (1991)
31. A. Rickman, G.T. Reed, B.L. Weiss, F. Namavar, Low-loss planar optical waveguides fabricated in SIMOX material. IEEE Photon. Technol. Lett. **4**(6), 633–635 (1992)
32. B.N. Kurdi, D.G. Hall, Optical waveguides in oxygen-implanted buried-oxide silicon-on-insulator structures. Opt. Lett. **13**(2), 175–177 (1988)
33. J. Schmidtchen, A. Splett, B. Schuppert, K. Petermann, Low loss integrated-optical rib-waveguides in SOI, in *1991 IEEE International Proceedings of the SOI Conference* (IEEE, 1991), pp. 142–143
34. A.G. Rickman, G.T. Reed, F. Namavar, Silicon-on-insulator optical rib waveguide loss and mode characteristics. J. Lightwave Technol. **12**(10), 1771–1776 (1994)
35. A.G. Rickman, G.T. Reed, Silicon-on-insulator optical rib waveguides: loss, mode characteristics, bends and y-junctions. IEEE Proc. Optoelectron. **141**(6), pp. 391–393 (1994)
36. C.K. Tang, A.K. Kewell, G.T. Reed, A.G. Rickman, F. Namavar, Development of a library of low-loss silicon-on-insulator optoelectronic devices. IEEE Proc. Optoelectron. **143**(5), 312–315 (1996)
37. A.G. Rickman, G.T. Reed, F. Namavar, Silicon-on-insulator optical rib waveguide circuits for fiber optic sensors. Proc. SPIE Distrib. Multipl. Fiber Opt. Sens. III **2071**, 190–196 (1993)
38. A. Sure, T. Dillon, J. Murakowski, C. Lin, D. Pustai, D.W. Prather, Fabrication and characterization of three-dimensional silicon tapers. Opt. Express **11**(26), 3555–3561 (2003)
39. Z. Lu, P. Yao, S. Venkataraman, D. Pustai, C. Lin, G. Schneider, J. Murakowski, S. Shi, D.W. Prather, June. Fiber-to-waveguide evanescent coupler for planar integration of silicon optoelectronic devices, in *Photonics Packaging and Integration IV*, vol. 5358 (International Society for Optics and Photonics, 2004), pp. 102–111
40. G.Z. Masanovic, V.M. Passaro, G.T. Reed, Dual grating-assisted directional coupling between fibers and thin semiconductor waveguides. IEEE Photonics Technol. Lett. **15**(10), 1395–1397 (2003)
41. V.R. Almeida, R.R. Panepucci, M. Lipson, Nanotaper for compact mode conversion. Opt. Lett. **28**(15), 1302–1304 (2003)
42. M. Lipson, Overcoming the limitations of microelectronics using Si nanophotonics: solving the coupling, modulation and switching challenges. Nanotechnology **15**(10), S622 (2004)

43. T. Shoji, T. Tsuchizawa, T. Watanabe, K. Yamada, H. Morita, Low loss mode size converter from 0.3 μm square Si wire waveguides to singlemode fibres. Electron. Lett. **38**(25), 1669–1670 (2002)
44. K. Petermann, Properties of optical rib-guides with large cross-section. Aeu Int. J. Electron. Commun. **30**(3), 139–140 (1976)
45. R.A. Soref, J. Schmidtchen, K. Petermann, Large single-mode rib waveguides in GeSi-Si and Si-on-SiO/sub 2. IEEE J. Quantum Electron. **27**(8), 1971–1974 (1991)
46. S.P. Pogossian, L. Vescan, A. Vonsovici, The single-mode condition for semiconductor rib waveguides with large cross section. J. Lightwave Technol. **16**(10), 1851–1853 (1998)
47. O. Powell, Single-mode condition for silicon rib waveguides. J. Lightwave Technol. **20**(10), 1851–1855 (2002)
48. O. Powell, Erratum to: Single-mode condition for silicon rib waveguides. J. Lightwave Technol. **21**(3), 868 (2003)
49. S.P. Chan, C.E. Png, S.T. Lim, G.T. Reed, V.M.N. Passaro, Single mode, polarisation independent waveguides in silicon-on-insulator. in *2004 Ist IEEE International Conference on Group Iv Photonics,* Jan 2004 (pp. 115–117)
50. T. Tsuchizawa, K. Yamada, H. Fukuda, T. Watanabe, J.I. Takahashi, M. Takahashi, T. Shoji, E. Tamechika, S.I. Itabashi, H. Morita, Microphotonics devices based on silicon microfabrication technology. IEEE J. Sel. Top. Quantum Electron. **11**(1), 232–240 (2005)
51. H. Yamada, T. Chu, S. Ishida, Y. Arakawa, Si photonic wire waveguide devices. IEEE J. Sel. Top. Quantum Electron. **12**(6), 1371–1379 (2006)
52. T. Chu, H. Yamada, S. Nakamura, M. Ishizaka, M. Tokushima, Y. Urino, S. Ishida, Y. Arakawa, Ultra-small silicon photonic wire waveguide devices. IEICE Trans. Electron. **92**(2), 217–223 (2009)
53. V.R. Almeida, Q. Xu, C.A. Barrios, M. Lipson, Guiding and confining light in void nanostructure. Opt. Lett. **29**(11), 1209–1211 (2004)
54. Q. Xu, V.R. Almeida, R.R. Panepucci, M. Lipson, Experimental demonstration of guiding and confining light in nanometer-size low-refractive-index material. Opt. Lett. **29**(14), 1626–1628 (2004)
55. https://www.comsol.com/
56. X. Tu, X. Xu, S. Chen, J. Yu, Q. Wang, Simulation demonstration and experimental fabrication of a multiple-slot waveguide. IEEE Photonics Technol. Lett. **20**(5), 333–335 (2008)
57. E. Jordana, J.M. Fedeli, P. Lyan, J.P. Colonna, P. Gautier, N. Daldosso, L. Pavesi, Y. Lebour, P. Pellegrino, B. Garrido, J. Blasco, Deep-UV lithography fabrication of slot waveguides and sandwiched waveguides for nonlinear applications. in *2007 4th IEEE International Conference on Group IV Photonics* (IEEE, Sept 2007), pp. 1–3
58. C.A. Barrios, High-performance all-optical silicon microswitch. Electron. Lett. **40**(14), 862–863 (2004)
59. C.A. Barrios, M. Lipson, Electrically driven silicon resonant light emitting device based on slot-waveguide. Opt. Express **13**(25), 10092–10101 (2005)
60. M.F.O. Hameed, R. Zaghloul, S.I. Azzam, S.S. Obayya, Ultrashort hybrid plasmonic transverse electric pass polarizer for silicon-on-insulator platform. Opt. Eng. **56**(1), 017107–017107 (2017)
61. M.F.O. Hameed, A.S. Saadeldin, E.M. Elkaramany, S.S. Obayya, label-free highly sensitive hybrid plasmonic biosensor for the detection of DNA hybridization. J. Lightwave Technol. **35**(22), 4851–4858 (2017)
62. J. Chiles, S. Fathpour, Silicon photonics beyond silicon-on-insulator. J. Opt. **19**(5), 053001 (2017)
63. B.J. Eggleton, B. Luther-Davies, K. Richardson, Chalcogenide photonics. Nat. Photonics **5**(3), 141–148 (2011)
64. Y.C. Chang, V. Paeder, L. Hvozdara, J.M. Hartmann, H.P. Herzig, Low-loss germanium strip waveguides on silicon for the mid-infrared. Opt. Lett. **37**(14), 2883–2885 (2012)

65. D.F. Logan, M. Giguere, A. Villeneuve, A.S. Helmy, Widely tunable mid-infrared generation via frequency conversion in semiconductor waveguides. Opt. Lett. **38**(21), 4457–4460 (2013)
66. P. Tai Lin, V. Singh, L. Kimerling, A. Murthy Agarwal, Planar silicon nitride mid-infrared devices. Appl. Phys. Lett. **102**(25), 251121 (2013)
67. R. Kitamura, L. Pilon, M. Jonasz, Optical constants of silica glass from extreme ultraviolet to far infrared at near room temperature. Appl. Opt. **46**(33), 8118–8133 (2007)
68. A. Sciuto, A. Alessandria, S. Libertino, S. Coffa, G. Coppola, Design, fabrication, and testing of an integrated Si-based light modulator: experimental evidence of plasma redistribution. in *Symposium on Integrated Optoelectronic Devices* (International Society for Optics and Photonics, Mar 2002), pp. 54–61
69. R. Soref, J. Larenzo, All-silicon active and passive guided-wave components for $\lambda = 1.3$ and 1.6 μm. IEEE J. Quant. Electron. **22**(6), 873–879 (1986)
70. H.M. Manasevit, W.I. Simpson, Single-Crystal Silicon on a Sapphire Substrate. J. Appl. Phys. **35**(4), 1349–1351 (1964)
71. M. Roser, S.R. Clayton, P.R. de La Houssaye, G.A. Garcia, High-mobility fully depleted thin-film SOS MOSFET's. IEEE Trans. Electron Devices **39**(11), 2665–2666 (1992)
72. E. Culurciello, *Silicon-on-sapphire circuits and systems* (McGraw-Hill Inc., 2009)
73. T. Baehr-Jones, A. Spott, R. Ilic, A. Spott, B. Penkov, W. Asher, M. Hochberg, Silicon-on-sapphire integrated waveguides for the mid-infrared. Opt. Express **18**(12), 12127–12135 (2010)
74. E.R. Dobrovinskaya, L.A. Lytvynov, V. Pishchik, *Sapphire: Material, Manufacturing, Applications* (Springer Science & Business Media, 2009)
75. F. Li, S.D. Jackson, C. Grillet, E. Magi, D. Hudson, S.J. Madden, Y. Moghe, C. O'Brien, A. Read, S.G. Duvall, P. Atanackovic, Low propagation loss silicon-on-sapphire waveguides for the mid-infrared. Opt. Express **19**(16), 15212–15220 (2011)
76. Z. Cheng, X. Chen, C.Y. Wong, K. Xu, C.K. Fung, Y.M. Chen, H.K. Tsang, Mid-infrared grating couplers for silicon-on-sapphire waveguides. IEEE Photonics J. **4**(1), 104–113 (2012)
77. Y. Zou, S. Chakravarty, P. Wray, R.T. Chen, Experimental demonstration of propagation characteristics of mid-infrared photonic crystal waveguides in silicon-on-sapphire. Opt. Express **23**(5), 6965–6975 (2015)
78. Y. Zou, S. Chakravarty, R.T. Chen, Mid-infrared silicon-on-sapphire waveguide coupled photonic crystal microcavities. Appl. Phys. Lett. **107**(8), 081109 (2015)
79. Y. Zou, S. Chakravarty, P. Wray, R.T. Chen, Mid-infrared holey and slotted photonic crystal waveguides in silicon-on-sapphire for chemical warfare simulant detection. Sens. Actuator B Chem. **221**, 1094–1103 (2015)
80. Y. Yue, L. Zhang, H. Huang, R.G. Beausoleil, A.E. Willner, Silicon-on-nitride waveguide with ultralow dispersion over an octave-spanning mid-infrared wavelength range. IEEE Photonics J. **4**(1), 126–132 (2012)
81. S. Khan, J. Chiles, J. Ma, S. Fathpour, Silicon-on-nitride waveguides for mid-and near-infrared integrated photonics. Appl. Phys. Lett. **102**(12), 121104 (2013)
82. Y. Zou, H. Subbaraman, S. Chakravarty, X. Xu, A. Hosseini, W.C. Lai, P. Wray, R.T. Chen, Grating-coupled silicon-on-sapphire integrated slot waveguides operating at mid-infrared wavelengths. Opt. Lett. **39**(10), 3070–3073 (2014)
83. Y. Chen, H. Lin, J. Hu, M. Li, Heterogeneously integrated silicon photonics for the mid-infrared and spectroscopic sensing. ACS Nano **8**(7), 6955–6961 (2014)
84. G.K. Celler, S. Cristoloveanu, Frontiers of silicon-on-insulator. J. Appl. Phys. **93**(9), 4955–4978 (2003)
85. Q.Y. Tong, U. Goesele, *Semiconductor Wafer Bonding: Science and Technology* (Wiley, 1999)
86. F. Namavar, E. Cortesi, B. Buchanan, P. Sioshansi, *Proceedings of IEEE SOS/SOI Technology Workshop* (1989), p. 117
87. T. Abe, M. Nakano, T. Ito, *Silicon-On-insulator Technology and Devices*, vol. 61, ed. by D. N. Schmidt (The Electrochemical Society, Pennington, New Jersey, 1990), pp. 90–96

88. K. Mitani, U.M. Gösele, Wafer bonding technology for silicon-on-insulator applications: a review. J. Electron. Mater. **21**(7), 669–676 (1992)
89. O. Kononchuk, B.Y. Nguyen, *Silicon-on-insulator (SOI) Technology: Manufacture and Applications* (Elsevier, 2014)
90. A. Marshall, S. Natarajan, *SOI Design* (Springer Science & Business Media, 2002)
91. P. Mumola, G. Gardopee, T. Feng, A. Ledger, P. Clapis, P. Miller, *Proceedings of the Semiconductor Wafer Bonding: Science, Technology and* Applications, vol. 410, ed. by M.A. Schmidt, T. Abe, C.E. Hunt, H. Baumgart (The Electrochemical Socity, Pennington, New Jersey, 1993), pp. 93–29
92. K. Mitani, SEMI Silicon on insulator (SOI), Manufacturing technology. Semicon. West **98**, H1 (1998)
93. D. Godbey, H. Hughes, F. Kub, M. Twigg, L. Palkuti, P. Leonov, J. Wang, A SiO. 7GeO. 3 strained-layer etch stop for the generation of thin layer undoped silicon. Appl. Phys. Lett. **56** (4), 373–375 (1990)
94. T. Yonehara, Silicon Wafer Bonding Technology for VLSI and MEMS Applications, in *EMIS Processing Series n° 1, Chapter 4*, vol. 53, ed. by S.S. Iyer, A.J. Auberton-Herve (2002)
95. T. Yonehara, ELTRAN; novel SOI wafer technology. JSAP Int. **4**, 10–16 (2001)
96. R.S. Burton, T.E. Schlesinger, Comparative analysis of the method-of-lines for three-dimensional curved dielectric waveguides. J. Lightwave Technol. **14**(2), 209–216 (1996)
97. N. Dagli, C. Fonstad, Analysis of rib dielectric waveguides. IEEE J. Quant. Electron. **21**(4), 315–321 (1985)

Chapter 5
Basic Principles of Biosensing

Mohamed Farhat O. Hameed, A. Samy Saadeldin, Essam M. A. Elkaramany and S. S. A. Obayya

Abstract Recently, optical sensors have been improved extensively due to the rising need of sensing applications in different specialties such as, medicine, military, environment, food quality control. The improvement of the photonic technologies based on the CMOS compatible silicon-on-insulator (SOI) and photonic crystal structures improves the sensing performance significantly. This chapter presents the basic principles of the sensing process. Additionally, it introduces the different configurations of optical sensors based on working principle, sensor design, and detection purpose.

Keywords Biosensors · Principles of biosensing · Phase-modulated sensors Intensity-modulated sensors · Polarization-modulated sensors · Wavelength-modulated sensors

M. F. O. Hameed (✉)
Center for Photonics and Smart Materials and Nanotechnology Engineering Program, Zewail City of Science and Technology, October Gardens, 6th of October City, Giza, Egypt
e-mail: mfarahat@zewailcity.edu.eg

M. F. O. Hameed
Mathematics and Engineering Physics Department, Faculty of Engineering, Mansoura University, Mansoura, Egypt

A. S. Saadeldin
Electronics and Communication Engineering Department, Akhbar Elyom Academy, 6th of October City, Egypt

A. S. Saadeldin · E. M. A. Elkaramany
Engineering Mathematics and Physics Department, Faculty of Engineering, Cairo University, Giza, Egypt

S. S. A. Obayya
Centre for Photonics and Smart Materials, Zewail City of Science and Technology, October Gardens, 6th of October City, Giza, Egypt
e-mail: sobayya@zewailcity.edu.eg

S. S. A. Obayya
Electronics and Communication Engineering Department, Faculty of Engineering, Mansoura University, Mansoura, Egypt

© Springer International Publishing AG, part of Springer Nature 2019

M. F. O. Hameed and S. Obayya (eds.), *Computational Photonic Sensors*, https://doi.org/10.1007/978-3-319-76556-3_5

5.1 Introduction

The optical sensor is an attractive technique for sensing applications. This is due to its high sensitivity, electrical and chemical passive nature, and immunity from electromagnetic interference. In some implementations, optical sensors have also lightweight with small-size devices. The sensing is a process of getting information from the environment which is the main function of the sensor [1]. This process consists of three stages: the sensing element, the transmission of the received information to processor, and information analysis. The interaction between the sensing element and the environment affects some features of the sensing element. The optical sensor depends on the detection of the change in intensity, phase, polarization, or resonance wavelength of the optical field due to the interaction with the environment. These features changes are the received information which is transmitted to the processing unit. The final stage, analysis, depends on the sensing mechanism and application. A schematic diagram for the sensing process is shown in Fig. 5.1.

The electric field of the light wave can be represented mathematically as

$$\vec{E}(\vec{r},t) = \overrightarrow{E_o}\,\sin(\vec{k}\cdot\vec{r} - \omega t + \varphi_o) \tag{5.1}$$

where E_o is the amplitude of the electric field, k is the wave number vector, ω is the angular frequency, and φ_o is the initial phase constant. The features of the sensing element can be one or some of these terms (depending on the application) of the electric field of the light wave represented in Eq. 5.1. Figure 5.2 shows how each feature can affect the electric field of the light wave. For example, the refractive

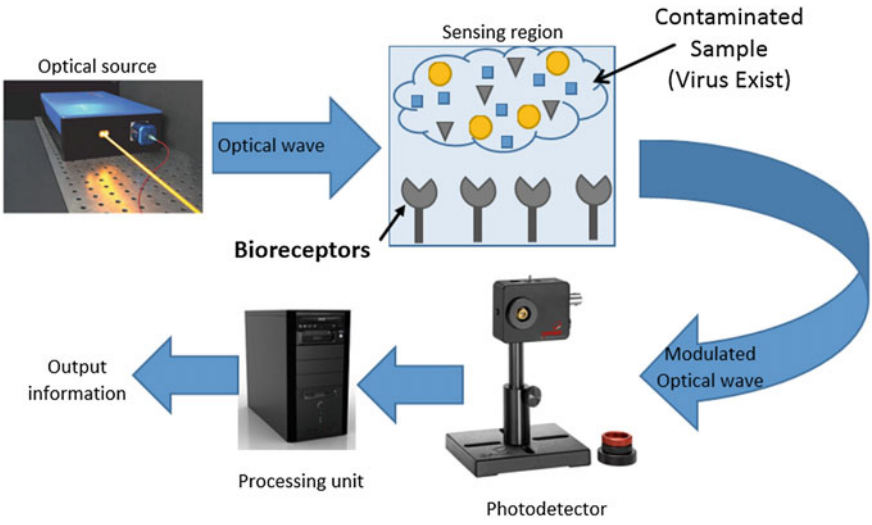

Fig. 5.1 Optical sensing system

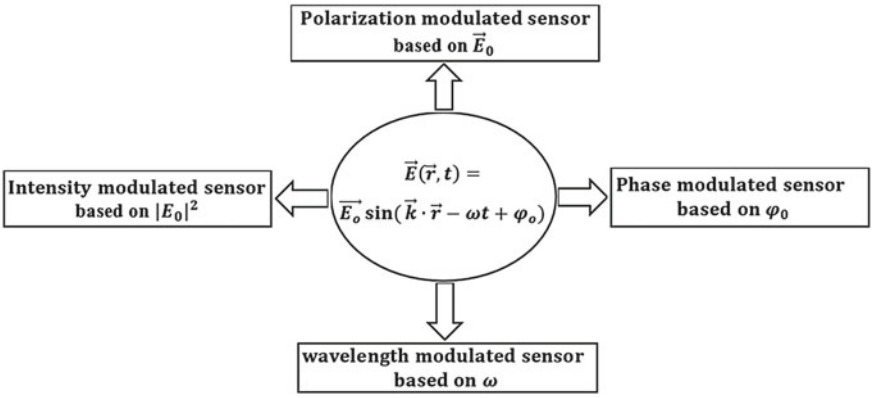

Fig. 5.2 Different sensing mechanisms

index (RI)-based sensor can detect the change in RI by two mechanisms. In the first one, the wavelength of the optical signal can be monitored through an optical spectrum analyzer (OSA), while in the second technique, the intensity changes of the output signal can be detected by using a photodetector (PD). Further, the phase change can be used as a sensing element based on interferometer structures such as Mach–Zehnder interferometer (MZI). The MZI depends on measuring the phase difference between its two arms. This phase shift is due to a perturbation occurrence in the sensing arm of the interferometer. Therefore, the output signal of that arm will differ in phase from the output signal of the other arms (reference arm). The polarization is also a feature that can be used in the sensing applications. Further, the polarimetric measurement can be used as a pressure sensor. The principle is based on monitoring the light intensity at the sensor output, modulated by the effect of applied pressure. In particular, by using input and output linear polarizers, it is possible to control the passage of only certain orientations of plane-polarized light, properly set by the input polarizer. Polarization changes induced by pressure influence alter the current state of light polarization proportionally to the pressure strength. Consequently, if the polarization state at the sensor output is not equal to that of the output polarizer, propagation of light is inhibited resulting in a light intensity reduction.

5.2 Classifications of the Optical Sensors

The optical sensors can be classified by different manners [2]. One of these classifications is based on the working principle. Another classification relies on the detection purpose. Also, the optical sensors can be categorized based on the sensor's configuration. These different classifications are shown in Fig. 5.3.

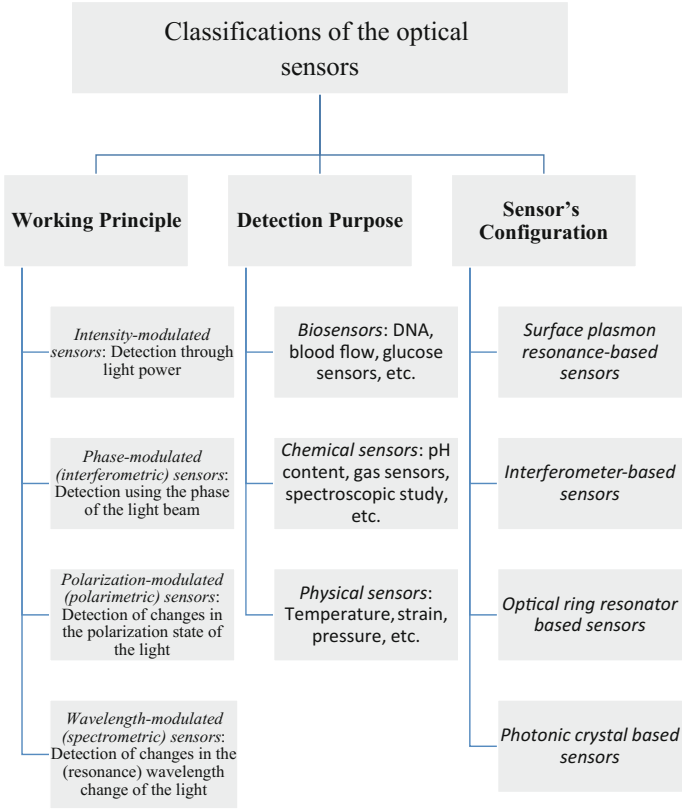

Fig. 5.3 Different classifications of the optical sensors

5.2.1 Classification Based on the Working Principle

5.2.1.1 Intensity-Modulated Optical Sensors

Intensity-modulated sensors are one of the earliest types and perhaps the simplest type of optical sensors. In this technique, the intensity of the transmitted light through the optical sensors will be modulated by different methods as bending, reflectance, or changing the propagation medium. The merits of this technique are ease of fabrication, simple detection system, simple signal processing requirements, and its low-cost performance.

Unlike the other sensing principles, a simple arrangement can be used to obtain the intensity modulation. However, the decrease of the sensor reliability occurs due to the attenuation and intensity instability of the signal due to bending, coupling misalignments, source power fluctuation, etc. To overcome this problem, the intensity referencing can be used where a portion of the input optical power is taken

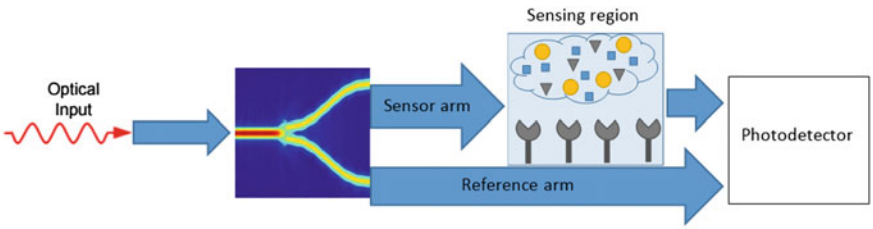

Fig. 5.4 Reference arm configuration

to observe the variation of the input power. A model of this method is shown in Fig. 5.4 [3]. In this case, the ratio between the power of the modulated signal to the power of the reference signal is used.

5.2.1.2 Phase-Modulated Optical Sensors

Phase-modulated sensors are based on detecting the phase difference of the light propagating on two different paths. These sensors are also called interferometric sensors. The interferometric sensors have high sensitivity due to the detection of the smallest change in the measurands. In this technique, the input light is split into two equal beams. One of these beams acts as a reference arm while the other beam is affected by the external stimuli. At the output of the sensor, these beams are re-merged which leads to forming an interference pattern. This pattern depends on the phase difference between the two beams which are linked to the amount of the measurand.

5.2.1.3 Wavelength-Modulated (Spectrometric) Optical Sensors

Wavelength-modulated sensors exhibit a change- in the propagating optical wavelength when interacted by an external perturbation. In this section, some common wavelength-based sensors will be discussed such as fluorescence sensors and Raman spectroscopy.

(1) *Fluorescence sensors*

Fluorescence technique depends on a light source directed to the receptors that is fixed on the sensing region to start the electronic transitions. The receptors will absorb the electromagnetic energy from the light source to reach an excited state. Then the receptors will return to its normal state by radiating a photon. This radiated photon is known as fluorescence [4]. When the receptors bind with the target molecules, the radiated photons change its energy (wavelength). This change in the energy of the radiated photon is an indication to the occurrence of the binding. The target molecules are labelled with fluorescent tags, such as dyes. The intensity of

the emitted fluorescence indicates the interaction strength between the target and the receptor molecules [5].

(2) *Raman Spectroscopy*

Raman spectroscopy depends on light scattering by molecules which lead to an exchange of energy between incident photon and scattered molecules. This exchange of energy may be from the scattered photon to the incident one or vice versa. This method could be mentioned either as Raman to Stokes scattering if the scattered photon has energy less than that of the incident one. However, Raman to anti-Stokes scattering occurs if the scattered photon has higher energy than that of the incident photon [6]. In Raman to Stokes scattering, the light interacts with the sample molecules with low-energy level to transfer to higher-energy level. Then the molecule radiates a photon in order to go back to the lower-energy level. The difference between incident and emitted photon energy is employed to change the vibration state of the molecule. However, in Raman to anti-Stokes scattering, the light interacts with the sample molecules with high-energy level to go to low-energy level with a photon radiation [7]. Raman signals are very weak and need high-precision optical receptors and powerful sources. This kind of sensors overcomes some of the shortcomings of fluorescence sensing such as the ability to sense analytes which do not exhibit fluorescence.

5.2.1.4 Polarization-Modulated (Polarimetric) Optical Sensors

The polarization state of the light wave that propagates along the optical sensor changes due to the difference in the phase velocity of the two polarization components in a birefringent sensor. The polarization state of the propagated light can be modulated by stress, strain, pressure, and temperature applied on the sensor. The polarimetric sensor can measure the polarization variation, and hence, the sensing parameter can be related [8]. For example, a symmetric deformation effect or temperature variation in a single-mode fiber influences the propagation constant (β) of the supported modes because of the changes in the fiber length (L) and the refractive indices of the core and the cladding regions. Under the influence of longitudinal strain (ε) or temperature (T), for single-mode fiber polarimetric sensors, the change in the phase difference can be written as [9]

$$\frac{\delta(\Delta\varphi)}{\delta X} = \Delta\beta\frac{\partial L}{\partial X} + L\frac{\partial(\Delta\beta)}{\partial X} \tag{5.2}$$

where X stands for temperature, pressure, or strain.

The change in polarization can be observed as a change in intensity as shown in Eq. 5.3. By correlating the output change in intensity due to the measurand, a polarimetric fiber sensor can be effectively used as a sensor for a variety of applications.

$$I_s(\lambda) = \frac{I_0}{2}[1 + \cos(\Delta\varphi)] \tag{5.3}$$

5.2.2 *Classification Based on the Sensor's Configuration*

5.2.2.1 Surface Plasmon Resonance

Surface plasmon resonance (SPR) [10–12] is one of the successful optical techniques which has applications in chemical and biochemical sensing [13]. In SPR technique, a transverse magnetic-polarized light causes the excitation of oscillations of electron density at the metal-dielectric interface [14]. This oscillation of electrons produces a wave known as surface plasmon wave (SPW). When the incident light (which carries energy as well as momentum) and the surface plasmon wave are matched, a resonance occurs which results in a sharp dip in the reflected light intensity as represented in Fig. 5.5.

The incident angle, wavelength of the light, and the dielectric constant for both metal and substrate are the parameters that affect the resonance condition. The sensing mechanism depends on the monitoring of the incident angle when the wavelength remains constant. The sharp dip occurs at the resonance angle. Similarly, the sensing mechanism can be through the monitoring of the wavelength while the incident angle remains constant. The resonance occurs at a specific wavelength. The dielectric media refractive index affects both the resonance incident angle and the resonance wavelength. So any variation in such refractive index will change the resonance wavelength or the resonance incident angle. The main

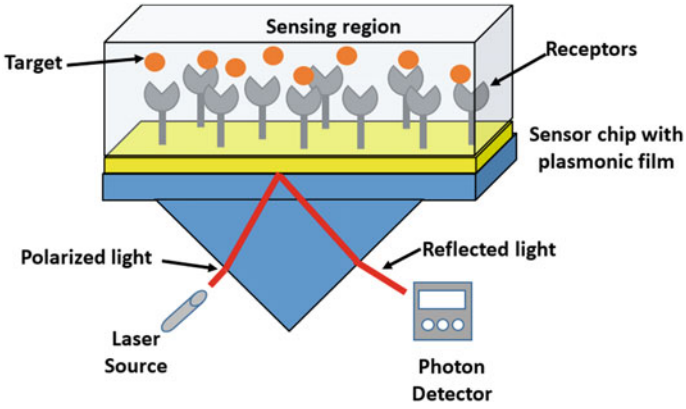

Fig. 5.5 Sensor chip detects the refractive index change in the immediate vicinity of a surface layer by the plasmonic resonance which is observed as a sharp shadow in the reflected light at an angle that depends on the effective index of the mode at the surface; this angle will be shifted when target-receptor binding occurs

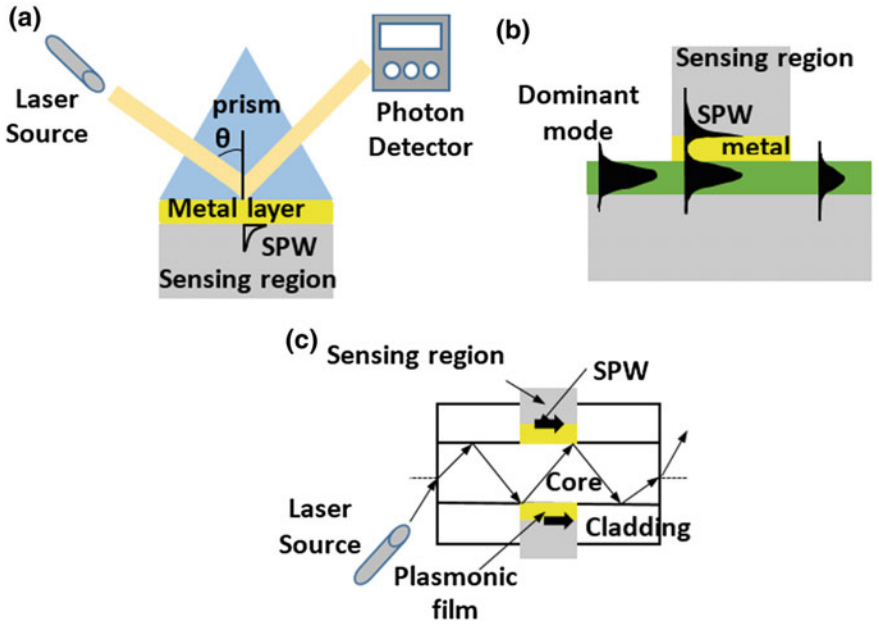

Fig. 5.6 Different coupling methods for SPR sensor configuration, **a** prism coupling, **b** waveguide coupling, and **c** optical fiber coupling

coupling methods for SPR sensors are prism coupling [15], waveguide coupling [16], and optical fiber coupling [17] as illustrated in Fig. 5.6. In the prism coupling technique shown in Fig. 5.6a, the excitation of the SPW is done by the evanescent field that is produced by the total reflected light at the interface between the prism and the metal layer. This evanescent field penetrates the metallic layer, and at the resonance condition, the propagation constants of the SPW and the evanescent field are matched. The matched propagation constant, as illustrated in Eq. 5.4, can excite the SPW.

$$\frac{2\pi}{\lambda} n_p \sin\theta = \beta_{sp.} \tag{5.4}$$

where λ is the incident wavelength, n_p is the prism refractive index, θ is the incident angle, and β_{sp} is the propagation constant of the SPW. However, the prism configuration is huge and hard to integrate. The SPW can be excited by the waveguide coupling to overcome the shortage in the prism coupling as shown in Fig. 5.6b. It is robust and easy to integrate with electrical and optical components. The excitation of the SPW through the waveguide is similarly to that of the prism coupling. Also, the optical fiber could be used to excite the SPW as shown in Fig. 5.6c where a part of the optical fiber is cut and replaced by a metal film.

5.2.2.2 Interferometric Optical Sensors

This type of sensors is based on detecting the optical phase change due to the light propagation along the sensor. Among the interferometer configuration, Mach–Zehnder architecture has high sensitivity for label-free optical biosensing. The interaction between the guided light through the sensor structure and the sensing region (analyte, in case of biosensing) is done through the evanescent field of the light. Alternatively, the core of the waveguide can be infiltrated by the analyte in case of slot/hollow waveguides.

The Mach–Zender interferometers (MZIs) can guide the light from the source into two single-mode waveguides. One of these waveguides has a sensing arm with the sensing layer, while the other one acts as a reference arm [18] as shown in Fig. 5.7.

The smallest change in the refractive index (homogenous sensing) or the thickness of the sensing layer (surface sensing) affects the effective index (Δn_{eff}) of the propagated mode which induces a phase shift in the propagated light wave in the sensing arm. This phase shift is equal to $\Delta n_{eff}\, k_0\, L$, where k_0 is the free-space wave number, L is the length of the sensing region. However, the reference arm has no contact with the sensing medium, and hence, no phase change occurs. The output of the MZI is the combination between the two separated waveguides (sensing arm and reference arm). Therefore, an interference occurs due to the phase shift φ produced by the effective indices difference between the sensing and reference arms. The interference converts this phase shift into a modulation of the optical output intensity satisfying the condition

$$\frac{I_{OUT}}{I_{IN}} = \frac{1}{2}[1 + \cos\varphi] \tag{5.5}$$

where I_{OUT}/I_{IN} is the ratio between optical output and input intensity of the MZI. The phase shift φ is defined as

$$\Delta\varphi = k_0 L\left[n_{eff}^{S} - n_{eff}^{R}\right] \tag{5.6}$$

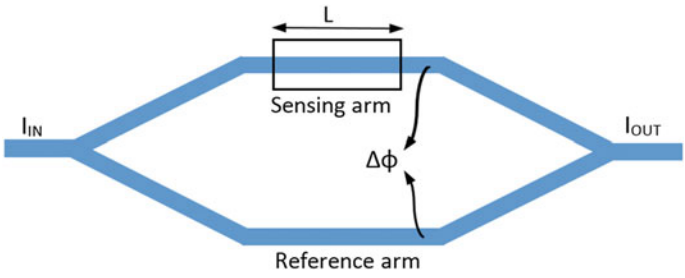

Fig. 5.7 Mach–Zehnder interferometer configuration

where (n_{eff}^{S}–n_{eff}^{R}) is the effective index difference between the sensing and reference arm.

The input optical power (I_{in}) is divided into the sensing arm and the reference arm, each with power of $I_{in}/2$. If there is no phase delay (i.e., $\Delta\varphi = 0$), the light of the two arm will be merged at the output of the MZI. In this case, the output power will equal to the input power (i.e., $I_{out} = I_{in}$). However, if there is a phase delay (i.e., $\Delta\varphi \neq 0$), the output power will be different from the input power (i.e., $I_{out} \neq I_{in}$) as follows:

$$I_{OUT} = I_{IN} \cos^2 \frac{\varphi}{2} = I_{IN} \cos^2 \frac{\pi \Delta n_{eff} L}{\lambda} \tag{5.7}$$

It is worth noting that as the length of the sensor increases, the sensing signal will be increased. Further, the MZI sensor has a cosine-dependent intensity function. Therefore, the maximum and minimum of the cosine function makes the signal change is difficult to resolve near these values in comparable to linear intensity response sensors.

The sensitivity S of the Mach–Zehnder interferometer sensor can be expressed as follows:

$$S = \frac{2\pi L}{\lambda} S_W \tag{5.8}$$

where S_w is the waveguide sensitivity. The sensitivity can be expressed for homogeneous sensing as follows:

$$S = \frac{2\pi L}{\lambda} \left(\frac{\partial n_{eff}}{\partial n_c} \right) \tag{5.9}$$

However, for surface sensing, S is given by

$$S = \frac{2\pi L}{\lambda} \left(\frac{\partial n_{eff}}{\partial \rho} \right) \tag{5.10}$$

where n_{eff} is the effective index of the propagating supported mode through the waveguide, n_c is the cladding medium refractive index, and ρ is the thickness of molecular layer deposited on guiding cover medium interface. The sensitivity of Mach–Zehnder-based sensor relies on sensing arm length, L. Further, the sensitivity of the MZI sensor may be affected by an external stimulus such as temperature which can cause an undesired shift in the propagating mode. Thus, a trade-off between device length and device sensitivity should be taken into account [19].

5.2.2.3 Ring Resonator Optical Sensors

Optical microring resonator is an emerging biosensing technology that has recently been under intensive investigation [20–23] for achieving high sensitivity. The microring resonator sensor has reduced the device size by some orders of magnitude without reducing the device sensitivity. Recently, the slot waveguide incorporated with ring resonator biosensors can achieve high sensitivity because of the light confinement in the slot region which allows a large light interaction with the sensing material. This configuration could be used as a biosensor by fixing the receptors on the top of the waveguide. When the flowing fluid, that includes the target molecules, be in contact with the receptors, the binding will occur at the surface of the waveguide. This binding will change the layer thickness on the surface of the waveguide or change the refractive index of that layer. As a result, the optical mode effective index will be changed which shifts the resonance wavelength by

$$\Delta\lambda = \frac{\Delta n_{eff} \cdot \lambda_{res}}{n_g} \tag{5.11}$$

where Δn_{eff} is the effective index change due to the binding, λ_{res} is the initial resonance wavelength, and n_g is the group index of the slot waveguide at the resonance wavelength and is given by:

$$n_g = n_{eff} - \lambda \frac{\Delta n_{eff}}{\Delta\lambda} \tag{5.12}$$

To enhance the sensor performance, the shift in the resonance wavelength, due to the binding event, should be increased as much as possible. This can be achieved by increasing the light-sensing medium interaction. At the resonance wavelength, the light is highly coupled to the ring resonator where a minimum transmission occurs in the slot-waveguide. Thus, the resonance wavelength (λ_{res}) can be detected by the photodetectors at the output port of the slot-waveguide.

A top view of the slot waveguide incorporated with a ring resonator is illustrated in Fig. 5.8. The light is coupled from the straight waveguide to the ring waveguide. The light wave that has wavelength that matches the resonance wavelength of the resonator is the only wave that can be coupled to the ring waveguide and vice versa. The slot waveguide consists of two nanowires close to each other and grown on a lower cladding layer. The sensing medium is the surface of the whole device that is in contact with the environment.

It is worth noting that many biosensors have been reported based on a slot waveguide incorporated ring resonators systems [24–27]. However, the ring resonator suffers from bending and coupling losses with the bus waveguides. Therefore, it is aimed to replace the ring resonator design with another device with smaller footprint. In [28, 29], a nanometer-scaled straight slotted resonator is

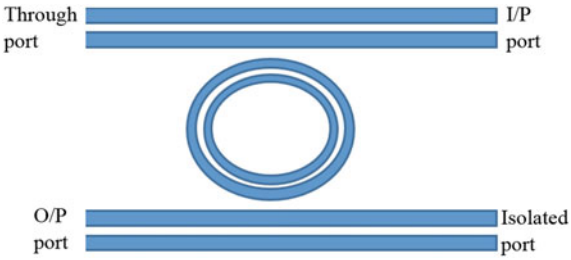

Fig. 5.8 Top view of the slot-waveguide-based microring resonator

incorporated with hybrid plasmonic slot-waveguide for DNA hybridization sensing instead of the microring resonator.

5.2.2.4 Photonic Crystal Optical Sensors

Another different configuration of optical sensors is the photonic crystal (PhC) [30] that has attracted intense interest in biosensing applications [31–35]. The PhC is a periodic structure with a photonic bandgap where the propagation through the PhC structure is forbidden. However, by inserting a defect in the periodic structure, a resonant mode can propagate in the PhC as shown in Fig. 5.9a. So, the transmission/reflection spectrum will have a sharp peak in the photonic bandgap due to the defect mode. The position of the sharp peak of the defect mode is strongly sensitive to the refractive index of the surrounding medium. Therefore, it could be used as a sensing signal to the change in refractive index (RI) due to the interaction between the receptors and the target molecules for biosensing applications. Beside the PhC waveguide sensors, there is another class of PhC sensors based on photonic crystal fiber (PCF) [36–41]. The PCF is a fiber cable with periodic air holes in the cladding region as shown in Fig. 5.9b. The PCF is an encouraging platform for sensing applications due to two main points. Firstly, the air holes can be used as a fluidic channel. Secondly, PCF has advantage in terms of light confinement mechanism that increases the interaction between the light and the sensing material which improves the sensor performance. Furthermore, the PCF air holes can act as holder for sample of volume up to a several nL/cm which is a desirable feature for biosensing applications.

5.3 Summary

Various optical sensing mechanisms have been reviewed in this chapter such as intensity-modulated sensors, phase-modulated sensors, and wavelength-modulated sensors. Additionally, different optical sensor configurations have been represented such as surface plasmon resonance, interferometric, optical ring resonator, and photonic crystal sensors.

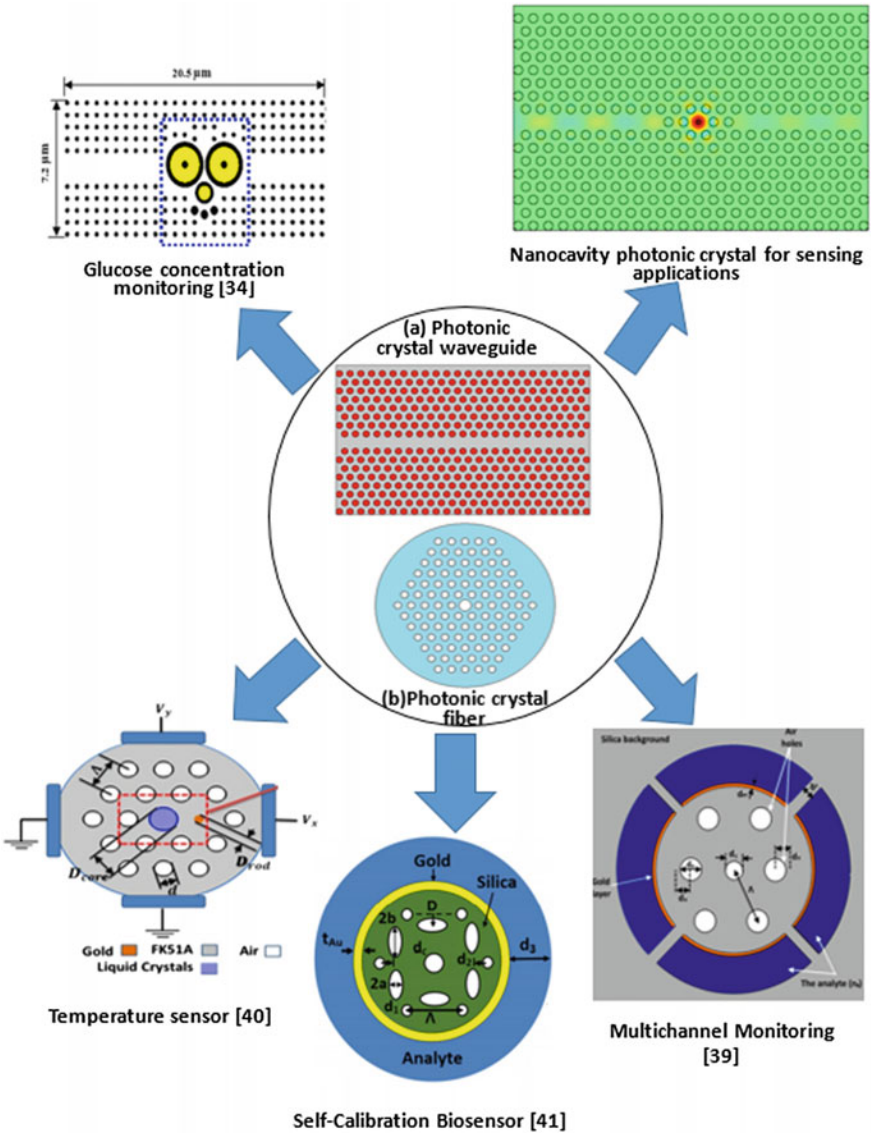

Fig. 5.9 **a** Photonic crystal waveguide, and **b** photonic crystal fiber-based biosensors

References

1. J.L. Santos, F. Farahi, *Handbook of Optical Sensors* (CRC Press Taylor & Francis Group, 2015)
2. G. Rajan, *Optical Fiber Sensors Advanced Techniques and Applications* (CRC Press Taylor & Francis Group, 2015)

3. G. Rajan, Y. Semenova, G. Farrell, An all-fiber temperature sensor based on a macro-bend single-mode fiber loop. Electron. Lett. **44**, 1123–1124 (2008)
4. L.M. Smith, J.Z. Saunders, R.J. Kaiser, P. Hughes, C.R. Dodd, C.R. Cornell, C. Heiner, S.B. H. Kent, L.E. Hood, Fluorescence detection in automated DNA sequence analysis. Nature **321**, 674–679 (1986)
5. R.B. Thompson(ed.), *Fluorescence Sensors and Biosensors* (CRC Press, 2005)
6. K. Kneipp, H. Kneipp, I. Itzkan, R.R. Dasari, M.S. Feld, Surface-enhanced Raman scattering and biophysics. J. Phys. Condens. Matter **14**(18), R597 (2002)
7. A. Tao, F. Kim, C. Hess, J. Goldberger, R. He, Y. Sun, Y. Xia, P. Yang, Langmuir−Blodgett silver nanowire monolayers for molecular sensing using surface-enhanced Raman spectroscopy. Nano Lett. **3**(9), 1229–1233 (2003)
8. T.R. Wolinski, Polarimetric optical fibers and sensors. Prog. Opt. **40**, 1–75 (2000)
9. T.R. Wolinski, P. Lesiak, A.W. Domanski, Polarimetric optical fiber sensors of a new generation for industrial applications. Bullet. Polish Acad. Sci. Tech. Sci. **56**(2), 125–132 (2008)
10. X. Fan, I.M. White, S.I. Shopova, H. Zhu, J.D. Suter, Y. Sun, Sensitive optical biosensors for unlabeled targets: a review. *Analytica chimica Acta* **620**(1), 8–26 (2008)
11. J. Homola, Present and future of surface plasmon resonance biosensors. Anal. Bioanal. Chem. **377**(3), 528–539 (2003)
12. K.S. Phillips, Q. Cheng, Recent advances in surface plasmon resonance based techniques for bioanalysis. Anal. Bioanal. Chem. **387**(5), 1831–1840 (2007)
13. M.A. Cooper, Optical biosensors in drug discovery. Nat. Rev. Drug Disc. **1**, 515–528 (2002)
14. E. Stenberg, B. Persson, H. Roos, C. Urbaniczky, Quantitative determination of surface concentration of protein with surface plasmon resonance using radiolabeled proteins. J. Colloid Inter. Sci. **143**, 513–526 (1991)
15. K. Matsubara, S. Kawata, S. Minami, Optical chemical sensor based on surface plasmon measurement. Appl. Opt. **27**(6), 1160–1163 (1988)
16. B. Liedberg, I. Lundström, E. Stenberg, Principles of biosensing with an extended coupling matrix and surface plasmon resonance. Sensors Actuat. B Chem. **11**(1–3), 63–72 (1993)
17. A.K. Sharma, R. Jha, B.D. Gupta, Fiber-optic sensors based on surface plasmon resonance: a comprehensive review. IEEE Sens. J. **7**(8), 1118–1129 (2007)
18. F. Prieto, B. Sepulveda, A. Calle, A. Llobera, C. Domínguez, A. Abad, A. Montoya, L.M. Lechuga, An integrated optical interferometric nanodevice based on silicon technology for biosensor applications. Nanotechnology **14**(8), 907 (2003)
19. A. Ymeti, J.S. Kanger, R. Wijn, P.V. Lambeck, J. Greve, Development of a multichannel integrated interferometer immunosensor, in Transducers' 01 Eurosensors XV (Springer, Berlin Heidelberg 2001), pp. 354–357
20. C.A. Barrios, M.J. Bañuls, V. González-Pedro, K.B. Gylfason, B. Sanchez, A. Griol, A. Maquieira, H. Sohlström, M. Holgado, R. Casquel, Label-free optical biosensing with slot-waveguides. Opt. Lett. **33**(7), 708–710 (2008)
21. V.R. Almeida, Q. Xu, C.A. Barrios, M. Lipson, Guiding and confining light in void nanostructure. Opt. Lett. **29**(11), 1209–1211 (2004)
22. Ian M. White, Xudong Fan, On the performance quantification of resonant refractive index sensors. Opt. Expr. **16**(2), 1020–1028 (2008)
23. X. Fan, I.M. White, H. Zhu, J.D. Suter, H. Oveys, Overview of novel integrated optical ring resonator bio/chemical sensors, in *International Society for Optics and Photonics Laser Resonators and Beam Control IX,* Feb. 2007 vol. 6452, p. 64520
24. T. Claes, J.G. Molera, K. De Vos, E. Schacht, R. Baets, P. Bienstman, Label-free biosensing with a slot-waveguide-based ring resonator in silicon on insulator. IEEE Photon. J. **1**(3), 197–204 (2009)
25. X. Tu, J. Song, T.Y. Liow, M.K. Park, J.Q. Yiying, J.S. Kee, M. Yu, G.Q. Lo, Thermal independent silicon-nitride slot waveguide biosensor with high sensitivity. Opt. Expr. **20**(3), 2640–2648 (2012)

26. F. Dell'Olio, V.M. Passaro, Optical sensing by optimized silicon slot waveguides. Opt. Express **15**(8), 4977–4993 (2007)
27. T. Dar, J. Homola, B.A. Rahman, M. Rajarajan, Label-free slot-waveguide biosensor for the detection of DNA hybridization. Appl. Opt. **51**(34), 8195–8202 (2012)
28. M.F.O. Hameed, A.S. Saadeldin, E.M. Elkaramany, S.S.A. Obayya, Label-free highly sensitive hybrid plasmonic biosensor for the detection of DNA hybridization. J. Lightwave Technol. **35**(22), 4851–4858 (2017)
29. S. Ghosh, B.M.A. Rahman, An innovative straight resonator incorporating a vertical slot as an efficient bio-chemical sensor. IEEE J. Sel. Top. Quant. Electron. **23**(2), 1–8 (2017)
30. B. Troia, A. Paolicelli, F. De Leonardis, V.M. Passaro, *Photonic crystals for optical sensing: A review* (In Advances in Photonic Crystals, InTech, 2013)
31. J. García-Rupérez, V. Toccafondo, M.J. Bañuls, A. Griol, J.G. Castelló, S. Peransi-Llopis, A. Maquieira, Single strand DNA hybridization sensing using photonic crystal waveguide based sensor, in *7th IEEE International Conference on Group IV Photonic*s (September 2010), 978-1-4244-6346-6, pp. 180–182
32. N. Griffete, H. Frederich, A. Maître, M.M. Chehimi, S. Ravaine, C. Mangeney, Photonic crystal pH sensor containing a planar defect for fast and enhanced response. J. Mater. Chem. **21**(34), 13052–13055 (2011)
33. H. Lin, Z. Yi, J. Hu, Double resonance 1-D photonic crystal cavities for single molecule mid-infrared photothermal spectroscopy: theory and design. Opt. Lett. **37**(8), 1304–1306 (2012)
34. N.F. Areed, M.F.O. Hameed, S.S.A. Obayya, Highly sensitive face-shaped label-free photonic crystal refractometer for glucose concentration monitoring. Opt. Quant. Electron. **49** (1), 5 (2017)
35. S. Jindal, S. Sobti, M. Kumar, S. Sharma, M.K. Pal, Nanocavity-coupled photonic crystal waveguide as highly sensitive platform for cancer detection. IEEE Sens. J. **16**(10), 3705–3710 (2016)
36. L. Xiao, W. Jin, M.S. Demokan, Photonic crystal fibers confining light by both index-guiding and bandgap-guiding: hybrid PCFs. Opt. Expr. **15**(24), 15637–15647 (2007)
37. X. Yang, C. Shi, R. Newhouse, J.Z. Zhang, C. Gu, Hollow-core photonic crystal fibers for surface-enhanced raman scattering probes. Int. J. Opt. 754610, 1–11 (2011)
38. A.M.R. Pinto, M. Lopez-Amo, Photonic crystal fibers for sensing applications. J. Sens. 598178, 1–21 (2012)
39. S.I. Azzam, M.F.O. Hameed, R.E.A. Shehata, A.M. Heikal, S.S.A. Obayya, Multichannel photonic crystal fiber surface plasmon resonance based sensor. Opt. Quant. Electron. **48**(2), 142 (2016)
40. M.F.O. Hameed, M.Y. Azab, A.M. Heikal, S.M. El-Hefnawy, S.S.A. Obayya, Highly sensitive plasmonic photonic crystal temperature sensor filled with liquid crystal. IEEE Photon. Technol. Lett. **28**(1), 59–62 (2016)
41. M.F.O. Hameed, Y.K. Alrayk, S.S.A. Obayya, Self-calibration highly sensitive photonic crystal fiber biosensor. IEEE Photon. J. **8**(3), 1–12 (2016)

Part II
Computational Modelling Techniques

Chapter 6
Finite Element Method for Sensing Applications

Khaled S. R. Atia, Souvik Ghosh, Ahmed M. Heikal, Mohamed Farhat O. Hameed, B. M. A. Rahman and S. S. A. Obayya

Abstract In this chapter, the fundamentals of the nodal finite element method (FEM) are presented, including the first-order element and second-order element. The nodal FEM is introduced for the scalar concept of the propagation constant of 2D waveguide cross section. Then, it is extended to include the time domain analysis under perfectly matched layer absorbing boundary conditions. A simple sensor based on optical grating is thereafter simulated using the time domain FEM. Also, the full vectorial analysis is discussed through the application of the penalty function method on the nodal FEM and the vector finite element method (VFEM).

K. S. R. Atia · A. M. Heikal · S. S. A. Obayya
Centre for Photonics and Smart Materials, Zewail City of Science and Technology, October Gardens, 6th of October City, Giza, Egypt
e-mail: Kh.satia@gmail.com

K. S. R. Atia
Advanced Research Complex, University of Ottawa, Ottawa ON K1N 6N5, Canada

A. M. Heikal
e-mail: aheikal@zewailcity.edu.eg

S. S. A. Obayya
e-mail: sobayya@zewailcity.edu.eg

S. Ghosh · B. M. A. Rahman
School of Mathematics, Computer Science and Engineering, City University of London, London EC1V 0HB, England
e-mail: B.M.A.Rahman@city.ac.uk

A. M. Heikal · S. S. A. Obayya
Faculty of Engineering, Department of Electronics and Communication Engineering, Mansoura University, Mansoura, Egypt

M. F. O. Hameed (✉)
Center for Photonics and Smart Materials and Nanotechnology Engineering Program, Zewail City of Science and Technology, October Gardens, 6th of October City, Giza, Egypt
e-mail: mfarahat@zewailcity.edu.eg

M. F. O. Hameed
Mathematics and Engineering Physics Department, Faculty of Engineering, Mansoura University, Mansoura, Egypt

© Springer International Publishing AG, part of Springer Nature 2019

M. F. O. Hameed and S. Obayya (eds.), *Computational Photonic Sensors*, https://doi.org/10.1007/978-3-319-76556-3_6

For the penalty function method, a global weighting factor is used to incorporate the effect of the divergence-free equation. In the VFEM, nodes are used to represent the orthogonal component of the field while the edges are used to represent the tangential component for accurate application of the boundary conditions. Finally, surface plasmon resonance photonic crystal fiber biosensor is introduced as an example of the full vectorial analysis using the VFEM.

Keywords Finite element method · Finite element time domain
Penalty function method · Full-vector finite element method · Edge finite element method

6.1 Introduction

In the finite element method (FEM) [1–5], corresponding functions, to which a variational principle is applied, are used where the computational domain is divided into so-called elements. Then, an equivalent discretization model for each element is constructed. After that, all element contributions in the analysis region are assembled. The FEM can be considered as a special type of Rayleigh–Ritz method, where piecewise polynomial functions are utilized for trial functions and a finite number of unknowns are used instead of the infinite degrees of freedom in the actual system. In analytical techniques without subdivision, analytical functions defined over the analysis region are used to describe the system. Therefore, these types of methods succeed only in simple geometries. The finite difference method (FDM) [6, 7] is one of the well-known forms of discretization process. FDM traditionally uses regular grids, where a rectangular grid with nodes at the intersection interface discretizes the computational window. Unfortunately, regular grids fail to describe curved and irregularly shaped geometries. The reason behind that is these nodes at the intersection of grid lines cannot be adjusted to set on the boundary of curved structures. Further, regular grids are not capable of accurately modeling fast variations in the field. On the other side, the FEM divides the analysis regions into elements, but, dissimilar to the FDM, these elements can take various shapes such as triangles or rectangles for 2D analysis and tetrahedral for 3D analysis. By using these shapes, the FEM allows using irregular grids. Hence, the FEM is more capable of modeling fast variation in the field than the FDM. Also, this approach can be easily extended to inhomogeneous and anisotropic materials. Moreover, the FEM technique can be constructed by the Galerkin method which is a weighted residual method as well as the variational method. The discussions, in this chapter, are restricted only to the Galerkin method. After the introduction, the rest of this chapter is organized as follows: An overview of the finite element method is presented. Then, the scalar finite element method for optical waveguide mode analysis is introduced. After that, the FEM is adopted for time domain analysis. Then, the penalty function method and the vector finite element are discussed for the full vectorial analysis of optical waveguides. Relying on the full vectorial analysis, a surface plasmon resonance photonic crystal fiber biosensor is investigated.

6.2 Finite Element Method Overview

6.2.1 Finite Element Procedure

The fundamental steps to build up the analysis of any photonic model using FEM can be listed as follows:

1. Discretization of the structure of one's interest into many smaller elements domains;
2. Setup of the interpolating equation by the values at the elemental nodes or boundaries to determine unknown parameter. It may be field or potential;
3. Assembling the individual equations of discretized elements to form global eigenvalue equations;
4. Solving the global equations using eigenvalue matrix solver;
5. Finally, post-processing of the eigenvalues and corresponding eigenvectors to obtain desired unknown parameters.

6.2.2 Computational Domain Discretization

The desired domain over which finite element method can be applied needs to be discretized into a large number of small domains, called elements. These elements can be chosen in such a way that its shape and size match closely with the geometry and the boundary curvatures of the computational domain of interest. These small elements altogether form a mesh that can be regular and irregular. Compared to the regular mesh distribution, the irregular mesh is much efficient in representing the desired domain. Finer elements can be accommodated in the regions of particular interest and coarse elements elsewhere. Thus, irregular meshing provides greater accuracy over regular meshing. For photonic computations, smaller mesh elements should be considered in the thin, narrow, and pointed regions, where the electromagnetic fields vary rapidly. In the areas where fields show a nearly constant distribution, a few elements might be sufficient for computations. It is also very important to select the shape and size of the boundary elements carefully so that those can match the complete boundary shape as far as possible. For that, several elemental geometries can be followed such as straight edge elements, iso-parametric elements, infinite elements, and edge elements. The straight edge elements include the triangles, rectangles, and quadrilaterals for 2D domains and tetrahedrals, prisms, bricks, and pyramids for 3D domains. These are mostly useful for the domains with less curved boundaries. The iso-parametric or curvilinear elements have curvatures on the edges, and their nodal positional coordinates are defined by the transformation of the local Cartesian coordinate to the global

curvilinear coordinates. These are useful for the geometries with curved boundaries. Higher-order elements are also applicable for these types of element family. For an open-space or unbounded photonic problem, the infinite mesh elements can be very useful. The shape function for the infinite elements decays exponentially in the directions, where the field extends to the infinity [8, 9]. Also, the perfectly matched layer based on coordinate stretching can efficiently truncate the computational domain causing the outgoing waves to decay without reflecting back to the computational domain.

6.2.3 Setup Element Interpolation

Once the domain is discretized with suitable elements, it is necessary to represent the element shape functions in terms of the variational unknown parameters. With the help of polynomial interpolation function or shape function, any continuous function over the computational domain can be approximated. The chosen function should have continuity within and across the boundaries of the elements. Without the continuity, the functions are not eligible for variational formulations and the electromagnetic field or potential cannot be calculated by summing up the individual contributions of elements. For a unique shape function for a specific element, the number of terms must be equal to the number of nodes in the element. The Pascal triangular structure in Fig. 6.1 exhibits a nice graphical representation of the relation between the element nodes number and the number of terms in the polynomial for a 2D domain discretization.

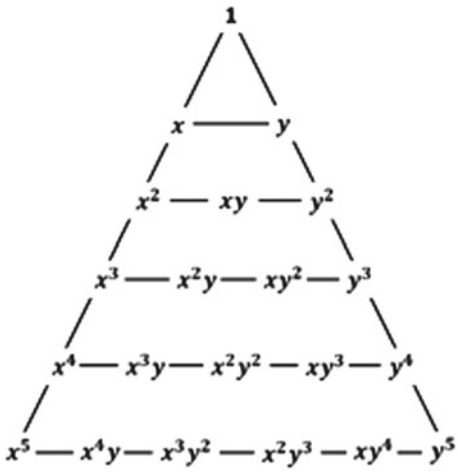

Fig. 6.1 Pascal triangle exhibiting the relationship between element nodes number and the number of terms in the shape function (N_i)

To construct the shape functions for the elements of different types, we introduce the Lagrange interpolation polynomials (L_i). For a linear triangular (2D) element and tetrahedral (3D) element, these Lagrange polynomials, which are also known as the area coordinates, are given by

$$L_i = \frac{1}{2A_e}[a_i + b_i x + c_i y] \quad for\, 2D \tag{6.1}$$

$$L_i = \frac{1}{2V_e}[a_i + b_i x + c_i y + d_i z] \quad for\, 3D \tag{6.2}$$

where A_e and V_e are the area and volume of the 2D triangular and 3D tetrahedral element, respectively. The subscript e denotes the element number. The a_i, b_i, c_i, and d_i are constant coefficients.

If we consider a point Q inside a discretized element, as shown in Fig. 6.2, we can get sub-elements from each element (sub-triangles and sub-tetrahedrals from triangular and tetrahedral elements, respectively). Now, the area and volume of those subregions can be expressed as follows:

The area defined by the point Q and nodes 2 and 3 is

$$\begin{aligned} A &= \frac{1}{2}\begin{bmatrix} 1 & x & y \\ 1 & x_2 & y_2 \\ 1 & x_3 & y_3 \end{bmatrix} \\ &= \frac{1}{2}[(x_2 y_3 - x_3 y_2) + (y_2 - y_3)x + (x_3 - x_2)y] \end{aligned} \tag{6.3}$$

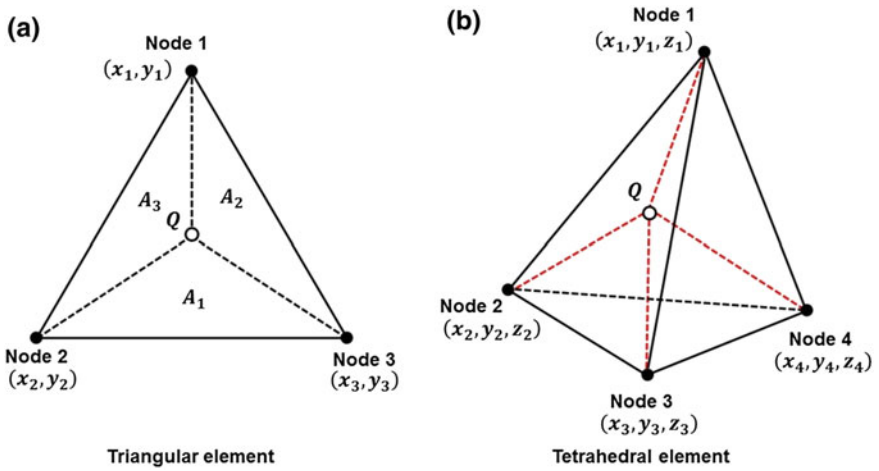

Fig. 6.2 **a** Linear triangular elements for 2D discretization and **b** linear tetrahedral elements for 3D discretization. The Q is taken as any point inside the element of arbitrary coordinate (x, y) for 2D and (x, y, z) for 3D

Similarly, the volume defined by the point Q and nodes 2, 3, and 4 is

$$V = \frac{1}{6}\begin{bmatrix} 1 & x & y & z \\ 1 & x_2 & y_2 & z_2 \\ 1 & x_3 & y_3 & z_3 \\ 1 & x_4 & y_4 & z_4 \end{bmatrix} \tag{6.4}$$

Reutilizing those constant coefficients (a_i^e, b_i^e, c_i^e for 2D and $a_i^e, b_i^e, c_i^e, d_i^e$ for 3D), the L_i^e functions for the all three nodes of a triangular element can be defined as

$$\begin{bmatrix} L_1 \\ L_2 \\ L_3 \end{bmatrix} = \frac{1}{A^e}\begin{bmatrix} A_1 \\ A_2 \\ A_3 \end{bmatrix} = \frac{1}{2A^e}\begin{bmatrix} a_1 & b_1 & c_1 \\ a_2 & b_2 & c_2 \\ a_3 & b_3 & c_3 \end{bmatrix} \tag{6.5}$$

Here, the Lagrange functions depend on the choice of point Q in the element. Similarly, for a 3D tetrahedral element, the Lagrange functions can be defined in a compact matrix form as

$$\begin{bmatrix} L_1 \\ L_2 \\ L_3 \\ L_4 \end{bmatrix} = \frac{1}{V^e}\begin{bmatrix} A_1 \\ A_2 \\ A_3 \\ A_4 \end{bmatrix} = \frac{1}{6V^e}\begin{bmatrix} a_1 & b_1 & c_1 & d_1 \\ a_2 & b_2 & c_2 & d_2 \\ a_3 & b_3 & c_3 & d_3 \\ a_4 & b_4 & c_4 & d_4 \end{bmatrix} \tag{6.6}$$

For 2D and 3D elements, the Lagrange functions depend on the elemental area and volume, respectively. Thus, these functions are also called as area and volume coordinates for 2D and 3D problems.

To formulate the shape function, at first each node of the element (linear and quadratic triangular or tetrahedral) is numbered as shown in Fig. 6.3. For a 2D element, the node numbers consist of three digits, whereas for a 3D element, it has four digits. The number of digits depends on the number of area or volume coordinates (Lagrange functions) required to define an element. For example, three area and four volume coordinates need to define 2D triangular and 3D tetrahedral elements, respectively. The nodes 1, 2, and 3 of a 2D linear triangular element are numbered as (100), (010), and (001), respectively. Thus, the shape function (N_i^e) correlated with node i can be expressed as [7]

$$N_i^e = Q_p^{(n)} L_1 Q_q^{(n)} L_2 Q_r^{(n)} L_3, \quad p + q + r = n \tag{6.7}$$

where p, q, r denote the individual digits of a node number and n denotes the element order. For example, p, q, and r of node 1 have the values of 1, 0, and 0, respectively. Here, the first multiplied term can be defined as

$$Q_p^{(n)} L_1 = \frac{n}{p!}\prod_{m=0}^{p-1}\Big((m+1)L_1 - m\Big) \tag{6.8}$$

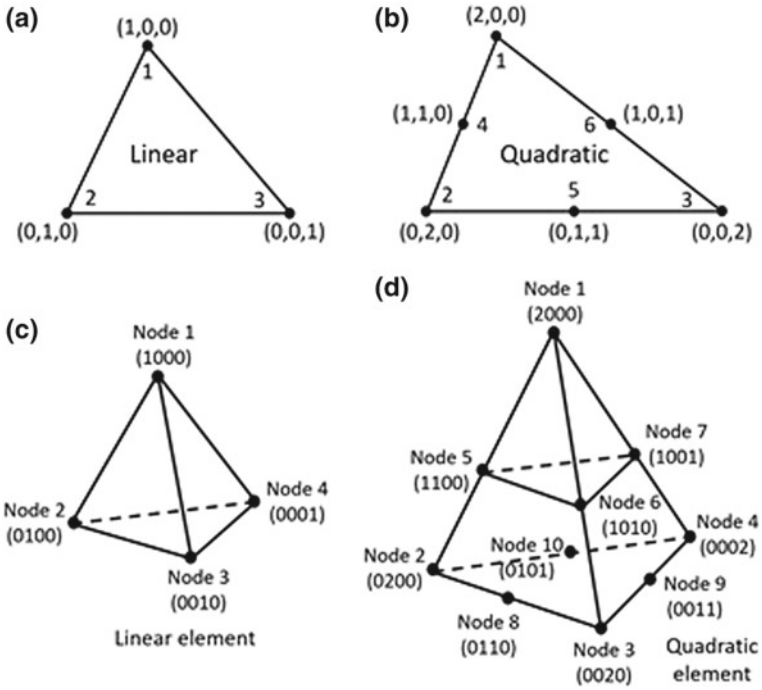

Fig. 6.3 Linear and quadratic elements and their node numbering scheme depending on the element order. **a** and **b** are the linear and quadratic 2D triangular elements, respectively. **c** and **d** are the liner and quadratic 3D tetrahedral elements, respectively

The other multiplied terms, $Q_q^{(n)}L_2$ and $Q_r^{(n)}L_3$, are defined as [8], where $Q_0^{(n)}$ is taken as 1. Thus, the relations between the shape functions and corresponding Lagrange polynomials for a linear triangular element shown in Fig. 6.3a can be formed with the help of Eqs. 6.7 and 6.8 as

$$\begin{aligned} N_1 &= Q_{p=1}^{(1)}L_1 Q_{q=0}^{(1)}L_2 Q_{r=0}^{(1)}L_3 = L_1 \\ N_2 &= Q_{p=0}^{(1)}L_1 Q_{q=1}^{(1)}L_2 Q_{r=0}^{(1)}L_3 = L_2 \\ N_3 &= Q_{p=0}^{(1)}L_1 Q_{q=0}^{(1)}L_2 Q_{r=1}^{(1)}L_3 = L_3 \end{aligned} \tag{6.9}$$

Similarly, for a 2D quadratic triangular element shown in Fig. 6.3b, the element order is 2 and we can get the shape functions as

$$\begin{aligned} N_1 &= Q^{(2)}_{p=2} L_1 Q^{(2)}_{q=0} L_2 Q^{(2)}_{r=0} L_3 = L_1(2L_1 - 1) \\ N_2 &= Q^{(2)}_{p=0} L_1 Q^{(2)}_{q=2} L_2 Q^{(2)}_{r=0} L_3 = L_2(2L_2 - 1) \\ N_3 &= Q^{(2)}_{p=0} L_1 Q^{(2)}_{q=0} L_2 Q^{(2)}_{r=3} L_3 = L_3(2L_3 - 1) \\ N_4 &= Q^{(2)}_{p=1} L_1 Q^{(2)}_{q=1} L_2 Q^{(2)}_{r=0} L_3 = 4L_1 L_2 \\ N_5 &= Q^{(2)}_{p=0} L_1 Q^{(2)}_{q=1} L_2 Q^{(2)}_{r=1} L_3 = 4L_2 L_3 \\ N_6 &= Q^{(2)}_{p=1} L_1 Q^{(2)}_{q=0} L_2 Q^{(2)}_{r=1} L_3 = 4L_1 L_3 \end{aligned} \tag{6.10}$$

In a similar fashion, a three-dimensional domain can be discretized with linear and quadratic tetrahedral elements (first order and second order). The numbering scheme of those elements is shown in Fig. 6.3c, d. The shape functions for those elements can also be written with the help of Eqs. 6.7 and 6.8 as

$$N_1 = Q^{(1)}_{p=1} L_1 Q^{(1)}_{q=0} L_2 Q^{(1)}_{r=0} L_3 Q^{(1)}_{s=0} L_4 = L_1 \tag{6.11}$$

and following the same steps for the other nodes,

$$N_2 = L_2, \quad N_3 = L_3, \quad N_4 = L_4 \tag{6.12}$$

Similar to the case of quadratic tetrahedral element, the shape functions can be listed as

$$\begin{aligned} &N_1 = L_1(2L_1 - 1), N_2 = L_2(2L_2 - 1), N_3 = L_3(2L_3 - 1), N_4 = 4L_1 L_2, \\ &N_5 = 4L_1 L_3, N_6 = 4L_1 L_4, N_7 = 4L_2 L_3, N_9 = 4L_3 L_4, N_{10} = 4L_2 L_4 \end{aligned} \tag{6.13}$$

Once the domain is discretized with sufficient number of elements of user's choice, any unknown function ϕ inside the element can be approximated in terms of the element coordinates and constant coefficients as

$$\phi^e_i = a_i + b_i x + c_i y \quad For\, 2D \tag{6.14}$$

$$\phi^e_i = a_i + b_i x + c_i y + d_i z \quad for\, 3D \tag{6.15}$$

with i being the node number per element

$$i = 1,\ 2,\ 3,\ 4 \tag{6.16}$$

Next, by solving the constant coefficients (a^e_i, b^e_i, c^e_i and d^e_i) in terms of ϕ^e_i and also solving the shape functions (N_i) for the specific element, the unknown function can be interpolated for an element as

$$\phi^e = \sum_i^n N_i \psi^e_i \tag{6.17}$$

6.3 Scalar Finite Element Method for Mode Analysis

The main advantages of the scalar finite element method (SC-FEM) are that the matrices produced in the eigenvalue equations are symmetric and small [10]. Also, SC-FEM does not suffer from the spurious problem. However, SC-FEM gives accurate results only when a homogeneous medium is considered or, in other words, when the boundary conditions are assumed, the field and its derivative are continuous. Here, we discuss the analysis of a 2D cross-sectional waveguide using the SC-FEM. However, the full vectorial analysis is discussed later in this chapter throughout the application of the penalty function method, and by introducing the vector finite element method, the field values are vectors and stored in the element edges. In SC-FEM, the nodal finite element is used where the field values are stored in the nodes.

There are two ways to solve optical waveguide problems [1, 11–13]: the variational methods and the weighted residual methods. Both methods yield similar eigenvalue equations which need to be solved.

In the variational methods, the computational domain shown in Fig. 6.4 is divided into number of segments and the variational principle is applied to the sum of the discretized functions of all segments.

In the variational principle, the solution of the waveguide problem requires to already know the function. Unlike the variational principle, the governing partial differential equation of electromagnetic wave propagation is already known. Therefore, the weighted residual methods, especially the Galerkin method, are very powerful in solving the electromagnetic wave equations.

6.3.1 Galerkin Method

The Galerkin method is a very powerful and a widely used tool not only in the FEM but also in the analysis methods such as spectral methods [14, 15].

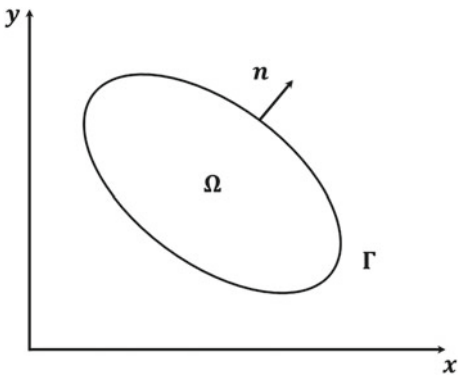

Fig. 6.4 Analysis domain

In this section, the Galerkin method is used to obtain the effective index n_{eff} by solving the scalar wave equation.

$$\frac{\partial}{\partial x}\left(p\frac{\partial \phi}{\partial x}\right)+\frac{\partial}{\partial y}\left(p\frac{\partial \phi}{\partial y}\right)+k_0^2\left(q-n_{eff}^2 p\right)\phi=0 \tag{6.18}$$

with

	ϕ	p	q
TE-wave	E_x	1	ε_r
TM-wave	H_x	$1/\varepsilon_r$	1

where ϕ is the wave function, k_0 is the free-space wave number, and ε_r is the material permittivity. E_x and H_x are, respectively, the electric field and magnetic field in the x-direction. Since ϕ is the exact solution to the wave equation, the right-hand side of Eq. 6.18 is definitely zero. However, the exact solution ϕ cannot be known. Therefore, an approximate solution $\tilde{\phi}$ to the wave equation is introduced. Thus, the previous equation can be rewritten as

$$\frac{\partial}{\partial x}\left(p\frac{\partial \tilde{\phi}}{\partial x}\right)+\frac{\partial}{\partial y}\left(p\frac{\partial \tilde{\phi}}{\partial y}\right)+k_0^2\left(q-n_{eff}^2 p\right)\tilde{\phi}=\mathrm{R} \tag{6.19}$$

We have to note that substituting the approximate solution $\tilde{\phi}$ in Eq. 6.18 makes the right-hand side does not equal zero; instead, the right-hand side equals the error residual R. The error residual R can be minimized thereafter by averagely forcing the error residual R to equal zero in the whole computational domain. Since the electromagnetic field is concentrated in the core where the refractive index is higher than the cladding, the weighting function must be introduced when forcing R to equal zero. By introducing the weight function ψ, we have

$$\iint \psi\left\{\frac{\partial}{\partial x}\left(p\frac{\partial \tilde{\phi}}{\partial x}\right)+\frac{\partial}{\partial y}\left(p\frac{\partial \tilde{\phi}}{\partial y}\right)+k_0^2\left(q-n_{eff}^2 p\right)\tilde{\phi}\right\}dxdy=0 \tag{6.20}$$

This procedure is termed as "the weighted residual method" in which the differential equation is multiplied by a weight function and the integration over the analysis domain is set to zero. Applying integration by parts or Green's divergence theorem to the derivative term, we get

$$\begin{aligned}&-\iint p\left(\frac{\partial \psi}{\partial x}\frac{\partial \tilde{\phi}}{\partial x}+\frac{\partial \psi}{\partial y}\frac{\partial \tilde{\phi}}{\partial y}\right)dxdy+\iint \psi k_0^2\left(q-n_{eff}^2 p\right)\tilde{\phi}\,dxdy\\&+\left[\int_\Gamma p\psi\frac{\partial \tilde{\phi}}{\partial n}\cdot n\,d\Gamma\right]=0\end{aligned} \tag{6.21}$$

where $\int_\Gamma d\Gamma$ is the line integral calculated at the boundary Γ surrounding the computational domain and $\partial/\partial n$ is the derivative with respect to the normal vector n. The Green divergence theorem converts the second derivative term in the integration of Eq. 6.20 into a first-order derivative and a line integral Eq. 6.21. The Galerkin method expands the wave function $\tilde{\phi}$ and the weight function ψ using the same basis function.

As mentioned before, the computational domain is firstly divided into small regions called elements. Then, the Galerkin procedure is applied to each element. After that, the contributions from all elements are summed up. The equation for element e in the divided elements can be expressed as

$$\begin{aligned} &-\iint_{\Omega_e} p\left(\frac{\partial \psi_e}{\partial x}\frac{\partial \tilde{\phi}_e}{\partial x}+\frac{\partial \psi_e}{\partial y}\frac{\partial \tilde{\phi}_e}{\partial y}\right)dxdy+\iint_{\Omega_e}\psi_e k_0^2\left(q-n_{eff}^2 p\right)\tilde{\phi}_e\,dx\,dy \\ &+\left[\int_{\Gamma_e} p\psi_e\frac{\partial \tilde{\phi}_e}{\partial n}\cdot n\,d\Gamma_e\right]=0 \end{aligned} \tag{6.22}$$

$\tilde{\phi}_e$ and ψ_e in element e are expressed using the same basis functions:

$$\tilde{\phi}_e=\psi_e=\sum_i^{M_e}\phi_{ei}N_i=[N_e]^T\{\phi_e\} \tag{6.23}$$

Here, M_e is the number of nodes in element e and T denotes transpose. $\{\phi_e\}$ and $[N_e]$ can be expressed as

$$\{\phi_e\}=\begin{pmatrix}\phi_1 & \phi_2 & \phi_3 & \cdots & \phi_{M_e}\end{pmatrix} \tag{6.24}$$

$$[N_e]=[N_1 \quad N_2 \quad N_3 \quad \ldots \quad N_{M_e}]^T \tag{6.25}$$

We have to note that the expansion coefficient ϕ_{ei} and the basis function N_i resemble the field component and the shape function. By substituting Eq. 6.23 into Eq. 6.22, we get

$$\begin{aligned} &\{\phi_e\}^T\iint_e -p\left\{\frac{\partial[N_e]}{\partial x}\frac{[N_e]^T}{\partial x}+\frac{[N_e]}{\partial y}\frac{[N_e]^T}{\partial y}\right\}dxdy\,\{\phi_e\} \\ &+\{\phi_e\}^T k_0^2\iint_e\left(q-n_{eff}^2 p\right)[N_e][N_e]^T dxdy\{\phi_e\}+\left[\int_{\Gamma_e} p\psi_e\frac{\partial \tilde{\phi}_e}{\partial n}\cdot n\,d\Gamma_e\right]=0 \end{aligned} \tag{6.26}$$

We can rewrite the previous equation as

$$\{\phi_e\}^T\left([A_e]+k_0^2[B_e]-\beta^2[C_e]\right)\{\phi_e\}+\left[\int_{\Gamma_e} p\tilde{\phi}_e\frac{\partial \tilde{\phi}_e}{\partial n}\cdot n\,d\Gamma_e\right]=0 \tag{6.27}$$

with

$$[A_e] = \iint_e -p\left\{\frac{\partial[N_e]}{\partial x}\frac{[N_e]^T}{\partial x} + \frac{[N_e]}{\partial y}\frac{[N_e]^T}{\partial y}\right\}dxdy \tag{6.28}$$

$$[B_e] = \iint_e q[N_e][N_e]^T dxdy \tag{6.29}$$

and

$$[C_e] = \iint_e p[N_e][N_e]^T dxdy \tag{6.30}$$

where β is the propagation constant and $\beta^2 = k_0^2 n_{eff}^2$ is the eigenvalue of the eigenvalue equation. Now, we sum up the contribution from all elements in the computational domain. Therefore, we get

$$\sum_e \{\phi_e\}^T\left([A_e] + k_0^2[B_e] - \beta^2[C_e]\right)\{\phi_e\} + \sum_e\left[\int_{\Gamma_e} p\tilde{\phi}_e \frac{\partial\tilde{\phi}_e}{\partial n}\cdot n\, d\Gamma_e\right] = 0 \tag{6.31}$$

where Σ_e extends over all elements in the computational domain. For simplicity, the previous equation can be written as

$$\{\phi\}^T\left([A] + k_0^2[B] - \beta^2[C]\right)\{\phi\} + \sum_e\left[\int_{\Gamma_e} p\tilde{\phi}_e \frac{\partial\tilde{\phi}_e}{\partial n}\cdot n\, d\Gamma_e\right] = 0 \tag{6.32}$$

where $\{\phi\}$, $[A]$, $[B]$, and $[C]$ are expressed as

$$\{\phi\} = \sum_e \{\phi_e\} \quad [A] = \sum_e [A_e] \quad [B] = \sum_e [B_e] \quad [C] = \sum_e [C_e] \tag{6.33}$$

If we assume $\tilde{\phi}_e$ and its normal derivative $\partial\tilde{\phi}_e/\partial n$ are continuous at the boundaries between elements, the second term in Eq. 6.32 is reduced to only a line integral surrounding the computational domain as the inner line integral cancels out each other. It is worth mentioning that this assumption is valid only for certain type of problems in which the computational domain contains only one material or when the difference between the dielectric constants in the computational domain is not significant. Finally, Eq. 6.32 can be written as

$$\{\phi\}^T\left([A] + k_0^2[B] - \beta^2[C]\right)\{\phi\} + \sum_e\left[\oint_\Gamma \tilde{\phi}\frac{\partial\tilde{\phi}}{\partial n}\cdot n\, d\Gamma\right] = 0 \tag{6.34}$$

When Neumann $(\partial\tilde{\phi}/\partial n = 0)$ or Dirichlet $(\tilde{\phi} = 0)$ boundary conditions are assumed, we can neglect the second term in Eq. 6.34 leaving only the first term. Since $\{\phi\}^T$ cannot equal zero, we can divide both sides by $\{\phi\}^T$ leading to

$$\left([A] + k_0^2[B] - \beta^2[C]\right)\{\phi\} = 0 \tag{6.35}$$

6.3.2 Stiffness and Mass Matrices

Here, the matrix elements for the first-order and second-order triangular elements are discussed. Starting from the eigenvalue equation (Eq. 6.35) derived earlier,

$$\left([A] + k_0^2[B] - \beta^2[C]\right)\{\phi\} = 0 \tag{6.36}$$

where

$$\begin{aligned}
[A] &= \sum_e \iint_e -p\left\{\frac{\partial[N_e]}{\partial x}\frac{[N_e]^T}{\partial x} + \frac{[N_e]}{\partial y}\frac{[N_e]^T}{\partial y}\right\}dxdy \\
[B] &= \sum_e \iint_e q[N_e][N_e]^T dxdy \\
[C] &= \sum_e \iint_e p[N_e][N_e]^T dxdy
\end{aligned} \tag{6.37}$$

Since p and q are constants over the elements, we have only the following two integrands to evaluate:

$$\iint_e \left\{\frac{\partial[N_e]}{\partial x}\frac{[N_e]^T}{\partial x} + \frac{[N_e]}{\partial y}\frac{[N_e]^T}{\partial y}\right\}dxdy \tag{6.38}$$

which is commonly known as the stiffness matrix, and

$$\iint_e [N_e][N_e]^T dxdy \tag{6.39}$$

which is known as the mass matrix.

To perform the integral calculus, we first need to explicitly express the area coordinates (Lagrange interpolation polynomials) L_1, L_2, and L_3 because the shape function $[N_e]$ is expressed by the area coordinates as mentioned earlier. The area coordinates can be expressed as

$$L_1 = \frac{Q_1(x - x_2) + R_1(y - y_2)}{2S_e} \tag{6.40}$$

$$L_2 = \frac{Q_2(x - x_3) + R_2(y - y_3)}{2S_e} \tag{6.41}$$

$$L_3 = \frac{Q_3(x - x_1) + R_3(y - y_1)}{2S_e} \tag{6.42}$$

where

$$\begin{aligned} Q_1 &= y_2 - y_3 \\ Q_2 &= y_3 - y_1 \\ Q_3 &= y_1 - y_2 \\ R_1 &= x_3 - x_2 \\ R_2 &= x_1 - x_3 \\ R_3 &= x_2 - x_1 \end{aligned} \tag{6.43}$$

and

$$S_e = \frac{1}{2}[(y_3 - y_1)(x_2 - x_1) - (x_3 - x_1)(y_2 - y_1)] \tag{6.44}$$

Now, for the first-order triangular element, the stiffness matrix can be expressed as

$$\begin{aligned} &\iint_e \left\{ \frac{\partial [N_e]}{\partial x} \frac{[N_e]^T}{\partial x} + \frac{[N_e]}{\partial y} \frac{[N_e]^T}{\partial y} \right\} dxdy \\ &= \iint_e \begin{pmatrix} \partial N_1/\partial x & \partial N_1/\partial y \\ \partial N_2/\partial x & \partial N_2/\partial y \\ \partial N_3/\partial x & \partial N_3/\partial y \end{pmatrix} \begin{pmatrix} \dfrac{\partial N_1}{\partial x} & \dfrac{\partial N_2}{\partial x} & \dfrac{\partial N_3}{\partial x} \\ \dfrac{\partial N_1}{\partial y} & \dfrac{\partial N_2}{\partial y} & \dfrac{\partial N_3}{\partial y} \end{pmatrix} dxdy \end{aligned} \tag{6.45}$$

where the derivatives can be evaluated from the area coordinates as

$$\frac{\partial N_1}{\partial x} = \frac{Q_1}{2S_e} \quad \frac{\partial N_2}{\partial x} = \frac{Q_2}{2S_e} \quad \frac{\partial N_3}{\partial x} = \frac{Q_3}{2S_e} \tag{6.46}$$

and

$$\frac{\partial N_1}{\partial y} = \frac{R_1}{2S_e} \quad \frac{\partial N_2}{\partial y} = \frac{R_2}{2S_e} \quad \frac{\partial N_3}{\partial y} = \frac{R_3}{2S_e} \tag{6.47}$$

Since all the derivatives are constants, Eq. 6.45 can be written as

$$\begin{aligned}&\iint_e \left\{ \frac{\partial [N_e]}{\partial x} \frac{[N_e]^T}{\partial x} + \frac{[N_e]}{\partial y} \frac{[N_e]^T}{\partial y} \right\} dxdy \\ &= \begin{pmatrix} \partial N_1/\partial x & \partial N_1/\partial y \\ \partial N_2/\partial x & \partial N_2/\partial y \\ \partial N_3/\partial x & \partial N_3/\partial y \end{pmatrix} \begin{pmatrix} \frac{\partial N_1}{\partial x} & \frac{\partial N_2}{\partial x} & \frac{\partial N_3}{\partial x} \\ \frac{\partial N_1}{\partial y} & \frac{\partial N_2}{\partial y} & \frac{\partial N_3}{\partial y} \end{pmatrix} S_e \end{aligned} \tag{6.48}$$

For the mass matrix, the resulted integral can be explicitly expressed as

$$\iint_e [N_e][N_e]^T dxdy = S_e \begin{pmatrix} 1/6 & 1/12 & 1/12 \\ 1/12 & 1/6 & 1/12 \\ 1/12 & 1/12 & 1/6 \end{pmatrix} \tag{6.49}$$

For the second-order triangular element, the stiffness matrix can be expressed as

$$\begin{aligned}&\iint_e \left\{ \frac{\partial [N_e]}{\partial x} \frac{[N_e]^T}{\partial x} + \frac{[N_e]}{\partial y} \frac{[N_e]^T}{\partial y} \right\} dxdy \\ &= \iint_e \begin{pmatrix} \partial N_1/\partial x & \partial N_1/\partial y \\ \partial N_2/\partial x & \partial N_2/\partial y \\ \partial N_3/\partial x & \partial N_3/\partial y \\ \partial N_4/\partial x & \partial N_4/\partial y \\ \partial N_5/\partial x & \partial N_5/\partial y \\ \partial N_6/\partial x & \partial N_6/\partial y \end{pmatrix} \begin{pmatrix} \frac{\partial N_1}{\partial x} & \frac{\partial N_2}{\partial x} & \frac{\partial N_3}{\partial x} & \frac{\partial N_4}{\partial x} & \frac{\partial N_5}{\partial x} & \frac{\partial N_6}{\partial x} \\ \frac{\partial N_1}{\partial y} & \frac{\partial N_2}{\partial y} & \frac{\partial N_3}{\partial y} & \frac{\partial N_4}{\partial y} & \frac{\partial N_5}{\partial y} & \frac{\partial N_6}{\partial y} \end{pmatrix} dxdy \end{aligned} \tag{6.50}$$

It is worth noting that the shape function derivatives are not constants but linear functions of the area coordinate. Therefore, after getting the shape function derivatives as described earlier using the area coordinates, the integration over the element has to be performed. Finally, the integrand of the second-order stiffness matrix can be written as

$$\iint_e \left\{ \frac{\partial [N_e]}{\partial x} \frac{[N_e]^T}{\partial x} + \frac{[N_e]}{\partial y} \frac{[N_e]^T}{\partial y} \right\} dxdy = \begin{pmatrix} a_{11} & a_{12} & a_{13} & a_{14} & a_{15} & a_{16} \\ a_{21} & a_{22} & a_{23} & a_{24} & a_{25} & a_{26} \\ a_{31} & a_{32} & a_{33} & a_{34} & a_{35} & a_{36} \\ a_{41} & a_{42} & a_{43} & a_{44} & a_{45} & a_{46} \\ a_{51} & a_{52} & a_{53} & a_{54} & a_{55} & a_{56} \\ a_{61} & a_{62} & a_{63} & a_{64} & a_{65} & a_{66} \end{pmatrix} \tag{6.51}$$

where

$$
\begin{aligned}
a_{11} &= (Q_1^2 + R_1^2)/4S_e \\
a_{22} &= (Q_2^2 + R_2^2)/4S_e \\
a_{33} &= (Q_3^2 + R_3^2)/4S_e \\
a_{12} = a_{21} &= -(Q_1Q_2 + R_1R_2)/12S_e \\
a_{13} = a_{31} &= -(Q_1Q_3 + R_1R_3)/12S_e \\
a_{23} = a_{32} &= -(Q_2Q_3 + R_2R_3)/12S_e \\
a_{14} = a_{41} &= (Q_1Q_2 + R_1R_2)/3S_e \\
a_{15} = a_{51} &= 0 \\
a_{16} = a_{61} &= (Q_1Q_3 + R_1R_3)/3S_e \\
a_{24} = a_{42} &= (Q_1Q_2 + R_1R_2)/3S_e \\
a_{25} = a_{52} &= (Q_2Q_3 + R_2R_3)/3S_e \\
a_{26} = a_{62} &= (Q_2Q_3 + R_2R_3)/3S_e \\
a_{34} = a_{43} &= 0 \\
a_{35} = a_{53} &= (Q_2Q_3 + R_2R_3)/3S_e \\
a_{36} = a_{63} &= (Q_1Q_3 + R_1R_3)/3S_e \\
a_{44} &= 2\left(Q_1^2 + Q_2^2 + Q_1Q_2 + R_1^2 + R_2^2 + R_1R_2\right)/3S_e \\
a_{55} &= 2\left(Q_3^2 + Q_2^2 + Q_3Q_2 + R_3^2 + R_2^2 + R_3R_2\right)/3S_e \\
a_{66} &= 2\left(Q_1^2 + Q_3^2 + Q_1Q_3 + R_1^2 + R_3^2 + R_1R_3\right)/3S_e \\
a_{45} = a_{54} &= 2\left(Q_2^2 + Q_2Q_3 + 2Q_1Q_3 + Q_1Q_2 + R_2^2 + R_2R_3 + 2R_1R_3 + R_1R_2\right)/3S_e \\
a_{46} = a_{64} &= 2\left(Q_1^2 + Q_1Q_2 + 2Q_2Q_3 + Q_1Q_3 + R_1^2 + R_1R_2 + 2R_2R_3 + R_1R_3\right)/3S_e \\
a_{56} = a_{65} &= 2\left(Q_3^2 + Q_1Q_3 + 2Q_1Q_2 + Q_2Q_3 + R_3^2 + R_1R_3 + 2R_1R_2 + R_2R_3\right)/3S_e
\end{aligned}
\tag{6.52}
$$

For the mass matrix, the resulted integral can be expressed explicitly as

$$
\begin{aligned}
&\iint_e [N_e][N_e]^T dxdy \\
&= S_e \begin{pmatrix}
1/30 & -1/180 & -1/180 & 0 & -1/45 & 0 \\
-1/180 & 1/30 & -1/180 & 0 & 0 & -1/45 \\
-1/180 & -1/180 & 1/30 & -1/45 & 0 & 0 \\
0 & 0 & -1/45 & 8/45 & 4/45 & 4/45 \\
-1/45 & 0 & 0 & 4/45 & 8/45 & 4/45 \\
0 & -1/45 & 0 & 4/45 & 4/45 & 8/45
\end{pmatrix}
\end{aligned}
\tag{6.53}
$$

We have thus obtained the local stiffness and mass matrix for the first-order element and the second-order element. To obtain the global stiffness and mass matrices, the local matrices are evaluated first for each element in the computational domain. Then, the evaluated matrices have to be summed up to form the global stiffness and mass matrices. Since the local matrices are symmetric, it is anticipated that the global matrices also are symmetric.

6.3.3 Assessment

A simple example to assess the finite element method is to compute the cutoff number of an air-filled rectangular waveguide [16] shown in Fig. 6.5.

This problem is a perfect assessment for the proposed method as it has an exact solution where the performance of the SC-FEM can be tested. Also, since the medium inside the waveguide is a homogeneous material and the material is bounded by a perfect electric conductor (PEC), SC-FEM is the excellent choice for this type of problems. The width of the waveguide is set $a = 1.2$ μm, and the height is $b = 1$ μm. The simulation wavelength is $\lambda = 1.5$ μm. The exact solution of the cutoff number can be calculated directly from the following relation:

$$Kc_{mn} = \sqrt{\left(\frac{m\pi}{a}\right)^2 + \left(\frac{n\pi}{b}\right)^2} \tag{6.54}$$

where m and n are eigennumbers that take integer values 0, 1, 2, …. According to the width and height of the presented waveguide, the fundamental cutoff for TM-wave ($m = 1$, $n = 1$) equals $Kc_{11} = 4.089437167421735$ (rad/m).

For the first-order element, the computational domain is divided into first-order triangular elements. Then, after evaluating the local matrices, the global matrices are assembled. Since the wave function ϕ equals zero at the boundary of the waveguide, it is convenient to reduce the order of the assembled matrices by removing the rows and columns corresponding to the nodes setting on the boundary. Finally, the eigenvalue equation Eq. 6.18 is solved for the eigenvalue β. Hence, the cutoff number can be evaluated numerically using the following relation:

$$Kc_{mn} = \sqrt{k_o^2 - \beta_{mn}^2} \tag{6.55}$$

Figure 6.6 shows the fundamental mode computed using the first-order triangular element after discretizing the computational domain into 3200 elements producing 1600 unknowns. The cutoff number computed is $Kc_{11} = 4.090541007769321$ rad/m with an error of $e = 0.001103840347586$.

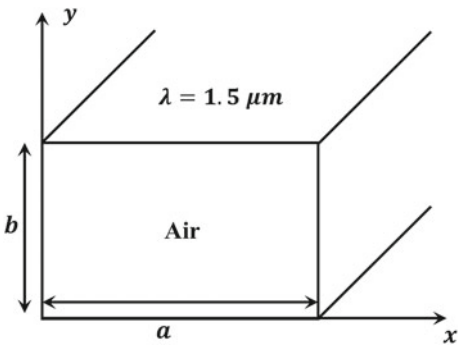

Fig. 6.5 Air-filled rectangular metallic waveguide

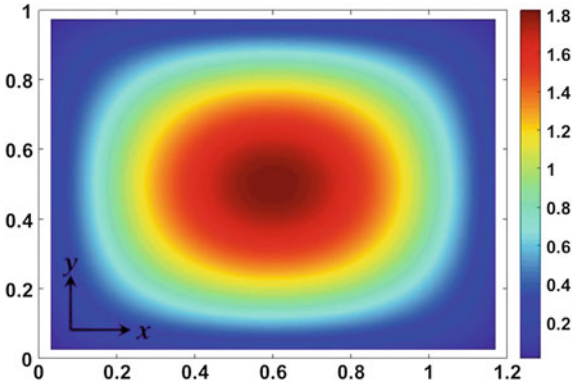

Fig. 6.6 Fundamental mode

For the second-order triangular element, the computational domain is discretized into 800s order elements which produce 1521 unknowns. Under these assumptions, The cutoff number computed is $Kc_{11} = 4.089451948101586\,\text{rad/m}$ with an error of $e = 0.000014780679851$. As may be noticed, the error produced by the second-order element is much less than that produced using first-order element, while using less number of unknowns.

6.3.4 Perfectly Matched Layer

Creating a practical FEM solver requires to include the effects of the simulation boundaries. As previously discussed, basic FEM boundary conditions set the field and its normal derivative at the boundary of the simulation region to zero which can be considered as the computational domain is in a metal box [12] or magnetic box. This approximation is not usually valid as in some cases we need to simulate the structures in open boundaries. Therefore, an artificial absorbing boundary condition termed perfectly matched layer (PML) [17] is used. It is a non-physical layer for wave equations. It is commonly used to truncate analysis region to mimic open boundary conditions. As it can be noticed from its name "perfectly matched," it is made to be matched with the nearby domain. In other words, the incident waves on the PML are not allowed to reflect. This feature advantages the PML over any other absorbing material. This property permits the PML to effectively absorb outgoing waves from the interior of the computational domain without reflecting them back into this domain.

In 1994, Berenger group developed the first PML [17] called "split-field PML" for using with Maxwell's equations. Since then it has become an area of research and several modified versions of PML for Maxwell's equations and other wave equations such as Schrodinger's equation have been developed. The split-field PML splits the electromagnetic field into two non-physical field components in the PML region. Later, a further improved formulation called uniaxial PML or UPML [18]

has earned popularity because of its efficiency and simplicity. UPML is described as an artificial anisotropic absorbing material. Although both UPML and split-field PML were initially derived by developing the conditions which force no reflection comes from the incident plane waves, both formulations were later proved to be comparable to a more neat approach termed stretched coordinate PML [19, 20]. Such approach uses the so-called coordinate transformation. The coordinate transformation maps one (or more) coordinate to a complex number. This approach is actually like an analytic continuation of the wave equation into complex coordinates, replacing the propagating wave by exponentially decaying one. This viewpoint of PML allows the extension for inhomogeneous media such as waveguides, as well as for other wave equations and other coordinate systems such as cylindrical coordinates. In this chapter, the stretched coordinate PML is used with a basic principle of replacing the original derivatives in the wave equation as follows:

$$\frac{\partial}{\partial x} \rightarrow \frac{s_x}{s}\frac{\partial}{\partial x} \quad \frac{\partial}{\partial y} \rightarrow \frac{s_y}{s}\frac{\partial}{\partial y} \tag{6.56}$$

where s, s_x, and s_y are the coordinate stretching parameters. By substituting this equation into Eq. 6.18, we get after some derivations

$$s_x \frac{\partial}{\partial x}\left(p\frac{s_x}{s}\frac{\partial \tilde{\phi}}{\partial x}\right) + s_y \frac{\partial}{\partial y}\left(p\frac{s_y}{s}\frac{\partial \tilde{\phi}}{\partial y}\right) + sk_0^2\left(q - n_{eff}^2 p\right)\tilde{\phi} = 0 \tag{6.57}$$

with

$$s = \begin{cases} 1 + j\frac{3c}{2n\omega_o d}\left(\frac{\rho}{d}\right)^2 \ln\,(R) & in\ PML\ region \\ 1 & otherwise \end{cases} \tag{6.58}$$

where ω_o is the angular frequency, d is the PML thickness, R is the theoretical reflection coefficient from the outer boundary of the PML, and ρ is the distance of the element from the beginning of the PML.

Figure 6.7 shows the computational domain including the PML and the definition of s_x and s_y.

This slight modification in the wave equation, in turn, modifies the SC-FEM matrices defined in Eq. 6.36 to be

$$\begin{aligned} [A] &= \sum_e \iint_e -p\left\{\frac{s_x^2}{s}\frac{\partial [N_e]}{\partial x}\frac{[N_e]^T}{\partial x} + \frac{s_y^2}{s}\frac{[N_e]}{\partial y}\frac{[N_e]^T}{\partial y}\right\} dxdy \\ [B] &= \sum_e \iint_e sq[N_e][N_e]^T dxdy \\ [C] &= \sum_e \iint_e sp[N_e][N_e]^T dxdy \end{aligned} \tag{6.59}$$

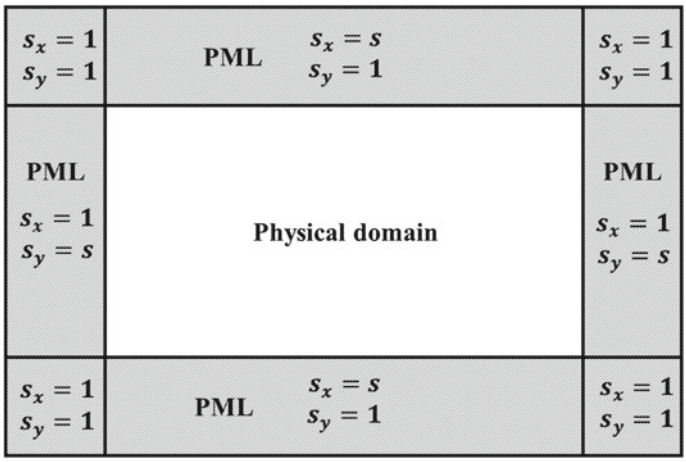

Fig. 6.7 Definition of the PML parameters s_x and s_y

6.3.5 Variations of the Conventional FEM

Several FEM analysis relies on the second-order triangular element due to the poor accuracy of the first-order triangular element [21–24]. However, for the conventional second-order element, the additional nodes located between the pairs of triangular vertices cannot be adjusted to set on the boundary of a curved structure. This problem was solved by using curvilinear elements [25]. Compared with conventional elements, curvilinear element approach converges faster for curved structures. However, the first-order element is often preferable because of its computational simplicity and easiness for adaptive mesh refinement. Moreover, most of mesh generation software rely on first-order triangular elements.

As a consequence, several research efforts have been dedicated to increase the accuracy of the first-order element. Recently, a new technique termed "smoothed Galerkin" has been introduced [26, 27]. This new technique relies on weakening the weak form ($W2$) as in mesh-free methods [28]. Beside approximating the field variable, $W2$ form approximates also the field derivatives via the gradient smoothing technique [29]. The high accuracy and the less sensitivity to mesh distortion are the most important features of $W2$ form. The accuracy of any method relying on the Galerkin form can be improved by using the smoothed Galerkin form that introduces a novel class of so-called smoothed finite element method (SFEM) for various mechanics problems. The shape function derivatives at element boundaries, in the conventional FEM, are numerically discontinuous which causes FEM poor performance. This disadvantage in FEM has been smartly overcome in SFEM by approximating the derivatives at the element boundaries to be continuous. The SFEM has been recently introduced for time domain analysis of photonic devices [30, 31].

6.3.6 Time Domain Methods

The rapid progress in the field of nanophotonics has sparked a series of fundamental research in the numerical methods that could cope up with this rapid progress. These numerical methods have been applied to solve Maxwell's equations in its both forms: frequency and time domains. Time domain solution to Maxwell's equations enjoys a paramount advantage over the frequency domain solution. This advantage is represented in the capability of covering a wide range of frequencies in a single simulation run. Also, time domain methods give the actual behavior of the interaction between light and photonic structures. Therefore, these methods are essential for design and performance prediction in real-time situations.

The finite difference method (FDM) is a very powerful and versatile method [6]. It gained its reputation from its computational simplicity and its applicability to several photonic problems. Based on the FDM, a time domain method termed "finite difference time domain (FDTD)" has been introduced [6]. The FDTD has been used widely in modeling photonic devices. It also has been extended to include several types of materials such as anisotropic, dispersive, and nonlinear materials. However, it suffers from inefficient discretization of irregularly shaped geometries. Such disadvantage stands against precise modeling of complex photonic structures and curved geometries such as photonic crystal fiber structures. This problem is commonly known as "the *staircasing* problem." Beside this problem, the conventional FDTD experiences stability problems where the time step size should satisfy the so-called Courant–Friedrichs–Lewy condition which makes the FDTD greatly sensitive to the step size choice. Such condition reduces the used time step size and consequently increases the overall computational time. Various variations of the FDTD have been proposed to overcome the stability problem. Based on the time domain beam propagation method (TD-BPM), a FDTD-BPM has been introduced. TD-BPM removes the fast varying field component leaving only the slowly varying field to be simulated [32, 33]. Such approximation has allowed a moderate time step size to be used. Also, a complex envelope alternating direction implicit technique (CE-ADI-FDTD) [7] and split step technique (SS-FDTD) [34] have been proposed to employ large time step size. Unlike the FDTD-BPM, CE-ADI-FDTD and SS-FDTD rely on simulating the coupled Maxwell's equations which require to solve three coupled equations at each time step causing more computational cost.

6.4 Finite Element Time Domain

Alternatively, the finite element method (FEM) provides a genuine solution to the *staircasing* problem. It has the ability to discretize the computational domain into triangular elements and accurately model curved and complex geometries. A variety of finite element time domain (FETD) techniques has been introduced over the

past decade. Generally speaking, there are two types of the FEM methods that are the nodal FEM and the edge FEM. In the nodal FEM, the field unknowns are stored at the vertices of the element, whereas in the edge FEM, the field unknowns are stored at the element edges instead of its vertices. The later has the ability to accurately include the boundary conditions, but it also suffers from its ill-conditioned-type resulted matrices. On the other hand, the nodal FEM produces well-conditioned matrices and also a better convergence rate. Relying on the edge basis functions, a vectorial solution to the time domain Maxwell's equations has been proposed [35]. Unfortunately, it yields a FDTD-like conditionally stable behavior. On the other hand, a solution to the curl-curl wave equation which solves one of Maxwell's equations field vectors has been presented [36]. This method is unconditionally stable; however, it produces a large system of equations that needs to be solved at each time step. Therefore, it is considered computationally expensive. Dissimilar to the vector shape function, the nodal shape function can be used to solve only one field component by solving the Helmholtz wave equation. Besides, it produces well-scaled matrices. Hence, the nodal shape functions are considered computationally efficient. Based on the nodal shape function, a solution to the time domain Maxwell's equations is made through the application of TD-BPM which permits the use of moderate time step size. FETD methods based on nodal shape function can be categorized into explicit and implicit schemes. In the explicit scheme, a mass lumping technique is used and the slowly varying wave equation is temporally discretized using central finite difference formula [13]. In this scheme, no linear system of equations is solved at each time step. However, one of the major disadvantages of this scheme is that it yields a conditionally stable time-marching algorithm where the time step size should satisfy the Courant–Friedrichs–Lewy condition to ensure the stability of the algorithm. Moreover, the used mass lumping technique severely affects the accuracy of the method. The second scheme discretizes the slowly varying wave equation in time domain yielding a linear system of equations to be solved at each time step. The advantage of the second scheme is that the produced time-marching algorithm is unconditionally stable which allows the use of moderate time step size. This scheme can be implemented by either discretizing the slowly varying wave equation using the unconditional stable Newmark-beta scheme [37] or by Padé approximation [21, 30]. The latter algorithm is less memory demanding as, unlike Newmark-beta method, it computes the field in the next time step using only the previous one.

6.4.1 Time Domain Wave Equation

Assuming the propagation is only in yz plane and there is no variation in x-direction, we can write the 2D time domain wave equation under the PML definition mentioned before as

$$\frac{-s}{c^2} q \frac{\partial^2 \phi}{\partial t^2} + \frac{\partial}{\partial y}\left(p \frac{s_y^2}{s} \frac{\partial \phi}{\partial y}\right) + \frac{\partial}{\partial z}\left(p \frac{s_z^2}{s} \frac{\partial \phi}{\partial z}\right) = 0 \tag{6.60}$$

In order to simulate large time step, the slowly varying wave approximation is introduced, in which, the fast varying wave component is removed leaving only the slow varying wave component. To do so, we assume the solution of Eq. 6.60 is composed of fast varying and slowly varying component as

$$\phi = \varphi \exp(j\omega_o t) \tag{6.61}$$

where φ is the slowly varying component of the electric or magnetic field. Further, $\exp(j\omega_o t)$ represents the fast varying component. Substituting this solution into Eq. 6.60 leads to

$$\frac{-s}{c^2} q \frac{\partial^2 \varphi}{\partial t^2} - \frac{2j\omega_o}{c^2} sq \frac{\partial \varphi}{\partial t} + \frac{\omega_o^2}{c^2} sq\varphi + \frac{\partial}{\partial y}\left(p \frac{s_y^2}{s} \frac{\partial \varphi}{\partial y}\right) + \frac{\partial}{\partial z}\left(p \frac{s_z^2}{s} \frac{\partial \varphi}{\partial z}\right) = 0 \tag{6.62}$$

Dividing the spatial domain into second-order triangular elements and applying the finite element procedure discussed earlier, we get

$$-\frac{1}{c^2}[M] \frac{d^2\{\varphi\}}{dt^2} - \frac{2j\omega_o}{c^2}[M] \frac{d\{\varphi\}}{dt} + \left([K] + \frac{\omega_o^2}{c^2}[M]\right)\{\varphi\} = 0 \tag{6.63}$$

where the finite element matrices $[K]$ and $[M]$ are given by

$$[K] = \sum_e \iint_e -p\left\{\frac{s_z^2}{s} \frac{\partial [N_e]}{\partial z} \frac{[N_e]^T}{\partial z} + \frac{s_y^2}{s} \frac{[N_e]}{\partial y} \frac{[N_e]^T}{\partial y}\right\} dzdy \tag{6.64}$$

and

$$[M] = \sum_e \iint_e sq[N_e][N_e]^T dzdy \tag{6.65}$$

6.4.2 Beam Propagation Technique

In order to propagate Eq. 6.63 in time, the derivatives in time have to be discretized. There are several formulations for time discretization; however, we restrict ourselves in this chapter to three well-known time discretization techniques which are the Newmark-beta technique [37], Crank–Nicolson [21] technique, and Padé approximation.

6.4.2.1 Newmark-Beta Technique

In Newmark-beta technique, the variation in time is approximated as a polynomial of second-order degree; therefore, the second-order and first-order derivatives in time are approximated as follows:

$$\frac{\partial^2\{\varphi\}}{\partial t^2} = \frac{\{\varphi\}_{i+1} - 2\{\varphi\}_i + \{\varphi\}_{i-1}}{\Delta t^2} \tag{6.66}$$

$$\frac{\partial\{\varphi\}}{\partial t} = \frac{\{\varphi\}_{i+1} - \{\varphi\}_{i-1}}{2\Delta t} \tag{6.67}$$

and the field variable is approximated as

$$\{\phi\} = \beta\{\varphi\}_{i+1} + (1-2\beta)\{\varphi\}_i + \beta\{\varphi\}_{i-1} \tag{6.68}$$

where Δt is the time step size between i-th and $i+1$-th time steps. β is the method stability parameter. In order to ensure the stability of this discretization technique, β should be chosen to satisfy the following condition

$$\beta \geq 0.25 \tag{6.69}$$

This discretization technique yields an implicit time-marching technique, where a system of linear equations needs to be solved at each time step. Also, this system is considered unconditionally stable. However, the Newmark-beta technique offers a way to discard the linear system of equations and hence makes the system explicit [13]. This can be made possible by allowing β to equal zero and scarificing the unconditional stability. In addition to the β condition, a mass lumping technique must be used which permits the mass matrices $[M]$ to be diagonal. The mass lumping technique can be made by

$$\left[\breve{M}_{e(i,i)}\right] = \sum_{jc}\left[M_{e(i,j)}\right] \tag{6.70}$$

In Eq. 6.70, the diagonal element of the new lumped mass matrix ($\breve{M}$) at a certain row "i " is the sum of all columns elements "jc" in the same certain row in the original mass matrix.

Unfortunately, this technique suffers from a serious stability problem as the stability condition given by Eq. 6.68 is not satisfied. Also, the mass lumping technique severely affects the accuracy of this method.

6.4.2.2 Crank–Nicolson Technique

In this technique, the second-order derivative in time is neglected. Therefore the accuracy of the method becomes severely affected as the resulted equation cannot handle higher-order modes. In this technique, the first-order derivative in time and the function are approximated as follows:

$$\frac{\partial\{\varphi\}}{\partial t} = \frac{\{\varphi\}_{i+1} - \{\varphi\}_i}{\Delta t} \tag{6.71}$$

and

$$\{\varphi\} = \theta\{\varphi\}_{i+1} + (1-\theta)\{\varphi\}_i \tag{6.72}$$

In order to ensure the stability of this discretization technique, θ should be chosen to satisfy the following condition:

$$\theta \geq 0.5 \tag{6.73}$$

This discretization technique also yields an implicit time-marching technique, where a system of linear equations needs to be solved at each time step. It also yields an unconditionally stable technique. However, the approximation of neglecting the second-order derivative in time is valid only for the paraxial approximation. Therefore, usually Padé approximation is used with the Crank–Nicolson algorithm [21, 30].

6.4.2.3 Padé Approximation

Padé approximation is a method used to approximate functions such as exponentials and square root. In this section, we adopt Padé approximation to reduce the second-order derivative in time to a first-order one. If we assume the solution of Eq. 6.63 is in the following form:

$$\{\varphi\} = e^{[A_c]t} \rightarrow \frac{\partial\{\varphi\}}{\partial t} = [A_c]e^{[A_c]t} \tag{6.74}$$

$$\frac{\partial^2\{\varphi\}}{\partial t^2} = [A_c]^2 e^{[A_c]t} \tag{6.75}$$

The second-order derivative in time can be rewritten as

$$\frac{\partial^2\{\varphi\}}{\partial t^2} = [A_c]\frac{\partial\{\varphi\}}{\partial t} \tag{6.76}$$

In the previous equation, the second-order derivative can be easily transformed into a first-order one by a characteristic matrix $[A_c]$ which can be evaluated from the solution of Eq. (6.63). Since getting the characteristic matrix is not as easy as expected; because it involves getting the square root of a matrix, Padé approximation is used to approximate the characteristic matrix $[A_c]$ as follows: Starting from Eq. 6.63, we can rewrite it in the following form:

$$\frac{1}{c^2}[M]\frac{\partial}{\partial t}\left(\frac{\partial\{\varphi\}}{\partial t}+2j\omega_o\{\varphi\}\right)=\left([K]+\frac{\omega_o^2}{c^2}[M]\right)\{\varphi\} \tag{6.77}$$

Dividing both sides by $(\partial\{\varphi\}/\partial t+j\omega_o\{\varphi\})$, we can get the following iterative equation

$$\frac{1}{c^2}[M]\frac{\partial}{\partial t}\bigg|_{i+1}=\frac{\left([K]+\frac{\omega_o^2}{c^2}[M]\right)}{\frac{\partial}{\partial t}\big|_i+2j\omega_o} \tag{6.78}$$

with initial condition

$$\frac{\partial}{\partial t}\bigg|_i=0 \tag{6.79}$$

The previous iterative formula can approximate the derivative in time using several iterations. In this work, the first iteration termed "Padé (1, 1)" is sufficed to approximate the derivative under the condition of using a moderate time step size. Hence, we have

$$\frac{1}{c^2}[M]\frac{\partial}{\partial t}\bigg|_{i=1}=\frac{\left([K]+\frac{\omega_o^2}{c^2}[M]\right)}{2j\omega_o} \tag{6.80}$$

By substituting Eq. 6.80 into Eq. 6.77, we have

$$\frac{-2j\omega_o}{c^2}\left[\tilde{M}\right]\frac{\partial\{\varphi\}}{\partial t}+\left([K]+\frac{\omega_o^2}{c^2}[M]\right)\{\varphi\}=0 \tag{6.81}$$

with

$$\left[\tilde{M}\right]=\left[[M]-\frac{c^2}{4\omega_o^2}\left([K]+\frac{\omega_o^2}{c^2}[M]\right)\right] \tag{6.82}$$

Finally, Eq. 6.81 can be discretized using Crank–Nicolson algorithm yielding the following recurrence relation:

$$[A]_i\{\varphi\}_{i+1} = [B]_i\{\varphi\}_{i+1} \tag{6.83}$$

with

$$[A]_i = \frac{-2j\omega_o}{c^2}[\tilde{M}] + 0.5\Delta t\left([K] + \frac{\omega_o^2}{c^2}[M]\right) \tag{6.84}$$

and

$$[B]_i = \frac{-2j\omega_o}{c^2}[\tilde{M}] - 0.5\Delta t\left([K] + \frac{\omega_o^2}{c^2}[M]\right) \tag{6.85}$$

The resulted system of equations is iteratively solved by using the BiCGSTAB algorithm [38].

6.4.3 Assessment

6.4.3.1 Single Mode Slab Waveguide (Perfectly Matched Layer Assessment)

The first assessment considered is the single mode slab waveguide shown in Fig. 6.8. The waveguide is excited by a pulse with a Gaussian profile in z-direction and a transverse profile φ_o corresponding to the fundamental mode of the planar waveguide. Therefore, the initial field at $t = 0$ is taken as

$$\varphi_o(y, z, t = 0) = \varphi_o(y) exp\left[-\left(\frac{z - z_o}{W_o}\right)^2\right] \cdot exp\left[-j\beta(z - z_o)\right] \tag{6.86}$$

where β is the propagation constant of the fundamental mode, z_o is the initial pulse position, and W_o is the spot size. During the simulation, W_o and z_o are taken as 2 μm and 20 μm, respectively. During the simulation, the time step size Δt and the

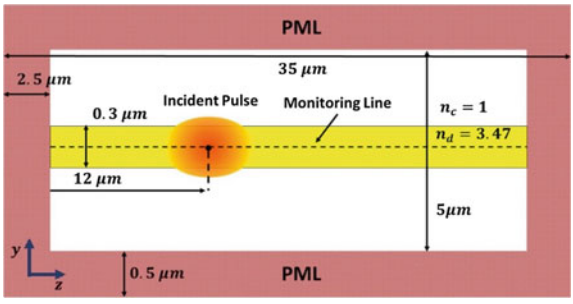

Fig. 6.8 Slab waveguide simulated

central wavelength λ_o are fixed to 1 fs and 1.55 μm, respectively. The problem is simulated for TE and TM modes. The computational domain is discretized into 1200 order triangular elements. The propagation of the injected pulse is monitored along the monitoring line placed at the center of the slab waveguide. Figure 6.9 shows the TE field on the monitoring line at a different time during the simulation.

Figure 6.9d shows the power computed at each time step during the simulation. Such a figure demonstrates the stability of the method. As it may be observed, the power is stable and normalized to 1 during the simulation which means that there is no non-physical amplification in the system. Until the propagated pulse hits the PML as it is shown in Fig. 6.9d, the power begins to drop down as an indication that the incident pulse is getting absorbed efficiently with a minimum reflection inside the PML.

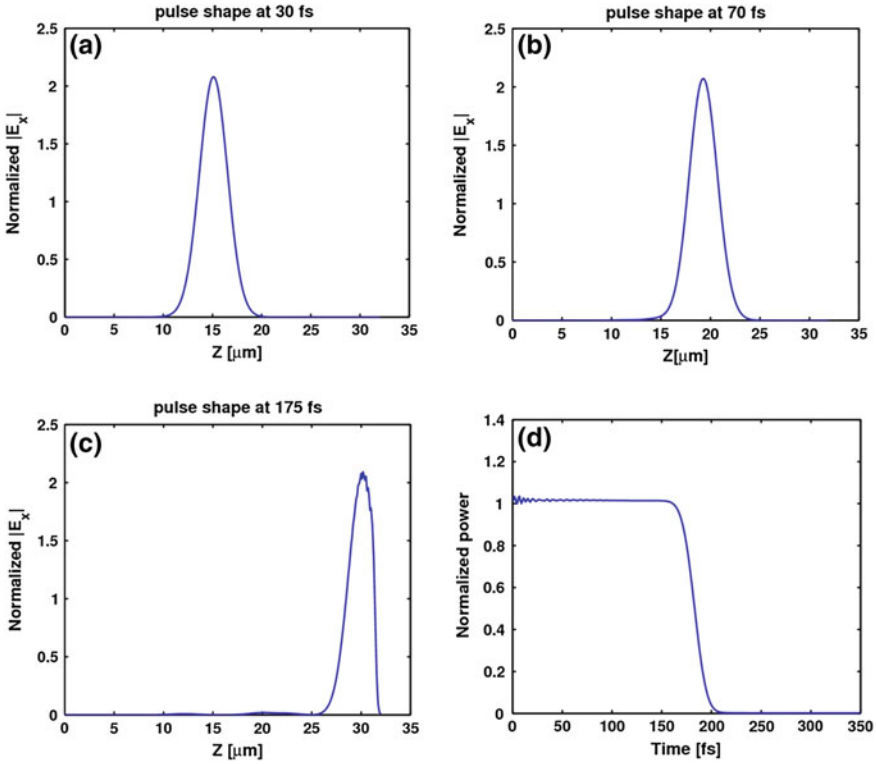

Fig. 6.9 Propagating pulse monitored inside the slab waveguide at **a** 30 fs, **b** 70 fs, and **c** 175 fs. **d** The power computed at each time step inside the slab waveguide

6.4.3.2 Optical Grating Sensor

The second assessment considered is an optical grating structure for gas sensing shown in Fig. 6.10, in which the gas is placed in the blue area. The structure is excited as described in the previous example. In this study, 220 time steps are used. The converged results are obtained by the proposed method when the computational domain is divided into 5780 structured non-uniform second-order triangular elements. This discretization produces 23835 unknowns. During the simulation run, the reflected pulse is monitored inside the waveguide at the monitoring point as shown in Fig. 6.10. By normalizing the fast Fourier transform of the reflected data to the input pulse spectrum, the reflection characteristics of the input pulse can be obtained.

In the first simulation, the refractive index of the gas is set to be equal $n_a = 1$. Figure 6.11a,b show the TE and TM mode reflection characteristics, respectively. However, in the second simulation, the refractive index of the gas is altered by 0.01. So, the refractive index is now equal $n_a = 1.01$. Figure 6.12 shows a comparison between the TE results obtained using $n_a = 1$ and $n_a = 1.01$. It may be noticed a shift between the two results. A quantitative measure of this shift directly refers to the sensitivity of the proposed sensor.

The sensitivity ($S = d\lambda_{peak}/dn$) of the proposed structure for the TE case is ~479 nm/RIU. On the other side, Fig. 6.13 shows a comparison between the TM results obtained using $n_a = 1$ and $n_a = 1.01$. It may be noticed a shift between the two results which is a bit higher than the TE case. The sensitivity of the proposed structure for the TM case is ~846 nm/RIU.

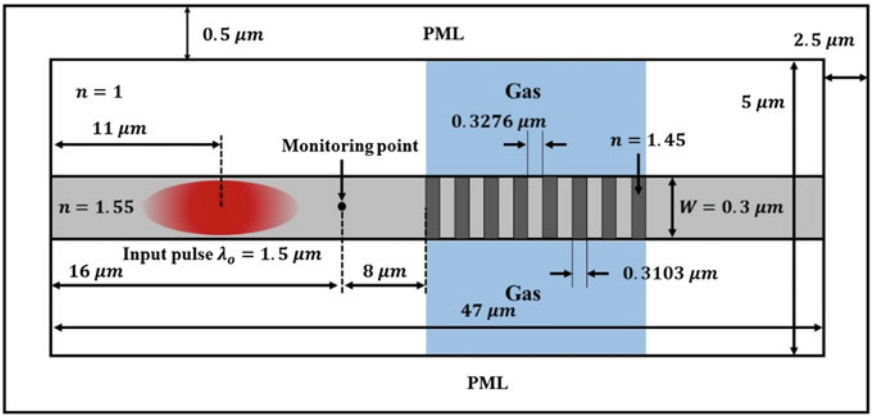

Fig. 6.10 Schematic diagram of the optical grating structure

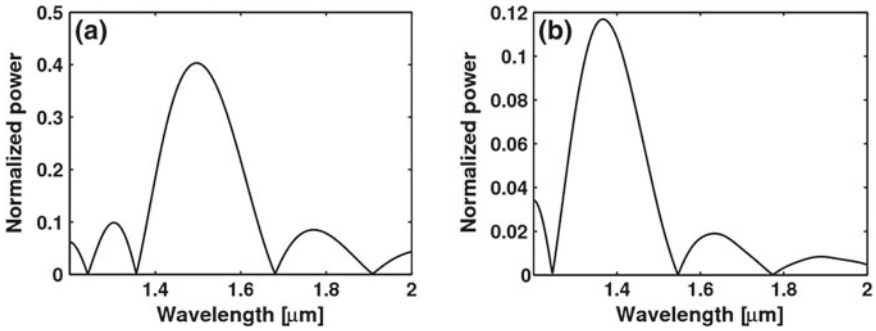

Fig. 6.11 Reflection characteristics for **a** TE mode and **b** TM mode

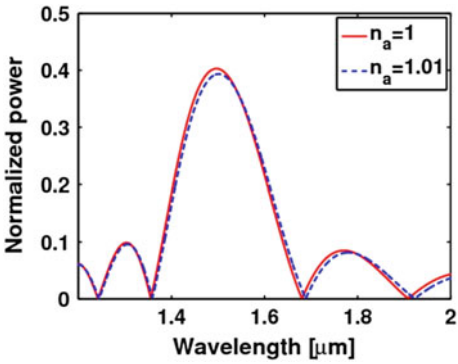

Fig. 6.12 Comparison between the TE reflection characteristics using $n_a = 1$ and $n_a = 1.01$, where n_a refers to the gas refractive index

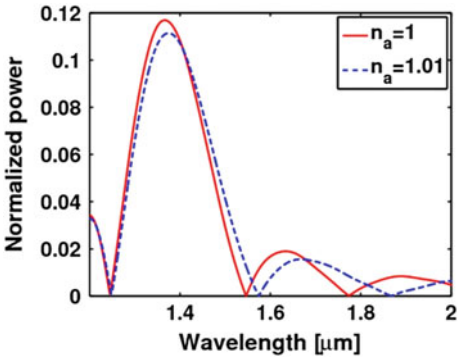

Fig. 6.13 Comparison between the TM reflection characteristics using $n_a = 1$ and $n_a = 1.01$, where n_a refers to the gas refractive index

6.5 Full Vectorial Finite Element

6.5.1 The Penalty Function Method

In the year of 1956, A. D. Berk [39] suggested several approaches to formulate the variational formulation based on different electromagnetic fields and its combinations. Generally, four different formulations can be considered, such as $E_z + H_z$, E-field, H-field, and E + H-field-based formulations. Both the E_z and H_z fields are continuous at the material interfaces. However, the $E_z + H_z$ formulation ends with a nonstandard eigenvalue problem. Extra computational effort needs to convert it into conventional standard form. As the E-field does not follow the continuity at the boundaries, the force boundary conditions need to implement externally in the E-field formulation. Among them, the H-field formulation is the most favorable one because the H-field components are naturally continuous at the material interfaces. Thus, no extra boundary conditions are needed to impose for this formulation. On the other hand, the E + H-field-based formulation results in six unknown field components compared to E- and H-field formulations without any extra benefits.

With all benefits and numerical advantages, we have followed the H-field formulation for our numerical studies. To minimize the energy associated with the functional, the minimum theorem is applied by setting $\delta\phi$ equal to zero.

$$\delta\phi = \langle \hat{\varepsilon}_r^{-1}(\nabla \times H), (\nabla \times H)\rangle - \omega^2 \langle \hat{\mu}_r H, H\rangle \tag{6.87}$$

Here, the parameters $\hat{\mu}_r$ and $\hat{\varepsilon}_r$ are the relative permeability and the relative permittivity tensors, respectively. The braces indicate the inner product with the equation form of

$$\langle A, B\rangle = \iint B^* \cdot A \, dxdy \tag{6.88}$$

The Euler form of the above equation follows Helmholtz's equation, but unfortunately that does not satisfy Maxwell's two divergence equations. This contaminates the eigenvalues and eigenvectors of the real modes with the presence of unwanted spurious solutions. Rahman and Davies proposed a successful way of spurious solution removal by balancing the curl and divergence parts with a penalty function method [8, 9]. A global weighting factor (α) close to the value of $\alpha = 1/n_{\text{eff}}^2$ was used to incorporate the effect of divergence equation ($\text{div} \cdot B = 0$), where n_{eff} denotes the effective index of the waveguide. This method has been very efficient to determine the accurate solution of a wide range of passive dielectric-based waveguides, particularly with all positive dielectric constants. The corresponding eigenvalue equation is (6.8), (6.9), (6.40)–(6.42).

$$\omega^2 = \frac{\iint (\nabla \times H)^* \varepsilon_r^{-1} (\nabla \times H)\, dxdy + \alpha \iint (\nabla . H)^* \varepsilon_r^{-1} (\nabla . H)\, dxdy}{\iint H^* \mu_r H\, dxdy} \tag{6.89}$$

For two-dimensional modal solutions, the field dependence $e^{j\omega t}$ is assumed throughout the direction of propagation (z-direction) which in turn results in the z-dependency as $e^{-j\beta z}$. This helps to reduce a three-dimensional problem into a two-dimensional one. For some special cases, we need a complete three-dimensional FEM code to simulate the device as a whole. In case of 3D electromagnetic resonator problems, the resonating mode fields are spread in all three directions. Thus, the same variational formulation with a direct z-dependency can be used for 3D FV-FEM formulation without considering the wave propagation assumption [40–43].

$$k^2 = \left(\frac{\omega}{c}\right)^2 = \frac{\iiint (\nabla \times H)^* \varepsilon_r^{-1} (\nabla \times H)\, dxdydz + \alpha \iiint (\nabla . H)^* \varepsilon_r^{-1} (\nabla . H)\, dxdydz}{\iiint H^* \mu_r H\, dxdydz} \tag{6.90}$$

After solving the global eigenvalue equation for the whole computational domain, the eigenvalues and corresponding eigenvectors can be obtained. Post-processing of those eigenvectors shows the quasi-TE and quasi-TM mode field distributions of the simulated waveguides and resonators.

6.5.2 Vector Finite Element

In most of the cases, the analysis of optical waveguides requires a rigorous vectorial analysis which includes accurate fulfillment of the boundary conditions. This is because the scalar FEM where the field and its derivatives are assumed continuous provides inaccurate results when the boundary conditions are significant in the problem. Several types of full vectorial finite element method (FV-FEM) have been introduced for the analysis of optical waveguides. The most serious problem associated with this approach is the appearance of spurious solutions, where an eigenvalue and associated eigenvector are in the high-frequency range, but not satisfying the divergence criteria and hence entirely unphysical. The penalty function method [44], discussed in the previous section, has been introduced to fix this problem, in which an arbitrary positive constant, called the penalty coefficient, is involved and the accuracy of solutions depends on its magnitude. This penalty coefficient forces the solution to be divergence free and hence overcome the issue of spurious modes. There is another serious problem in the full vectorial approach. The FV-FEM approach is difficult in dealing with corner singularities and interface singularities as was explained by Birman [45] and Birman and Solomyak [46]. Recently, the vector finite element method (VFEM) with the lowest-order

mixed-interpolation-type triangular elements, namely constant edge elements for transverse components of the electric field or magnetic field and linear nodal elements for the axial one, has been developed [47]. The use of mixed-interpolation-type elements provides a direct solution for propagation constants and avoids spurious solutions. In this section, the mixed interpolation elements, including first order and second order, is discussed.

6.5.2.1 Full Vectorial Equation

By considering an optical waveguide with a cross section in *xy* plane, the following full-vector wave equation can be derived from Maxwell's equation

$$\nabla \times ([p] \times \phi) - k_o^2 [q] \phi = 0 \tag{6.91}$$

with

$$[p] = \begin{bmatrix} \frac{s_x^2}{s} p_x & 0 & 0 \\ 0 & \frac{s_y^2}{s} p_y & 0 \\ 0 & 0 & \frac{s_z^2}{s} p_z \end{bmatrix} \tag{6.92}$$

$$[q] = \begin{bmatrix} sq_x & 0 & 0 \\ 0 & sq_y & 0 \\ 0 & 0 & sq_z \end{bmatrix} \tag{6.93}$$

where ϕ denotes either the electric field E or the magnetic field H, and the components of $[p]$ and $[q]$ are given in the following table.

	ϕ	p_x	p_y	p_z	q_x	q_y	q_z
Electric field	E	1	1	1	n_x^2	n_y^2	n_z^2
Magnetic field	H	$1/n_x^2$	$1/n_y^2$	$1/n_z^2$	1	1	1

where n_x, n_y, and n_z are, respectively, the refractive indices in x, y, and z directions. Multiplying Eq. 6.91 by test function ψ and applying Green's divergence theorem, we get

$$\iint_{\Omega} (\nabla \times \psi)^* ([p] \times \phi) - k_o^2 [q] \psi^* \phi = 0 \tag{6.94}$$

where the asterisk denotes conjugate transpose. In the Galerkin technique, the function and the test function are expanded using the same basis. Then, the computational domain Ω is divided into triangular elements as shown in Fig. 6.14. Figure 6.14a is a first-order mixed-interpolation-type triangular element which

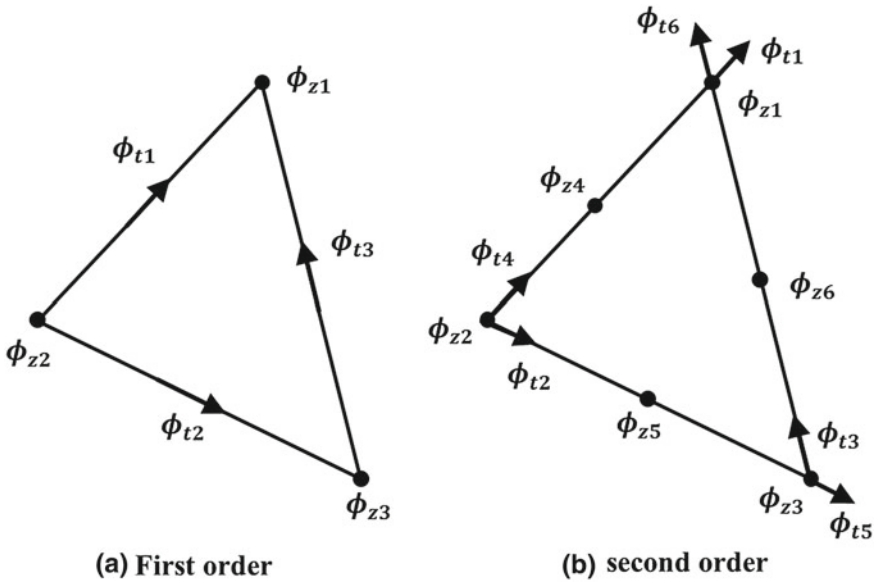

Fig. 6.14 Mixed-interpolation-type triangular element: **a** constant edge and linear nodal elements and **b** linear edge and quadratic nodal elements

consists of constant edge element with three unknowns associated with the edges (ϕ_{t1}, ϕ_{t2}, and ϕ_{t3}) and first-order nodal element with three unknowns (ϕ_{z1}, ϕ_{z2}, and ϕ_{z3}). Figure 6.14b is a higher-order mixed-interpolation-type triangular element which consists of linear edge element with six unknowns associated with the edges (ϕ_{t1}, ϕ_{t2}, … ϕ_{t6}) and second-order nodal element with six unknowns (ϕ_{z1}, ϕ_{z2}, … ϕ_{z6}) (Fig. 6.14).

The tangential components ϕ_x, ϕ_y and the axial component ϕ_z in each element are expressed as

$$\phi = \begin{bmatrix} \phi_x \\ \phi_y \\ \phi_z \end{bmatrix} = \begin{bmatrix} \{U\}^T \{\phi_t\}_e \\ \{V\}^T \{\phi_t\}_e \\ j\{N\}^T \{\phi_z\}_e \end{bmatrix} \tag{6.95}$$

where $\{\phi_t\}_e$ is the edge variable in the transverse plane for each element, and $\{\phi_z\}_e$ is the nodal axial field vector for each element. The shape function vectors $\{U\}$ and $\{V\}$ for the constant edge element and linear nodal element are given as

$$\{U\} = \frac{1}{2S_e} \begin{bmatrix} w_1(y_3 - y) \\ w_2(y_1 - y) \\ w_3(y_2 - y) \end{bmatrix} \tag{6.96}$$

$$\{V\} = \frac{-1}{2S_e} \begin{bmatrix} w_1(x_3 - x) \\ w_2(x_1 - x) \\ w_3(x_2 - x) \end{bmatrix} \tag{6.97}$$

And, for the linear edge and second-order element, $\{U\}$ and $\{V\}$ are expressed as

$$\{U\} = \frac{1}{2S_e} \begin{bmatrix} w_1 b_2 L_1 \\ w_2 b_3 L_2 \\ w_3 b_1 L_3 \\ -w_1 b_1 L_2 \\ -w_2 b_2 L_3 \\ -w_3 b_3 L_1 \end{bmatrix} \tag{6.98}$$

$$\{V\} = \frac{1}{2S_e} \begin{bmatrix} w_1 c_2 L_1 \\ w_2 c_3 L_2 \\ w_3 c_1 L_3 \\ -w_1 c_1 L_2 \\ -w_2 c_2 L_3 \\ -w_3 c_3 L_1 \end{bmatrix} \tag{6.99}$$

whereas the shape function $\{N\}$ is defined as in the scalar FEM. The coefficient $w_k (k = 1, 2, 3)$ is given as

$$w_k = \begin{cases} \sqrt{b_m^2 + c_m^2} & for\, b_m \le 0,\ c_m > 0 \\ -\sqrt{b_m^2 + c_m^2} & for\, b_m \ge 0,\ c_m < 0 \end{cases} \tag{6.100}$$

where a, b, and c are defined as mentioned before as

$$\begin{aligned} a_k &= x_l y_m - x_m y_l \\ b_k &= y_l - y_m \\ c_k &= x_m - x_l \end{aligned} \tag{6.101}$$

with k, l, and m being indices that progress modulo 3 (cyclically around the three vertices of the triangle).

It is worth noting that the unit tangential vector on the side between two corner points (x_k, y_k) and (x_l, y_l), t_k, is given by

$$t_k = \left(\frac{c_m}{l_k}\right)\hat{x} - \left(\frac{b_m}{l_k}\right)\hat{y} \tag{6.102}$$

It can be noticed from the definition of the shape functions in Eqs. 6.96 and 6.97 for the constant edge and Eqs. 6.98 and 6.99 for linear edge that the following relation is satisfied

$$\phi_{tk} = \left(\phi_{xk}\hat{x} + \phi_{yk}\hat{y}\right) \cdot t_k \tag{6.103}$$

where ϕ_{xk} and ϕ_{yk} are the values of ϕ_x and ϕ_y at any point on the side length of the triangle $|w_k|$, respectively, and thus, the tangential component ϕ_t is constant along each side of the triangle. For the linear edge elements, the following relations are satisfied for the higher-order element:

$$\begin{aligned}
\phi_{t1} &= \left(\phi_{x1}\hat{x} + \phi_{y1}\hat{y}\right) \cdot t_1 \\
\phi_{t2} &= \left(\phi_{x2}\hat{x} + \phi_{y2}\hat{y}\right) \cdot t_2 \\
\phi_{t3} &= \left(\phi_{x3}\hat{x} + \phi_{y3}\hat{y}\right) \cdot t_3 \\
\phi_{t4} &= \left(\phi_{x2}\hat{x} + \phi_{y2}\hat{y}\right) \cdot t_1 \\
\phi_{t5} &= \left(\phi_{x3}\hat{x} + \phi_{y3}\hat{y}\right) \cdot t_2 \\
\phi_{t6} &= \left(\phi_{x1}\hat{x} + \phi_{y1}\hat{y}\right) \cdot t_3
\end{aligned} \tag{6.104}$$

Substituting Eq. 6.95 into Eq. 6.94, we obtain the following final eigenvalue problem which gives a solution for the propagation constant and the corresponding field distribution directly:

$$[K_{tt}]\{\phi_t\} - \beta^2\left(\left[[M_{tt}] + [K_{tz}][K_{zz}]^{-1}[K_{zt}]\right]\right)\{\phi_t\} = 0 \tag{6.105}$$

with

$$\begin{aligned}
[K_{tt}] = \sum_e \iint_e & k_o^2\left(q_x\{U\}\{U\}^T + q_y\{V\}\{V\}^T\right) - \left(p_z\{U_y\}\{U_y\}^T + p_z\{V_x\}\{V_x\}^T\right) \\
& + \left(p_z\{U_y\}\{V_x\}^T + p_z\{V_x\}\{U_y\}^T\right) dxdy
\end{aligned} \tag{6.106}$$

$$[K_{tz}] = [K_{zt}]^T = \sum_e \iint_e \left(p_y\{U\}\{N_x\}^T + p_x\{V\}\{N_y\}^T\right) dxdy \tag{6.107}$$

$$[K_{zz}] = \sum_e \iint_e k_o^2 q_z\{N\}\{N\}^T - \left(p_x\{N_y\}\{N_y\}^T + p_y\{N_x\}\{N_x\}^T\right) dxdy \tag{6.108}$$

$$[M_{tt}] = \sum_e \iint_e \left(p_y\{U\}\{U\}^T + p_x\{V\}\{V\}^T\right) dxdy \tag{6.109}$$

where U_y and U_x are, respectively, the derivatives of U in x and y. Also, V_y and V_x are, respectively, the derivatives of V in x and y. Further, N_y and N_x are, respectively, the derivatives of N in x and y. The final equation Eq. 6.105 is then solved for the eigenvalue β directly. It is worth noting that Eq. 6.105 contains only the edge variables in the transverse plane $\{\phi_t\}$.

6.5.2.2 Application

The use of full vectorial approaches is essential in computational modeling of photonic devices such as biomedical sensors [48–50] and polarization handling devices including plasmonic structures [51], polarization rotators [52–55], polarizers [56], polarization filters [57], polarization splitters [58], and couplers [59]. In this study, the FV-FEM is used to model and analyze surface plasmon photonic crystal fiber (PCF) biosensor. Figure 6.15 shows the cross section of the suggested PCF biosensor. The proposed PCF design relies on using two rings of air holes in the core region with a central air hole. The air holes of the outer ring have a small diameter d_1 and are arranged in hexagonal shape with a hole pitch Λ. The two air holes along x-axis are shifted by a distance d_2, as shown in Fig. 6.15. The center of each hole in the inner ring is located at a normal distance D to the line between the centers of two neighboring holes in the outer ring, as shown in Fig. 6.15. The air holes of the inner ring have elliptical shape with minor and major diameters $2a$ and $2b$, respectively, while the central hole has a diameter d_c. The air holes in the inner ring are used to control the confinement of the two core-guided modes through the core region. Additionally, the air hole at the center of the structure is utilized to reduce the effective refractive index in the central core area to facilitate the matching between the core-guided modes and the surface plasmon modes. Further, a uniform gold layer of thickness t_{Au} is used to coat the PCF microstructure surrounded by a slot of thickness d_3 to house the analyte. The permittivity of the gold has been obtained from Johnson and Christy [60]. Further, the suggested design has a silica background material which has the following Sellmeier Eq. (61):

$$n_s^2(\lambda) = 1 + \frac{B_1\lambda^2}{\lambda^2 - C_1} + \frac{B_2\lambda^2}{\lambda^2 - C_2} + \frac{B_3\lambda^2}{\lambda^2 - C_3} \tag{6.110}$$

where n_s is the refractive index of the silica and λ is the wavelength in μm. Additionally, B_1, B_2, and B_3 are given by 0.6961663, 0.4079426, and 0.8974794, while C_1, C_1, and C_1 are equal to 0.00467914826 μm^2, 0.0135120631 μm^2, and

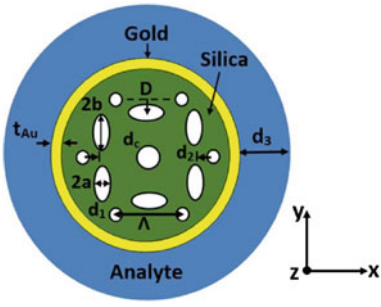

Fig. 6.15 Cross section of surface plasmon resonance photonic crystal fiber biosensor [48]

97.9340025 μm^2, respectively. In this assessment, the VFEM is used to find the quasi-TE and quasi-TM core-guided modes and plasmonic modes for the suggested biosensor. The fundamental quasi-TE mode refers to the fundamental H_y^{11} or E_x^{11} modes, while the fundamental quasi-TM mode refers to the fundamental H_x^{11} or E_y^{11} modes. The computational window is set to 10 × 10 μm, and the cross section is divided into 17170 triangular elements, with 99883 degrees of freedom for the employed elements. In this study, the initial geometrical parameters are taken as $\Lambda = 1.5$ μm, $d_1 = 0.15$ μm, $d_2 = \Lambda/1.5$, $d_c = 0.45$ μm, $d_3 = 1.3$ μm, d3, $t_{Au} = 40$ nm, $D = 0.15$ μm, b = 0.5 μm, and a = 0.25 μm. In addition, the water analyte has a refractive index of $n_a = 1.33$.

Figure 6.16 shows the dispersion relations of the E_{11}^{x} and E_{11}^{y} polarized core-guided modes and surface plasmon modes, SP_1^{x} and SP_1^{y}. In addition, the confinement losses of the two fundamental core-guided modes are shown in Fig. 6.16.

The confinement loss is calculated from

$$Loss = \frac{40\pi}{\ln(10)\lambda} \times im(n_{eff}) \times 10^4 \approx 8.686 \times Im(n_{eff}) \times 10^4 \qquad (6.111)$$

where $im(n_{eff})$ is the imaginary part of the complex effective index of the core-guided mode. As the wavelength increases, the confinement of the fundamental core modes through the core region and, hence, their effective indices decrease, as shown in Fig. 6.16. In addition, Fig. 6.16 reveals that the resonant attenuation peaks occur at the resonance wavelengths $\lambda = 0.6868$ μm and 0.708 μm according to the quasi-TM and quasi-TE polarized modes, respectively. This is due to the phase matching between the core-guided modes and the surface plasmon modes SP_1^{y} and SP_1^{x}, at the corresponding resonance wavelengths. Further, phase matching occurs between the SP_2^{x} and the E_{11}^{x} modes at $\lambda = 0.6605$ μm. However, the resonance spectral width of the TE mode at $\lambda = 0.708$ μm is much narrower than that at $\lambda = 0.6605$ μm. The narrower spectral width can filter the spectral noise more effectively, which results in a lower spectral deviation from the actual center of the

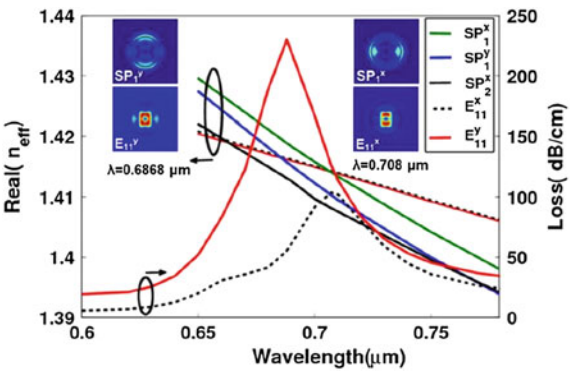

Fig. 6.16 Dispersion relations of the quasi-TE and quasi-TM polarized core-guided modes and surface plasmon modes. Confinement losses of the two polarized core modes are also shown in this figure. The inset field plots show the E_{11}^{x}, E_{11}^{y}, SP_1^{x}, and SP_1^{y} modes at the corresponding resonance wavelengths [48]

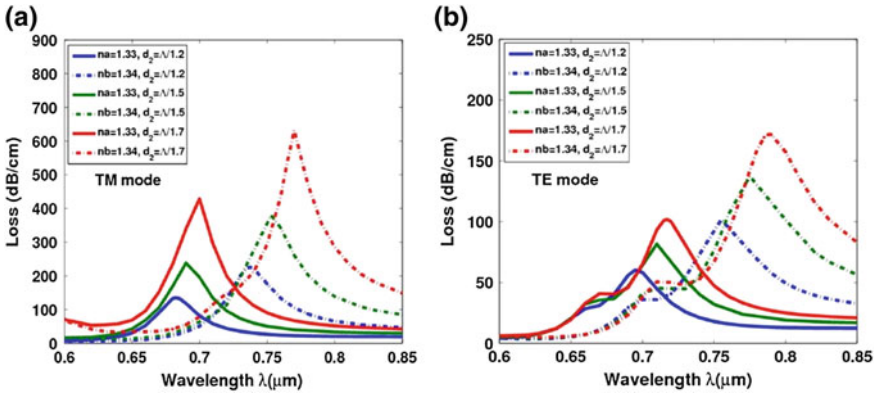

Fig. 6.17 Calculated losses of the **a** quasi-TM and **b** quasi-TE fundamental core modes with wavelength variation at different values of d_2 when the analyte refractive index is changed from $n_a = 1.33$ to $n_a = 1.34$ [48]

resonance. Therefore, the resonance wavelength of $\lambda = 0.708$ μm can be detected accurately and hence will be considered for the subsequent simulations. The inset of Fig. 6.16 shows the electric field distribution for the main components E_{11}^x and E_{11}^y of the quasi-TE and quasi-TM modes and the surface plasmon modes at the resonance wavelengths. It is evident from the core-guided field plots that the leakage of the quasi-TM mode into the analyte filled slot is greater than that of the quasi-TE mode. Therefore, the losses of the quasi-TM mode are greater than those of the quasi-TE modes. It should be noted that the sensor device length is inversely proportional to its modal loss. Therefore, the optimization of the PCF structural geometrical parameters can control the design length of the PCF sensor with comparable sensitivities. This feature is important for the practical considerations when integrating the proposed sensor into a complete sensor system.

The effect of the shift distance d_2 is investigated, while the other parameters are kept constant at their initial values. Figure 6.17a and b shows the variation of the loss spectra of the quasi-TM and quasi-TE polarized guided modes, respectively, with the wavelength at different values of $d_2 = \Lambda/1.2$, $d_2 = \Lambda/1.5$, and $\Lambda/1.7$, at two different analyte refractive indices: $n_a = 1.33$ and $n_b = 1.34$. As the distance d_2 increases, the index contrast between the core and cladding regions and, hence, the effective index of the core-guided modes decrease, as shown in Fig. 6.18. Figure 6.18 shows the wavelength-dependent effective indices of the quasi-TM core modes and surface plasmon modes. Therefore, the leakage of the core-guided modes toward the metallic layer increases by increasing the d_2 value. Consequently, the confinement losses of the two polarized modes and the corresponding resonance wavelengths increase by increasing the shift distance d_2, as shown in Figs. 6.17 and 6.18. Further, the resonance wavelengths are shifted by changing the analyte refractive index from 1.33 to 1.34. At $d_2 = \Lambda/1.2$,$d_2 = \Lambda/1.5$, and $d_2 = \Lambda/1.7$, the resonance peaks of the quasi-TM mode are changed from wavelength of 0.682 μm,

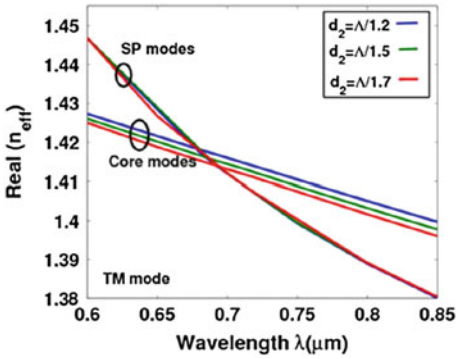

Fig. 6.18 Variation of the real part of the effective indices of the quasi-TM core-guided modes and surface plasmon modes at different d_2/Λ ratios [48]

0.690 μm, and 0.700 μm to 0.738 μm, 0.753 μm, and 0.770 μm as the analyte refractive index changes from 1.33 to 1.34, respectively. However, the resonance wavelengths of the quasi-TE modes are varied from 0.695 μm, 0.710 μm, and 0.711 μm to 0.755 μm0.755 μm, and 0.789 μm, respectively. This transduction technique can be utilized to detect the change of the analyte refractive index.

In this study, the sensitivity of the proposed sensor is calculated according to the wavelength interrogation method. In this approach, the shift of the plasmonic peak is used to detect the analyte refractive index changes. Therefore, the sensitivity can be expressed in terms of the resonance peak wavelength λ_{peak} in the loss spectra and the analyte refractive index $n_{analyte}$ as follows:

$$S_\lambda(\lambda) = \frac{\partial \lambda_{peak}}{\partial n_{analyte}} \quad (\text{nm/RIU}) \tag{6.112}$$

It is found that the suggested sensor sensitivities are equal to 5600, 6300, and 7000 nm/RIU according to the quasi-TM modes at $d_2 = \Lambda/1.2$, $\Lambda/1.5$, and $\Lambda/1.7$, respectively. However, sensitivities of 6000, 6500, and 7200 nm/RIU, respectively, are obtained based on the quasi-TE modes.

6.6 Summary

In this chapter, the nodal finite element method under the scalar approach has been discussed for the first-order and second-order triangular elements. In SC-FEM, the assumed boundary conditions are the continuity of the field and its derivatives. Under these assumptions, the nodal finite element has been assessed throughout an air-filled rectangular waveguide surrounded by a perfect electric conductor. Further, for suppressing the outgoing waves from the physical domain, the coordinate stretching perfectly matched layer has been discussed. Also, based on the nodal finite element, the FEM has been introduced to time domain analysis where several techniques for propagation such as Newmark-beta scheme, Crank–Nicolson

scheme, and Padé approximation has been introduced and discussed. Under the perfectly matched layer approach, the propagation inside a slab waveguide has been presented as an indication of the efficient absorption of the outgoing waves by the perfectly matched layer. The finite element time domain formulation has then been utilized to analyze a simple sensor based on optical grating. The results show that the TM reflection provides more sensitivity than the TE case because the evanescent waves in the TM-wave are higher than those in the TE-wave. Furthermore, for accurate inclusion of the boundary conditions to get accurate results for optical waveguide analysis, the penalty function method and the vector finite element method have been discussed. In the penalty function method, a global factor is used to incorporate the imposition of the divergence-free field condition. In VFEM, unlike the nodal FEM, the tangential component of the electric field has been introduced as a vector and consequently the shape functions used are vectors. The vector finite element method under the first-order triangular element and the second-order triangular elements has been discussed. Moreover, using the vector finite element formulation, a highly sensitive photonic crystal fiber biosensor has been introduced, where its analysis is based on the vectorial analysis of the 2D cross section of the photonic crystal fiber. The sensitivity of the presented sensor has been discussed. It has been shown that high sensitivities of 7000 nm/RIU and 7200 nm/RIU can be obtained for the quasi-TM and quasi-TE modes, respectively.

References

1. M. Koshiba, *Optical Waveguide Theory by the Finite Element Method* (KTK Scientific, 1992)
2. Zienkiewitz, *The Finite Element Method* (New York, McGraw-Hill, 1973)
3. M.V.K. Chari, P.P. Silvester, *Finite Elements in Electrical and Magnetic Field Problems* (Chechester, Wiley, 1980)
4. E. Yamashita, *Analysis Methods for Electromagnetic Wave Problems* (Boston, Artech House, 1990)
5. D.B. Davidson, *Computational Electromagnetics for RF and Microwave Applications* (Cambridge, Cambridge University Press, 2005)
6. A. Taflov, *Computational Electrodynamics: The Finite Difference Time Domain Method* (Artech, 1995)
7. D. Pinto, S.S.A. Obayya, Improved complex-envelope alternating-direction-implicit finite-difference-time-domain method for photonic-bandgap cavities. J. Lightwave Technol. **25**(1), 440–447 (2007)
8. B. Rahman, J. Davis, Finite-element solution of integrated optical waveguides. J. Lightwave Technol. **2**(5), 682–688 (1984)
9. B.M. Azizur Rahman, Finite-element analysis of optical and microwave waveguide problems. IEEE Trans. Microwave Theor. Techniq. **32**(1), 20–28 (1984)
10. K. Kawano, T. Kitoh, Introduction to Optical Waveguide Analysis: Solving Maxwell's Equations and the Schrodinger's Equation (New York, wiley, 2001)
11. M. Koshiba, H. Saitoh, M. Eguchi, K. Hirayama, Simple scaler finite element approach to optical waveguides. IEE Proc. J. **139**, 166–171 (1992)
12. S.S.A. Obayya, *Computational Photonics* (Wiley, 2011)
13. S.S.A. Obayya, Efficient finite-element-based time-domain beam propagation analysis of Optical integrated circuits. IEEE J. Quant. Electron. **40**(5), 591–595 (2004)

14. T. Itoh, R. Mittra, Spectral domain approach for calculation the dispersion characteristics of microstrip lines. IEEE Trans. Microwave Theor. Tech. MTT21 496–499 (1973)
15. A. Abdrabou, A.M. Heikal, S.S.A. Obayya, Efficient rational Chebyshev pseudo-spectral method with domain decomposition for optical waveguides modal analysis. Opt. Express **24** (10), 10495–10511 (2016)
16. D.M. Pozar, *Microwave Engineering* (Wiley, Hoboken, NJ, 2012)
17. J. Berenger, A perfectly matched layer for the absorption of electromagnetic waves. J. Comput. Phys. **114**, 185–200 (1994)
18. S.D. Gedney, An anisotropic perfectly matched layer absorbing media for the truncation of FDTD latices. Antennas Prop. IEEE Trans. **44**, 1630–1639 (1996)
19. W.C. Chew, W.H. Weedon, A 3D perfectly matched medium from modifie Maxwell's equations with stretched coordinates. Microwave Opt. Technol. Lett. **7**, 590–604 (1994)
20. W.C. Chew, J.M. Jin, E. Michielssen, complex coordinate stretching as a generalized absorbing boundary condition. Microwave Opt. Technol. Lett. **15**(6), 363–369 (1997)
21. M. Koshiba, Y. Tsuji, M. Hikari, Time-domain beam propagation method and its application to photonic crystal circuits. J. Lightwave Technol. **18**(1), 102–110 (2000)
22. V.F. Rodríguez-Esquerre, M. Koshiba, Finite element analysis of photonic crystal cavities: time and frequency domain. J. Lightwave Technol. **23**(3), 1514–1521 (2005)
23. T. Fujisawa, M. Koshiba, time-domain beam propagation method for nonlinear optical propagation analysis. J. Lightwave Tech. **22**(2), 684–691 (2004)
24. V.F. Rodríguez-Esquerre, M. Koshiba, E.H.-Figueroa, Frequency-dependent envelope finite element time domain analysis of dispersion materials. Microwave Opt. Tech. Lett. **44**(1), 13–16 (2004)
25. A. Niiyama, M. Koshiba, Y. Tsuji, An efficient scalar finite element formulation for nonlinear optical channel waveguides. J. Lightwave Technol. **13**(9), 1919–1925 (1995)
26. G.R. Liu, A Generalized gradient smoothing technique and the smoothed bilinear form for Galerkin formulation of a wide class of computational methods. Int. J. Comput. Methods (2008)
27. K.S.R. Atia, S.S.A. Obayya, Novel gradient smoothing method-based time domain beam propagation analysis of optical integrated circuits. Signal Process. Photon. Commun. JM3A–23 (2015)
28. G.R. Liu, *Meshfree Methods: Moving Beyond the Finite Element Method* (CRC Press, 2009)
29. J.R. LeVeque, *Finite Volume Methods for Hyperbolic Problems* (Cambridge, Cambridge, 2002)
30. K.S.R. Atia, A.M. Heikal, S.S.A. Obayya, Efficient smoothed finite element time domain beam propagation method for photonic devices. Opt. Exp. **23**(17), 22199–22213 (2015)
31. K.S.R. Atia, A.M. Heikal, S.S.A. Obayya, Time-domain beam propagation method based on gradient smoothing technique for dispersive materials, in *Progress in Electromagnetics Research symposium* (PIERS) (2015)
32. P.L. Liu, Q. Zhao, F.S. Choa, Slow-wave finite-difference beam propagation method. IEEE Photon. Technol. Lett. **7**(8), 890–892 (1995)
33. G.H. Jin, J. Harari, J.P. Vilcot, D. Decoster, An improved time domain beam propagation method for integrated optics components. IEEE Photon. Technol. Lett. **9**(3), 117–122 (1997)
34. J. Lee, B. Fornberg, A split step approach for the 3-D Maxwell's equations. J. Comput. Appl. Math. **158**(2), 485–505 (2003)
35. M. Movahhedi, A. Abdipour, Alternating direction implicit formulation for the finite element time domain method. IEEE Trans. Microwave Theor. Technol. **55**(6), 1322–1331 (2007)
36. J.F. Lee, WETD-A finite element time-domain approach for solving Maxwell's equations. IEEE Microwave Guided Wave Lett. **4**(1), 11–13 (1994)
37. V.F. Rodríguez-Esquerre, H.E. Hernández-Figueroa, Novel time-domain step-by-step scheme for integrated optical applications. IEEE Photon. Technol. Lett. **13**(4), 311–313 (2001)
38. H.A. Van der Vorst, Bi-CGSTAB: a fast and smoothly converging variant of Bi-CG for the solution of nonsymmetric linear systems. SIAM J. Sci. Stat. **13**(2), 631–644 (1992)

39. A.D. Berk, Variational principles for electromagnetic resonators and waveguides. IRE Trans. Antennas Propagat. **4**(2) (1956)
40. K.T.V. Grattan, B.T. Meggitt, Optical Fiber Sensor Technology: Fundamental (US, Springer, 2000)
41. T. Dar, J. Homola, B.M.A. Rahman, M. Rajarajan, Label-free slot-waveguide biosensor for the detection of DNA hybridization. Appl. Opt. **51**(34) (2012)
42. C. Koos, P. Vorreau, T. Vallaitis, P. Dumon, W. Bogaerts, R. Baets et al., All-optical high-speed signal processing with silicon–organic hybrid slot waveguides. Nat. Photonics. **3**(4) (2009)
43. Barrios CA, Banuls MJ, Gonzalez-Pedro V, Gylfason KB, Sanchez, Griol A, et al. Label-free optical biosensing with slot-waveguides. Opt. Lett. **33**(7) 2008
44. M. Koshiba, K. Hayata, M. Suzuki, Vectorial finite-element formulation without spurious solutions for dielectric waveguide problems. Electron. Lett. **20**, 409–410 (1984)
45. Sh Birman, M. The, Maxwell operator for a resonator with inward edges. Vestnik Leningradskogo Universiteta. Matematika. **19**, 1–8 (1986)
46. S.M. Birman, Z.M. Solomyak, Maxwell operator in regions with nonsmooth boundaries. Siberian Malh. J. **28**, 12–24 (1987)
47. F. Kikuchi, Mixed and penalty formulations for finite element analysis of an eigenvalue problem in electromagnetism. Compur. Methods Appl. Mech. Eng. **64**, 509–521 (1987)
48. M.F.O. Hameed, Y.K.A. Alrayk, S.S.A. Obayya, Self-calibration highly sensitive photonic crystal fiber biosensor. IEEE Photon. **8**(3) (2016)
49. M.F.O. Hameed, M. El-Azab, A.M. Heikal, S.M. El-Hefnawy, S.S.A. Obayya, Highly sensitive plasmonic photonic crystal temperature sensor filled with liquid crystal. IEEE Photon. Technol. Lett. **28**(1) (2015)
50. S.I. Azzam, R.E.A. Shehata, M.F.O. Hameed, A.M. Heikal, S.S.A. Obayya, Multichannel photonic crystal fiber surfrace plasmon resonance based sensor. J. Opt. Quant. Electron. **48** (142) (2016)
51. F.F.K. Hussain, A.M. Heikal, M.F.O. Hameed, J. El-Azab, W.S. Abdelaziz, S.S.A. Obayya, Dispersion characteristics of asymmetric channel plasmon polariton waveguide. IEEE J. Quant. Electron. **50**(6) (2014)
52. M.F.O. Hameed, S.S.A. Obayya, H.A. El-Mikati, Passive polarization converters based on photonic crystal fiber with L-shaped core region. IEEE J. Lightwave Technol. **50**(6) (2012)
53. M.F.O. Hameed, A.M. Heikal, S.S.A. Obayya, Novel passive polarization rotator based on spiral photonic crystal fiber. IEEE Photon. Technol. Lett. **25**(16) (2013)
54. M.F.O. Hameed, S.S.A. Obayya, R.J. Wiltshire, Beam propagation analysis of polarization rotation in soft glass nematic liquid crystal photonic crystal fibers. IEEE Photon. Technol. Lett. **22**(3) (2010)
55. M.F.O. Hameed, A.M. Heikal, S.S.A. Obayya, Passive polarization converters based on photonic crystal fibers. IEEE Photon. Technol. Lett. **22**(3) (2010)
56. S.I. Azzam, M.F.O. Hameed, N.F.F. Areed, S.S.A. Obayya, H. El-Mikati et al., Proposal of ultracompact CMOS compatible TE-/TM-pass polarizer based on SOI platform. IEEE Photon. Technol. Lett. **33**(13) (2015)
57. A.M. Heikal, F.F.K. Hussain, M.F.O. Hameed, S.S.A. Obayya, Efficient polarization filter design based on plasmonic photonic crystal fiber. IEEE J. Lightwave Technol. **33**(13) (2015)
58. S.S.A. Obayya, M.F.O. Hameed, N.F.F. Areed, *Computational Liquid Crystal Photonics: Fundamentals* (Wiley, Modelling and Applications, 2016)
59. M.F.O. Hameed, S.S.A. Obayya, K. Al-Begain, A.M. Nasr, M.L. Abo el Maaty, Coupling characteristics of a soft glass nematic liquid crystal photonic crystal fiber coupler. IET Optoelectron. **3**(6) (2009)
60. M.F.O. Hameed, A.M. Heikal, B.M. Younis, M.M. Abdelrazzak, S.S.A. Obayya, Ultra-high tunable liquid crystal plasmonic photonic crystal fiber polarization filter. Opt. Exp. **23**(6), 7007–7020 (2015)
61. B.M. Younis, A.M. Heikal, M.F.O. Hameed, S.S.A. Obayya, Enhancement of plasmonic liquid photonic crystal fiber. Plasmonics p. 1–7 (2016)

Chapter 7
FDTD in Cartesian and Spherical Grids

Mohammed Hadi, Atef Elsherbeni, Ravi Bollimuntha and Melinda Piket-May

Abstract The numerical dispersion relation is derived for the finite-difference time-domain method when implemented on spherical grids using Maxwell's equations in spherical coordinates. Derivation is appropriately based on elementary spherical functions which renders the resulting numerical dispersion relation valid for all spherical FDTD space including near the singular regions at the origin and along the z-axis. Accuracy of this relation is verified through convergence tests to the continuous-space limit and the Cartesian FDTD limit far from the origin. Numerical dispersion analyses are carried out to demonstrate numerical wavenumber error bounds and their dependence on absolute position as well as on spherical solutions' modes. The chapter is concluded by visiting the existing challenges of designing absorbing boundary conditions for spherical FDTD when the grid truncation is in the near vicinity of the origin. Such a design challenge can be effectively studied in the future with the aid of the derived spherical FDTD numerical dispersion relation.

Keywords Finite-difference time-domain (FDTD) method · Spherical FDTD
Numerical dispersion · Absorbing boundary conditions (ABCs)
Spherical coordinates · Perfectly matched layer (PML) ABCs
Spherical Bessel and Hankel functions

Numerically modeling an electromagnetics phenomenon often requires judicious selections of modeling parameters to optimize simulation efficiency to maintain a tolerable error upper bound. In the case of finite-difference time-domain (FDTD) methods, temporal and spatial discrete steps need to be managed to avoid using unnecessarily small steps that will require overuse of computing resources. For example, halving the spatial step in any given dimension would double the overall

M. Hadi · A. Elsherbeni (✉)
Colorado School of Mines, Golden, CO, USA
e-mail: aelsherb@mines.edu

R. Bollimuntha · M. Piket-May
University of Colorado at Boulder, Boulder, CO, USA

© Springer International Publishing AG, part of Springer Nature 2019

M. F. O. Hameed and S. Obayya (eds.), *Computational Photonic Sensors*, https://doi.org/10.1007/978-3-319-76556-3_7

required memory and quadruple the simulation runtime. Linking these resource demanding discrete steps to predetermined error bounds for FDTD methods is accomplished through the discrete equivalent of the trivial dispersion relation $\omega^2\mu\epsilon = \beta^2$. Every FDTD variant produces its own unique "numerical dispersion relation" which is a function of the algorithm's discrete steps, frequency, and the host medium's intrinsic parameters. Furthermore, this numerical dispersion relation can be solved for the numerical counterpart of the wavenumber β, which in turn is used to precisely predict algorithmic errors for any given set of intrinsic and discrete modeling parameters.

Deriving an FDTD algorithm's numerical dispersion relation is a well-established and documented exercise in the literature [1]. Basically, a discrete equivalent of a harmonic solution is injected into the algorithm's update equations, and the resulting expressions are then distilled to produce the numerical dispersion relation. A quick validity test of this resulting relation can be conducted by taking the limits as all discrete steps approach zero to produce the continuous-space dispersion relation mentioned earlier. Since most FDTD variants are based on Cartesian coordinates, the appropriate harmonic solutions used always have the form of plane waves as in $\exp[-\jmath(\beta_x x + \beta_y y + \beta_z z - \omega t)]$. The reason behind this choice is the fact that Cartesian-based FDTD algorithms fundamentally propagate plane waves through their Cartesian grids. Therefore, any problem-specific solution would materialize as a superposition of these plane waves.

On the other hand, when an FDTD algorithm is based on a different coordinate system such as cylindrical or spherical, corresponding native harmonic solutions need to be used in order to produce the correct numerical dispersion relation. This chapter will specifically target a second-order FDTD based on spherical coordinate systems. It will start by reviewing the established approach of deriving the numerical dispersion relation for second-order Cartesian FDTD. This initial treatment will serve as a reference approach when dealing with spherical FDTD, as well as a benchmark to highlight both similarities and critical differences in the error-producing mechanisms of both FDTD variants. The chapter will then proceed to derive in detail the spherical FDTD numerical dispersion relation and concludes with comparative analysis of numerical error behaviors and mesh design metrics.

7.1 Cartesian FDTD

For FDTD implementations in Cartesian coordinates, the six electromagnetic field components are represented in a digital space such that they easily conform to applications of Ampere's and Faraday's laws as shown in Fig. 7.1. In other words, each electric field component is surrounded by four transverse magnetic field components aligned along a closed loop. Extending this implementation to all three dimensions results in a uniformly populated digital mesh where each field component is sampled every Δx, Δy, and Δz along the x, y, and z dimensions, respectively. Furthermore, the sub-grid hosting all electric field-only components

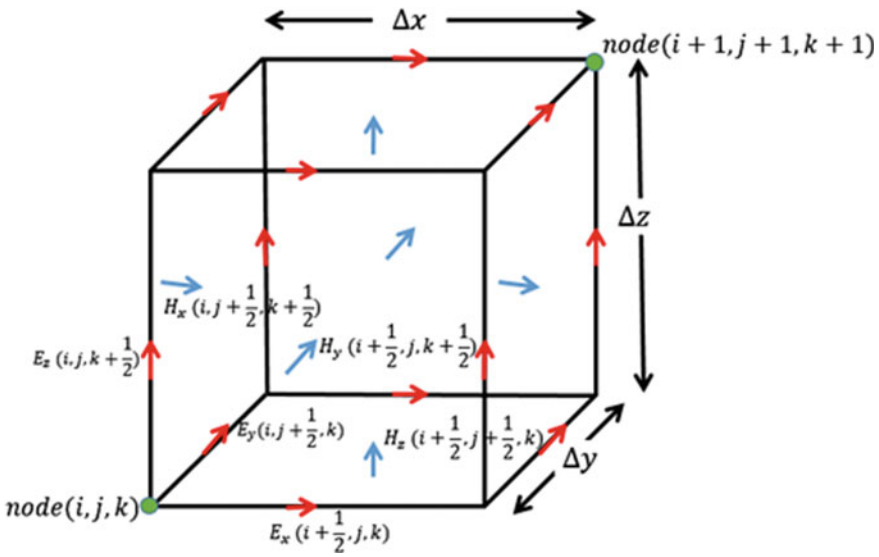

Fig. 7.1 Building block of Yee cell for Cartesian FDTD algorithm

turns out to be offset from the magnetic fields sub-grid by $\Delta x/2$, $\Delta y/2$, and $\Delta z/2$, as can be seen in Fig. 7.1.

Maxwell's curl equations in source-free, loss-free media are

$$\epsilon \frac{\partial \overline{E}}{\partial t} = \nabla \times \overline{H}, \tag{7.1}$$

$$-\mu \frac{\partial \overline{H}}{\partial t} = \nabla \times \overline{E}, \tag{7.2}$$

which can be expanded using Cartesian del operators and readied for conversion into discrete form, as

$$\begin{aligned}
\epsilon \frac{\partial E_x}{\partial t} &= \frac{\partial H_z}{\partial y} - \frac{\partial H_y}{\partial z}, \\
\epsilon \frac{\partial E_y}{\partial t} &= \frac{\partial H_x}{\partial z} - \frac{\partial H_z}{\partial x}, \\
\epsilon \frac{\partial E_z}{\partial t} &= \frac{\partial H_y}{\partial x} - \frac{\partial H_x}{\partial y}, \\
-\mu \frac{\partial H_x}{\partial t} &= \frac{\partial E_z}{\partial y} - \frac{\partial E_y}{\partial z}, \\
-\mu \frac{\partial H_y}{\partial t} &= \frac{\partial E_x}{\partial z} - \frac{\partial E_z}{\partial x}, \\
-\mu \frac{\partial H_z}{\partial t} &= \frac{\partial E_y}{\partial x} - \frac{\partial E_x}{\partial y}.
\end{aligned}$$

Using either these differential forms or their integral form equivalents (modified Ampere's and Faraday's laws) in conjunction with the field distributions of Fig. 7.1 will produce the same set of finite-difference equations

$$
\begin{aligned}
\epsilon \frac{E_x|_{i,j,k}^{n+\frac{1}{2}} - E_x|_{i,j,k}^{n-\frac{1}{2}}}{\Delta t} &= \frac{H_z|_{i,j+\frac{1}{2},k}^{n} - H_z|_{i,j-\frac{1}{2},k}^{n}}{\Delta y} - \frac{H_y|_{i,j,k+\frac{1}{2}}^{n} - H_y|_{i,j,k-\frac{1}{2}}^{n}}{\Delta z},\\
\epsilon \frac{E_y|_{i,j,k}^{n+\frac{1}{2}} - E_y|_{i,j,k}^{n-\frac{1}{2}}}{\Delta t} &= \frac{H_x|_{i,j,k+\frac{1}{2}}^{n} - H_x|_{i,j,k-\frac{1}{2}}^{n}}{\Delta z} - \frac{H_z|_{i+\frac{1}{2},j,k}^{n} - H_z|_{i-\frac{1}{2},j,k}^{n}}{\Delta x},\\
\epsilon \frac{E_z|_{i,j,k}^{n+\frac{1}{2}} - E_z|_{i,j,k}^{n-\frac{1}{2}}}{\Delta t} &= \frac{H_y|_{i+\frac{1}{2},j,k}^{n} - H_y|_{i-\frac{1}{2},j,k}^{n}}{\Delta x} - \frac{H_x|_{i,j+\frac{1}{2},k}^{n} - H_x|_{i,j-\frac{1}{2},k}^{n}}{\Delta y},\\
-\mu \frac{H_x|_{i,j,k}^{n+\frac{1}{2}} - H_x|_{i,j,k}^{n-\frac{1}{2}}}{\Delta t} &= \frac{E_z|_{i,j+\frac{1}{2},k}^{n} - E_z|_{i,j-\frac{1}{2},k}^{n}}{\Delta y} - \frac{E_y|_{i,j,k+\frac{1}{2}}^{n} - E_y|_{i,j,k-\frac{1}{2}}^{n}}{\Delta z},\\
-\mu \frac{H_y|_{i,j,k}^{n+\frac{1}{2}} - H_y|_{i,j,k}^{n-\frac{1}{2}}}{\Delta t} &= \frac{E_x|_{i,j,k+\frac{1}{2}}^{n} - E_x|_{i,j,k-\frac{1}{2}}^{n}}{\Delta z} - \frac{E_z|_{i+\frac{1}{2},j,k}^{n} - E_z|_{i-\frac{1}{2},j,k}^{n}}{\Delta x},\\
-\mu \frac{H_z|_{i,j,k}^{n+\frac{1}{2}} - H_z|_{i,j,k}^{n-\frac{1}{2}}}{\Delta t} &= \frac{E_y|_{i+\frac{1}{2},j,k}^{n} - E_y|_{i-\frac{1}{2},j,k}^{n}}{\Delta x} - \frac{E_x|_{i,j+\frac{1}{2},k}^{n} - E_x|_{i,j-\frac{1}{2},k}^{n}}{\Delta y},
\end{aligned}
$$

where i, j, k, n are integer counters for spatial and temporal steps along x, y, z, t dimensions, respectively. An important observation here is the way that electric field components are offset by $\Delta t/2$ in time from magnetic field components. This is a critical algorithmic design choice for FDTD as it results in a set of equations that do not need to be evaluated simultaneously. Therefore, these equations can be rearranged to produce six explicit "update equations" where each field component can be evaluated at any given time step using only field values already evaluated in previous time steps. Henceforth, FDTD wave propagation in time is effected through full update equations sweep of all electric field components in the digital mesh, followed by a similar sweep of all magnetic field components, with each pair of sweeps representing one Δt time increment.

Clearly, the discrete nature of FDTD grids means that FDTD wave solutions incur numerical errors that can only diminish by using higher mesh densities where $\Delta x, \Delta y, \Delta z \ll \lambda_{\min}$, and $\Delta t \ll T_{\min}$, the smallest wavelength and shortest wave period expected in the simulation, respectively. One of the error sources concerns the second-order finite-differencing which is on the order of $O(\Delta^2)$ where Δ is any of the four discrete steps used for simulation. This error source is of little concern in practical FDTD simulations, mainly because it affects field amplitudes uniformly and negligibly. A far more critical error source is the one induced in the wavenumber, β, since it appears in the phase of every propagated wave within the FDTD mesh in the form of $e^{j\beta r}$. However small the error is, if the wave propagates far enough it incurs enough cumulative phase error to cause serious simulation errors, especially when the simulation size extends multiples of wavelengths.

Thankfully, this particular error source can be precisely predicted by solving the FDTD algorithm-specific numerical dispersion relation.

Deriving this formula start by assuming each of the six electromagnetic field components to be of the plane wave form

$$F = Ae^{-\jmath(\beta_x x + \beta_y y + \beta_z z - \omega t)}, \tag{7.3}$$

which in its discrete form is expressed as

$$\tilde{F} = Ae^{-\jmath(\tilde{\beta}_x i\Delta x + \tilde{\beta}_y j\Delta y + \tilde{\beta}_z k\Delta z - \omega n\Delta t)},$$

where the symbol $\tilde{\beta}$ represents the numerical wavenumber that the FDTD algorithm is expected to effectively render within its simulation. Injecting this elementary wave function into the E_x update equation, as an example, yields the successive reductions.

$$\begin{aligned}
\frac{\epsilon E_x}{\Delta t}\left(e^{\jmath\omega\Delta t/2} - e^{-\jmath\omega\Delta t/2}\right) &= \frac{H_z}{\Delta y}\left(e^{-\jmath\tilde{\beta}_y\Delta y/2} - e^{\jmath\tilde{\beta}_y\Delta y/2}\right) - \frac{H_y}{\Delta z}\left(e^{-\jmath\tilde{\beta}_z\Delta z/2} - e^{\jmath\tilde{\beta}_z\Delta z/2}\right), \\
\jmath\epsilon E_x\frac{\sin(\omega\Delta t/2)}{\Delta t/2} &= -\jmath H_z\frac{\sin(\tilde{\beta}_y\Delta y/2)}{\Delta y/2} + \jmath H_y\frac{\sin(\tilde{\beta}_z\Delta z/2)}{\Delta z/2}, \\
\epsilon D_t E_x &= D_y H_z - D_z H_y.
\end{aligned} \tag{7.4}$$

Extending this treatment to the remaining five update equations yields a set of equations that can be expressed in the following matrix form

$$\begin{bmatrix}
-\epsilon D_t & 0 & 0 & 0 & -D_z & +D_y \\
0 & -\epsilon D_t & 0 & +D_z & 0 & -D_x \\
0 & 0 & -\epsilon D_t & -D_y & +D_x & 0 \\
0 & +D_z & -D_y & -\mu D_t & 0 & 0 \\
-D_z & 0 & +D_x & 0 & -\mu D_t & 0 \\
+D_y & -D_x & 0 & 0 & 0 & -\mu D_t
\end{bmatrix}
\begin{bmatrix} E_x \\ E_y \\ E_z \\ H_x \\ H_y \\ H_z \end{bmatrix} = 0, \tag{7.5}$$

with all the discrete operators given by

$$\begin{aligned}
D_t &= \jmath\frac{\sin(\omega\Delta t/2)}{\Delta t/2}, \\
D_x &= -\jmath\frac{\sin(\tilde{\beta}_x\Delta x/2)}{\Delta x/2}, \\
D_y &= -\jmath\frac{\sin(\tilde{\beta}_y\Delta y/2)}{\Delta y/2}, \\
D_z &= -\jmath\frac{\sin(\tilde{\beta}_z\Delta z/2)}{\Delta z/2}.
\end{aligned}$$

The numerical dispersion relation is then directly obtained by setting the determinant of the above square matrix to zero which yields

$$\mu\epsilon D_t^2 = D_x^2 + D_y^2 + D_z^2. \tag{7.6}$$

This numerical dispersion relation can now be solved for the numerical wavenumber given any prescribed set of mesh parameters and operating frequency. Conversely, it can be used as a design metric to specify an upper bound of mesh coarseness that maintains a prescribed upper bound of numerical wavenumber error.

The plane wave function (7.3) can be used to derive the numerical dispersion relation for any FDTD variant provided that the respective update equations were derived from Maxwell's equations that use the Cartesian del operator $\nabla \equiv \overline{a}_x \partial/\partial x + \overline{a}_y \partial/\partial y + \overline{a}_z \partial/\partial z$. If the del operator is based on, say, cylindrical or spherical wave functions, then the use of Cartesian wave functions will not yield the appropriate numerical dispersion relation. This restriction is further complicated by the fact that different electromagnetic field components will most probably require different forms of elementary functions. This is a complication that does not apply to Cartesian-based FDTD variants since both the Cartesian wave function and its derivatives have the same $e^{\mathrm{j}\beta r}$ dependence.

7.2 Spherical FDTD Update Equations

The expansion of the spatial ∇ operators of (7.1)–(7.2) into spherical coordinates results in

$$\epsilon \frac{\partial E_r}{\partial t} = \frac{1}{r \sin\theta}\left[\frac{\partial(\sin\theta H_\phi)}{\partial\theta} - \frac{\partial H_\theta}{\partial\phi}\right], \tag{7.7}$$

$$\epsilon \frac{\partial E_\theta}{\partial t} = \frac{1}{r}\left[\frac{1}{\sin\theta}\frac{\partial H_r}{\partial\phi} - \frac{\partial(rH_\phi)}{\partial r}\right], \tag{7.8}$$

$$\epsilon \frac{\partial E_\phi}{\partial t} = \frac{1}{r}\left[\frac{\partial(rH_\theta)}{\partial r} - \frac{\partial H_r}{\partial\theta}\right], \tag{7.9}$$

$$-\mu \frac{\partial H_r}{\partial t} = \frac{1}{r \sin\theta}\left[\frac{\partial(\sin\theta E_\phi)}{\partial\theta} - \frac{\partial E_\theta}{\partial\phi}\right], \tag{7.10}$$

$$-\mu \frac{\partial H_\theta}{\partial t} = \frac{1}{r}\left[\frac{1}{\sin\theta}\frac{\partial E_r}{\partial\phi} - \frac{\partial(rE_\phi)}{\partial r}\right], \tag{7.11}$$

$$-\mu \frac{\partial H_\phi}{\partial t} = \frac{1}{r}\left[\frac{\partial(rE_\theta)}{\partial r} - \frac{\partial E_r}{\partial\theta}\right]. \tag{7.12}$$

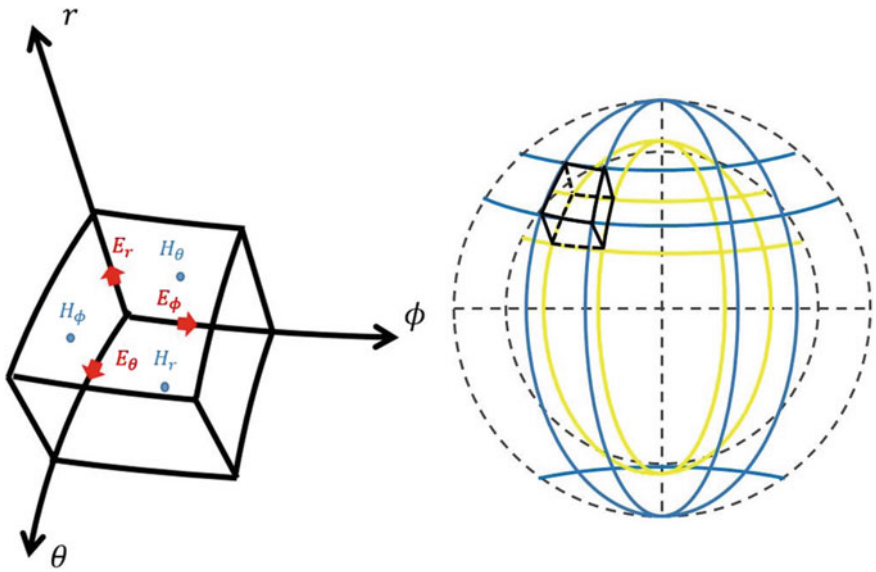

Fig. 7.2 Building block cell for spherical FDTD

Spherical FDTD is based on similar staggered fields mesh to Cartesian FDTD, except the building block cell is conforming to spherical coordinates as shown in Fig. 7.2. The complete set of update equations is given then by

$$\epsilon \frac{E_r|_{i,j,k}^{n+1} - E_r|_{i,j,k}^{n}}{\Delta t} = \frac{\Delta\theta/2}{i\Delta r \sin(j\Delta\theta)\sin(\Delta\theta/2)} \cdot \left[\frac{\sin((j+\frac{1}{2})\Delta\theta) H_\phi|_{i,j+\frac{1}{2},k}^{n+\frac{1}{2}} - \sin((j-\frac{1}{2})\Delta\theta) H_\phi|_{i,j-\frac{1}{2},k}^{n+\frac{1}{2}}}{\Delta\theta} - \frac{H_\theta|_{i,j,k+\frac{1}{2}}^{n+\frac{1}{2}} - H_\theta|_{i,j,k-\frac{1}{2}}^{n+\frac{1}{2}}}{\Delta\phi} \right], \tag{7.13}$$

$$\epsilon \frac{E_\theta|_{i,j,k}^{n+1} - E_\theta|_{i,j,k}^{n}}{\Delta t} = \frac{1}{i\Delta r} \left[\frac{H_r|_{i,j,k+\frac{1}{2}}^{n+\frac{1}{2}} - H_r|_{i,j,k-\frac{1}{2}}^{n+\frac{1}{2}}}{\sin(j\Delta\theta)\Delta\phi} - \frac{(i+\frac{1}{2}) H_\phi|_{i+\frac{1}{2},j,k}^{n+\frac{1}{2}} - (i-\frac{1}{2}) H_\phi|_{i-\frac{1}{2},j,k}^{n+\frac{1}{2}}}{1} \right], \tag{7.14}$$

$$\epsilon \frac{E_\phi|_{i,j,k}^{n+1} - E_\phi|_{i,j,k}^{n}}{\Delta t} = \frac{1}{i\Delta r} \left[\frac{(i+\frac{1}{2}) H_\theta|_{i+\frac{1}{2},j,k}^{n+\frac{1}{2}} - (i-\frac{1}{2}) H_\theta|_{i-\frac{1}{2},j,k}^{n+\frac{1}{2}}}{1} - \frac{H_r|_{i,j+\frac{1}{2},k}^{n+\frac{1}{2}} - H_r|_{i,j-\frac{1}{2},k}^{n+\frac{1}{2}}}{\Delta\theta} \right], \tag{7.15}$$

$$-\mu\frac{H_r|_{i,j,k}^{n+\frac{1}{2}}-H_r|_{i,j,k}^{n-\frac{1}{2}}}{\Delta t}=\frac{\Delta\theta/2}{i\Delta r\,\sin(j\Delta\theta)\sin(\Delta\theta/2)}$$
$$\cdot\left[\frac{\sin((j+\frac{1}{2})\Delta\theta)E_\phi|_{i,j+\frac{1}{2},k}^{n}-\sin((j-\frac{1}{2})\Delta\theta)E_\phi|_{i,j-\frac{1}{2},k}^{n}}{\Delta\theta}-\frac{E_\theta|_{i,j,k+\frac{1}{2}}^{n}-E_\theta|_{i,j,k-\frac{1}{2}}^{n}}{\Delta\phi}\right], \tag{7.16}$$

$$-\mu\frac{H_\theta|_{i,j,k}^{n+\frac{1}{2}}-H_\theta|_{i,j,k}^{n-\frac{1}{2}}}{\Delta t}=\frac{1}{i\Delta r}\left[\frac{E_r|_{i,j,k+\frac{1}{2}}^{n}-E_r|_{i,j,k-\frac{1}{2}}^{n}}{\Delta\phi\,\sin(j\Delta\theta)}-\frac{(i+\frac{1}{2})E_\phi|_{i+\frac{1}{2},j,k}^{n}-(i-\frac{1}{2})E_\phi|_{i-\frac{1}{2},j,k}^{n}}{1}\right], \tag{7.17}$$

$$-\mu\frac{H_\phi|_{i,j,k}^{n+\frac{1}{2}}-H_\phi|_{i,j,k}^{n-\frac{1}{2}}}{\Delta t}=\frac{1}{i\Delta r}\left[\frac{(i+\frac{1}{2})E_\theta|_{i+\frac{1}{2},j,k}^{n}-(i-\frac{1}{2})E_\theta|_{i-\frac{1}{2},j,k}^{n}}{1}-\frac{E_r|_{i,j+\frac{1}{2},k}^{n}-E_r|_{i,j-\frac{1}{2},k}^{n}}{\Delta\theta}\right], \tag{7.18}$$

with the index counters i,j,k,n now corresponding to the spherical coordinates variables r,θ,ϕ,t, respectively. Equations (7.14), (7.15), (7.17), and (7.18) are derived using strictly second-order finite-differences. Equations (7.13) and (7.16), on the other hand, were derived through using the modified Ampere's and Faraday's laws as they give a better representation of the finite cell areas in spherical coordinates. For example, when Ampere's Law is applied to the cell surface hosting $E_r|_{i,j,k}$, the surface integral of the displacement current produces

$$\int\epsilon\frac{\partial\overline{E}}{\partial t}\cdot d\overline{s}=\int_{\theta-\Delta\theta/2}^{\theta+\Delta\theta/2}\int_{\phi-\Delta\phi/2}^{\phi+\Delta\phi/2}\epsilon\frac{\partial E_r|_{i,j,k}}{\partial t}r^2\sin\theta' d\theta' d\phi'=\epsilon\frac{\partial E_r|_{i,j,k}}{\partial t}2r^2\Delta\phi\sin\theta\sin(\Delta\theta/2).$$

Special update equations along the z-axis ($\theta=0,\pi$) and at the origin ($r=0$) are needed. Furthermore, a wraparound joining condition needs to be enforced explicitly since along the k counter (corresponding to ϕ variable), field values at $k=0,N_\phi$ should be matched as they occupy identical physical positions.

Figure 7.3 illustrates the spherical FDTD cell facet used to update the $E_r|_{i,j=0,k}$ and $E_r|_{i,j=N_\theta,k}$ field components along the z-axis. The facet is actually concave, conforming to an outer surface of a sphere of radius $r=i\Delta r$. Using the modified Ampere's law, $\int\epsilon\frac{\partial\overline{E}}{\partial t}\cdot d\overline{s}=\oint\overline{H}\cdot d\overline{\ell}$, the left-hand side produces

$$\int\epsilon\frac{\partial\overline{E}}{\partial t}\cdot d\overline{s}=\epsilon\frac{\partial E_r|_{i,0,k}}{\partial t}\int_{\phi=0}^{2\pi}\int_{\theta=0}^{\Delta\theta/2}r^2\sin\theta d\theta d\phi=2\pi\epsilon r^2(1-(\cos\Delta\theta/2))\frac{\partial E_r|_{i,0,k}}{\partial t},$$

while the right-hand side produces

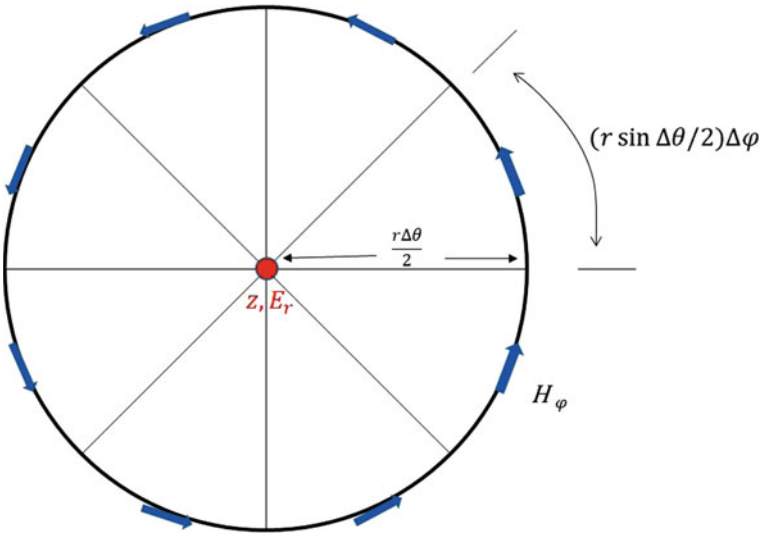

Fig. 7.3 Configuration of spherical FDTD cell facet for the purpose of deriving the $E_r|_{i,j=0,k}$ and $E_r|_{i,j=N_\theta,k}$ update equations, along the and both combine to produce the final$z$-axis

$$\oint \overline{H} \cdot d\overline{\ell} = \int_{\phi=0}^{2\pi} H_\phi r \sin\theta d\phi = r\Delta\phi \sin(\Delta\theta/2) \sum_{k=0}^{N_\phi - 1} H_\phi|_{i,\frac{1}{2},k},$$

and both combine to produce the final special update equation

$$\epsilon \frac{E_r|_{i,0,k}^{n+1} - E_r|_{i,0,k}^{n}}{\Delta t} = \frac{\Delta\phi \sin(\Delta\theta/2)}{2\pi r(1 - \cos(\Delta\theta/2))} \sum_{k=0}^{N_\phi - 1} H_\phi|_{i,\frac{1}{2},k}^{n+\frac{1}{2}}. \tag{7.19}$$

Because of geometric and trigonometric symmetries, the matching update equation along the negative z-axis will have a similar form,

$$\epsilon \frac{E_r|_{i,N_\theta,k}^{n+1} - E_r|_{i,N_\theta,k}^{n}}{\Delta t} = \frac{\Delta\phi \sin(\Delta\theta/2)}{2\pi r(1 - \cos(\Delta\theta/2))} \sum_{k=0}^{N_\phi - 1} H_\phi|_{i,N_\theta-\frac{1}{2},k}^{n+\frac{1}{2}}. \tag{7.20}$$

The integers N_θ and N_ϕ are the number of spherical FDTD cells along the θ and ϕ dimensions, respectively.

The H_r field nodes located $\Delta\theta/2$ off the z-axis also require a special update equation. Applying Faraday's law, $-\int \mu \frac{\partial \overline{H}}{\partial t} \cdot d\overline{s} = \oint \overline{E} \cdot d\overline{\ell}$, on the H_r-centered facet of Fig. 7.4, the left-hand side produces

$$-\int \mu \frac{\partial \overline{H}}{\partial t} \cdot d\overline{s} = -\mu \frac{\partial H_r|_{i,\frac{1}{2},k}}{\partial t} \int_{\theta=0}^{\Delta\theta} \int_{\phi=\phi_k-\Delta\phi/2}^{\phi_k+\Delta\phi/2} r^2 \sin\theta d\theta d\phi = -\mu\Delta\phi r^2(1 - \cos\Delta\theta) \frac{\partial H_r|_{i,\frac{1}{2},k}}{\partial t},$$

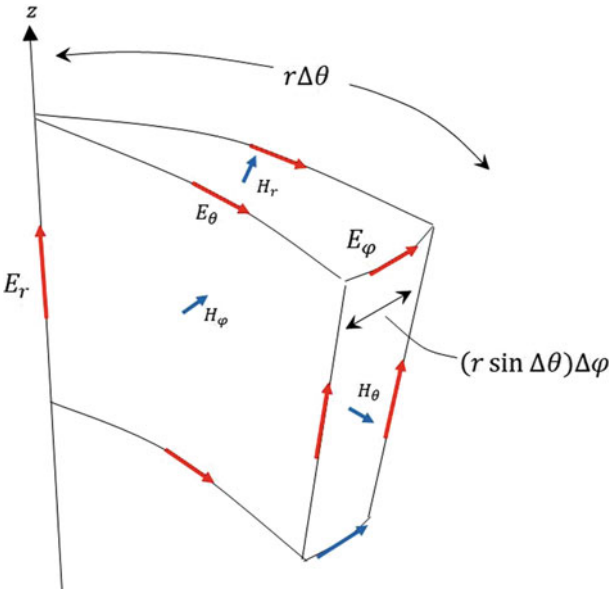

Fig. 7.4 Configuration of spherical FDTD cell facet for the purpose of deriving the $H_r|_{i,j=\frac{1}{2},k}$ update equation, around the z-axis

while the right-hand side produces

$$\oint \overline{E} \cdot d\overline{\ell} = \int_{\theta=0}^{\Delta\theta} E_\theta|_{i,\frac{1}{2},k-\frac{1}{2}} r d\theta + \int_{\phi=\phi_k-\Delta\phi/2}^{\phi_k+\Delta\phi/2} E_\phi|_{i,1,k} r \sin\Delta\theta d\phi + \int_{\theta=\Delta\theta}^{0} E_\theta|_{i,\frac{1}{2},k+\frac{1}{2}} r d\theta$$
$$= r\Delta\theta E_\theta|_{i,\frac{1}{2},k-\frac{1}{2}} + r\Delta\phi \sin\Delta\theta E_\phi|_{i,1,k} - r\Delta\theta E_\theta|_{i,\frac{1}{2},k+\frac{1}{2}},$$

and both combine, with $1-\cos\Delta\theta = 2\sin^2(\Delta\theta/2)$, to produce the update equation

$$-\mu \frac{H_r|_{i,\frac{1}{2},k}^{n+\frac{1}{2}} - H_r|_{i,\frac{1}{2},k}^{n-\frac{1}{2}}}{\Delta t} = \frac{\Delta\theta/2}{i\Delta r \sin^2(\Delta\theta/2)} \left[\frac{\sin\Delta\theta}{\Delta\theta} E_\phi|_{i,1,k}^n - \frac{E_\theta|_{i,\frac{1}{2},k+\frac{1}{2}}^n - E_\theta|_{i,\frac{1}{2},k-\frac{1}{2}}^n}{\Delta\phi} \right]. \tag{7.21}$$

Similarly, the matching update equation at $j = N_\theta - \frac{1}{2}$ can be found to be

$$-\mu \frac{H_r|_{i,N_\theta-\frac{1}{2},k}^{n+\frac{1}{2}} - H_r|_{i,N_\theta-\frac{1}{2},k}^{n-\frac{1}{2}}}{\Delta t} = \frac{\Delta\theta/2}{i\Delta r \sin^2(\Delta\theta/2)} \left[-\frac{\sin\Delta\theta}{\Delta\theta} E_\phi|_{i,N_\theta-1,k}^n - \frac{E_\theta|_{i,N_\theta-\frac{1}{2},k+\frac{1}{2}}^n - E_\theta|_{i,N_\theta-\frac{1}{2},k-\frac{1}{2}}^n}{\Delta\phi} \right]. \tag{7.22}$$

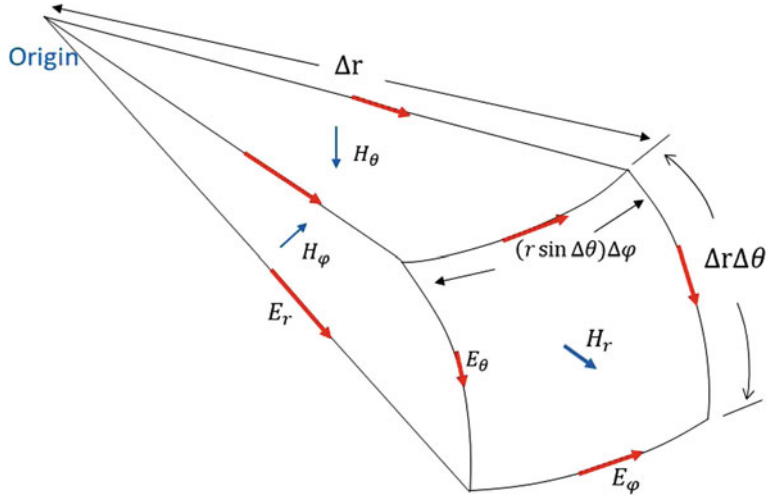

Fig. 7.5 Configuration of spherical FDTD cell facets for the purpose of deriving $H_\theta|_{i=\frac{1}{2},j,k}$ and $H_\phi|_{i=\frac{1}{2},j,k}$ update equations, around the origin

Next the special update equations for H_ϕ and H_θ field nodes located on the $r=\Delta r/2$ surface are derived. With the help of H_ϕ-centered facet in Fig. 7.5, the left-hand side of Faraday's law produces

$$-\int \mu\frac{\partial \overline{H}}{\partial t}\cdot d\overline{s} = -\mu\frac{\partial H_\phi|_{\frac{1}{2},j,k}}{\partial t}\int_{r=0}^{\Delta r}\int_{\theta=\theta_j-\Delta\theta/2}^{\theta_j+\Delta\theta/2} r dr d\theta = -\frac{\mu\Delta\theta(\Delta r)^2}{2}\frac{\partial H_\phi|_{\frac{1}{2},j,k}}{\partial t},$$

while the right-hand side produces

$$\oint \overline{E}\cdot d\overline{\ell} = \int_{r=0}^{\Delta r} E_r|_{\frac{1}{2},j-\frac{1}{2},k}dr + \int_{\theta=\theta_j-\Delta\theta/2}^{\theta_j+\Delta\theta/2} E_\theta|_{1,j,k}\Delta r d\theta + \int_{r=\Delta r}^{0} E_r|_{\frac{1}{2},j+\frac{1}{2},k}dr$$
$$= \Delta r E_r|_{\frac{1}{2},j-\frac{1}{2},k} + \Delta r\Delta\theta E_\theta|_{1,j,k} - \Delta r E_r|_{\frac{1}{2},j+\frac{1}{2},k},$$

and both combine to produce the update equation

$$-\mu\frac{H_\phi|_{\frac{1}{2},j,k}^{n+\frac{1}{2}} - H_\phi|_{\frac{1}{2},j,k}^{n-\frac{1}{2}}}{\Delta t} = \frac{1}{\Delta r/2}\left[E_\theta|_{1,j,k}^{n} - \frac{E_r|_{\frac{1}{2},j+\frac{1}{2},k}^{n} - E_r|_{\frac{1}{2},j-\frac{1}{2},k}^{n}}{\Delta\theta}\right]. \tag{7.23}$$

Using now the H_θ-centered facet of the same Fig. 7.5, the left-hand side of Faraday's law produces

$$-\int \mu\frac{\partial \overline{H}}{\partial t}\cdot d\overline{s} = -\mu\frac{\partial H_\theta|_{\frac{1}{2},j,k}}{\partial t}\int_{r=0}^{\Delta r}\int_{\phi=\phi_k-\Delta\phi/2}^{\phi_k+\Delta\phi/2} r\sin\theta dr d\phi = -\frac{\mu\Delta\phi(\Delta r)^2\sin\theta}{2}\frac{\partial H_\theta|_{\frac{1}{2},j,k}}{\partial t},$$

while the right-hand side produces

$$\oint \overline{E} \cdot d\overline{\ell} = \int_{r=0}^{\Delta r} E_r|_{\frac{1}{2},j,k+\frac{1}{2}} dr + \int_{\phi=\phi_k+\Delta\phi/2}^{\phi_k-\Delta\phi/2} E_\phi|_{1,j,k} \Delta r \sin\theta d\phi + \int_{r=\Delta r}^{0} E_r|_{\frac{1}{2},j,k-\frac{1}{2}} dr$$
$$= \Delta r E_r|_{\frac{1}{2},j,k+\frac{1}{2}} - \Delta r \sin\theta \Delta\phi E_\phi|_{1,j,k} - \Delta r E_r|_{\frac{1}{2},j,k-\frac{1}{2}},$$

and both combine to produce the update equation

$$-\mu \frac{H_\theta|^{n+\frac{1}{2}}_{\frac{1}{2},j,k} - H_\theta|^{n-\frac{1}{2}}_{\frac{1}{2},j,k}}{\Delta t} = \frac{1}{\Delta r/2}\left[\frac{E_r|^n_{\frac{1}{2},j,k+\frac{1}{2}} - E_r|^n_{\frac{1}{2},j,k-\frac{1}{2}}}{\Delta\phi \sin j\Delta\theta} - E_\phi|^n_{1,j,k}\right]. \tag{7.24}$$

Now that the spherical FDTD set of update equations is complete, it should be recognized that some of the update equations remain near-singular close to the origin or the z-axis, due to the presence of $i\Delta r$ or $\sin j\Delta\theta$, respectively. Although the special update equations above avoided the singular limits $i=0$ and $j=0, N_\theta$, the remaining worst-case scenarios, $i=\frac{1}{2}$ and $j=\frac{1}{2}, N_\theta - \frac{1}{2}$, are unavoidable and their effect on algorithm accuracy will remain, especially at very small Δr and $\Delta\theta$ spatial increments. An extremely fine spherical FDTD mesh in these neighborhoods is certainly not desirable for this and other computational efficiency reasons. It is important, however, to maintain the ability to quantify algorithmic errors for all space, and especially within the near-singular regions. In other words, the numerical dispersion relation needs to be sensitive to these near-singular behaviors.

7.3 Spherical FDTD Numerical Dispersion Relation

With the aim of producing a numerical dispersion relation that represents the discrete form of the Helmholtz wave equation in spherical space,

$$\frac{1}{h_n^{(2)}(\beta r)} \frac{d}{dr}\left(r^2 \frac{dh_n^{(2)}(\beta r)}{dr}\right) + \frac{1}{\sin\theta P_n^m(\cos\theta)} \frac{d}{d\theta}\left(\sin\theta \frac{dP_n^m(\cos\theta)}{d\theta}\right) - \left(\frac{m}{\sin\theta}\right)^2 + \beta^2 r^2 = 0, \tag{7.25}$$

the required harmonic functions need to be of Schelkunoff's form [2, 3]. Limiting the treatment to TE^r (or $E_r = 0$) outgoing spherical waves, an electric vector potential function of the form

$$F = \beta r h_n^{(2)}(\beta r) P_n^m(\cos\theta) e^{-j(m\phi - \omega t)}, \tag{7.26}$$

where $h_n^{(2)}$ is the forward-traveling spherical Hankel function and P_n^m the associated Legendre function, can be used to produce the remaining electromagnetic field components via

$$E_\theta = -\frac{1}{r\sin\theta}\frac{\partial F}{\partial \phi} = \mathcal{E}_\theta \frac{\beta}{\sin\theta} h_n^{(2)}(\beta r) P_n^m(\cos\theta) e^{-J(m\phi-\omega t)}, \tag{7.27}$$

$$E_\phi = \frac{1}{r}\frac{\partial F}{\partial \theta} = \mathcal{E}_\phi \beta \sin\theta h_n^{(2)}(\beta r) P_n'^m(\cos\theta) e^{-J(m\phi-\omega t)}, \tag{7.28}$$

$$H_r = \frac{1}{J\omega\mu}\left(\frac{\partial^2}{\partial r^2}+\beta^2\right)F = \mathcal{H}_r \beta^2 M(\beta r) P_n^m(\cos\theta) e^{-J(m\phi-\omega t)}, \tag{7.29}$$

$$H_\theta = \frac{1}{J\omega\mu r}\frac{\partial^2 F}{\partial r \partial \theta} = \mathcal{H}_\theta \frac{\beta\sin\theta}{r} N(\beta r) P_n'^m(\cos\theta) e^{-J(m\phi-\omega t)} \tag{7.30}$$

$$H_\phi = \frac{1}{J\omega\mu r\sin\theta}\frac{\partial^2 F}{\partial r \partial \phi} = \mathcal{H}_\phi \frac{\beta}{r\sin\theta} N(\beta r) P_n^m(\cos\theta) e^{-J(m\phi-\omega t)}, \tag{7.31}$$

All the redacted constants were grouped into the field amplitudes and

$$M(\beta r) = \beta r h_n^{(2)}(\beta r) + 2h_n'^{(2)}(\beta r) + \beta r h_n''^{(2)}(\beta r),$$
$$N(\beta r) = h_n^{(2)}(\beta r) + \beta r h_n'^{(2)}(\beta r).$$

Following the earlier approach with Cartesian FDTD, the above field quantities are introduced into the spherical FDTD update equations with the understanding that $\beta \to \tilde{\beta}$, $r = i\Delta r$, $\theta = j\Delta\theta$, and $\phi = k\Delta\phi$. For example, Eq. (7.14), once the midpoint in time is shifted from $n+\frac{1}{2}$ to n, results in

$$\epsilon \frac{e^{J\omega\Delta t/2} - e^{-J\omega\Delta t/2}}{\Delta t}\frac{\tilde{\beta}\mathcal{E}_\theta}{\sin\theta} h_n^{(2)}(\tilde{\beta} r) P_n^m(\cos\theta) =$$
$$\frac{e^{-Jm\Delta\phi/2} - e^{Jm\Delta\phi/2}}{r\sin(\theta)\Delta\phi}\mathcal{H}_r\tilde{\beta}^2 M(\tilde{\beta} r) P_n^m(\cos\theta) - \frac{N\left(\tilde{\beta}(r+\Delta r/2)\right) - N\left(\tilde{\beta}(r-\Delta r/2)\right)}{r\Delta r}\frac{\tilde{\beta} P_n^m(\cos\theta)}{\sin\theta}\mathcal{H}_\phi. \tag{7.32}$$

Applying a similar treatment to the remaining update Eqs. (7.15)–(7.18) and simplifying the expressions eventually produces the matrix equation

$$\begin{bmatrix} -\epsilon D_t & 0 & +D_\phi^H & 0 & -D_r^H \\ 0 & -\epsilon D_t & -D_\theta^H & +D_r^H & 0 \\ +D_\phi^E & -D_\theta^E & -\mu D_t & 0 & 0 \\ 0 & D_r^E & 0 & -\mu D_t & 0 \\ -D_r^E & 0 & 0 & 0 & -\mu D_t \end{bmatrix} \begin{bmatrix} \mathcal{E}_\theta \\ \mathcal{E}_\phi \\ \mathcal{H}_r \\ \mathcal{H}_\theta \\ \mathcal{H}_\phi \end{bmatrix} = 0, \tag{7.33}$$

where

$$D_t = J\frac{\sin\omega\Delta t/2}{\Delta t/2}, \tag{7.34}$$

$$D_r^E = \frac{r^+ h_n^{(2)}(\tilde{\beta} r^+) - r^- h_n^{(2)}(\tilde{\beta} r^-)}{\Delta r N(\tilde{\beta} r)}, \tag{7.35}$$

$$D_r^H = \frac{N(\tilde{\beta} r^+) - N(\tilde{\beta} r^-)}{r \Delta r h_n^{(2)}(\tilde{\beta} r)}, \tag{7.36}$$

$$D_\theta^E = \frac{h_n^{(2)}(\tilde{\beta} r)}{\tilde{\beta} r M(\tilde{\beta} r)} \frac{\Delta\theta/2}{\sin\ \Delta\theta/2} \frac{\sin^2\theta^+ P_n^{'m}(\cos\ \theta^+) - \sin^2\theta^- P_n^{'m}(\cos\ \theta^-)}{\Delta\theta\ \sin\ \theta P_n^m(\cos\ \theta)}, \tag{7.37}$$

$$D_\theta^H = \frac{\tilde{\beta} M(\tilde{\beta} r)}{r h_n^{(2)}(\tilde{\beta} r)} \frac{P_n^m(\cos\ \theta^+) - P_n^m(\cos\ \theta^-)}{\Delta\theta\ \sin\ \theta P_n^{'m}(\cos\ \theta)}, \tag{7.38}$$

$$D_\phi^E = -J \frac{\sin\ m\Delta\phi/2}{\Delta\phi/2} \frac{h_n^{(2)}(\tilde{\beta} r)}{\tilde{\beta} r M(\tilde{\beta} r)} \frac{\Delta\theta/2}{\sin(\Delta\theta/2)} \frac{1}{\sin^2\theta}, \tag{7.39}$$

$$D_\phi^H = -J \frac{\sin\ m\Delta\phi/2}{\Delta\phi/2} \frac{\tilde{\beta} M(\tilde{\beta} r)}{r h_n^{(2)}(\tilde{\beta} r)},$$

$$r\pm = r \pm \frac{\Delta r}{2},$$

$$\theta^\pm = \theta \pm \frac{\Delta\theta}{2}.$$

From the above matrix equation, the spherical FDTD dispersion relation can be derived by setting the system's determinant to zero;

$$\mu\epsilon D_t^2 = D_r^E D_r^H + D_\theta^E D_\theta^H + D_\phi^E D_\phi^H, \tag{7.40}$$

with the expanded form

$$\begin{aligned} \mu\epsilon \left(\frac{\sin(\omega\Delta t/2)}{\Delta t/2}\right)^2 &= \frac{1}{(r\ \sin\ \theta)^2} \left(\frac{\sin(m\Delta\phi/2)}{\Delta\phi/2}\right)^2 \frac{\Delta\theta/2}{\sin(\Delta\theta/2)} \\ &- \frac{r^+ h_n^{(2)}(\tilde{\beta} r^+) - r^- h_n^{(2)}(\tilde{\beta} r^-)}{\Delta r N(\tilde{\beta} r)} \cdot \frac{N(\tilde{\beta} r^+) - N(\tilde{\beta} r^-)}{r \Delta r h_n^{(2)}(\tilde{\beta} r)} \\ - \frac{1}{(r\ \sin\ \theta)^2} \frac{\Delta\theta/2}{\sin(\Delta\theta/2)} &\frac{\sin^2\theta^+ P_n^{'m}(\cos\ \theta^+) - \sin^2\theta^- P_n^{'m}(\cos\ \theta^-)}{\Delta\theta P_n^m(\cos\theta)} \cdot \frac{P_n^m(\cos\ \theta^+) - P_n^m(\cos\ \theta^-)}{\Delta\theta P_n^{'m}(\cos\ \theta)}. \end{aligned} \tag{7.41}$$

It can be shown, with the help of some trigonometric identities and the first derivative definition, that

$$\lim_{\Delta t \to 0} D_t^2 = -\omega^2,$$

$$\lim_{\Delta r \to 0} D_r^E D_r^H = \frac{\beta^2 r h_n^{''(2)}(\beta r) + 2\beta h_n^{'(2)}(\beta r)}{r h_n^{(2)}(\beta r)},$$

$$\lim_{\Delta \theta \to 0} D_\theta^E D_\theta^H = \frac{-\sin^2\theta P_n^{''m}(\cos\theta) + 2\cos\theta P_n^{'m}(\cos\theta)}{r^2 P_n^m(\cos\theta)},$$

$$\lim_{\substack{\Delta\phi \to 0 \\ \Delta\theta \to 0}} D_\phi^E D_\phi^H = -\left(\frac{m}{r\sin\theta}\right)^2.$$

Assembling all these limits into (7.40) reduces this numerical dispersion relation to the continuous-space limit as

$$\omega^2\mu\epsilon = \left(\frac{m}{r\sin\theta}\right)^2 - \left(\beta^2 \frac{h_n^{''(2)}(\beta r)}{h_n^{(2)}(\beta r)} + \frac{2\beta}{r}\frac{h_n^{'(2)}(\beta r)}{h_n^{(2)}(\beta r)}\right) - \frac{1}{r^2}\left(\sin^2\theta \frac{P_n^{''m}(\cos\theta)}{P_n^m(\cos\theta)} - 2\cos\theta \frac{P_n^{'m}(\cos\theta)}{P_n^m(\cos\theta)}\right). \tag{7.42}$$

Finally, if we take the spherical Helmholtz wave equation in its separated variables form [2]

$$\frac{1}{h_n^{(2)}(\beta r)}\frac{d}{dr}\left(r^2 \frac{dh_n^{(2)}(\beta r)}{dr}\right) + \frac{1}{\sin\theta P_n^m(\cos\theta)}\frac{d}{d\theta}\left(\sin\theta \frac{dP_n^m(\cos\theta)}{d\theta}\right) - \left(\frac{m}{\sin\theta}\right)^2 + \beta^2 r^2 = 0, \tag{7.43}$$

and convert the ordinary derivatives $\frac{d}{dr}$ and $\frac{d}{d\theta}$ to derivatives with respect to the arguments $\frac{d}{d(\beta r)}$ and $\frac{d}{d(\cos\theta)}$, respectively, we can produce

$$\beta^2 = \left(\frac{m}{r\sin\theta}\right)^2 - \left(\beta^2 \frac{h_n^{''(2)}(\beta r)}{h_n^{(2)}(\beta r)} + \frac{2\beta}{r}\frac{h_n^{'(2)}(\beta r)}{h_n^{(2)}(\beta r)}\right) - \frac{1}{r^2}\left(\sin^2\theta \frac{P_n^{''m}(\cos\theta)}{P_n^m(\cos\theta)} - 2\cos\theta \frac{P_n^{'m}(\cos\theta)}{P_n^m(\cos\theta)}\right). \tag{7.44}$$

A simple comparison of (7.42) with (7.44) would result in the succinct dispersion relation for lossless spherical space, thus finally validating the accuracy of the derived spherical FDTD dispersion relation in (7.40);

$$\omega^2\mu\epsilon = \beta^2.$$

This continuous limit is realized everywhere in the discrete spherical FDTD space except for the regions

$$r \le \frac{\Delta r}{2}, \theta \le \frac{\Delta\theta}{2}, \theta \ge \pi - \frac{\Delta\theta}{2},$$

as they involve the special update equations discussed earlier which differ from those used to derive the numerical dispersion relation (7.40).

7.4 Numerical Dispersion Analysis

The numerical dispersion relation (7.40) is solved for the numerical wavenumber $\tilde{\beta}$ given a prescribed set of mesh parameters, intrinsic medium parameters (free space assumed), and frequency (1 GHz assumed). The selected time step is [4]

$$\Delta t = \frac{\sqrt{\mu\epsilon}}{\sqrt{\left(\frac{1}{\Delta r}\right)^2 + \left(\frac{1}{\Delta r \Delta\theta}\right)^2 + \left(\frac{1}{\Delta r \sin(\Delta\theta)\Delta\phi}\right)^2}}, \tag{7.45}$$

based on the smallest dimensions in the designed spherical FDTD mesh. Figure 7.6 compares numerical wavenumber solutions from the derived dispersion relation at three different mesh resolutions in terms of spherical FDTD cells per radial wavelength. As expected, calculated error decreases and stabilizes as the normalized radial distance exceeds unity. Closer to the origin, however, higher mesh densities are certainly needed if wave solutions integrity is to be maintained. The numerical wavenumber also becomes complex-valued near the origin which affects wave solution amplitudes as well as their phases. Negative imaginary $\tilde{\beta}$ values cause the waves to attenuate while positive values cause them to grow artificially. Each of the curves is limited on the left by $r_{\min} = \Delta r = \lambda/R$ to avoid the Hankel function singularity at $r = \Delta r/2$ in Eq. (7.35)–(7.36).

Figure 7.7 demonstrates the sensitivity of numerical wavenumber solutions to n, the variable which dictates the mode order along the θ dimension. As the order increases, so goes the error. If solutions from the problem at hand are expected to exhibit vital behavior at high n orders, then a finer mesh resolution is called for. On the other hand, there is limited solutions sensitivity to m, the mode order along the ϕ dimension, as demonstrated in Fig. 7.8. It should be remembered here that the spherical wave function (7.26) dictates that $m \leq n$ for any given spherical mode.

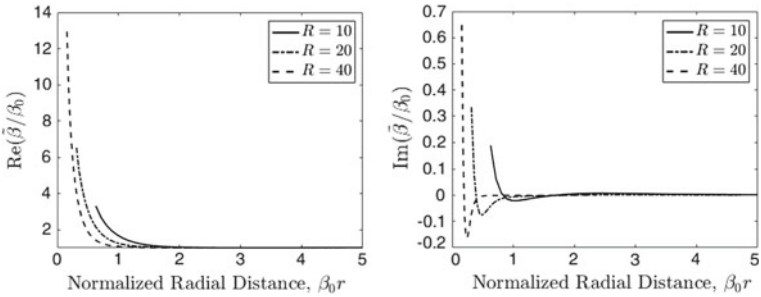

Fig. 7.6 Wavenumber error growth approaching the origin at three R cells per radial wavelength values. $N_\theta = 20$, $N_\phi = 40$, $m = 2$, $n = 2$, $\phi = 36^\circ$, and $\theta = 27^\circ$

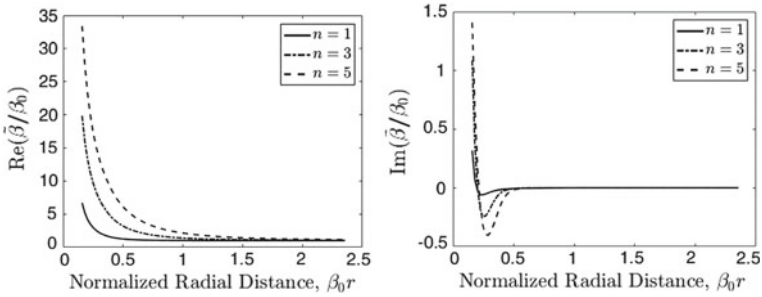

Fig. 7.7 Wavenumber error sensitivity to n modes. Same parameters as in Fig. 7.6 except for $m = 0$, $R = 40$, and n is variable

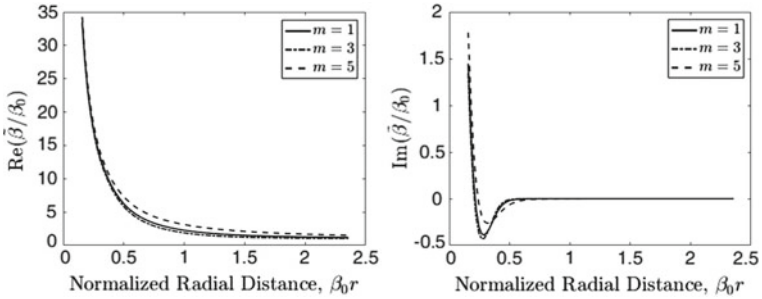

Fig. 7.8 Wavenumber error sensitivity to m modes. Same parameters as in Fig. 7.6 except for $n = 5$, $R = 40$, and m is variable

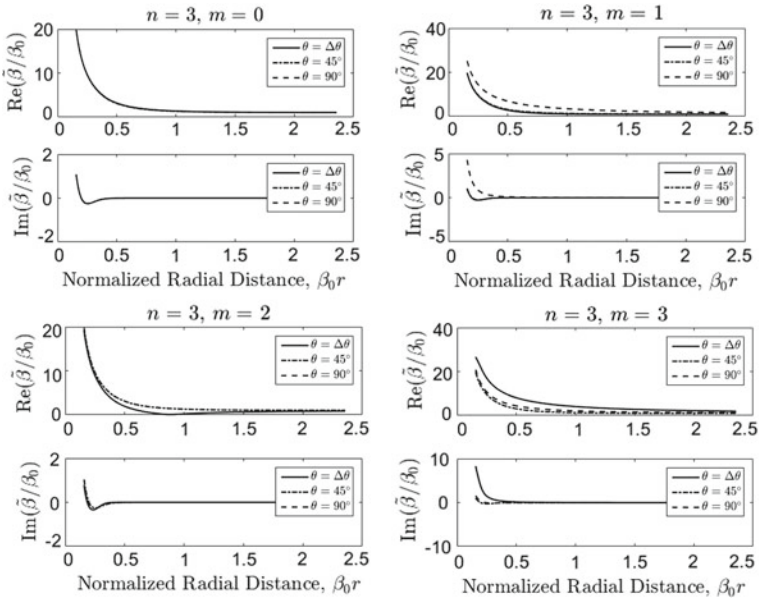

Fig. 7.9 Wavenumber error sensitivity to absolute θ position at different modes. Same parameters as in Fig. 7.6 except for $R = 40$, $n = 3$, and m is variable

Sensitivity analysis of wavenumber solutions with respect to absolute θ position can be disrupted by the inherent singularities in the numerical dispersion relation. The locations of these singularities vary with (m, n) values as they affect the associated Legendre functions present in the denominators of D_θ^E and D_θ^H. Figure 7.9 shows that wavenumber solutions remain relatively unchanged with θ at low m values and change minimally as m approaches n.

7.5 Absorbing Boundary Conditions

Outgoing spherical waves in a spherical space, continuous or discrete as in spherical FDTD, have a standing wave nature along both θ and ϕ dimensions. If the spherical domain is terminated along either of these two dimensions, then appropriate boundary conditions can be constructed using modal analysis. That leaves only wave propagation along the r dimension requiring absorbing boundary termination when modeling unbounded structures. This fact suggests that a spherical FDTD absorbing boundary layer can be constructed as a regular distortion-less layer with a profiled loss factor, from zero at the inner boundary of the layer to some maximum loss factor value at the outer boundary. This type of absorbing boundary condition (ABC) has been proven to fail for Cartesian FDTD [5]. It will be demonstrated here that it actually works for spherical FDTD and matches the performance of Berenger's perfectly matched layer (PML) ABC [6].

7.5.1 Perfectly Matched Layer ABC

PML absorbing boundary conditions are basically a set of added layers of FDTD cells tacked on to the outer boundary of the numerical model. In the case of spherical FDTD, these layers (typically 10–20 cells deep) comprise spherical shells. The update equations within the PML region match those within the interior model, with the exception that a profiled loss factor is introduced to a portion of every field component therein. Said portion is only limited to the $\partial/\partial r$ related part of the component's update equation. To effect this treatment for spherical FDTD, Eqs. (7.8), (7.9), (7.11), and (7.12) need to be split into the following set of pairs

$$\epsilon \frac{\partial E_{\theta\phi}}{\partial t} = \frac{1}{r \sin\theta} \frac{\partial H_r}{\partial \phi}, \tag{7.46}$$

$$\epsilon \frac{\partial E_{\theta r}}{\partial t} + \sigma_r E_{\theta r} = -\frac{1}{r} \frac{\partial (r H_\phi)}{\partial r}, \tag{7.47}$$

$$\epsilon \frac{\partial E_{\phi\theta}}{\partial t} = -\frac{1}{r} \frac{\partial H_r}{\partial \theta}, \tag{7.48}$$

$$\epsilon \frac{\partial E_{\phi r}}{\partial t} + \sigma_r E_{\phi r} = \frac{1}{r} \frac{\partial (r H_\theta)}{\partial r}, \tag{7.49}$$

$$-\mu \frac{\partial H_{\theta\phi}}{\partial t} = \frac{1}{r \sin\theta} \frac{\partial E_r}{\partial \phi}, \tag{7.50}$$

$$-\mu \frac{\partial H_{\theta r}}{\partial t} - \sigma_r^* H_{\theta r} = -\frac{1}{r} \frac{\partial (r E_\phi)}{\partial r}, \tag{7.51}$$

$$-\mu \frac{\partial H_{\phi\theta}}{\partial t} = -\frac{1}{r} \frac{\partial E_r}{\partial \theta}, \tag{7.52}$$

$$-\mu \frac{\partial H_{\phi r}}{\partial t} - \sigma_r^* H_{\phi r} = \frac{1}{r} \frac{\partial (r E_\theta)}{\partial r}, \tag{7.53}$$

where σ_r, σ_r^* are artificially introduced electric and magnetic conductivities that adhere to the matching condition $\sigma_r^*/\mu = \sigma_r/\epsilon$. Furthermore, the split field components are summed algebraically when they are needed in the right-hand side of PML region update equations, as in $E_\theta = E_{\theta\phi} + E_{\theta r}$.

The corresponding spherical FDTD equations within the PML region are

$$\epsilon \frac{E_{\theta\phi}|_{i,j,k}^{n+1} - E_{\theta\phi}|_{i,j,k}^{n}}{\Delta t} = \frac{H_r|_{i,j,k+\frac{1}{2}}^{n+\frac{1}{2}} - H_r|_{i,j,k-\frac{1}{2}}^{n+\frac{1}{2}}}{i\Delta r \sin(j\Delta\theta)\Delta\phi}, \tag{7.54}$$

$$\epsilon \frac{E_{\theta r}|_{i,j,k}^{n+1} - E_{\theta r}|_{i,j,k}^{n}}{\Delta t} + \sigma_r \frac{E_{\theta r}|_{i,j,k}^{n+1} + E_{\theta r}|_{i,j,k}^{n}}{2} = -\frac{(i+\frac{1}{2}) H_\phi|_{i+\frac{1}{2},j,k}^{n+\frac{1}{2}} - (i-\frac{1}{2}) H_\phi|_{i-\frac{1}{2},j,k}^{n+\frac{1}{2}}}{i\Delta r}, \tag{7.55}$$

$$\epsilon \frac{E_{\phi\theta}|_{i,j,k}^{n+1} - E_{\phi\theta}|_{i,j,k}^{n}}{\Delta t} = -\frac{H_r|_{i,j+\frac{1}{2},k}^{n+\frac{1}{2}} - H_r|_{i,j-\frac{1}{2},k}^{n+\frac{1}{2}}}{i\Delta r \Delta\theta}, \tag{7.56}$$

$$\epsilon \frac{E_{\phi r}|_{i,j,k}^{n+1} - E_{\phi r}|_{i,j,k}^{n}}{\Delta t} + \sigma_r \frac{E_{\phi r}|_{i,j,k}^{n+1} + E_{\phi r}|_{i,j,k}^{n}}{2} = \frac{(i+\frac{1}{2}) H_\theta|_{i+\frac{1}{2},j,k}^{n+\frac{1}{2}} - (i-\frac{1}{2}) H_\theta|_{i-\frac{1}{2},j,k}^{n+\frac{1}{2}}}{i\Delta r}, \tag{7.57}$$

$$-\mu \frac{H_{\theta\phi}|_{i,j,k}^{n+\frac{1}{2}} - H_{\theta\phi}|_{i,j,k}^{n-\frac{1}{2}}}{\Delta t} = \frac{E_r|_{i,j,k+\frac{1}{2}}^{n} - E_r|_{i,j,k-\frac{1}{2}}^{n}}{i\Delta r \Delta\phi \sin(j\Delta\theta)}, \tag{7.58}$$

$$-\mu \frac{H_{\theta r}|_{i,j,k}^{n+\frac{1}{2}} - H_{\theta r}|_{i,j,k}^{n-\frac{1}{2}}}{\Delta t} - \sigma_r^* \frac{H_{\theta r}|_{i,j,k}^{n+\frac{1}{2}} + H_{\theta r}|_{i,j,k}^{n-\frac{1}{2}}}{2} = -\frac{(i+\frac{1}{2}) E_\phi|_{i+\frac{1}{2},j,k}^{n} - (i-\frac{1}{2}) E_\phi|_{i-\frac{1}{2},j,k}^{n}}{i\Delta r}, \tag{7.59}$$

$$-\mu\frac{H_{\phi\theta}|_{i,j,k}^{n+\frac{1}{2}}-H_{\phi\theta}|_{i,j,k}^{n-\frac{1}{2}}}{\Delta t}=-\frac{E_r|_{i,j+\frac{1}{2},k}^{n}-E_r|_{i,j-\frac{1}{2},k}^{n}}{i\Delta r\Delta\theta}, \tag{7.60}$$

$$-\mu\frac{H_{\phi r}|_{i,j,k}^{n+\frac{1}{2}}-H_{\phi r}|_{i,j,k}^{n-\frac{1}{2}}}{\Delta t}-\sigma_r^{*}\frac{H_{\phi r}|_{i,j,k}^{n+\frac{1}{2}}+H_{\phi r}|_{i,j,k}^{n-\frac{1}{2}}}{2}=\frac{(i+\frac{1}{2})E_\theta|_{i+\frac{1}{2},j,k}^{n}-(i-\frac{1}{2})E_\theta|_{i-\frac{1}{2},j,k}^{n}}{i\Delta r}. \tag{7.61}$$

The PML conductivity profile is typically polynomial graded from zero to $\sigma_{\max}$;

$$\sigma(L)=\sigma_{\max}\left(\frac{L}{d}\right)^{n_\sigma}, \tag{7.62}$$

where L is the radial distance from the innermost PML interface, $d=\Delta r\times$(the number of PML Layers) is the PML depth and $n_\sigma\approx 2-4$. Finally, $\sigma_{\max}$ is chosen following Gedney's empirical suggestion for Cartesian FDTD PML implementations [7];

$$\sigma_{\max}=\frac{0.8(n_\sigma+1)}{\eta_0\Delta r\sqrt{\mu_r\epsilon_r}}, \tag{7.63}$$

where η_0 is free space intrinsic impedance and μ_r,ϵ_r are the relative permeability and permittivity, if different from unity.

7.5.2 Distortion-Less Absorbing Shell ABC

For the distortion-less absorbing shell (DAS) ABC, spherical FDTD update equations remain un-split and the electric and magnetic conductivities are introduced as add-on terms as if modeling an isotropic lossy medium. The distortion-less condition is maintained by enforcing $\sigma^*/\mu=\sigma/\epsilon$. This approach fails for Cartesian FDTD except for normally incident waves. Since spherical wave harmonics are basically traveling waves along r and standing waves along θ and ϕ, DAS is expected to work just as efficiently as PML.

7.5.3 ABC Simulation Comparison

To compare the two ABC approaches, a test model is constructed with $\Delta r=\lambda/40$ at 1 GHz, $\Delta\theta=\pi/12$, and $\Delta\phi=\pi/8$. The ABC layers start at $r=1.5\lambda$. Two observation points were tracked at $r=0.75\lambda$, $\theta=45^\circ, 105^\circ$, and $\phi=0$. The source is an impressed $\mathrm{TE_{mn}}=\mathrm{TE_{01}}$ (H_r) field distribution over a spherical shell of radius

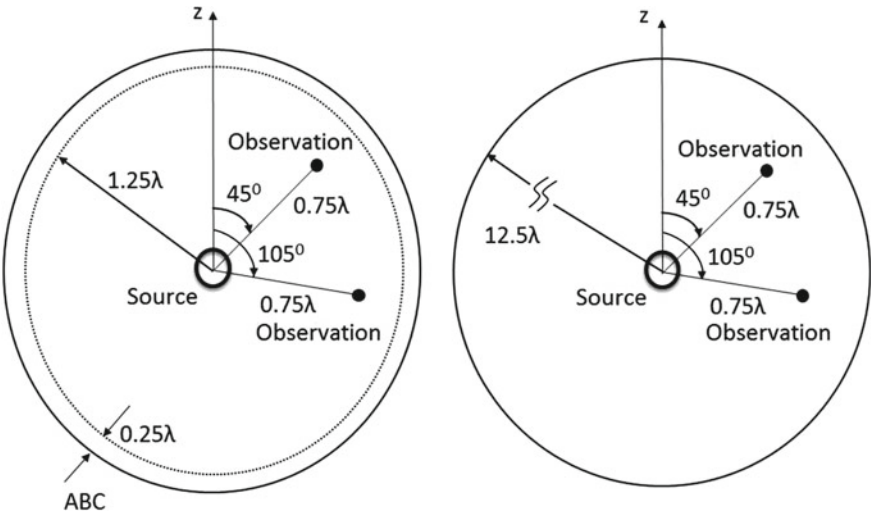

Fig. 7.10 Structure of the PML and DAS testing models. The absorptive performance of the ABC layers in the left model is compared at the same observation point with the results from the larger reference model on the right

$r = \Delta r$. Results from test simulation are compared with a larger reference model with similar parameters, except that the outer radius is at $r = 12.5\lambda$ (See Fig. 7.10). Duration of simulations was terminated before reflections from the larger reference boundaries could contaminate fields at the observation points.

Figure 7.11 compares the two ABC approaches in terms of the maximum value of the normalized error in the E_ϕ component at the observation points

$$\left| \frac{E_{obs} - E_{ref}}{E_{ref}|_{max}} \right|, \tag{7.58}$$

for different loss profile configurations. Several observations can be made here. First, both ABC approaches give nearly identical results, suggesting that the extra memory and computing demands of PML field splitting are unnecessary. Second, absorption efficiency is not affected by θ position. Third, the empirical formula derived for Cartesian FDTD (7.63) is usable for spherical FDTD. However, additional absorption performance is attainable through further optimization. From Fig. 7.11, the empirical formula produced, for $n_\sigma = 2$, $\sigma_{\max} = 0.85$ S/m which afforded -25 dB error, whereas the optimum $\sigma_{\max} = 80$ dB resulted in -30 dB. Fourth and most important, spherical FDTD ABC normalized errors are much higher compared to Cartesian FDTD which are in the range of -100 dB [7, 8].

Clearly, ABC design and performance for spherical FDTD deviate considerably from those for Cartesian FDTD. The sample analysis above serves as a warning against simple attempts to borrow ABC design parameters from Cartesian FDTD. Appropriate spherical FDTD ABC design requires more thorough analysis of the

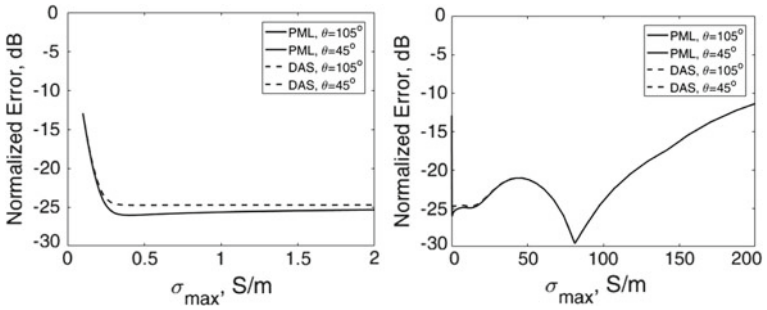

Fig. 7.11 Comparison of DAS and PML absorption performances at two different observation points

algorithm and underlying error-governing equations. The numerical dispersion relation derived in this chapter can serve as an important tool toward this goal as well as toward appropriate designs for other spherical FDTD modeling tools.

7.6 Conclusion

Many of the modeling decisions and tools for spherical FDTD require intimate knowledge of its underlying numerical dispersion relation. Merely copying the design metrics used for Cartesian FDTD will produce poor performance at best and may cause the simulation to fail outright if the region of interest is in close proximity to the origin. The spherical FDTD numerical dispersion relation has been derived in this chapter using the appropriate spherical harmonic solutions of the governing Maxwell's equations in spherical coordinates. Sensitivity of the incurred numerical errors to mesh design parameters has also been analyzed. This presentation lays the foundation for optimizing modeling tools specifically for spherical FDTD. For example, the chosen PML parameters in this chapter were based on PML analysis and conclusions from Cartesian FDTD. A potential future work would be to derive such parameters using reflection analysis of multilayered spherical boundaries which would directly benefit from the numerical dispersion relation derived here.

References

1. A. Elsherbeni, D. Veysel, *The Finite-Difference Time-Domain Method for Electromagnetics with MATLAB Simulations, 2nd Edition* (SciTech Publishing Inc. an Imprint of the IET, Edison, NJ, 2015)
2. R.F. Harrington, *Time-Harmonic Electomagnetic Fields* (McGraw-Hill, New York, NY, 1961)
3. C.A. Balanis, *Advanced Engineering Electromagnetics* (Wiley, New York, NY, 1989)

4. O. Franek, G. Pedersen, J. Andersen, Numerical modeling of a spherical array of monopoles using FDTD method. IEEE Trans. Antennas Propag. **54**(7), 1952–1963 (2006)
5. A. Taflove, S. Hagness, *Computational Electrodynamics: The Finite-Difference Time-Domain Method for Electromagnetics, 3rd Edition* (Artech House Inc., Norwood, MA, 2005)
6. J.-P. Berenger, A perfectly matched layer for the absorption of electromagnetics waves. J. Computat. Phys. **114**(2), 185–200 (1994)
7. S.D. Gedney, An anisotropic perfectly matched layer-absorbing medium for the truncation of FDTD lattices. IEEE Trans. Antennas Propag. **44**(12), 1630–1639 (1996)
8. M.F. Hadi, Near-Field PML optimization for low and high order FDTD algorithms using closed-form predictive equations. IEEE Trans. Antennas Propag. **59**(8), 2933–2942 (2011)

Part III
Photonic Crystal Fiber Sensors

Chapter 8
Temperature Sensors Based on Plasmonic Photonic Crystal Fiber

Mohammad Y. Azab, Mohamed Farhat O. Hameed and S. S. A. Obayya

Abstract In this chapter, two novel highly sensitive surface plasmon resonance photonic crystal fiber (PCF) temperature sensors based on liquid crystal (LC) or alcohol mixture are presented and studied. Through this chapter, the coupling characteristics between the core-guided mode inside the PCF core infiltrated with either nematic LC or alcohol mixture and surface plasmon mode around the surface of nanogold wire are studied in detail. The structural geometrical parameters of the proposed designs, such as hole pitch, number of metallic rods, core diameter, and metallic rod diameter, are optimized to achieve highly temperature sensitivity. The suggested alcohol-based sensor offers high sensitivity of 3 nm/°C and 4.9 nm/°C for transverse electric (TE) and transverse magnetic (TM) polarizations, respectively. Moreover, the alcohol core sensor operates over a wider range of temperatures from −4 °C to 53 °C. In addition, the suggested LC-based sensor of compact device length of 20 μm proved to surpass the sensitivity of the recent temperature sensors. Using the LC instead of alcohol has improved the sensitivity to 10 nm/°C.

M. Y. Azab · M. F. O. Hameed (✉)
Mathematics and Engineering Physics Department, Faculty of Engineering, Mansoura University, Mansoura 35516, Egypt
e-mail: mfarahat@zewailcity.edu.eg

M. F. O. Hameed
Center for Photonics and Smart Materials and Nanotechnology Engineering Program, Zewail City of Science and Technology, October Gardens, 6th of October City, Giza, Egypt

S. S. A. Obayya
Centre for Photonics and Smart Materials, Zewail City of Science and Technology, October Gardens, 6th of October City, Giza, Egypt
e-mail: sobayya@zewailcity.edu.eg

S. S. A. Obayya
Electronics and Communication Engineering Department, Faculty of Engineering, Mansoura University, Mansoura, Egypt

© Springer International Publishing AG, part of Springer Nature 2019

M. F. O. Hameed and S. Obayya (eds.), *Computational Photonic Sensors*, https://doi.org/10.1007/978-3-319-76556-3_8

The results are calculated using full-vectorial finite-element method with irregular meshing capabilities and perfect matched layer boundary conditions.

Keywords Temperature sensors · Photonic crystal fiber · Liquid crystal Surface plasmon · Alcohol

8.1 Introduction

Surface plasmon resonance (SPR) sensors based on photonic crystal fibers (PCFs) aroused much interest in recent years [1–3]. This is due to the high dependence of the surface plasmon on the index of refraction of the dielectric surrounding the metal/dielectric interface. A good example is the design of PCF with capillaries filled with metallic nanowires, where plasmonic modes are excited on the metal surface [2]. The resonance peak occurs when the real part of the effective index of the core mode is equal to that of the SPR mode at a particular wavelength. As a result, maximum power transfer occurs to the surface plasmon mode from the core mode with maximum losses. It is worth noting that PCF-based temperature sensor should be filled with liquid material with temperature coefficient. Consequently, the refractive index of the filling liquid and hence the effective refractive index of the PCF design will be temperature dependent. Therefore, SPR PCF temperature sensor can be realized.

Great efforts have been exerted in designing temperature sensors based on PCFs. A SP PCF temperature sensor has been reported [2] with a large central hole filled with LC material and coated by gold layer which offers sensitivity of 4 nm/°C. Additionally, a coupling between core modes and surface plasmon modes was demonstrated by Peng et al. [3]. In Ref. [3], the second layer has airholes filled with a liquid characterized by a large thermo-optic coefficient which offers sensitivity of 0.072 nm/°C. Further, liquid sealed (LS) PCF sensor with sensitivity of 0.0166 nm/°C based on in-line modal interferometers was proposed in [4]. Also, SPR sensor based on PCF filled with different concentrations of analyte and silver nanowires [5] was reported with sensitivity of 2.7 nm/°C. Moreover, Hu et al. [6] have investigated PCF directional coupler sensor filled with NLC with sensitivity of 3.86 nm/°C. Furthermore, high sensitivity of 4 nm/°C was achieved based on SPR PCF filled with a mixture of chloroform and ethanol with silver nanowires around the core region [7].

In this chapter, two novel designs of SPR temperature sensors based on PCF have been presented and analyzed. The suggested PCF sensors have a metal wire next to the core region as shown in Fig. 8.1. Resonance peaks are supported by the metal wire which is sensitive to the temperature variation by using alcohol mixture as a sensing medium for the first design and NLC for the second design. The temperature variation will affect the effective refractive indices of both LC material and alcohol mixture. This leads to a shift in the resonance wavelength. The temperature change can be detected by measuring the wavelength shift of the resonance

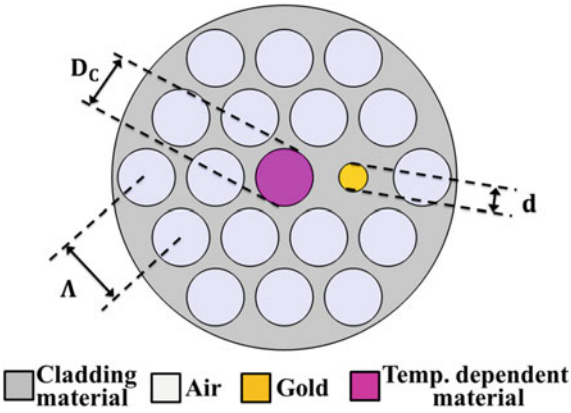

Fig. 8.1 Cross section of the suggested SPR PCF temperature sensor

peak. The suggested alcohol SPR PCF sensor has a background material of silica while the other design based on the NLC has a fluorite crown glass of type FK51A.

The first design with alcohol mixture in the core region achieves high sensitivity of 3 nm/°C which is comparable to those in the literature over a wide range of detection from −4 to 53 °C. On the other hand, in the second design, the refractive index of the FK51A is close to that of the ordinary index n_o of the liquid crystal. As a result, the efficiency of the coupling between the plasmonic modes and core modes is improved. Therefore, high sensitivity for temperature variation as high as 10 nm/°C can be attained for temperature range from 30 to 50 °C. The reported sensitivity is much higher than the recent temperature sensors in the literature [2–7].

8.2 Alcohol-Based SPR PCF Temperature Sensor

8.2.1 Design Considerations

Figure 8.1 represents a cross section of the suggested SPR PCF. The first design is based on silica glass as a background material. Further, the central hole has a diameter D_C and is infiltrated with alcohol mixture. The hole next to the core region from the right is replaced by a gold nanowire with diameter d. The core is infiltrated with alcohol mixture consisting of ethanol and chloroform [7]. Both ethanol and chloroform have temperature-dependent refractive indices that can be determined from the following relation [7]:

$$n_x = n_0 + \frac{dn}{dT}(T_x - T_0) \tag{1}$$

where n_0 is the refractive index at reference temperature T_0 which is equal to 1.36 and 1.44 for ethanol and chloroform at 20 °C, respectively, n_x is the refractive index

of ethanol or chloroform at temperature T_x. Additionally, to calculate the refractive index n of the resultant mixture, the mixing ratio must be considered as follows [7]:

$$\frac{n^2-1}{n^2+2} = \varnothing_1 \frac{n_1^2-1}{n_1^2+2} + \varnothing_2 \frac{n_2^2-1}{n_2^2+2} \tag{2}$$

where n_1 and n_2 are the refractive indices for ethanol and chloroform at a specific temperature, $\varnothing_1$ and $\varnothing_2$ are the volume fractions for ethanol and chloroform in the mixture. According to [7], it is convenient to use a volume ratio for ethanol to chloroform of 4:6. In this study, a temperature range from −4 to 53 °C is considered with four steps (−4, 15, 34, and 53). The corresponding alcohol mixture refractive indices according to the above equations are 1.39, 1.4, 1.41, and 1.42 for temperature values of 53 °C, 34 °C, 15 °C, and −4 °C, respectively. Additionally, the wavelength-dependent relative permittivity of the gold wire is given by [8]:

$$\varepsilon_{\mathrm{Au}}(\omega) = \varepsilon_\infty - \frac{\omega_\mathrm{p}^2}{\omega(\omega + \mathrm{i}\omega_\tau)} \tag{3}$$

where $\varepsilon_\infty, \omega_\mathrm{p}$ and ω_τ are equal to 9.75, 1.36 × 10^{16} rad/s and 1.45 × 10^{14} rad/s, respectively. Further, the Sellmeier equation of the silica glass n_s is taken as [9]:

$$\mathrm{n_s^2}(\lambda) = 1 + \frac{\mathrm{B_1}\lambda^2}{\lambda^2 - \mathrm{C_1}} + \frac{\mathrm{B_2}\lambda^2}{\lambda^2 - \mathrm{C_2}} + \frac{\mathrm{B_3}\lambda^2}{\lambda^2 - \mathrm{C_3}} \tag{4}$$

where λ is the wavelength in μm. Additionally, B_1, B_2, and B_3 are fixed to 0.6961663, 0.4079426, and 0.8974794 while C_1, C_2, and C_3 are equal to 0.00467914826 μm^2, 0.0135120631 μm^2, and 97.9340025 μm^2, respectively.

8.2.2 Numerical Results and Discussion

The analysis of the suggested sensor is carried out using the full-vectorial finite-element method (FVFEM) [10] on a circular computational domain of radius 6 μm with 63131 degrees of freedom and minimum element size of 0.0008 μm. Additionally, a perfect matched layer (PML) is used as a boundary condition to truncate the computational domain. Figure 8.2 shows the variation of the real part of the effective index of the quasi-TE core-guided mode and quasi-TE SP mode with the wavelength. In addition, the confinement loss of the core mode is also shown in Fig. 8.2 which is calculated using the following equation [9]:

$$\alpha(\mathrm{dB/m}) = 40\ \pi \mathrm{Im}(\mathrm{neff})/(\ln(10)\lambda) \tag{5}$$

In this study, the geometrical parameters are taken as $\Lambda = 2.4$ μm, $D_C = 2$ μm, T = 34 °C, and $d = 1000$ nm. It may be seen from Fig. 8.2 that at $\lambda = 1337$ nm, the

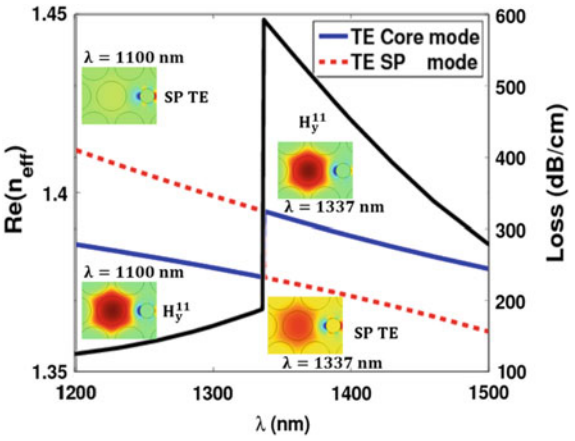

Fig. 8.2 Variation of the effective index and loss of the quasi-TE core mode H_y^{11} and the SP mode with the wavelength. Inset: field plots of the H_y^{11} of the quasi-TE core mode and SP mode at different wavelengths

effective indices of the quasi-TE core mode H_y^{11} and SP mode are equal. At the resonance wavelength, the matching condition is achieved with maximum loss for the core-guided mode as shown in Fig. 8.2. In addition, the field plots of the x-component of the quasi-TE core mode and the TE SP mode are shown in Fig. 8.2. It is evident from the inset of Fig. 8.2 that at $\lambda = 1100$ nm away from the resonance wavelength, the field of the quasi-TE core mode is well confined to the core region, while the field of the SP mode exists only around the surface of the gold rod. Additionally, at the resonance wavelength of 1337 nm, there is a similarity between the field plots of both the quasi-TE core mode and the TE SP mode where the matching takes place as shown in Fig. 8.2.

The efficiency of the proposed sensor can be studied by calculating its sensitivity to temperature change over the specified range (−4 °C:53 °C). The sensitivity of the proposed design can be calculated according to the wavelength interrogation method given by [9]:

$$S_\lambda(\lambda) = \frac{\partial \lambda_{peak}(T)}{\partial T} (\text{nm}/^\circ\text{C}) \tag{6}$$

where $S_\lambda(\lambda)$ is the sensitivity defined by the shift of λ_{peak} per unit temperature degree, where λ_{peak} is the wavelength corresponding to the resonance peak in the loss spectra. Additionally, the sensitivity of the reported sensor is calculated using the amplitude-based method given by [9]:

$$S_A = -\frac{\partial(\alpha(\lambda, T))/\partial T}{\alpha(\lambda, T)} \left(^\circ\text{C}^{-1}\right) \tag{7}$$

where α(λ, T) represents the propagation loss of the core-guided mode as a function of the wavelength at temperature T.

To achieve the maximum possible sensitivity for the proposed design, the geometrical parameters are studied including the hole pitch Λ, the core diameter D_C, and the gold rod diameter d. The analysis is carried out for the first structure where the resonance wavelength is calculated at different temperatures −4, 15, 34, and 53 °C while the cladding airholes diameter is fixed at 2 μm. First, the effect of the hole pitch is studied with three different values 2.3 μm, 2.4 μm, and 2.5 μm while the core radius and the gold rod diameter are fixed at 2 μm and 1000 nm, respectively. It may be seen from Fig. 8.3a, d that for Λ = 2.3 μm, the resonance occurs at 1370 nm, 1324 nm, 1277 nm, and 1230 nm for temperature values of 53 °C, 34 °C, 15 °C, and −4 °C, respectively. As a result, the corresponding wavelength sensitivities are equal to 2.42, 2.47, and 2.47 nm/°C. Further, amplitude sensitivities of 0.0113 $°C^{-1}$, 0.0214 $°C^{-1}$, and 0.0178 $°C^{-1}$ are achieved for temperature ranges (53 °C:34 °C), (34 °C:15 °C), and (15 °C:−4 °C), respectively, as shown in Table 8.1. It is also evident from Fig. 8.3b, e that when the hole pitch is increased to 2.4 μm, the corresponding wavelength sensitivities also increase to 2.63, 2.68, and 2.63 nm/°C for temperature ranges (53 °C:34 °C), (34 °C:15 °C), and (15 °C:−4 °C), respectively. However, the amplitude sensitivity increases only for temperature range (53 °C:34 °C), while it slightly decreases for (34 °C:15 °C) and remains constant for (15 °C:−4 °C) temperature range as shown in Table 8.1. Additionally, Table 8.1 and Fig. 8.3c, f show that if the hole pitch is further increased to 2.5 μm, the wavelength sensitivity increases while there is a slight decrease in the amplitude sensitivity.

Next, the impact of the core diameter is studied, while the values of the hole pitch and gold rod diameter are fixed at 2.5 μm and 1000 nm, respectively. Figure 8.4a, d shows that at core diameter of 1.8 μm, the achieved wavelength

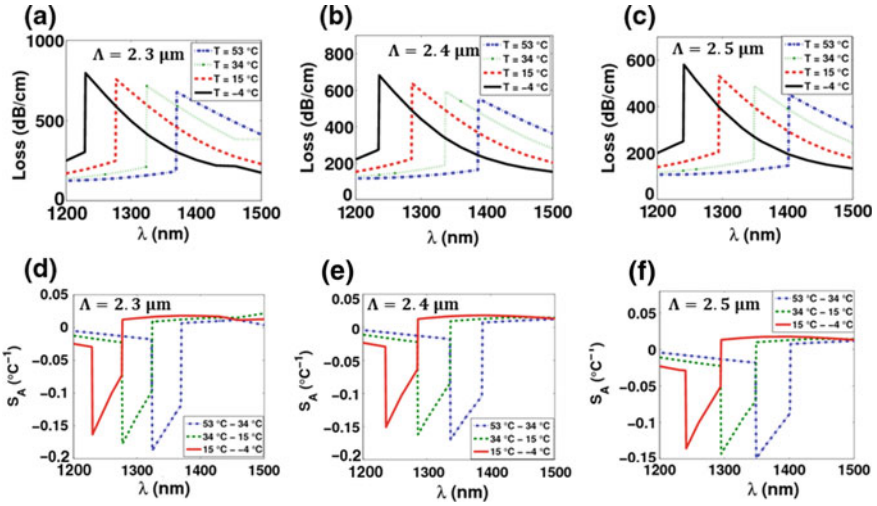

Fig. 8.3 Variation of the quasi-TE core mode losses and amplitude sensitivity with the wavelength at different temperatures, at **a**, **d** Λ = 2.3 μm, **b**, **e** Λ = 2.4 μm, and **c**, **f** Λ = 2.5 μm

Table 8.1 Summary of the resonance wavelength λ_0, wavelength sensitivity S_λ and amplitude sensitivity S_A at different structural geometrical parameters for the TE polarization

Parameter		λ_o (nm)				S_λ (nm/°C)			S_A (°C^{-1})		
		53 °C	34 °C	15 °C	−4 °C	53–34	34–15	15–4	53–34	34–15	15–4
Λ (μm)	2.3	1370	1324	1277	1230	2.42	2.47	2.47	0.0113	0.0214	0.0178
	2.4	1387	1337	1286	1236	2.63	2.68	2.63	0.0120	0.0148	0.0178
	2.5	1402	1349	1295	1241	2.78	2.84	2.84	0.0116	0.0145	0.0176
D_C (μm)	1.8	1381	1330	1280	1231	2.68	2.63	2.57	0.0112	0.0135	0.0164
	2	1402	1349	1295	1241	2.78	2.84	2.84	0.0116	0.0145	0.0176
	2.2	1414	1359	1303	1247	2.89	2.94	2.94	0.0109	0.0155	0.0188
d_{rod} (nm)	*900*	*1358*	*1302*	*1245*	*1188*	*2.94*	*3*	*3*	*0.0102*	*0.0156*	*0.0194*
	1000	1414	1359	1303	1247	2.89	2.94	2.94	0.0109	0.0155	0.0188
	1100	1462	1409	1354	1299	2.78	2.89	2.89	0.0122	0.0150	0.0179

sensitivities are 2.68, 2.63, and 2.57 nm/°C for temperature ranges of (53 °C:34 °C), (34 °C:15 °C), and (15 °C:−4 °C). Further, the corresponding amplitude sensitivities are equal to 0.0112 °C^{-1}, 0.0135 °C^{-1}, 0.0164 °C^{-1} for the same temperature ranges, respectively, as seen from Table 8.1. It is also evident from Fig. 8.4b, e, c and Table 8.1 that the wavelength and amplitude sensitivities are increased by increasing the core diameter to 2.2 μm. However, the amplitude sensitivity slightly decreases at core diameter of 2.2 μm for the temperature range (53 °C:34 °C) as may be seen from Fig. 8.4f and Table 8.1.

The effect of the gold rod diameter is next studied while the hole pitch and core diameter are fixed at 2.5 μm and 2.2 μm, respectively. It may be seen from Fig. 8.5a, d that at gold rod diameter of 900 nm, the resonance occurs at wavelength of

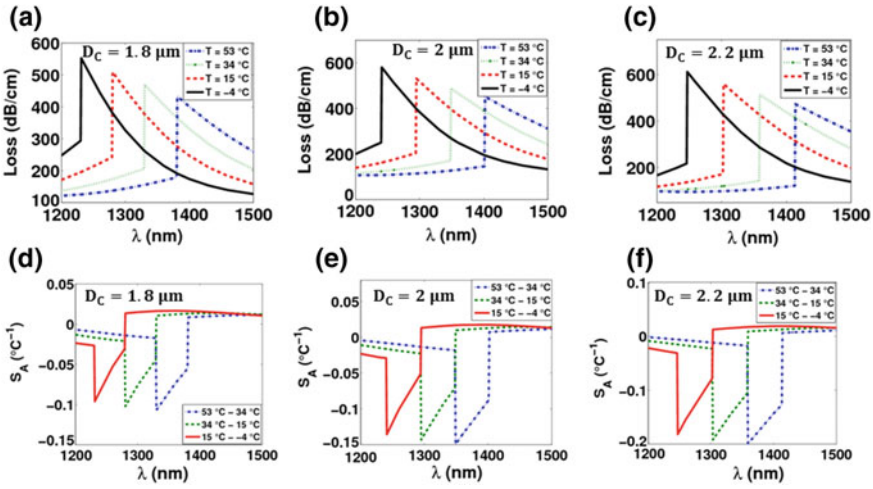

Fig. 8.4 Variation of the quasi-TE core mode losses and amplitude sensitivity with the wavelength at different temperatures, at **a**, **d** D_c = 1.8 μm, **b**, **e** D_c = 2 μm, and **c**, **f** D_c = 2.2 μm

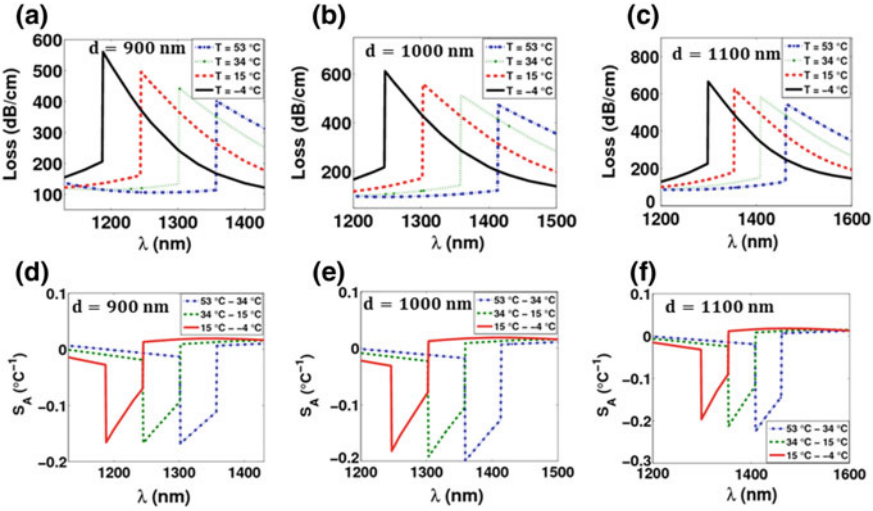

Fig. 8.5 Variation of the quasi-TE core mode losses and amplitude sensitivity with the wavelength at different temperatures, at **a**, **d** d = 900 nm, **b**, **e** d = 1000 nm, and **c**, **f** d = 1100 nm

1358 nm, 1302 nm, 1245 nm, and 1188 nm at temperature values of 53 °C, 34 °C, 15 °C, and −4°C, respectively. The resultant wavelength sensitivities are equal to 2.94 nm/°C, 3 nm/°C, and 3 nm/°C for temperature ranges of (53 °C:34 °C), (34 °C:15 °C), and (15 °C:−4 °C), respectively, as seen from Table 8.1. In addition, the corresponding amplitude sensitivities are equal to 0.0102, 0.0156, and 0.0194 $°C^{-1}$ for the same temperature ranges. When the gold rod diameter is changed to 1000 nm, both the wavelength sensitivities and amplitude sensitivities are decreased except for the amplitude sensitivity for temperature range (53 °C:34 °C) where it slightly increases, as shown in Fig. 8.5b, e and Table 8.1. Moreover, if the gold rod diameter is further increased to 1100 nm, the wavelength sensitivities and amplitude sensitivities are decreased over the whole temperature range except for temperature range of (53 °C:34 °C) where the amplitude sensitivity slightly increases as shown in Fig. 8.5f.

The performance of the suggested design is also tested for linear sensing capability. Figure 8.6 represents the variation of the resonance wavelength with the temperature variation. As may be seen from Fig. 8.6, the suggested sensor has an excellent linear fitting accuracy with linear fitting equation of the form:

$$\lambda_{res} = 2.9842 \times T + 1200.1 \ (nm) \tag{8}$$

In addition, the achieved R value is equal to 1. As a result, unknown temperatures within the specified range can be detected efficiently.

The analysis of the proposed sensor based on quasi-TM modes is also reported. Figure 8.7 shows the variation of the effective index of the quasi-TM core mode

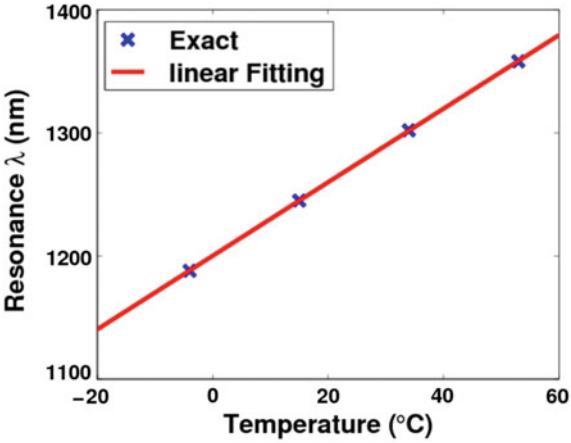

Fig. 8.6 Linear fitting for the variation of the resonance wavelength with the temperature

and the TM SP mode with the wavelength. The analysis is performed at T = 34 °C, $\Lambda = 2.4$ μm, $D_C = 2$ μm, and $d = 1000$ nm. In addition, the confinement loss of the quasi-TM core mode is shown in Fig. 8.7 to justify the coupling where a maximum loss occurs. Moreover, the inset of Fig. 8.7 shows the field plots of the main components for both the quasi-TM core mode H_x^{11} and the TM SP mode at different wavelengths. As shown in Fig. 8.7, the matching is attained at $\lambda = 1421$ nm between the quasi-TM core mode and the TM SP mode. Further, the field plots of the quasi-TM core mode and the TM SP mode are nearly the same at the coupling wavelength of 1421. However, away from the resonance wavelength, the field of the quasi-TM core mode is confined to the core region while the field of the TM SP mode exists only around the metal surface as shown in the inset of Fig. 8.7.

It is worth noting that the suggested sensor can be used efficiently using both TE and TM polarizations. The analysis shows that if the same optimized parameters for the TE polarization case is used for the TM case, the achieved sensitivities for the

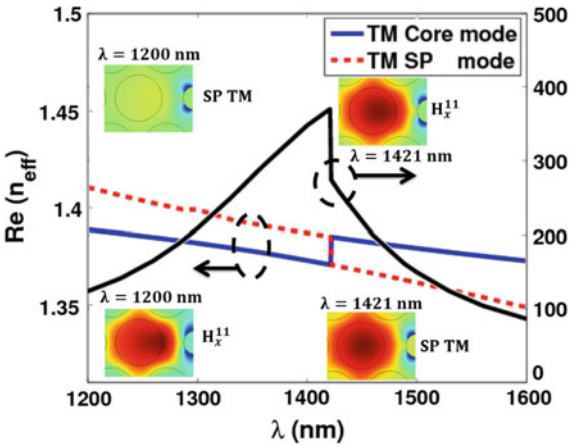

Fig. 8.7 Variation of the effective index and loss of the quasi-TM core mode and the SP TM modes with the wavelength

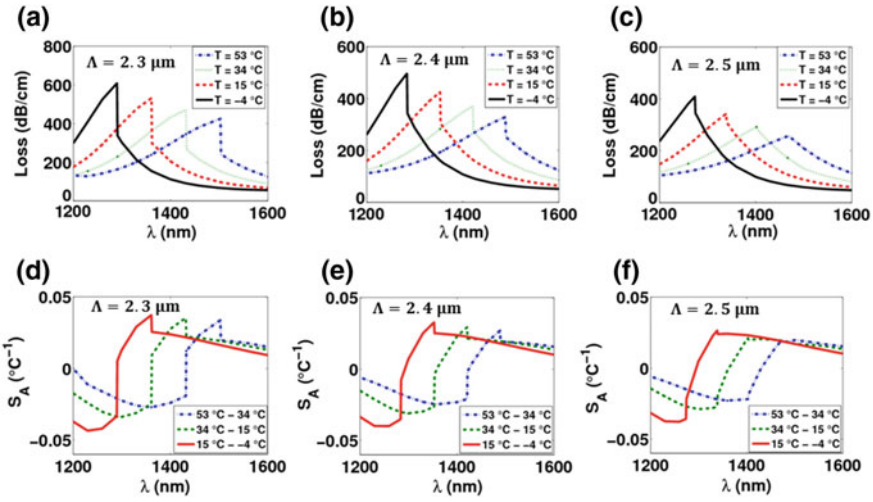

Fig. 8.8 Variation of the quasi-TM core mode losses and amplitude sensitivity with the wavelength at different temperatures, at **a**, **d** $\Lambda = 2.3$ μm, **b**, **e** $\Lambda = 2.4$ μm, and **c**, **f** $\Lambda = 2.5$ μm

TM case are equal to 3.73 nm/°C, 3.84 nm/°C, and 3.84 nm/°C for temperature ranges of (53 °C:34 °C), (34 °C:15 °C), and (15 °C:−4 °C), respectively. However, if a complete study is performed for the TM polarization such that only TM modes are considered, different results can be obtained.

First, the effect of the hole pitch is considered, while the other parameters are fixed at $D_C = 2$ μm and $d = 1000$ nm. Figure 8.8 represents the variation of the confinement loss of the quasi-TM core mode with the wavelength at different temperatures and for different hole pitch values. Additionally, the amplitude sensitivity is added for different values of the hole pitch. It is revealed from Fig. 8.8a, d that for $\Lambda = 2.3$ μm, the resonance peaks occur at $\lambda = 1504$ nm, 1432 nm, 1361 nm, and 1290 nm for temperature values of 53° C, 34 °C, 15 °C, and −4 °C, respectively. These resonance peaks result in wavelength sensitivities of 3.78 nm/°C, 3.73 nm/°C, and 3.73 nm/°C for temperature ranges of (53 °C:34 °C), (34 °C:15 °C), and (15 °C:−4 °C), respectively. Further, the corresponding amplitude sensitivities are 0.0336, 0.0353, and 0.0373°C^{-1} for the same temperature ranges. The numerical results of the current study are summarized in Table 8.2. When the hole pitch is increased to 2.5 μm, the distance between the alcohol core and the gold rod increases which decreases the interaction between TM core mode and SP mode and hence the wavelength sensitivity as shown in Fig. 8.8c, f and Table 8.2. Furthermore, increasing the distance between the core and the gold rod will decrease the power transfer between them as well as the amplitude sensitivity as shown in Table 8.2.

Next, an analysis of the alcohol core diameter is performed, while the other parameters are fixed at $\Lambda = 2.3$ μm and $d = 1000$ nm. It may be seen from Fig. 8.9a, d that at core diameter of 1.8 μm, the coupling between the quasi-TM core mode and

Table 8.2 Summary of the resonance wavelength λ_0, wavelength sensitivity S_λ, and amplitude sensitivity S_A at different structural geometrical parameters for the TM polarization

Parameter		λ_o (nm)				S_λ (nm/°C)			S_A (°C^{-1})		
		53 °C	34 °C	15 °C	−4 °C	53–34	34–15	15–4	53–34	34–15	15–4
Λ (μm)	2.3	1504	1432	1361	1290	3.78	3.73	3.73	0.0336	0.0353	0.0373
	2.4	1489	1421	1353	1284	3.57	3.57	3.63	0.0268	0.0292	0.0326
	2.5	1468	1403	1339	1274	3.42	3.36	3.42	0.0197	0.0211	0.0264
D_C (μm)	1.8	1410	1358	1306	1251	2.73	2.73	2.89	0.0202	0.0243	0.0292
	2	1504	1432	1361	1290	3.78	3.73	3.73	0.0336	0.0353	0.0373
	2.2	1590	1501	1410	1320	4.68	4.78	4.73	0.0404	0.0411	0.0417
d_{rod} (nm)	*900*	*1541*	*1451*	*1358*	*1266*	*4.73*	*4.89*	*4.84*	*0.0400*	*0.0407*	*0.0416*
	1000	1590	1501	1410	1320	4.68	4.78	4.73	0.0404	0.0411	0.0417
	1100	1631	1545	1456	1368	4.52	4.68	4.63	0.0405	0.0411	0.0416

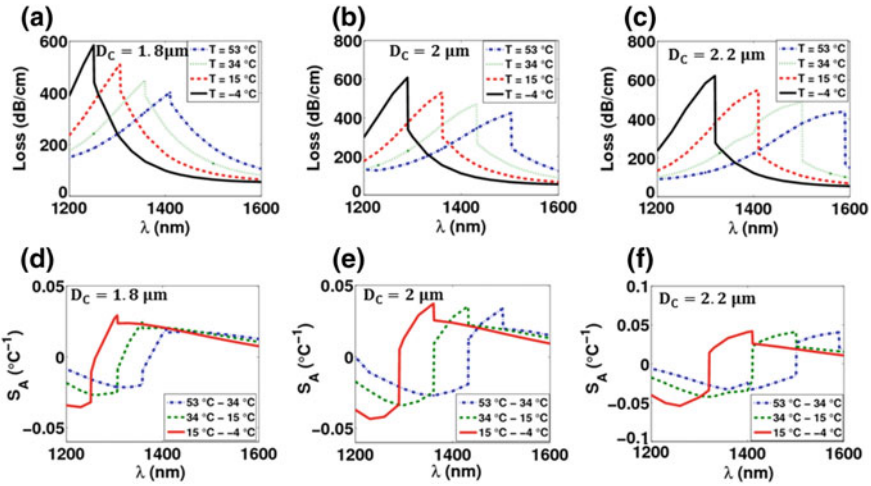

Fig. 8.9 Variation of the quasi-TM core mode losses and amplitude sensitivity with the wavelength at different temperatures, at **a**, **d** D_c = 1.8 μm, **b**, **e** D_c = 2 μm, and **c**, **f** D_c = 2.2 μm

the TM SP mode takes place at $\lambda = 1410$ nm, 1358 nm, 1306 nm, and 1251 nm at temperatures of 53 °C, 34 °C, 15 °C, and −4 °C, respectively As a result, for temperature ranges of (53 °C:34 °C), (34 °C:15 °C), and (15 °C:−4 °C), the achieved wavelength sensitivities are: 2.73 nm/°C, 2.73 nm/°C, and 2.89 nm/°C, while the amplitude sensitivity is equal to 0.0202 °C^{-1}, 0.0243 °C^{-1}, and 0.0292 °C^{-1}, respectively. If the core diameter is increased to 2.2 μm, the distance between the core region and the gold rod will be decreased. As a result, both the wavelength sensitivity and the amplitude sensitivity are increased as shown in Fig. 8.9 and

Table 8.2. Therefore, the alcohol core diameter of 2.2 μm will be taken in the subsequent simulations.

The effect of the gold rod diameter is next studied, while the other parameters are fixed at their optimum values of $\Lambda = 2.3$ μm and $D_C = 2.2$ μm. Figure 8.10 represents the change in the confinement loss and amplitude sensitivity of the quasi-TM core mode with the wavelength at different gold rod diameters 900, 1000, and 1100 nm for different temperatures. According to Fig. 8.10a, d, the resonance peaks result in wavelength sensitivities of 4.73 nm/°C, 4.89 nm/°C, and 4.84 nm/°C, for temperature ranges of (53 °C:34 °C), (34 °C:15 °C), and (15 °C: −4 °C), respectively. In addition, the corresponding amplitude sensitivities are 0.0400, 0.0407, and 0.0416 $°C^{-1}$ for the same temperature ranges. Figure 8.10b, e along with Table 8.2 shows that using a gold rod with diameter of 1000 nm results in a decrease in the wavelength sensitivities. However, as the gold rod diameter increases, the area of the metal surface increases. Therefore, more power transfer occurs between the core mode and the SP mode which results in a slight increase in the amplitude sensitivity. If the gold rod diameter is further increased to 1100 nm, the wavelength sensitivities are further decreased over all temperature ranges as shown in Fig. 8.10c, f. On the other hand, Table 8.2 shows that increasing the gold rod diameter to 1100 nm has nearly no effect on the amplitude sensitivities.

The performance linearity of the suggested sensor is tested based on the TM mode. Figure 8.11 shows the change in the resonance wavelength with the temperature variation. The fitting of the curve points proves that the behavior of the suggested sensor for the TM polarization is excellently linear. Further, R coefficient for the fitting curve is equal to 0.999988 with linear fitting equation as follows:

$$\lambda_{res} = 4.8316 \times T + 1285.6 \tag{9}$$

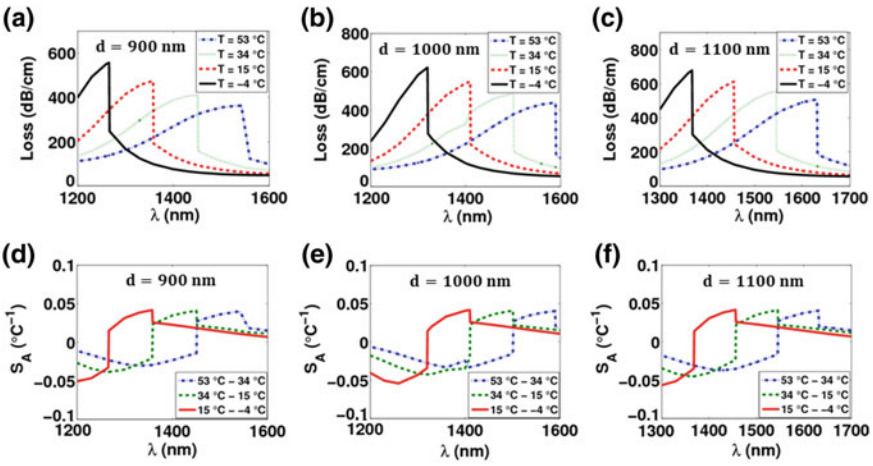

Fig. 8.10 Variation of the quasi-TM core mode losses and amplitude sensitivity with the wavelength at different temperatures, at **a**, **d** d = 900 nm, **b**, **e** d = 1000 nm and **c**, **f** d = 1100 nm

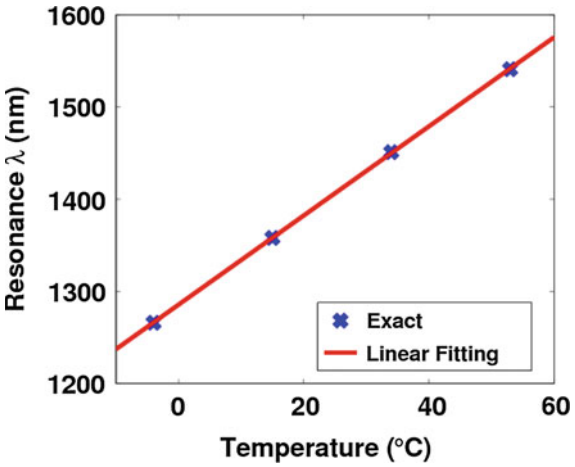

Fig. 8.11 Linear fitting for the variation of the resonance wavelength with the temperature

Based on the previous study, the optimum case is achieved for the TE polarization at hole pitch, core diameter, and gold rod diameter values of 2.5 μm, 2.2 μm, and 900 nm, respectively. The achieved wavelength sensitivities are 2.94 nm/°C, 3 nm/°C, and 3 nm/°C with amplitude sensitivities of $0.0102°C^{-1}$, $0.0156°C^{-1}$, and $0.0194°C^{-1}$ for temperature ranges of (53 °C:34 °C), (34 °C:15 °C), and (15 °C:−4 °C), respectively. For the TM polarization at the same design parameters of ($\Lambda = 2.5$ μm, $D_C = 2.2$ μm, and $d = 900$ nm), the reported wavelength sensitivities are 3.73, 3.84, and 3.84 nm/°C. If the design parameters are optimized for the TM case, the achieved wavelength sensitivities are 4.73, 4.89, and 4.84 nm/°C. The reported sensitivities are comparable to those in the literature [2–7] for the TE case, while the values for the TM case surpass slightly those in the literature. Moreover, the analysis shows that if the same optimized parameters for the TM polarization case is used for the TE case, the achieved sensitivity for the TE case is equal to 2.31 nm/°C, 2.31 nm/°C, and 2.36 nm/°C for temperature ranges of (53 °C:34 °C), (34 °C:15 °C), and (15 °C:−4 °C), respectively. In order to further increase the sensor sensitivity, a second design based on LC-filled core is suggested and analyzed in the next section.

8.3 NLC SPR PCF Temperature Sensor

8.3.1 Design Considerations

Figure 8.12 represents a cross section of the suggested LC PCF SPR temperature sensor with different numbers of metal rods. The reported structure is based on two rings of airholes characterized with diameter d and arranged in a triangular lattice with a hole pitch Λ. The FK51A [8] is used as a background material. The hole in

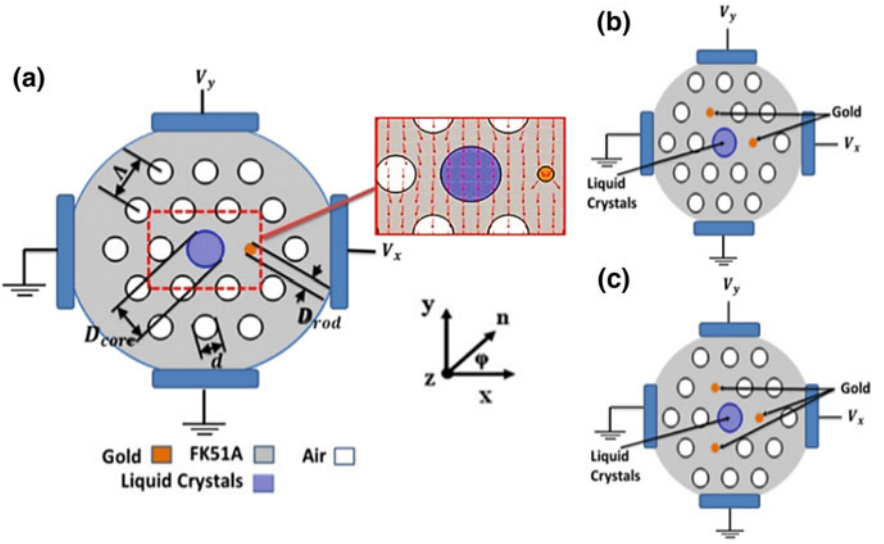

Fig. 8.12 Cross section of the NLC SPR PCF temperature sensor with **a** One, **b** Two, and **c** Three metallic nanorods. Inset: Electric potential and electric field distribution through the structure at $V_y = 250$ V [13]

the center has a diameter D_{core} and is infiltrated with type E7 NLC [8]. The hole next to the core region from the right is replaced by a gold rod with diameter D_{rod}. Further, two sets of electrodes are used to control the state of the LC molecules.

The NLC is an anisotropic material, with direction-dependent properties. The dielectric permittivity of the LC has the diagonal form of $[n_e^2\ n_o^2\ n_o^2]$ with rotation angle $\varphi = 0°$ when $V_x = V_0$, and $V_y = 0$ where φ stands for the rotation angle of the director of the LC molecules, and n_o and n_e are the ordinary and extraordinary refractive indices of the NLC material, respectively. However, the NLC molecules will be oriented along y-axis when $V_x = 0$, and $V_y = V_0$ with $\varphi = 90^o$ and $\varepsilon_r = [n_o^2\ n_e^2\ n_o^2]$. The wavelength-dependent values of n_e and n_o [11] are given by

$$n_{e,o} = A_{e,o} + \frac{B_{e,o}}{\lambda^2} + \frac{C_{e,o}}{\lambda^4} \tag{10}$$

where λ is the wavelength and A_e, B_e, C_e, A_o, B_o, and C_o are temperature-dependent coefficients of the Cauchy model which can be found at different temperatures in [11, 12].

The Sellmeier equation of the FK51A material is obtained from [8]:

$$n^2(\lambda) = 1 + \frac{A_1\lambda^2}{\lambda^2 - B_1} + \frac{A_2\lambda^2}{\lambda^2 - B_2} + \frac{A_3\lambda^2}{\lambda^2 - B_3} \tag{11}$$

where n(λ) is the wavelength-dependent refractive index of the FK51A, $A_1 = 0.971247817$, $A_2 = 0.2169014$, $A_3 = 0.9046517$, $B_1 = 0.00472302\ \mu m^2$, $B_2 = 0.01535756\ \mu m^2$, and $B_3 = 168.68133\ \mu m^2$.

Additionally, the wavelength-dependent relative permittivity of the gold wire is also taken from Eq. (3). Further, both the FK51A ($\sim 10^{-6}$/K) [14] and the gold have thermo-optical coefficients which are much smaller than that of the NLC which justifies neglecting them in the analysis. However, thermo-optical coefficients of other types of glasses with positive thermal expansion coefficient and relatively large thermo-optical constant such as F2 glass [15] should be considered.

8.3.2 Numerical Results and Discussion

In order to ensure that the electric field and the vertical electric potential (V_y) have uniform distribution inside the NLC core region, an important analysis is made where Gauss law is solved along with the electric potential–electric field relation given by [16]:

$$\nabla \cdot D = \rho, E = -\nabla V \tag{12}$$

where D represents the displacement field, E is the electric field, V is the electric potential, and ρ is the charge density which vanishes for a dielectric material. The FVFEM [10] is used to solve the two equations over a square-shaped (side = 6 × Λ) computational domain as shown in Fig. 8.12. The vertical electrodes' voltage is taken as $V_y = 250$ V which is greater than Fréedericksz threshold [17]. The degree of freedom is equal to 175249 with minimum element size of 0.00045 μm and Dirichlet boundary conditions for the electric potential. It may be seen from the inset figure that the electric field and the electric potential are uniform in the region inside the NLC core while they have a slight change near the gold rod. Therefore, the metallic rod will not affect the uniformity of the electric field through the NLC core.

The analysis of the suggested sensor is carried out using the FVFEM [10] on the same computational domain with 175294 degrees of freedom and minimum element size of 0.0008 μm. Additionally, a perfect matched layer (PML) is used as a boundary condition. Figure 8.13 shows the variation of the effective indices with the wavelength for quasi-TE (X-polarized) and quasi-TM (Y-polarized) core modes and surface plasmon (SP) modes. Additionally, the loss spectrum of the two polarized core modes is shown in Fig. 8.13. In this study, Λ, D_{core}, D_{rod}, and T are initially equal to 3.75 μm, 3.4 μm, 800 nm, and 20 °C, respectively. It is evident from Fig. 8.13a that matching occurs between the SP mode (SP_x^1) and quasi-TE core mode (H_y^{11}) at wavelength of 1493 μm. Therefore, the loss spectrum of the quasi-TE core mode has a peak at the resonance wavelength. However, no coupling occurs between the quasi-TM mode and SP modes as shown in Fig. 8.13b. At $\varphi = 90°$, $\varepsilon_r = [n_o^2\ n_e^2\ n_o^2]$; therefore, the quasi-TE core mode is affected by n_o while

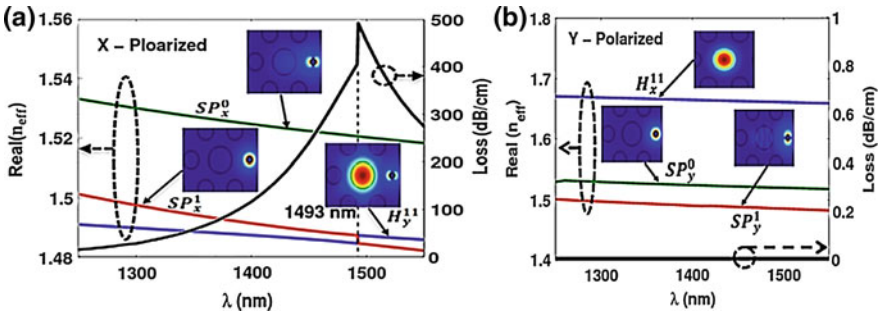

Fig. 8.13 Variation of the effective index and loss of the **a** quasi-TE and **b** quasi-TM core modes and the SP modes with the wavelength [13]

the quasi-TM core mode relies on n_e. As a result, the effective indices for the quasi-TM core modes will be greater than those for the SP modes which prevent the coupling occurrence. Therefore, the coupling between the quasi-TE mode and the SP modes and its effect on the performance of the proposed sensor will be studied thoroughly in the following simulations.

To justify our choice of using FK51A glass rather than silica as a background material, an analysis is also made for the loss spectrum using silica as a background material. In this study, the silica glass has a wavelength which is dependent on refractive index n_s given by Eq. (4).

Figure 8.14 shows the loss variation of the quasi-TE mode when silica or FK51A is used as a background material. It is revealed from this figure that there is no resonance when the silica is used as a background material. However, a resonance occurs in the case of FK51A at a wavelength of 1493 nm. It is worth nothing

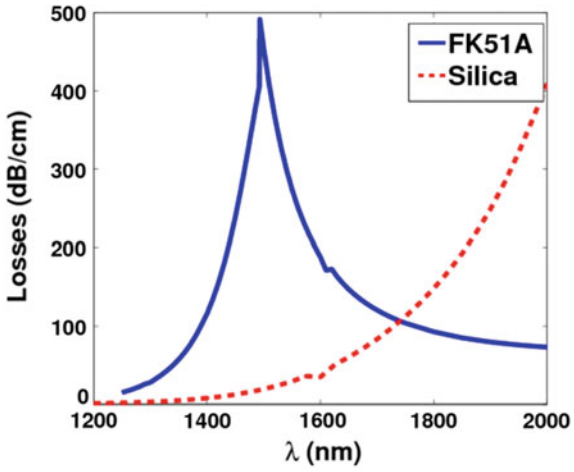

Fig. 8.14 Spectra curve for loss of the quasi-TE core mode using two different background materials, silica and FK51A [13]

that it is possible to fabricate optical fibers using FK51A through stack and draw mechanism as reported in [18]. Therefore, FK51A is chosen as a background material for the suggested sensor.

The temperature-sensing mechanism depends mainly on the temperature-dependent LC molecules. The sensitivity of the proposed design can be calculated according to the wavelength and the amplitude interrogation methods given by Eqs. (6) and (7), respectively. In order to obtain highly sensitive temperature sensor, the structural geometrical parameters have been studied. The effect of the number of gold rods is first investigated. The analysis is carried out by calculating the losses versus wavelength for different temperatures 30, 40, and 50 °C where the other parameters are fixed at $D_{core} = 3$ μm, $D_{rod} = 800$ nm, and $\Lambda = 3.75$ μm. Figure 8.15 shows the variation of the confinement loss of the quasi-TE core mode with the wavelength variation at different temperatures and for different number of gold rods. It is revealed from Fig. 8.15a that the use of one rod only results in resonance wavelengths of 1593 nm, 1499 nm, and 1415 nm according to temperatures of 30, 40, and 50 °C, respectively. Therefore, a shift ($\Delta\lambda$) of 94 nm and 84 nm is achieved when the temperature is changed from 30 °C to 40 °C and from 40 °C to 50 °C, respectively. As a result, sensitivity of 9.4 nm/°C and 8.4 nm/°C is obtained at the corresponding temperature ranges. The reported sensitivity is much higher than 2.7 nm/°C, 3.86 nm/°C, and 4 nm/°C reported in [5–7] respectively. However, sensitivity of 9.1 nm/°C and 8.4 nm/°C is offered by using two rods as shown in Fig. 8.15b according to the resonance wavelengths of 1580 nm, 1489 nm, and 1405 nm at T = 30 °C, 40 °C, and 50 °C, respectively. On the other hand, sensitivity of 8.9 nm/°C and 8.3 nm/°C is obtained over the same temperature

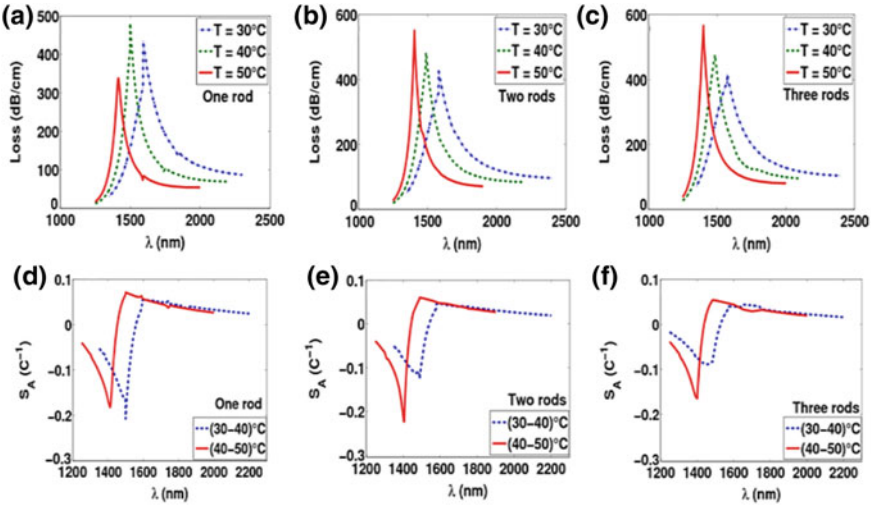

Fig. 8.15 Variation of the quasi-TE core mode losses in (dB/cm) with the wavelength at different temperatures, with **a** One, **b** Two, and **c** Three gold rods. Variation of the corresponding amplitude sensitivities with the wavelength is shown in Fig. 8.15**d**, **e**, and **f**, respectively [13]

Table 8.3 Summary of the resonance wavelength λ_0, wavelength sensitivity S_λ, and amplitude sensitivity S_A at different structural geometrical parameters. [13]

Parameter		λ_o (nm)			S_λ (nm/°C)		S_A ($°C^{-1}$)	
		30 °C	40 °C	50 °C	30–40	40–50	30–40	40–50
No. of rods	1	1593	1499	1415	9.4	8.4	0.207	0.182
	2	1580	1489	1405	9.1	8.4	0.126	0.223
	3	1573	1484	1401	8.9	8.3	0.089	0.164
D_{core} (μm)	3	1593	1499	1415	9.4	8.4	0.207	0.182
	3.4	1510	1425	1353	8.5	7.2	0.278	0.129
	4	1434	1361	1296	7.3	6.5	0.213	0.137
D_{rod} (nm)	600	1423	1354	1292	6.9	6.2	0.132	0.093
	800	1593	1499	1415	9.4	8.4	0.207	0.182
	1000	1712	1612	1512	10.0	10.0	0.20	0.20

ranges, (from 30 °C to 40 °C) and (from 40 °C to 50 °C), respectively, due to three rods as realized from Fig. 8.15c. It may be also seen from Fig. 8.15 that the loss of the quasi-TE core mode with only one rod is smaller than those obtained by using two and three rods.

The same analysis for the geometrical parameters is carried out using the amplitude interrogation method. It is evident from Fig. 8.15d that the maximal amplitude sensitivity has values of 0.207 $°C^{-1}$ and 0.182 $°C^{-1}$ when one gold rod is used for temperature ranges (from 30 °C to 40 °C) and (from 40 °C to 50 °C), respectively. However, if two gold rods are used, the maximal amplitude sensitivity drops to 0.126 $°C^{-1}$ for temperature range (from 30 °C to 40 °C), while it increases to 0.223 $°C^{-1}$ for temperature range (from 40 °C to 50 °C) as shown in Fig. 8.15e. Further, Fig. 8.15f reveals that if three gold rods are used, the maximal amplitude sensitivity will be decreased to 0.0891 $°C^{-1}$ and 0.164 $°C^{-1}$ according to temperature ranges (from 30 °C to 40 °C) and (from 40 °C to 50 °C), respectively. Table 8.3 summarizes the resonance wavelength, wavelength interrogation sensitivity, and maximal amplitude sensitivity at different structural geometrical parameters.

Next, the effect of the NLC core diameter on the sensor performance is studied. Figure 8.16 shows the loss and amplitude sensitivity variation with the wavelength at three different temperatures 30, 40, and 50 °C. In this investigation, one gold rod of diameter 800 nm is used for different core diameters. The resonance wavelengths and the corresponding sensor sensitivities are also reported in Table 8.3. It is found that at $D_{core} = 3$ μm, sensor sensitivities of 9.4 nm/°C and 8.4 nm/°C are reported for temperature ranges (from 30 °C to 40 °C) and (from 40 °C to 50 °C), respectively. Additionally, maximal amplitude sensitivity of 0.207 and 0.182 $°C^{-1}$ is obtained for the same temperature ranges as shown in Fig. 8.16d. When the core diameter is further increased to 3.4 and 4 μm, the sensor sensitivity will be decreased as reported in Table 8.3.

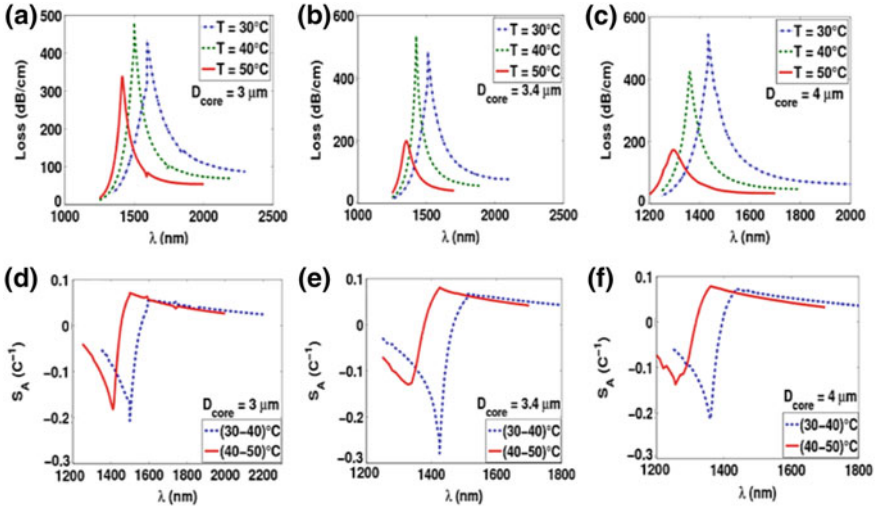

Fig. 8.16 Variation of the quasi-TE core mode losses and amplitude sensitivity with the wavelength at different temperatures, at **a**, **d** $D_{core} = 3$ μm, **b**, **e** $D_{core} = 3.4$ μm, and **c**, **f** $D_{core} = 4$ μm [13]

The effect of the gold rod diameter at $D_{core} = 3$ μm is also investigated and reported in Fig. 8.17 and Table 8.3. The numerical results show that at $D_{rod} = 1000$ nm, an ultra-high sensitivity of 10.0 nm/°C is achieved for detection range 30–50 °C that guarantees linear sensor operation. Further, maximal amplitude sensitivity of approximately 0.2 $°C^{-1}$ is obtained for the same temperature range as realized from Fig. 8.17f. To achieve an optimum design for the sensor which has <1.0 dB total leakage losses for the quasi-TE mode, a compact length of 20 μm can fulfill this requirement. Furthermore, the LC core biosensor has a high linearity for measurement over the specified temperature range (30 °C:50 °C) as shown in Fig. 8.18.

Table 8.4 shows a comparison between the achieved results and other related recent researches reported in the literature in terms of the resonance wavelength and wavelength sensitivity. Table 8.4 clarifies that the obtained sensitivities in this work are higher than those reported in the literature.

Finally, a tolerance study for the different structure geometrical parameters of the NLC-based sensor has been investigated. It is found that the NLC core radius, metal rod diameter, hole pitch, and cladding hole radius have a tolerance of ±5% at which the sensor sensitivity is still greater than 9.0 nm/°C. Therefore, the suggested design has less sensitivity to geometrical parameters variations through the fabrication process.

The fabrication of the proposed PCF SPR sensor can be accomplished by the use of popular stack and draw technique [19] since the structure depends on the widely used triangular lattice PCF. Through careful process control, the airholes can be arranged with high accuracy, and hence, the gaps between the hollow channels that

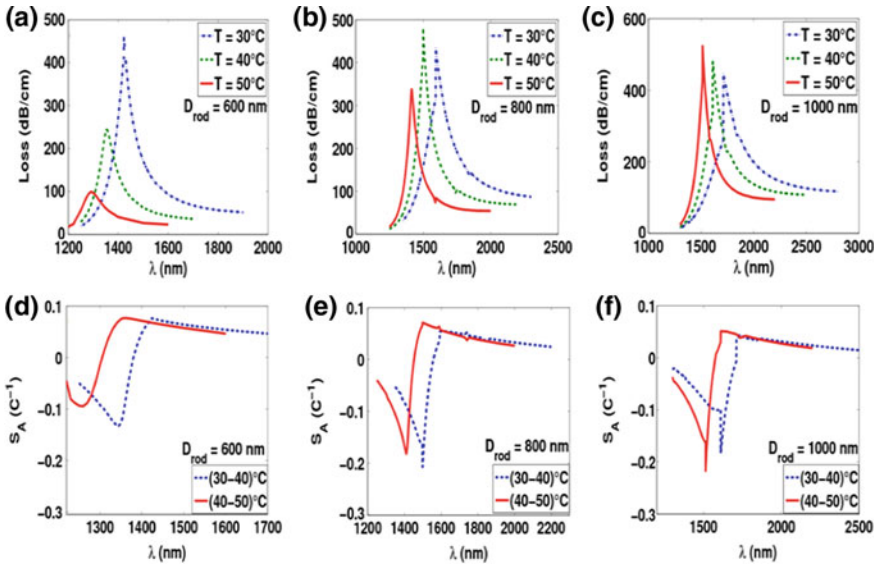

Fig. 8.17 Variation of the quasi-TE core mode losses and amplitude sensitivity at different temperatures versus the wavelength, at **a**, **d** $D_{rod} = 600$ nm, **b**, **e** $D_{rod} = 800$ nm, and **c**, **f** $D_{rod} = 1000$ nm [13]

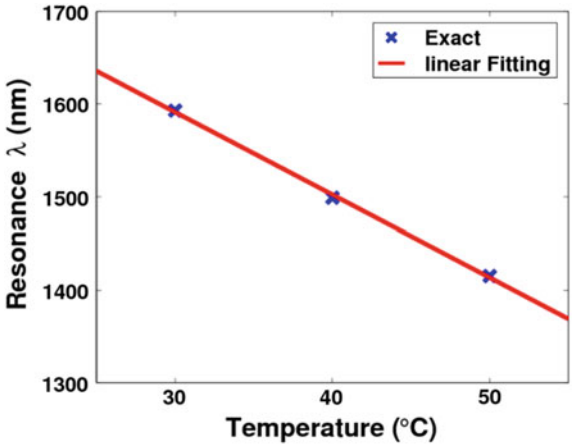

Fig. 8.18 Linear fitting for the variation of the resonance wavelength with the temperature [13]

will be filled by the gold can be controlled efficiently. The pressure-filling technique can be used for selectively filling the PCF with the gold rods [20]. In this regard, the Ti:Sa-laser assisted polymer gluing can be used to selectively open or inflate the airholes with diameter down to 500 nm. Then, high pressure is required to fill the hollow channels in a PCF with the required metal at its melting point.

Table 8.4 Comparison between the resonance wavelength and wavelength sensitivity of the suggested designs and others in the literature

Research		λ_o (nm)				S_λ (nm/°C)		
Current work	LC core	–	30 °C	40 °C	50 °C	–	30–40 °C	40–50 °C
		–	1712	1612	1512	–	10.0	10.0
	Alcohol core	−4 °C	15 °C	34 °C	53 °C	−4–15 °C	15–34 °C	34–53 °C
		1188	1245	1302	1358	3	3	2.94
Ref. [5]		10 °C	20 °C	30 °C	40 °C	10–20 °C	20–30 °C	30–40°C
		612	593	580	530	1.9	1.3	5.0
Ref. [6]		27.3 °C	37.4 °C	43.9 °C	53.5 °C	27.3–37.4 °C	37.4–43.9 °C	43.9–53.5 °C
		1576	1562	1585	1553	1.386	3.538	3.333
Ref. [7]		−4 °C	15 °C	34 °C	53 °C	−4–15 °C	15–34 °C	34–53 °C
		1004	928	871	828	4	3	2.263

Moreover, Huang et al. [21] reported that the central hole can be infiltrated by either the NLC or alcohol mixture such that the filling of the large central hole occurs sooner than the smaller background holes. Then, the PCF required length can be cleaved with filled central hole. Additionally, the light can be coupled to the proposed design such that the PCF is spliced to a standard single-mode fiber (SMF) followed by using a laser source to launch the light directly to the SMF [22]. Leon-Saval et al. [22] have ensured experimentally the efficiency of this technique which makes an interface between the SMF and PCF with low losses.

8.4 Summary

Novel designs of highly sensitive SPR temperature sensors based on NLC-PCF and alcohol-PCF are proposed and analyzed. The suggested designs are based on NLC and alcohol mixture as temperature-dependent materials. The reported LC core sensor has high sensitivity of 10 nm/°C for a temperature range from 30 to 50 °C. However, the temperature range is limited by the nematic range of the E7 material between its melting point and ~60 °C. To the best of our knowledge, it is the highest sensitivity reported in the literature. The temperature range of the suggested sensor can be broadened by employing alcohol mixture as an alternative material. The alcohol mixture achieves sensitivities of 3 nm/°C and 4.9 nm/°C corresponding to TE polarization and TM polarization, respectively, over wider temperature range from −4 to 53 °C.

References

1. F.F.K. Hussain, A.M. Heikal, M.F.O. Hameed, J. El-Azab, W.S. Abdelaziz, S.S.A. Obayya, Dispersion characteristics of asymmetric channel plasmon polariton waveguides. IEEE J. Quant. Electron. **50**(6), 474–482 (2014)
2. S.S.A. Obayya, M.F.O. Hameed, N.F.F. Areed, *Liquid Crystal Photonic Crystal Fiber Sensors* (Wiley, Computational Liquid Crystal Photonics, 2016)
3. Y. Peng, J. Hou, Z. Huang, Q. Lu, Temperature sensor based on surface plasmon resonance within selectively coated photonic crystal fiber. Appl. Opt. **51**(26), 6361–6367 (2012)
4. S.-J. Qiu, Y. Chen, F. Xu, Y.-Q. Lu, Temperature sensor based on an isopropanol-sealed photonic crystal fiber in-line interferometer with enhanced refractive index sensitivity. Opt. Lett. **37**(5), 863–865 (2012)
5. Y. Lu, M.T. Wang, C.J. Hao, Z.Q. Zhao, J.Q. Yao, Temperature sensing using photonic crystal fiber filled with silver nanowires and liquid. IEEE Photon. J. **6**(3), 6801307 (2014)
6. D.J.J. Hu et al., A compact and temperature-sensitive directional coupler based on photonic crystal fiber filled with liquid crystal 6CHBT. IEEE Photon. J. **4**(5), 2010–2016 (2012)
7. N. Luan, R. Wang, W. Lv, Y. Lu, J. Yao, Surface plasmon resonance temperature sensor based on photonic crystal fibers randomly filled with silver nanowires. Sensors **14**(9), 16035–16045 (2014)
8. M.F.O. Hameed, A.M. Heikal, B.M. Younis, M. Abdelrazzak, S.S.A. Obayya, Ultra-high tunable liquid crystal-plasmonic photonic crystal fiber polarization filter. Opt. Exp. **23**(6), 7007–7020 (2015)
9. E.K. Akowuah, T. Gorman, H. Ademgil, S. Haxha, G.K. Robinson, J.V. Oliver, Numerical analysis of a photonic crystal fiber for biosensing applications. IEEE J. Quant. Electron. **48** (11), 1403–1410 (2012)
10. S.S.A. Obayya, B.M.A. Rahman, K.T.V. Grattan, Accurate finite element modal solution of photonic crystal fibres. IEE Proc. Optoelectron. **152**(5), 241–246 (2005)
11. M.F.O. Hameed, S.S.A. Obayya, Ultrashort silica liquid crystal photonic crystal fiber polarization rotator. Opt. Lett. **39**(4), 1077–1080 (2014)
12. M.F.O. Hameed, S.S.A. Obayya, K. Al Begain, A.M. Nasr, M.I. Abo El Maaty, Coupling characteristics of a soft glass nematic liquid crystal photonic crystal fibre coupler. IET Optoelectron. **3**(6), 264–273 (2009)
13. M.F.O. Hameed, M.Y. Azab, A.M. Heikal, S.M. ElHefnawy, S.S.A. Obayya, Highly sensitive plasmonic photonic crystal temperature sensor filled with liquid crystal. IEEE PTL **28**, 59–62 (2015)
14. *TIE-19: Temperature Coefficient of Refractive Index*, SCHOTT Technical Information, SCHOTT North America, Inc., (New York, NY, USA, 2012) pp. 1–12
15. M.F.O. Hameed, S.S.A. Obayya, K. Al-Begain, M.I. Abo el Maaty, A.M. Nasr, Modal properties of an index guiding nematic liquid crystal based photonic crystal fiber. J. Lightwave Technol. **27**(21), 4754–4762 (2009)
16. M.Y. Azab, M.F.O. Hameed, S.M. El-Hefnawy, S.S.A. Obayya, Ultra-compact liquid crystal dual core photonic crystal fibre multiplexer–demultiplexer. IET Optoelectron. **10**(1), 1–7 (2015)
17. Y. Jeong, B. Yang, B. Lee, H.S. Seo, S. Choi, K. Oh, Electrically controllable long-period liquid crystal fiber gratings. IEEE Photon. Technol. Lett. **12**(5), 519–521 (2000)
18. C.A.G. Kalnins, H. Ebendorff-Heidepriem, N.A. Spooner, T.M. Monro, Radiation dosimetry using optically stimulated luminescence in fluoride phosphate optical fibres. Opt. Mater. Exp. **2**(1), 62–70 (2012)
19. P. Russell, Photonic crystal fibers. Science **299**(5605), 358–362 (2003)

20. H.W. Lee, Plasmonic photonic crystal fiber, in Max Plank Institute of Science and Light, Ph. D. dissertation, (Erlangen, Germany, 2012)
21. Y. Huang, Y. Xu, A. Yariv, Fabrication of functional microstructured optical fibers through a selective-filling technique. Appl. Phys. Lett. **85**(22), 5182–5184 (2004)
22. S.G. Leon-Saval et al., Splice-free interfacing of photonic crystal fibers. Opt. Lett. **30**(13), 1629–1631 (2005)

Chapter 9
Microstructured Optical Fiber-Based Plasmonic Sensors

Ahmmed A. Rifat, Md. Rabiul Hasan, Rajib Ahmed and Andrey E. Miroshnichenko

Abstract Surface plasmon resonance (SPR) is a considerably growing optical sensing approach which has been employed in wide range of applications including medical diagnostics, biological and chemical analyte detection, environmental monitoring, and food safety to security. SPR sensing technique shows high sensitive nature due to small change of sample refractive index, compared to other optical sensing techniques. Recently, microstructured optical fiber-based plasmonic sensors have shown great development due to its compact structure and light controlling capabilities in unprecedented ways. The goal of this chapter is to (1) describe the principle operation of plasmonic sensors, (2) discuss the optical properties of plasmonic materials, (3) compare and contrast the different types of microstructured optical fiber-based plasmonic sensors, and (4) highlight the main challenges of microstructured plasmonic sensors and possible solutions.

Keywords Surface plasmon resonance · Microstructured optical fiber Optical fiber sensors · Optical sensing and sensors

A. A. Rifat (✉) · A. E. Miroshnichenko
Nonlinear Physics Centre, Research School of Physics & Engineering, Australian National University, Acton, ACT 2601, Australia
e-mail: RifatAhmmed.Aoni@anu.edu.au

Md. Rabiul Hasan
Department of Electronics & Telecommunication Engineering, Rajshahi University of Engineering & Technology, Rajshahi 6204, Bangladesh

R. Ahmed
Nanotechnology Laboratory, School of Engineering, University of Birmingham, Birmingham B15 2TT, UK

A. E. Miroshnichenko
School of Engineering and Information Technology, University of New South Wales, Canberra, ACT 2600, Australia

© Springer International Publishing AG, part of Springer Nature 2019

M. F. O. Hameed and S. Obayya (eds.), *Computational Photonic Sensors*, https://doi.org/10.1007/978-3-319-76556-3_9

9.1 Introduction

Over the last three decades, surface plasmon resonance (SPR) has been considered as the key technology for numerous sensing applications. SPR sensors are powerful and effective tool that have been widely used in biosensing [1, 2], bioimaging [3], chemical detection [4–7], water testing [8], aqueous sample detection [9, 10], food safely [11, 12], environmental monitoring [13], biological analyte detection [4, 14], and gas detections [15, 16] (Fig. 9.1). Due to ongoing advancement of SPR technology, it has been also employed in optoelectronic devices such as optical tunable filters [17, 18], optical modulators [19, 20], film thickness monitoring [21, 22], and SPR imaging [23, 24]. Additionally, SPR technology enables integration of nanoelectronic and nanophotonic components with the aim to obtain ultra-compact optoelectronic devices [25, 26]. In 1907, the origin of SPR was first theoretically formulated by Zenneck [27], where it was demonstrated that surface electromagnetic

Fig. 9.1 Applications of surface plasmon resonance sensors

waves can be observed at the boundary of two mediums when one medium is lossless and another medium is either lossy dielectric or metal. In 1909, Sommerfeld first observed that surface waves are fast and attenuate exponentially with height above the interface [28]. The actual progress of SPR was carried out by Ritchie. In 1957, physical existence of the surface waves at the metal–dielectric interface was demonstrated [29].

Conventional prism-coupling-based SPR sensors are classified into two categories: Kretschmann [30] and Otto configurations [31]. The operating principle of both these sensors is attenuated total reflection (ATR). Although Kretschmann-based configuration SPR sensors are widely employed due to their excellent sensing performances, they suffer from several limitations. In general, these SPR sensors are bulky and made with moving optical and mechanical parts. As a result, they are not portable and cannot be used for remote sensing applications [6]. Moreover, practical implementation of spectral-based measurement is costly and scope for scaling down the sensor size is limited. To effectively overcome such potential difficulties, optical fiber-based SPRs are introduced [32–35]. Optical fibers are simple and have lightweight. Moreover, due to flexible design of the optical fiber it is possible to reduce the sensor size to a great extent, which can be potentially used for remote sensing applications [35]. Optical fiber-based SPR sensors provide higher dynamic range for detection and high resolution; however, they are applicable only for narrow acceptance angles [36]. Several optical fiber SPR sensors have been reported by both theoretical and experimental investigations [32–35].

Recently, photonic crystal fiber (PCF)-based SPR sensors have been extensively studied due to their unusual and appealing optical characteristics over the conventional optical fiber [37–56]. The optical properties of the PCF (such as confinement loss, single-mode propagation, birefringence, etc.) can be easily tailored, which eventually enable to control the performance of the sensor [57–60]. By changing the structural parameters such as pitch, air hole dimension, and number of air hole rings, it is possible to operate the sensor at the optimum condition [42, 50]. Current fabrication technologies are well-developed that permit practical realization of the PCF sensors. However, experimental characterizations of PCF-based SPR sensors are not matured enough to date. Therefore, existing PCF sensors are mostly demonstrated by numerical analysis. Finite element method (FEM) is a powerful numerical technique, which is widely adopted to characterize the optical properties of PCF sensors. Besides, spectral (wavelength)- and intensity (amplitude or phase)-based numerical calculations are used to evaluate the sensing performance of the PCF SPR sensors [61].

In this chapter, current developments of SPR sensors are introduced and discussed. We will mainly focus on the review of the PCF-based SPR sensors and their potential applications in medical diagnostics and industrial settings. First, fundamentals of SPR technology and optical properties of several plasmonic materials (silver, copper, aluminum, gold, graphene, and niobium) are discussed. Then, we introduce several optical fiber-based SPR sensors and discuss how it overcomes the major limitations of prism-based SPR sensors. Later, recent advances of existing

PCF-based SPR sensors are discussed, which consist of comparisons among several PCF structures in terms of sensitivity, resolution, and fabrication feasibility. Finally, research gaps of this field are addressed and potential future detections to overcome them are discussed.

9.2 Fundamentals of Surface Plasmon Resonance

Inside a conductor (metal), there are lots of free electrons and an assembly of the electrons can be considered as plasma excitations. At the same time, there are equal numbers of positive charged ions from lattice so the total charge density in the conductor is zero. If an external field is applied, the electrons will be moving toward the positive region, and at the same time, the positive ion will be moving as opposite to the electrons. Due to such transport, a longitudinal oscillation will be introduced in the conductor which is known as surface plasmons (SPs) [62]. To support the SPs, a conductor and dielectric interface is required. In general, a metal and dielectric interface is used to support the surface plasmon oscillations. Due to these oscillations and a certain resonance condition, surface plasmon waves (SPWs) are generated that propagates along the metal–dielectric surface. Such SPs support only transverse magnetic (TM)-polarized electromagnetic field since there is no solution of Maxwell's equations for transverse electric (TE)-polarized case. Therefore, for SPW only the TM-polarized electric field exists. This wave is decayed exponentially in the metal. This SPW is characterized by the propagation constant as [63]

$$\beta = \frac{\omega}{c}\sqrt{\frac{\varepsilon_{\mathrm{M}}\varepsilon_{\mathrm{D}}}{\varepsilon_{\mathrm{M}}+\varepsilon_{\mathrm{D}}}} \tag{9.1}$$

where ω is the angular frequency, c is the speed of light in vacuum, and ε_{M} and ε_{D} are the dielectric permittivities of metal and dielectric medium, respectively. According to the above equations, property of the SPW is dependent on the property of two materials, i.e., the metal and the dielectric media.

To create the surface plasmon oscillation, it is required to excite the electrons in the conductor. Therefore, imposing the light (EM field) is necessary on the surface. The electrical permittivity for the conductor (metal) is negative, and the electrical permittivity for the dielectric is positive. In the dielectric medium, the propagation constant (maximum) can be written as [64]

$$\beta = \frac{\omega}{c}\sqrt{\varepsilon_S} \tag{9.2}$$

where ε_{S} is the dielectric permittivity of sensing medium. It is stated that the propagation constant for surface plasmon wave is higher than the propagation constant of light in the dielectric medium. As a result, surface plasmon cannot be

excited with the normal light; it requires the light with extra momentum or energy with the same polarization state as the SPW. Moreover, the propagation constant should be matched with the surface plasmon wave.

PCF-based SPR sensors operate based on the guided evanescent field. When the light propagates through the core by the mechanism of total internal reflection (TIR), then a part of the electromagnetic field that propagates from the cladding is called the evanescent field. In PCF SPR sensor structure, evanescent field penetrates through the cladding region and hits on the plasmonic metal surface which excites the free electrons from the metallic surface. When the frequency of the incident photon and the frequency of the free electrons are matched, the electrons start to resonate and at this condition SPW is generated on the metal–dielectric interface. At the resonance condition, a sharp loss peak appears which is very sensitive to the small refractive index (RI) variation of the dielectric medium. Mathematically, resonance will occur when the real effective refractive index (n_{eff}) of core-guided mode and surface plasmon polariton (SPP) mode value are equal. At the resonance condition, maximum energy transfers from the core-guided mode to the SPP mode [42]. Due to the change of refractive index of the dielectric media (sample analyte), n_{eff} of SPP will change resulting in a loss peak and the resonant wavelength shift. This indicates the phase-matching wavelength changes with the change of sample/analyte refractive index. Unknown sample could be detected by observing the variation of loss peak due to the change of analyte RI [61].

9.3 Optical Properties of Plasmonic Materials

PCF-based SPR sensors mostly use gold, copper, silver, and aluminum as the active plasmonic materials [65]. From the optical point of view, silver can be regarded as one of the potential candidates for plasmonic material [66]. The positive attributes of silver are no interband transition in the visible wavelength spectrum, low optical damping, narrow resonance peak, and a plasma wavelength (137 nm) deep in the ultraviolet wavelength range [67]. However, in the presence of aqueous solution it creates brittle oxide layers, which obstructs its widespread applications as plasmonic sensors [68]. Although such formation of oxide layer can be strongly prevented by depositing bimetallic layer on the top of the silver [69, 70], this additional layer will deteriorate the performance of the sensor. Compared to silver, aluminum has not attracted much attention due to its high optical damping, oxidation issue, and interband transition loss [71].

Current SPR sensors mostly rely on gold as the plasmonic material due to several advantages. Gold is chemically inert, biocompatible, long-term stable, and easy to structure. Moreover, gold does not suffer from oxidation issue [67, 72]. However, it has slightly higher optical damping and has broadened resonance wavelength peak leading to false positive analyte detection [44]. Copper is another potential plasmonic material possessing almost same optical damping and interband transition as gold in the wavelength range of 600–750 nm [73]. Unfortunately,

copper is also prone to oxidation. Recently, graphene is used on the top of the copper or silver in order to prevent the oxidation issue [74, 75]. Graphene is chemically inert and mechanically strong that keeps it isolated from contacting with aqueous solution [76]. Copper–graphene- [74] and silver–graphene [42]-based PCF SPR sensors possess long-term stability and stable performance. These widely used plasmonic materials are unfeasible when the thickness of the films is scaled down below ten nanometers because it leads to discontinuous film [77, 78]. Moreover, conventional plasmonic materials show poor adhesion strength with silica glass that requires additional adhesion layer. Employing such adhesion layer causes more damping loss; therefore, the performance of the sensor reduces significantly [66].

Niobium is a novel plasmonic material having strong chemical resistivity and high mechanical stability [79]. The adhesion strength of niobium film with silica glass is so strong that does not require an adhesion layer. Moreover, in contrast to gold, niobium provides continuous film when the thickness of the film falls below ten nanometers [80, 81]. Furthermore, after depositing niobium film on the silica surface, several atomic protection layers are naturally formed [82]. Although this layer has no optical functionality, it prevents the film from external perturbations of the environment. Recently, indium tin oxide (ITO)-based SPR sensors have achieved increased attention due to low bulk plasma frequency [43]. Moreover, its optical damping is almost same as gold and silver [83, 84].

9.4 Fiber Optic-Based Plasmonic Sensors

In contrast to prism-coupling SPR sensors, fiber optic-based SPR sensors provide several advantages such as simple and flexible design, ease of miniaturization, and capability for remote sensing and vivo measurements [51]. The prim-coupling configuration of the conventional SPR system is replaced by the core, where light is guided by the total internal reflection (TIR) mechanism. In fiber optic SPR sensors, certain portion of the silica cladding is removed and a metal layer is deposited on it. Later on, the metal layer is coated with a dielectric sensing layer. A light source is used to launch the light from an end of the fiber, which propagates by TIR mechanism. The generated evanescent field creates SPs at the fiber core–metal interface.

In general, fiber optic plasmonic sensors are based on either transmission or reflection properties of the guided light [51]. Fiber optic sensors based on transmission probe consist of plasmonic metal and immobilized ligand to detect the unknown analytes [56, 85]. On the other hand, sensors based on reflection probe use a mirror to reflect backlight to the fiber. Based on the transmission probe, several fiber optic plasmonic sensors have been explored in the literature, where plasmonic materials are placed on the etched cladding section. They include single-mode fibers (SMFs) [86], multi-mode fibers (MMFs) [87], wagon wheel fiber [88], U-shaped fiber [89], D-shaped fiber [90], tapered fiber [66, 91, 92], and

Bragg grating fibers [93]. Recently, side-polished single-mode optical fiber-based SPR sensor has been demonstrated for simple and cost-effective biochemical detections (see Fig. 9.2a(i)) [94]. With varying refractive index from 1.32 to 1.40, the highest sensitivity of 4365.5 nm/RIU and figure of merit (FOM) of 51.61 RIU^{-1} were reported (Fig. 9.2a(ii)). Niobium nanofilm was deposited on the tapered optical fiber in order to observe a dielectric-loaded niobium surface plasmon excitation (see Fig. 9.2b) [66]. The cross-sectional view of the sensor is shown in Fig. 9.2b(i). The cross-sectional view of the taper fiber optic sensor with different materials is shown in Fig. 9.2b(ii). Poynting vector distributions of dielectric and

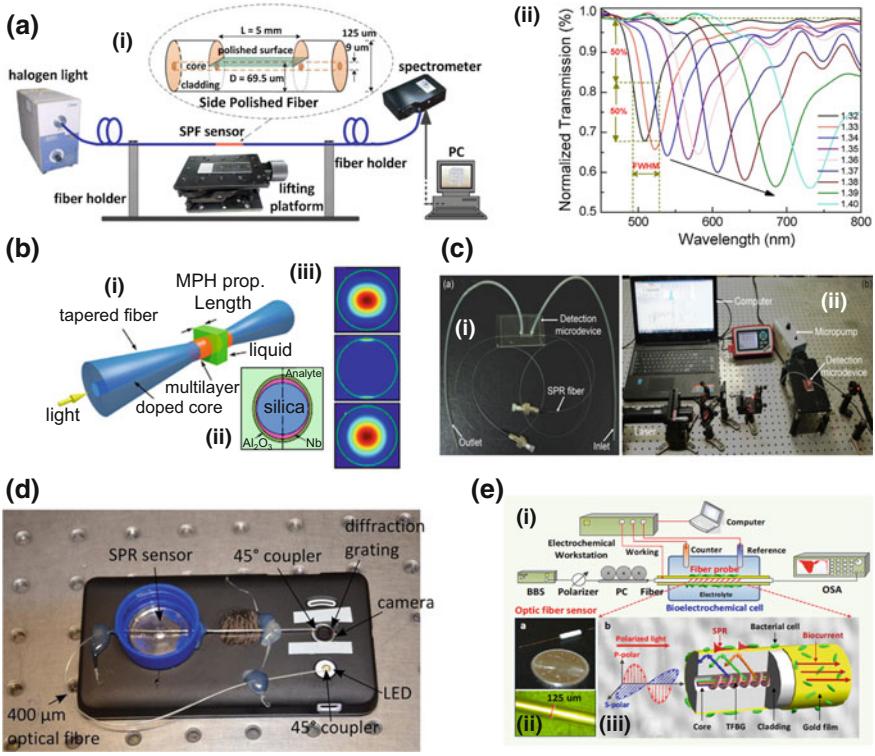

Fig. 9.2 Fiber optic-based SPR sensors. **a(i)** Schematic diagram to test the refractive index using side-polished D-shaped fiber and **(ii)** normalized transmission spectra due to the variation of analyte refractive index from 1.32 to 1.40 [94]. **b(i)** Schematic diagram of the plasmonic taper fiber with the multilayer structure, **(ii)** cross-sectional view showing different materials of the sensor, and **(iii)** Poynting vector distribution of the fundamental and SPP mode. Reprinted with permission from Macmillan Publishers Ltd. [66]. **c(i)** Microdevice installed with the SPR fiber sensor head and **(ii)** the experimental setup for the detection of polymerase chain reaction amplification with SPR fiber sensor system. Reprinted with permission from Elsevier B.V. [95]. **d** Smartphone-based fiber optic SPR sensor for pregnancy test. Reprinted with permission from Optical Society of America [96]. **e(i)** Schematic of the plasmonic fiber optic sensing system for in situ biofilm monitoring, **(ii)** SEM image of the gold-coated optic fiber sensor, and **(iii)** the zoomed configuration of the gold-coated sensor probe. Reprinted with permission from the American Chemical Society [97]

SPP mode are shown in Fig. 9.2b(iii). The proposed plasmonic sensor shows low modal attenuation of 4 dB/mm and refractive index sensitivity of 15 μm/mm with analyte index of 1.42. A SPR optical fiber sensor for the detection of polymerase chain reaction amplification has been reported by Nguyen et al. [95] using bimetallic (Ag/Al) coating (see Fig. 9.2c). A smartphone-based optical fiber sensor has been reported by Bremer and Roth [96] for concentration measurements on aqueous solutions and pregnancy testing (see Fig. 9.2d). A sensitivity of 5.96×10^{-4} RIU/pixel was obtained in the sensing range between 1.33 and 1.36. Recently, electrochemical SPR fiber optic sensor has been proposed for in situ monitoring of electroactive biofilms (see Fig. 9.2e) [97].

9.5 Photonic Crystal Fiber-Based Plasmonic Sensors

PCF is a new class of optical fiber that consists of a core and cladding with periodic arrangement of air hole arrays [98]. Such periodic arrangement of the air holes controls the propagation characteristics of the PCFs. The light guiding mechanism in PCF is modified TIR and photonic band gap [99, 100]. In contrast to conventional optical fiber, PCF-based SPR sensors offer several advantages. By varying the air hole dimension and number of rings in a PCF, it is possible to control the guiding properties of the PCF. In general, PCFs are compact and can be fabricated in micron scale. Unlike prism-coupling and conventional optical fiber-based SPR sensors, PCF-based SPR sensors provide potential platform for downscaling the sensor size. Moreover, the unique features of PCFs have opened a new window for realizing nanosensors. Several cladding structures including hexagonal, octagonal, circular, square, and hybrid can be used to modify the evanescent field; thereby, it is possible to obtain the optimum sensing performance [101]. Furthermore, single-mode propagation can be obtained by properly choosing the core–cladding diameter. Single-mode guidance provides sharp resonance peak that increases the sensitivity of a sensor [102]. The detection accuracy and sensitivity of the PCF SPR sensors can be optimized by changing the structural parameters such as pitch and air hole dimensions. Besides, sensor length can be extended by setting the fiber parameters in such a way that exhibits minimum propagation loss. In practice, depositing the metal layer on the PCF is a difficult task. The existing fabrication technologies can be employed to deposit the metal layer inside or outside of the PCFs. Based on the metal deposition on the PCF, SPR sensors are classified into two major categories. They are internally and externally metal-coated SPR sensors.

9.5.1 Internally Metal-Coated PCF SPR Sensors

The internally metal-coated PCF SPR sensors are based on the deposition of metal layer on the inner air hole(s), which are filled by the analyte. To date, several PCF

structures have been explored where metal layer is placed inside the PCF and liquid analytes are selectively filled into the inner air hole(s) [39, 41–43, 103–107]. Very recently, diamond ring fiber (DRF)-based SPR sensor has been proposed (see Fig. 9.3a) by numerical investigations [108]. This is an all-silica fiber containing a ring capillary with thickness of 0.94 μm. The diameter of the core is 3.23 μm. A thin layer of gold is deposited on the inner wall of the capillary. The DRF contains two large cavities, which simplify the metal coating process. Moreover, this sensor does not require selective infiltration of the liquid sample. The evanescent field created from the fundamental core-guided mode reaches at the metal boundary, which resembles free electrons from its surface. Due to the interaction of emitted electrons and evanescent field, SPW is generated that propagates along the metal–dielectric surface. The electric field distribution of the fundamental core-guided mode and SPP mode is shown in Fig. 9.3b. When the effective index of core-guided mode and SPP mode is equal, a phase-matching condition occurs at a particular wavelength known as the resonance wavelength. Under this condition, confinement loss peak is observed at the resonance wavelength (see Fig. 9.3c) resulting in maximum power transfer from the core-guided mode to the SPP mode. The confinement loss can be computed from the following equation $\alpha(\text{dB/cm}) = 8.686 \times (2\pi/\lambda)\ \text{Im}(n_{\text{eff}}) \times 10^4$, where $\text{Im}(n_{\text{eff}})$ is the

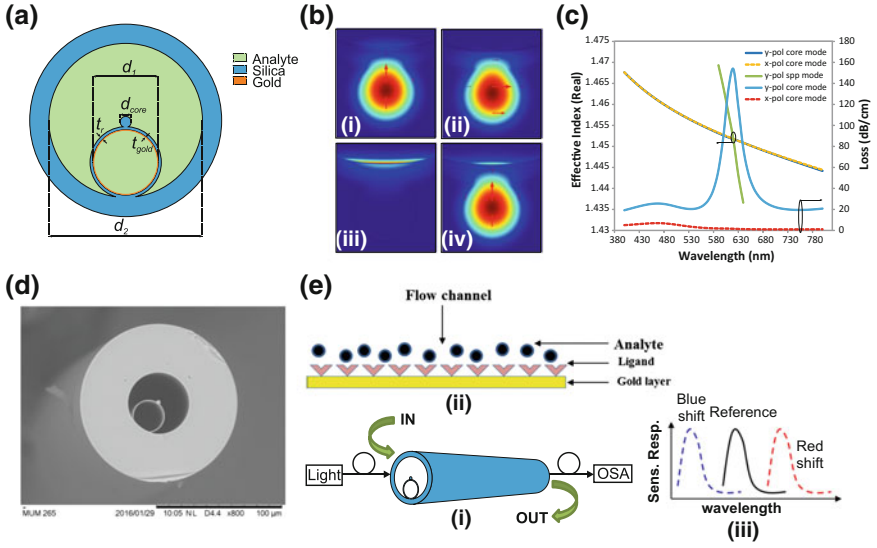

Fig. 9.3 **a** Cross-sectional view of the DRF showing different materials used in the structure. **b** Fundamental mode field distributions of the **(i)** *y*-polarized core mode, **(ii)** *x*-polarized core mode, **(iii)** *y*-polarized SPP mode at 580 nm, and **(iv)** *y*-polarized core mode at 620 nm. **c** Dispersion relation between core-guided mode and SPP mode at analyte refractive index of 1.33. **d** SEM image of the DRF. **e(i)** Generalized sensing setup using the DRF, **(ii)** analyte flow mechanism for DRF-based sensor, and **(iii)** sensing response observed from the computer. Reprinted with permission from Springer [108]

imaginary part of the effective mode index. The proposed DRF is fabricated using the stack-and-draw method, and the scanning electron microscope (SEM) image is shown in Fig. 9.3d. Figure 9.3e(i)–(ii) shows the generalized experimental setup that can be implemented based on the DRF–SPR sensor. Broadband supercontinuum laser source can be lunched to the SMF. The propagating light can be coupled to the DRF by using the butt-coupling technique. Due to the interaction of the evanescent field with the ligand, the effective index of SPP mode expected to be changed. As a result, blue or red shift will occur as shown in the sensing response curve (see Fig. 9.3e(iii)). The output light can be coupled with the optical spectrum analyzer (OSA), and it can be processed using computer.

The performance of SPR sensors can be analyzed using wavelength sensitivity (spectral-based analysis), amplitude sensitivity (intensity-based analysis), and sensor resolution. The wavelength sensitivity of a sensor can be expressed as [109]

$$S_\lambda(\mathrm{nm/RIU}) = \Delta\lambda_{\mathrm{peak}}/\Delta n_{\mathrm{a}} \tag{9.3}$$

where $\Delta\lambda_{\mathrm{peak}}$ is the peak wavelength shift due to any change of analyte RI and Δn_a is the change of the two successive analyte RIs. On the other hand, amplitude sensitivity can be manipulated by the following equation [45, 109]

$$S_A(\mathrm{RIU}^{-1}) = -\frac{1}{\alpha(\lambda, n_{\mathrm{a}})}\frac{\partial\alpha(\lambda, n_{\mathrm{a}})}{\partial n_{\mathrm{a}}} \tag{9.4}$$

where $\alpha(\lambda, n_a)$ is the confinement loss at refractive index of n_a and $\partial\alpha(\lambda, n_a)$ is the confinement loss difference due to two adjacent analyte RIs. In the sensing range between 1.33 and 1.39, the DRF-based SPR sensor shows maximum wavelength and amplitude sensitivity of 6000 nm/RIU and 508 RIU^{-1}, respectively. Assuming instrumental resolution of 0.1 nm and avoiding practical noise influence, the calculated wavelength resolution is 1.67×10^{-5} RIU. Besides, amplitude resolution of 1.97×10^{-5} RIU is reported, while it is assumed that 1% transmitted intensity can be detected by the sensor. A liquid core PCF with two selectively analyte-filled channels has been demonstrated, where graphene–silver coating was used to improve the sensing performance (see Fig. 9.4a(i)) [42]. The phase-matching conditions are shown in Fig. 9.4a(ii) for analyte index of 1.47 and 1.49, respectively. It was reported that at optimum design parameters it is possible to obtain maximum wavelength and amplitude sensitivity of 3000 nm/RIU and 418 RIU^{-1}, respectively. The corresponding sensor resolutions are 3.33×10^{-5} and 2.4×10^{-5} RIU, respectively. Moreover, another PCF SPR sensor has been proposed by Yang et al. using graphene–silver bimetallic configuration [110]. In this sensor, two rings hexagonal PCF was considered, where six air holes of the second ring were selectively infiltrated by the analyte. In the sensing range between 1.33 and 1.34, maximum wavelength and amplitude sensitivity of 2520 nm/RIU and 72.47 RIU^{-1}, respectively. The selectively analyte-filled PCF SPR sensor proposed by Fan et al. shows average wavelength sensitivity of 7040 and 7017 nm/RIU using gold and silver as the plasmonic material, respectively [105]. Moreover, the

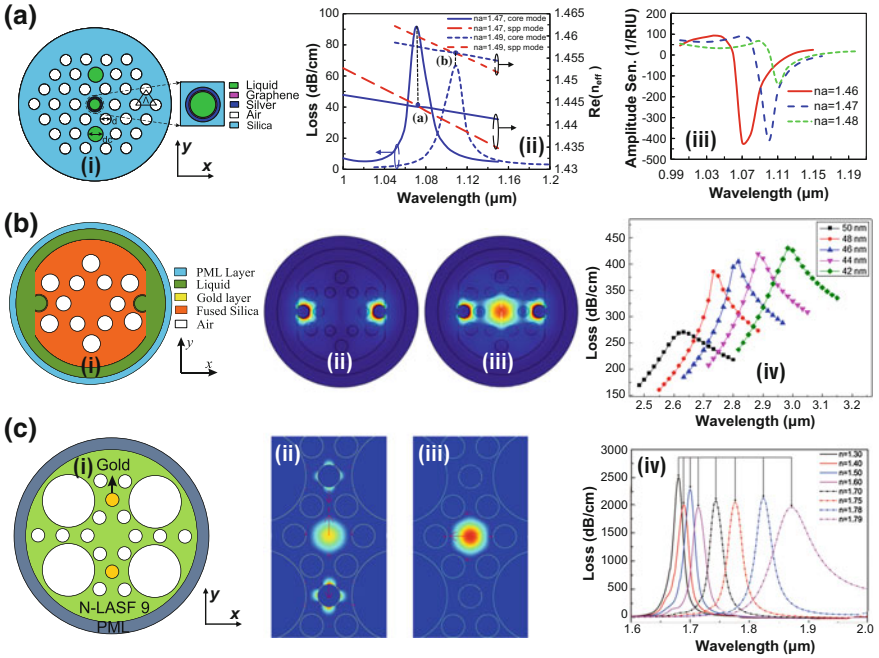

Fig. 9.4 Internally metal-coated PCF SPR sensors. **a(i)** Cross-sectional view of the liquid core PCF with selectively analyte-filled sensor, **(ii)** dispersion relation between core-guided mode and SPP mode at analyte refractive index of 1.47 and 1.49, and **(iii)** amplitude sensitivity as a function of wavelength for analyte refractive index of 1.46, 1.47, and 1.48. Reprinted with permission from MDPI AG [42]. **b(i)** Cross-sectional view of the open ring PCF sensor, **(ii)** optical field distribution of the plasmonic mode, **(iii)** optical field distribution of the fundamental core-guided mode, and **(iv)** loss spectra for the variation of gold layer thickness. Reprinted with permission from Optical Society of America [112]. **c(i)** Cross-sectional view of the gold nanowire-based PCF sensor, **(ii)** optical field distribution of the plasmonic mode, **(iii)** optical field distribution of the fundamental core-guided mode, and **(iv)** loss spectra for the variation of analyte refractive index [113]

reported figure of merit (FOM) for gold and silver was 73.8 and 5.9 RIU^{-1} at analyte refractive index of 1.40. Very recently, multi-coating PCF SPR sensor proposed by Li et al. employs tantalum pentoxide (Ta_2O_5) on gold in order to further improve the sensitivity [111]. The proposed sensor shows average wavelength sensitivity of 9180 nm/RIU and maximum amplitude sensitivity of 1739.26 RIU^{-1}, respectively.

In practice, it is a difficult task to selectively filling the air holes with the analyte. To overcome this limitation, PCF SPR sensor having open rings channels was proposed [112]. The analyte can be injected into the channels automatically, and size of the open rings can be controlled according to the molecular concentrations of the analyte. The hollow-core open ring PCF sensor operates in the mid-infrared region and can be used to detect low refractive indices between 1.23 and 1.29 (see Fig. 9.4b(i)) [112]. Mode field distribution of the core-guided mode, SPP mode,

and loss variations due to analyte index change is shown in Fig. 9.4b(ii)–(iii). With optimum design parameters, average wavelength sensitivity of 5500 nm/RIU and maximum amplitude sensitivity of 333.8 RIU^{-1} were reported. In practice, disposition of metal on several air holes maintaining uniform thickness is unfeasible from the fabrication point of view. Nanowire-based PCF sensors provide viable way to eliminate those issues. To date, several PCF SPR sensors have been realized using silver and gold nanowires [114–116]. Recently, silver nanowire-based PCF SPR glucose sensor has been proposed showing high average wavelength sensitivity of 19009.17 nm/RIU and amplitude sensitivity of 513.68 RIU^{-1} [52]. Gold nanowire-based PCF SPR sensor (see Fig. 9.4c(i)) proposed by An et al. can be used to detect analyte refractive index from 1.30 to 1.79 [113]. It contains four large air holes that make it easier to inject the analyte. The electric field distributions of the core-guided mode, SPP mode, and confinement loss for different analyte refractive index are shown in Fig. 9.4c(ii)–(iii). In the sensing range between 1.30 and 1.63, average wavelength sensitivity of 100 nm/RIU and in the sensing range between 1.63 and 1.79, average wavelength sensitivity of 3233 nm/RIU were reported. Very recently, hollow-core silver nanowire-based PCF SPR sensor has been proposed having large detection range from 1.33 to 1.50 [117]. The proposed sensor shows maximum wavelength sensitivity of 1800 nm/RIU when analyte index is varied from 1.33 to 1.34. Nanowire-based PCF can be fabricated by implementing the Taylor wire method [90]. Table 9.1 shows the performance comparison among existing internally metal-coated PCF SPR sensors.

9.5.2 Externally Metal-Coated PCF SPR Sensors

To potentially overcome the major limitations such as the requirements for selective infiltration of liquids, metal coating of several air holes, and complex fabrication, externally metal-coated PCF SPR sensors have been proposed. Unlike internally metal-coated PCF sensors, plasmonic materials are deposited on the outer surface of the PCF facilitating straightforward sensing mechanism. Based on the structural configurations, external metal-coated PCF SPR sensors are generally three types: slotted PCF sensors, D-shaped PCF sensors, and improved external PCF sensors.

9.5.2.1 Slotted PCF SPR Sensors

Slotted PCF SPR sensors are mainly developed in order to detect multiple analytes. Various structural configurations have been proposed in the literature for this purpose [50, 118–121]. The PCF-based SPR sensor proposed by Hassani et al. was used for the detection of biolayer thickness (see Fig. 9.5a(i)) [119]. Plasmonic gold and biolayer were deposited outside the PCF surface. Six smaller air holes are placed near the gold surface to control the coupling strength between core-guided mode and SPP mode. The central air hole was used to maintain the phase-matching

Table 9.1 Performance comparison of the internally metal-coated PCF SPR sensors

References	Characteristics	RI range	Interrogation type	Sensitivity	Resolution (RIU)
[42]	Graphene–silver deposited core with selective analyte channels	1.46–1.49	Wavelength	3000 nm/RIU	3.33×10^{-5}
			Amplitude	418 RIU^{-1}	2.4×10^{-5}
[43]	Polymer PCF coated with conducting metal oxide	1.33–1.35	Wavelength	2000 nm/RIU	5×10^{-5}
			Amplitude	80 RIU^{-1}	12×10^{-5}
[48]	Selectively filled silver nanowires	1.33–1.335	Wavelength	N/A	4.5×10^{-5}
			Amplitude	203 RIU^{-1}	4.9×10^{-5}
[103]	Multi-hole single-mode PCF	1.33–1.35	Wavelength	2000 nm/RIU	5×10^{-5}
			Amplitude	370 RIU^{-1}	2.7×10^{-5}
[104]	Selectively gold coating with analyte-filled core PCF	1.46–1.485	Wavelength	2280 nm/RIU	N/A
			Wavelength	−4354.3 nm/RIU	N/A
[105]	Analyte-filled PCF with selective coating	1.40–1.42	Wavelength	7040 nm/RIU	N/A
			Wavelength	7017 nm/RIU	N/A
[107]	PCF with large size microfluidic channels	1.33–1.39	Wavelength	2000 nm/RIU	5×10^{-6}
			Amplitude	300 RIU^{-1}	3.3×10^{-5}
[108]	Diamond ring PCF	1.33–1.39	Wavelength	6000 nm/RIU	1.67×10^{-5}
			Amplitude	508 RIU^{-1}	1.97×10^{-5}
[110]	Graphene–silver bimetallic layer PCF	1.33–1.35	Wavelength	2520 nm/RIU	3.97×10^{-5}
			Amplitude	72.47 RIU^{-1}	N/A
[111]	Analyte-filled multi-coated PCF	1.40–1.44	Wavelength	9180 nm/RIU	1.09×10^{-5}
			Amplitude	1739.26 RIU^{-1}	5.75×10^{-6}
[112]	Open ring channels PCF	1.23–1.29	Wavelength	5500 nm/RIU	7.69×10^{-6}
			Amplitude	333.8 RIU^{-1}	N/A
[113]	Gold nanowires with large size channels	1.30–1.79	Wavelength	3233 nm/RIU	3.09×10^{-5}
			Amplitude	N/A	N/A
[116]	Hollow-core PCF with silver-filled nanowire	1.10–1.60	Wavelength	14,240 nm/RIU	N/A
			Amplitude	N/A	N/A

characteristics. The mode field distributions of the core-guided mode and SPP mode at 575 nm are shown in Fig. 9.5a(ii)–(iii). It is demonstrated that with gold layer thickness of 50 nm, a wavelength shift of 23 nm can be obtained when biolayer thickness is increased from 0 to 10 nm (see Fig. 9.5a(iv)). Recently, a multi-channel PCF-based sensor has been proposed, where plasmonic silver is coated with the gold (see Fig. 9.5b(i)) [122]. The loss spectrum of the quasi-TM and TM fundamental core modes for analyte refractive index of 1.33 and 1.34 are shown in Fig. 9.5b(ii)–(iii). The proposed bimetallic SPR sensor shows maximum wavelength sensitivity of 4750 nm/RIU and 4300 nm/RIU for quasi-TM and TM fundamental core mode, respectively. The major limitation of this sensor is the high confinement loss, which potentially limits its length. In general, the signal strength

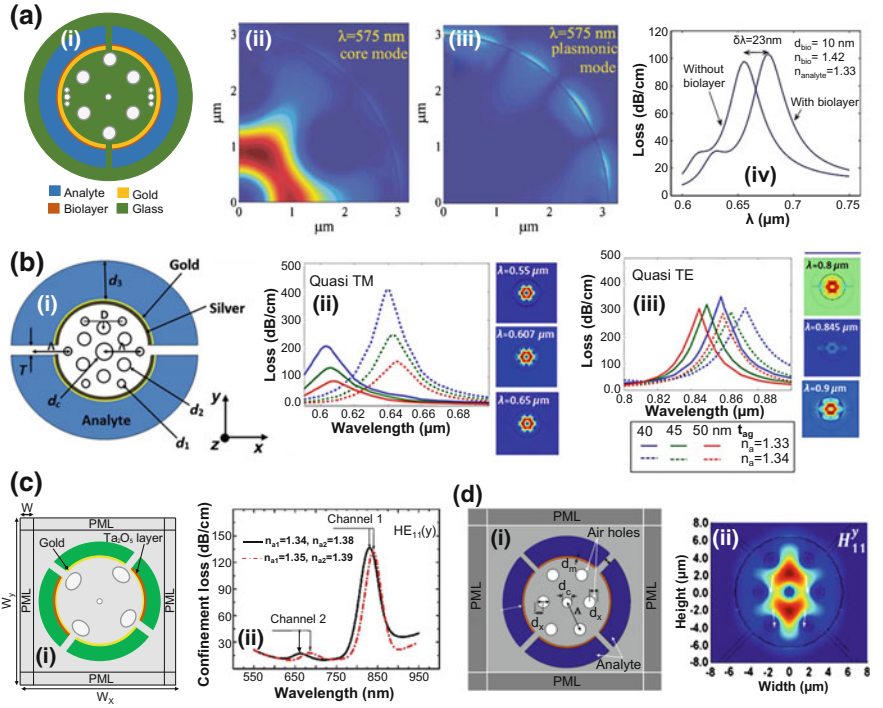

Fig. 9.5 Slotted PCF SPR sensors. **a(i)** Cross-sectional view of the slotted PCF sensor with the air hole defects in the near vicinity of the gold layers, **(ii)** optical field distribution of the fundamental mode, **(iii)** optical field distribution of the SPP mode, and **(iv)** effect of inserting biolayer on the loss spectra. Reprinted with permission from Optical Society of America [119]. **b(i)** Cross-sectional view of the bimetallic-slotted PCF sensor, **(ii)** loss spectra for the variation of silver layer thickness in quasi-TM mode, and **(iii)** loss spectra for the variation of silver layer thickness in quasi-TE mode. Reprinted with permission from SPIE [122]. **c(i)** Cross-sectional view of the PCF sensor with elliptical air holes, and **(ii)** loss spectra for the variation of analyte refractive index. Reprinted with permission from Optical Society of America [50]. **d(i)** Cross-sectional view of the PCF sensor with four microfluidic channels, and **(ii)** optical field distribution of the fundamental mode. Reprinted with permission from Springer [118]

of the PCF with high confinement loss exhibits fast decay. As a result, it will be difficult to obtain measurable signal at the output end.

The PCF SPR sensor proposed by Otupiri et al. consists of elliptical air holes and four microfluidic channels [50], which can detect multi-analytes having different refractive indices (see Fig. 9.5c(i)). The designed sensor can be used as the self-referencing mode making it suitable for eliminating external perturbations such as temperature variations, instrumental noises. The confinement losses for two different channels are shown in Fig. 9.5c(ii). It is reported that maximum wavelength sensitivity of 4600 nm/RIU and amplitude sensitivity of 425 RIU^{-1} can be obtained at gold layer thickness of 50 nm. A single ring hexagonal PCF sensor with four microfluidic channels has been demonstrated, where four modes are separately studied for multi-analyte detections (see Fig. 9.5d(i)) [118]. The birefringence property is used that exhibits different effective refractive indices for *x*-polarized and *y*-polarized modes. Due to this fact, one of the fundamental modes (either *x*- or *y*-polarized mode) shows higher confinement loss. The mode field distribution of the fundamental *y*-polarized HE_{11} mode is shown in Fig. 9.5d(ii). The proposed sensor shows maximum wavelength sensitivity of 2400 nm/RIU in *y*-polarized HE_{11} mode. Based on the birefringence property, another slotted PCF sensor has been proposed showing maximum wavelength sensitivity of 2000 nm/RIU and 1700 nm/RIU in *x*-polarized HE_{11} mode and *y*-polarized HE_{11} mode, respectively. In addition to multi-analytes detection, this slotted PCF sensor can be used for the detection of bulk and surface sensitivities.

9.5.2.2 D-Shaped PCF SPR Sensors

Recently, D-shaped PCF sensors have attracted much attention due to its definite advantages over other externally metal-coated sensors. In D-shaped PCF sensor, the top of the cladding is etched out in order to obtain a flat surface. Both the plasmonic material and analyte sample are placed on that flat surface. Most of the internally and externally metal-coated PCF sensors are based on the metal coating on the circular surface. In general, obtaining a uniform circular surface is difficult since it associates with unwanted surface roughness. Taking advantage from the flat surface, D-shaped PCF sensors provide possibilities for homogeneous coating with minimal surface roughness [123]. The unknown analyte can be detected by simply flowing on the flat surface. Moreover, plasmonic materials are deposited near to the core resulting in strong interaction of the core-guided mode and SPP mode. Due to such strong coupling, D-shaped PCF sensors show comparatively higher sensitivity than other PCF sensors. Currently, several D-shaped PCF sensors have been explored in order to enhance the performance [46, 47, 124–130]. Very recently, a D-shaped PCF sensor has been proposed using gold as the plasmonic material and titanium dioxide (TiO_2) for shifting the resonance wavelength from visible to near-infrared (see Fig. 9.6a(i)) [123]. Since plasmonic gold is deposited near the core, the evanescent field can easily reach to the metal surface. The electric field distributions of the fundamental core-guided mode and SPP mode are also shown in

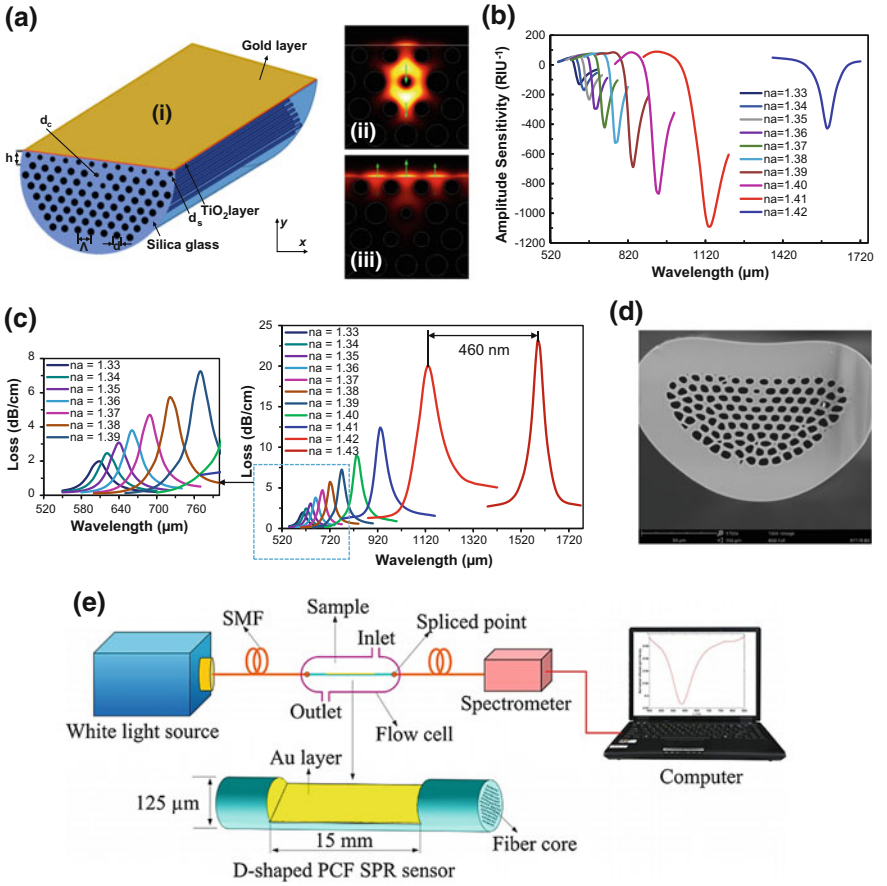

Fig. 9.6 **a(i)** 3D view of the D-shaped PCF sensor, **(ii)** electric field distribution of the fundamental core-guided mode, and **(iii)** electric field distribution of the SPP mode. **b** Amplitude sensitivity for the variation of analyte refractive index from 1.33 to 1.42. **c** Loss spectra for the variation of analyte refractive index from 1.33 to 1.43. **d** SEM image of the D-shaped PCF. **e** Generalized sensing setup using the D-shaped PCF. Reprinted with permission from IEEE [123]

Fig. 9.6a(ii)–(iii). In the sensing range between 1.33 and 1.43, the D-shaped sensor shows maximum amplitude sensitivity of 1086 RIU^{-1} (Fig. 9.6b) with sensing resolution of 9.2 $\times$ 10^{-6} RIU. It is also reported that maximum resonance wavelength shift of 460 nm can be obtained when analyte refractive index is varied from 1.42 to 1.43 (Fig. 9.6c).

The reported theoretical wavelength sensitivity and resolution are 46,000 nm/RIU and 2.2 $\times$ 10^{-6} RIU, respectively. The SEM image of the proposed D-shaped is shown in Fig. 9.6d. The general setup for detecting unknown analytes using D-shaped PCF is shown in Fig. 9.6e. Broadband white light source can be used to couple input light to the D-shaped PCF through a SMF. An analyte flow cell is

maintained on the flat surface region. The inlet and outlet of the flow cell can be obtained through a pump. The output light is again coupled to the SMF. The spectrometer is used to observe the output obtained from the SMF.

The hollow-core D-shaped PCF has been experimentally demonstrated having average wavelength sensitivity of 2336.2 nm/RIU [131] (see Fig. 9.7a(i)). The optical field distribution of the hollow-core D-shaped sensor is shown in Fig. 9.7a (ii). Compared to exposed core PCF sensor, this sensor shows higher sensitivity. Normalized light intensity of the proposed sensor due to the change of analyte refractive index is shown in Fig. 9.7a(iii). Due to structural simplicity, this sensor is convenient and suitable for practical sensing applications. The D-shaped PCF sensor proposed by Luan et al. can be potentially used for fast response and distributed sensing (see Fig. 9.7b(i)) [128]. The performance of this sensor has been

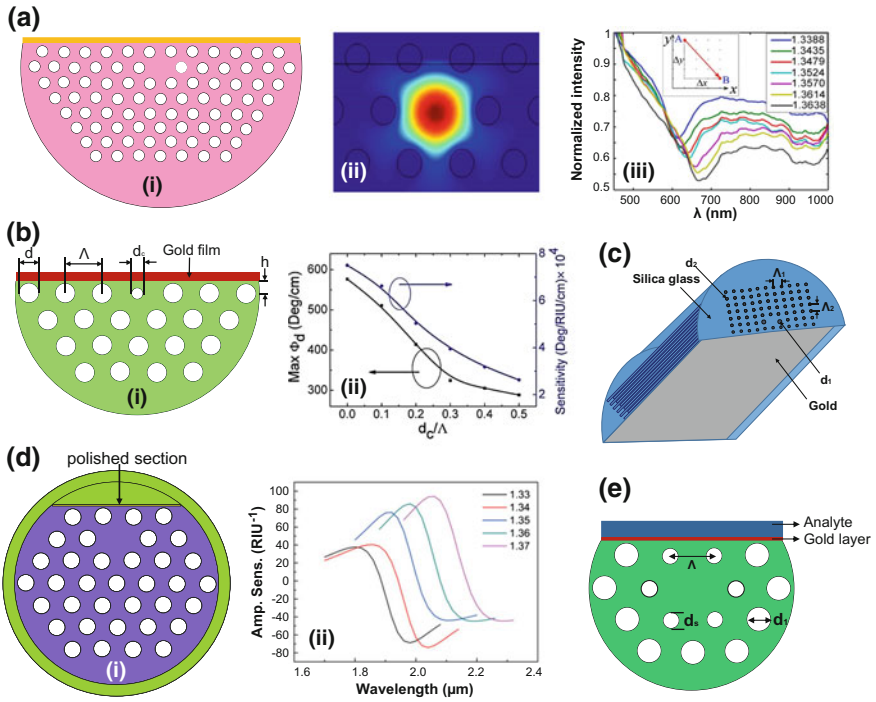

Fig. 9.7 D-shaped PCF SPR sensors. **a(i)** Cross-sectional view of the hollow-core D-shaped PCF sensor, **(ii)** optical field distribution of the fundamental mode, **(iii)** normalized intensity for different analyte refractive index [131]. **b(i)** Cross-sectional view of the D-shaped PCF sensor with external gold coating, **(ii)** variations of phase sensitivity and wavelength sensitivity due to the change of d_c/Λ. Reprinted with permission from Optical Society of America [128]. **c** Cross-sectional view of the D-shaped PCF with rectangular lattice air holes [46]. **d(i)** Cross-sectional view of the quasi-D-shaped PCF sensor and **(ii)** amplitude sensitivity for the variation of analyte refractive index from 1.33 to 1.37. Reprinted with permission from IEEE [132]. **e** Cross-sectional view of the hollow-core D-shaped PCF sensor with hexagonal lattice. Reprinted with permission from Springer [133]

demonstrated using wavelength, amplitude, and phase sensitivity. Variations of phase sensitivity and wavelength sensitivity due to the change of d_c/Λ are shown in Fig. 9.7b(ii). When the analyte refractive index is changed from 1.33 to 1.34, it shows wavelength sensitivity of 2900 nm/RIU, amplitude sensitivity of 120 RIU^{-1}, and phase sensitivity of 50,300 deg/RIU/cm. Another D-shaped PCF has been proposed having rectangular lattice air holes (see Fig. 9.7c) [46]. Two larger air holes are placed near the core to create birefringence in the structure resulting in higher FOM about 478.3 RIU^{-1}. Very recently, a quasi-D-shaped PCF SPR sensor has been proposed by An et al. using graphene and indium tin oxide (ITO) layers operating in the near-infrared wavelengths (see Fig. 9.7d(i)) [132]. In contrast to other D-shaped PCFs, this PCF structure is comparatively simple and easy to fabricate due to smaller polishing section. Moreover, it shows comparatively lower confinement loss than that of reported in other PCFs. Due to low confinement losses, the length of sensor can be enlarged making it suitable for remote sensing applications. Simulation results show maximum wavelength sensitivity of 10,693 nm/RIU and amplitude sensitivity of 95 RIU^{-1} at analyte refractive index of 1.37. The hollow-core D-shaped PCF sensor has been proposed using ITO as the plasmonic material [134]. This PCF also uses birefringence effect by employing two larger air holes near the core. It shows maximum wavelength sensitivity of 6000 nm/RIU, amplitude sensitivity of 148 RIU^{-1}, and phase sensitivity of 1.2×10^6 deg/RIU/cm. Besides, the D-shaped PCF has been proposed (see Fig. 9.7e) showing high average wavelength sensitivity of 7700 nm/RIU and resolution of 1.30×10^{-5} RIU [133]. Although D-shaped PCF sensors provide high sensitivity and eliminate the issue of uniform thickness, it requires accurate polishing of the predefined section. Moreover, few D-shaped PCF sensors show high confinement loss to polish out the upper air holes [46, 128, 133]. The high confinement loss potentially reduces the sensor length making them unsuitable for remote sensing applications.

9.5.2.3 Improved External Approach of PCF SPR Sensors

The improved PCF SPR sensors can be realized by putting plasmonic material and sensing medium outside the PCF structure. To date, several PCF sensors have been proposed based on improved external approach [37, 44, 109, 135–139]. The multi-core flat fiber (MCFF)-based PCF has been proposed (see Fig. 9.8a), where gold, TiO_2, and sensing layers are sequentially employed [109]. The MCFF operates in the near-infrared region and can be used to detect analyte having high refractive index from 1.46 to 1.48. This PCF provides easier fabrication since gold and TiO_2 layers are placed outside the PCF structure. Moreover, it requires coating of the flat surface rather than the circular one. The phase-matching condition and mode field distribution of the fundamental mode and SPP mode are shown in Fig. 9.8b. Since core of the MCFF is close to the gold layer, it provides strong interaction between core-guided mode and SPP mode.

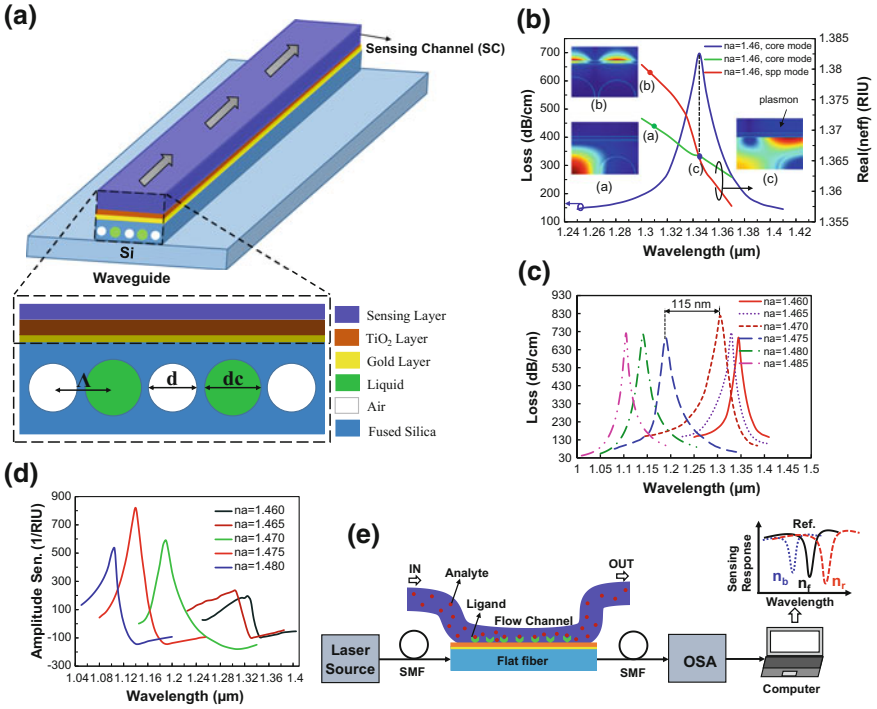

Fig. 9.8 **a** Schematic of the MCFF-based sensor. **b** Dispersion relation between core-guided mode and SPP mode with electric field distribution of the fundamental core-guided mode and SPP mode. **c** Loss spectra for the variation of analyte refractive index from 1.46 to 1.485. **d** Amplitude sensitivity for the variation of analyte refractive index from 1.46 to 1.485. **e** Generalized sensing setup using the MCFF. Reprinted with permission from Optical Society of America [109]

When the analyte refractive index is varied from 1.47 to 1.475, it shows maximum resonance wavelength shift of 115 nm (Fig. 9.8c). Amplitude sensitivity as a function of wavelength for the variation of analyte refractive index from 1.46 to 1.485 is shown in Fig. 9.8d. Simulation analysis shows maximum wavelength sensitivity of 23,000 nm/RIU and amplitude sensitivity of 820 RIU^{-1}. Due to fewer number of air holes, the proposed MCFF exhibits high confinement loss. The process of analyte flow through the sensing layer and typical sensing response is shown in Fig. 9.8e. Due to high linearity and very high sensitivity, the MCFF can be potentially used in high refractive index analyte detections.

Very recently, a hollow-core PCF SPR sensor has been reported in Fig. 9.9a(i) with maximum wavelength sensitivity of 4000 nm/RIU and amplitude sensitivity of 478 RIU^{-1} [140]. This PCF sensor eliminates major design issues due to its simple structure and minimum design parameters. It consists of hexagonal lattice cladding having four missing air holes in the second ring. The evanescent field produced from the core-guided mode penetrates through the missing air holes resulting in a strong interaction with metal surface as shown in Fig. 9.9a(ii)–(iii). The highest confinement loss for analyte refractive index of 1.37 is 60 dB/cm, and R^2 of 0.9868

are also demonstrated in Fig. 9.9a(iv). The proposed structure proposed by Liu et al. consists of seven air holes with annular analyte channel (Fig. 9.9b(i)) [141]. Due to fewer air holes in the cladding and smaller curved gold surface, fabrication of this sensor is comparatively easy. Moreover, perturbation with outer channel can be ignored since analyte channel is placed on the outermost layer. It is reported that wavelength sensitivity can be enhanced up to 7500 nm/RIU using extra graphene layer in the outer surface of the PCF. Variation of confinement loss with width of analyte channel for different operating wavelengths is shown in Fig. 9.9b(ii). The copper–graphene-based PCF sensor (see Fig. 9.9c(i)) shows average wavelength sensitivity of 2000 nm/RIU and amplitude sensitivity of 140 RIU^{-1} in the sensing range between 1.33 and 1.37 [136]. Two air holes in the cladding are scaled down in order to permit light propagating through their surrounding silica area. The scaled down air holes are kept close to the copper surface making intense interaction with evanescent field with metallic surface. The linear fitting of the resonance

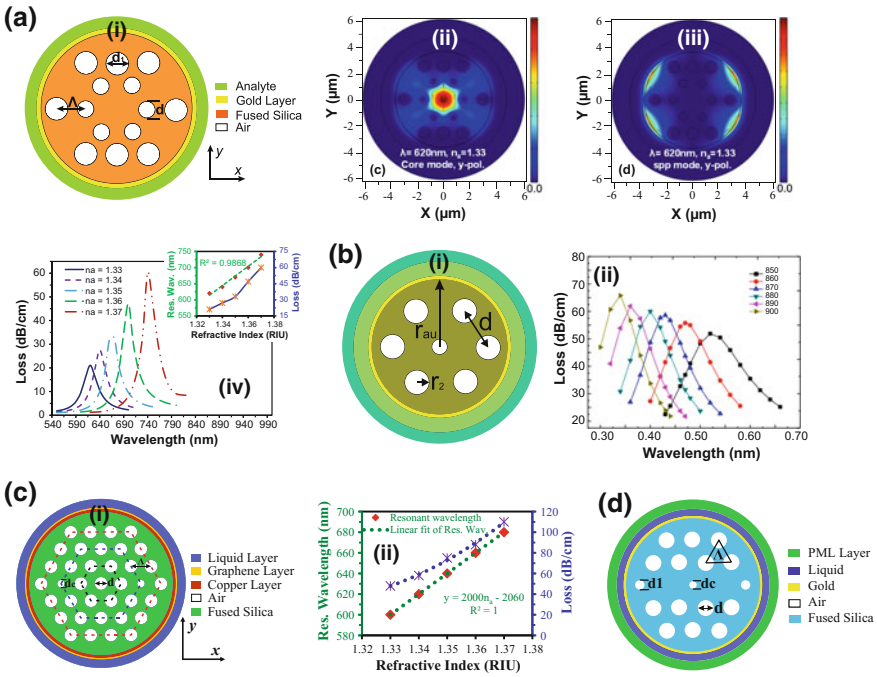

Fig. 9.9 Improved external approach of PCF SPR sensors. **a(i)** Cross-sectional view of the hollow-core PCF sensor, **(ii)** mode field distribution of the core-guided mode, **(iii)** mode field distribution of the SPP mode, and **(iv)** loss spectra for the variation of analyte refractive index from 1.33 to 1.37. Reprinted with permission from SPIE [140]. **b(i)** Cross-sectional view of the annular core PCF sensor and **(ii)** dependence of optical loss on the analyte channel width for different wavelengths [141]. **c(i)** Cross-sectional view of the copper–graphene-based PCF sensor and **(ii)** linear fitting of the resonance wavelengths. Reprinted with permission from IEEE [136]. **d** Cross-sectional view of the hexagonal lattice PCF sensor with external sensing. Reprinted with permission from IEEE [45]

Table 9.2 Performance comparison of the externally metal-coated PCF SPR sensors

References	Characteristics	RI range	Interrogation type	Sensitivity	Resolution (RIU)
[45]	Gold-coated PCF with external sensing approach	1.33–1.37	Wavelength	4000 nm/RIU	2.5×10^{-5}
			Amplitude	320 RIU^{-1}	3.125×10^{-5}
[50]	Multi-channel PCF with elliptical air holes	1.33–1.36	Wavelength	4600 nm/RIU	2.0×10^{-5}
			Amplitude	425 RIU^{-1}	2.0×10^{-5}
[109]	Multi-core flat fiber	1.46–1.485	Wavelength	23,000 nm/RIU	4.35×10^{-6}
			Amplitude	820 RIU^{-1}	1.22×10^{-5}
[118]	Four microfluidic slots	1.33–1.34	Wavelength	2400 nm/RIU	N/A
			Amplitude	N/A	N/A
[122]	Silver–gold bimetallic layer with multi-channels	1.33–1.35	Wavelength	4750 nm/RIU	2.1×10^{-5}
			Amplitude	1555 RIU^{-1}	6.43×10^{-6}
[123]	D-shaped fiber with gold deposited on titanium dioxide	1.33–1.43	Wavelength	46,000 nm/RIU	2.2×10^{-6}
			Amplitude	1086 RIU^{-1}	9.2×10^{-6}
[128]	Hollow-core D-shaped fiber	1.33–1.34	Wavelength	2900 nm/RIU	N/A
			Amplitude	120 RIU^{-1}	N/A
[132]	Quasi-D-shaped fiber with external graphene over ITO	1.33–1.38	Wavelength	10,693 nm/RIU	9.35×10^{-6}
			Amplitude	95 RIU^{-1}	1.05×10^{-4}
[134]	D-shaped PCF coated with indium tin oxide	1.28–1.34	Wavelength	6000 nm/RIU	1.6×10^{-7}
			Amplitude	148 RIU^{-1}	N/A
[136]	Copper–graphene-based PCF	1.33–1.37	Wavelength	2000 nm/RIU	5×10^{-5}
			Amplitude	140 RIU^{-1}	7.1×10^{-5}
[140]	Hollow-core PCF with external gold layer	1.33–1.37	Wavelength	4000 nm/RIU	2.5×10^{-5}
			Amplitude	478 RIU^{-1}	2.1×10^{-5}
[141]	PCF with annular analyte channel	1.38–1.42	Wavelength	7500 nm/RIU	1.33×10^{-5}
			Amplitude	513 RIU^{-1}	N/A

wavelength is shown in Fig. 9.9c(ii), where reported R^2 value is 1. Due to simple design and very high linearity, the proposed sensor has great potential for numerous sensing applications. Based on the birefringence effect, another simple PCF sensor has been demonstrated (Fig. 9.9d) having maximum wavelength sensitivity of 4000 nm/RIU and amplitude sensitivity of 320 RIU^{-1} [45]. Table 9.2 shows the performance comparison of the externally metal-coated PCF SPR sensors.

9.6 Future Directions

PCF-based SPR sensors are the key platform for numerous applications especially in biosensing, chemical sensing, and organic chemical sensing. All these sensing fields have potential opened area of research associated with PCF sensors. Although PCF SPR sensor is a topic of great interest, significant advancement has not been made from the point of device deployment. The major limitation of PCF SPR sensors is the fabrication challenges. Due to this fact, most of researches on PCF sensors are carried out by theoretical and simulation models. There are some experimental studies have been reported [52, 61, 115]; however, they are applicable for limited applications. Therefore, experimental investigation in order to use PCF sensors in practical applications can be a potential future work. Besides, detection of biological and biochemical analytes having wide range of refractive indices can be studied. PCF-based sensors are only implemented in laboratory-based experiments, which limit their capability for commercialization. A mobile analytical system can be developed in order to use it in field-based biosensing. Future progress of such systems can lead to highly robust, user-friendly, and compact PCF-based nanosensors.

One of the important challenges is to detect a particular molecule from a group of molecules. In general, a given system may contain undesirable molecules with similar properties. These unwanted molecules interact with the sensor causing false refractive index change. As a result, the performance of the sensor such as sensitivity, detection limit, and sensing resolution is greatly affected. The detection of the target molecules is problematic when the concentration of unwanted molecules is higher than that of target molecules. Another open issue of PCF SPR sensors is the effect of environmental perturbations such as temperature, humidity, vibration, and instrumental noise. These unwanted facts cause serious performance errors. Although few techniques have been developed to eliminate those issues, they are not matured enough [40, 142]. The current PCF sensors should be made consumers-friendly by fabricating them with simple and low-cost method. The PCF sensors should be able to reduce the test costs and rapid detections of unknown analytes.

The key challenge of PCF SPR sensors is the uniformity of the metal coating. In internally metal-coated PCF sensors, multiple air holes are selectively coated with plasmonic materials. From the fabrication point of view, it is really difficult to maintain uniform coating on selective air holes of the PCF. The externally

metal-coated PCF sensors require single metal coating, which is placed on the outer surface of the PCF. However, depositing metal on the circular surface creates huge surface roughness. Several physical methods such as vacuum evaporation [143], thermal evaporation [144], and RF sputtering [145] can be used for metal coating. Besides, several chemical methods such as chemical vapor deposition (CVD) [146], atomic layer deposition (ALD) [147], and wet-chemistry deposition [148] can be also used to deposit metal layer. However, none of these techniques provide guaranteed uniformity of the metal coating. These practical limitations are the main obstacles for employing PCF SPR sensors in practical applications. Few studies have been performed on Surface-Enhanced Raman Scattering (SERS) [149, 150], which is an important topic of metal nanoparticle-modified PCF. Research on SERS can be extended for the detection of low concentration without using fluorescent labeling. Moreover, SPR-like sensing technologies for THz frequencies are not matured. Several polymer materials such as TOPAS, HDPA, LDPA, and Teflon can be replaced by the silica background, and polaritonic materials can be used for THz sensing [100, 151].

9.7 Conclusions

In this chapter, recent advancements and challenges of PCF SPR sensors are reviewed and discussed. At first, we discuss the fundamentals of SPR and working mechanism of PCF SPR sensors. Then, we classify the PCF SPR sensors based on the location of plasmonic material deposition. Recently, results of internally metal-coated PCF SPR sensors are demonstrated and compared. We categorize the externally metal-coated PCF SPR sensors into three types: slotted PCF sensors, D-shaped PCF sensors, and improved PCF sensors. We also discuss and compare with recently proposed designs of these three categories. The study of SPR technique and PCF technology is the potential platform for level-free sensing. Progress on PCF SPR sensors is in initial stage; however, based on the experimental advancements achieved to date, PCF SPR can be regarded as an emerging sensing platform. In contrast to conventional prism-based SPR sensors, experimental setup of PCF-based sensors is relatively simple and cost-effective. Moreover, PCF SPR sensors have the potential to detect various types of biological and biochemical analytes. Although numerous simulation analyses have been performed on PCF SPR sensors, further experimental investigations are required for implementing them in practical applications such as medical diagnostics, food safety, and environmental monitoring.

References

1. C.E. Berger, J. Greve, Differential SPR immunosensing. Sens. Actuators B Chem. **63**, 103–108 (2000)
2. I. Stemmler, A. Brecht, G. Gauglitz, Compact surface plasmon resonance-transducers with spectral readout for biosensing applications. Sens. Actuators B Chem. **54**, 98–105 (1999)
3. Y. Fang, Label-free cell-based assays with optical biosensors in drug discovery. Assay Drug Dev. Technol. **4**, 583–595 (2006)
4. J. Homola, Surface plasmon resonance sensors for detection of chemical and biological species. Chem. Rev. **108**, 462–493 (2008)
5. R. Jorgenson, S. Yee, A fiber-optic chemical sensor based on surface plasmon resonance. Sens. Actuators B Chem. **12**, 213–220 (1993)
6. B.D. Gupta, R.K. Verma, Surface plasmon resonance-based fiber optic sensors: principle, probe designs, and some applications. J. Sens. **2009** (2009)
7. B. Lee, S. Roh, J. Park, Current status of micro-and nano-structured optical fiber sensors. Opt. Fiber Technol. **15**, 209–221 (2009)
8. C. Mouvet, R. Harris, C. Maciag, B. Luff, J. Wilkinson, J. Piehler et al., Determination of simazine in water samples by waveguide surface plasmon resonance. Anal. Chim. Acta **338**, 109–117 (1997)
9. C.P. Cahill, K.S. Johnston, S.S. Yee, A surface plasmon resonance sensor probe based on retro-reflection. Sens. Actuators B Chem. **45**, 161–166 (1997)
10. Y.-C. Cheng, W.-K. Su, J.-H. Liou, Application of a liquid sensor based on surface plasma wave excitation to distinguish methyl alcohol from ethyl alcohol. Opt. Eng. **39**, 311–314 (2000)
11. J. Homola, J. Dostálek, S. Chen, A. Rasooly, S. Jiang, S.S. Yee, Spectral surface plasmon resonance biosensor for detection of staphylococcal enterotoxin B in milk. Int. J. Food Microbiol. **75**, 61–69 (2002)
12. V. Koubová, E. Brynda, L. Karasová, J. Škvor, J. Homola, J. Dostálek et al., Detection of foodborne pathogens using surface plasmon resonance biosensors. Sens. Actuators B Chem. **74**, 100–105 (2001)
13. A. Nooke, U. Beck, A. Hertwig, A. Krause, H. Krüger, V. Lohse et al., On the application of gold based SPR sensors for the detection of hazardous gases. Sens. Actuators B Chem. **149**, 194–198 (2010)
14. B. Liedberg, C. Nylander, I. Lunström, Surface plasmon resonance for gas detection and biosensing. Sens. Actuators **4**, 299–304 (1983)
15. G. Ashwell, M. Roberts, Highly selective surface plasmon resonance sensor for NO2. Electron. Lett. **32**, 2089–2091 (1996)
16. M. Niggemann, A. Katerkamp, M. Pellmann, P. Bolsmann, J. Reinbold, K. Cammann, Remote sensing of tetrachloroethene with a micro-fibre optical gas sensor based on surface plasmon resonance spectroscopy. Sensors and Actuators B: Chemical **34**, 328–333 (1996)
17. P.J. Kajenski, Tunable optical filter using long-range surface plasmons. Opt. Eng. **36**, 1537–1541 (1997)
18. Y. Wang, Voltage-induced color-selective absorption with surface plasmons. Appl. Phys. Lett. **67**, 2759–2761 (1995)
19. J.S. Schildkraut, Long-range surface plasmon electrooptic modulator. Appl. Opt. **27**, 4587–4590 (1988)
20. G.T. Sincerbox, J.C. Gordon, Small fast large-aperture light modulator using attenuated total reflection. Appl. Opt. **20**, 1491–1496 (1981)
21. K.S. Johnston, S.R. Karlsen, C.C. Jung, S.S. Yee, New analytical technique for characterization of thin films using surface plasmon resonance. Mater. Chem. Phys. **42**, 242–246 (1995)
22. T. Akimoto, S. Sasaki, K. Ikebukuro, I. Karube, Refractive-index and thickness sensitivity in surface plasmon resonance spectroscopy. Appl. Opt. **38**, 4058–4064 (1999)

23. Y.-D. Su, S.-J. Chen, T.-L. Yeh, Common-path phase-shift interferometry surface plasmon resonance imaging system. Opt. Lett. **30**, 1488–1490 (2005)
24. L. Wang, R.J.H. Ng, S. Safari Dinachali, M. Jalali, Y. Yu, J.K. Yang, Large area plasmonic color palettes with expanded gamut using colloidal self-assembly. ACS Photonics **3**, 627–633 (2016)
25. S.A. Maier, Plasmonics: The promise of highly integrated optical devices. IEEE J. Sel. Top. Quantum Electron. **12**, 1671–1677 (2006)
26. S.P. Burgos, H.W. Lee, E. Feigenbaum, R.M. Briggs, H.A. Atwater, Synthesis and characterization of plasmonic resonant guided wave networks. Nano Lett. **14**, 3284–3292 (2014)
27. J. Zenneck, Über die Fortpflanzung ebener elektromagnetischer Wellen längs einer ebenen Leiterfläche und ihre Beziehung zur drahtlosen Telegraphie. Ann. Phys. **328**, 846–866 (1907)
28. A. Sommerfeld, Über die Ausbreitung der Wellen in der drahtlosen Telegraphie. Ann. Phys. **333**, 665–736 (1909)
29. R. Ritchie, Plasma losses by fast electrons in thin films. Phys. Rev. **106**, 874 (1957)
30. E. Kretschmann, H. Raether, Radiative decay of non radiative surface plasmons excited by light. Zeitschrift für Naturforschung A **23**, 2135–2136 (1968)
31. A. Otto, Excitation of nonradiative surface plasma waves in silver by the method of frustrated total reflection. Zeitschrift für Physik **216**, 398–410 (1968)
32. M. Piliarik, J. Homola, Z. Manıková, J. Čtyroký, Surface plasmon resonance sensor based on a single-mode polarization-maintaining optical fiber. Sens. Actuators B Chem. **90**, 236–242 (2003)
33. D. Monzón-Hernández, J. Villatoro, High-resolution refractive index sensing by means of a multiple-peak surface plasmon resonance optical fiber sensor. Sens. Actuators B Chem. **115**, 227–231 (2006)
34. D. Monzón-Hernández, J. Villatoro, D. Talavera, D. Luna-Moreno, Optical-fiber surface-plasmon resonance sensor with multiple resonance peaks. Appl. Opt. **43**, 1216–1220 (2004)
35. B. Gupta, A.K. Sharma, Sensitivity evaluation of a multi-layered surface plasmon resonance-based fiber optic sensor: a theoretical study. Sens. Actuators B Chem. **107**, 40–46 (2005)
36. M. Skorobogatiy, A.V. Kabashin, Photon crystal waveguide-based surface plasmon resonance biosensor. Appl. Phys. Lett. **89**, 143518 (2006)
37. B. Gauvreau, A. Hassani, M.F. Fehri, A. Kabashin, M. Skorobogatiy, Photonic bandgap fiber-based surface plasmon resonance sensors. Opt. Express **15**, 11413–11426 (2007)
38. A. Hassani, B. Gauvreau, M.F. Fehri, A. Kabashin, M. Skorobogatiy, Photonic crystal fiber and waveguide-based surface plasmon resonance sensors for application in the visible and near-IR. Electromagnetics **28**, 198–213 (2008)
39. Q. Wei, L. Shu-Guang, X. Jian-Rong, X. Xü-Jun, Z. Lei, Numerical analysis of a photonic crystal fiber based on two polarized modes for biosensing applications. Chin. Phys. B **22**, 074213 (2013)
40. B. Shuai, L. Xia, Y. Zhang, D. Liu, A multi-core holey fiber based plasmonic sensor with large detection range and high linearity. Opt. Express **20**, 5974–5986 (2012)
41. B. Shuai, L. Xia, D. Liu, Coexistence of positive and negative refractive index sensitivity in the liquid-core photonic crystal fiber based plasmonic sensor. Opt. Express **20**, 25858–25866 (2012)
42. A.A. Rifat, G.A. Mahdiraji, D.M. Chow, Y.G. Shee, R. Ahmed, F.R.M. Adikan, Photonic crystal fiber-based surface plasmon resonance sensor with selective analyte channels and graphene-silver deposited core. Sensors **15**, 11499–11510 (2015)
43. J.N. Dash, R. Jha, SPR biosensor based on polymer PCF coated with conducting metal oxide. IEEE Photonics Technol. Lett. **26**, 595–598 (2014)
44. J.N. Dash, R. Jha, Graphene-based birefringent photonic crystal fiber sensor using surface plasmon resonance. IEEE Photonics Technol. Lett. **26**, 1092–1095 (2014)

45. A. Rifat, G.A. Mahdiraji, Y. Sua, Y. Shee, R. Ahmed, D.M. Chow et al., Surface plasmon resonance photonic crystal fiber biosensor: a practical sensing approach. IEEE Photon. Technol. Lett. **27**, 1628–1631 (2015)
46. L. Peng, F. Shi, G. Zhou, S. Ge, Z. Hou, C. Xia, A surface plasmon biosensor based on a D-shaped microstructured optical fiber with rectangular lattice. IEEE Photonics J. **7**, 1–9 (2015)
47. F. Shi, L. Peng, G. Zhou, X. Cang, Z. Hou, C. Xia, An elliptical core D-shaped photonic crystal fiber-based plasmonic sensor at upper detection limit. Plasmonics **10**, 1263–1268 (2015)
48. A.K. Mishra, S.K. Mishra, B.D. Gupta, SPR based fiber optic sensor for refractive index sensing with enhanced detection accuracy and figure of merit in visible region. Opt. Commun. **344**, 86–91 (2015)
49. Q. Liu, S. Li, H. Chen, J. Li, Z. Fan, High-sensitivity plasmonic temperature sensor based on photonic crystal fiber coated with nanoscale gold film. Appl. Phys. Express **8**, 046701 (2015)
50. R. Otupiri, E.K. Akowuah, S. Haxha, Multi-channel SPR biosensor based on PCF for multi-analyte sensing applications. Opt. Express **23**, 15716–15727 (2015)
51. Y. Zhao, Z.-Q. Deng, J. Li, Photonic crystal fiber based surface plasmon resonance chemical sensors. Sens. Actuators B Chem. **202**, 557–567 (2014)
52. X. Yang, Y. Lu, M. Wang, J. Yao, A photonic crystal fiber glucose sensor filled with silver nanowires. Opt. Commun. **359**, 279–284 (2016)
53. J.N. Dash, R. Jha, Highly sensitive D shaped PCF sensor based on SPR for near IR. Opt. Quantum Electron. **48**, 137 (2016)
54. M.F.O. Hameed, M.Y. Azab, A. Heikal, S.M. El-Hefnawy, S. Obayya, Highly sensitive plasmonic photonic crystal temperature sensor filled with liquid crystal. IEEE Photonics Technol. Lett. **28**, 59–62 (2016)
55. C. Liu, F. Wang, J. Lv, T. Sun, Q. Liu, C. Fu et al., A highly temperature-sensitive photonic crystal fiber based on surface plasmon resonance. Opt. Commun. **359**, 378–382 (2016)
56. S. Singh, S.K. Mishra, B.D. Gupta, Sensitivity enhancement of a surface plasmon resonance based fibre optic refractive index sensor utilizing an additional layer of oxides. Sens. Actuators A **193**, 136–140 (2013)
57. M.R. Hasan, M.I. Hasan, M.S. Anower, Tellurite glass defect-core spiral photonic crystal fiber with low loss and large negative flattened dispersion over S + C + L + U wavelength bands. Appl. Opt. **54**, 9456–9461 (2015)
58. M.R. Hasan, M.S. Anower, M.I. Hasan, A Polarization Maintaining Single-Mode Photonic Crystal Fiber for Residual Dispersion Compensation. IEEE Photonics Technol. Lett. **28**, 1782–1785 (2016)
59. M.R. Hasan, M.S. Anower, M.I. Hasan, Polarization maintaining highly nonlinear photonic crystal fiber with closely lying two zero dispersion wavelengths. Opt. Eng. **55**, 056107–056107 (2016)
60. R. Ahmmed, R. Ahmed, S.A. Razzak, Design of large negative dispersion and modal analysis for hexagonal, square, FCC and BCC photonic crystal fibers, in *2013 International Conference on Informatics, Electronics & Vision (ICIEV)* (2013), pp. 1–6
61. A.A. Rifat, R. Ahmed, A.K. Yetisen, H. Butt, A. Sabouri, G.A. Mahdiraji et al., Photonic crystal fiber based plasmonic sensors. Sens. Actuators B Chem. **243**, 311–325 (2017)
62. J. Homola, Present and future of surface plasmon resonance biosensors. Anal. Bioanal. Chem. **377**, 528–539 (2003)
63. J. Homola, Electromagnetic theory of surface plasmons, in *Surface plasmon resonance based sensors* (2006), pp. 3–44
64. A.K. Sharma, R. Jha, B. Gupta, Fiber-optic sensors based on surface plasmon resonance: a comprehensive review. IEEE Sens. J. **7**, 1118–1129 (2007)
65. K.M. McPeak, S.V. Jayanti, S.J. Kress, S. Meyer, S. Iotti, A. Rossinelli et al., Plasmonic films can easily be better: rules and recipes. ACS Photonics **2**, 326–333 (2015)

66. T. Wieduwilt, A. Tuniz, S. Linzen, S. Goerke, J. Dellith, U. Hübner et al., Ultrathin niobium nanofilms on fiber optical tapers–a new route towards low-loss hybrid plasmonic modes. Sci. Rep. **5** (2015)
67. P.B. Johnson, R.-W. Christy, Optical constants of the noble metals. Phys. Rev. B **6**, 4370 (1972)
68. G.V. Naik, V.M. Shalaev, A. Boltasseva, Alternative plasmonic materials: beyond gold and silver. Adv. Mater. **25**, 3264–3294 (2013)
69. S.A. Zynio, A.V. Samoylov, E.R. Surovtseva, V.M. Mirsky, Y.M. Shirshov, Bimetallic layers increase sensitivity of affinity sensors based on surface plasmon resonance. Sensors **2**, 62–70 (2002)
70. N.D. Orf, O. Shapira, F. Sorin, S. Danto, M.A. Baldo, J.D. Joannopoulos et al., Fiber draw synthesis. Proc. Natl. Acad. Sci. **108**, 4743–4747 (2011)
71. M.A. Ordal, R.J. Bell, R.W. Alexander, L.L. Long, M.R. Querry, Optical properties of fourteen metals in the infrared and far infrared: Al, Co, Cu, Au, Fe, Pb, Mo, Ni, Pd, Pt, Ag, Ti, V, and W. Appl. Opt. **24**, 4493–4499 (1985)
72. P.G. Etchegoin, E. Le Ru, M. Meyer, Erratum: an analytic model for the optical properties of gold. J. Chem. Phys. **125**, 164705 (2006); J. Chem. Phys. **127**, 189901 (2007)
73. P.R. West, S. Ishii, G.V. Naik, N.K. Emani, V.M. Shalaev, A. Boltasseva, Searching for better plasmonic materials. Laser Photonics Rev. **4**, 795–808 (2010)
74. V. Kravets, R. Jalil, Y.-J. Kim, D. Ansell, D. Aznakayeva, B. Thackray et al., Graphene-protected copper and silver plasmonics. Sci. Rep. **4** (2014)
75. M. Schriver, W. Regan, W.J. Gannett, A.M. Zaniewski, M.F. Crommie, A. Zettl, Graphene as a long-term metal oxidation barrier: worse than nothing. ACS Nano **7**, 5763–5768 (2013)
76. M.M. Huq, C.-T. Hsieh, Z.-W. Lin, C.-Y. Yuan, One-step electrophoretic fabrication of a graphene and carbon nanotube-based scaffold for manganese-based pseudocapacitors. RSC Adv. **6**, 87961–87968 (2016)
77. I. Doron-Mor, Z. Barkay, N. Filip-Granit, A. Vaskevich, I. Rubinstein, Ultrathin gold island films on silanized glass. Morphology and optical properties. Chem. Mater. **16**, 3476–3483 (2004)
78. S. Szunerits, V.G. Praig, M. Manesse, R. Boukherroub, Gold island films on indium tin oxide for localized surface plasmon sensing. Nanotechnology **19**, 195712 (2008)
79. C. Granata, A. Vettoliere, M. Russo, B. Ruggiero, Noise theory of dc nano-SQUIDs based on Dayem nanobridges. Phys. Rev. B **84**, 224516 (2011)
80. A. Troeman, S. van der Ploeg, E. Il'Ichev, H.-G. Meyer, A. A. Golubov, M. Y. Kupriyanov et al., Temperature dependence measurements of the supercurrent-phase relationship in niobium nanobridges. Phys. Rev. B **77**, 024509 (2008)
81. M. Schmelz, Y. Matsui, R. Stolz, V. Zakosarenko, T. Schönau, S. Anders et al., Investigation of all niobium nano-SQUIDs based on sub-micrometer cross-type Josephson junctions. Supercond. Sci. Technol. **28**, 015004 (2014)
82. K. Sokhey, S. Rai, G. Lodha, Oxidation studies of niobium thin films at room temperature by X-ray reflectivity. Appl. Surf. Sci. **257**, 222–226 (2010)
83. S. Franzen, Surface plasmon polaritons and screened plasma absorption in indium tin oxide compared to silver and gold. J. Phys. Chem. C **112**, 6027–6032 (2008)
84. C. Rhodes, M. Cerruti, A. Efremenko, M. Losego, D. Aspnes, J.-P. Maria et al., Dependence of plasmon polaritons on the thickness of indium tin oxide thin films. J. Appl. Phys. **103**, 093108 (2008)
85. R.K. Verma, B.D. Gupta, Surface plasmon resonance based fiber optic sensor for the IR region using a conducting metal oxide film. JOSA A **27**, 846–851 (2010)
86. A. Tubb, F. Payne, R. Millington, C. Lowe, Single-mode optical fibre surface plasma wave chemical sensor. Sens. Actuators B Chem. **41**, 71–79 (1997)
87. W. Peng, S. Banerji, Y.-C. Kim, K.S. Booksh, Investigation of dual-channel fiber-optic surface plasmon resonance sensing for biological applications. Opt. Lett. **30**, 2988–2990 (2005)

88. Y. Zhang, C. Zhou, L. Xia, X. Yu, D. Liu, Wagon wheel fiber based multichannel plasmonic sensor. Opt. Express **19**, 22863–22873 (2011)
89. R. Verma, B. Gupta, Theoretical modelling of a bi-dimensional U-shaped surface plasmon resonance based fibre optic sensor for sensitivity enhancement. J. Phys. D Appl. Phys. **41**, 095106 (2008)
90. S.-F. Wang, M.-H. Chiu, R.-S. Chang, Numerical simulation of a D-type optical fiber sensor based on the Kretchmann's configuration and heterodyne interferometry. Sens. Actuators B Chem. **114**, 120–126 (2006)
91. Y.-C. Kim, W. Peng, S. Banerji, K.S. Booksh, Tapered fiber optic surface plasmon resonance sensor for analyses of vapor and liquid phases. Opt. Lett. **30**, 2218–2220 (2005)
92. M.-C. Navarrete, N. Díaz-Herrera, A. González-Cano, Ó. Esteban, Surface plasmon resonance in the visible region in sensors based on tapered optical fibers. Sens. Actuators B Chem. **190**, 881–885 (2014)
93. B. Špačková, J. Homola, Theoretical analysis of a fiber optic surface plasmon resonance sensor utilizing a Bragg grating. Opt. Express **17**, 23254–23264 (2009)
94. J. Zhao, S. Cao, C. Liao, Y. Wang, G. Wang, X. Xu et al., Surface plasmon resonance refractive sensor based on silver-coated side-polished fiber. Sens. Actuators B Chem. **230**, 206–211 (2016)
95. T.T. Nguyen, K.T.L. Trinh, W.J. Yoon, N.Y. Lee, H. Ju, Integration of a microfluidic polymerase chain reaction device and surface plasmon resonance fiber sensor into an inline all-in-one platform for pathogenic bacteria detection. Sens. Actuators B Chem. **242**, 1–8 (2017)
96. K. Bremer, B. Roth, Fibre optic surface plasmon resonance sensor system designed for smartphones. Opt. Express **23**, 17179–17184 (2015)
97. Y. Yuan, T. Guo, X. Qiu, J. Tang, Y. Huang, L. Zhuang et al., Electrochemical surface plasmon resonance fiber-optic sensor: in situ detection of electroactive biofilms. Anal. Chem. **88**, 7609–7616 (2016)
98. M.R. Hasan, S. Akter, T. Khatun, A.A. Rifat, M.S. Anower, Dual-hole unit-based kagome lattice microstructure fiber for low-loss and highly birefringent terahertz guidance. Opt. Eng. **56**, 043108–043108 (2017)
99. T.A. Birks, J.C. Knight, P.S.J. Russell, Endlessly single-mode photonic crystal fiber. Opt. Lett. **22**, 961–963 (1997)
100. M.R. Hasan, M.S. Anower, M.I. Hasan, S. Razzak, Polarization maintaining low-loss slotted core kagome lattice THz fiber. IEEE Photonics Technol. Lett. **28**, 1751–1754 (2016)
101. M.R. Hasan, M.A. Islam, A.A. Rifat, M.I. Hasan, A single-mode highly birefringent dispersion-compensating photonic crystal fiber using hybrid cladding. J. Mod. Opt. **64**, 218–225 (2017)
102. R. Slavík, J. Homola, J. Čtyroký, Single-mode optical fiber surface plasmon resonance sensor. Sens. Actuators B Chem. **54**, 74–79 (1999)
103. D. Gao, C. Guan, Y. Wen, X. Zhong, L. Yuan, Multi-hole fiber based surface plasmon resonance sensor operated at near-infrared wavelengths. Opt. Commun. **313**, 94–98 (2014)
104. W. Qin, S. Li, Y. Yao, X. Xin, J. Xue, Analyte-filled core self-calibration microstructured optical fiber based plasmonic sensor for detecting high refractive index aqueous analyte. Opt. Lasers Eng. **58**, 1–8 (2014)
105. Z. Fan, S. Li, Q. Liu, G. An, H. Chen, J. Li et al., High sensitivity of refractive index sensor based on analyte-filled photonic crystal fiber with surface plasmon resonance. IEEE Photonics J. **7**, 1–9 (2015)
106. X. Yu, Y. Zhang, S. Pan, P. Shum, M. Yan, Y. Leviatan et al., A selectively coated photonic crystal fiber based surface plasmon resonance sensor. J. Opt. **12**, 015005 (2009)
107. P. Bing, J. Yao, Y. Lu, Z. Li, A surface-plasmon-resonance sensor based on photonic-crystal-fiber with large size microfluidic channels. Opt. Appl **42**, 493–501 (2012)
108. W.L. Ng, A.A. Rifat, W.R. Wong, G. Mahdiraji, F.M. Adikan, A novel diamond ring fiber-based surface plasmon resonance sensor. Plasmonics, 1–6 (2017)

109. A.A. Rifat, G. Mahdiraji, Y.M. Sua, R. Ahmed, Y. Shee, F.M. Adikan, Highly sensitive multi-core flat fiber surface plasmon resonance refractive index sensor. Opt. Express **24**, 2485–2495 (2016)
110. X. Yang, Y. Lu, B. Liu, J. Yao, Analysis of graphene-based photonic crystal fiber sensor using birefringence and surface plasmon resonance. Plasmonics **12**, 489–496 (2017)
111. D. Li, W. Zhang, H. Liu, J. Hu, G. Zhou, High sensitivity refractive index sensor based on multicoating photonic crystal fiber with surface plasmon resonance at near-infrared wavelength. IEEE Photonics J. **9**, 1–8 (2017)
112. C. Liu, L. Yang, X. Lu, Q. Liu, F. Wang, J. Lv et al., Mid-infrared surface plasmon resonance sensor based on photonic crystal fibers. Opt. Express **25**, 14227–14237 (2017)
113. G. An, S. Li, X. Yan, X. Zhang, Z. Yuan, H. Wang et al., Extra-broad photonic crystal fiber refractive index sensor based on surface plasmon resonance. Plasmonics **12**, 465–471 (2017)
114. X. Fu, Y. Lu, X. Huang, J. Yao, Surface plasmon resonance sensor based on photonic crystal fiber filled with silver nanowires. Opt. Appl **41**, 941–951 (2011)
115. Y. Lu, M. Wang, C. Hao, Z. Zhao, J. Yao, Temperature sensing using photonic crystal fiber filled with silver nanowires and liquid. IEEE Photonics J. **6**, 1–7 (2014)
116. Y. Lu, X. Yang, M. Wang, J. Yao, Surface plasmon resonance sensor based on hollow-core PCFs filled with silver nanowires. Electron. Lett. **51**, 1675–1677 (2015)
117. N. Luan, J. Yao, A hollow-core photonic crystal fiber-based SPR sensor with large detection range. IEEE Photonics J. (2017)
118. S.I. Azzam, M.F.O. Hameed, R.E.A. Shehata, A. Heikal, S.S. Obayya, Multichannel photonic crystal fiber surface plasmon resonance based sensor. Opt. Quant. Electron. **48**, 142 (2016)
119. A. Hassani, M. Skorobogatiy, Photonic crystal fiber-based plasmonic sensors for the detection of biolayer thickness. J. Opt. Soc. Am. B **26**, 1550 (2009)
120. E.K. Akowuah, T. Gorman, H. Ademgil, S. Haxha, G.K. Robinson, J.V. Oliver, Numerical analysis of a photonic crystal fiber for biosensing applications. IEEE J. Quantum Electron. **48**, 1403–1410 (2012)
121. R. Otupiri, E. Akowuah, S. Haxha, H. Ademgil, F. AbdelMalek, A. Aggoun, A novel birefrigent photonic crystal fiber surface plasmon resonance biosensor. IEEE Photonics J. **6**, 1–11 (2014)
122. M.F.O. Hameed, Y.K. Alrayk, A.A. Shaalan, W.S. El Deeb, S.S. Obayya, Design of highly sensitive multichannel bimetallic photonic crystal fiber biosensor. J. Nanophotonics **10**, 046016–046016 (2016)
123. A.A. Rifat, R. Ahmed, G.A. Mahdiraji, F.M. Adikan, Highly sensitive d-shaped photonic crystal fiber-based plasmonic biosensor in visible to near-IR. IEEE Sens. J. **17**, 2776–2783 (2017)
124. M. Tian, P. Lu, L. Chen, C. Lv, D. Liu, All-solid D-shaped photonic fiber sensor based on surface plasmon resonance. Opt. Commun. **285**, 1550–1554 (2012)
125. Z. Tan, X. Li, Y. Chen, P. Fan, Improving the sensitivity of fiber surface plasmon resonance sensor by filling liquid in a hollow core photonic crystal fiber. Plasmonics **9**, 167–173 (2014)
126. J.N. Dash, R. Jha, On the performance of graphene-based D-shaped photonic crystal fibre biosensor using surface plasmon resonance. Plasmonics **10**, 1123–1131 (2015)
127. D.F. Santos, A. Guerreiro, J.M. Baptista, SPR microstructured D-type optical fiber sensor configuration for refractive index measurement. IEEE Sens. J. **15**, 5472–5477 (2015)
128. N. Luan, R. Wang, W. Lv, J. Yao, Surface plasmon resonance sensor based on D-shaped microstructured optical fiber with hollow core. Opt. Express **23**, 8576–8582 (2015)
129. Z. Fan, S. Li, H. Chen, Q. Liu, W. Zhang, G. An et al., Numerical analysis of polarization filter characteristics of D-shaped photonic crystal fiber based on surface plasmon resonance. Plasmonics **10**, 675–680 (2015)
130. Z. Tan, X. Hao, Y. Shao, Y. Chen, X. Li, P. Fan, Phase modulation and structural effects in a D-shaped all-solid photonic crystal fiber surface plasmon resonance sensor. Opt. Express **22**, 15049–15063 (2014)

131. Y. Chen, Q. Xie, X. Li, H. Zhou, X. Hong, Y. Geng, Experimental realization of D-shaped photonic crystal fiber SPR sensor. J. Phys. D Appl. Phys. **50**, 025101 (2016)
132. G. An, S. Li, H. Wang, X. Zhang, Metal Oxide-Graphene-Based Quasi-D-Shaped Optical Fiber Plasmonic Biosensor. IEEE Photonics J. **9**, 1–9 (2017)
133. R.K. Gangwar, V.K. Singh, Highly sensitive surface plasmon resonance based D-shaped photonic crystal fiber refractive index sensor. Plasmonics, 1–6 (2016)
134. T. Huang, Highly sensitive SPR sensor based on D-shaped photonic crystal fiber coated with indium tin oxide at near-infrared wavelength. Plasmonics **12**, 583–588 (2017)
135. X. Yang, Y. Lu, M. Wang, J. Yao, An exposed-core grapefruit fibers based surface plasmon resonance sensor. Sensors **15**, 17106–17114 (2015)
136. A.A. Rifat, G.A. Mahdiraji, R. Ahmed, D.M. Chow, Y. Sua, Y. Shee et al., Copper-graphene-based photonic crystal fiber plasmonic biosensor. IEEE Photonics J. **8**, 1–8 (2016)
137. V. Popescu, N. Puscas, G. Perrone, Power absorption efficiency of a new microstructured plasmon optical fiber. JOSA B **29**, 3039–3046 (2012)
138. V. Popescu, N. Puscas, G. Perrone, Strong power absorption in a new microstructured holey fiber-based plasmonic sensor. JOSA B **31**, 1062–1070 (2014)
139. A. Rifat, G.A. Mahdiraji, Y. Shee, M.J. Shawon, F.M. Adikan, A novel photonic crystal fiber biosensor using surface plasmon resonance. Proced. Eng. **140**, 1–7 (2016)
140. A.A. Rifat, M.R. Hasan, R. Ahmed, H. Butt, Photonic crystal fiber-based plasmonic biosensor with external sensing approach. J. Nanophotonics **12503**, 1 (2018)
141. C. Liu, L. Yang, W. Su, F. Wang, T. Sun, Q. Liu et al., Numerical analysis of a photonic crystal fiber based on a surface plasmon resonance sensor with an annular analyte channel. Opt. Commun. **382**, 162–166 (2017)
142. I.M. White, X. Fan, On the performance quantification of resonant refractive index sensors. Opt. Express **16**, 1020–1028 (2008)
143. R. Klenk, T. Walter, H.W. Schock, D. Cahen, A model for the successful growth of polycrystalline films of CuInSe2 by multisource physical vacuum evaporation. Adv. Mater. **5**, 114–119 (1993)
144. M.C. Barnes, D.-Y. Kim, H.S. Ahn, C.O. Lee, N.M. Hwang, Deposition mechanism of gold by thermal evaporation: approach by charged cluster model. J. Cryst. Growth **213**, 83–92 (2000)
145. L. Armelao, D. Barreca, G. Bottaro, G. Bruno, A. Gasparotto, M. Losurdo et al., RF-sputtering of gold on silica surfaces: evolution from clusters to continuous films. Mater. Sci. Eng., C **25**, 599–603 (2005)
146. P.J. Sazio, A. Amezcua-Correa, C.E. Finlayson, J.R. Hayes, T.J. Scheidemantel, N.F. Baril et al., Microstructured optical fibers as high-pressure microfluidic reactors. Science **311**, 1583–1586 (2006)
147. M.B. Griffiths, P.J. Pallister, D.J. Mandia, S.N.T. Barry, Atomic layer deposition of gold metal. Chem. Mater. **28**, 44–46 (2015)
148. J.A. Sioss, C.D. Keating, Batch preparation of linear Au and Ag nanoparticle chains via wet chemistry. Nano Lett. **5**, 1779–1783 (2005)
149. Z. Chen, Z. Dai, N. Chen, S. Liu, F. Pang, B. Lu et al., Gold nanoparticles-modified tapered fiber nanoprobe for remote SERS detection. IEEE Photonics Technol. Lett. **26**, 777–780 (2014)
150. M.K.K. Oo, Y. Han, R. Martini, S. Sukhishvili, H. Du, Forward-propagating surface-enhanced Raman scattering and intensity distribution in photonic crystal fiber with immobilized Ag nanoparticles. Opt. Lett. **34**, 968–970 (2009)
151. M.R. Hasan, M.A. Islam, M. Anower, S. Razzak, Low-loss and bend-insensitive terahertz fiber using a rhombic-shaped core. Appl. Opt. **55**, 8441–8447 (2016)

Chapter 10
Multifunctional Plasmonic Photonic Crystal Fiber Biosensors

Mohammad Y. Azab, Mohamed Farhat O. Hameed, Abed M. Nasr and S. S. A. Obayya

Abstract In this chapter, two novel designs of compact surface plasmon resonance multifunctional biosensors based on nematic liquid crystal (NLC) and Alcohol mixture photonic crystal fibers (PCFs) are proposed and studied. The suggested sensors have a central hole filled either with NLC or alcohol mixture as temperature-dependent materials. Further, another large hole filled with liquid analyte has a gold nanorod as a plasmonic material. Therefore, the proposed sensors can be used for temperature and analyte refractive index sensing via the coupling between the core-guided modes in the central hole and the surface plasmon modes around the gold nanorod. The effects of the structure geometrical parameters are studied to maximize the sensitivity of the PCF biosensors. The numerical analysis is carried out using full-vectorial finite element method with perfectly matched layer boundary conditions. The reported multifunctional NLC-based sensor offers high sensitivity of 5 nm/°C and 3700 nm/RIU (refractive index unit) for temperature and analyte refractive index sensing, respectively. In addition, the alcohol mixture PCF sensor achieves high-temperature sensitivity of 13.1 nm/°C with high analyte

M. Y. Azab · M. F. O. Hameed (✉) · A. M. Nasr
Mathematics and Engineering Physics Department, Faculty of Engineering, Mansoura University, Mansoura 35516, Egypt
e-mail: mfarahat@zewailcity.edu.eg

M. F. O. Hameed
Center for Photonics and Smart Materials and Nanotechnology Engineering Program, Zewail City of Science and Technology, October Gardens, 6th of October City, Giza, Egypt

S. S. A. Obayya
Centre for Photonics and Smart Materials, Zewail City of Science and Technology, October Gardens, 6th of October City, Giza, Egypt
e-mail: sobayya@zewailcity.edu.eg

S. S. A. Obayya
Electronics and Communication Engineering Department, Faculty of Engineering, Mansoura University, Mansoura, Egypt

© Springer International Publishing AG, part of Springer Nature 2019

M. F. O. Hameed and S. Obayya (eds.), *Computational Photonic Sensors*, https://doi.org/10.1007/978-3-319-76556-3_10

refractive index sensitivity of 12700 nm/RIU. To the best of the authors' knowledge, it is the first time to introduce PCF biosensor with high sensitivity for temperature and analyte refractive index sensing as well. Further, the achieved sensitivity values of the alcohol sensor are far higher than those reported in the literature.

Keywords Multifunctional sensors · Photonic crystal fiber · Liquid crystal Surface plasmon · Alcohol

10.1 Introduction

Plasmonics sensors based on photonic crystal fibers (PCFs) have recently aroused interests in the field of optical sensing [1–4]. The sensing mechanism depends mainly on the coupling between the surface plasmon modes (SPMs) around a metal surface and the core-guided modes inside a near medium. The coupling takes place when the real part of the effective indices of a core mode and surface plasmon mode are equal. Therefore, matching exists and maximum power transfer occurs from the core-guided mode to the SPM and resonance is attained. The resonance happens at a specific wavelength with a determined refractive index for the surrounding medium. When the medium refractive index changes, a shift in the resonant wavelength occurs, and hence, the sensor sensitivity can be detected.

Numerous researches have been directed for designing temperature and analyte biosensors based on PCFs. In this regard, a tunable optical filter sensor has been demonstrated using NLC where a minimum refractive index detectivity of 10^{-5} is achieved [5]. Ismail et al. [6] have reported 1-D Bragg grating photonic crystal temperature sensor with sensitivity of 0.014 nm/°C at which the temperature variation affects the characteristics of an insulated-gate bipolar transistor. In addition, liquid sealed PCF sensor based on in-line modal interferometers with slight better sensitivity of 0.0166 nm/°C was reported by Qiu et al. [7]. Further, a coupling between core modes and SPMs was demonstrated by Peng et al. [8] with sensitivity of 0.072 nm/°C. Furthermore, a surface plasmon resonance (SPR) temperature sensor based on PCF filled with different concentrations of analyte and silver nanowires [9] was reported with sensitivity of 2.7 nm/°C. Additionally, Hu et al. [10] have proposed a directional coupler sensor based on nematic liquid crystal (NLC) PCF with sensitivity of 3.86 nm/°C. Moreover, a temperature sensor based on SPR PCF filled with a liquid mixture of ethanol and chloroform achieved sensitivity of 4 nm/°C [4]. Recently, the use of the NLCs as a sensing medium along with SPR on nanogold wire offers high sensitivity of 10 nm/°C as reported by Hameed et al. [11].

On the other hand, concerning the analyte refractive index biosensing, Hassani and Skorobogatiy [1] have reported biosensors with sensitivity of 3000 nm/RIU. Additionally, Akowuah et al. [12] have presented SPR PCF biosensor with sensitivity of 4000 nm/RIU. Furthermore, PCF biosensor for multi-analyte/multichannel

sensing with spectral sensitivities of 2000 nm/RIU and 1500 nm/RIU according to the HE_{11}^{x} and HE_{11}^{y} modes, respectively, was proposed by Akowuah et al. [13]. Moreover, Otupiri et al. [14] have presented SPR birefringent PCF with spectral sensitivities of 1700 nm/RIU and 2000 nm/RIU using HE_{11}^{y} and HE_{11}^{x} modes, respectively. Qin et al. [15] have also reported PCF biosensor selectively filled with the analyte with sensitivity of 4354.3 nm/RIU and 2280 nm/RIU for two resonance peaks. Furthermore, a self-calibration biosensor based on SP PCF has been designed in [16] which has sensitivity of 6700 nm/RIU for the y-polarized core mode and 10000 nm/RIU for the x-polarized core mode. The corresponding resolutions are equal to 1.49×10^{-5} RIU and 1.0×10^{-5} RIU, respectively. However, such a configuration [16] depends on elliptical-shaped holes, which will be difficult for fabrication. Additionally, a multichannel PCF sensor is introduced in [17] which is based on four microfluidic slots with their surfaces metalized to enable the excitation of the SPR modes. The reported sensor [17] has relatively high sensitivities up to 2200, 2400, 2200, and 2400 nm/RIU according to the H_x^{11}, H_y^{11}, H_x^{12}, and H_y^{12} modes, respectively. Moreover, a multichannel sensor presented in [18] is based on a bimetallic configuration with two microfluidic slots and asymmetric core region. The reported sensor achieves high sensitivity of about 4750 nm/RIU and 4300 nm/RIU with corresponding resolutions of 2.1×10^{-5} RIU, and 2.33×10^{-5} RIU according to the quasi-transverse magnetic (TM) and quasi-transverse electric (TE) modes, respectively. Furthermore, a SP PCF temperature sensor has been reported [19] with a large central hole filled with LC material and coated by gold layer which offers sensitivity of 4 nm/°C. Additionally, Areed et al. [20] presented a refractometer for glucose concentration monitoring based on two-dimensional photonic crystal (PhC) with face-shaped defect filled with the analyzed analyte. The proposed sensor [20] offers linear sensitivity of 359 nm/RIU with an average quality factor of 477.

In this chapter, two novel multifunctional SPR-based PCF sensors are presented and analyzed. The first design uses liquid crystals (LCs) as a temperature-dependent material, while the second structure relies on alcohol mixture for temperature sensing. The proposed biosensors have a triangular lattice with a central hole filled with a temperature-dependent material. Further, the adjacent hole is filled with the analyte sample. A gold nanorod is added into the filled analyte hole which facilitates the coupling for both temperature and analyte refractive index sensing. The resonance wavelength supported by the gold nanorod is affected by the change in temperature or analyte refractive index. Therefore, the change in the resonance wavelength can be used to detect the temperature or the analyte refractive index variations. The first SPR PCF sensor has a fluorite crown of type FK51A [11] as a background material. The refractive index of the FK51A is close to that of the ordinary index of the NLC, which improves the coupling efficiency between the core modes and plasmonic modes. However, the second design includes silica glass as a background material. The analysis of the reported biosensors is performed using Comsol Multiphysics software package [21] based on finite element method (FEM) with perfectly matched layer (PML) boundary conditions [22]. The

numerical simulations for the LC core sensor demonstrate that a temperature sensitivity as high as 5 nm/°C can be achieved. Further, high refractive index sensitivity of 3700 nm/RIU (refractive index unit) can be attained by the same sensor. The achieved sensitivity values of the LC sensor are comparable to those in the literature [4, 6, 7, 9, 11, 13, 16–20] with temperature and analyte refractive index-sensing capabilities. In addition, the second sensor with alcohol mixture achieves very high-temperature sensitivity of 13.1 nm/°C which is superior to all those reported in the literature. Moreover, the alcohol mixture sensor has a high refractive index sensitivity of 12700 nm/RIU which is also far higher than the achieved sensitivities of the proceeding sensors with temperature and analyte refractive index-sensing capabilities.

10.2 NLC-SPR PCF Sensor

10.2.1 Design Considerations

Figure 10.1 presents the cross section of the suggested multifunctional biosensors. The proposed designs have two rings of airholes arranged in a triangular lattice with a hole pitch Λ and airhole diameter d. In addition, the central hole with diameter D_C is filled with temperature-dependent material and the right adjacent hole with diameter D_W is infiltrated with the analyte sample. Further, a gold nanorod with diameter D_{rod} is added to the left corner of the analyte-filled hole. In the first design, the FK51A is chosen as a background material rather than silica glass as shown in Fig. 10.2. This is due to the coupling enhancement between the quasi-TE core

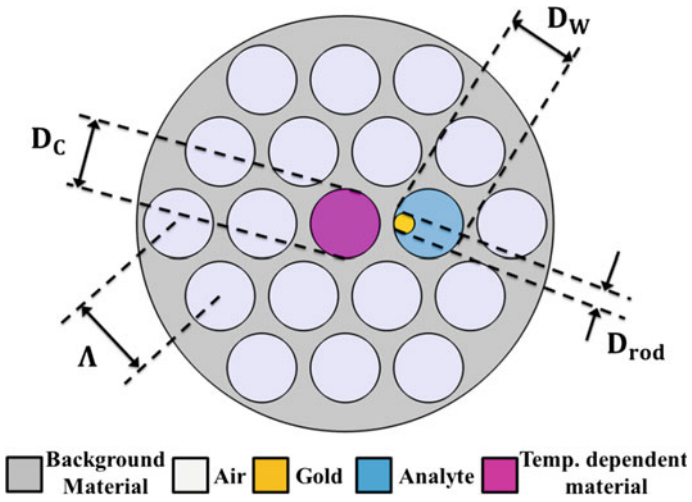

Fig. 10.1 Cross section of the multifunction SPR-PCF biosensor

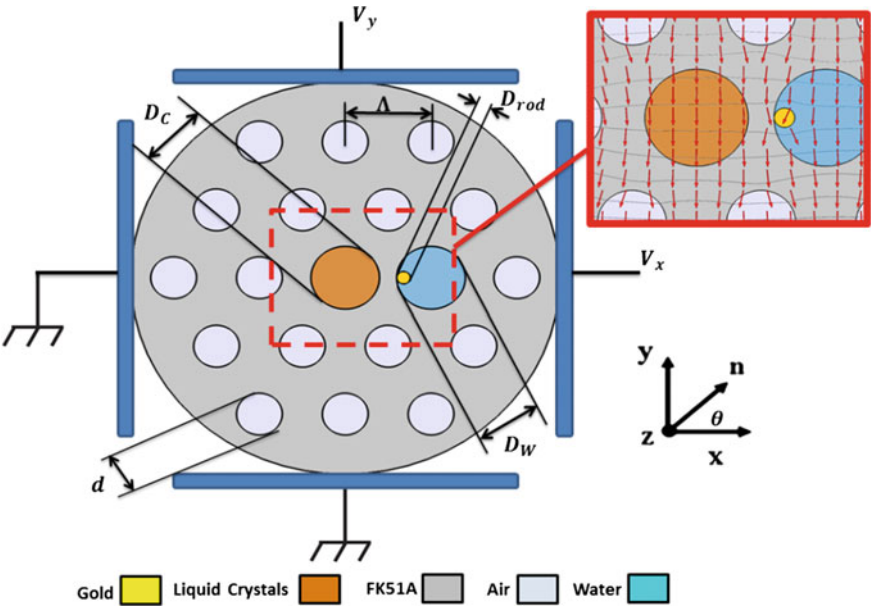

Fig. 10.2 Cross section of the suggested multifunctional biosensor. Inset: electric potential and electric field distribution through the structure at $V_x = V_y = V_0 = 100V$ [24]

modes and the surface plasmon modes using the FK51A [11]. It is worth noting that it is possible to fabricate optical fibers using FK51A through stack and draw mechanism as reported by Kalnins et al. [23]. Therefore, FK51A is chosen as a background material for the suggested multifunctional sensor. The refractive index of the FK51A material is obtained from the Sellmeier equation [11]:

$$n^2(\lambda) = 1 + \frac{A_1\lambda^2}{\lambda^2 - B_1} + \frac{A_2\lambda^2}{\lambda^2 - B_2} + \frac{A_3\lambda^2}{\lambda^2 - B_3} \tag{10.1}$$

where $n(\lambda)$ is the wavelength-dependent refractive index of the FK51A, $A_1 = 0.971247817$, $A_2 = 0.2169014$, $A_3 = 0.9046517$, $B_1 = 0.00472302\ \mu m^2$, $B_2 = 0.01535756\ \mu m^2$, and $B_3 = 168.68133\ \mu m^2$.

The central hole of the first design is filled with NLC of type E7. Figure 10.2 also shows that two sets of electrodes are used to control the orientation of the NLC molecules in both x and y directions. According to the anisotropic property of the NLCs, their optical properties are direction dependent. The control of the tilt angle φ of the director of the NLC shown in the inset of Fig. 10.2 can be carried out via the two pairs of electrodes [25]. The electrodes in the x direction are used to align the molecules in the x direction with $V_x = V_0$ and $V_y = 0$. As a result, the dielectric permittivity would take the diagonal form $\varepsilon_r = [n_e^2\ n_o^2\ n_o^2]$ where n_e and n_o are the extraordinary and ordinary refractive indices of the NLC material, respectively. On

the other hand, when $V_x = 0$, and $V_y = V_0$, the NLC molecules are oriented along y direction with a tilt angle 90° which results in a relative permittivity of $\varepsilon_r = [n_o^2\ n_e^2\ n_o^2]$. The ordinary and extraordinary refractive indices of the NLCs are temperature dependent according to [26]:

$$n_{e,o} = A_{e,o} + \frac{B_{e,o}}{\lambda^2} + \frac{C_{e,o}}{\lambda^4} \tag{10.2}$$

where λ is the wavelength and A_e, B_e, C_e, A_o, B_o, and C_o are temperature-dependent coefficients of the Cauchy model which can be found at different temperatures in [27]. In addition, the gold nanorod has a wavelength-dependent relative permittivity [3] as follows:

$$\varepsilon_{Au}(\omega) = \varepsilon_\infty - \frac{\omega_p^2}{\omega(\omega + i\omega_\tau)} \tag{10.3}$$

where $\varepsilon_\infty = 9.75$, $\omega_p = 1.36 \times 10^{16}$ rad/s, and $\omega_\tau = 1.45 \times 10^{14}$ rad/s.

10.2.2 Numerical Results and Discussion

First, it is needed to ensure the uniformity of the NLC molecules alignment under the application of an external potential. This can be achieved by studying the electric potential V and the electric field E distributions in the NLC core region. The Gauss Law is solved along with the electric potential–electric field relation as given by [28]:

$$\nabla \cdot D = 0,\ E = -\nabla V \tag{10.4}$$

where D is the displacement field, E is the electric field, V is the electric potential. In this study, the FEM via Comsol Multiphysics software package [21] is used to solve the two equations over a rectangular-shaped computational domain of width = 6Λ, and height = 5.46Λ. The electrodes voltage is taken as 100 V which is greater than the Fréedericksz threshold [29]. In this investigation, d, Λ, D_{LC}, D_W, D_{rod}, n_w, and T are initially equal to 2 μm, 3.75 μm, 3 μm, 3 μm, 600 nm, 1.33, and 30 °C, respectively. The degree of freedom is equal to 101579 with minimum element size of 0.00045 μm. Further, Dirichlet boundary conditions are used for the electric potential. It is clear from the inset of Fig. 10.2 that the electric potential and the electric field are uniform inside the NLC core region with a slight change near the gold nanorod. Therefore, the gold nanorod will not affect the uniformity of the electric field through the NLC core.

The analysis of the reported biosensor is also carried out using the Comsol Multiphysics software package [21] on a circular computational domain with radius of 2.5Λ. Additionally, PML is used as a boundary condition to truncate the

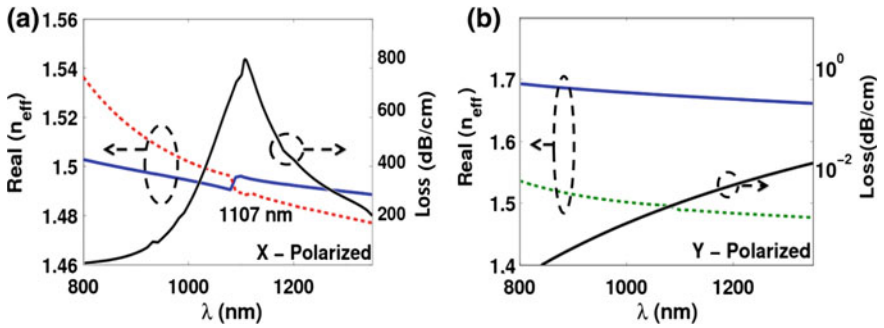

Fig. 10.3 Variation of the wavelength-dependent effective indices and losses at $D_{rod} = 800$ nm of the **a** quasi-TE core mode and **b** quasi-TM core mode and the surface plasmon modes [24]

computational domain with 213973 degrees of freedom and minimum element size of 0.0008 μm. The values of the hole pitch, airhole diameters, and the tilt angle are fixed at $\Lambda = 3.75$ μm, d = 2 μm, and $\varphi = 90°$. The analysis is carried out at T = 30 °C, $n_W = 1.33$, $D_{LC} = 3$ μm, $D_W = 3$ μm, $D_{rod} = 800$ nm. The variation of the real part of the effective indices of the quasi-TE (E_x^{11}) and quasi-TM (E_y^{11}) core-guided modes, and the SPM is shown in Fig. 10.3. The wavelength-dependent loss spectra of the two polarized core modes are also shown in Fig. 10.3. It is evident from Fig. 10.3a that the coupling occurs only between the quasi-TE (E_x^{11}) and SPM (SP_x^0) at resonance wavelength of λ = 1107 nm. On the other hand, there is no coupling between the quasi-TM core (E_y^{11}) and SP modes as shown in Fig. 10.3b.

Figure 10.4a, c shows the field plots of the main components E_x^{11} and E_y^{11} of the quasi-x-polarized and quasi-y-polarized mode, respectively. Further, the E_x and E_y components of the SP mode are also shown in Fig. 10.4b. It may be seen from Fig. 10.4a, b that at the resonance wavelength, the field plots of the SPM and fundamental quasi-x-polarized core mode are similar. However, away from the resonance wavelength, the core mode is well confined in the NLC core at $\lambda = 800$ nm while the SPM exists at the metallic nanorod interface. For y-polarized

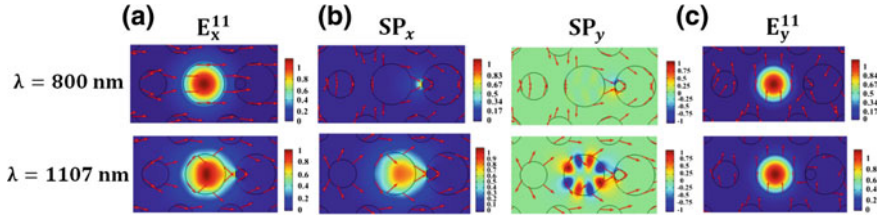

Fig. 10.4 Field plot at λ = 800 and 1107 nm for **a** x-component of quasi-TE core mode, **b** x and y components of the SP mode, and **c** y-component of the quasi-TM core mode [24]

mode, there is no coupling between the surface plasmon mode and y-polarized core mode. Therefore, the study will be concerned with the quasi-TE modes only.

The sensing mechanism depends mainly on the variation of the refractive index of a specific medium with the change of a physical property such as temperature and analyte refractive index. Then, a shift in the resonance wavelength occurs, and hence, the sensitivity can be determined. The sensitivity of the desired physical property can be calculated according to the wavelength interrogation method given by:

$$S_\lambda(\lambda) = \frac{\partial \lambda_{peak}(\psi)}{\partial \psi} \tag{10.5}$$

where λ_{peak} is the wavelength corresponding to the resonance peak in the loss spectra for a specific physical property ψ. The suggested multifunctional sensor can be used for sensing two physical parameters, temperature T and analyte refractive index n_w at a time. The sensitivity can be also calculated according to the amplitude interrogation method as follows:

$$S_A = -\frac{\partial(\alpha(\lambda, \psi))/\partial \psi}{\alpha(\lambda, \psi)} \tag{10.6}$$

where $\alpha(\lambda, \psi)$ represents the propagation loss of the core-guided mode as a function of the wavelength at a specific physical property value ψ (temperature or analyte refractive index). It is worth noting that the study of the sensitivity according to one parameter is investigated while the other parameter is kept constant. The following analysis concerns the study of the structural geometrical parameters to obtain the design that has high sensitivity for temperature and analyte refractive index.

A. **Refractive Index Sensitivity**

The sensing of the analyte refractive index change has many related applications including glucose monitoring in blood samples. The analyte refractive index can be changed due to the change of the glucose concentration as reported by Daly et al. [30]. Therefore, the detection of the analyte refractive index variation could help determine the change in the glucose concentration. In this study, the sensitivity of the analyte refractive index sensing is first investigated while the temperature is kept constant at 30 °C. The thermoelectric module can be used to control the temperature as experimentally described by Wolinski et al. [31, 32]. This can control the temperature within large range of 10–120 °C with 0.1 °C long-term stability and electric field regulation in the 0–1000 V range with frequencies from 50 Hz to 2 kHz. The effect of the gold nanorod diameter is initially studied. The analysis is performed by calculating the losses variation with the wavelength at different analyte refractive indices n_w, 1.33 and 1.34. However, the other parameters are fixed at $D_{LC} = 3$ μm, $D_W = 3$ μm, $d = 2.0$ μm, $\Lambda = 3.75$ μm. The wavelength and amplitude sensitivities at $n_w = 1.33$ and 1.34 are shown in Fig. 10.5 at different gold nanorod diameters, and the results are reported in Table 10.1. It is evident

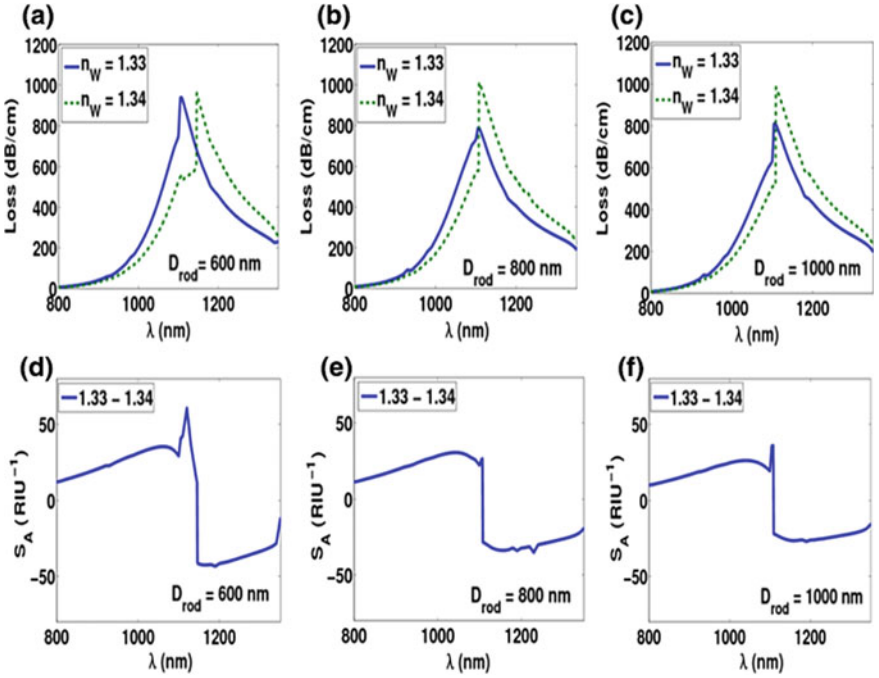

Fig. 10.5 Variation of quasi-TE core mode loss and amplitude sensitivity with the wavelength at different analyte refractive indices, at **a**, **d** D_{rod} = 600 nm, **b**, **e** D_{rod} = 800 nm, and **c**, **f** D_{rod} = 1000 nm [24]

from Fig. 10.5 that the resonance wavelength increases by increasing the analyte refractive index from 1.33 to 1.34. As the analyte refractive index increases, the effective index of the surface plasmon mode SP_x^0 increases as shown in Fig. 10.6 while the quasi-TE core modes are slightly affected by the analyte refractive index variation (except at the resonance point) due to the well confinement in the LC core. Therefore, the shift in the resonance wavelength occurs toward long wavelength region as revealed from Fig. 10.6. It is also evident from Fig. 10.5 and Table 10.1 that at D_{rod} = 600 nm, the shift in the resonance wavelength is greater than those obtained at D_{rod} = 800 and 1000 nm. Therefore, the proposed sensor has high sensitivity of 3900 nm/RIU with a corresponding amplitude sensitivity of 60.75 RIU^{-1} within index range 1.33–1.34 as shown in Table 10.1. As D_{rod} is further increased to 1000 nm, the amplitude sensitivity and wavelength sensitivity are decreased to 36.04 RIU^{-1} and 300 nm/RIU, respectively. Therefore, D_{rod} is fixed at 600 nm in the subsequent simulations.

The effect of the analyte core diameter is next studied at two different analyte refractive indices, 1.33 and 1.34. However, the other parameters are fixed at D_{LC} = 3 μm, D_{rod} = 600 nm, d = 2.0 μm, Λ = 3.75 μm, and T = 30 °C. Figure 10.7 shows the variation of the wavelength-dependent quasi-TE core mode

Table 10.1 Summary of the resonance wavelength, wavelength sensitivity, and amplitude sensitivity for analyte refractive index sensing at different structural geometrical parameters [24]

Parameter		λ_o(nm)		S_λ(nm/RIU)	S_A(RIU^{-1})
		1.33	1.34	1.33 – 1.34	1.33 – 1.34
D_{rod} (nm)	600	1107	1146	3900	60.75
	800	1107	1108	100	30.59
	1000	1106	1109	300	36.04
D_W (μm)	2.6	1130	1167	3700	47.77
	3	1107	1046	3900	60.75
	3.4	1108	1108	0	39.84

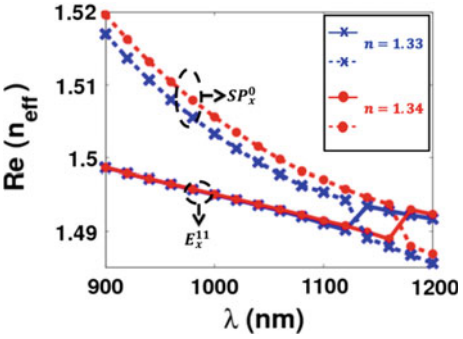

Fig. 10.6 Variation of the real part of the effective indices of the surface plasmon modes and quasi-TE core modes with the wavelengths at $D_{rod} = 600$ nm for two different refractive indices 1.33 and 1.34 [24]

losses and amplitude sensitivities at different analyte refractive indices and at different D_W values, 2.6, 3.0, and 3.4 μm. It is evident from this figure that at $D_W = 2.6$ μm, the corresponding wavelength and amplitude sensitivities are equal to 3700 nm/RIU and 47.77 RIU^1, respectively. When D_w is increased to 3.0 μm, both wavelength and amplitude sensitivities are increased to 3900 nm/RIU and 60.75 RIU^{-1}, respectively. As D_w is further increased to 3.4 μm, the refractive index variation has no effect on the resonance wavelength as reported in Table 10.1. Figure 10.8 shows the resonance wavelength variation with the analyte refractive index at $D_{rod} = 600$ nm, $D_W = 2.6$ μm, and T = 30 °C. It may be noted from this figure that the performance of the suggested biosensor has high linearity over analyte refractive index change from 1.33 to 1.35. Therefore, the proposed biosensor can be used as a self-calibration sensor within unknown analyte refractive

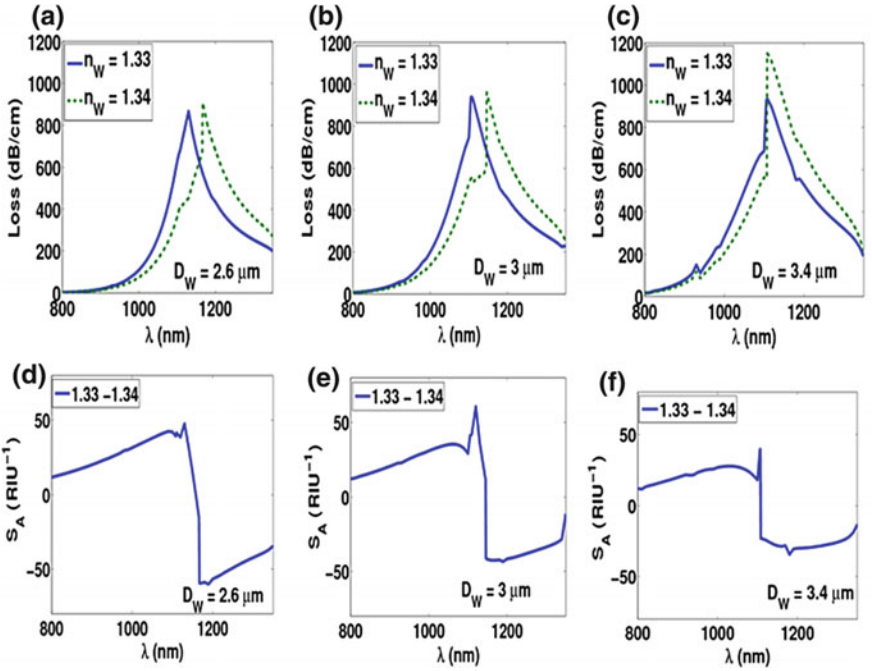

Fig. 10.7 Variation of quasi-TE core mode loss and amplitude sensitivity with the wavelength at different analyte refractive indices, at **a**, **d** $D_W = 2.6$ μm, **b**, **e** $D_W = 3.0$ μm, and **c**, **f** $D_W = 3.4$ μm [24]

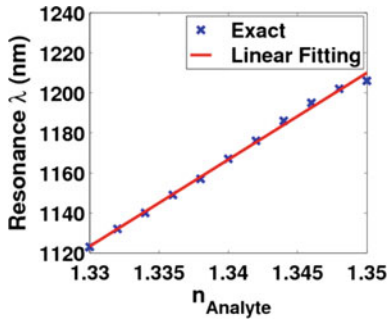

Fig. 10.8 Linear fitting for the variation of the resonance wavelength with the analyte refractive index change [24]

index range from 1.33 to 1.35. In addition, the fitting accuracy is comparable with other reported biosensors [16, 33, 34].

B. Temperature Sensitivity

The suggested sensor can be also used for detecting the temperature variation. The temperature sensing is based on the change of the ordinary and extraordinary refractive indices of the NLC molecules with the change in temperature. Therefore,

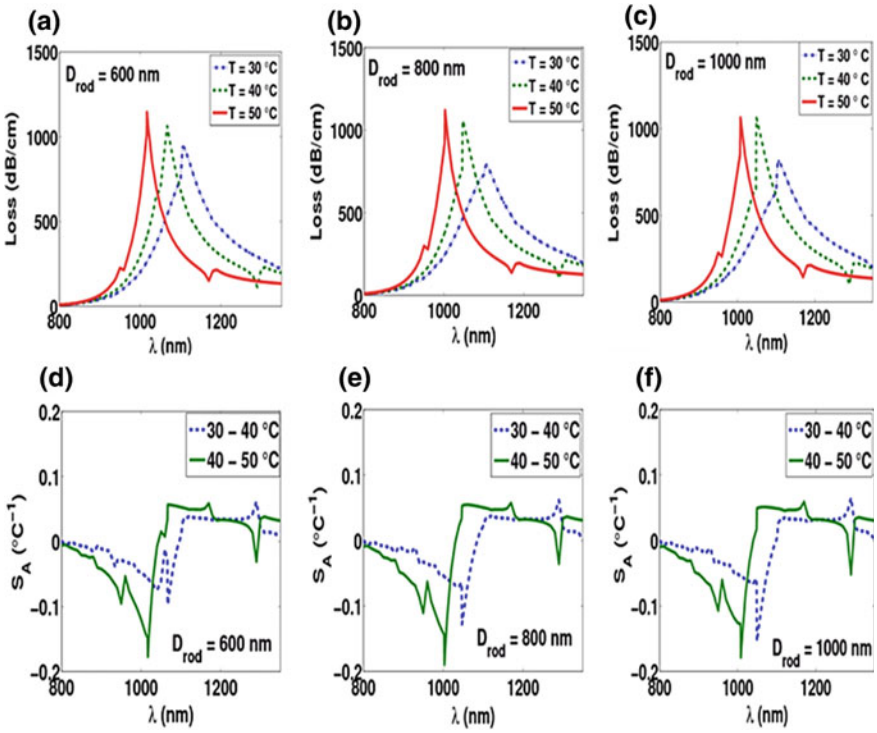

Fig. 10.9 Variation of the quasi-TE core mode loss in (dB/cm) and amplitude sensitivity with the wavelength at different temperatures, and at **a**, **d** D_{rod} = 600 nm, **b**, **e** D_{rod} = 800 nm, and **c** D_{rod} = 1000 nm [24]

the resonance wavelength is changed with the temperature variation. Consequently, the sensitivity of the reported design for the temperature variation is next studied. It should be noted that the thermo-optical coefficients of the FK51A (∼10 − 6/K) [35] and the gold are much lower than that of the NLC material and are therefore not taken into consideration. The analysis is carried out by calculating the losses versus the wavelength at different temperatures 30, 40, and 50 °C where the other parameters are fixed at $D_{LC} = 3\,\mu m$, $D_W = 3\,\mu m$, $d = 2.0\,\mu m$, $\Lambda = 3.75\,\mu m$, and $n_W = 1.33$. Figure 10.9 shows the loss and amplitude sensitivity variation with the wavelength at three different temperatures 30, 40, and 50 °C and at different D_{rod} values. The resonance wavelengths and corresponding sensor sensitivities are summarized in Table 10.2. It may be noted from Fig. 10.9 that the resonance wavelength decreases by increasing the temperature. As the temperature increases, the effective indices of the quasi-TE core-guided modes increase due to the confinement of the core modes inside the LC core as shown in Fig. 10.10. However, the surface plasmon modes are independent on the temperature variation with well confinement around the metallic nanorod. Therefore, the shift in the resonance wavelength occurs toward shorter wavelength. It is also found that at D_{rod} = 600

Table 10.2 Summary of the temperature resonance wavelength, wavelength sensitivity, and amplitude sensitivity at different structural geometrical parameters [24]

Parameter		λ_o(nm)			S_λ(nm/°C)		S_A(°C^{-1})	
		30 °C	40 °C	50 °C	30-40	40-50	30-40	40-50
D_{rod} (nm)	600	1107	1067	1017	4	5	0.038	0.056
	800	1107	1047	1003	6	4.4	0.037	0.055
	1000	1106	1049	1008	5.7	4.1	0.034	0.051
D_W (μm)	2.6	1130	1081	1030	4.9	5.1	0.048	0.07
	3	1107	1067	1017	4	5	0.038	0.056
	3.4	1108	1048	1017	6	3.1	0.029	0.041

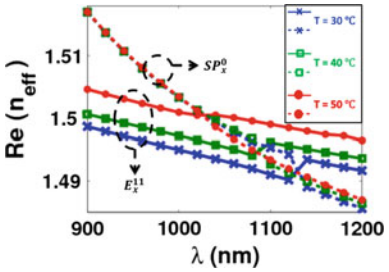

Fig. 10.10 Variation of the real part of the effective indices of the surface plasmon modes and quasi-TE core modes with the wavelengths at $D_{rod} = 600$ nm for three different temperatures 30, 40 and 50 °C [24]

nm, sensor sensitivities of 4 nm/°C and 5 nm/°C are achieved for temperature ranges 30 °C–40 °C and 40 °C–50 °C, respectively. Additionally, maximal amplitude sensitivity of 0.038 °C^{-1} and 0.056 °C^{-1} is obtained for the same temperature ranges as shown in Fig. 10.9. When the gold rod diameter is further increased to 800 and 1000 nm, the sensor sensitivity will be decreased as shown in Table 10.2.

Next, the effect of analyte-filled core diameter D_w is studied. The losses analysis versus wavelength is also carried out at three different temperatures, 30, 40, and 50 °C, while the other parameters are fixed at $D_{LC} = 3$ μm, $D_{rod} = 600$ nm, $d = 2.0$ μm, $\Lambda = 3.75$ μm, and $n_w = 1.33$. Figure 10.11 shows that at $D_W = 2.6$ μm, the corresponding sensitivities are equal to 4.9 and 5.1 nm/°C for temperature ranges 30 °C–40 °C and 40 °C–50 °C, respectively. Further, the corresponding amplitude sensitivities are equal to 0.048 and 0.07 °C^{-1} for the same temperature ranges. When D_W is increased to 3 and 3.4 μm, the wavelength and amplitude sensitivities are decreased as revealed from Table 10.2.

The linearity of the temperature sensing behavior is also tested by studying the variation of the resonance wavelength with the temperature as shown in Fig. 10.12. It may be seen from this figure that the proposed biosensor has a good linearity over

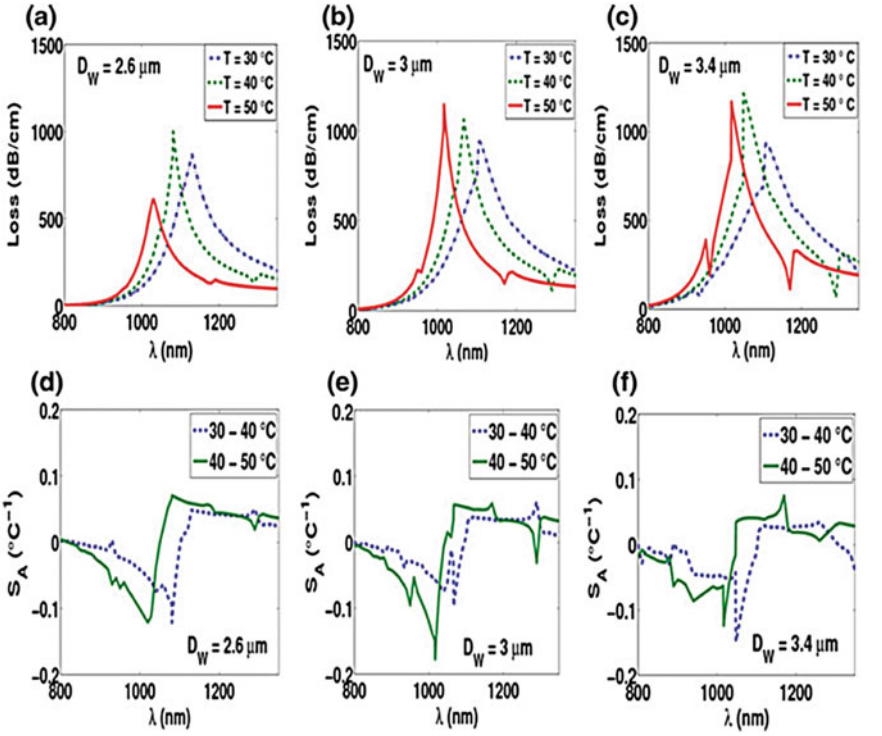

Fig. 10.11 Variation of quasi-TE core mode loss and amplitude sensitivity with the wavelength at different temperatures, at **a**, **d** D_W = 2.6 µm, **b**, **e** D_W = 3.0 µm, and **c**, **f** D_W = 3.4 µm [24]

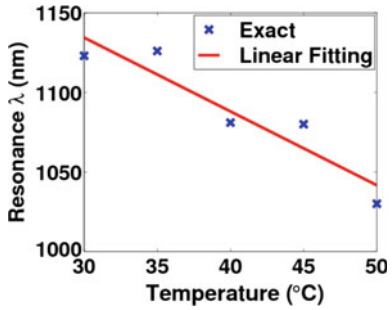

Fig. 10.12 Linear fitting for the variation of the resonance wavelength with the temperature [24]

temperature range from 15 to 50 °C with an average sensitivity of 3.3 nm/°C which is comparable to that reported in [16, 33, 34]. The analysis is carried out at D_{rod} = 600 nm, D_W = 2.6 µm, and n_w = 1.33. It may be also noted that the linearity of the suggested temperature sensor is less than that for analyte refractive index sensing. This is due to the temperature-dependent ordinary and extraordinary refractive indices of the NLC material [26]. The n_e of the NLC material of type E7

decreases from 1.7096 to 1.6438 by increasing the temperature from 15 to 50 °C, at wavelength of 1.55 μm. However, the ordinary index n_o decreases from 1.5034 to 1.5017 by increasing the temperature from 15 to 35 °C. As the temperature is further increased to 50 °C, the n_o increases to 1.5089 at $\lambda = 1.55$ μm. The sensing linearity can be increased by using different types of LCs or another temperature-dependent liquid (such as alcohol) [4]. It should be also noted that the temperature range of the suggested sensor is comparable to that reported in [4, 9–11]. The studied temperature range is dependent on the NLC phase that exists between its melting point and ~60 °C. However, the temperature range supported by the suggested sensor can be increased by using an alternative NLC material with a much wider nematic range such as those used in the current thin-film-transistor liquid crystal display market.

It is worth noting that the sensor device length is inversely proportional to its modal loss. Therefore, the PCF structural geometrical parameters are optimized to control the sensor device length with comparable sensitivity. For practical considerations, this point should be taken into our account when integrating the proposed sensor into a complete sensor system. The suggested device length should fulfill the requirement that the total leakage loss for the quasi-TE mode will not exceed 0.1 dB. Therefore, the required device length can be as compact as 10 μm.

It may be noticed from Tables 10.1 and 10.2 that high sensitivities of 5 nm/°C and 3700 nm/RIU are achieved for temperature and analyte refractive indexing sensing at the same geometrical parameters. In order to prove that the reported multifunctional biosensor has more robust to the perturbation introduced during the fabrication process, a fabrication tolerance study is performed. It should be noted that the tolerance of a specific parameter is studied at constant values of the other design parameters at their optimum values. It is revealed from the numerical results that the proposed sensor has a fabrication tolerance of ±5% for D_W, D_{rod} and the position of the nanorod inside the analyte-filled hole at which the sensitivities of the temperature and analyte refractive index monitoring are still better than 3.4 nm/°C and 3700 nm/RIU, respectively, which ensure the robustness of the designed biosensor for fabrication imperfection.

A further analysis is carried out where all cladding airholes, except the water-filled hole, are filled with NLC. It is found that adding LCs to the other cladding holes has no effect on the sensitivity for temperature range 30–40 °C. However, the sensitivity is slightly enhanced from 5.1 to 5.6 nm/°C through temperature range 40–50 °C. On the other hand, the infiltration of only central hole is much easier than infiltrating all the cladding holes with LCs. Further, the suggested design has advantages in terms of low material cost. Therefore, the suggested design is the better choice for the multifunction biosensor.

10.3 Alcohol-Based SPR-PCF Multifunction Sensor

10.3.1 Design Considerations

In this study, the multifunctional sensor have the same design shown in Fig. 10.1, where the central hole is infiltrated by an alcohol mixture as a temperature-dependent material instead of the NLC.

The alcohol mixture in the central hole consists of ethanol and chloroform which have temperature-dependent refractive indices that can be determined from the following relation [4]:

$$n_x = n_0 + \frac{dn}{dT}(T_x - T_0) \tag{10.7}$$

where n_0 is the refractive index at reference temperature T_0 which is equal to 1.36 and 1.44 for ethanol and chloroform at 20 °C, respectively, n_x is the refractive index of chloroform or ethanol at temperature T_x. Further, in order to find the resultant refractive index n of the mixture, the mixing ratio must be considered as follows [4]:

$$\frac{n^2-1}{n^2+2} = \varnothing_1 \frac{n_1^2-1}{n_1^2+2} + \varnothing_2 \frac{n_2^2-1}{n_2^2+2} \tag{10.8}$$

where n_1 and n_2 are the refractive indices for ethanol and chloroform at a specific temperature, $\varnothing_1$ and $\varnothing_2$ are the volume fractions for ethanol and chloroform in the mixture. It is found that a volume ratio for ethanol to chloroform of 4:6 has proven to be reliable as reported in [4]. According to [4], a temperature range $(-4°C: 53°C)$ has a corresponding refractive index for alcohol mixture of (1.42:1.39). The specified range is studied through four points (−4 °C, 15 °C, 34 °C and 53 °C) which corresponds to refractive indices of (1.42, 1.41, 1.4, and 1.39), respectively, for alcohol mixture. Moreover, the gold has a wavelength-dependent relative permittivity obtained from Eq. (10.3). Furthermore, the silica glass has a wavelength-dependent refractive index n_s calculated from the following Sellmeier equation [13]:

$$n_s^2(\lambda) = 1 + \frac{B_1\lambda^2}{\lambda^2 - C_1} + \frac{B_2\lambda^2}{\lambda^2 - C_2} + \frac{B_3\lambda^2}{\lambda^2 - C_3} \tag{10.9}$$

where λ is the wavelength in μm. Additionally, B_1, B_1, and B_3 are taken as 0.6961663, 0.4079426, and 0.8974794 while C_1, C_2, and C_3 are equal to 0.00467914826 μm^2, 0.0135120631 μm^2, and 97.9340025 μm^2, respectively.

10.3.2 Numerical Results and Discussion

The FVFEM is used to carry out the analysis of the proposed PCF sensor based on the commercial software package Comsol Multiphysics [21]. The computational domain is specified as a circle of radius $2.5 \times \Lambda$ with minimum element size of 0.0008 μm and 100329 degrees of freedom. In addition, a PML layer is used to truncate the computational domain. The variation of the real part of the effective index of refraction for the quasi-TE core-guided mode and quasi-TE SP mode with the wavelength is shown in Fig. 10.13a. In addition, the confinement loss of the core mode is also shown in Fig. 10.13. Moreover, the variations of the effective indices of the quasi-core-guided TM mode and the SP TM mode and the confinement loss of the TM core mode with the wavelength are shown in Fig. 10.13b. Furthermore, the field plots for both the fundamental core mode E_x^{11} and the x-polarized SP mode are illustrated in Fig. 10.13a, while the field plots of the fundamental core mode E_y^{11} and the y-polarized SP mode are shown in Fig. 10.13b. The analysis is carried out at a temperature value of 34 °C, analyte refractive index of $n_a = 1.33$, $\Lambda = 2.4\,\mu m$, $D_C = 2\,\mu m$, and $d = 600\,nm$. Figure 10.13a shows that at $\lambda = 962\,nm$, the quasi-TE core mode has the same effective index of the TE SP mode. As a result, the coupling condition is achieved where maximum loss occurs for the core-guided mode as shown in Fig. 10.13a. However, away from

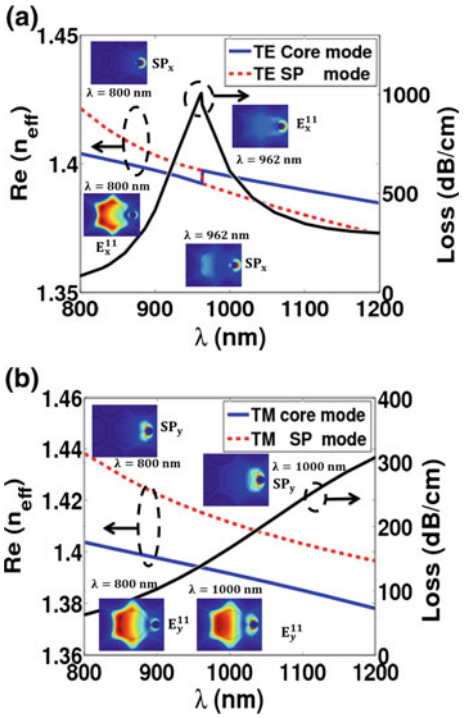

Fig. 10.13 Variation of the wavelength-dependent effective indices and losses of the **a** quasi-TE core mode and **b** quasi-TM core mode and the surface plasmon modes. Inset: Field plots of the quasi-TE, quasi-TM core modes, TE SP and TM SP mode at different wavelengths

$\lambda = 962$ nm, the effective indices of the quasi-TE core mode and SP mode are unequal and their field plots are different. On the other hand, the effective indices of the quasi-TM core mode and the TM SP mode are divergent from each other throughout the specified range of wavelengths. As a result, no coupling occurs between the quasi-TM core mode and the TM SP mode. Therefore, the following study will be concerned with the quasi-TE modes only.

To study the performance of the proposed design, the sensitivity of such sensor should be calculated over the specified range of temperature (− 4 °C: 53 °C) and for analyte refractive index range (1.33:1.4) using the wavelength interrogation method, which is defined by Eq. (10.5). Further, the sensitivity of the proposed sensor can be also calculated using the amplitude-based method given by Eq. (10.6). The study of the geometrical structural parameters is needed to achieve the maximum sensitivity for both temperature and analyte refractive index sensing. The studied parameters are the hole pitch Λ, the diameter of the central hole containing the alcohol D_C, and the gold rod diameter d, while the cladding airholes have a fixed diameter of 2 μm.

A. **Refractive Index Sensitivity**

To study the sensitivity of the proposed design to the change in the refractive index of the analyte, the temperature is kept constant at 15 °C which corresponds to alcohol mixture refractive index value of 1.41. First, the effect of the hole pitch is investigated while the other two parameters are fixed at $D_C = 2$ μm and $d = 600$ nm. Figure 10.14 shows the variation of the confinement loss of the quasi-TE core mode with the wavelength at different analyte refractive indices (1.33, 134) and for different hole pitch values. It may be seen from Fig. 10.14a, d that at $\Lambda = 2.3$ μm, the

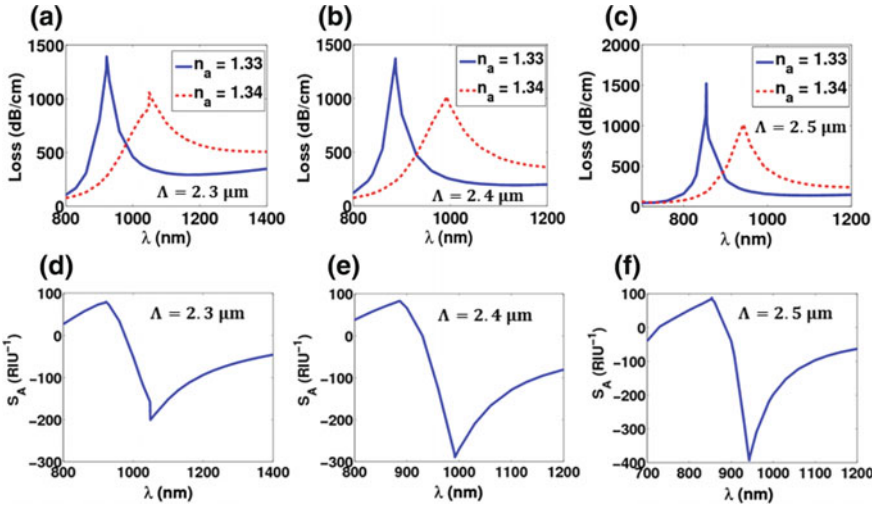

Fig. 10.14 Variation of quasi-TE core mode loss and amplitude sensitivity with the wavelength at different analyte refractive indices, at **a**, **d** $\Lambda = 2.3$ μm, **b**, **e** $\Lambda = 2.4$ μm, and **c**, **f** $\Lambda = 2.5$ μm

Table 10.3 Summary of the resonance wavelength, wavelength sensitivity, and amplitude sensitivity for analyte refractive index sensing at different structural geometrical parameters

Parameter		λ_o(nm)		S_λ(nm/RIU)	S_A(RIU^{-1})
		1.33	1.34	1.33 – 1.34	1.33-1.34
Λ (μm)	2.3	922	1049	12700	79.845
	2.4	887	992	10500	83.153
	2.5	854	943	8900	88.090
D_C (μm)	1.8	888	997	10900	82.869
	1.9	906	1024	11800	80.575
	2	922	1049	12700	79.845
d_{rod} (nm)	400	929	1018	8900	63.985
	500	933	1045	11200	70.045
	600	922	1049	12700	79.845

corresponding resonance wavelengths are equal to 922 nm and 1049 nm. These resonance peaks result in a wavelength sensitivity of 12700 nm/RIU and a corresponding amplitude sensitivity of 79.845 RIU^{-1}. When the hole pitch is increased to 2.4 μm, the shift in the resonance peaks $\Delta\lambda$ decreases to 105 nm which reduces the wavelength sensitivity to 10500 nm/RIU as shown in Fig. 10.14b, e with a slight increase in the amplitude sensitivity. Figure 10.14c, f shows that when the hole pitch is further increased to 2.5 μm, the wavelength sensitivity decreases to 8900 nm/RIU while the amplitude sensitivity slightly increases to 88.09 RIU^{-1}. The calculated values of the wavelength and amplitude sensitivities are reported in Table 10.3.

Next, the effect of the alcohol core diameter is considered while the other two parameters are fixed at $\Lambda = 2.3$ μm and $d = 600$ nm. Figure 10.15 shows the variation of the confinement loss of the quasi-TE core mode with the wavelength at different analyte refractive indices and for different core diameters. It is worth noting that the hole pitch is fixed at 2.3 μm which achieves the highest wavelength sensitivity. It may be seen from Fig. 10.15a, d that at $D_C = 1.8$ μm, the resonance wavelengths for analyte refractive indices of 1.33 and 1.34 are equal to 888 nm and 997 nm, respectively. The calculated wavelength and amplitude sensitivities are 10900 nm/RIU and 82.869 RIU^{-1}, respectively. If the core diameter is increased to 1.9 μm, the silica distance between the core region and the metal surface is decreased which facilitates the coupling between the SP and core modes and increases the wavelength sensitivity as shown in Fig. 10.15b. Moreover, increasing the core diameter to 2 μm also increases the wavelength sensitivity to 12700 nm/RIU and slightly decreases the amplitude sensitivity as shown in Table 10.3.

The impact of the gold nanorod diameter is also considered, while the other two parameters are fixed at their optimum values at $\Lambda = 2.3$ μm and $D_C = 2$μm.

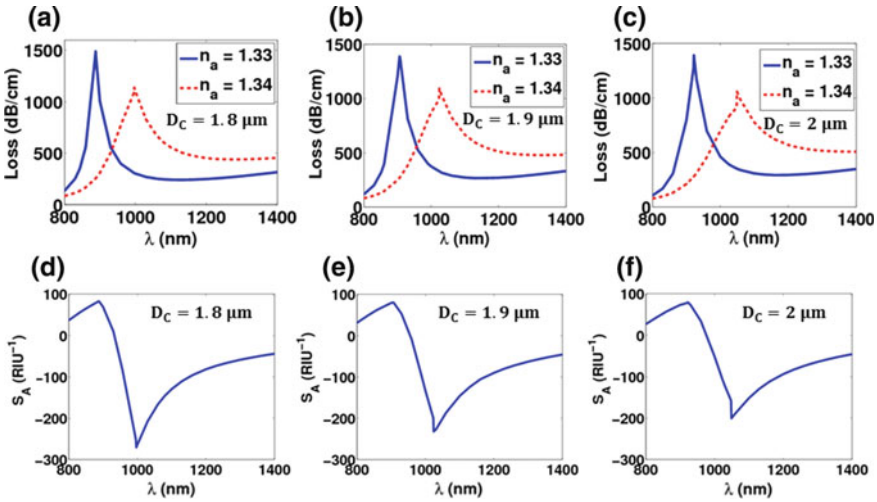

Fig. 10.15 Variation of the quasi-TE core mode loss and amplitude sensitivity with the wavelength at different analyte refractive indices, at **a**, **d** $D_C = 1.8\,\mu m$, **b**, **e** $D_C = 1.9\,\mu m$, and **c**, **f** $D_C = 2\,\mu m$

Figure 10.16a, d shows that using gold nanorod diameter of 400 nm gives a rise to resonance peaks at λ of 929 nm and 1018 nm corresponding to analyte refractive index of 1.33 and 1.34, respectively. The resultant wavelength sensitivity and amplitude sensitivity are equal to 8900 nm/RIU and 63.985 RIU^{-1}, respectively. It is also evident from Fig. 10.16 that as the gold nanorod diameter is increased to 600 nm, the surface area of the metal increases which improves the interaction between the core mode and SP mode. Therefore, the wavelength and amplitude sensitivities are improved as may be seen from Table 10.3.

B. Temperature Sensitivity

The sensitivity of the proposed multifunctional biosensor for temperature variation is next studied in temperature range from −4 to 53°C and reported in Table 10.4, while the analyte refractive index is fixed at $n_a = 1.33$. The first analysis is carried out for the change in the hole pitch while the other two parameters are fixed at $D_C = 2\,\mu m$ and $d = 600$ nm. The variation of the confinement loss of the quasi-TE core mode with the wavelength at different temperatures and for different hole pitch values is shown in Fig. 10.17. As may be seen from Fig. 10.17a, d that at $\Lambda = 2.3\,\mu m$, the coupling between the quasi-TE core mode and the SP mode occurs at $\lambda = 1273$ nm, 1024 nm, 922 nm, and 860 nm for temperature values of 53 °C, 34 °C, 15 °C and −4 °C, respectively. The corresponding wavelength sensitivities for temperature ranges (53 °C: 34 °C), (34 °C: 15 °C), and (15 °C: − 4 °C) are 13.1 nm °C, 5.36 nm /°C and 3.26 nm /°C, respectively, as shown in Table 10.4. Additionally, the resultant amplitude sensitivities are equal to 0.0185, 0.0325 and 0.0396 $°C^{-1}$ for the same temperature ranges. When Λ is increased to 2.4 µm, the

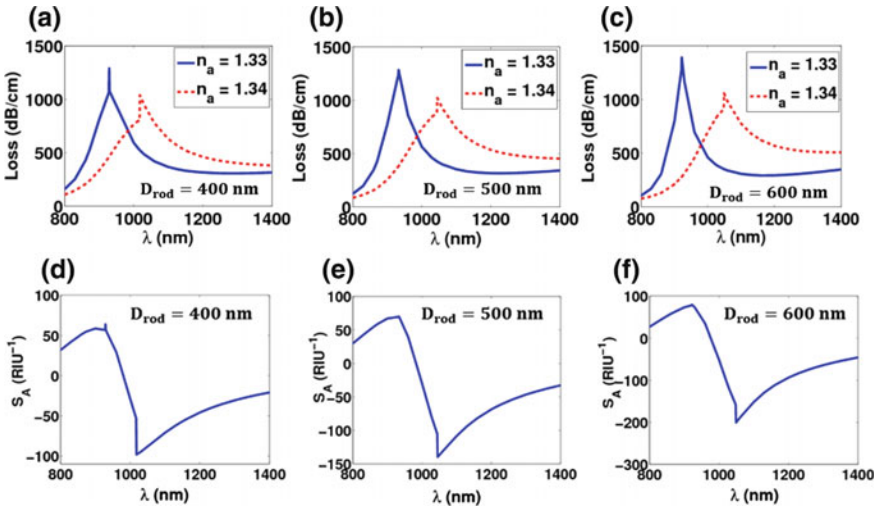

Fig. 10.16 Variation of the quasi-TE core mode loss and amplitude sensitivity with the wavelength at different analyte refractive indices, at **a**, **d** $D_{rod} = 400$ nm, **b**, **e** $D_{rod} = 500$ nm, and **c**, **f** $D_{rod} = 600$ nm

Table 10.4 Summary of the temperature resonance wavelength, wavelength sensitivity, and amplitude sensitivity at different structural geometrical parameters

Parameter		λ_o(nm)				S_λ(nm/°C)			S_A(°C^{-1})		
		53°C	34 °C	15 °C	-4 °C	53-34°C	34-15°C	15--4°C	53-34°C	34-15°C	15--4°C
Λ (μm)	2.3	1273	1024	922	860	13.1	5.36	3.26	0.0185	0.0325	0.0396
	2.4	1102	962	887	839	7.36	3.94	2.52	0.0268	0.0356	0.0412
	2.5	990	907	854	820	4.36	2.78	1.78	0.0292	0.0362	0.0429
D_C (μm)	1.8	1080	958	888	843	6.42	3.68	2.36	0.0260	0.0349	0.0396
	1.9	1160	991	906	852	8.89	4.47	2.84	0.0233	0.0332	0.394
	2	1273	1024	922	860	13.1	5.36	3.26	0.0185	0.0325	0.0396
d_{rod} (nm)	400	1146	1015	929	873	6.89	4.52	2.94	0.0167	0.0234	0.0294
	500	1206	1028	933	870	9.36	5	3.31	0.0181	0.0278	0.0347
	600	1273	1024	922	860	13.1	5.36	3.26	0.0185	0.0325	0.0396

shift between the resonance peaks decreases resulting in a decrease in the wavelength sensitivity as shown in Fig. 10.17b. On the other hand, as the pitch value increases, the difference in the loss values between the different peaks increases which slightly improves the amplitude sensitivity as seen from Fig. 10.17e. If the hole pitch is further increased to 2.5 μm, the shift between the resonance peaks and hence the wavelength sensitivity is further decreased while the amplitude sensitivity is slightly increased as presented in Table 10.4.

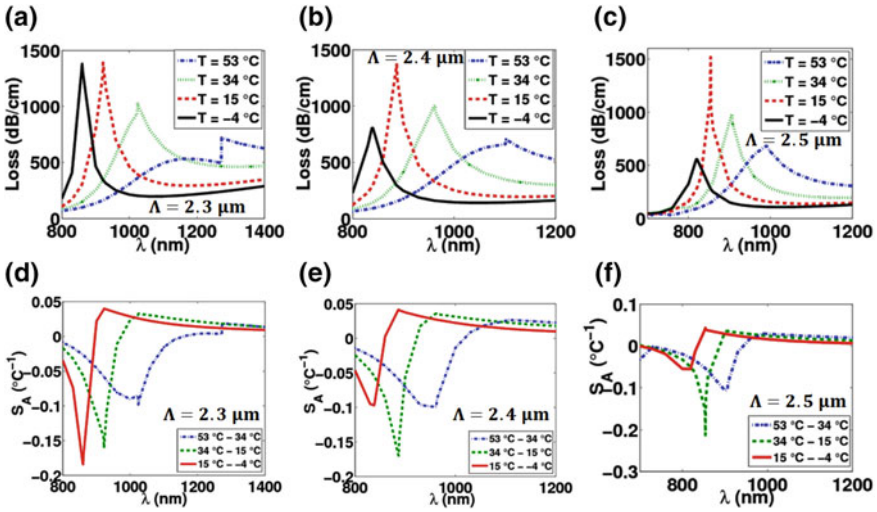

Fig. 10.17 Variation of the quasi-TE core mode loss and amplitude sensitivity with the wavelength at different temperatures, at **a**, **d** $\Lambda = 2.3\,\mu m$, **b**, **e** $\Lambda = 2.4\,\mu m$, and **c**, **f** $\Lambda = 2.5\,\mu m$

Next, the effect of the alcohol core diameter is studied while the other two parameters are fixed at $\Lambda = 2.3\,\mu m$ and $d = 600\,nm$. Figure 10.18 shows the variation of the confinement loss for the quasi-TE core mode with the wavelength at different temperatures and for different core diameters. At $D_C = 1.8\,\mu m$, the

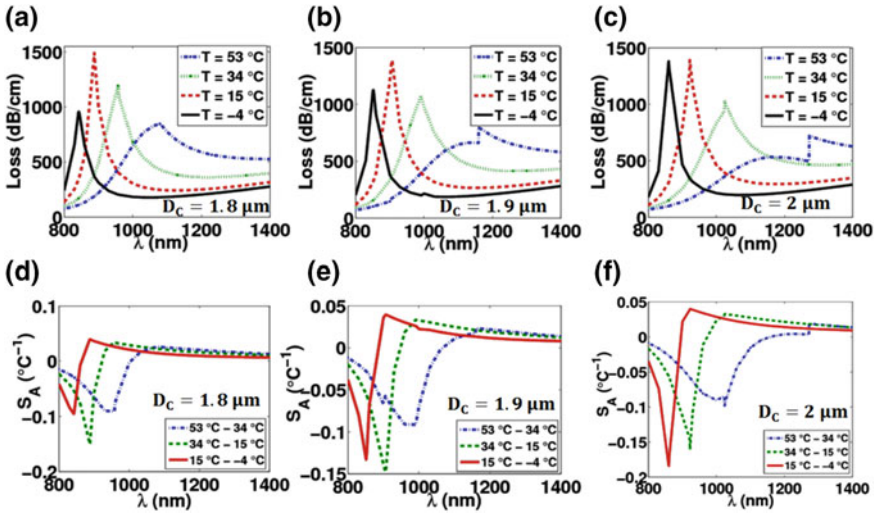

Fig. 10.18 Variation of the quasi-TE core mode loss and amplitude sensitivity with the wavelength at different temperatures, at **a**, **d** $D_C = 1.8\,\mu m$, **b**, **e** $D_C = 1.9\,\mu m$, and **c**, **f** $D_C = 2\,\mu m$

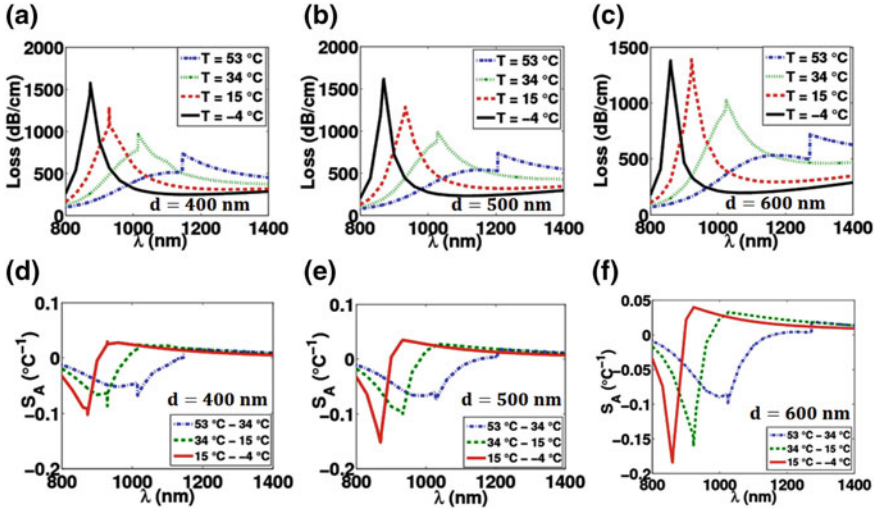

Fig. 10.19 Variation of the quasi-TE core mode loss and amplitude sensitivity with the wavelength at different temperatures, at **a**, **d** $D_{rod} = 400$ nm, **b**, **e** $D_{rod} = 500$ nm, and **c**, **f** $D_{rod} = 600$ nm

resonance wavelengths at different temperatures of 53 °C, 34 °C, 15 °C and –4 °C are equal to 1080 nm, 958 nm, 888 nm and 843 nm, respectively, as shown in Fig. 10.18a and Table 10.4. The resultant wavelength sensitivities are 6.42 nm/°C, 3.68 nm/°C, and 2.36 nm/°C, for the specified temperature range (53 °C: −4 °C), as may be seen from Table 10.4. The corresponding amplitude sensitivities are equal to 0.0260, 0.0349 $°C^{-1}$ and 0.0396 $°C^{-1}$ for the same temperature range. It is also evident from Table 10.4 that if the core diameter is increased to 2 µm, the wavelength sensitivity is increased to 13.1 nm/°C, 5.36 nm/°C and 3.26 nm/°C for temperature range (53 °C: 34 °C), (34 °C: 15 °C), and (15 °C: −4 °C), respectively.

Next, the effect of the gold nanorod D_{rod} diameter is studied, while the hole pitch and the alcohol core diameter are fixed at their optimum values of $\Lambda = 2.3$ µm and $D_C = 2$ µm. As shown in Fig. 10.19a, d, at gold nanorod diameter of 400 nm, the coupling occurs at resonance wavelengths of 1146 nm, 1015 nm, 929 nm, and 873 nm for temperature values of 53 °C, 34 °C, 15 °C and −4°C, respectively. Accordingly, for temperature ranges of (53 °C: 34 °C), (34 °C: 15 °C), and (15 °C: −4 °C), the achieved wavelength sensitivities are 6.89 nm/°C, 4.52 nm/°C, and 2.94 nm/°C, respectively, as shown in Table 10.4. Additionally, the corresponding amplitude sensitivities are equal to 0.0167, 0.0234 and 0.0294 $°C^{-1}$. As may be seen from Fig. 10.19, if the gold rod diameter is increased to 600 nm, the interaction between the SP modes and the core-guided modes increases. As a result, an increase in the wavelength sensitivities and the amplitude sensitivities occurs as shown in Table 10.4.

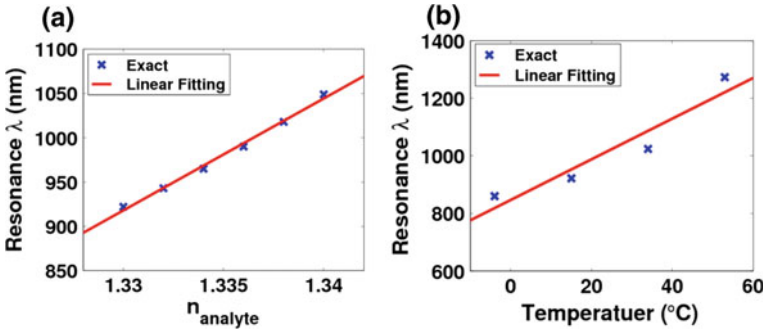

Fig. 10.20 Linear fitting for the variation of the resonance wavelength with the **a** analyte refractive index and **b** temperature

The performance linearity of the suggested sensor is finally studied throughout the temperature and analyte refractive index detection range. Figure 10.20a shows the variation of the resonance wavelength with the analyte refractive index at $\Lambda = 2.3\,\mu m$, $D_C = 2\,\mu m$, $d = 600\,nm$ and $T = 15\ ^\circ C$. It may be noted from this figure that the suggested biosensor has high linearity over analyte refractive index change from 1.33 to 1.34. In addition, the resonance wavelength variation with the temperature is shown in Fig. 10.20b at the same geometrical parameters and at analyte refractive index of 1.33. It may be seen from Fig. 10.20b that the suggested sensor has an acceptable linear behavior over the specified temperature range. Moreover, the accuracy of the linear fitting is close to those reported in [16, 33, 34].

The performance of the suggested multifunctional biosensors is compared to other sensors in the literature [4, 9–11, 13–15] to clarify the advantage of the current work over the preceding ones as shown in Table 10.5. The table shows the dynamic detection range and the average sensitivity of the previously reported and current biosensors. It is evident from this table that the temperature sensitivities of the proposed biosensors are greater than that reported in [4, 9, 10] while the temperature sensitivity of the LC core multifunctional sensor is smaller than that of the NLC-PCF temperature sensor [11]. However, the proposed LC core design is a multifunctional sensor with glucose monitoring capabilities with high sensitivity. Further, the sensitivity of the analyte refractive index change of our design is greater than that obtained by the multichannel sensors [13, 14]. Furthermore, the sensitivity is comparable with the counterparts reported in [12, 15] for the case of LC core while it is far higher for the case of the alcohol core. Additionally, the previously reported SPR-PCF sensors [1, 9–11, 15] are operated for sensing one parameter only such as temperature [4, 9–11] or analyte refractive index [13–15]. In comparison to bifunctional biosensors, Peng et al. [36] have implemented fiber sensor with two cascaded SPR sensing areas. Therefore, the sensitivity of each area is different than the other sensing area. However, this is on the expense of increasing the length of the sensor [36]. Further, Xiao et al. [37] have reported biosensor for detecting temperature and refractive index changes based on

Table 10.5 Comparison between the previously published sensors and the suggested designs

Fiber design		Sensing function & Range	Average S_λ	Multi-function
Fiber filled with silver nanowires and liquid [9]		Temperature 0 – 40°C	2.7 nm/°C	No
Directional coupler filled with liquid crystal [10]		Temperature 27.3 – 37.4°C 43.9 – 53.5°C	3.86 nm/°C	No
Randomly filled with silver nanowires [4]		Temperature -4 – 15°C	4 nm/°C	No
Plasmonic photonic crystal temperature sensor [11]		Temperature 30 – 50°C	10 nm/°C	No
Biosensor for an aqueous environment [12]		Refractive index 1.33 – 1.34	4000 nm/RIU	No
PCF biosensor [13]		Refractive index 1.33 – 1.34	2000 (HE_x^{11}) nm/RIU 1667 (HE_y^{11}) nm/RIU	No
PCF birefringent biosensor [14]		Refractive index 1.33 – 1.34	2000 (HE_x^{11}) nm/RIU 1700 (HE_y^{11}) nm/RIU	No
Analyte-filled core SPR PCF [15]		Refractive index 1.46 -1.485, 1.50 –1.52	4354(peak1) nm/RIU 2280(peak2) nm/RIU 2660(peak1) nm/RIU 4240(peak2) nm/RIU	No
Isopropanol-sealed PCF [7]		Refractive index 1.3577 – 1.3739	275.296 nm/RIU	Yes
		Temperature 23.7 – 66.1 ℃	166 pm/℃	
This work	LC core	Refractive index 1.33 – 1.34	3900 nm/RIU	Yes
		Temperature 30 – 50°C	5 nm/°C	
	Alcohol core	Refractive index 1.33 – 1.34	12700 nm/RIU	Yes
		Temperature -4 – 53°C	13.1 nm/°C	

Kretschamann SPR sensor. However, this sensor has disadvantages in terms of larger sensing area than that of the fiber sensors.

The proposed SPR-PCF biosensors are based on a triangular lattice of airholes which is widely fabricated using the well-known stack and draw method [38]. In this technique, the airholes can be arranged with high accuracy through careful process control. Further, the fused array preform technique can be used to fabricate PCF with airhole diameters of typically 0.1 microns or more [39]. The reported design has a nanorod that is attached to the left corner of a large hole. In this regard, Luan et al. [4] have successfully fabricated PCF with silver nanorods that are attached to the inner surface of the desired capillaries by using capillary force and air pressure. Additionally, polymer glue can be used to stick the rod at the desired position. Then, an unfocused ultra-violate irradiation will be applied through the structure to harden the glue without affecting the remaining structural materials as reported by Lee [40]. In order to selectively fill the large hole attached with the nanorod with the analyte, silicone glue can be used to block the other holes. Then, one end of the PCF is submerged into the analyte solution, and hence, the unblocked hole will be filled by the fluid under capillary forces. Further, the infiltration of the central hole with Alcohol mixture or NLCs can be accomplished using the same technique reported by Huang et al. [41]. The PCF required length can be cleaved with filled central hole. The coupling between the laser source and the proposed structure is carried out by splicing it to a standard single-mode fiber (SMF) and then launching the light from a laser source direct to the SMF as explained by Leon-Saval et al. [42].

10.4 Summary

Two novel designs of multifunctional highly sensitive SPR biosensors based on SPR LC-PCF and alcohol mixture-filled PCF are presented and analyzed. The LC core-based sensors could sense both temperature and analyte refractive index with high sensitivity of 5 nm/°C over temperature range $(30\,°C: 50\,°C)$ and 3700 nm/RIU over analyte refractive index range (1.33:1.34), respectively. In addition, the alcohol core sensor achieves an ultra-high-temperature sensitivity of 13.1 nm/°C over temperature range $(-4\,°C: 53\,°C)$ with a high refractive index sensitivity of 12700 nm/RIU over analyte refractive index range (1.33:1.34). Therefore, the suggested sensors show great potential for biosensing, glucose monitoring, and microfluidic sensing applications. Additionally, the suggested biosensors have advantages in terms of simplicity of fabrication. Further, the reported LC core-based biosensor has a fabrication tolerance of $\pm 5\%$ at which the sensitivities of the temperature and analyte refractive index are still better than 3.4 nm/°C and 3700 nm/RIU, respectively, which ensure the robustness of the reported biosensor for fabrication errors.

References

1. A. Hassani, M. Skorobogatiy, Design of the microstructured optical fiber-based surface plasmon resonance sensors with enhanced microfluidics. Opt. Expr. **14**, 11616–11621 (2006)
2. E.K. Akowuah, T. Gorman, H. Ademgil, S. Haxha, G. Robinson, J. Oliver, Surface-plasmon-resonance sensor based on three-hole microstructured optical fiber. Opt. Exp. **16**, 8427–8432 (2008)
3. M.F.O. Hameed, Y.K.A. Alrayk, A.A. Shaalan, S.S.A. Obayya, Novel multichannel surface plasmon resonance photonic crystal fiber biosensor, SPIE Photon. Europe (2016)
4. N. Luan, R. Wang, W. Lv, Y. Lu, J. Yao, Surface plasmon resonance temperature sensor based on photonic crystal fibers randomly filled with silver nanowires. Sensors **14**, 16035–16045 (2014)
5. I. Abdulhalim, Optimized guided mode resonant structure as thermooptic sensor and liquid crystal tunable filter. Chin. Opt. Lett. **7**(8), 667–670 (2009)
6. M.A. Ismail, N. Tamchek, M.R. Abu Hassan, K.D. Dambul, J. Selvaraj, N. Abd Rahim, S.R. Sandoghchi, F.R.M. Adikan, A fiber bragg grating—bimetal temperature sensor for solar panel inverters. Sensors **11**, 8665–8673 (2009)
7. S.-J. Qiu., Y. Ch., F. Xu, Y.Q. Lu, Temperature sensor based on an isopropanol-sealed photonic crystal fiber in-line interferometer with enhanced refractive index sensitivity. Opt. Lett. **37**(5), 863–865 (2012)
8. Y. Peng, J. Hou, Z. Huang, Q. Lu, Temperature sensor based on surface plasmon resonance within selectively coated photonic crystal fiber. Appl. Opt. **51**(26), 6361–6367 (2012)
9. Y. Lu, M.T. Wang, C.J. Hao, Z.Q. Zhao, J.Q. Yao, Temperature sensing using photonic crystal fiber filled with silver nanowires and liquid. IEEE Photon. J. **6**(3), 6801307 (2014)
10. D.J.J. Hu, P.P. Shum, J.L. Lim, Y. Cui, K. Milenko, Y. Wang, T. Wolinski, A compact and temperature-sensitive directional coupler based on photonic crystal fiber filled with liquid crystal 6CHBT. IEEE Photon. J. **4**(5), 2010–2016 (2012)
11. M.F.O. Hameed, M.Y. Azab, A.M. Heikal, S.M. ElHefnawy, S.S.A. Obayya, Highly sensitive plasmonic photonic crystal temperature sensor filled with liquid crystal. IEEE PTL **28**, 59–62 (2015)
12. E.K. Akowuah, T. Gorman, H. Ademgil, S. Haxha, G. Robinson, J. Oliver, A novel compact photonic crystal fibre surface plasmon resonance biosensor for an aqueous environment, in *Photonic Crystals—Innovative Systems, Lasers and Waveguides*, Dr. Alessandro Massaro (ed.), ISBN: 978-953-51-0416-2 (2012)
13. E.K. Akowuah, T. Gorman, H. Ademgil, S. Haxha, G.K. Robinson, J.V. Oliver, Numerical analysis of a photonic crystal fiber for biosensing applications. IEEE J. Quant. Electron. **48**, 1403–1410 (2012)
14. R. Otupiri, E.K. Akowuah, S. Haxha, H. Ademgil, F. AbdelMalek, A. Aggoun, A novel birefrigent photonic crystal fiber surface plasmon resonance biosensor. IEEE Photon. J. **6**(4), 1–11 (2014)
15. W. Qin, S. Li, Y. Yao, X. Xin, J. Xue, Analyte-filled core self-calibration microstructured optical fiber based plasmonic sensor for detecting high refractive index aqueous analyte. Opt. Laser Eng. **58**, 1–8 (2014)
16. M.F.O. Hameed, Y.K.A. Alrayk, S.S.A. Obayya, Self-calibration highly sensitive photonic crystal fiber biosensor. IEEE Photon. J. **8**(3), 1–12 (2016)
17. S.I. Azzam, M.F.O. Hameed, R. Eid, A. Shehata, A.M. Heikal, S.S.A. Obayya, Multichannel photonic crystal fiber surface plasmon resonance based sensor. Opt. Quant. Electron **48**(2) (2016)
18. M.F.O. Hameed, Y.K.A. Alrayk, A.A. Shaalan, W.S. El Deeb, S.S.A. Obayya, Design of highly sensitive multichannel bimetallic photonic crystal fiber biosensor. J. Nanophoton. **10** (4), 046016 (2016)
19. S.S.A. Obayya, M.F.O. Hameed, N.F.F. Areed, Liquid crystal photonic crystal fiber sensors, in *Computational Liquid Crystal Photonics*. (Wiley, 2016)

20. N.F.F. Areed, M.F.O. Hameed, S.S.A. Obayya, Highly sensitive face-shaped label-free photonic crystal refractometer for glucose concentration monitoring. Opt. Quant. Electron. (2016)
21. COMSOL Multiphysics Inc. http://www.comsol.com
22. S.S.A. Obayya, B.M.A. Rahman, K.T.V. Grattan, Accurate finite element modal solution of photonic crystal fibres. IEE Proc.: Optoelectron. **152**(5), 241–246 (2005)
23. C. Kalnins, H. Ebendorff-Heidepriem, N. Spooner, T. Monro, Radiation dosimetry using optically stimulated luminescence in fluoride phosphate optical fibers. Opt. Mat. Exp. **2**, 62 (2012)
24. M.Y. Azab, M.F.O. Hameed, S.S.A. Obayya, Multi-functional optical sensor based on plasmonic photonic liquid crystal fibers, Opt. Quant. Electron. **49**(2) (2017)
25. D.C. Zografopoulos, E.E. Kriezis, T.D. Tsiboukis, Photonic crystal-liquid crystal fibers for single-polarization or high birefringence guidance. Opt. Exp. **14**(2), 914–925 (2006)
26. M.F.O. Hameed, S.S.A. Obayya, K. Al-Begain, M.I. Abo el Maaty, A.M. Nasr, Modal properties of an index guiding nematic liquid crystal based photonic crystal fiber. J. Lightwave Technol. **27**(21), 4754–4762 (2009)
27. M.F.O. Hameed, S.S.A. Obayya, K. Al Begain, A.M. Nasr, M.I. Abo El Maaty, Coupling characteristics of a soft glass nematic liquid crystal photonic crystal fibre coupler. IET Optoelectron. **3**(6), 264–273 (2009)
28. M.Y. Azab, M.F.O. Hameed, S.M. El-Hefnawy, S.S.A. Obayya, Ultra-compact liquid crystal dual core photonic crystal fibre multiplexer–demultiplexer. IET Optoelectron. **10**(1), 1–7 (2015)
29. P. Alexandros, D.C. Zografopoulos, E. Kriezis, In-line polarization controller based on liquid-crystal photonic crystal fibers. J. Lightwave Technol. **29**, 2560–2569 (2011)
30. D. Daly, G.Clark, Optical measurement of glucose content of the aqueous humor, in *Lein Applied Diagnostics* (2004)
31. T.R. Wolinski, K. Szaniawska, S. Ertman, P. Lesiak, A.W. Domanski, R. Dabrowski, E. Nowinowski-Kruszelnicki, J. Wojcik, Influence of temperature and electrical fields on propagation properties of photonic liquid-crystal fibres. Meas. Sci. Technol. **17**(5), 985–991 (2006)
32. T.R. Wolinski, S. Ertman, A. Czapla, P. Lesiak, K. Nowecka, A.W. Domanski, E. Nowinowski-Kruszelnicki, R. Dabrowski, J. Wojcik, Polarization effects in photonic liquid crystal fibers. Meas. Sci. Technol. **18**(10), 3061–3069 (2007)
33. C. Zhou, Theoretical analysis of double-microfluidic-channels photonic crystal fiber sensor based on silver nanowires. Opt. Commun. **288**, 42–46 (2013)
34. A.A. Rifat, G.A. Mahdiraji, D.M. Chow, Y.G. Shee, R. Ahmed, F.R.M. Adikan, Photonic crystal fiberbased surface plasmon resonance sensor with selective analyte channels and graphene-silver deposited core. Sensors **15**, 11499–11510 (2015)
35. *TIE-19: Temperature Coefficient of Refractive Index*, SCHOTT Technical Information, SCHOTT North America, Inc., New York, NY, USA, July 2012, pp. 1–12
36. W. Peng, S. Banerji, Y.C. Kim, K.S. Booksh, Investigation of dual-channel fiber-optic surface plasmon resonance sensing for biological applications. Opt. Lett. **30**, 2988–2990 (2005)
37. F. Xiao, D. Michel, G. Li, A. Xu, K. Alameh, Simultaneous measurement of refractive index and temperature based on surface plasmon resonance sensors. J. Lightwave Technol. **32**, 3567–3571 (2014)
38. P. Russell, Photonic crystal fibers. Science **299**(5605), 358–362 (2003)
39. P. Falkenstein, B.L. Justus, *Fused Array Preform Fabrication of Holey Optical Fibers* (Google Patents, 2013)
40. H. Lee, *Plasmonic Photonic crystal Fiber*, PhD, Max Plank Institute (2012)
41. Y. Huang, Y. Xu, A. Yariv, Fabrication of functional microstructured optical fibers through selective filling technique. Appl. Phys. Lett. **85**, 5182–5184 (2004)
42. S.G. Leon-Saval, T.A. Birks, N.Y. Joly, A.K. George, W.J. Wadsworth, G. Kakarantzas, P.S. J. Russel, Splice-free interfacing of photonic crystal fibers. Opt. Lett. **30**(13), 1629–1631 (2005)

Chapter 11
Photonic Crystal Fiber Pressure Sensors

Zhengyong Liu and Hwa-Yaw Tam

Abstract This chapter introduces photonic crystal fibers (PCFs) specifically designed for pressure sensors, including PCF fabrication to introduce birefringence and pressure sensor design incorporating the PCFs. Simulation and experimental results for pressure sensors incorporating two common principles, grating and interferometry, are presented. The flexibility of designing PCF microstructures means PCF pressure sensors with very high sensitivity and accuracy are relatively easily fabricated, compared with conventional methods based on single-mode fibers, microcavities, or electrical methods. Various PCF-based pressure sensor performances are compared. Pressure sensitivity varies with the employed principle, and we show that polarimetric techniques provide the highest sensitivity compared with other types. Higher sensor sensitivity and resolution allows for a large measurement dynamic range. The proposed novel pressure sensors will meet the increasing requirements and have many applications for pressure monitoring, e.g., oil industry and biomedical detection.

Keywords Photonic crystal fiber · Pressure sensor · Fiber bragg grating Interferometry · High birefringence

List of Abbreviations

PCF	Photonic crystal fiber
FBG	Fiber Bragg grating
SMF	Single-mode fiber
FPI	Fabry-Pérot interferometer
MZI	Mach-Zehnder interferometer
SI	Sagnac interferometer
TIR	Total internal refraction
M-TIR	Modified total internal refraction

Z. Liu (✉) · H.-Y. Tam
Photonics Research Centre, Department of Electrical Engineering, The Hong Kong Polytechnic University, Hung Hum, Kln, Hong Kong, China
e-mail: zhengyong.liu@connect.polyu.hk

© Springer International Publishing AG, part of Springer Nature 2019

M. F. O. Hameed and S. Obayya (eds.), *Computational Photonic Sensors*, https://doi.org/10.1007/978-3-319-76556-3_11

PBG-PCF	Photonic bandgap photonic crystal fiber
PM-PCF	Polarization-maintaining photonic crystal fiber
LPG	Long period grating
BBS	Broadband source
OSA	Optical spectrum analyzer
TC-PCF	Twin-core photonic crystal fiber
DR	Dynamic range
MOF	Microstructured optical fiber

11.1 Introduction

Fiber-optic pressure sensors have attracted increasing interest due to the intrinsic properties of optical fibers, such as compact size, rigidity, insensitivity to electromagnetic interference, long-distance measurements, and multiplexing [1]. Most commercial pressure sensors are based on electrical approaches, which have high failure rates when implemented in high-temperature applications. However, fiber-optic sensors have shown good performance in environments up to 250 °C. Fiber-optic sensors are also electrically free and suitable for applications in explosive or corrosive environments. Optical fiber sensors are an indispensable technology in the oil and gas industry [2], which often experiences extreme conditions. For example, real-time fluid pressure monitoring within offshore oil field boreholes is operationally and safety essential, but very challenging. Sensors can be subjected to high pressure (>100 MPa) and temperature (>200 °C), yet require high resolution (<0.0001 MPa), which requires a dynamic range of 10^6 (i.e., 120 dB). Fiber-optic sensors provide a new opportunity to sense a wide range of critical parameters in the oil and gas industry, such as pressure, temperature, vibration, flow [3].

Conventional fiber-optic pressure sensors employ single-mode fibers (SMFs), which are commercially available and widely used for telecommunication due to low loss transmission and handling simplicity. SMFs consist of a solid core and cladding approximately 8 and 125 μm in diameter, respectively. Most pressure sensors are based on fiber Bragg grating (FBG) technology, inscribed into the fiber core. Figure 11.1 demonstrates a feasible sensing system based on FBG arrays within a single fiber, which is often utilized for downhole applications to measure pressure, temperature, and flow simultaneously. Long measurement distance capability (>10 km) is desirable for downhole applications. In addition to the active measurement line, sensors are often packaged in small diameter conduits (e.g., internal diameter = 6 mm), as shown in Fig. 11.1

Low propagation loss and electrically free characteristics mean it is feasible to install fiber-optic pressure sensing systems for long-distance measurements.

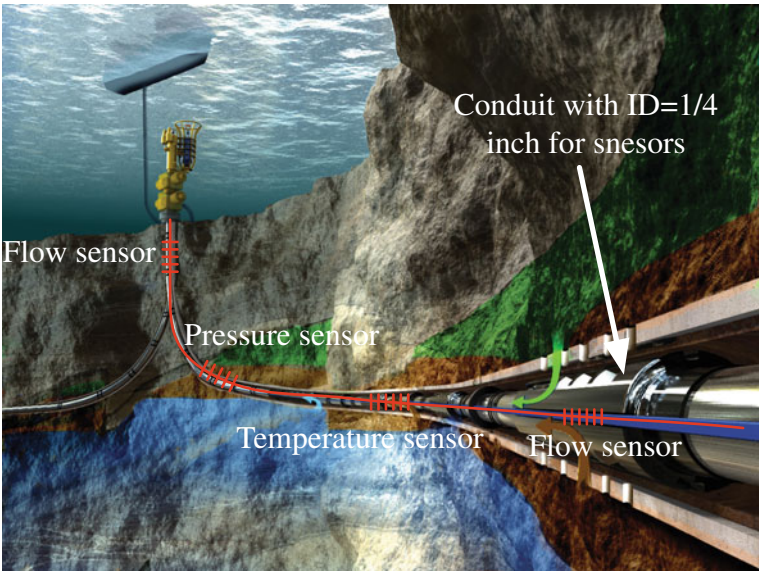

Fig. 11.1 Fiber Bragg grating-based sensing system for downhole applications (permission obtained from [4])

However, FBG pressure sensitivity on SMFs is of the order 4 pm/MPa [5], which is insufficient to achieve good performance. Although transducers transfer the external pressure to FBG axial strain, which improves pressure sensitivity to tens of pm/MPa, the sensor head becomes too bulky for many applications [6]. Nevertheless, the FBG technique is advanced, mature, and reliable [7]. Poor pressure sensitivity results from employing SMFs. Therefore, the novel specialty fibers are desirable for the sensing applications.

Interferometry has been employed for pressure sensors, e.g., Fabry–Pérot interferometers (FPIs) [8, 9] and Mach–Zehnder interferometers (MZIs) [10], using micromachined SMFs. FPIs have been developed for medical pressure detection using sensitive films to construct the Fabry–Pérot cavity [8], one of a range of useful, promising, and commercially available SMF sensors. FISO Technologies Inc., a private company, is focused on developing FPI products for medical and life sciences. Current commercial FPI probes are sufficiently sensitive and detect very slight pressure change. The necessarily simple SMF structure limits pressure sensitivity and resolution, which provides large research space for improvement.

The special designs of the microstructured optical fibers could improve the pressure sensitivity dramatically owing to the flexibility of the airhole arrangement. Several types of those pressure sensors including those based on gratings and interferometry have been reported. In 2008, Fu et al. reported that the pressure sensitivity could be enhanced up to 3.42 nm/MPa by configuring a Sagnac

interferometer based on polarization-maintaining photonic crystal fiber (PM-PCF) [11]. This kind of approach is promising in the downhole applications with high temperature up to 293 °C [12]. Similar polarimetric pressure sensors employing the fiber intrinsic birefringence have been reported [13–20] and can achieve polarimetric sensitivity as high as -76 rad $\times$ MPa^{-1} m^{-1} [16]. High sensitivity is possible thanks to the asymmetrical airhole structure of the PCFs, e.g., side holes [16, 17], two large holes adjacent to the core [11], "butterfly" airhole arrangement [13], elliptical core [19, 20].

Furthermore, PCF-based pressure sensors are more critical and practical in recent years. In 2016, the temperature-compensated distributed sensing scheme using PM-PCF was demonstrated [21]. The temperature cross talk was measured by the temperature-induced Brillouin frequency shift, while the pressure sensing is realized by measuring the birefringence changes through exciting and probing the Brillouin dynamic gratings. Moreover, the novel mechanism of anti-resonant guidance was utilized as well to sense pressure in hollow-core fiber, showing a sensitivity of 3.592 nm/MPa [22]. FBGs written in specialty fiber (i.e., "butterfly" airhole arrangement) were reported in the year of 2017 to measure high pressure over an operating temperature range from 40 to 290 °C [23]. Even though the pressure sensitivity is only 33 pm/MPa due to the grating-based approach, it achieves low-temperature cross-sensitivity of 0.6 kPa/°C. In the same year, Osório et al. reported a simple design of special microstructured optical fiber that has an embedded core in the wall of capillary. The demonstrated pressure sensitivity can be up to 10.4 nm/MPa. However, the free-space coupling is employed, which is not acceptable in many applications.

This chapter presents the principles, types, and applications for novel photonic crystal fiber (PCF)-based pressure sensors. PCFs were first proposed and demonstrated by Phillip Russel and are optical fibers with microstructures formed by periodic airholes along the fiber [24–26]. The airholes are arranged in a hexagonal structure, and the fiber core is either solid (pure silica or metallic ion-doped silica) or hollow, depending on the desired cross-sectional structure. Optical and mechanical PCF properties can be easily tuned simply by modifying the microstructure, i.e., the arrangement of airholes. Techniques have been developed that allow simple fabrication of microstructures along with the fiber, many sensors have been produced using various structures, and their physical and biomedical parameters have been monitored [27, 28]. This chapter focuses on pressure sensors in particular.

11.2 Photonic Crystal Fibers

Since the first endless single-mode PCFs were fabricated in the 1990s, PCFs have become an important and rapidly developing area of research and development of optical fibers [29, 30]. They differ from conventional SMFs in that PCF cladding is composed of one or several layers of airholes hexagonally stacked along with the

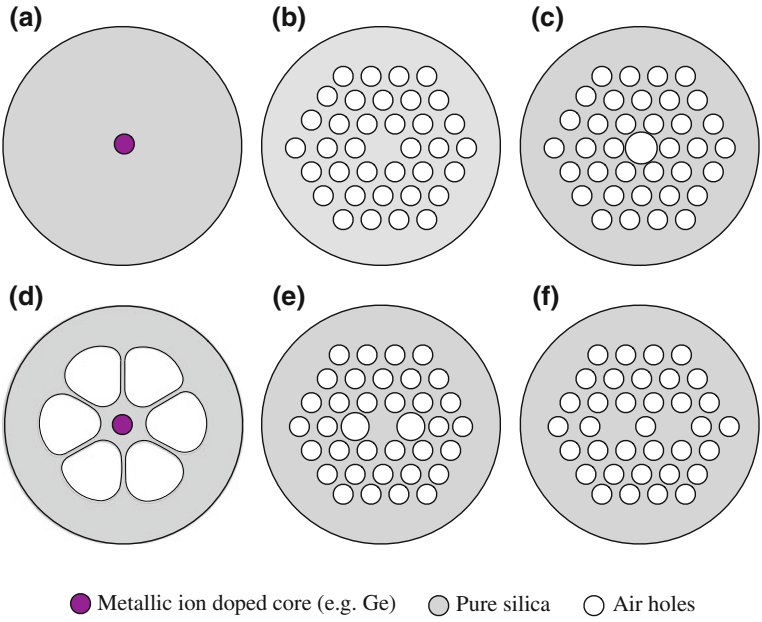

Fig. 11.2 Typical cross sections for **a** single-mode fiber (SMF), **b** solid-core photonic crystal fiber (PCF), **c** hollow-core PCF, **d** six-hole PCF, **f** polarization-maintaining PCF, and **g** twin-core PCF

fiber length, as shown in Fig. 11.2. Generally, SMF cores are doped with germanium to increase the refractive index, whereas PCF cores contain pure silica for index guides or an open hole for hollow-core PCFs.

Conventional SMFs consist of doped core and silica cladding, where the core has a slightly higher index than the cladding to provide total internal refraction (TIR) and support light propagation. Generally, PCFs are composed of a single material, i.e., fused silica. The PCF core is pure silica with an index = 1.444 at 1550 nm. The periodic airholes reduce the average refractive index of the cladding, providing an index profile similar to conventional step index fibers. This mechanism is called modified total internal refraction (M-TIR), and these are regarded as index-guiding PCFs [25], as shown in Figs. 11.2b, e, and f.

Alternatively, PCF cores can be hollow, as shown in Fig. 11.2c, which also guide the light following photonic bandgap theory. For these PCFs, the core index is lower than that of the cladding, and only specific wavelength regimes falling within the bandgap can be guided. The hollow core is implemented by removing capillaries from a triangular lattice of holes, with 7 or 19 cells missing (commonly) [31]. These fibers are also called photonic bandgap PCFs (PBG-PCFs) [25].

Index-guiding PCF cores can also be doped with metallic ions to modify the core properties in desirable ways, as shown in Fig. 11.2d. For example, germanium-doped PCF cores enable FBGs to be inscribed within the core similar to conventional SMFs [32]. Additionally, airholes in the cladding mean pressure-induced stress transferred

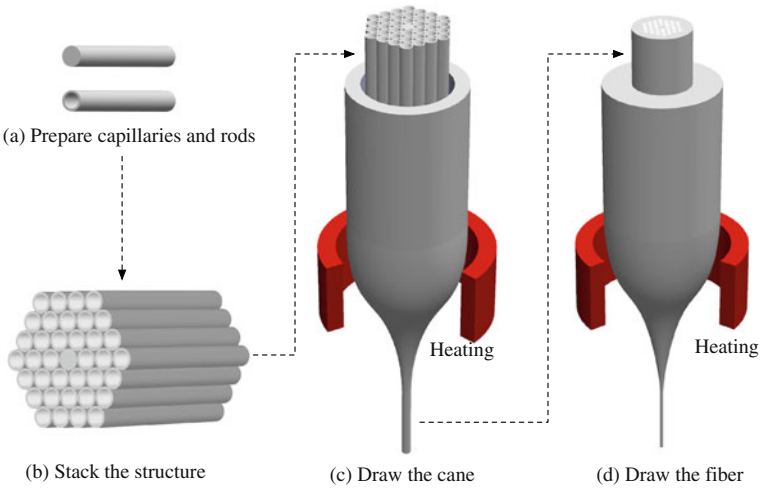

Fig. 11.3 Typical photonic crystal fiber (PCF) fabrication using two draw stages

to the core changes with the PCF structure type, consequently improving pressure sensitivity.

Several PCF fabrication approaches have been developed, such as extrusion [33], drilling [34], and stacking [35], to introduce the desired airhole structure [36]. The stack and draw technique is the most popular due to its ease, flexibility, and efficiency of stacking the structures, as shown in Fig. 11.3. Capillaries and rods with the same diameter are first drawn from a large silica tube and preformed. The preform is stacked with a hexagonal structure using the capillaries, and the center capillary is replaced with a silica rod core. A cane with the desired microstructure is drawn from the stacked preform and then inserted into a jacket tube with a precise inner and outer diameter. The PCF is fabricated by re-drawing the jacket tube with the cane inside. Typical drawing temperatures are 1900–1950 °C, somewhat less than that used to draw SMFs, to maintain the airhole structure [37]. Thus, PCF structure can be easily modified by changing the arrangement of airholes and rods during stacking. Consequently, the pressure-induced stress distribution across fiber facets can be tuned to obtain high-performance pressure sensors.

To develop PCFs into pressure sensors, the fibers should have either photosensitivity, to enable FBG inscription, or special structures to facilitate interferometry. Consider the Sagnac interferometer (SI) as an example, which requires birefringent fibers. The flexibility of PCF fabrication techniques means high birefringence can be simply introduced by an appropriate airhole distribution. High birefringence means the core can support two orthogonal linearly polarized modes with different effective indexes over a wide wavelength range. In conventional fibers, i.e., not birefringent PCFs, those orthogonal modes have the same effective index and can be regarded as a single mode. The polarization with large effective index is called the slow axis, and the other the fast axis. Birefringence is the difference of effective index between the orthogonal modes, $B = |n_x - n_y|$, where n_x

and n_y are the effective index of x- and y-polarized modes, respectively. Birefringence of PCFs can be expressed in three parts

$$B = B_G + B_S^i + B_S^e, \tag{11.1}$$

where B_G is the geometrical component induced by core asymmetry; B_S^i is the interior stress of the core, i.e., the self-stress induced by the difference of thermal expansion between the asymmetrical core and outer cladding; and B_S^e is the exterior stress of the core caused by the stress-applying parts of the cladding. Thus, B is highly dependent on the fiber structure, which provides large birefringence from asymmetry of the core shape (e.g., elliptical core) and asymmetrical stress induced by the cladding (e.g., asymmetrical airhole distribution or stress-applying dopants).

Stacking asymmetrical airholes in the cladding or introducing an elliptical core produces PCFs with high birefringence. The first high birefringence PCF was made by Ortigosa-Blach et al. at the University of Bath in 2000 [38]. Their design broke the hexagonal structure with twofold rotational symmetry around a central line of smaller airholes and produced $B = 3.85 \times 10^{-3}$. Subsequently, different high birefringence PCFs have been proposed and fabricated with $B = 10^{-4}$ to 10^{-2}. For these polarization-maintaining PCFs (PM-PCFs), a structure of two large airholes adjacent to the core is widely used and commercially available from NKT Photonics (PM-1550-01©). The beat length of this fiber is less than 4 mm, corresponding to $B \approx 4 \times 10^{-4}$ at 1550 nm, and it has low propagation loss (1.3 dB/km) [39].

This type of structure has been developed within our research group into various sensors, including SI-based pressure sensors with pressure sensitivity = 3.4 nm/MPa [11]. We also modified the structure by introducing an elliptical core doped with germanium, obtaining ultrahigh birefringence $B = 1.1 \times 10^{-2}$ [40]. The fiber enables FBGs to be inscribed in the core, and its ability to discriminate pressure and temperature simultaneously was demonstrated by detecting the shift of two widely separated Bragg peaks due to the ultrahigh birefringence. Other special structures inducing birefringence include large side hole [41], butterfly type [19, 42], super lattice [43, 44], and elliptical airhole [45–47] PCFs. Asymmetry in the core directly leads to interior stress within the core, further increasing birefringence. These types of PCFs show good performance for pressure sensing, such as elliptical core [48, 49] and suspended elliptical core [37] PCFs. The details of pressure sensors based on birefringent PCFs are described in the following sections.

11.3 Types and Principles of Photonic Crystal Fiber-Based Pressure Sensors

Figure 11.4 shows the two main types of PCF pressure sensors: grating- and interferometry-based. FBGs and long-period gratings (LPGs) can be inscribed on PCFs and utilized to measure pressure. Sagnac, Fabry–Pérot, and Mach–Zehnder interferometers are widely employed to configure pressure sensors.

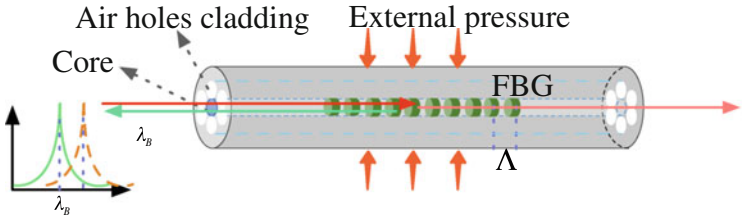

(a) FBG-based PCF pressure sensor

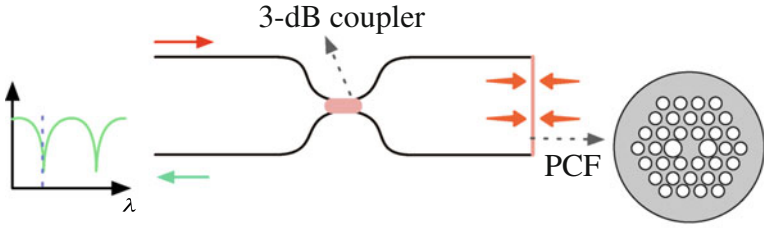

(b) SI-based PCF pressure sensor

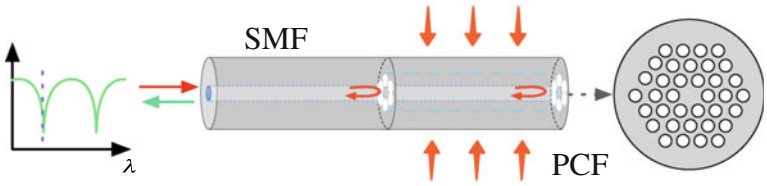

(c) FPI-based PCF pressure sensor

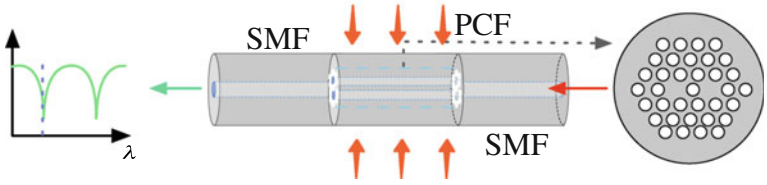

(d) MZI-based PCF pressure sensor

Fig. 11.4 Typical pressure sensor configurations based on photonic crystal fibers (PCFs)

11.3.1 Grating-Based Photonic Crystal Fiber Pressure Sensors

Normally, the core must be photosensitive, such as germanium-doped silica, to fabricate Bragg gratings on PCFs, with the grating formed from photoinduced refractive index change by UV lasers (193, 213, 248, or 266 nm wavelength) [50, 51]. However, high-power femtosecond or CO_2 lasers can also be used to inscribe the gratings [52], which do not require photosensitivity, but directly induce physical damage or deformation. Typically, it is more difficult to inscribe FBGs on PCFs using UV lasers compared to conventional SMFs, because the honeycomb airhole structure can diffract the laser beam and result in non-uniform interference patterns within the core. The problem is accentuated for larger air-filling fractions or thinner airhole wall thickness. Higher power UV lasers with superior beam quality and alignment can assist with this issue. When using the phase mask technique, the modulated index pitch along the fiber depends on the phase mask, whereas it is inversely proportional to the angle between two laser beams if an interferometric approach is employed. The Bragg wavelength can be expressed as

$$\lambda_B = 2n_{eff}\Lambda, \tag{11.2}$$

where λ_B is the reflected Bragg wavelength, n_{eff} is the effective index of the guided mode in the microstructured optical fiber (MOF), and Λ is the FBG pitch. When the FBG is subjected to pressure, e.g., hydrostatic oil or water, this induces a change in the effective index and the grating pitch proportionally with the pressure, and the Bragg wavelength shifts correspondingly,

$$\Delta\lambda_B(P)/\lambda_B = \Delta\Lambda(P)/\Lambda + \Delta n_{eff}(P)/n_{eff}, \tag{11.3}$$

where $\Delta\lambda_B(P)$, $\Delta\Lambda(P)$, and $\Delta n_{eff}(P)$ are the pressure-induced change in Bragg wavelength, grating pitch, and effective index, respectively. Silica's refractive index changes with external pressure due to the photo-elastic effect, and hence, the effective index of the guided mode also varies with the applied pressure. Since silica glass is isotropic, the index variation after applying pressure can be expressed as [53]

$$\begin{cases} n_x = n(\lambda)_{silica} - C_1 \cdot \sigma_x - C_2 \cdot \sigma_y - C_2 \cdot \sigma_z \\ n_y = n(\lambda)_{silica} - C_2 \cdot \sigma_x - C_1 \cdot \sigma_y - C_2 \cdot \sigma_z \\ n_z = n(\lambda)_{silica} - C_2 \cdot \sigma_x - C_2 \cdot \sigma_y - C_1 \cdot \sigma_z \end{cases}, \tag{11.4}$$

where σ_i is the stress component in ith direction ($i = x, y, z$); $n(\lambda)_{silica}$ is the silica glass index, which depends on wavelength as well due to dispersion; and C_1 and C_2 are the stress optic coefficients for silica (6.5×10^{-13} and 4.2×10^{-12} m^2/N, respectively) [54]. The pressure-induced index change can be obtained by calculating the effective index of the guided mode under pressure. Figure 11.5 shows the

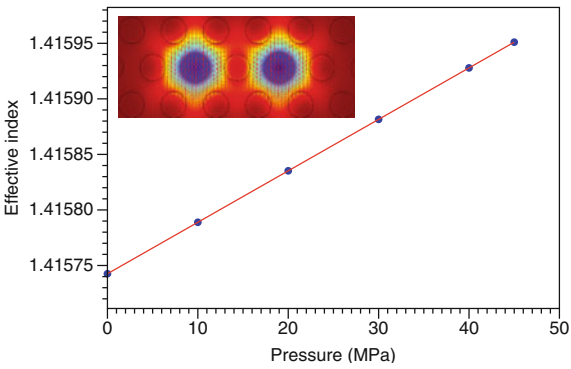

Fig. 11.5 Calculated effective index for guided even mode in a twin-core photonic crystal fiber (PCF)

effective index of the guided even mode in a twin-core PCF (Fig. 11.2f) with respect to external pressure applied to the fiber. The effective index increases with increasing applied pressure. The index pressure dependence varies with the airhole structure, and hence, high-sensitivity PCF pressure sensors can be fabricated by modifying the structure appropriately.

Pressure-induced changes in grating pitch can be regarded as the total strain, ε_z, along the fiber, including compression or elongation at the grating position. Figure 11.6 shows that the external pressure can induce radial, $\varepsilon_{z,\ radial}$, and axial, $\varepsilon_{z,\ axial}$, strains from the side surface and end facet of the fiber. Total FBG strain is the sum of the radial and axial strain caused by the applied pressure. Strain transfer is somewhat different from SMFs, which are fully solid, due to the airholes. Thus, the FBG is elongated due to the radial strain and compressed due to the axial strain [32].

Axial strain transferred to the grating position can be expressed as

$$\varepsilon_{z,\,axial} = -\frac{A}{A_0} \cdot P, \tag{11.5}$$

where P is the external pressure, A is the total cross-sectional area of the fiber, and A_0 is the silica area. Axial strain can be increased by introducing larger airholes. Thus, pressure sensitivity FBG on SMFs (−4 pm/MPa) is much lower than FBG on PCFs (−13 pm/MPa for grapefruit and −18 pm/MPa for single-ring suspended fiber with large airhole area configurations) [55]. Bragg wavelength for FBG on PCFs shows blueshift, which means that axial strain from external pressure has the dominant role in determining pressure sensitivity.

Figure 11.7 shows the pressure response as the wavelength shift for FBGs written on in-house fabricated ultrahigh birefringence PCF and single-ring suspended fiber. Pressure sensitivity can be improved approximately fivefold using larger airholes compared to SMFs and other PCFs. The ultrahigh birefringence PCF shows different pressure responses for the polarized peaks. Temperature dependence was approximately 11 pm/°C, which implies that this type of grating allows simultaneous measurement of pressure and temperature.

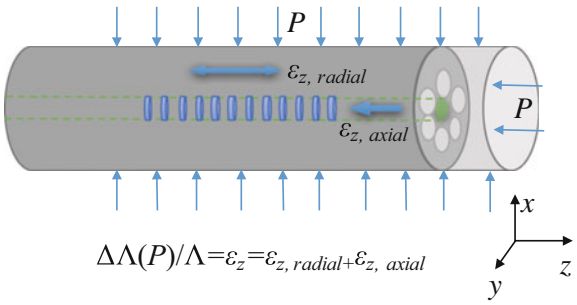

Fig. 11.6 Strain transfer induced by external pressure on a fiber Bragg grating (FBG) inscribed photonic crystal fiber (PCF)

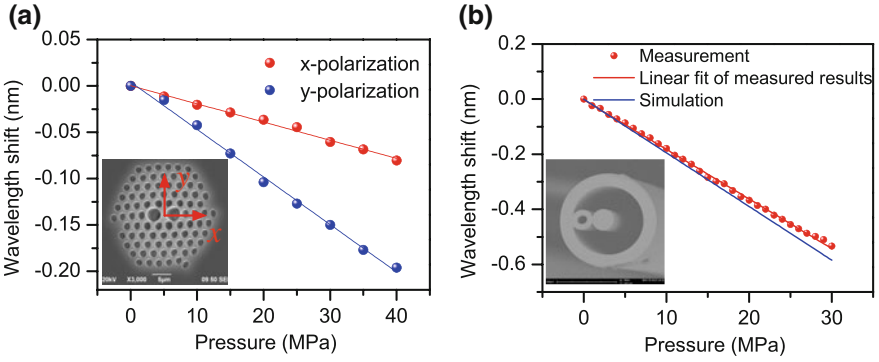

Fig. 11.7 Fiber Bragg grating pressure response written on **a** ultrahigh birefringence photonic crystal fiber (PCF) and **b** single-ring suspended fiber with large airhole area. Insets show the scanning electron microscopic images. Pressure sensitivity of ultrahigh birefringence PCF = −1.96 pm/MPa for *x*-polarized peak, and −5.13 pm/MPa for *y*-polarized peak, 18 pm/MPa (experiment), and 19.4 pm/MPa (simulation) for single-ring suspended fiber. (Adapted from [40, 55])

11.3.2 Sagnac Interferometer-Based Pressure Sensors

Interferometry is also widely employed for pressure sensors, based on either SI, FPI, or MZI systems. The flexibility of the PCF structure means an SI based on high birefringence PCF can be configured to measure pressure [11]. Section 11.2 of this chapter introduced PCF birefringence by breaking the fiber structure symmetry. High birefringence can be induced by asymmetrical cladding, elliptical core, or asymmetric stress applied to the core. Highly birefringent fibers are desirable to construct an SI, as shown in Fig. 11.4b, where PM-PCF is spliced between two single-mode fibers of a 3-dB coupler, forming a loop. The 3-dB coupler splits the input broadband source light into two counter propagating beams that interfere

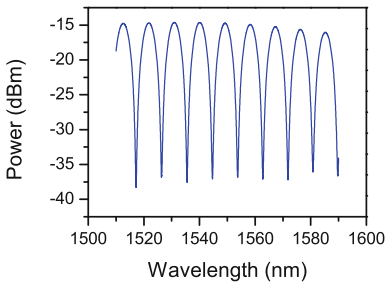

Fig. 11.8 Transmission spectrum from a Sagnac interferometers (SI) based on a commercial 0.35 m polarization-maintaining photonic crystal fiber (PM-PCF)

either constructively or destructively at the coupler. Interference transmission can be detected from the other port of the coupler. Figure 11.8 shows an example of SI transmission spectrum, using a 0.35 m commercial PM-PCF (NKT Photonics, PM-1550-01).

The spacing of two adjacent SI dips can be expressed as

$$G(\lambda) = \frac{\lambda^2}{\Delta\lambda \cdot L} \approx \frac{\lambda_1 \cdot \lambda_2}{\Delta\lambda \cdot L}, \tag{11.6}$$

where G and L are the PCF group birefringence and length, respectively; λ_1 and λ_2 are the wavelengths of two adjacent dips; and $\Delta\lambda$ is the fringe spacing. Figure 11.8 shows fringe spacing of 9 nm, which corresponds to group birefringence of 7.6×10^{-4} and beat length <4 mm. The phase difference between the fast and slow light can be expressed as

$$\varphi = \frac{2\pi}{\lambda} B(\lambda) \cdot L, \tag{11.7}$$

where $B(\lambda) = |n_x - n_y|$ is the phase birefringence and is wavelength dependent due to dispersion. The relationship between group and phase birefringence can be obtained via

$$G(\lambda) = B(\lambda) - \lambda \frac{dB(\lambda)}{d\lambda}. \tag{11.8}$$

When the PM-PCF is subject to high pressure oil, the refractive indexes, i.e., n_x, n_y, change due to photo-elastic effects as described in Eq. (11.4), which causes changes to the interference spectrum. Since the phase of one dip is always $2\ k\pi$ ($k \in I$), SI pressure sensitivity can be calculated from the derivative of Eq. (11.7) with respect to pressure,

$$\frac{d\lambda}{dP} = \frac{\lambda}{G(\lambda)} \cdot \frac{dB(\lambda)}{dP}, \tag{11.9}$$

where $dB(\lambda)/dP$ is determined by the pressure-induced index change and is related to the airhole structure, with different structures producing different stress distributions. Figure 11.9 shows the pressure response for three PCFs with different airhole structures, as indicated by wavelength shifts based on SI. Pressure sensitivity of commercial PM-PCF ≈ 3.9 nm/MPa, which is almost matched by the six-hole suspended-core fiber (3.3 nm/MPa). The fiber sensitivities are similar because their birefringence is similar (4×10^{-4}) and the pressure-induced strain transferred to the core from the slow and fast axis is comparative, which determines the term $dB(\lambda)/dP$ in Eq. (11.9). However, the in-house developed semicircular hole fiber (Fig. 11.9c) exhibits pressure sensitivity = 44 nm/MPa, more than a tenfold improvement. This fiber has two semicircle holes along the fast axis that breaks the pressure-induced strain transference to the core via this axis. Thus, pressure sensitivity can be significantly improved by modifying the PCF airhole structure, and sensitivity for SI systems is generally much higher than that based on the FBG technique.

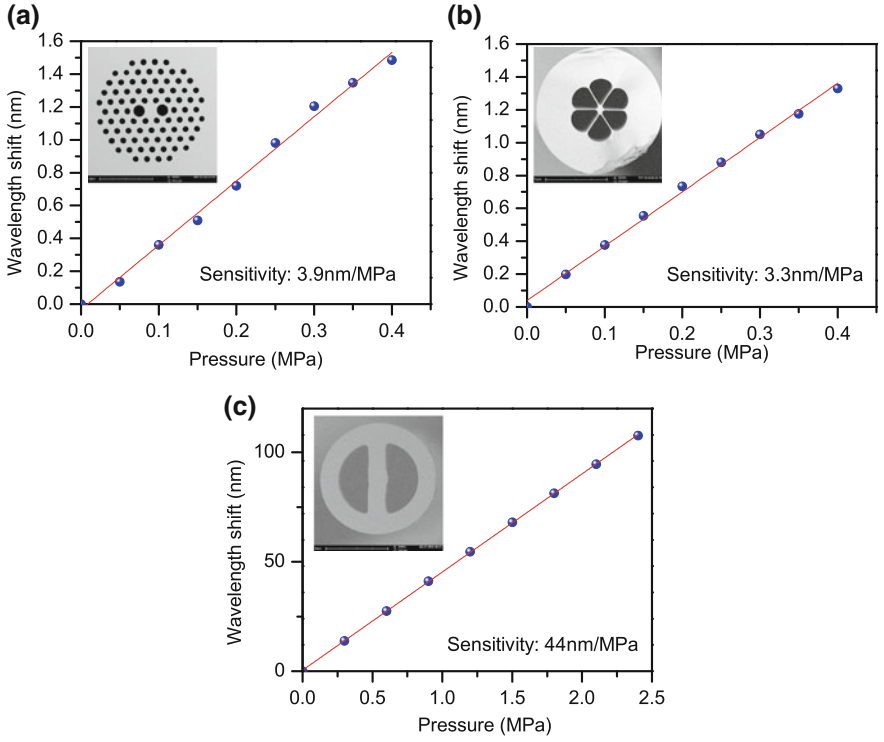

Fig. 11.9 Hydrostatic oil pressure response in wavelength shift for **a** commercial PM-PCF, **b** six-hole suspended-core fiber, and **c** semicircular hole fiber. Insets show the fiber cross-sectional structures

11.3.3 Fabry–Pérot Interferometer-Based Pressure Sensors

Fabry–Pérot interferometers have also been constructed to measure pressure. There are many ways to configure FPIs, where the FP cavity needs to be along the light propagating direction. The FP can be constructed by a film coating on the fiber end facet [56], forming an air cavity in the core [57], a FBG pair [58], or two material interfaces [59]. Since PCF cores can be pure silica, in contrast to SMF cores that require dopant (e.g., germanium) to increase the refractive index, Fresnel reflection facets of the FP cavity can be implemented by splicing the PCF between two SMF sections [59, 60], forming the FP cavity from the spliced connections and PCF core, as shown in Fig. 11.10.

Since the index difference between the PCF core and SMF is small (approximately 0.01), multiple reflections at the interfaces can be neglected and interference is regarded as a two-beam configuration. The spectrum can be expressed as

$$I(\lambda) = I_1 + I_2 + 2\sqrt{I_1 I_2}\cos\left(\frac{4\pi n_{neff} L}{\lambda} + \varphi_0\right), \tag{11.10}$$

where I_1 and I_2 are the intensities of the reflection beams at the two PCF and SMF interfaces, n_{eff} is the effective index of the fundamental PCF mode, L is the PCF length, and φ_0 is the initial phase. When the PCF is subject to high pressure, silica refractive index changes with the pressure due to photo-elastic effects, following the same relationship as Eq. (11.4). Total PCF length will also extend slightly under the radial pressure. Similar to the SI case, the phase of one FP interference spectrum dip is always 2 $k\pi$. Therefore, the wavelength change at one dip induced by the pressure can be expressed as

$$\frac{\Delta\lambda}{\lambda} = \frac{\Delta n_{eff}}{n_{eff}} + \frac{\Delta L}{L} = \frac{\Delta n_{eff}}{n_{eff}} + \varepsilon_z, \tag{11.11}$$

where ε_z is the total strain induced by the pressure on the FP cavity.

To measure the response, 1- and 2-mm-long PCFs were used to construct an FPI and then placed in a pressure-controlled chamber [59]. Pressure was increased from 0 to 40 MPa with 5 MPa step and the reflection spectrum recorded for each

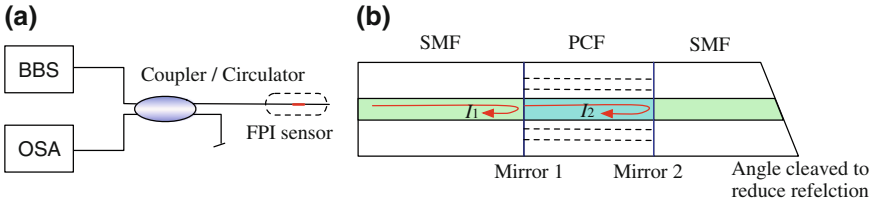

Fig. 11.10 Photonic crystal-based Fabry–Pérot interferometer. BBS = broadband source, OSA = optical spectrum analyzer

pressure. The 1- and 2-mm-based FPIs show similar pressure sensitivity (−5.57 and −5.77 pm/MPa, respectively). The pressure-induced change in effective index and strain was calculated using the finite element method (4.22×10^{-6} and -7.97×10^{-6} MPa^{-1}, respectively) [59]. Therefore, pressure sensitivity from Eq. (11.11) is equal to −5.8 pm/MPa at 1550 nm. Thus, experimental and simulation results show good agreement.

Since pressure sensitivity only depends on the change of fiber length, the various fiber lengths should have the same sensitivity, which is consistent with the experimental outcome. This is advantageous to design compact sensors using very short PCFs. Since the change of external pressure only causes corresponding variation in the effective index for the fundamental mode and axial strain, which are the same as FBG-based pressure sensors, the different pressure sensor types show similar pressure sensitivity, as expected from Eqs. (11.11) and (11.3). Nevertheless, since FPI and FBG-based pressure sensors have simpler configuration compared to SI, they are more suitable for practical applications to measure high pressure.

11.3.4 Mach–Zehnder Interferometer-Based Pressure Sensors

Mach–Zehnder interferometers (MZIs) can be configured to measure pressure using PCFs as well. In contrast to FPIs, which require a cavity, MZIs only require two light beams propagating forward. This can be implemented using two cores [61], two separate beams [62], two optical modes [63] (e.g., core and cladding modes), etc. We propose a novel design twin-core PCF (TC-PCF) that propagates supermodes in *x*- and *y*-polarized directions to measure pressure [61]. MZI interference has intrinsic interferometer characteristics and occurs when two light beams have a certain phase shift. Typically, external pressure induces perturbation in either one or both beams when the MZI is placed in such an environment.

The TC-PCF supports supermodes of the even and odd modes in *x* and *y* polarizations. Since the supermodes are propagating along two fiber cores, the beams couple with each other simultaneously. Figure 11.11a shows the setup to measure transmission spectrum using a 110 cm TC-PCF, and Fig. 11.11b shows the resultant interference spectrum. Interference was modulated due to a combination of interferences occurring in *x* and *y* polarizations. Fringe spacing is measured to be 0.676 nm.

Total intensity measured at the output end can be expressed as

$$I(\lambda) = 1 - \cos\left[\frac{\pi}{\lambda}(\Delta n_{x,g} + \Delta n_{y,g})L\right] \cdot \cos\left[\frac{\pi}{\lambda}(\Delta n_{x,g} - \Delta n_{y,g})L\right], \tag{11.12}$$

where $\Delta n_{x,g}$ and $\Delta n_{y,g}$ are the index differences between even and odd modes in *x*- and *y*-polarized directions, respectively, and L is the TC-PCF length.

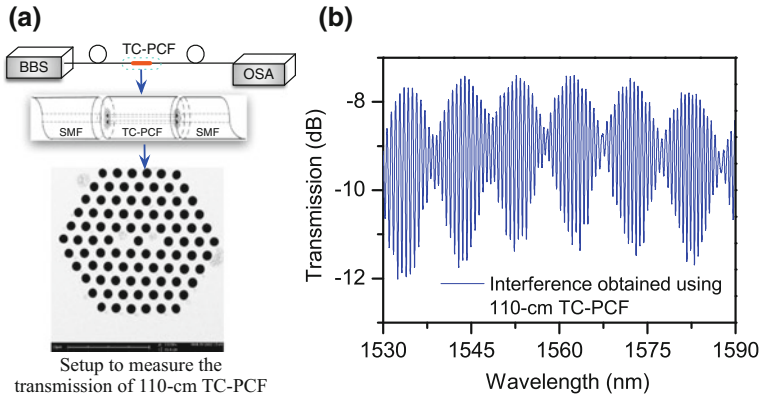

Fig. 11.11 Transmission interference using 110 cm twin-core photonic crystal fiber (TC-PCF): **a** equipment setup to measure the spectra and scanning electron microscopic TC-PCF image and **b** corresponding transmission spectrum of the interference. (Adapted from [61])

The transmission spectrum is modulated by the last term in Eq. (11.12). Considering small wavelength range, fringe spacing can be approximated as

$$\Delta\lambda = \frac{2\lambda^2}{(\Delta n_{x,g} + \Delta n_{y,g})L}. \tag{11.13}$$

The index difference of even and odd modes was calculated using the finite element method based on the actual TC-PCF cross-sectional structure, as shown in Fig. 11.11a. Index difference = 3.745×10^{-3} and 3.386×10^{-3} at x and y polarizations, respectively. Thus, fringe spacing = 0.613 nm at 1550 nm, which shows good consistency with the measured result (0.676 nm, Fig. 11.11b).

Similar to Eq. (11.4), the photo-elastic effect when the fiber is subject to pressure causes index differences between the even and odd modes; i.e., interference spectrum changes reflect pressure changes. Figure 11.12 shows the pressure response obtained using the proposed TC-PCF-based MZI. The wavelength of one dip in the

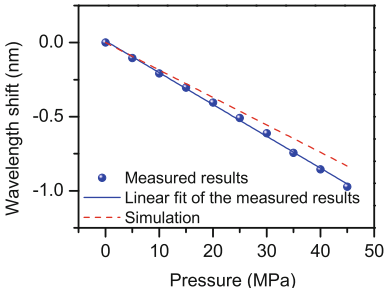

Fig. 11.12 Pressure response of twin-core photonic crystal fiber (TC-PCF)-based MZI. Experimental and calculated pressure sensitivity = −21 and −19 pm/MPa, respectively. (Adapted from [61])

transmission spectrum was recorded as the pressure increased to 45 MPa with 5 MPa step. Measured pressure sensitivity ≈−21 pm/MPa, which is consistent with the calculated −19 pm/MPa using the above theory.

11.4 Photonic Crystal Fiber Pressure Sensor Characteristics

11.4.1 Sensitivity and Resolution

Sensitivity is a key parameter to evaluate the developed pressure sensors. Pressure sensitivity of PCF-based pressure sensors varies with the fundamental principles used. In particular, PCF pressure sensors that employ the difference of two polarized modes show much higher sensitivity, e.g., the SI rocking filter. Other types using the dependence of the fundamental mode index on pressure have lower sensitivity, such as FBGs on SMFs or PCFs, and PCF-based FPIs. Pressure sensitivity of the former type can achieve up to tens of nm for 1 MPa pressure variation, whereas only tens of pm for the latter type. Table 11.1 provides state-of-the-art pressure sensors utilizing PCFs and other principles. Sensitivity, resolution, and temperature dependence were chosen for the comparison.

Table 11.1 shows that PCF-based pressure sensors vary greatly with the underlying principle. Typically, FBG-based approaches show lower pressure sensitivity compared with interferometers. Microstructured optical fibers (MOFs) with large airholes in the cross section give better pressure sensitivity. For example, the single-ring suspended fiber discussed in this chapter achieved sensitivity = −18 pm/MPa, a ~fivefold improvement over SMFs with no airholes. Two reflection peaks occur for FBGs written in polarization-maintaining fibers due to the two polarization modes. Thus, individual peaks can be used to measure pressure and temperature responses [40, 64]. Pressure sensitivity of the slow and fast axes was approximately 5 and 2–3 pm/MPa, respectively, but temperature dependence of the peaks was similar (approximately 11 pm/°C). Although pressure sensitivity is low, this type of pressure sensor is also promising and feasible for simultaneous pressure and temperature measurement. FPI and MZI-based pressure sensors have similar sensitivity (a few to tens of pm/MPa) as FBG-based sensors. This is because the pressure mainly induced change in the fundamental guiding mode index in PCFs, which hardly gives too large discrimination due to the similar photo-elastic coefficient of silica. In such cases, different airhole structures result in minor differences.

Polarimetric schemes to measure pressure based on polarization-maintaining fibers show quite different results. Pressure sensors based on Sagnac loop interferometers show very high sensitivity, the largest (44,000 pm/MPa) being the in-house fabricated two semicircular holes fiber, as shown in Fig. 11.9c. This sensitivity is approximately 11,000 times larger than FBGs in SMFs, i.e., better

Table 11.1 Comparison of state-of-the-art photonic crystal fiber (PCF) and other microstructured optical fiber (MOF)-based pressure sensors

Fiber type	Principle	Pressure sensitivity (pm/MPa)	Resolution 1 pm interrogator (kPa)	Temperature dependence (pm/°C)
Commercial PM-PCF [64]	FBG	−3.6 (*fast axis*) −5.4 (*slow axis*)	277 (*fast axis*) 185 (*slow axis*)	10.51
Ultrahigh birefringence PM-PCF [40]	FBG	−1.9 (*fast axis*) −5.1 (*slow axis*)	526 (*fast axis*) 196 (*slow axis*)	11
SMF [5]	FBG	~4	250	~10
Two large side-hole fiber [65]	Regenerated FBG	10.9	91	0.15
Grapefruit MOF [32]	FBG	−12.86	77	~12
Single-ring suspended fiber [55]	FBG	−18	55	12.02
Endless single-mode PCF [66]	LPG	112	8.93	~0.35
Solid-core honeycomb PCF [59]	FPI	−5.8	172	~13
Four-hole suspended-core fiber [67]	FPI	−6.8	147	−11
Twin-core PCF [61]	Modal coupling MZI	−21	47	12.4
Commercial PM-PCF [11]	SI	3420	0.292	−2.2
Six-hole suspended-core fiber [37]	SI	2816	0.355	~1
Butterfly MOF [19]	SI	~6850	0.146	~7
Two-semicircle-hole fiber	SI	44,000	0.023	~10
High birefringence PM-PCF [68]	Rocking filter	3300	0.303	1.38
Butterfly MOF [13]	Rocking filter	–72,600 to −97,300	0.014	−28 to −79

than 4 orders of magnitude, and still exceeds commercial PM-PCF sensitivity (3,420 pm/MPa). Resolution for discriminating pressure can be as small as 20 Pa when considering the interrogator resolution (1 pm). This significant sensitivity improvement is attributed to the dependence of birefringence with pressure; i.e., the

refractive index difference between the two polarized modes is considered, rather than only one mode.

The rocking filter scheme shows even higher pressure sensitivity (97,300 pm/MPa) than the SI scheme using the same fiber, e.g., butterfly MOF. The rocking filter uses the grating structure to couple one polarization beam with the other one to achieve resonance dips in the transmission spectrum. The shift of dips is encoded with pressure changes. Several resonance peaks are available, and sensitivity is dependent on the peak selection [13]. For the rocking filter, polarimetric sensitivity ($K_p = 2\pi/\lambda \times$ (dB/dP)) and group birefringence have vital roles in determining sensitivity, which is similar to SI and related to the asymmetrical stress distribution induced by the applied pressure. Therefore, both SI and rocking filter exhibit very high sensitivity as well as high resolution. Since SI based on the two semicircular holes fiber has larger sensitivity than butterfly MOF, it can be anticipated that even better performance in terms of sensitivity and resolution can be achieved by employing the rocking filter with this fiber.

Temperature dependence varies from approximately 1–10 pm/°C, which can cause cross-sensitivity issues using grating, FPI, or MZI schemes. However, this can be neglected for SIs or rocking filters due to their high sensitivity. Furthermore, the flexibility of modifying PCF geometry means it would be relatively simple and promising to develop PCF pressure sensors with even better performance to meet the strict demands of the oil industry.

11.4.2 Dynamic Range

Dynamic range (DR) of the measurement determines the capability of the pressure sensors. DR low limit is related to the pressure sensor resolution, signal interrogation noise level, and equipment resolution. DR high limit is dependent on the sensor fracture threshold, which is large for silica fiber. Hydrostatic oil pressures >100 MPa have been successfully measured using optical fibers [69]. DR of PCF pressure sensors can be defined by the maximum detectable pressure over the minimum limit,

$$DR(\mathrm{dB}) = 20 \times \log_{10}\left(\frac{P_{\max}}{P_{\min}}\right), \tag{11.14}$$

where $P_{\max}$ and $P_{\min}$ are the maximum pressure and minimum pressure the sensor can detect, respectively. Ideally, P_{min} refers to the pressure sensor resolution if zero system noise was present, and no inaccuracy detection in spectral shift was available. Taking the SI on the two semicircular holes fiber and butterfly MOF rocker filter as examples, sensor resolution can be 0.023 and 0.014 kPa, respectively (Table 11.1) and hence DR ≈ 133 and 137 dB, respectively, if taking the maximum pressure of 100 MPa into account.

However, in practice, sensor resolution will be lower than the theoretical estimate due to measurement inaccuracy, spectral instability, and signal noise. The interferometric schemes provide narrower resonance dips and would be expected to provide better practical detection accuracy. In particular, the Sagnac loop and rocking filter are based on polarimetric techniques, and SMF polarization changes randomly with even slight perturbation, which leads to spectral instability. Therefore, pressure discrimination accuracy will also be reduced.

11.5 Photonic Crystal Fiber-Based Pressure Sensor Applications

Basically, the property of the photosensitivity enables the PCFs to be inscribed with FBGs, which are widely developed into various sensors, including pressure sensor. However, the sensing performance in terms of the pressure sensitivity based on gratings varies from a few to tens of pm/MPa, too small for minor pressure detection. The flexibility of fabricating PCFs in asymmetrical geometry extends the possibility of developing pressure sensors with better performance. Compared with all the fiber-optic pressure sensors, those based on polarimetric approaches exhibit superior pressure sensitivity, which consequently show better discrimination resolution under the same conditions, as shown in Table 11.1. Birefringence is an essential property to configure polarimetric pressure sensors, which are more promising. The index difference of the two orthogonally polarized modes with respect to pressure is taken into account to characterize and enhance the sensitivity. There are various strategies to design the airhole structure of PCFs in order to introduce the high birefringence. But the key technique is to introduce asymmetrical stress distribution to the core as presented in Sect. 11.2. Although the polarimetric PCF pressure sensors possesses high sensitivity compared to grating-based pressure sensors, the bandwidth of the signal valleys/peaks is typically broader than FBGs, which leads to large measurement uncertainty and high detection limit. Furthermore, since the polarization is employed, the system would be sensitive to the polarization perturbations unless additional approaches are taken for stabilization, e.g., the use of polarization scrambler, polarization-maintaining fiber. Therefore, these shortcomings could be overcome accordingly by designing the sensors properly.

Nevertheless, PCF-based pressure sensors with high sensitivity and a large dynamic range would be extremely useful in the oil and gas industry, especially in harsh environments where conventional electronic sensors cannot sustain operation. The inherent passivity of the fiber approach enables sensors to be used for high-pressure and temperature measurement. Temperatures in deep wells can reach 250 °C, and oil pressures >100 MPa can be expected. In these situations, PCF sensors would be very suitable to quantify slight pressure variations due to their high sensitivity. Although the sensors exhibit different temperature dependences,

these can be easily compensated by using separate gratings or simultaneous measurements with proper sensing schemes. Temperature variation can be neglected if the change is small and SIs or rocking filters with low-temperature cross-sensitivity are utilized.

To push PCF sensors into industrial applications, functionality and long-term reliability under the downhole conditions must be addressed and demonstrated practically for operators. This should include reliable packaging, temperature robustness, mechanical strength, vibration robustness, etc. [7]. Compared with FBG on SMF using mechanical transducers to improve sensitivity, PCF pressure sensors possess significantly superior intrinsic sensitivity without requiring additional transducers and consequential increased sensing headspace. Mature FBG technology has been successfully applied in the oil industry over the past decades [70], but few PCF-based pressure sensors have been in practical use. This leaves a large development space for PCF pressure sensors to be adapted for the oil and gas industry. The high sensitivity achieved by unique airhole structures makes it possible and advantageous to monitor slight oil pressure variations.

PCF pressure sensors with high sensitivity and resolution could also be employed to measure biomedical pressure [71], which could be promising for monitoring local blood pressure in real time, especially when conducting minimally invasive surgery. Normally, blood pressure <120/80 mm Hg (systolic/diastolic) in blood vessels, i.e., <16 kPa. However, hypertensive patients can exhibit blood pressure >160 mmHg (i.e., >20 kPa). The best resolution for SI using the two semicircular holes fiber was 0.023 kPa, corresponding to approximately 0.17 mmHg, which could provide good discrimination for slight blood pressure changes in the vessel. To implement this application, PCF-based pressure sensor performance must be improved in terms of resolution, stability, and suitable packaging. Appropriate fiber geometry and sensing schemes need to be developed.

11.6 Summary

This chapter presented pressure sensors based on photonic crystal fibers (PCFs) or microstructured optical fibers (MOFs). The PCF fabrication process was briefly explained, focusing on introducing birefringence due to asymmetrical distribution of stress in or on the core. Birefringence is the key property that can be easily tuned by modifying the fiber geometry and employed in SI configurations to improve pressure sensitivity. FBG- and interferometry-based schemes (i.e., FPI, SI, and MZI) were presented in terms of their underlying principle and specific sensing configurations. Several MOFs that were designed and fabricated in-house were included to illustrate the range of potential PCF pressure sensors.

Resolution and other performance characteristics of some state-of-the-art PCF pressure sensors were compared. Sensors incorporating polarimetric techniques using PCFs with high birefringence exhibited the highest pressure sensitivity (44,000, −97,300 pm/MPa) compared to other pressure sensor types. The high

sensitivity meant that higher resolution could also be achieved, which is important for determining the smallest detectable pressure.

Large dynamic range >130 dB was achievable by reducing spectral instability and increasing measurement accuracy. Ideally, minimum detectable pressure should be 10–20 Pa, and there remains room for further improvement.

It would be promising to apply those novel PCF pressure sensors in the oil and gas industry to monitor pressure in real time. The high resolution also suggests potential applications in biomedical pressure monitoring, particularly for minimally invasive surgery. In principle, slight blood vessel pressure changes could be locally monitored in real time. However, the technology requires optimization and improvement in terms of fiber and sensor design, reliability, sensing and packaging schemes, etc.

Acknowledgements This project is financially supported by The Hong Kong Polytechnic University under project 1-ZVGB.

References

1. K.T.V. Grattan, T. Sun, Fiber optic sensor technology: an overview. Sens. Actuators A Phys. **82**, 40–61 (2000)
2. H. Nakstad, J.T. Kringlebotn, Oil and Gas Applications: Probing oil fields. Nat. Photonics **2**, 147–149 (2008)
3. A.D. Kersey, Optical fiber sensors for permanent downwell monitoring applications in the oil and gas industry. IEICE Trans. Electron. **83**, 400–404 (2000)
4. Emerson company, http://www2.emersonprocess.com/en-IN/news/pr/Pages/509-Roxar.aspx
5. M. Xu, L. Reekie, Y. Chow, J.P. Dakin, Optical in-fibre grating high pressure sensor. Electron. Lett. **29**, 398–399 (1993)
6. D. Song, Z. Wei, J. Zou, S. Yang, E. Du, H. Cui, Pressure sensor based on fiber Bragg grating and carbon fiber ribbon-wound composite cylindrical shell. Sensors (Peterborough, NH) **9**, 828–831 (2009)
7. P.M. Nellen, P. Mauron, A. Frank, U. Sennhauser, K. Bohnert, P. Pequignot, P. Bodor, H. Brändle, Reliability of fiber Bragg grating based sensors for downhole applications. Sens. Actuators A Phys. **103**, 364–376 (2003)
8. É. Pinet, Fabry-Pérot fiber-optic sensors for physical parameters measurement in challenging conditions. J Sens. **2009**, 1–9 (2009)
9. S. Watson, M.J. Gander, W.N. MacPherson, J.S. Barton, J.D.C. Jones, T. Klotzbuecher, T. Braune, J. Ott, F. Schmitz, Laser-machined fibers as Fabry-Perot pressure sensors. Appl. Opt. **45**, 5590–5596 (2006)
10. Z. Li, C. Liao, Y. Wang, L. Xu, D. Wang, X. Dong, S. Liu, Q. Wang, K. Yang, J. Zhou, Highly-sensitive gas pressure sensor using twin-core fiber based in-line Mach-Zehnder interferometer. Opt. Express **23**, 6673 (2015)
11. H.Y. Fu, H.Y. Tam, L.-Y. Shao, X. Dong, P.K.A. Wai, C. Lu, S.K. Khijwania, Pressure sensor realized with polarization-maintaining photonic crystal fiber-based Sagnac interferometer. Appl. Opt. **47**, 2835–2839 (2008)
12. H.Y. Fu, C. Wu, M.L.V. Tse, L. Zhang, K.D. Cheng, H.Y. Tam, B. Guan, C. Lu, High pressure sensor based on photonic crystal fiber for downhole application. Appl. Opt. **49**, 2639–2643 (2010)

13. A. Anuszkiewicz, G. Statkiewicz-Barabach, T. Borsukowski et al., Sensing characteristics of the rocking filters in microstructured fibers optimized for hydrostatic pressure measurements. Opt. Express **20**, 23320 (2012)
14. F.C. Fávero, S.M.M. Quintero, C. Martelli, A.M.B. Braga, V.V. Silva, I.C.S. Carvalho, R.W. A. Llerena, L.C.G. Valente, Hydrostatic pressure sensing with high birefringence photonic crystal fibers. Sensors **10**, 9698–9711 (2010)
15. E. Chmielewska, W. Urbańczyk, W.J. Bock, Measurement of pressure and temperature sensitivities of a Bragg grating imprinted in a highly birefringent side-hole fiber. Appl. Opt. **42**, 6284–6291 (2003)
16. A. Anuszkiewicz, T. Martynkien, P. Mergo, M. Makara, W. Urbanczyk, Sensing and transmission characteristics of a rocking filter fabricated in a side-hole fiber with zero group birefringence. Opt. Express **21**, 12657 (2013)
17. J. Clowes, S. Syngellakis, M. Zervas, Pressure sensitivity of side-hole optical fiber sensors. Photonics Technol. Lett. IEEE **10**, 857–859 (1998)
18. K. Naeem, B.H. Kim, B. Kim, Y. Chung, Simultaneous multi-parameter measurement using Sagnac loop hybrid interferometer based on a highly birefringent photonic crystal fiber with two asymmetric cores. Opt. Express **23**, 3589 (2015)
19. T. Martynkien, G. Statkiewicz-Barabach, J. Olszewski et al., Highly birefringent microstructured fibers with enhanced sensitivity to hydrostatic pressure. Opt. Express **18**, 15113–15121 (2010)
20. R. Kaul, Pressure sensitivity of rocking filters fabricated in an elliptical-core optical fiber. Opt. Lett. **20**, 1000–1001 (1995)
21. L. Teng, H. Zhang, Y. Dong, D. Zhou, T. Jiang, W. Gao, Z. Lu, L. Chen, X. Bao, Temperature-compensated distributed hydrostatic pressure sensor with a thin-diameter polarization-maintaining photonic crystal fiber based on Brillouin dynamic gratings. Opt. Lett. **41**, 4413–4416 (2016)
22. M. Hou, F. Zhu, Y. Wang, Y. Wang, C. Liao, S. Liu, P. Lu, Antiresonant reflecting guidance mechanism in hollow-core fiber for gas pressure sensing. Opt. Express **24**, 27890 (2016)
23. J.-Y. Huang, J. Van Roosbroeck, J. Vlekken, A.B. Martinez, T. Geernaert, F. Berghmans, B. Van Hoe, E. Lindner, C. Caucheteur, FBGs written in specialty fiber for high pressure/high temperature measurement. Opt. Express **25**, 17936 (2017)
24. P. Russell, Photonic crystal fibers. Science **299**, 358–362 (2003)
25. S.T. Philip, J. Russell, Photonic-crystal fibers. J Light Technol **24**, 4729–4749 (2006)
26. J.C. Knight, Photonic crystal fibres. Nature **424**, 847–851 (2003)
27. O. Frazão, J.L. Santos, F.M. Araújo, L.A. Ferreira, Optical sensing with photonic crystal fibers. Laser Photon Rev. **2**, 449–459 (2008)
28. A.M.R. Pinto, M. Lopez-Amo, Photonic crystal fibers for sensing applications. J. Sens. **2012**, 1–21 (2012)
29. T.A. Birks, J.C. Knight, P.S. Russell, Endlessly single-mode photonic crystal fiber. Opt. Lett. **22**, 961–963 (1997)
30. J. Knight, T. Birks, P. Russell, All-silica single-mode optical fiber with photonic crystal cladding. Opt. Lett. **21**, 1547–1549 (1996)
31. G. Humbert, J. Knight, G. Bouwmans, P. Russell, D. Williams, P. Roberts, B. Mangan, Hollow core photonic crystal fibers for beam delivery. Opt. Express **12**, 1477–1484 (2004)
32. C. Wu, B.-O. Guan, Z. Wang, X. Feng, Characterization of pressure response of bragg gratings in grapefruit microstructured fibers. J. Light Technol. **28**, 1392–1397 (2010)
33. V.V.R. Kumar, A. George, W. Reeves, J. Knight, P. Russell, F. Omenetto, A. Taylor, Extruded soft glass photonic crystal fiber for ultrabroad supercontinuum generation. Opt. Express **10**, 1520–1525 (2002)
34. A. Argyros, M.A. van Eijkelenborg, M.C. Large, I.M. Bassett, Hollow-core microstructured polymer optical fiber. Opt. Lett. **31**, 172–174 (2006)
35. M.H. Frosz, J. Nold, T. Weiss, A. Stefani, F. Babic, S. Rammler, P.S.J. Russell, Five-ring hollow-core photonic crystal fiber with 1.8 dB/km loss. Opt. Lett. **38**, 2215–2217 (2013)

36. J. Laegsgaard, A. Bjarklev, Microstructured optical fibers-fundamentals and applications. J. Am. Ceram. Soc. **89**, 2–12 (2006)
37. Z. Liu, C. Wu, M.-L.V. Tse, H.-Y. Tam, Fabrication, characterization, and sensing applications of a high-birefringence suspended-core fiber. J. Light Technol. **32**, 2113–2122 (2014)
38. A. Ortigosa-Blanch, J. Knight, W. Wadsworth, Highly birefringent photonic crystal fibers. Opt. Lett. **25**, 1325–1327 (2000)
39. K. Suzuki, H. Kubota, S. Kawanishi, M. Tanaka, M. Fujita, Optical properties of a low-loss polarization-maintaining photonic crystal fiber. Opt. Express **9**, 676–680 (2001)
40. Z. Liu, C. Wu, M.-L.V. Tse, C. Lu, H.-Y. Tam, Ultrahigh birefringence index-guiding photonic crystal fiber and its application for pressure and temperature discrimination. Opt. Lett. **38**, 1385–1387 (2013)
41. C. Wu, J. Li, X. Feng, B.O. Guan, H.Y. Tam, Side-hole photonic crystal fiber with ultrahigh polarimetric pressure sensitivity. J Light Technol. **29**, 943–948 (2011)
42. K. Chah, N. Linze, C. Caucheteur et al., Temperature-insensitive polarimetric vibration sensor based on HiBi microstructured optical fiber. Appl. Opt. **51**, 6130–6138 (2012)
43. D. Chen, M.L. Vincent Tse, H.Y. Tam, Super-lattice structure photonic crystal fiber. Prog. Electromagn. Res. M **11**, 53–64 (2010)
44. M.-L.V. Tse, Z. Liu, L.-H. Cho, C. Lu, P.-K.A. Wai, H. Tam, Superlattice microstructured optical fiber. Mater. (Basel) **7**, 4567–4573 (2014)
45. Y. Yue, G. Kai, Z. Wang et al., Highly birefringent elliptical-hole photonic crystal fiber with squeezed hexagonal lattice. Opt. Lett. **32**, 469–471 (2007)
46. F. Beltrán-Mejía, G. Chesini, E. Silvestre, A.K. George, J.C. Knight, C.M.B. Cordeiro, Ultrahigh-birefringent squeezed lattice photonic crystal fiber with rotated elliptical air holes. Opt. Lett. **35**, 544–546 (2010)
47. N.A. Issa, M.A. van Eijkelenborg, M. Fellew, F. Cox, G. Henry, M.C.J. Large, Fabrication and study of microstructured optical fibers with elliptical holes. Opt. Lett. **29**, 1336–8 (2004)
48. T.P. Hansen, J. Broeng, S.E.B. Libori, E. Knudsen, A. Bjarklev, J.R. Jensen, H. Simonsen, Highly birefringent index-guiding photonic crystal fibers. IEEE Photonics Technol Lett **13**, 588–590 (2001)
49. W. Urbanczyk, T. Martynkien, W.J. Bock, Dispersion effects in elliptical-core highly birefringent fibers. Appl. Opt. **40**, 1911–1920 (2001)
50. K.O. Hill, G. Meltz, Fiber Bragg grating technology fundamentals and overview. J. Light Technol. **15**, 1263–1276 (1997)
51. N. Groothoff, J. Canning, E. Buckley, K. Lyttikainen, J. Zagari, Bragg gratings in air-silica structured fibers. Opt. Lett. **28**, 233–235 (2003)
52. C.M. Jewart, Q. Wang, J. Canning, D. Grobnic, S.J. Mihailov, K.P. Chen, Ultrafast femtosecond-laser-induced fiber Bragg gratings in air-hole microstructured fibers for high-temperature pressure sensing. Opt. Lett. **35**, 1443–1445 (2010)
53. A.D. Yablon, Optical and mechanical effects of frozen-in stresses and strains in optical fibers. IEEE J. Sel. Top. Quantum Electron. **10**, 300–311 (2004)
54. W. Primak, D. Post, Photoelastic constants of vitreous silica and its elastic coefficient of refractive index. J. Appl. Phys. **30**, 779 (1959)
55. L. Htein, Z. Liu, H.-Y. Tam, Hydrostatic pressure sensor based on fiber Bragg grating written in single-ring suspended fiber, in Proceedings of the SPIE 9916, Sixth Eur Work Opt Fibre Sensors 99161R (2016)
56. G. Liu, Q. Sheng, W. Hou, M. Han, High-resolution, large dynamic range fiber-optic thermometer with cascaded Fabry-Perot cavities. Opt. Lett. **41**, 5134 (2016)
57. F. Xu, D. Ren, X. Shi, C. Li, W. Lu, L. Lu, L. Lu, B. Yu, High-sensitivity Fabry-Perot interferometric pressure sensor based on a nanothick silver diaphragm. Opt. Lett. **37**, 133 (2012)
58. Y.O. Barmenkov, D. Zalvidea, S. Torres-Peiró, J.L. Cruz, M.V. Andrés, Effective length of short Fabry-Perot cavity formed by uniform fiber Bragg gratings. Opt. Express **14**, 6394–6399 (2006)

59. C. Wu, H.Y. Fu, K.K. Qureshi, B.-O. Guan, H.Y. Tam, High-pressure and high-temperature characteristics of a Fabry-Perot interferometer based on photonic crystal fiber. Opt. Lett. **36**, 412–414 (2011)
60. W. Zhou, W.C. Wong, C.C. Chan, L.-Y. Shao, X. Dong, Highly sensitive fiber loop ringdown strain sensor using photonic crystal fiber interferometer. Appl. Opt. **50**, 3087–3092 (2011)
61. Z. Liu, M.-L.V. Tse, C. Wu, D. Chen, C. Lu, H.-Y. Tam, Intermodal coupling of supermodes in a twin-core photonic crystal fiber and its application as a pressure sensor. Opt. Express **20**, 21749–21757 (2012)
62. Y. Wang, M. Yang, D.N. Wang, S. Liu, P. Lu, Fiber in-line Mach-Zehnder interferometer fabricated by femtosecond laser micromachining for refractive index measurement with high sensitivity. J. Opt. Soc. Am. B **27**, 370–374 (2010)
63. H.Y. Choi, M.J. Kim, B.H. Lee, All-fiber Mach-Zehnder type interferometers formed in photonic crystal fiber. Opt. Express **15**, 5711–5720 (2007)
64. B. Guan, D. Chen, Y. Zhang, Bragg gratings in pure-silica polarization-maintaining photonic crystal fiber. Photonics Technol. Lett. IEEE **20**, 1980–1982 (2008)
65. T. Chen, R. Chen, C. Jewart, B. Zhang, K. Cook, J. Canning, K.P. Chen, Regenerated gratings in air-hole microstructured fibers for high-temperature pressure sensing. Opt. Lett. **36**, 3542–3544 (2011)
66. W.J. Bock, J. Chen, P. Mikulic, T. Eftimov, M. Korwin-Pawlowski, Pressure sensing using periodically tapered long-period gratings written in photonic crystal fibres. Meas. Sci. Technol. **18**, 3098–3102 (2007)
67. S.H. Aref, M.I. Zibaii, M. Kheiri et al., Pressure and temperature characterization of two interferometric configurations based on suspended-core fibers. Opt. Commun. **285**, 269–273 (2012)
68. G. Statkiewicz-Barabach, A. Anuszkiewicz, W. Urbanczyk, J. Wojcik, Sensing characteristics of rocking filter fabricated in microstructured birefringent fiber using fusion arc splicer. Opt. Express **16**, 17258–17268 (2008)
69. W.J. Bock, A.W. Domański, T.R. Woliński Influence of high hydrostatic pressure on beat length in highly birefringent single-mode bow tie fibers. Appl. Opt. **29** 3484–8 (1990)
70. X. Qiao, Z. Shao, W. Bao, Q. Rong, Fiber bragg grating sensors for the oil industry. Sensors **17**, 429 (2017)
71. P. Roriz, O. Frazão, A.B. Lobo-Ribeiro, J.L. Santos, J.A. Simões, Review of fiber-optic pressure sensors for biomedical and biomechanical applications. J. Biomed. Opt. **18**, 50903 (2013)

Chapter 12
Development of Photonic Crystal Fiber-Based Gas/Chemical Sensors

Ahmmed A. Rifat, Kawsar Ahmed, Sayed Asaduzzaman, Bikash Kumar Paul and Rajib Ahmed

Abstract The development of highly sensitive and miniaturized sensors that capable of real-time analytes detection is highly desirable. Nowadays, toxic or colorless gas detection, air pollution monitoring, harmful chemical, pressure, strain, humidity, and temperature sensors based on photonic crystal fiber (PCF) are increasing rapidly due to its compact structure, fast response, and efficient light-controlling capabilities. The propagating light through the PCF can be controlled by varying the structural parameters and core–cladding materials; as a result, evanescent field can be enhanced significantly which is the main component of the PCF-based gas/chemical sensors. The aim of this chapter is to (1) describe the principle operation of PCF-based gas/chemical sensors, (2) discuss the important PCF properties for optical sensors, (3) extensively discuss the different types of microstructured optical fiber-based gas/chemical sensors, (4) study the effects of different core–cladding shapes, and fiber background materials on sensing performance, and (5) highlight the main challenges of PCF-based gas/chemical sensors and possible solutions.

Keywords Photonic crystal fiber · Optical fiber sensors · Gas sensor Chemical sensors · Optical sensing and sensors

A. A. Rifat (✉)
Nonlinear Physics Centre, Research School of Physics & Engineering, Australian National University, Acton, Act 2601, Australia
e-mail: RifatAhmmed.Aoni@anu.edu.au

K. Ahmed
Department of Information and Communication Technology, Mawlana Bhashani Science and Technology University, Santosh, Tangail 1902, Bangladesh

S. Asaduzzaman · B. K. Paul
Department of Software Engineering, Daffodil International University, Sukrabad, Dhaka 1207, Bangladesh

R. Ahmed
Nanotechnology Laboratory, School of Engineering, University of Birmingham, Birmingham B15 2TT, UK

© Springer International Publishing AG, part of Springer Nature 2019

M. F. O. Hameed and S. Obayya (eds.), *Computational Photonic Sensors*, https://doi.org/10.1007/978-3-319-76556-3_12

12.1 Introduction

Optical sensor devices have been taken as an alternative to conventional solid-state planar, brittle, less flexible, and rigid electronic devices [1]. Electronic devices have some major limitations such as high manufacturing cost, complex procedure, slower response time, and reliability as compared to the optical sensors. Electronic devices are also affected with electromagnetic (EM) and thermal noise or interference [2]. Nowadays, physical sensing based on optical platform used to sense and monitor complex environment and its surrounding such as temperature, humidity, strain, stress, pressure, and torsion having important applications in wearable sensors, robotics, health and safety monitoring [3–8]. Therefore, optical sensor devices have been found the suitable alternative for the gas, chemical, and oil-sensing applications, due to its advantages of low cost, less noise/interference, higher sensitivity, fast response, reliability, and compactness [9–11].

Since last decades, photonic crystal fiber has been shown great development in optical sensing [12–15]. Due to advance optical instrumentations, the field of fiber optics is no longer limited to telecommunication applications. PCF also known as holey fiber consists of periodically ordered microscopic cylindrical airholes running through the full length of the fiber. The standard PCF is made with fused silica (SiO_2) that has a regular pattern of voids or airholes that run parallel to its axis. Unlike traditional optical fibers, both the core and cladding are made from the same material. The structural view of PCF is shown in Fig. 12.1. Due to unique advantages of PCFs such as design freedom, light-controlling capabilities, faster detection response, and miniaturized structure, it has been received considerable attention in developing opto-devices and sensors. Moreover, modifying the structural parameters of PCFs, such as airhole diameters, pitch size, and number of rings, evanescent field can be controlled; as a result, it will find the large scale of possible applications, especially in sensing.

The first working PCF emerged from the drawing tower in late 1995. PCF was practically fabricated for the first time in 1996 by Birks et al. [16]. The first

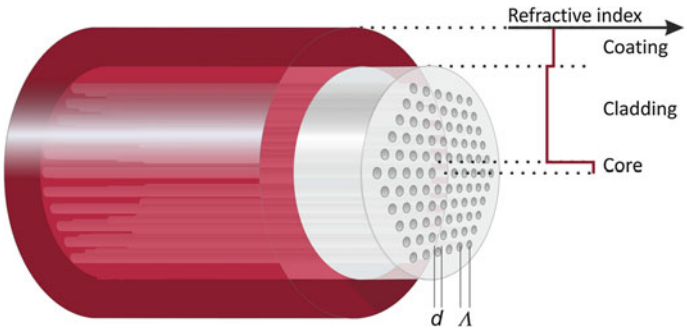

Fig. 12.1 Standard photonic crystal fiber structure

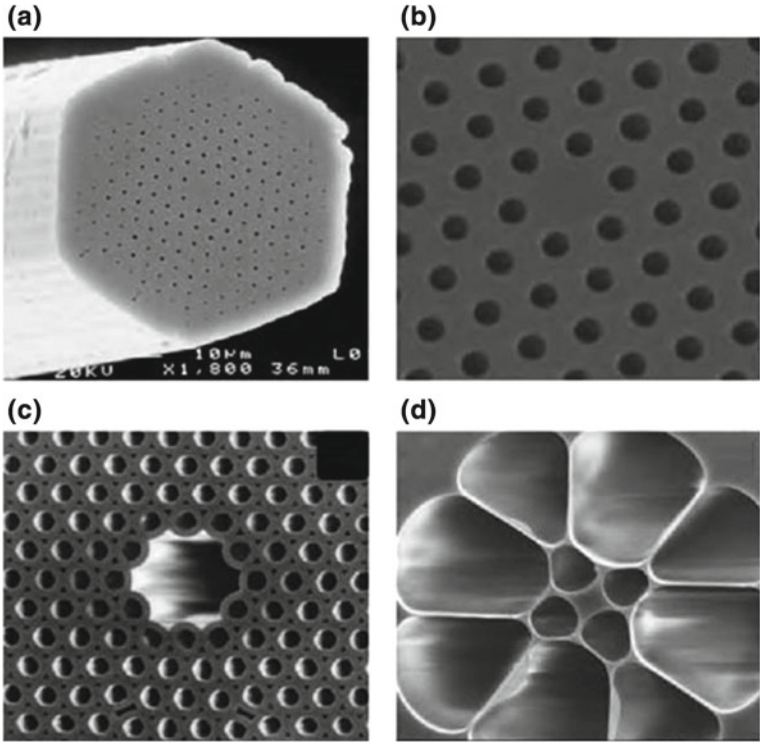

Fig. 12.2 **a** First working PCF. **b** Low loss solid core PCF. **c** The first hollow-core PCF. **d** A small core PCF extruded from Schott SF6 glass [16, 17]

fabricated PCF is shown in Fig. 12.2a. There are mainly two types of PCF, one is index-guiding PCF and another is photonic band gap (PBG) PCF. The cross-sectional diagram of index-guided photonic crystal fiber is shown in Fig. 12.2b. Photonic bandgap guiding occurs by surrounding the core of an optical fiber with the cladding region which contains airholes running along the length of the fiber. The cross-sectional diagram of photonic bandgap is shown in Fig. 12.2c. Recently, researchers are more interested in special type of PCF where both core and cladding are microstructured (see Fig. 12.2d).

Nowadays, PCF has been attracted much attention for its incredible performance and broad range of applications such as filters [18], switches [19, 20], electro-optical modulators [21, 22], polarization converters [23], and sensors [24–28]. Since last few decades, PCF has been considered and widely investigated as a suitable candidate for the optical sensing. Highly sensitive liquid and gas sensors are playing an important role in industrial processes especially for detecting toxic and flammable gases or liquids to overcome the safety issues [29]. So, it has become one of the key challenges to enhance the performance of liquid and gas sensors. Photonic crystal fiber-based liquid and gas sensors have been shown

excellent performance in terms of sensitivity response. In recent years, researchers have been shown great interest on the development of PCF-based sensors for environmental and safety monitoring [30, 31]. A wide variety of PCF-based sensing techniques have been reported by changing different geometric parameters of the PCF to get higher sensitivity, detection accuracy, and faster response time. Performance of the PCFs can be enhanced by regular or irregular geometric structure like hexagonal [32], octagonal [33], decagonal [34], square [35], honeycomb cladding [36], elliptical [37], and kagome [38]. Development of regular or irregular PCF structure leads to achieve more efficiency as well as use it in multipurpose like gas sensing, chemical sensing, bio sensing, cancer cell detection, medical science, temperature sensing, illuminations, machining, and welding applications because of its smaller size, lighter weight, chemically inertness, higher bandwidth, longer repeater span, electromagnetic immunity, and many other intriguing properties [39–41].

Researchers are trying to improve the performance of the PCF-based sensors following different geometric shape of cladding and filling different transparent material in the core and cladding. However, doping material will cause high cost and also led to the complex fabrication process. As a result, considering practical point of view, a simple PCF structure is required with high sensitivity virtues. Park et al. [42] proposed a new type of index-guided PCF to enhance sensing capability by introducing a hollow high index ring defect that consists of the central airhole surrounded by a high index GeO_2 doped SiO_2 glass ring. They showed that fraction of evanescent field was increased by increasing the diameter of central airhole; hence, the sensitivity was improved and kept the diameter smaller than cladding holes diameters for the physical realization of effective index guiding. Olyaee et al. [43] showed sensitivity 13.23% by increasing the diameter of the holes located in the inner ring and reduced confinement losses to 3.77×10^{-6} dB/m by increasing the airhole diameters located in the outer ring at the wavelength 1.33 μm. Ademgil et al. [44] proposed a microstructured core and cladding PCF for liquid sensing and found the sensitivity of 20.10% at the wavelength $\lambda = 1.33$ μm. According to the reported papers, it has been observed that both relative sensitivity and confinement loss are improved. But these are not the significant value for a gas sensor. To increase the relative sensitivity and lower the confinement loss, more research has to be done. An effective way to increase the performance of gas sensor is to design a simple PCF structure which will allow more penetration of the evanescent fields.

In this chapter, sensitivity and guiding properties of various index-guiding PCFs-based gas/chemical sensors as well as liquid sensors are extensively discussed. The finite element method (FEM) with perfectly matched boundary layer (PML) conditions is extensively used for the computational study of PCF-based gas/chemical sensors; as a result, we also described the PML effect on sensing. The important sensor parameters such as sensitivity and confinement loss effect due to change of pitch, number of rings, airhole diameters, and air filling fractions (AFF) are investigated. Recent advances of existing PCF-based gas/chemical sensors are discussed, which consist of comparisons among several PCF structures in

terms of relative sensitivity and fabrication feasibility. Finally, research gaps of this field are addressed and potential future detections to overcome them are discussed.

12.2 Fundamentals of PCF-Based Sensors

12.2.1 Sensing Mechanism of PCF-Based Sensors

The criteria's for which PCFs are used as a sensor

- **Absorbance** measured in a transparent medium.
- **Reflectance** measured in non-transparent media, usually using an immobilized indicator.
- **Luminescence** based on the measurement of the intensity of light emitted by a chemical reaction in the receptor system.
- **Fluorescence** measured as the positive emission effect caused by irradiation.
- **Refractive index** measured as the result of a change in solution composition.
- **Opto-thermal effect** based on a measurement of the thermal effect caused by light absorption.
- **Light scattering** based on effects caused by particles of definite size present in the sample.

Among these criteria's, absorbance property is widely used for sensing applications which followed by the absorption spectroscopy for practical realization. In recent years, absorption techniques are also used to detect the gas/chemicals. We have discussed the absorption spectroscopy in the following paragraph.

Fundamentals of Absorption Spectroscopy

The quality of gas assimilation lines can be utilized to perform quantitative estimation of gas. The sensitivity of the analytes is derived from the output optical power, and it is followed by the Beer–Lambert law [43, 45] as follows.

$$I(\lambda) = I_0(\lambda) \exp(-r\alpha_m lc) \tag{12.1}$$

where I_0 is the emerging optical intensity of light passing through the targeted analyte and I is the intensity of light for investigation. The relative sensitivity coefficient is r, α_m is the absorption coefficient, l is proportional to the line strength, and c is the concentration of the sample analyte.

The absorbance of the sample is defined as [25];

$$A = -\log_{10}\left(\frac{I_0}{I}\right) = r\alpha_m lc \tag{12.2}$$

Table 12.1 Absorption wavelength and line strength of some common gases [45]

Molecule	Absorption wavelength (μm)	Line strength (cm^{-2} atm^{-1})	Descriptions
Acetylene (C_2H_2)	1.533	$\sim 20 \times 10^{-2}$	Extremely flammable
Hydrogen iodide (HI)	1.541	0.775×10^{-2}	Highly toxic, colorless
Ammonia (NH_3)	1.544	0.925×10^{-2}	Toxic, irritating and destructive to tissues
Carbon monoxide (CO)	1.567	0.0575×10^{-2}	Combustion product, toxic, colorless
Carbon dioxide (CO_2)	1.573	0.048×10^{-2}	Main greenhouse gas
Hydrogen sulfide (H_2S)	1.578	0.325×10^{-2}	Toxic, colorless, flammable
Methane (CH_4)	1.667, 1.33	1.5×10^{-2}	Flammable, greenhouse gas
Hydrogen fluoride (HF)	1.330	32.5×10^{-2}	Toxic, colorless, extremely corrosive
Hydrogen bromide (HBr)	1.341	0.0525×10^{-2}	Highly toxic, colorless
Nitrogen dioxide (NO_2)	0.800	0.125×10^{-2}	Greenhouse gas
Oxygen (O_2)	0.761	0.01911×10^{-2}	Strong oxidizer, supports and vigorously accelerates combustion

The molecule shows different properties in their different states. Some gases are extremely flammable and hazardous that can be detected by PCF. The flammable gases may cause exploitation and fire in any industries as well as residential areas. Some gases are toxic that may cause different types of diseases. Few gases may cause cancer and other disorders as well. Table 12.1 shows the detailed description and absorption wavelength.

The PCF-sensing mechanism depends on the absorption lines of the corresponding gases. By the effective refractive index of the related gas which can be detected shows modal intensities at the core region. Gas species with absorption in near IR region and line strength are listed in Table 12.1. By the absorption cell, gases can be detected between any ranges of wavelength (see Fig. 12.3).

Figure 12.4 exhibits the schematic block diagram of the checked wavelength direct absorption spectroscopy system, which is used for methane ID. Light from a tenable laser source (TLS) is dispatched into a solitary mode fiber (SMF). The SMF is butt-coupled to the HC-PBF using a 3-turn positioner. An opening is left between

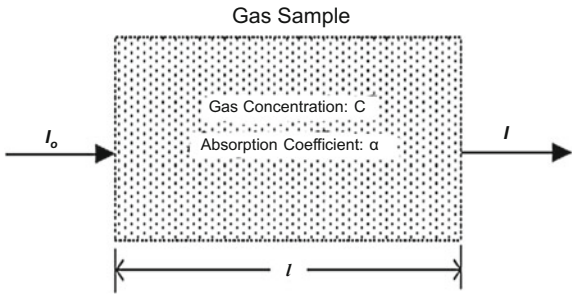

Fig. 12.3 Guided absorption cell

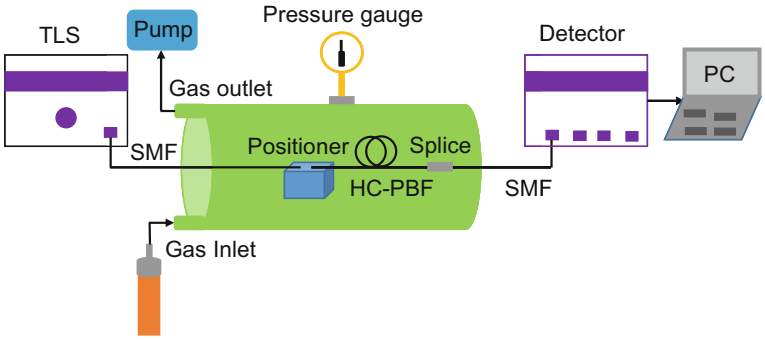

Fig. 12.4 Direct absorption spectroscopy system [46]

the terminations of the fibers to allow the gas access into the focal point of the HC-PBF. The other side of the HC-PBF is joined to a single mode fiber (SMF) using a business roundabout section splicer as described in [45]. The incapacitating of this splicer is around 1 dB. The light transmitted through the HC-PBF is measured using a Ge-identifier. A PC is used to control the tuneable laser and accumulate data from power meter which contain the locator. The open end of the HC-PBF is set in a settled vacuum chamber. Finally, a pump is used to clear the fiber before stacking with the adjusted joining of the targeted gas.

To measure the methane maintenance territory, use the two HC-PBF cells. The setup of absorption spectroscopy showed up in figure (Fig. 12.4). Consequently, the vacuum chamber is required to clear first, then it is stacked with a balanced mix of 18,750 ppmv (parts per million volumes) methane in air at a relative weight of 1 bar.

Resulting allows sufficient time for the gas to thoroughly diffuse into the fiber, and a transmission extent is recorded. The intentional territory is then established to a reach accumulated with void cells, yielding the ingestion in light of methane. From the methane maintenance band, it can be seen that the methane has generally more grounded absorption at 1331.55 nm.

12.2.2 Applications of PCF-Based Sensors

Due to unique optical properties of PCFs, it has been found large scale of potential applications. There are many applications in PCF-based sensors and some of them are listed below:

- **Gas sensor**: Gases are colorless and can be toxic. But different gas has different absorption line based on its absorption spectrum length as well as refractive index. PCF has been used to detect those colorless gases [47]. PCF-based gas sensor has the capability to detect CO that is commonly known as silent killer [43].
- **Chemical Sensor**: Chemicals are massively used in the industrial applications. In some cases, it is bounded to detect some unwanted chemical and those are poisonous for human body. Based on the internal structure of the chemical, their refractive index is also different. Each chemical has its unique refractive index like for benzene (n = 1.366), ethanol (n = 1.354), water (n = 1.33). Based on these refractive index, chemical can be detected by PCF by passing the chemical through the core region [48].
- **Biosensor**: Biosensor is a device that can sense the numerous biological molecules and/or antibodies, enzymes with the presence of associated chemical or analyte. Nowadays, PCFs are used to detect biological substances like urine glucose, pH, serum protein [49].
- **Temperature Sensor**: Temperature measurement is a key issue in industrial and environmental health monitoring purposes. The conventional temperature measurement mechanism is not suitable. PCF-based temperature sensors are most popular for temperature sensing because of its simple and cost-effective detection capabilities. To date, several number of PCF-based temperature sensors have been reported [50, 51].
- **Refractive Index Sensor**: Refractive index-based sensors are vastly using in optical sensing area. Based on the refractive index of different specimen, different applications are already employed among them surface plasmon resonance (SPR) is notable [52, 53].
- **Corrosion Sensor**: The deterioration and loss of a material are commonly known as corrosion. With the development of PCF-based corrosion sensors, it can be easily monitored the present structural condition of aircraft [54], steel [55], and other materials.
- **Pressure Sensor**: Pressure is a common behavior in case of gaseous and liquid chemicals. Moreover the revolutionary changes in the optical field, PCF-based pressure sensor played the significant role by measuring the pressure inside the patient body especially for urodynamic and cardiovascular assessment [56].
- **Humidity and Moister Sensor**: To predict the present state of the atmospheric condition some weather forecasting parameters are needed to be calculated. Among them, humidity is exceedingly crucial. Nowadays, PCF-based humidity and pressure sensors are using widely [57, 58].

- **Flying Particle Sensor**: Different particles are generally present in the environment (like in open air). But the particles are too tiny that it cannot be easily detected. Some radioactive substance may be present in the different areas air, and those are flying randomly. This type of sensor can be used in radioactive areas to monitor the environment [59].
- **Transverse Load Sensing**: Utilizing the mechanism of light propagation property load can be sensed. Optical fiber can directly use to sense load in the transverse direction [60].

12.2.3 Advantages of PCF-Based Sensors

By varying PCF structure (like hexagonal, octagonal, decagonal) and also varying the structural core–cladding size with different arrangement, propagating light can be tailored significantly. For the PCF-based sensors, evanescent field is the key element. Due to PCFs light-controlling capability, evanescent field can be tailored intensely; as a result, sensor performance can be improved significantly.

12.2.4 Optical/Guiding Properties of PCF Sensors

The better optical guiding properties ensure the application of PCFs as gas/chemical sensors. Optical properties are the core area of research on PCF. The sensor guiding properties of the PCFs are discussed below stepwise in details [12, 61].

Relative Sensitivity

First and foremost nature of a PCF used as sensor is needed to compute the relative sensitivity response. Relative sensitivity response of a PCF denoted the sensing capacity of the proposed PCF. Relative sensitivity is symbolized by r, and it can be calculated through the following equation [47];

$$r = \frac{n_s}{\mathrm{Re}[n_{eff}]} f \tag{12.3}$$

where n_s is the refractive index of target gas species, typically consider as 1 and Re [n_{eff}] is the real part of the effective mode index. Here, f is the fraction of holes power by total optical power which can be defined as [62]:

$$f = \frac{\int_{holes} \mathrm{Re}(E_x H_y - E_y H_x) dxdy}{\int_{total} \mathrm{Re}(E_x H_y - E_y H_x) dxdy} \tag{12.4}$$

Here, E_x, E_y, H_x, and H_y are the transverse electric and magnetic field of the guided mode, respectively.

Confinement loss

Confinement loss or leakage loss occurs due to leaky nature of the mode and irregular arrangement of airholes. Those airholes are playing the role of dielectric medium. Confinement loss also depends on transmitted wavelength, parameter shape and size, number of holes, and rings. A circular-shaped anisotropic perfectly matched layer (C-APML) is used to satisfy the boundary condition which avoids unwanted electromagnetic reflection at the boundary of PCF. By this term, confinement loss or leakage loss can be calculated by the imaginary part of the effective refractive index. The confinement loss or leakage loss can be calculated by the following equation [63]:

$$L_c(\mathrm{dB/m}) = 8.686\, K_0 Im\left(n_{eff}\right) \times 10^6 \tag{12.5}$$

where $K_0 = 2\pi/\lambda$, is the wave number and $\mathrm{Im}[n_{\mathrm{eff}}]$ is the imaginary part of the effective refractive index.

Birefringence

Birefringence is one of the crucial properties of PCFs. It is highly influential for polarization maintaining fiber (PMF). Birefringence is a property of a PCF which comes from some geometric asymmetry based on airholes position. Highly structural asymmetry of PCF, especially first ring of the PCF, produces higher order of birefringence, and structural symmetry of PCF has no influence to produce birefringence. The mathematical formulation of birefringence can be expressed as [64],

$$B(\lambda) = \left| n_{eff}^{x} - n_{eff}^{y} \right| \tag{12.6}$$

Beat length

Another wavelength-dependent parameter is beat length. Beat length is a significant argument to discover the birefringent optical fibers. It defines the optical signal transmission length along the fiber when the phase difference of two orthogonal polarization states varies 360° or 2π radians. This property leads to periodic power exchange between two orthogonal components. This period is called beat length which can be evaluated by the following expression [65]:

$$L_B(\lambda) = \frac{\lambda}{B(\lambda)} \tag{12.7}$$

V-Parameter

A PCF can be single mode or multimode. A cutoff value always present there for determining the fiber for modal analysis. If the value of V is less than or equal to 2.405, then it indicates the single mode operations; otherwise, it permits multimode

operations. The single mode response for step index fiber can be determined by the V-parameter which is defined by [66]:

$$V_{eff} = \frac{2\pi}{\lambda} a \sqrt{n_{co}^2 - n_{cl}^2} \tag{12.8}$$

Here, n_{co} and n_{cl} are the refractive index of core and cladding; a is the radius of the fiber core. The fraction of optical power in a certain mode is bounded inside a fiber core determined by V number. The lower V-value indicates the optical power fraction is low and vice versa.

Effective Area

Effective mode area is generally considered as the light carrying region. For fundamental propagating mode, electric field (E) distribution occurs inside the core; as a result, effective mode area (EMA) of a PCF can be determined by the following equation [32]:

$$A_{eff} = \frac{\left(\iint |E(x,y)|^2 dxdy\right)^2}{\iint |E(x,y)|^4 dxdy} \tag{12.9}$$

For high bit rate data transmission system (especially for telecommunication), large effective mode area is required. On the contrary, lower EMA is preferable for nonlinear applications.

Nonlinearity

High-optical power density is provided by a small effective area for which the nonlinear effects would be significant. The nonlinear effective or nonlinearity is closely related with the effective area and also nonlinear coefficient of the PCF background material in associated with the operating wavelength λ. The nonlinear coefficient can be examined by the following equation [32]:

$$\gamma = \left(\frac{2\pi}{\lambda}\right)\left(\frac{n_2}{A_{eff}}\right) \tag{12.10}$$

where n_2 is the nonlinear refractive index. Nonlinear effects are very advantageous in different optical devices and optical applications such as broadband amplification, channel demultiplexing, wavelength conversion, soliton formation, optical switching and many more applications. Nevertheless, higher orders of nonlinearity are responsible for supercontinuum generation (SCG).

Splice Loss

Splice loss is another important parameter for fiber design consideration. Generally, for longer distance signal carrying or longer distance optical communication aspect

two fibers are experienced by joining or splicing. It is very sensitive issue because due to small mismatch of the fibers during the splicing will led to the large signal attenuation. Splice loss occurs during the splicing between PCF and the single mode fiber. Splice loss can be calculated by the following equation [32]:

$$L_S = -20\log_{10}\frac{2W_{SMF}W_{PCF}}{W_{SMF}^2 + W_{PCF}^2} \tag{12.11}$$

where W_{SMF} and W_{PCF} are the mode field diameters of the single mode fiber and PCF, respectively.

Refractive Index

Transparent materials are highly used for PCF fabrication. The common transparent material silica has been used extensively for the PCF fabrication. Even as a standard PCF, silica fiber has been considered till now. Due to the technological advancement, different types of transparent materials such as tellurite, graphene, ZBLAN, and TOPAS have also been shown great interest. These are all the basic material characteristics which completely depend on refractive index. Refractive index is a material itself property which can be increased or decreased by doping other materials based on the different applications.

12.3 Overview of PCF-Based Gas/Chemical Sensors

12.3.1 Conventional Optical Fiber Sensors

Optical fiber-based surface plasmon resonance (SPR) sensor has been reported by Mishra et al. [67], for the detection of hydrogen sulfide gas. The schematic diagram of the experimental setup is shown in Fig. 12.5. To utilize the SPR-based gas sensor, nickel oxide doped ITO thin film has been used. Gas chamber having the facility with inlet and outlet was used, and the fiber probe was inserted into the gas chamber. The unpolarized light lunched at one end of the fiber and at the other end of the fiber is connected to the spectrometer. To study the SPR response of the hydrogen sulfide gas, the gas chamber was evacuated with the help of a rotary pump and the reference signal was recorded.

Recently, optical fiber-based SPR sensor for the detection of ammonia gas has also been reported [68]. The sensitivity of the sensor with optimized thickness of BCP layer is 1.891 nm/ppm and is larger than the sensitivity values obtained in the cases of Ag/BCP and Cu/BCP-coated probes for the concentration range 1–10 ppm of the ammonia gas.

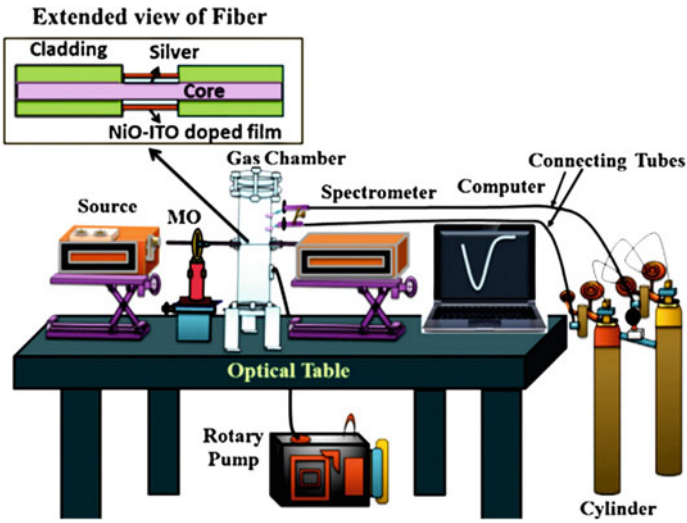

Fig. 12.5 Conventional optical fiber sensor [67]

12.3.2 PCF-Based Sensors

Based on geometrical structure, different types of PCFs have been reported for the gas/chemical sensing. The most common and modest PCF-based sensor structure is hexagonal structure. Moreover, circular, square, octagonal structures have also been reported. These types of shapes are constructed based on the orientation of airholes

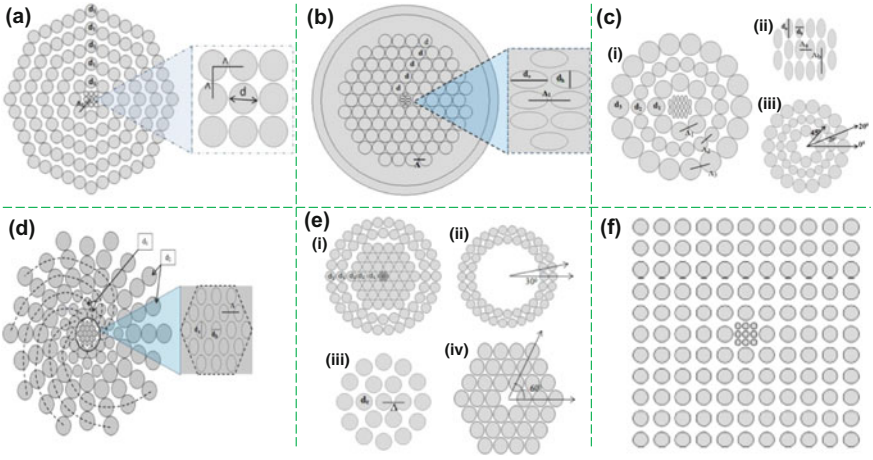

Fig. 12.6 Different types of PCF-based sensors. **a** Octagonal, **b** hexagonal, **c** hybrid, **d** spiral, **e** hybrid combined, and **f** Square

in the cladding region. For the various architectural shapes, light guiding mechanism through the fiber may have different manner. Here, from the design prospective, different types of PCF-based sensor are shown in Fig. 12.6. Figure 12.6 shows the different types of PCF such as octagonal (Fig. 12.6a), hexagonal (Fig. 12.6b), hybrid (Fig. 12.6c), spiral (Fig. 12.6d), hybrid combined (Fig. 12.6e), and square (Fig. 12.6f)-based chemical/gas sensors.

12.4 Guiding Properties Controlling Parameters of PCFs

Guiding properties or so-called optical properties can be controlled by some fundamental parameters of PCF. By recent vibrating research, it has been concluded that pitch, air filling ratio, diameters of airholes of both core and cladding significantly affect the result of wave guiding properties. In this section, a brief discussion on the sensor performance controlling parameters and their effects have been outlined.

12.4.1 Pitch Effects on Sensing

In PCF, airholes exists through the entire fiber; those are forming on silica background. These airholes are organized in a well-defined geometrical pattern. The hole-to-hole distance more specifically center-to-center distance of two adjacent airholes is called pitch (see Fig. 12.7). By altering, pitch sensitivity of PCFs can improve.

Figure 12.8 shows the pitch effect on relative sensitivity of PCF. The figures (see Fig. 12.8a–c) illustrates that smaller the pitch led to the higher relative sensitivity because the lower pitch value induces the lower space between airholes which result congested airholes. These airholes direct the evanescent field through the core region.

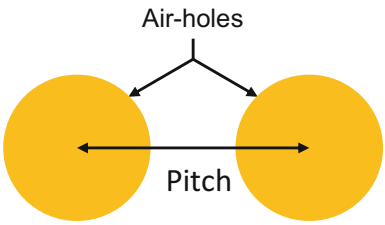

Fig. 12.7 Pitch of PCF

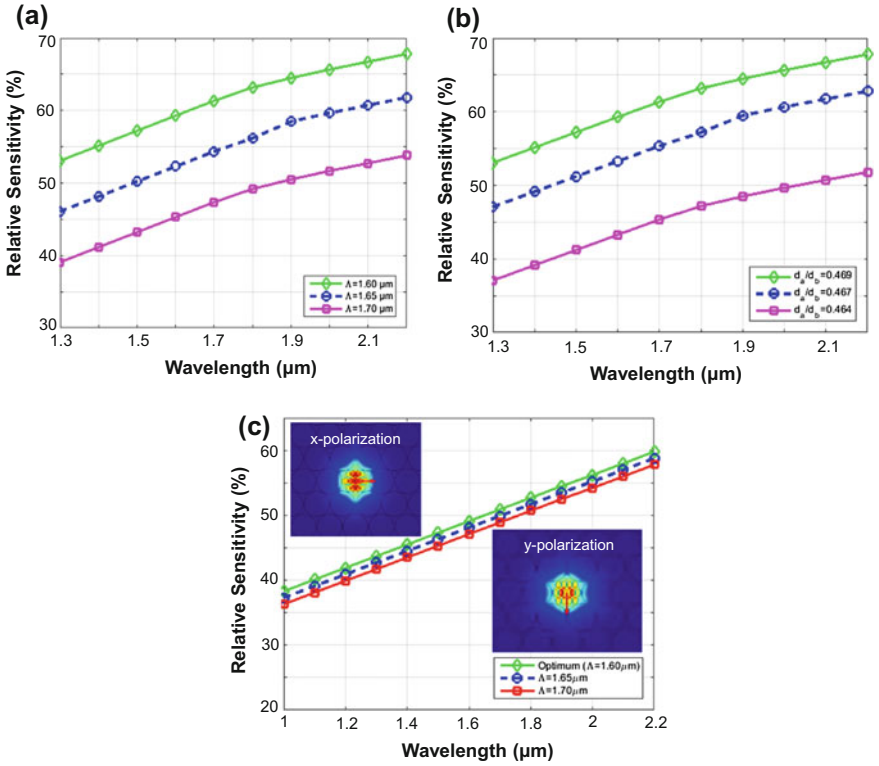

Fig. 12.8 Analysis the pitch effect on relative sensitivity of PCF [12]

12.4.2 Diameter Effects on Sensing

Diameter has significant effects on relative sensitivity. These diameters mean air-holes diameter of core region as well as cladding region. By changing the diameters, relative sensitivity can be tailored. In Fig. 12.9a, b, it is observed that the larger diameters show higher relative sensitivity.

12.4.3 Air Filling Ratio Effects on Sensing

Air filling ratio is the ratio between diameters of airhole and pitch. The air filling ratio is another controlling parameter of relative sensitivity of PCF sensors. By changing both diameter and pitch at a certain ratio together air filling ratio changes, there exists a cutoff air filling ratio which is require to maintain. The cutoff value of the air filling ratio is set as level of 0.95. Figure 12.10 illustrates that relative

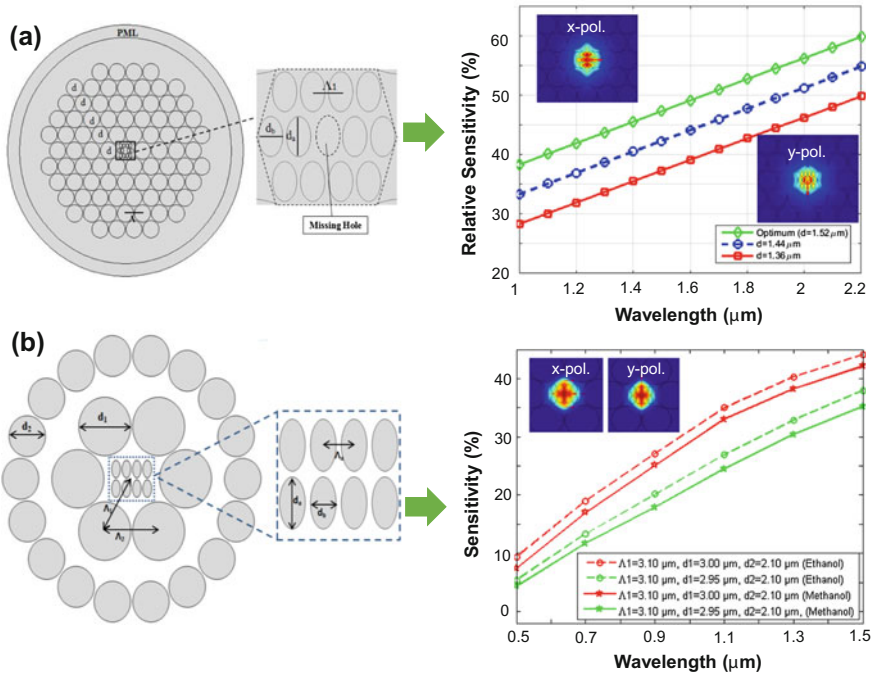

Fig. 12.9 Analysis the diameter effect on relative sensitivity with **a** hexagonal PCF, **b** hybrid PCF [12, 69]

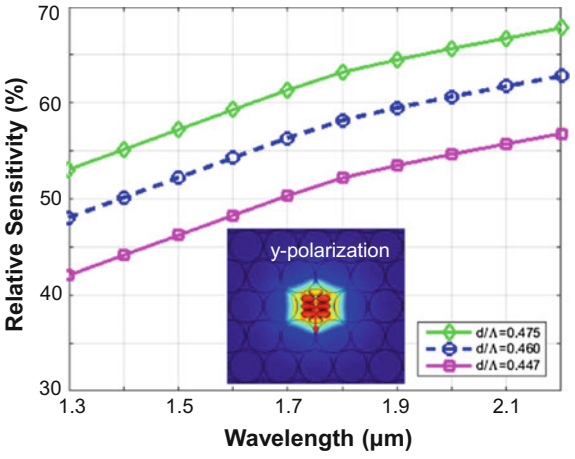

Fig. 12.10 Analysis the effect of air filling ratio on relative sensitivity of PCF [47]

sensitivity changes a lot due to small change of air filling ratio. The air filling ratio can define by the following equation

$$\text{Air filling ratio} = \frac{d(Diameter)}{\Lambda(pitch)} \tag{12.12}$$

12.5 Core-Shaped Effects on Sensing

In PCF-based gas/chemical sensors, core is a key parameter in terms of sensor performance. Generally, gases and chemicals are filled through the core; as a result, core shape has effects on sensing. According to Fig. 12.11, it is visible that an elliptical hole in a rhombic orientation shows the higher sensitivity responses than the other orientation of airholes at the innermost core region.

12.5.1 Hollow-Core PCF-Based Sensors

Recently, a simple hollow-core PCF (HC-PCF) where core is doped with different material which has been reported for gas sensing [70] (see Fig. 12.12a). The operating wavelength varied from 0.8 to 1.60 μm to investigate the different guiding properties. At wavelength λ = 1.60 μm, it shows the maximum sensitivity response of 19.94% (Fig. 12.12b) and at the same time, it also reduces the confinement loss to 2.74×10^{-4} dB/m.

A hybrid structure photonic crystal fiber-based gas sensor is presented in Fig. 12.13a to detect toxic and colorless gases. Numerical study showed that

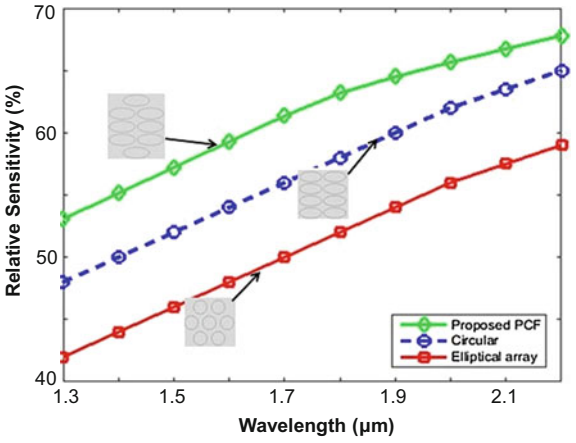

Fig. 12.11 Core shape effect on relative sensitivity [47]

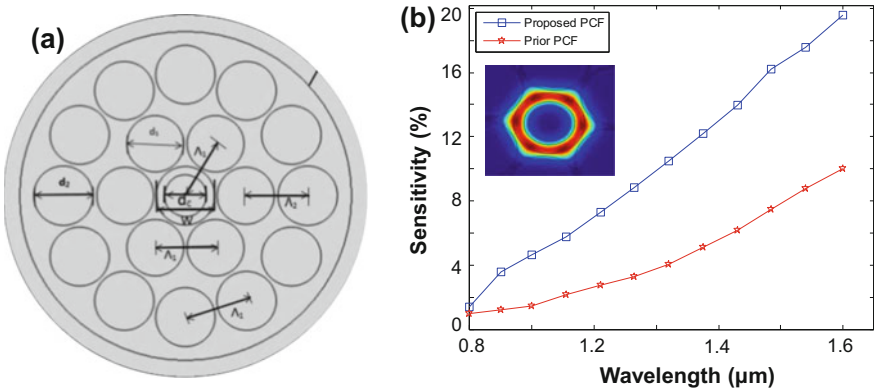

Fig. 12.12 **a** Cross-sectional view of doped material-based hollow-core PCF. **b** Sensitivity as a function of wavelength [70]

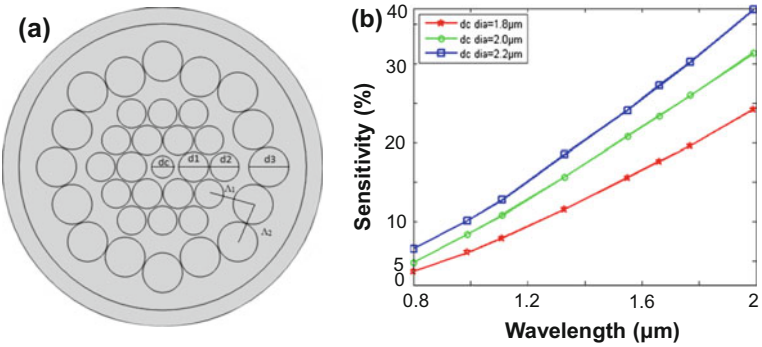

Fig. 12.13 **a** Cross-sectional view of hollow-core-based hybrid PCF. **b** Sensitivity as a function of wavelength

sensitivity response of this hybrid PCF sensor enhanced to 15.67% (Fig. 12.13b). The confinement loss or leakage loss decreased to 1.12×10^{-7} dB/m by acquainting an octagonal ring of airholes in the outer cladding. This sensor works in wider range of wavelength from 0.8 to 2 μm.

Two different structures of HC-PCF have been presented in Fig. 12.14a, b [71]. The numerical result shows that hexagonal PCF (consist with six airholes in the first ring) shows 2.22 times higher sensitivity responses compared to the octagonal PCF (consist with eight airholes in the first ring) (Fig. 12.14c). Octagonal PCF also exhibits low confinement loss. These PCFs have been reported to sense the lower refractive index-based gases (toxic/flammable) at a wide range of wavelength from 0.8 to 2 μm [71].

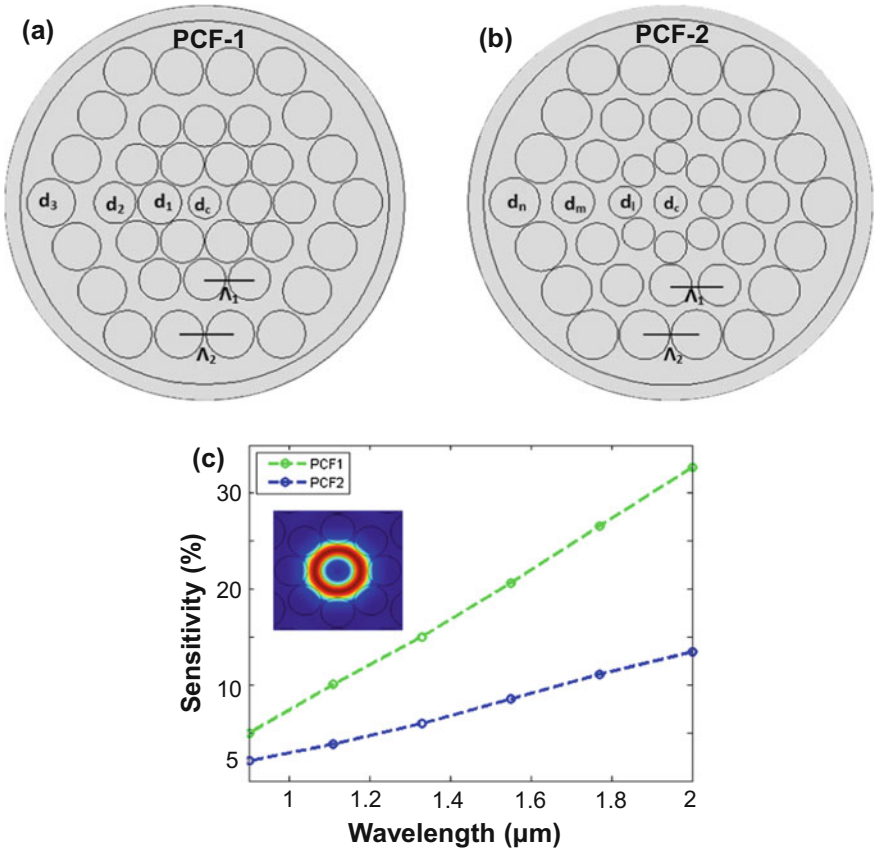

Fig. 12.14 Cross-sectional view of **a** hexagonal, **b** octagonal PCF, and **c** comparison of two HC-PCFs based on sensitivity [71]

12.5.2 Slotted-Core PCF-Based Sensors

Slotted-core PCF is widely used in terahertz communication applications. However, recently it shows great interest in sensing applications as well. Recently, Asaduzzaman et al. reported a slotted-core PCF for gas sensing (Fig. 12.15a) [72]. Numerical result reveals that slotted-core PCF is more suitable for the sensing application, and it shows the maximum relative sensitivity of 48.26%. By using slotted-shaped airholes, relative sensitivity response increased a lot than the prior PCFs which is presented in Fig. 12.15b.

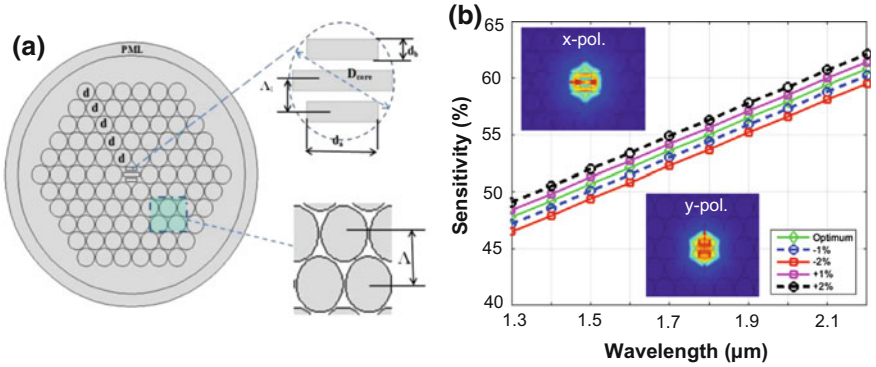

Fig. 12.15 **a** Cross-sectional view of slotted-core PCF. **b** Sensitivity as a function of wavelength (inset shows the x- and y-polarized modes) [72]

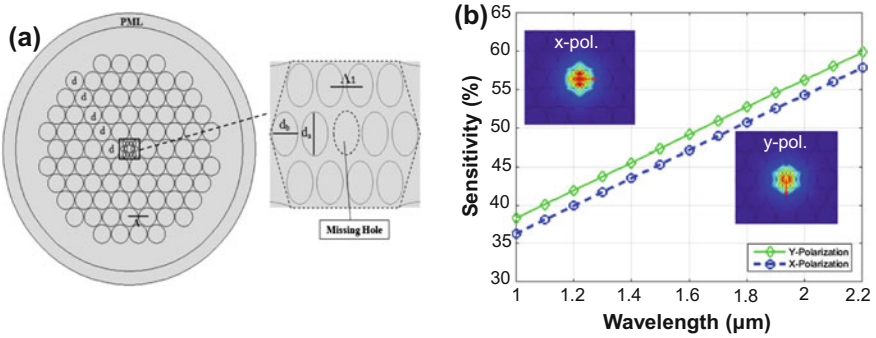

Fig. 12.16 **a** Cross-sectional view of microarray core-based PCF and **b** sensitivity as a function of wavelength [29]

12.5.3 Microstructured Core PCF-Based Sensors

Recently, PCF with microarray pattern core has been reported by Asaduzzaman et al. [12] (Fig. 12.16a). The core region contains vertically arranged elliptical holes which enhanced the relative sensitivity responses. The elliptical holes are arranged in hexagonal shape with missing holes at center. It shows the maximum sensitivity response of 43.7% (Fig. 12.16b). The structural geometric parameters also tuned to optimize the sensor performance.

Asaduzzaman et al. [47] reported a microcore PCF-based gas sensor for detecting colorless or toxic gases and monitoring air pollution by measuring gas condensate components in production facilities (Fig. 12.17a). According to the computational results, the high relative sensitivity response of 53.07% is obtained at 1.33-μm wavelength for optimum parameters which is shown in Fig. 12.17b. Here,

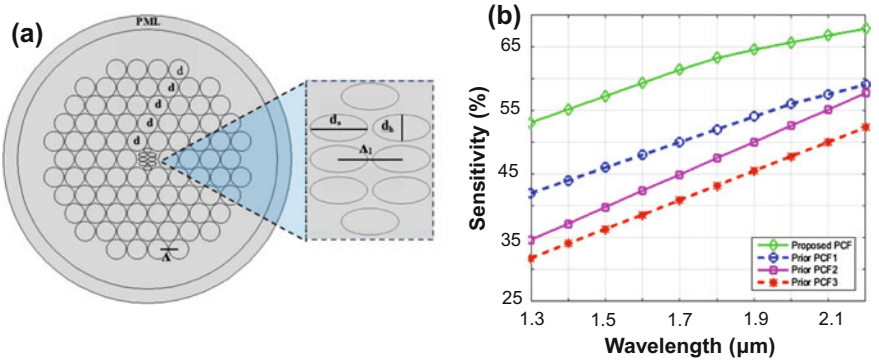

Fig. 12.17 **a** Elliptical holes array core-based PCF and **b** sensitivity as a function of wavelength [47]

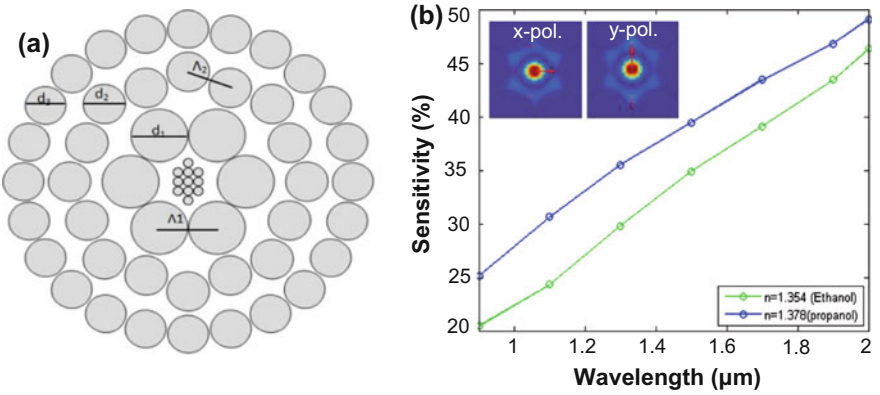

Fig. 12.18 **a** Cross-sectional view of PCF with microarray-circular hole-based core and **b** sensitivity as a function of wavelength [73]

elliptical-shaped holes are arranged in an elliptical manner which led to the higher sensitivity response than the previous reported sensor [47].

A circular photonic crystal fiber (C-PCF)-based chemical sensor presented in Fig. 12.18a [73]. It investigated the detection of ethanol and propanol chemical compound. For both chemicals (n = 1.354, n = 1.378), proposed C-PCF sensor shows higher relative sensitivity response compared to reported results in Fig. 12.12b and Fig. 12.14b (Fig. 12.18b).

12.6 Cladding Effects on Sensing

Cladding is the outer layer of photonic crystal fibers which helps to concentrate light through the core region. Cladding has significant influence in reducing confinement loss and guiding light to pass through the center core which may result more power at core region. Shape of cladding means the different geometrical organization of airholes surrounding the core region. Different cladding shape has very small impact on PCF-based gas sensing. Different cladding structure-based PCF gas sensors are shown in Fig. 12.19. It is visible that hybrid shape PCF shows better relative sensitivity compared to the circular PCF [74]. Hybrid means asymmetric arrangement of airholes at cladding region such as hexagonal, octagonal, or in circular manner.

Cladding air filling ratio also affects the relative sensitivity. Figure 12.20 reveals that higher air filling ratio introduces the higher relative sensitivity which increases with respect to wavelength.

Cladding airhole diameters are also responsible for changing in relative sensitivity. The larger airhole at outer layer of cladding reduces the confinement loss but has very less effects on relative sensitivity. On the other hand, larger airhole at inner most layer of cladding increases the sensitivity but no significant effects on confinement loss. Besides, the increment of airhole diameters in cladding increases the relative sensitivity which shows in Fig. 12.21.

Figure 12.22 exhibits the effects of inner layer and outer layer airholes effects on the relative sensitivity. According to Fig. 12.22b, it is clearly visible that first-cladding layer airhole diameters have significant effects on sensing. With the increase of first airhole diameters, sensitivity increases significantly. On the contrary, third-layer/ring diameter variation has no significant effects on sensing (Fig. 12.22c).

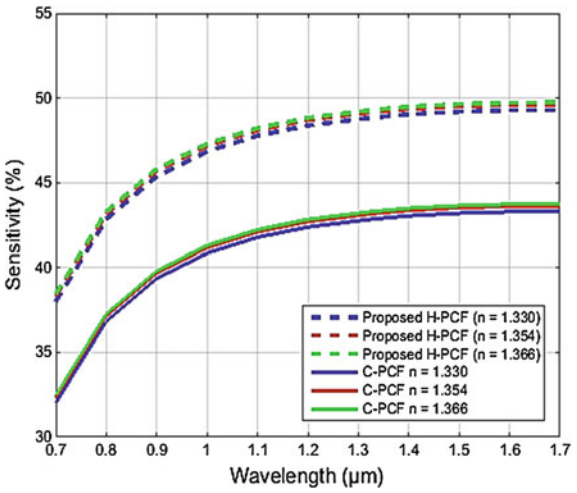

Fig. 12.19 Cladding shape effects on relative sensitivity [74]

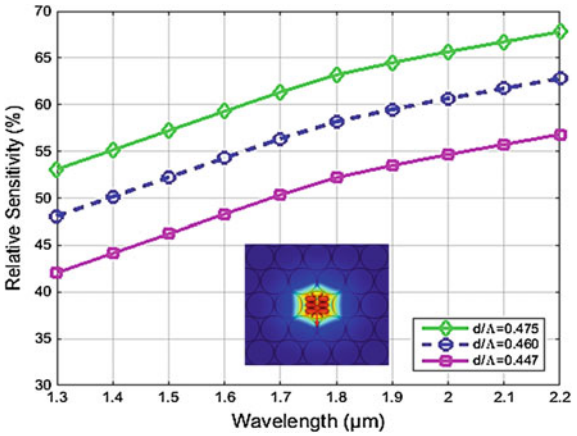

Fig. 12.20 Cladding air filling ratio effect on relative sensitivity [47]

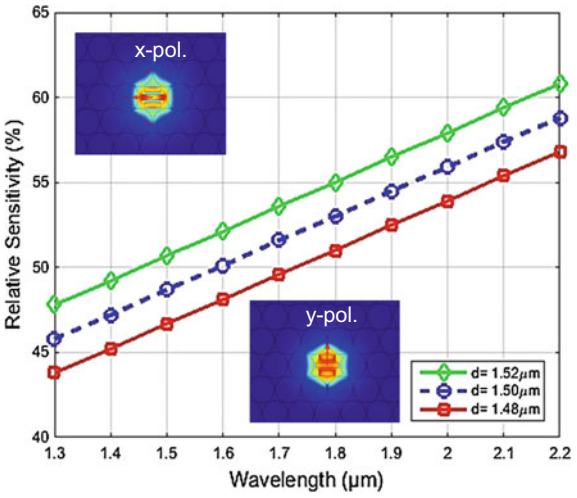

Fig. 12.21 Analysis the cladding diameter effect on relative sensitivity [72]

According to Fig. 12.23, it is also agree with the previous argument that first cladding layer is the important layer which has substantial effects on sensing performance. Figure 12.23a shows a two-ring-based hybrid PCF. Figure 12.23b shows the two different cases, one is for ethanol and another one is methanol gas. Both cases show the same result that due to increase in first layer airhole diameters, sensitivity increases significantly.

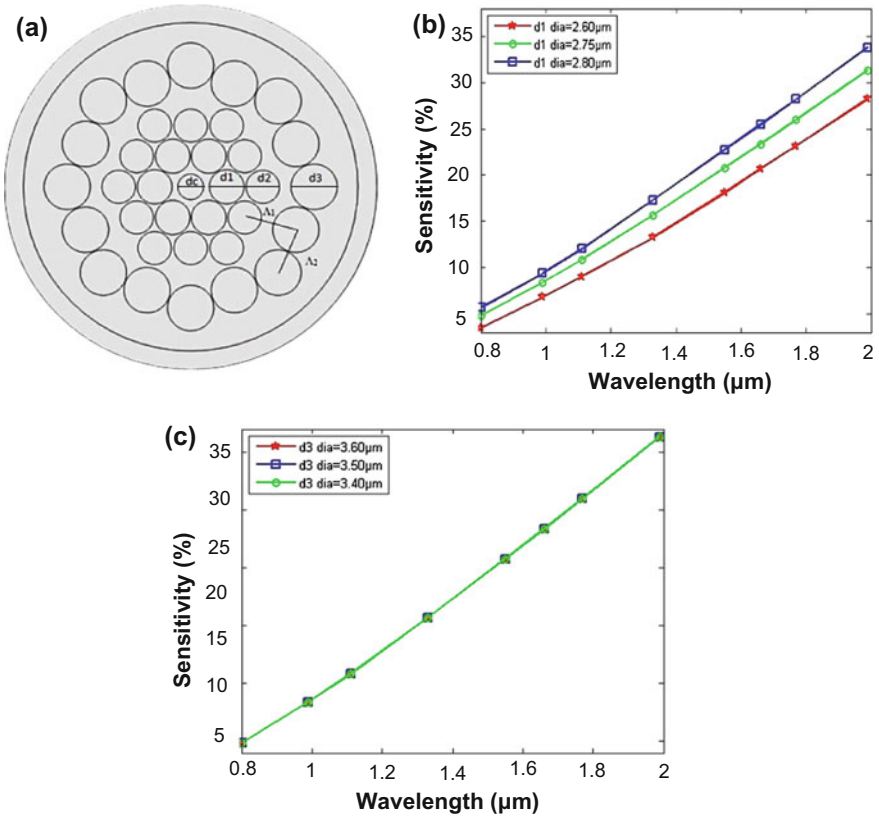

Fig. 12.22 **a** Cross-sectional view of hybrid PCF, **b**, and **c** cladding diameter (layer-based) effects on relative sensitivity

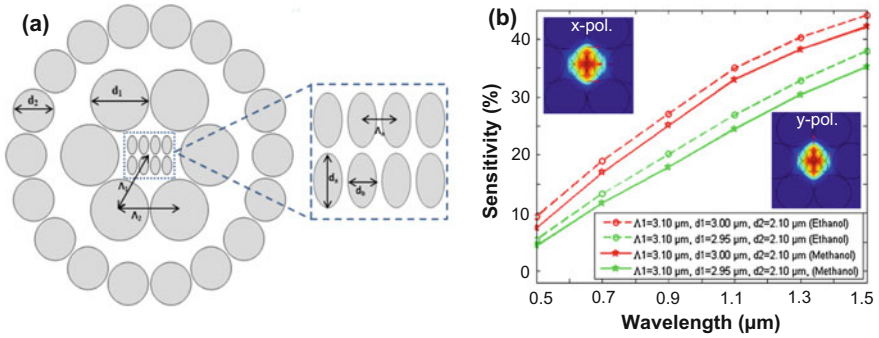

Fig. 12.23 **a** Cross-sectional view of two-ring hybrid PCF and **b** sensitivity effects due to change of first layer cladding diameters [69]

12.7 Perfectly Matched Layer (PML) Effects on Sensing

Perfectly matched layer is an artificial layer that was primarily developed by the researcher Berenger [75]. It is the outermost layer of the PCF that enclosed the cladding region. Absorption boundary layer is needed to diminish the incident unwanted electromagnetic radiation which employs the role of absorption boundary condition (ABC) [76]. Generally, PCF-based gas/chemical sensors depth is set as 10% of the cladding region. The width of the PML does not have much effects on sensitivity response. However, it has effects on confinement loss measurement [77].

12.8 Fiber Background Material Effects on Sensing

Recently, Kawsar et al. [78] investigated the effect of background materials on sensing performance (Fig. 12.24). Figure 12.24a shows the cross-sectional view of the reported sensor structure. It focuses the effect of background material on relative sensitivity at the operating wavelength 1.2–2 μm wavelength. The relative sensitivity rapidly increases with respect to wavelength. Normally, silica is used as a background material. However, they explored three different materials such as crown glass, silica, and ZBLAN as background materials with tiny airholes in core regions. From Fig. 12.24b, it can be illustrated that although, initially, silica shows the highest sensing performance, after crossing the operating wavelength 1.6 μm, ZBLAN shows the maximum sensitivity. The core-guided fundamental mode with x- and y-polarization for background material crown glass (i and ii), silica (iii and iv), and ZBLAN (v and vi) is shown in Fig. 12.24c. Finally, it can be said that background materials also have strong influence on sensor performance.

12.9 Future Directions and Conclusions

In this chapter, we discuss the optical properties of PCF and working principle of PCF-based gas/chemical sensors. We also extensively discuss the different types of PCF-based gas/chemical sensors and also the effects of core–cladding and background materials on the sensing performance. The conventional PCF can be fabricated by following the standard stack-and-draw fiber fabrication method [79]. However, irregular PCF such as octagonal, decagonal, circular, kagome, and hybrid structures fabrication is still challenging. Although the fabrication of irregular PCFs is complex, nowadays it can be done by different fiber fabrication techniques. Sol–gel technique [80] is a modern innovation for PCF fabrication which enables to contrast diameter and pitch of any size of airholes. Besides, sol–gel casting [81], extrusion [82], drilling [83] methods are suitable alternative to fabricate such irregular PCF structure. The use of chemical and gas sensors in industries is

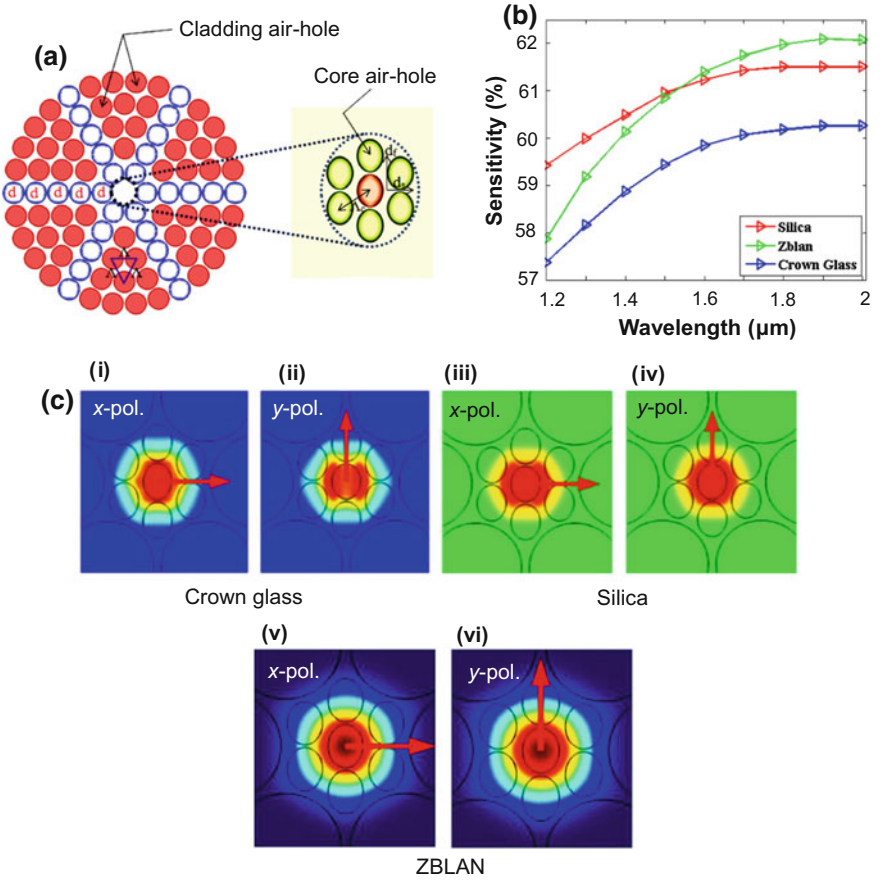

Fig. 12.24 **a** Cross-sectional view of the PCF sensor, **b** sensitivity as a function of wavelength, and **c** core-guided fundamental mode with different background materials i and ii crown glass, iii and iv silica, and v and vi ZBLAN [78]

becoming more popular. Moreover, toxic and harmful gases and chemicals are injurious and can cause an exploitation. Optical sensor more specifically photonic crystal fiber-based sensors has proved its ability to detect toxic gases and chemicals. Although numerous computational works have been done for PCF-based gas/chemical sensing, only a limited number of works have been explored experimentally. Additional experimental investigations are required to practically implement the PCF-based gas/chemical sensors.

The future aspects of the PCF-based gas/chemical sensors are as follows

- Need to simplify the PCF structure so that it can easily be fabricated.
- For PCF-based gas/chemical sensors, core region is very important because generally, gases and chemicals are flow through the core. A result needs to make a suitable core structure to absorb the light as much as possible.
- The propagation loss needs to control which is important for the practical realization. Otherwise, light will immediately vanish after launching the light one end of the fiber; as a result, it will not able to generate the measurable signal at the output end.
- Selective gas/chemical infiltrations are required in most of the reported PCF-based gas/chemical sensors. This is another challenge issue for practical realization. Its alternative solution could be external gas/chemical-sensing approaches.

References

1. T.N. Do, Y. Visell, Stretchable, twisted conductive microtubules for wearable computing, robotics, electronics, and healthcare. Sci. Rep. **7** (2017)
2. D. Ahuja, D. Parande, Optical sensors and their applications. J. Sci. Res. Rev. **1**, 060–068 (2012)
3. J.C. Yeo, C.T. Lim, Emerging flexible and wearable physical sensing platforms for healthcare and biomedical applications. Microsyst. Nanoeng. **2** (2016)
4. S.A. Morin, R.F. Shepherd, S.W. Kwok, A.A. Stokes, A. Nemiroski, G.M. Whitesides, Camouflage and display for soft machines. Science **337**, 828–832 (2012)
5. S. Gong, W. Schwalb, Y. Wang, Y. Chen, Y. Tang, J. Si et al., A wearable and highly sensitive pressure sensor with ultrathin gold nanowires. Nat. Commun. **5**, 3132 (2014)
6. S. Xu, Y. Zhang, L. Jia, K.E. Mathewson, K.-I. Jang, J. Kim et al., Soft microfluidic assemblies of sensors, circuits, and radios for the skin. Science **344**, 70–74 (2014)
7. M. Kaltenbrunner, T. Sekitani, J. Reeder, T. Yokota, K. Kuribara, T. Tokuhara et al., An ultra-lightweight design for imperceptible plastic electronics. Nature **499**, 458 (2013)
8. I.E. Araci, B. Su, S.R. Quake, Y. Mandel, An implantable microfluidic device for self-monitoring of intraocular pressure. Nat. Med. **20**, 1074–1078 (2014)
9. W. Ding, Y. Jiang, R. Gao, Y. Liu, High-temperature fiber-optic Fabry-Perot interferometric sensors. Rev. Sci. Instrum. **86**, 055001 (2015)
10. S. Liu, K. Yang, Y. Wang, J. Qu, C. Liao, J. He et al., High-sensitivity strain sensor based on in-fiber rectangular air bubble. Sci. Rep. **5**, 7624 (2015)
11. Y. Liu, D. Wang, W. Chen, Crescent shaped Fabry-Perot fiber cavity for ultra-sensitive strain measurement. Sci. Rep. **6** (2016)
12. S. Asaduzzaman, B.K. Paul, K. Ahmed, Enhancement of sensitivity and birefringence of a gas sensor on micro-core based photonic crystal fiber, in *2016 3rd International Conference on Electrical Engineering and Information Communication Technology (ICEEICT)* (2016), pp. 1–4
13. N.L. Andrews, R. Ross, D. Munzke, C. van Hoorn, A. Brzezinski, J.A. Barnes et al., In-fiber Mach-Zehnder interferometer for gas refractive index measurements based on a hollow-core photonic crystal fiber. Opt. Express **24**, 14086–14099 (2016)
14. X. Feng, W. Feng, C. Tao, D. Deng, X. Qin, R. Chen, Hydrogen sulfide gas sensor based on graphene-coated tapered photonic crystal fiber interferometer. Sens. Actuators B Chem. **247**, 540–545 (2017)

15. Y. Zhao, Z.-Q. Deng, J. Li, Photonic crystal fiber based surface plasmon resonance chemical sensors. Sens. Actuators B Chem. **202**, 557–567 (2014)
16. T.A. Birks, J.C. Knight, P.S.J. Russell, Endlessly single-mode photonic crystal fiber. Opt. Lett. **22**, 961–963 (1997)
17. R. Cregan, B. Mangan, J. Knight, T. Birks, P.S.J. Russell, P. Roberts et al., Single-mode photonic band gap guidance of light in air. Science **285**, 1537–1539 (1999)
18. M. Arjmand, R. Talebzadeh, Optical filter based on photonic crystal resonant cavity. Optoelectron. Adv. Mater.-Rapid Commun. **9**, 32–35 (2015)
19. K. Fasihi, High-contrast all-optical controllable switching and routing in nonlinear photonic crystals. J. Lightwave Technol. **32**, 3126–3131 (2014)
20. K. Cui, Q. Zhao, X. Feng, Y. Huang, Y. Li, D. Wang et al., Thermo-optic switch based on transmission-dip shifting in a double-slot photonic crystal waveguide. Appl. Phys. Lett. **100**, 201102 (2012)
21. J.-M. Brosi, C. Koos, L.C. Andreani, M. Waldow, J. Leuthold, W. Freude, High-speed low-voltage electro-optic modulator with a polymer-infiltrated silicon photonic crystal waveguide. Opt. Express **16**, 4177–4191 (2008)
22. Y. Gao, R.-J. Shiue, X. Gan, L. Li, C. Peng, I. Meric et al., High-speed electro-optic modulator integrated with graphene-boron nitride heterostructure and photonic crystal nanocavity. Nano Lett. **15**, 2001–2005 (2015)
23. H. Xuan, J. Ma, W. Jin, W. Jin, Polarization converters in highly birefringent microfibers. Opt. Express **22**, 3648–3660 (2014)
24. Y.-H. Chang, Y.-Y. Jhu, C.-J. Wu, Temperature dependence of defect mode in a defective photonic crystal. Opt. Commun. **285**, 1501–1504 (2012)
25. Y. Liu, H. Salemink, All-optical on-chip sensor for high refractive index sensing in photonic crystals. EPL (Europhys. Lett.) **107**, 34008 (2014)
26. A.A. Rifat, R. Ahmed, A.K. Yetisen, H. Butt, A. Sabouri, G.A. Mahdiraji et al., Photonic crystal fiber based plasmonic sensors. Sens. Actuators B Chem. **243**, 311–325 (2017)
27. P. Hu, X. Dong, W.C. Wong, L.H. Chen, K. Ni, C.C. Chan, Photonic crystal fiber interferometric pH sensor based on polyvinyl alcohol/polyacrylic acid hydrogel coating. Appl. Opt. **54**, 2647–2652 (2015)
28. A.A. Rifat, M.R. Hasan, R. Ahmed, H. Butt, Photonic crystal fiber-based plasmonic biosensor with external sensing approach. J. Nanophotonics **12**, 012503 (2017)
29. M. Pushkarsky, M. Webber, O. Baghdassarian, L. Narasimhan, C.K.N. Patel, Laser-based photoacoustic ammonia sensors for industrial applications. Appl. Phys. B Lasers Opt. **75**, 391–396 (2002)
30. G. Whitenett, G. Stewart, K. Atherton, B. Culshaw, W. Johnstone, Optical fibre instrumentation for environmental monitoring applications. J. Opt. A Pure Appl. Opt. **5**, S140 (2003)
31. J.P. Carvalho, H. Lehmann, H. Bartelt, F. Magalhães, R. Amezcua-Correa, J.L. Santos, et al., Remote system for detection of low-levels of methane based on photonic crystal fibres and wavelength modulation spectroscopy. J. Sens. **2009** (2009)
32. R.A. Aoni, R. Ahmed, M.M. Alam, and S. Razzak, Optimum design of a nearly zero ultra-flattened dispersion with lower confinement loss photonic crystal fibers for communication systems. Int. J. Sci. Eng. Res. **4** (2013)
33. M.S. Habib, M.S. Habib, S.A. Razzak, M.A. Hossain, Proposal for highly birefringent broadband dispersion compensating octagonal photonic crystal fiber. Opt. Fiber Technol. **19**, 461–467 (2013)
34. S.A. Razzak, M.A.G. Khan, F. Begum, S. Kaijage, Guiding properties of a decagonal photonic crystal fiber. J. Microwaves Optoelectron. Electromagn. Appl. (JMOe) **6**, 44–49 (2007)
35. R. Ahmmed, R. Ahmed, S.A. Razzak, Design of large negative dispersion and modal analysis for hexagonal, square, FCC and BCC photonic crystal fibers, in *2013 International Conference on Informatics, Electronics & Vision (ICIEV)* (2013), pp. 1–6.
36. Y. Hou, F. Fan, Z.-W. Jiang, X.-H. Wang, S.-J. Chang, Highly birefringent polymer terahertz fiber with honeycomb cladding. Opt. Int. J. Light Electron Opt. **124**, 3095–3098 (2013)

37. R. Hao, Z. Li, G. Sun, L. Niu, Y. Sun, Analysis on photonic crystal fibers with circular air holes in elliptical configuration. Opt. Fiber Technol. **19**, 363–368 (2013)
38. M.R. Hasan, S. Akter, T. Khatun, A.A. Rifat, M.S. Anower, Dual-hole unit-based kagome lattice microstructure fiber for low-loss and highly birefringent terahertz guidance. Opt. Eng. **56**, 043108–043108 (2017)
39. J. Hecht, *Understanding fiber optics* (Jeff Hecht, 2015)
40. E. Udd, Fiber optic sensors based on the Sagnac interferometer and passive ring resonator. Fiber opt. Sens. Introduc.Eng. Sci. (1991)
41. P. Sharan, S. Bharadwaj, F.D. Gudagunti, P. Deshmukh, Design and modelling of photonic sensor for cancer cell detection, in *2014 International Conference on the IMpact of E-Technology on US (IMPETUS)* (2014), pp. 20–24.
42. J. Park, S. Lee, S. Kim, K. Oh, Enhancement of chemical sensing capability in a photonic crystal fiber with a hollow high index ring defect at the center. Opt. Express **19**, 1921–1929 (2011)
43. S. Olyaee, A. Naraghi, V. Ahmadi, High sensitivity evanescent-field gas sensor based on modified photonic crystal fiber for gas condensate and air pollution monitoring. Opt. Int. J. Light Electron Opt. **125**, 596–600 (2014)
44. H. Ademgil, Highly sensitive octagonal photonic crystal fiber based sensor. Opt. Int. J. Light Electron Opt. **125**, 6274–6278 (2014)
45. W. Jin, H. Ho, Y. Cao, J. Ju, L. Qi, Gas detection with micro-and nano-engineered optical fibers. Opt. Fiber Technol. **19**, 741–759 (2013)
46. E. Austin, A. van Brakel, M.N. Petrovich, D.J. Richardson, Fibre optical sensor for C 2 H 2 gas using gas-filled photonic bandgap fibre reference cell. Sens. Actuators B Chem. **139**, 30–34 (2009)
47. S. Asaduzzaman, K. Ahmed, Proposal of a gas sensor with high sensitivity, birefringence and nonlinearity for air pollution monitoring. Sens. Bio-Sens. Res. **10**, 20–26 (2016)
48. K. Ahmed, M. Morshed, Design and numerical analysis of microstructured-core octagonal photonic crystal fiber for sensing applications. Sens. Bio-Sens. Res. **7**, 1–6 (2016)
49. S. Asaduzzaman, K. Ahmed, T. Bhuiyan, T. Farah, Hybrid photonic crystal fiber in chemical sensing. SpringerPlus **5**, 748 (2016)
50. Q. Liu, S. Li, H. Chen, Z. Fan, J. Li, Photonic crystal fiber temperature sensor based on coupling between liquid-core mode and defect mode. IEEE Photonics J. **7**, 1–9 (2015)
51. Y. Lu, M. Wang, C. Hao, Z. Zhao, J. Yao, Temperature sensing using photonic crystal fiber filled with silver nanowires and liquid. IEEE Photonics J. **6**, 1–7 (2014)
52. Y. Al-Qazwini, A. Noor, Z. Al-Qazwini, M.H. Yaacob, S. Harun, M. Mahdi, Refractive index sensor based on SPR in symmetrically etched plastic optical fibers. Sens. Actuators A **246**, 163–169 (2016)
53. T. Takeo, H. Hattori, Optical fiber sensor for measuring refractive index. Jpn. J. Appl. Phys. **21**, 1509 (1982)
54. K. Cooper, J. Elster, M. Jones, R. Kelly, Optical fiber-based corrosion sensor systems for health monitoring of aging aircraft, in *2001 IEEE Systems Readiness Technology Conference on AUTOTESTCON Proceedings* (2001), pp. 847–856.
55. K.T. Wan, C.K. Leung, Durability tests of a fiber optic corrosion sensor. Sensors **12**, 3656–3668 (2012)
56. L. Alwis, T. Sun, K. Grattan, Optical fibre-based sensor technology for humidity and moisture measurement: review of recent progress. Measurement **46**, 4052–4074 (2013)
57. C. Bariain, I.R. Matías, F.J. Arregui, M. López-Amo, Optical fiber humidity sensor based on a tapered fiber coated with agarose gel. Sens. Actuators B Chem. **69**, 127–131 (2000)
58. D. Bykov, O. Schmidt, T. Euser, P.S.J. Russell, Flying particle sensors in hollow-core photonic crystal fibre. Nat. Photonics **9**, 461 (2015)
59. Y. Wang, N. Li, X. Huang, M. Wang, Fiber optic transverse load sensor based on polarization properties of π-phase-shifted fiber Bragg grating. Opt. Commun. **342**, 152–156 (2015)

60. M.S. Islam, B.K. Paul, K. Ahmed, S. Asaduzzaman, M.I. Islam, S. Chowdhury et al., Liquid-infiltrated photonic crystal fiber for sensing purpose: design and analysis. Alexandria Eng. J. (2017)
61. K. Ahmed, M.S. Islam, B.K. Paul, Design and numerical analysis: effect of core and cladding area on hybrid hexagonal microstructure optical fiber in environment pollution sensing applications. Karbala Int. J. Mod. Sci. **3**, 29–38 (2017)
62. W.L. Ng, A.A. Rifat, W.R. Wong, D.C. Tee, F.R. Mahamd Adikan, Enhancement of evanescent field exposure in a photonic crystal fibre with interstitial holes. J. Mod. Opt. **64**, 1544–1549 (2017)
63. A.A. Rifat, R. Ahmed, G.A. Mahdiraji, F.M. Adikan, highly sensitive d-shaped photonic crystal fiber-based plasmonic biosensor in visible to near-IR. IEEE Sens. J. **17**, 2776–2783 (2017)
64. M. De, R.K. Gangwar, V.K. Singh, Designing of highly birefringence, dispersion shifted decagonal photonic crystal fiber with low confinement loss. Photonics Nanostruct. Fundam. Appl. **26**, 15–23 (2017)
65. L. Xin, L. Ying, X. Guo, Modular interference characteristics and beat length of a two-hole photonic crystal fiber, in *International Symposium on Optoelectronic Technology and Application 2016* (2016), pp. 101550T–101550T-7
66. M.R. Hasan, M.A. Islam, A.A. Rifat, A single mode porous-core square lattice photonic crystal fiber for THz wave propagation. J. Eur. Opt. Soc. Rapid Publ. **12**, 15 (2016)
67. S.K. Mishra, S. Rani, B.D. Gupta, Surface plasmon resonance based fiber optic hydrogen sulphide gas sensor utilizing nickel oxide doped ITO thin film. Sens. Actuators B Chem. **195**, 215–222 (2014)
68. S.K. Mishra, S. Bhardwaj, B.D. Gupta, Surface plasmon resonance-based fiber optic sensor for the detection of low concentrations of ammonia gas. IEEE Sens. J. **15**, 1235–1239 (2015)
69. S. Asaduzzaman, K. Ahmed, M.F.H. Arif, M. Morshed, Proposal of a simple structure photonic crystal fiber for lower indexed chemical sensing, in *2015 18th International Conference on Computer and Information Technology (ICCIT)* (2015), pp. 127–131
70. M. Morshed, S. Asaduzzaman, M.F.H. Arif, K. Ahmed, Proposal of simple gas sensor based on micro structure optical fiber in *2015 International Conference on Electrical Engineering and Information Communication Technology (ICEEICT)* (2015), pp. 1–5
71. S. Das, V. Jayaraman, SnO 2: a comprehensive review on structures and gas sensors. Prog. Mater Sci. **66**, 112–255 (2014)
72. S. Asaduzzaman, K. Ahmed, B.K. Paul, Slotted-core photonic crystal fiber in gas-sensing application, in *SPIE/COS Photonics Asia* (2016), pp. 100250O–100250O-9
73. S. Asaduzzaman, M.F.H. Arif, K. Ahmed, P. Dhar, Highly sensitive simple structure circular photonic crystal fiber based chemical sensor, in *2015 IEEE International WIE Conference on Electrical and Computer Engineering (WIECON-ECE)* (2015), pp. 151–154
74. S. Asaduzzaman, K. Ahmed, M.F.H. Arif, M. Morshed, Application of microarray-core based modified photonic crystal fiber in chemical sensing, in *2015 International Conference on Electrical & Electronic Engineering (ICEEE)* (2015), pp. 41–44
75. J.-P. Berenger, A perfectly matched layer for the absorption of electromagnetic waves. J. Comput. Phys. **114**, 185–200 (1994)
76. T. Uno, Y. He, S. Adachi, Perfectly matched layer absorbing boundary condition for dispersive medium. IEEE Microwave Guided Wave Lett. **7**, 264–266 (1997)
77. B.K. Paul, K. Ahmed, S. Asaduzzaman, M.S. Islam, Folded cladding porous shaped photonic crystal fiber with high sensitivity in optical sensing applications: design and analysis. Sens. Bio-Sens. Res. **12**, 36–42 (2017)
78. K. Ahmed, I. Islam, B.K. Paul, S. Islam, S. Sen, S. Chowdhury et al., Effect of photonic crystal fiber background materials in sensing and communication applications. Mat. Discov. (2017)
79. G. Amouzad Mahdiraji, D.M. Chow, S. Sandoghchi, F. Amirkhan, E. Dermosesian, K.S. Yeo et al., Challenges and solutions in fabrication of silica-based photonic crystal fibers: an experimental study. Fiber Integr. Opt. **33**, 85–104 (2014)

80. R.T. Bise, D. Trevor, Solgel-derived microstructured fibers: fabrication and characterization, in *Optical Fiber Communication Conference* (2005), p. OWL6
81. H. El Hamzaoui, Y. Ouerdane, L. Bigot, G. Bouwmans, B. Capoen, A. Boukenter et al., Sol-gel derived ionic copper-doped microstructured optical fiber: a potential selective ultraviolet radiation dosimeter. Opt. Express **20**, 29751–29760 (2012)
82. H. Ebendorff-Heidepriem, P. Petropoulos, S. Asimakis, V. Finazzi, R.C. Moore, K. Frampton et al., Bismuth glass holey fibers with high nonlinearity. Opt. Express **12**, 5082–5087 (2004)
83. J. Knight, T. Birks, P.S.J. Russell, D. Atkin, All-silica single-mode optical fiber with photonic crystal cladding. Opt. Lett. **21**, 1547–1549 (1996)

Part IV
Silicon-on-Insulator Sensors

Chapter 13
Silicon Nanowires for DNA Sensing

Mohamed Farhat O. Hameed, A. Samy Saadeldin, Essam M. A. Elkaramany and S. S. A. Obayya

Abstract Highly sensitive hybrid plasmonic slot waveguide (HPSW) biosensors based on silicon on insulator (SOI) are proposed and analyzed for DNA hybridization detection. The reported designs are based on increasing the light interaction with the sensing region by using slot waveguide with plasmonic material. Due to the high index contrast and plasmonic effect, an ultrahigh optical confinement is achieved in the low-index regions which enables the detection of the smallest change in the analyte refractive index with high sensitivity. The normalized power confinement, power density, effective index of the supported modes by the HPSWs are analyzed to achieve high power confinement through the suggested biosensors, and hence, high sensitivity can be obtained. The HPSWs are also incorporated with straight slotted resonator to calculate the sensitivity of the proposed design. In this study, two different plasmonic materials (gold and titanium

M. F. O. Hameed (✉)
Center for Photonics and Smart Materials and Nanotechnology Engineering Program, Zewail City of Science and Technology, October Gardens, 6th of October City, Giza, Egypt
e-mail: mfarahat@zewailcity.edu.eg

M. F. O. Hameed
Mathematics and Engineering Physics Department, Faculty of Engineering, Mansoura University, Mansoura, Egypt

A. Samy Saadeldin
Electronics and Communication Engineering Department, Akhbar Elyom Academy, 6th of October City, Egypt
e-mail: ahmed_samy2086@yahoo.com

A. Samy Saadeldin · E. M. A. Elkaramany
Engineering Mathematics and Physics Department, Faculty of Engineering, Cairo University, Giza, Egypt

S. S. A. Obayya
Centre for Photonics and Smart Materials, Zewail City of Science and Technology, October Gardens, 6th of October City, Giza, Egypt
e-mail: sobayya@zewailcity.edu.eg

S. S. A. Obayya
Electronics and Communication Engineering Department, Faculty of Engineering, Mansoura University, Mansoura, Egypt

© Springer International Publishing AG, part of Springer Nature 2019

M. F. O. Hameed and S. Obayya (eds.), *Computational Photonic Sensors*, https://doi.org/10.1007/978-3-319-76556-3_13

nitride) are used for the proposed designs. The simulation results are calculated using full vectorial finite element method (FVFEM). The reported biosensors have high sensitivity of 1890.4 nm/RIU (refractive index unit) with a detection limit of 2.65×10^{-6} RIU with gold material and 1190 nm/RIU with a detection limit of 4.2×10^{-6} RIU based on titanium nitride material, which are the highest in the literature to the best of our knowledge.

Keywords DNA hybridization · Optical biosensors · Slot waveguide SOI · Surface plasmon

13.1 Introduction

Optical biosensors [1] have attracted the attention during the last years since they can be used in many applications such as monitoring molecular reaction, environmental monitoring, and medical diagnostics. There are two types of biosensors, label-based sensor and label-free sensor. Label-based detection can change molecule's binding properties and therefore decrease the detection reliability [2]. However, label-free biosensing has advantages in terms of real-time monitoring with no label requirement [3]. The biosensing mechanism depends on detecting the refractive index change due to the biomolecule interaction. The refractive index change can be measured by homogenous sensing or surface sensing. Homogenous sensing can detect the variation of the effective indices of the supported modes due to the change of the medium refractive index as a result of biomolecule binding. However, surface sensing is based on the change of the mode effective index because of the alternation of the thickness of the thin layer of receptors owing to the biomolecule binding [4].

There are different platforms such as photonic crystal [5] and silicon on insulator (SOI) [6] that can be used for biosensing applications. Among different optical sensors such as directional couplers [7], photonic crystal fibers [8–10], photonic crystal cavities [11], and Bragg grating-based fabry–perot resonators [12], the slot waveguide biosensors have advantages in terms of light confinement in the low-index region due to the discontinuity of the electric field at the interface between the nanowires and the slot design [3]. Therefore, the interaction of the light with the sensing material increases which improves the sensor sensitivity. However, in most optical waveguide biosensors, the light is confined in the high-index region, so the interaction of the light with the sensing material is limited. Therefore, biosensors based on SOI slot waveguide have been studied extensively. In [13], a label-free biosensor based on SOI microring cavities for the detection of protein concentration down to 10 ng/ml was proposed and minimum detectable refractive index change of 10^{-5} RIU was achieved. Barrios et al. [14] have demonstrated label-free molecule detection by using an integrated biosensor based on a Si_3N_4/SiO_2 slot waveguide to detect the bovine serum albumin (BSA) and anti-BSA molecular binding with sensitivity of 1.8 and 2.3 nm/(ng/mm^2), respectively. Additionally, Claes et al. [15] have presented label-free biosensor using SOI slot

waveguide-based ring resonator for protein sensing with sensitivity of 298 nm/RIU. Further, a directional coupler-based integrated optical chemical sensor using two SOI slot waveguides with minimum detectable refractive index change of 5×10^{-5} RIU was proposed [16]. A double-slot hybrid plasmonic waveguide was also used as an active sensing arm of Mach–Zehnder interferometer-based liquid sensor with sensitivity of 1061 nm/RIU [17]. Ishizaka et al. [18] have also presented a metal-assisted silicon slot waveguide for gas detection with sensitivity of 458 nm/RIU. In [19], miniature microring resonator sensor based on a hybrid plasmonic waveguide has been presented with sensitivity of 580 nm/RIU. Further, a theoretical investigation for biosensor using a metal–insulator–silicon waveguide has been proposed by Kwon [20] with sensitivity of 430 nm/RIU. Furthermore, hybrid plasmonic waveguides based on metal coating of dielectric ridges have been reported for sensing applications [21]. Additionally, Bahrami et al. [22] have presented dual polarization measurements in the hybrid plasmonic biosensors. Yun et al. [23] have also introduced a numerical study on refractive index sensor based on hybrid plasmonic mode with sensitivity of 1080 nm/RIU. In [24], a hybrid plasmonic microcavity with an air-filled gap for sensing applications has been proposed with sensitivity of 100 nm/RIU. Ghosh et al. [25] have also reported an innovative straight resonator incorporating a vertical slot as an efficient biochemical sensor with sensitivity of 820 nm/RIU. The biosensors based on SOI slot waveguide have been also studied for the detection of deoxyribonucleic acid (DNA) hybridization. The DNA hybridization means that single-stranded DNA (ssDNA) hybridizes with another complementary homologous single-stranded DNA to perform double-stranded DNA (dsDNA) [2]. The ssDNA (probe) is immobilized by an attachment to a solid surface (by linker layer (glue) on silicon nanowire). During the flow of the aqueous solution containing complementary ssDNA, the homologous DNA (target) will hybridize the probe ssDNA, while the non-homologous DNA will not be attached. Li et al. [26] have reported a label-free biosensor based on concentric ring resonators for detecting the DNA hybridization with sensitivity of 683 nm/RIU. A label-free biosensor using the slot waveguide-based ring resonator for the detection of DNA hybridization was also optimized to improve the sensitivity to 856 nm/RIU [3]. A silicon multiple-slot-based ring resonator optical sensor with sensitivity of 912 nm/RIU was also introduced [27]. Moreover, the demonstration of a label-free horizontal slot waveguide based on Mach–Zehnder interferometer biosensor for the detection of DNA hybridization was reported with sensitivity of 893.5 nm/RIU [28].

It is worth noting that most of the previously reported DNA biosensors [3, 26–28] depend on all-dielectric materials with complex structures. Further, the maximum achieved sensitivity was equal to 893.5 nm/RIU [28] based on Mach–Zehnder interferometer. By introducing surface plasmon polaritons (SPPs) to the biosensor design, we can confine the light strongly to the surface of the metal and thereby strongly increase the interaction between the light and the sensing medium. The SPPs are electromagnetic interaction between surface free electrons of a metal and the fields of the incident light.

This chapter introduces a novel design of highly sensitive hybrid plasmonic slot waveguide (HPSW) for detecting the DNA hybridization with high sensitivity. The reported design can increase the light interaction with the sensing region and enhance the field confinement by using plasmonic sidewalls and plasmonic substrate along with the slot waveguide. Therefore, three slots are formed between plasmonic rails and silicon nanowires. Consequently, the light is well confined in the three low-index regions. So, the light interaction with the sensing material increases and hence the sensitivity can be improved. The sensitivity of the proposed sensor is based on a shift in the resonance wavelength due to the DNA hybridization. It is worth noting that many biosensors have been reported based on a slot waveguide-incorporated ring resonator systems. However, the ring resonator suffers from bending and coupling losses with the bus waveguides. Therefore, it is aimed to replace the ring resonator design with another device with smaller footprint. At the resonance wavelength, the light is highly coupled to the resonator part where a minimum transmission occurs in the middle slot region. Thus, the resonance wavelength (λ_{res}) can be detected by the photodetectors at the output port of the suggested design. Further, the reported biosensor is designed with sensing ability around the well-known telecommunication wavelength, $\lambda = 1550$ nm. The proposed biosensor has also advantages in terms of compactness with nanometer dimension and high-scale integration. Also, the fabrication of the suggested design is easier than that of other complex devices. Furthermore, a much higher device sensitivity of 1890.4 nm/RIU with detection limit of 2.65×10^{-6} RIU can be achieved with gold material which is the highest sensitivity in the literature to the best of our knowledge. If the gold material is replaced by TiN, the achieved sensitivity is equal to 1190 nm/RIU with detection limit of 4.2×10^{-6} RIU.

The chapter will be organized as follows: The design consideration of the suggested design is introduced in Sect. 13.2. The proposed structure is studied with gold as a plasmonic material in Sect. 13.3 to optimize the geometrical parameters to achieve high power confinement through the suggested biosensor, and hence, high sensitivity can be achieved. Then, the analysis of the reported configuration incorporated with the straight slotted resonator is introduced to calculate the sensitivity of the reported biosensor. Additionally, the previous study is repeated with titanium nitride (TiN) as an alternative plasmonic material. Finally, conclusion will be drawn.

13.2 Design Considerations

Figure 13.1 shows the proposed hybrid plasmonic slot waveguide (HPSW) for the detection of the DNA hybridization. It consists of two silicon nanowires close to each other depositing on a plasmonic layer of thickness $t_{plasm} = 50$ nm and sandwiched between two plasmonic rails. The refractive indices of the silicon, silicon oxide, and water are taken as 3.476, 1.45, and 1.33, respectively, at the operating wavelength of 1550 nm. The silicon nanowire is coated with linker layer (silanes) that has a refractive index of 1.42 [29] with thickness of 1 nm. Then, the ssDNA

(probe layer) of thickness 8 nm is added with refractive index of 1.456. When the hybridization occurs, the refractive index of the ssDNA will be changed to that of dsDNA which is equal to 1.53 [3, 26], while the layer thickness remains unchanged. Therefore, homogenous sensing can be achieved.

The slot waveguide has height GH = 320 nm, width GW = 170 nm, slot width SW = 100 nm, and slot width between plasmonic and silicon nanowire PSW = 100 nm for the initial simulation study. The full vectorial finite element method (FVFEM) [30, 31] based on Comsol Multiphysics software package [32] is used with minimum element size of 0.003 nm and total number of elements of 75,959. Additionally, the number of degrees of freedom is equal to 675,078, and the total cross-sectional area is 1.5 μm × 0.6 μm. Further, perfect matched layer (PML) boundary condition is used to truncate the computational domain and calculate the confinement losses of the two polarized modes.

The suggested design can be fabricated based on the following steps. The plasmonic layer is first coated on the Si wafer covered by the SiO_2 layer. The silicon is then deposited onto the plasmonic surface [33–35]. Next, the silicon layer is etched to form a slot waveguide as shown in Fig. 13.1. The plasmonic rails are then deposited onto the plasmonic surface to form plasmonic slot waveguide. The ultrathin and stable monolayer of silane can be formed around the surface of the Si ridges with thickness of 10–17 Å depending on silane concentration. Further, the deposition technique of the 1 nm silane around the Si ridges can be obtained as reported in [36]. In this regard, the Si ridge should be cleaned by sonication in ethanol/water. Further, a mixture of hydrogen peroxide and sulfuric acid is used to oxidize the Si ridge. The sample is then washed, dried, and immersed in the silane

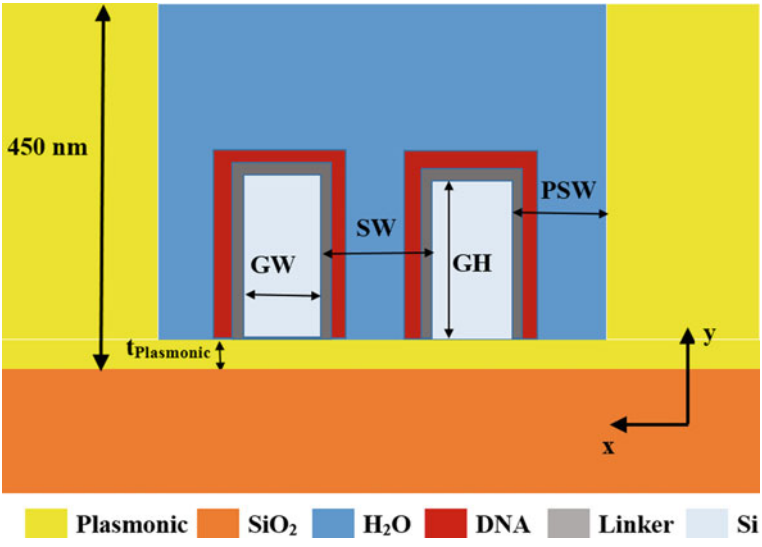

Fig. 13.1 Cross section of the suggested HPSW biosensor [1]

solution. Consequently, the deposition layer will be obtained through the solution of silane in toluene within 18 h at room temperature.

In the next section, the proposed structure in Fig. 13.1 is first studied with gold as a plasmonic material, then with titanium nitride (TiN) as an alternative plasmonic material. It is aimed to optimize the geometrical parameters to obtain high power confinement through the suggested biosensor, and hence, high sensitivity can be achieved.

13.3 Simulation Results

13.3.1 HPSW with Gold as a Plasmonic Material

Gold and silver are the two most useful metals because they have low ohmic losses and high DC conductivity. The silver has higher detection accuracy than the gold. However, the sliver has a low chemical stability because of its oxidation due to the interaction with air and water. Therefore, it is difficult to give a reproducible result and hence the silver-based sensor is not reliable for practical applications [37]. Consequently, the gold is used for the suggested design.

The relative permittivity of the gold can be obtained from [38]:

$$\varepsilon_{Au}(\omega) = \varepsilon_{\infty} - \frac{\omega_p^2}{\omega(\omega + i\omega_\tau)} \tag{13.1}$$

where $\varepsilon_{\infty} = 9.75$, $\omega_p = 1.36 \times 10^{16}$ (rad/s), and $\omega_\tau = 1.45 \times 10^{14}$ (rad/s).

The FVFEM is used to calculate the supported quasi-transverse electric (TE) and quasi-transverse magnetic (TM) modes. It is found that the quasi-TE mode has

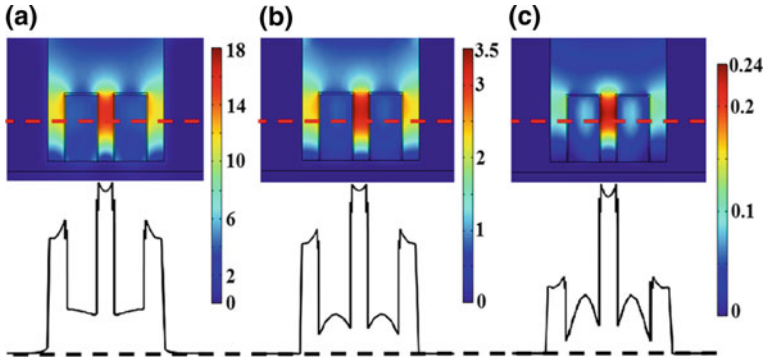

Fig. 13.2 Confinement in the slot regions for the suggested design at λ = 1.55 μm **a** norm E component for the quasi-TE mode, **b** E_x component for the quasi-TE mode, and **c** power flow P_z for the quasi-TE mode. Insets are the field plots and power flow along x-axis (red dash lines are referred to the cross section along x-axis) [1]

higher confinement in the slot regions than the quasi-TM mode. Figure 13.2a, b shows the norm and x-components of the quasi-TE polarized mode at wavelength of 1.55 μm. The corresponding field plots along the x-axis at the center of the waveguide are also shown as insets in Fig. 13.2a, b. It may be seen from Fig. 13.2 that the field of the quasi-TE mode is highly confined in the slot regions due to the high index contrast and plasmonic enhancement. The power flow P_z for the quasi-TE mode is also confined in the slot regions as shown in Fig. 13.2c. Therefore, the performance of the suggested biosensor will be studied based on the quasi-TE mode.

In order to increase the confinement of the light in the sensing regions and hence improve the biosensor sensitivity, the different geometrical parameters are studied. The effect of the high-index region width GW on the effective index, n_{eff}, of the quasi-TE mode is first investigated. In this investigation, the silicon nanowire height is taken as GH = 320 nm, slot width of SW = 100 nm, and slot width between gold and silicon nanowire is PSW = 100 nm.

Figure 13.3 shows the variation of the effective index of the quasi-TE mode for the ssDNA and dsDNA cases with the silicon nanowire width GW. Figure 13.3 also shows the change in the effective index δn_{eff} due to the binding of the ssDNA with the complementary ssDNA to form the dsDNA after the hybridization occurrence. The change in the effective index can be defined as $\delta n_{eff} = n_{eff\_dsDNA} - n_{eff\_ssDNA}$. The δn_{eff} is obtained by simulating the proposed design with ssDNA layer above the linker layer; then, the ssDNA is replaced by dsDNA. It may be noted from Fig. 13.3 that when the silicon nanowire width increases, its volume and hence the effective index of the quasi-TE mode increase. Further, the n_{eff} of the quasi-TE mode in the ssDNA case is smaller than that of the dsDNA case because the refractive index of the ssDNA is less than that of the dsDNA. It is also revealed from Fig. 13.3 that the maximum change in the effective index is obtained at GW = 200 nm. However, the suitable silicon nanowire width is taken as 170 nm due to the well confinement of the mode inside the slots as shown in Fig. 13.2a.

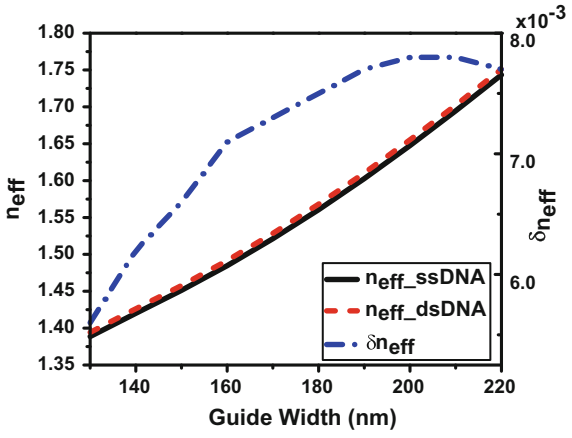

Fig. 13.3 Variation of the n_{eff} of the quasi-TE mode of the suggested design with ssDNA and dsDNA layers and δn_{eff} with the silicon nanowire width GW [1]

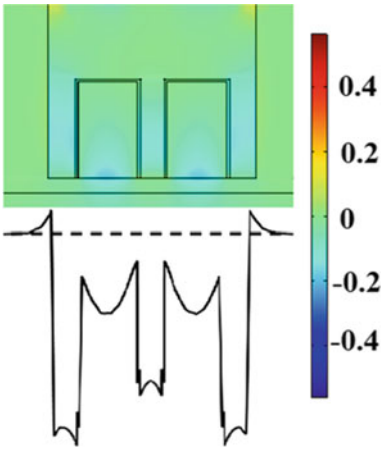

Fig. 13.4 E_x component for the quasi-TE mode at GW = 200 nm [1]

At GW = 200 nm, the electric field is not strongly confined in the slot region as shown in Fig. 13.4, which leads to a weak light interaction with the sensing region.

The proposed design presents high power confinement in the low-index regions which leads to high light interaction with the sensing material, and a higher sensitivity can be achieved. The normalized power confinement in the three low-index regions is equal to 67% where the normalized power confinement is defined as the power in a region normalized to the total power. The power density is obtained by dividing this normalized power confinement with the area of that region [28]. Figure 13.5 shows the variation of the power density of the quasi-TE mode in the DNA layer with the silicon nanowire width GW. It is evident that the power density of the quasi-TE mode for the ssDNA case is higher than that of the dsDNA because the refractive index of the ssDNA is less than that of the dsDNA. Therefore, higher refractive index contrast is achieved with the ssDNA layer which offers more field enhancement in the low-index regions due to normal electric field discontinuity. Also it may be seen from this figure that the maximum power density is achieved at GW = 170 nm which confirms our choice for that value.

The effect of the slot width SW on the effective index of the quasi-TE mode is next investigated. During this study, the silicon nanowire width is fixed at GW = 170 nm, silicon nanowire height GH = 320 nm, and slot width between the gold and the silicon nanowire is PSW = 100 nm. Figure 13.6 shows the variation of the effective index of the quasi-TE mode in the ssDNA and dsDNA cases with the SW value. It may be seen from Fig. 13.6 that as the slot width decreases, the change in the effective index increases and the field becomes more confined in the low-index region leading to higher sensitivity.

Figure 13.7 shows the power density variation of the quasi-TE mode of the suggested design at different DNA layers with the slot width SW. It may be seen from this figure that the highest power densities using the ssDNA and dsDNA layers are obtained at slot width SW = 60 nm. However, there is a fabrication

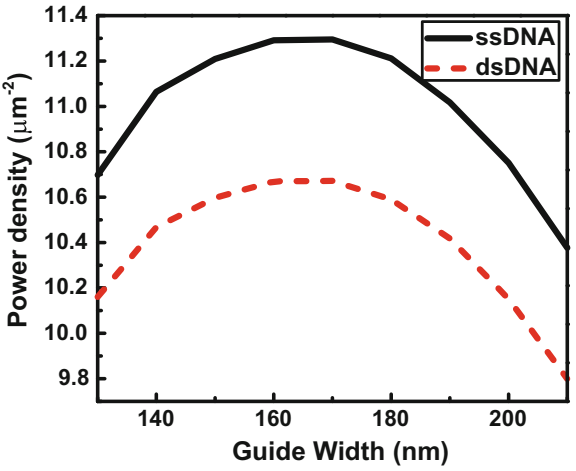

Fig. 13.5 Variation of the power density of the quasi-TE mode of the suggested design in the ssDNA and dsDNA layers with the silicon nanowire width GW [1]

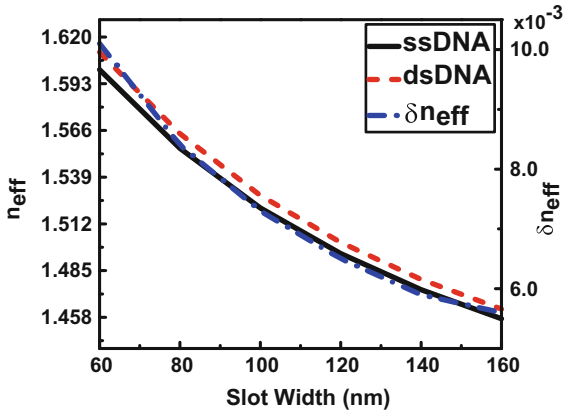

Fig. 13.6 Variation of the n_{eff} of the quasi-TE mode of the suggested design with the ssDNA and dsDNA layers and δn_{eff} with the slot width SW [1]

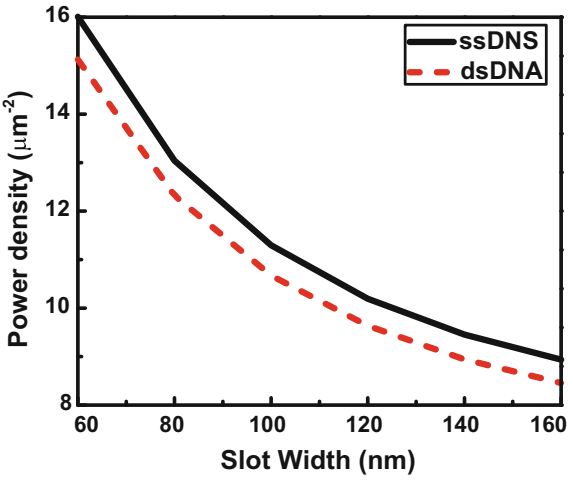

Fig. 13.7 Variation of the power density of the quasi-TE mode of the suggested design with the slot width SW [1] using ssDNA and dsDNA layers

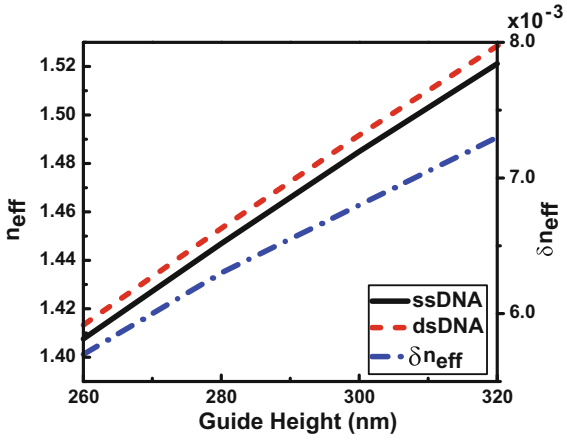

Fig. 13.8 Variation of the n_{eff} of the quasi-TE mode of the suggested design and δn_{eff} with the silicon nanowire height GH [1] using the ssDNA and dsDNA layers

limitation for slot width of less than 100 nm [3]. According to fabrication technologies, SW = 100 nm is suggested as a suitable design.

The effect of the silicon nanowire height GH on the effective index of the quasi-TE mode is also investigated as shown in Fig. 13.8. It is evident from this figure that the effective indices of the quasi-TE modes in both ssDNA and dsDNA cases increase by increasing the GH value due to the increase in the silicon volume. It is also revealed from Fig. 13.8 that the change in the effective index of the quasi-TE mode increases by increasing the silicon nanowire height and the maximum δn_{eff} is obtained at GH = 320 nm.

Figure 13.9 shows the variation of the effective index of the quasi-TE mode and the change in the effective index with the slot width between the gold and silicon nanowires (PSW) using the ssDNA and dsDNA layers. It may be seen that the effective indices of the quasi-TE modes in both ssDNA and dsDNA cases are increased as the PSW decreases. It may be also noted from Fig. 13.9 that the change

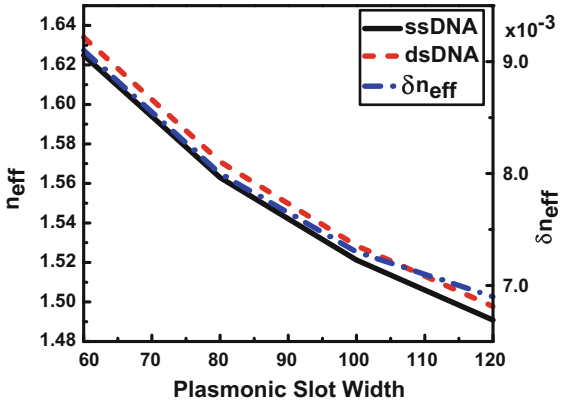

Fig. 13.9 Variation of the n_{eff} of the quasi-TE mode of the suggested design using the ssDNA and dsDNA layers and δn_{eff} with the slot width between gold and silicon nanowire (PSW) [1]

in the effective index decreases by increasing the PSW. The PSW = 100 nm is a suitable design according to the fabrication technologies.

The effects of the metal width, metal height, and thickness of the bottom metallic layer (t_{plasm}) on the power density through the ssDNA and dsDNA layers have been also calculated. In these investigations, the effect of the t_{plasm} is studied while the metal width and metal height are fixed at 200 nm and 400 nm, respectively. Further, the impact of the metal width on the power density is analyzed, while the t_{plasm} and metal height are equal to 50 nm and 400 nm, respectively. Then, the metal height effect on the power density is investigated, while the t_{plasm} and metal width are taken as 50 nm and 200 nm, respectively. The numerical results show that the effects of the metal width, metal height, and thickness of bottom metallic layer on the calculated power density through the DNA layers are small in the ranges of $t_{plasm} > 25$ nm, metal width > 100 nm, and metal height > 300 nm. Therefore, the metal width, metal height, and thickness of the bottom metallic layer are taken as 200 nm, 400, and 50 nm, respectively.

The plasmonic material (gold) in the suggested design plays an important role in improving the biosensor sensitivity. This can be achieved by increasing the power density through the DNA layers which increases the light–sensing medium interaction. Therefore, a complete analysis has been made to ensure the impact of the plasmonic material. In these investigations, GW = 170 nm, GH = 320 nm, SW = 100 nm, and PSW = 100 nm. Figure 13.10 shows the power density variation with the guide width for the suggested hybrid design (case 1), the proposed design without plasmonic material (case 2), the reported design with plasmonic side rails only (case 3), and the biosensor design with bottom metallic layer only (case 4). It may be seen from this figure that the reported hybrid plasmonic biosensor (case 1) achieves the higher power density in the ssDNA and dsDNA layers and hence higher sensitivity than the other studied cases. Further, the plasmonic bottom layer (case 4) increases the power density over that without using plasmonic material at all (case 2).

In order to detect the DNA hybridization, the HPSW can be incorporated in a resonating system as shown in Fig. 13.11. The resonating structure allows us to detect the occurrence of the binding (hybridization) by calculating the shift in the resonance wavelength due to the cladding refractive index change from the ssDNA to the dsDNA cases.

The HPSW is incorporated here with hybrid straight resonator as shown in Fig. 13.11. It may be seen from this figure that the slot waveguide inside the straight resonator is also coated with ssDNA layer to enhance the sensitivity of the reported design. The straight resonator has the same geometrical dimensions of the previously optimized slot waveguide. The length of the straight resonator can be obtained from the wavelength of the fundamental longitudinal mode that resonates in the cavity as suggested in [25]

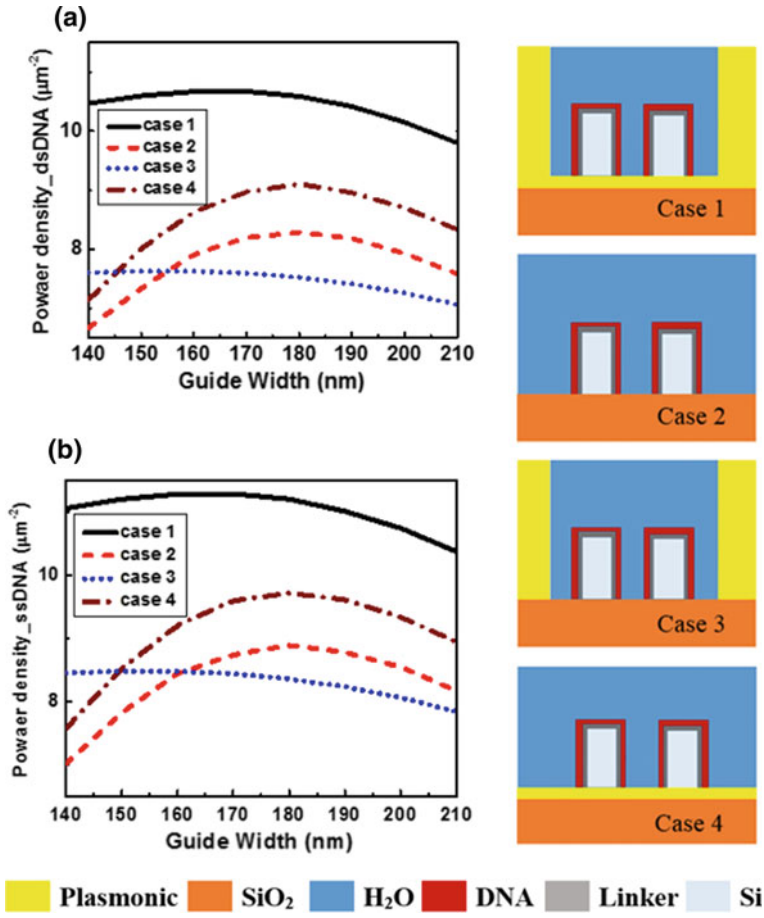

Fig. 13.10 Variation of the power density of the quasi-TE mode of the suggested design through the **a** dsDNA and **b** ssDNA layers with the silicon nanowire width GW for the studied four cases [1]

$$\lambda_{res} = \frac{2Ln_{eff}}{m} \tag{13.2}$$

where m is the longitudinal mode order inside the cavity (m = 1 for the fundamental mode), and 2L denotes the round trip length of the electromagnetic wave in the resonator. The numerical results show that the resonator length plays an important role in the coupling process. However, the length of the HPSW (L_{HPSW}) has a slight effect on the coupling process. For example, the resonator length is equal to 495 nm at λ_{res} = 1550 nm. As the length of the HPSW is increased from 500 nm to 750 nm, the resonance wavelength is slightly changed from 1532.07 nm to 1535.7 nm, respectively. Therefore, a HPSW length of 750 nm is chosen for the suggested design.

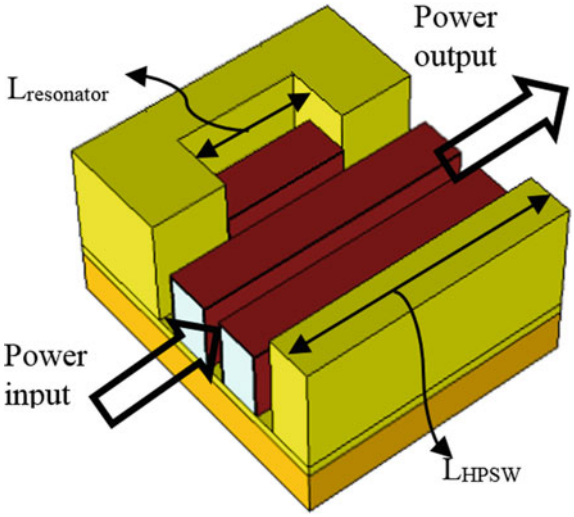

Fig. 13.11 Three-dimensional diagram of the HPSW incorporated with straight resonator (the two arrows referred to the power input/output of the electromagnetic field) [1]

The device sensitivity is related to the variation of transducing optical parameters which is, in our case, the resonance wavelength shift and can be calculated from [3]

$$S_D = \frac{\delta \lambda_{res}}{\delta n} \tag{13.3}$$

In this study, the optimum geometrical parameters of the HPSW structure are equal to GW = 170 nm, SW = 100 nm, GH = 320 nm, and PSW = 100 nm. These geometrical parameters have been chosen to improve the biosensor sensitivity and confirm a strong mode confinement through the slot regions beside the DNA layers. The three-dimensional HPSW shown in Fig. 13.11 is simulated by 3D-FVFEM based on Comsol Multiphysics software package [32] with total number of elements of 440,641 and degrees of freedom of 2,804,664.

Figure 13.12 shows the x-component of the steady-state electric field of the supported quasi-TE mode at wavelengths of 1360 and 1535.7 nm. Further, a resonance wavelength shift of 13.8 nm is achieved due to the hybridization as shown in Fig. 13.13. Figure 13.13 shows the transmission S_{21} parameter for the ssDNA and dsDNA cases. Therefore, HPSW incorporated with straight resonator achieved high sensitivity of 1890.4 nm/RIU. The detection limit is also an important parameter, which can be defined as the ratio between sensor resolution and device sensitivity. The sensor resolution depends on the wavelength resolution of the light source. The sensor resolution was taken as 5 pm [13]. Therefore, the detection limit or the minimum detectable refractive index of 2.65×10^{-6} RIU can be obtained.

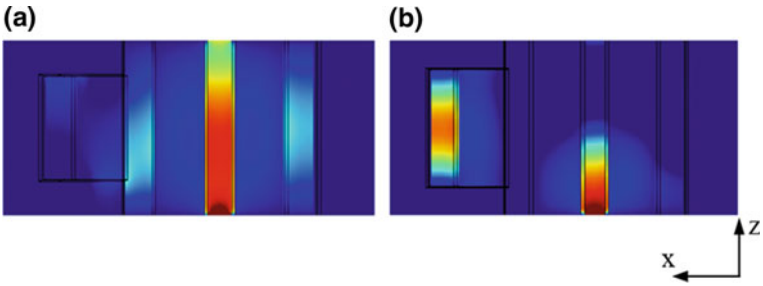

Fig. 13.12 The x-component of the electric field of the supported quasi-TE mode at wavelength of **a** 1360 nm and **b** 1535.7 nm (resonance) [1]

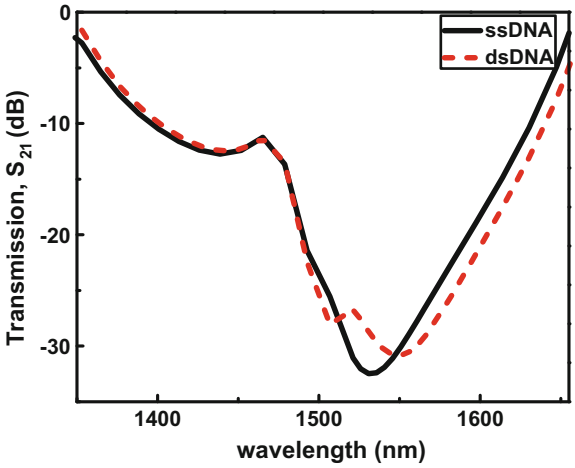

Fig. 13.13 Wavelength-dependent S_{21} parameter for the ssDNA and dsDNA cases [1]

In order to ensure that the reported biosensor is robust to the fabrication errors, a tolerance study has been performed for the design parameters. Table 13.1 shows the tolerance of the different geometrical parameters of the suggested design. It is evident from this table that the reported biosensor has a tolerance of ±5% at which the sensitivity is still better than 1750 nm/RIU which is higher than those reported in the literature [3, 8–23].

13.3.2 HPSW with TiN as an Alternative Plasmonic Material

The surface plasmon polaritons (SPPs) can confine the light strongly to the surface of the metal and thereby strongly increase the interaction between the light and the

Table 13.1 Tolerance of different geometric parameters of the proposed design

Parameter	Tolerance (%)	$\delta\lambda_{res}$ (nm)	Sensitivity (nm/RIU)
Guide width (GW)	+5	13.4	1835.7
	−5	13.59	1861.6
Guide height (GH)	+5	13.31	1823.5
	−5	12.9	1767.1
Slot width (SW)	+5	12.8	1753.4
	−5	13.9	1911.5
Metal slot width (PSW)	+5	13.5	1852.6
	−5	13.85	1897.1

sensing material. However, at optical frequencies, interband transition loss will occur [39]. Therefore, the interest has aimed to discover alternative plasmonic materials with low losses. The alternative plasmonic materials such as titanium nitride, zirconium nitride, and tantalum nitride have many advantages such as tunable optical properties, lower loss, high thermal stability, high chemical stability, biocompatibility, epitaxial growth on a large number of substrates, and compatibility with CMOS technology.

The relative permittivity of the TiN is calculated by the Drude–Lorentz model [40]:

$$\varepsilon_{TiN}(\omega) = \varepsilon_b - \frac{\omega_p^2}{\omega(\omega + i\gamma_p)} + \frac{f_1\omega_1^2}{(\omega_1^2 - \omega^2 + i\omega\gamma_1)} \tag{13.4}$$

where $\varepsilon_b = 2.485$, $\omega_p = 5.953$ eV, $\gamma_p = 0.5142$ eV, $f_1 = 2.0376$, $\omega_1 = 3.9545$ eV, and $\gamma_1 = 2.4852$ eV.

FVFEM [30, 31] is used to calculate the supported slot waveguide modes. Figure 13.14a, b shows the norm component of the electric field and the power flow P_z of the supported mode, respectively. The field and power plots of the supported mode along the x-axis at the center of the waveguide are also shown as insets in Fig. 13.14a, b. It may be seen from Fig. 13.14 that the quasi-TE slot waveguide mode field and power are highly confined in the slot regions due to the high index contrast and plasmonic enhancement. Therefore, the performance of the HPSW biosensor based on TiN will be also studied based on the quasi-TE mode.

The geometrical parameters of the reported design are studied to increase the mode confinement through the slot regions and enhance the biosensor sensitivity. The effect of the silicon nanowire width, GW, is firstly investigated, while the other parameters are fixed at their initial values. Figure 13.15a shows the variation of the effective index of the quasi-TE mode for the ssDNA and dsDNA cases with the silicon nanowire width GW. The change in the effective index δn_{eff} due to DNA hybridization is also shown in Fig. 13.15a. It is evident from this figure that the effective index of the supported mode increases due to the increase in the silicon

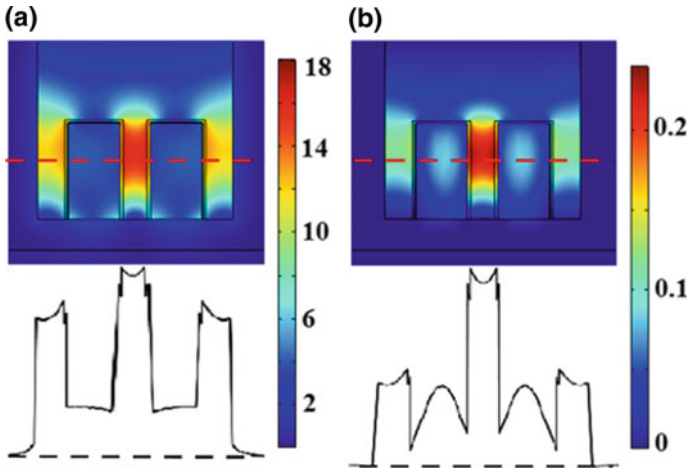

Fig. 13.14 Confinement in the slot regions of the suggested design at $\lambda = 1550$ nm **a** norm component of the quasi-TE slot waveguide mode and **b** power flow P_z of the quasi-TE slot waveguide mode. Insets are the field plots and power flow along x-axis (red dash lines are referred to the cross section along x-axis) [40]

nanowire width. Further, the refractive index of the ssDNA is less than that of the dsDNA. Therefore, the n_{eff} of the quasi-TE slot waveguide mode in the ssDNA case is smaller than that of the dsDNA case as shown in Fig. 13.15a. It may be seen from this figure that the maximum change in the effective index is obtained at GW = 170 nm; therefore, it will be taken as an optimum width for the subsequent simulation.

Next, the effect of the slot width SW on the effective index of the supported mode is investigated. In this study, the other parameters are fixed at GW = 170 nm, GH = 320 nm, and PSW = 100 nm. The variations of the effective index of the supported mode in the ssDNA and dsDNA cases and δn_{eff} with the slot width SW value are shown in Fig. 13.15b. It may be noted from this figure that the δn_{eff} increases by decreasing the SW, where high confinement is achieved in the slot regions which enhances the biosensor sensitivity. In this regard, the maximum change in the effective index is obtained at SW = 60 nm. However, the suitable value is 100 nm due to fabrication limitation for slot width.

Figure 13.15c shows the effect of the slot width between the TiN and silicon nanowires (PSW) on the effective index of the quasi-TE slot waveguide mode and the δn_{eff}. It may be seen that the effective indices of the quasi-TE modes in both ssDNA and dsDNA cases are increased by decreasing the PSW. It may be also noted from Fig. 13.15c that the change in the effective index decreases by increasing the PSW. The PSW = 100 nm is a suitable design according to the fabrication technologies.

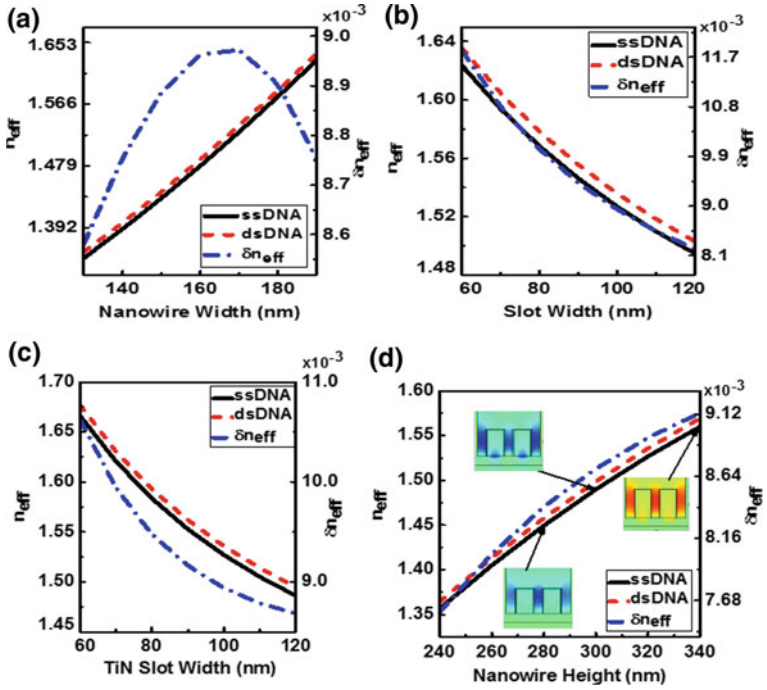

Fig. 13.15 Variation of the n_{eff} of the quasi-TE slot waveguide mode of the suggested design with ssDNA and dsDNA layers and δn_{eff} with the **a** silicon nanowire width GW, **b** slot width SW, **c** slot width between TiN and silicon nanowire PSW, and **d** silicon nanowire height GH, field plots at GH = 280 nm, 300, and 340 nm as insets at $\lambda = 1550$ nm [40]

Figure 13.15d shows the variation of δn_{eff} and the effective index of the quasi-TE slot waveguide mode with the silicon nanowire height GH. It may be seen from this figure that the δn_{eff} and the effective indices of the quasi-TE modes in both ssDNA and dsDNA cases increase by increasing the GH value due to the increase in the silicon volume. It is also revealed from Fig. 13.15d that the maximum δn_{eff} is obtained at GH = 340 nm. However, the silicon nanowire height of 280 nm is chosen due to the well confinement of the mode inside the slots as shown in inset plots. At GH = 340 nm, the electric field is confined inside the silicon core as shown in Fig. 13.15d, which leads to a weak light interaction with the sensing region. Also it is found that as the nanowire height increases, the field confinement in the silicon core increases.

It is worth noting that the suggested design can improve the sensitivity due to strong light-sensing region interaction with high power confinement in the low-index regions. The normalized power confinement in the three low-index regions is equal to 67% at $\lambda = 1550$ nm.

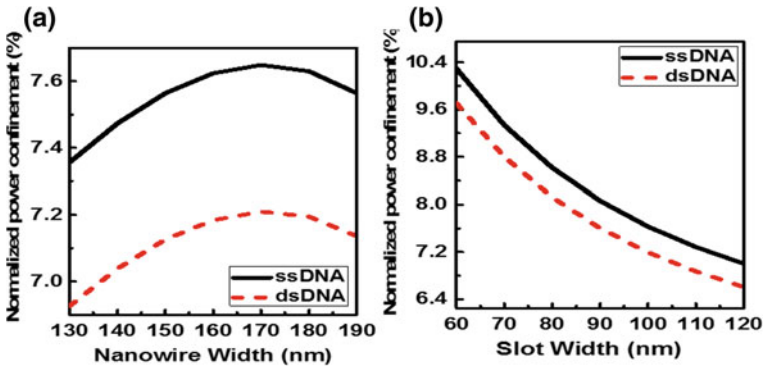

Fig. 13.16 Variation of the normalized power confinement of the supported quasi-TE mode of the reported design for the ssDNA and dsDNA cases with **a** the silicon nanowire width GW and **b** the slot width SW [40]

Figure 13.16a shows the variation of the normalized power confinement of the quasi-TE slot waveguide mode through the DNA layer with the silicon nanowire width GW, while the rest parameters are taken as GH = 280 nm, SW = 100 nm, and PSW = 100 nm. Since the refractive index of the ssDNA is smaller than that of the dsDNA, higher refractive index contrast and hence more field enhancement occur in the slot regions due to normal electric field discontinuity. Consequently, the normalized power confinement of the quasi-TE slot waveguide mode for the ssDNA case is higher than that of the dsDNA as shown in Fig. 13.16a. It may be also seen from Fig. 13.16a that the highest normalized power confinement is obtained at nanowire width of 170 nm which confirms our choice of that value. Figure 13.16b shows the variation of the normalized power confinement of the quasi-TE slot waveguide mode through the DNA layer with the SW. It is evident from this figure that the highest normalized power confinements are obtained at SW = 60 nm. However, there is a fabrication limitation for slot width of less than 100 nm. According to fabrication technologies, SW = 100 nm is suggested as a suitable design.

The resonator system can be introduced with the suggested HPSW to detect the DNA hybridization as shown in Fig. 13.11. Therefore, the change in effective index of the supported quasi-TE mode, as hybridization occurs, will produce a shift in the resonance wavelength. In this study, the optimum geometrical parameters of the HPSW structure based on TiN are equal to GW = 170 nm, SW = 100 nm, GH = 280 nm, and PSW = 100 nm. The geometrical parameters of the straight resonator are taken as those of the HPSW. The resonator length is equal to 310 nm at λ_{res} = 1550 nm. As the length of the HPSW is increased from 400 nm to 537 nm, the resonance wavelength is slightly changed from 1458 nm to 1460.323 nm, respectively. Therefore, a HPSW length of 537 nm is chosen for the suggested design.

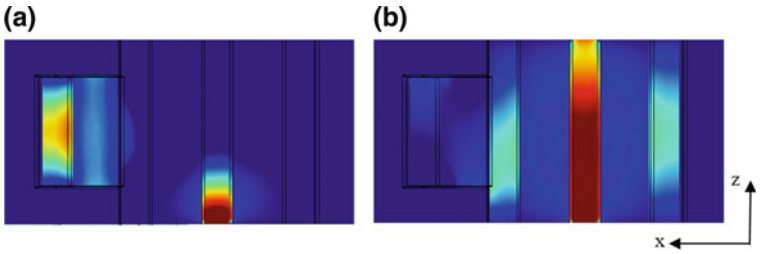

Fig. 13.17 The x-component of the electric field of the supported mode at wavelength of **a** 1460.323 nm (resonance) and **b** 1250 nm, respectively [40]

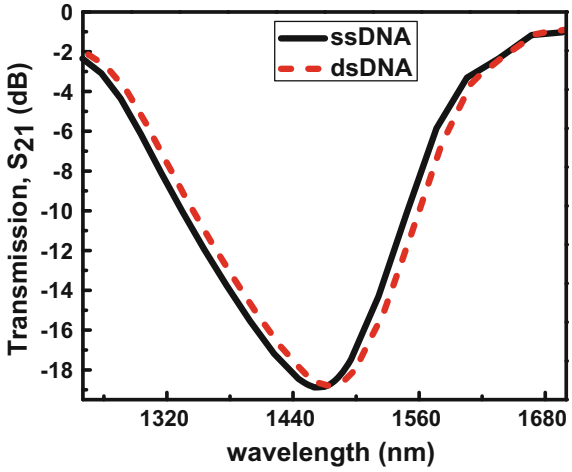

Fig. 13.18 Wavelength-dependent transmission coefficient S_{21} for the ssDNA and dsDNA cases [40]

The HPSW incorporated with the straight resonator is simulated by 3D-FVFEM based on Comsol Multiphysics software package. The steady state of the x-component of the electric field of the supported mode (ssDNA case) is shown in Fig. 13.17a, b at different wavelengths 1460.323 nm (resonance) and 1250 nm. It may be noted from this figure that the field is well coupled to the resonator waveguide at which minimum transmission is obtained. The resonance wavelength for the ssDNA case is 1460.323 nm, while the resonance wavelength for the dsDNA case is 1470.33 nm. Consequently, the resonance wavelength shift is 10 nm and the biosensor sensitivity is equal to 1190 nm/RIU. Figure 13.18 shows the transmission, S_{21} parameter, for the HPSW incorporated with the straight resonator using the ssDNA and dsDNA layers. Table 13.2 shows a comparison between the device sensitivity of the reported designs with those in the literature. It may be noted from Table 13.2 that the suggested designs with gold or TiN have the highest sensitivities in the literature to the best of authors' knowledge.

Table 13.2 Comparison between the sensitivity of the suggested designs with those in the literature

Design	Detection purpose	Resonance Wavelength shift (nm)	Resonance wavelength (nm)	Device sensitivity $\mathbf{S_D} = \boldsymbol{\delta\lambda_{res.}/\delta n}$ (nm/RIU)
Ref. [15]	Protein	2.2	1561	298
Ref. [26]	DNA hybridization	3.634	1558	683
Ref. [3]	DNA hybridization	6.12	1550	856
Ref. [28]	DNA hybridization	6.33	1550	893.5
Ref. [27]	Organic molecules	4.99	1548	912
Ref. [17]	Aqueous solutions of 2-propanol	6.4	1554	1061
The suggested design using gold [1]	DNA hybridization	13.8	1535.7	1890.4
The suggested design using TiN [40]	DNA hybridization	10	1460.323	1190

13.4 Summary

The full vectorial finite element methods (2D and 3D) are used in this work to study and optimize the HPSW biosensors for the detection of the DNA hybridization to achieve maximum sensitivity. The detection of the DNA hybridization occurs by detecting the variation of the refractive index of the sensing material when the ssDNA (probe) binding with the complementary ssDNA (target) occurs to form the dsDNA and complete the hybridization process. It has been shown that the effective index and power confinement of the quasi-TE mode supported by the biosensors are highly dependent on the change in the refractive index of the sensing material. The reported HPSW biosensors based on straight slotted resonator have high sensitivity of 1890.4 nm/RIU with a detection limit of 2.65×10^{-6} RIU with gold material and 1190 nm/RIU with a detection limit of 4.2×10^{-6} RIU based on titanium nitride material which are the highest in the literature.

References

1. M.F.O. Hameed, A.S. Saadeldin, E.M.A. Elkaramany, S.S.A. Obayya, Label-free highly sensitive hybrid plasmonic biosensor for the detection of DNA hybridization. J. Lightwave Technol. 1–1 (2017)
2. W. Cox, V. Singer, Fluorescent DNA hybridization probe preparation using amine modification and reactive dye coupling. Biotechniques **36**, 114–122 (2004)
3. T. Dar, J. Homola, B. Rahman, M. Rajarajan, Label-free slot-waveguide biosensor for the detection of DNA hybridization. Appl. Opt. **51**, 8195–8202 (2012)
4. F. Dell'Olio'Olio, V. Passaro, Optical sensing by optimized silicon slot waveguides. Opt. Express **15**, 4977–4993 (2007)
5. S.S.A. Obayya, M.F.O. Hameed, N.F.F. Areed, *Computational Liquid Crystal Photonics* (Wiley, 2016)
6. S.I. Azzam, M.F.O. Hameed, N.F.F. Areed, M.M. Abd-Elrazzak, H. El-Mikaty, S.S.A. Obayya, Proposal of an ultracompact CMOS-compatible TE-/TM-Pass polarizer based on SoI platform. **26**(16), 1633–1636 (2014)
7. B. Luff, R. Harris, J. Wilkinson, R. Wilson, D. Schiffrin, Integrated optical directional coupler biosensor.Opt. Lett. **21**, 618–620 (1996)
8. S.I. Azzam, M.F.O. Hameed, R.E.A. Shehata, A.M. Heikal, S.S.A. Obayya, Multichannel photonic crystal fiber surface plasmon resonance based sensor. Opt. Quantum Electron. **48**(2), 142 (2016)
9. M.F.O. Hameed, M.Y. Azab, A.M. Heikal, S.M. El-Hefnawy, S.S.A. Obayya, Highly sensitive plasmonic photonic crystal temperature sensor filled with liquid crystal. IEEE Photonics Technol. Lett. **28**(1), 59–62 (2016)
10. M.F.O. Hameed, Y.K.A. Alrayk, S.S.A. Obayya, Self-calibration highly sensitive photonic crystal fiber biosensor. IEEE Photonics **8**(3). 1–12 (2016)
11. L. Rindorf, J. Jenson, M. Dufva, L. Pedersen, P. Hiby, O. Bang, Photonic crystal fiber long-period gratings for biochemical sensing. Opt. Express **14**, 8224–8231 (2006)
12. W. Hopman, P. Pottier, D. Yudistira, J. Lith, P. Lambeck, R. De La Rue, A. Driessen, H. Hoekstra, R. de Ridder, Quasi-one-dimensional photonic crystal as a compact building-block for refractometric optical sensors. IEEE J. Sel. Top. Quantum Electron. **11**, 11–16 (2005)
13. K. Vos, I. Bartolozzi, E. Schacht, P. Bienstman, R. Baets, Silicon-on-insulator microring resonator for sensitive and label-free biosensing. Opt. Express **15**, 7610–7615 (2007)
14. C. Barrios, M. Banuls, V. Gonzalez-Pedro, K. Gylfason, B. Sanchez, A. Griol, A. Maquieira, H. Sohlstrom, M. Holgado, R. Casquel, Label-free optical biosensing with slotwaveguides. Opt. Lett. **33**, 708–710 (2008)
15. T. Claes, J. Molera, K. De Vos, E. Schacht, R. Baets, P. Bienstman, Label-free biosensing with a slot waveguide based ring resonator in silicon on insulator. IEEE Photonics J. **1**, 197–204 (2009)
16. V. Passaro, F. Dell'Olio, C. Ciminelli, M. Armenise, Efficient chemical sensing by coupled slot SOI waveguides. Sens. Actuators B Chem. **150**, 417–424 (2010)
17. X. Sun, D. Dai, L. Thyl´en, L. Wosinski, High-sensitivity liquid refractive-index sensor based on a mach-zehnder interferometer with a double-slot hybrid plasmonic waveguide. Opt. Express **23**(20), 25688–25699 (2015)
18. Y. Ishizaka, S. Makino, T. Fujisawa, K. Saitoh, A metal-assisted silicon slot waveguide for highly sensitive gas detection. IEEE Photonics J. **9** (2017)
19. L. Zhou, X. Sun, X. Li, J. Chen, Miniature microring resonator sensor based on a hybrid plasmonic waveguide. Sensors **11**(7), 6856–6867 (2011)
20. M. Kwon, Theoretical investigation of an interferometer-type plasmonic biosensor using a metal-insulator-silicon waveguide. Plasmonics **5**(4), 347–354 (2010)
21. V. Zenin, S. Choudhury, S. Saha, V. Shalaev, A. Boltasseva, S. Bozhevolnyi, Hybrid plasmonic waveguides formed by metal coating of dielectric ridges. Opt. Express **25**(11), 12295 (2017)

22. F. Bahrami, M. Alam, J. Aitchison, M. Mojahedi, Dual polarization measurements in the hybrid plasmonic biosensors. Plasmonics **8**(2), 465–473 (2013)
23. J. Yun, J. Kim, K. Lee, Y. Lee, B. Lee, Numerical study on refractive index sensor based on hybrid-plasmonic mode, in *Proceedings of the SPIE 10323, 25th International Conference on Optical Fiber Sensors* (2017)
24. M. Zhang, B. Liu, G. Wu, D. Chen, Hybrid plasmonic microcavity with an air-filled gap for sensing applications. Opt. Commun. **380**, 6–9 (2016)
25. S. Ghosh, B. Rahman, An innovative straight resonator incorporating a vertical slot as an efficient bio-chemical sensor. IEEE J. Sel. Top. Quantum Electron. **23**(2) (2017)
26. X. Li, Z. Zhang, S. Qin, T. Wang, F. Liu, M. Qiu, Y. Su, Sensitive label-free and compact biosensor based on concentric silicon-on-insulator microring resonators. Appl. Opt. **48**, F90–F94 (2009)
27. I. Khodadad, N. Clarke, M. Khorasaninejad, D. Henneke, S. Saini, Optimization of multiple-slot waveguides for biochemical sensing. Appl. Opt. **53**, 5169–5178 (2014)
28. C. Viphavakit, M. Komodromos, C. Themistos, W. Mohammed, K. Kalli, B. Rahman, Optimization of a horizontal slot WG biosensor to detect DNA hybridization. Appl. Opt. **54**(15), 4881–4888 (2015)
29. M. Malinsky, K. Kelly, G. Schatz, R. Van Duyne, Chain length dependence and sensing capabilities of the localized surface plasmon resonance of silver nanoparticles chemically modified with alkanethiol self-assembled monolayers. J. Am. Chem. Soc. **123**, 1471–1482 (2001)
30. S. Obayya, *Computational Photonics* (Wiley, Chichester, West Sussex, UK, 2011)
31. S.Obayya, N. Somasiri, B. Rahman, K. Grattan, Full vectorial finite element modeling of novel polarization rotators. Opt. and Quantum Electron. **35**(4), 297–312 (2003)
32. https://www.comsol.com/
33. A. Krasavin, A. Zayats, Three-dimensional numerical modeling of photonic integration with dielectric-loaded SPP waveguides. Phy. Rev. B **78**, 045425 (2008)
34. A. Krasavin, A. Zayats, Passive photonic elements based on dielectric-loaded surface plasmon polariton waveguides. Appl. Phy. Lett. **90**, 211101 (2007)
35. B. Steinberger, A. Hohenau, H. Ditlbacher, A. Stepanov, A. Drezet, F. Aussenegg, A. Leitner, J. Krenn, Dielectric stripes on gold as surface plasmon waveguides. Appl. Phy. Lett. **88**, 094104 (2006)
36. A. Papra, N. Gadegaard, N. Larsen, Characterization of ultrathin poly(ethylene glycol) monolayers on silicon substrates. Langmuir **17**, 1457–1460 (2001)
37. T. Dar, Numerical characterization of label-free optical biosensors. Ph.D. Dissertation, School of Engineering and Mathematical Sciences, City University, London, United Kingdom (2015)
38. A.M. Heikal, M.F.O. Hameed, S.S.A. Obayya, Improved trenched channel plasmonic waveguide. J. Lightwave Technol. **31**(13), 2184–2191 (2013)
39. G. Naik, V. Shalaev, A. Boltasseva, Alternative plasmonic materials: beyond gold and silver. Adv. Mater. **25**(24), 3264–3294 (2013)
40. M.F.O. Hameed, A.S. Saadeldin, E.M.A. Elkaramany, S.S.A. Obayya, Detection of DNA hybridization by hybrid alternative plasmonic biosensor, Proc. SPIE 10672, Nanophotonics VII, 106722H (4 May 2018); doi: 10.1117/12.2306299

Chapter 14
Compact Photonic SOI Sensors

Souvik Ghosh, Tuffail Dar, Charusluk Viphavakit, Chao Pan, N. Kejalakshmy and B. M. A. Rahman

Abstract Besides well matured optical fiber-based sensors, emerging compact down-scaled nanowires, slot waveguides and resonators are now under researcher's consideration due to their high sensitivities and on-chip fabrication possibilities. Along with pure dielectric based waveguides and resonators, clever engineering of sub-wavelength field confinement and modal propagation loss in plasmonic nanowire and hybrid plasmonic slot waveguides also showing promising results in the field of photonic sensing. Numerically efficient, versatile finite element method based approaches are used for rigorous analyses, design, and optimizations of these complex optical guided-wave structures. All these sensor devices can exploit the well-developed state-of-the-art fabrication technologies.

Keywords Optical sensors · Biosensors · Silicon photonics
Finite element method

14.1 Introduction

The maturity of photonic technology not only enlighten the telecommunication industries through its high-speed data transmission but also shows a great potential in many diverse fields of applications. One of the key application has been in optical sensing. Each year, billions of dollars are invested in research and development of accurate and non-hazardous sensing technologies. All these demands impose a considerable amount of responsibility on scientists and researchers. These increased legislative requirements drive us for the innovation and development of integrated, compact, nano dimensioned photonic devices for sensing. Our focus here to present the accurate computational approaches needed for design and optimization of compact integrated photonic sensors.

S. Ghosh · T. Dar · C. Viphavakit · C. Pan · N. Kejalakshmy · B. M. A. Rahman (✉)
School of Mathematics, Computer Science, and Engineering, City University of London, Clerkenwell EC1V 0HB, UK
e-mail: b.m.a.rahman@city.ac.uk

© Springer International Publishing AG, part of Springer Nature 2019

M. F. O. Hameed and S. Obayya (eds.), *Computational Photonic Sensors*, https://doi.org/10.1007/978-3-319-76556-3_14

The broadened applications of photonics show a great potential in sensing applications for accurate measurement of chemical, physical and biological parameters, such as humidity, temperature, a range of selective gases, stress, strain, pressure, displacements, surface roughness, microscopic living substance, DNA hybridizations etc. Photonic sensors can easily be designed with pure dielectric materials or noble metals which make those reliable in hazardous conditions where other conventional sensors are unsafe due to fire, electrical short-circuit, high temperature, corrosive environment, and radiation risk and high electromagnetic interferences. On the other hand, for medical and bio-chemical sensing with lower weight, compact size with high precision sensitivity is highly desirable. Dielectric material and noble metal-based optical waveguides and resonators would serve those purposes for both invasive and non-invasive cases due to a much greater efficiency for detection of small refractometric changes and nano footprint. Although, fiber optic sensors are well-developed and most commercially available sensors are fiber based, the advancement in fabrication technology leads researchers to consider innovative high index contrast and composite material based sensor designs.

The design of a new system often includes individual component assessment and its effectiveness for the specially required purpose. Analytical, semi-analytical and numerical modeling of the devices are often considered to achieve an accurate and optimized design for evaluation of potential performance and unfavorable features of the device. Thus, advanced photonics modelings are helpful to predict and understand the complex sensor characteristics before expensive production and experimental validation. A complete sensing device comprises of many distributed complex optical components and waveguides. Understanding of exact fundamental physics of light guidance and wave propagation characteristics through optical components are necessary for their effective use. Several modeling methods have already been proposed based on analytical and semi-analytical approaches. A pure analytical and semi-analytical method exhibits its inability or inefficiency for the solution of practical waveguides where optical power confined in the transverse plane. Analytical approach only can solve the planar waveguide by analyzing the transcendental equations by taking field continuity at the material interfaces. In the years of 1969 and 1970 Maracatili [1], Goell [2] and Knox and Toulios [3] have introduced semi-analytical methods which can only provide solutions for simple waveguides. However, these methods also inadequate for the analyses of complex waveguide geometries containing inhomogeneous and anisotropic materials. Over last 40 years, several methods have been developed such as the matrix methods [4], the mode matching method [5], the finite difference method [6], the method of lines [7] and the spectral index method [8]. Beside these approximated approaches the full-vectorial finite element method (FV-FEM) shows its high efficiency for design and optimizations of complex structured waveguides and resonators [9–12]. Any arbitrarily shaped waveguide geometry with isotropic and anisotropic multilayered materials can easily be handled by this powerful numerical tool. Simple mathematical formulations and clever use of memory management algorithm for sparse matrices can make this method suitable for readily available computer workstations.

14.2 Integrated Slot Waveguide for Sensing

Optical waveguides initially developed for the advancement of the telecommunications. However, their efficient light-matter interactions, noise immunity, precise detection and dedicated flexible geometry make them suitable for sensing applications. Nowadays, circularly symmetric optical waveguide i.e. optical fibers are widely used for label-free macro, micro, and even nano-scale detections. Different fiber modulation designs, such as clad polishing for high evanescent light-matter interactions, intrinsic and extrinsic fiber interferometry arrangements, fiber Bragg gratings (FBG) and luminescent-based sensors could be used to dealing with specific sensing problem. Developments and applications of the fiber-based sensor are discussed in [13, 14]. But the fiber designs and productions are still limited to telecommunication applications. Thus, compared to the fiber optic sensors, the nano-dimensioned, high index contrast rib, channel, hollow-core and slot waveguides have attracted the considerable attentions in sensing based applications. Both the labeling-based and label-free sensing processes can be exploited by these exotic waveguide designs. They can be fabricated with standard lithographic techniques which results in low-cost mass production on a single-chip. Additionally, SOI based high index contrast waveguiding incorporates sensor integration with other electronic and optical components on the same chip. The rib, channel, and strip waveguides confines the lightwave in the high index core surrounded by low index medium. Here, the light guiding is based on the total internal reflection (TIR) and only a modest fraction of evanescent light tail interacts with the surrounded sensing analytes. Another interesting structure, the dielectric coated metallic hollow-core waveguide, reported by Saito et al. [15] is advantageous for biochemical liquid and gas sensing due to its light guiding mechanism through a low index core medium. It works as an absorption cell and its performance is highly wavelength dependent. However, length of this waveguide is much larger (few meters) compared to the integrated waveguides (few microns). On the other hand, the integrated slot waveguide has a unique light guiding mechanism that confines light in a low index slot. This nanometer wide gap/slot is formed in between two high index dielectrics, dielectric-metal or metal-metal strips. Thus, the electric field normal to the high and low index interface becomes discontinuous. Depending upon the slot orientations, the waveguide could be either vertical, horizontal or a combination of both, forming a cross-slot. In case of both vertical and horizontal slot waveguides, the dominant electric field components (E_x and E_y) of the quasi-TE and TM mode, respectively, encounters discontinuities at the material interfaces. Thus, instead of an evanescent field i.e. a small fraction of the guided field for conventional waveguides, a large field enhancement has been observed for a dielectric and metal-dielectric based slot waveguides. An intense power density in the slot results in a strong light-matter interaction that makes this structure more attractive for extensive label-based, label-free and opto-mechanical sensing applications. The detection of analyte refractometric change is a major sensing mechanism for integrated optical sensors. According to problem demand, the distinct waveguide can be designed and incorporated into suitable transducer devices, such as interferometers

Table 14.1 An overview of the dielectric and hybrid plasmonic slot waveguide based photonic sensors

Sensor type	Operating wavelength	Target element	Sensitivity (S) and/or detection limit (DL)	Evaluation method	References
$Si_3N_4 - SiO_2$ based micro ring resonator	~1.3 μm	DI H_2O-ethanol solution, RI: 1.33–1.42	$S = 212$ nm/RIU $DL = 2 \times 10^{-4}$ RIU	Experimental	[16]
$Si_3N_4 - SiO_2$ based micro ring resonator	~1.3 μm	Label-free sensing: BSA and anti-BSA	BSA $S = 3.2$ nm/(ng/mm^2), DL =16 pg/mm^2 Anti-BSA $S = 1.8$ nm/(ng/mm^2), $DL = 28$ pg/mm^2	Experimental	[17]
Coupled slot SOI waveguides	1.55 μm	Glucose/water solution	0.1 g/L 10^{-5} RIU	Theory and simulations	[18]
Three SOI coupled slot waveguides	1.55 μm	Glucose/water solution ethanol/DI water solution	$S = -172$ RIU^{-1} (glucose/water) $S = 155$ RIU^{-1} (ethanol/water)	Theory and simulation	[19]
SOI based slot waveguide	1.55 μm	Bulk sensing: RI: 1.333–1.335 Surface sensing: Bio-layer, RI: 1.45	Waveguide sensitivities[a]	Simulations	[20]
Si_3N_4–SiO_2 based triple slot waveguide	1.3 μm	Bulk sensing: RI: 1.45–1.46	20% greater waveguide sensitivity than single slot[a]	Simulations and experiments	[21]
Si_3N_4 slot waveguide ring resonator	~1.55 μm	Bulk sensing: DI H_2O–NaCl solution Surface sensing: bilayer (ploy-sodium-4-styrenesulfonate/ poly-allylamine hydrochloride)	Bulk sensing: $S = 1730$ (2π)/RIU and $DL = 1.29 \times 10^{-5}$ RIU Surface sensing: $S =$ 60 nm/(ngmm^{-2}) and $DL = 0.155$ pgmm^{-2}	Simulations and experiments	[22]

(continued)

Table 14.1 (continued)

Sensor type	Operating wavelength	Target element	Sensitivity (S) and/or detection limit (DL)	Evaluation method	References
Si single and double slot microrings	~1.55 μm	Bulk sensing: water	Waveguide sensitivity[a]	Simulations	[23]
Si multiple slot based ring resonator	~1.55 μm	Water solution	$S = 912$ nm/RIU	Simulations	[24]
SOI vertical slot ring resonator	~1.55 μm	Bulk sensing: NaCl/water solution	$S = 298$ nm/RIU $DL = 4.2 \times 10^{-5}$ RIU	Simulations and experiments	[25]
Loop mirror based slot waveguide	~1.55 μm	Bulk sensing: air, water	$S = 6 \times 10^3$ nm/RIU	Simulations	[26]
Si_3N_4 slot based Mach-Zehnder interferometer (MZI)	~1.55 μm	Bulk sensing: streptavidin solution	$S = 1864\ \pi$/RIU $DL = 1$ pg/ml	Simulations and experiments	[27]
Grating assisted Si_3N_4 strip and slot waveguide coupler	~1.55 μm	Bulk sensing: water solution	$S = 10^5$ nm/RIU	Simulations	[28]
Au based plasmonic vertical slot cavity	~1.55 μm	Bulk sensing: water, acetone	$S = 600$ nm/RIU	Simulations	[29]
Double slot hybrid plasmonic MZI	~1.55 μm	Bulk sensing: isopropanol solution	$S = 1061$ nm/RIU	Simulations and experiments	[30]
Double slot plasmonic ring resonator	~1.55 μm	Bulk sensing: isopropanol	$S = 687.5$ nm/RIU $DL = 5.37 \times 10^{-6}$ RIU	Simulations and experiments	[31]
SOI based suspended slot waveguide	2.25 μm	Bulk sensing	Waveguide sensitivity = 1.123	Simulations and experiments	[32]

(continued)

Table 14.1 (continued)

Sensor type	Operating wavelength	Target element	Sensitivity (S) and/or detection limit (DL)	Evaluation method	References
Au/Si hybrid plasmonic miroing resonator	~1.55 μm	Bulk sensing: water solution	S = 580 nm/RIU	Simulations	[33]
SOI slot with sidewall Bragg gratings	~1.55 μm	Bulk sensing: multi-analyte	S = 291.93 nm/RIU $DL = 10^{-6}$ RIU	Simulations	[34]
SOI micro ring resonator	Near-IR	Acetylene gas	490 nm/RIU 10^{-4} RIU	Simulation and experiment	[35]
Silicon-on-nitride (SON) vertical slot waveguide	Mid-IR	NH_3 gas	DL = 5 ppm	Simulations	[36]
Si rib slot waveguide	Mid-IR	Gases: N_2O, CO and CH_4	DL = 0.2 ppm (N_2O) DL = 0.44 ppm (CO) DL = 36 ppm (CH_4)	Simulations	[37]

[a]A specific waveguide sensitivity is not mentioned in the report. Depending on the design parameters the waveguide sensitivities may have different values. Consult the corresponding article for sensitivity values

and resonators. The mode shift of the waveguide due to light-matter interaction introduces a corresponding phase change which results in a detectable interference fringe shift at the output. Several integrated interferometer mechanisms, such as Mach-Zehnder (MZI), Young (YI), coupler interferometers (CI) are often used as transducing device for sensing. They are highly efficient to make a very small measurement that is not possible by any other means. In resonator sensors, the resonating wavelength shift measures the refractive index changes that arise due to bio-chemical bindings. Thus, high index contrast dielectrics, noble metal and composite material based slot and waveguide sensors could be considered as a one step towards future. Table 14.1 gives an overview of the recently published works on the photonic sensors based on dielectric and hybrid plasmonic slot waveguides with different sensing architectures.

In this chapter, we are presenting dielectric, noble metal and composite material based slot and nanowire for biochemical liquid, gas and vapor sensing. For these results, we used the two and three-dimensional finite element mode solvers and the least-squares boundary residual (LSBR) method for junction analyses. These computational methods are discussed in detail in Chap. 6.

14.3 Detection of DNA Hybridization by Vertical and Horizontal Slot Waveguide

The light confinement in the void nanostructure was first reported by Almeida et al. in 2004 [38], since then the slot waveguide became an intriguing area of research in integrated photonics waveguiding and especially for sensing. A slot waveguide design comprises of the formation of a low index slot region by bringing two narrow high index waveguides close together that are operating below their modal cut-off regions. The lightwave propagates through the low index slot region in between two high index cores. This low index guiding could be justified with the help of electromagnetic boundary condition derivable from Maxwell's equations. It demands that for a high index contrast dielectric interface, the normal component of electric flux density (**D**) must be continuous, i.e. $D_{n1} = D_{n2}$. This, on the other hand, results in a discontinuity of the corresponding electric field (E_n). Thus, a much higher electric field amplitude could be observed in the low index region which enhances and strongly confines the light power into the slot. Utilizing this phenomenon, a much effective light-analyte interaction could be obtained in case of both surface and bulk sensing. The *surface sensing* or *contact sensing* is mostly exploited to measure the refractive index changes of ultra-thin layered film on the waveguides and/or into slot region. An ultra-thin adlayer of receptor molecules uses on guiding material to immobilize the targeted analyte. The binding interaction between the target analyte and adlayer changes the complete (adlayer + analyte) sensing layer thickness that influences the effective index of the guided optical mode. The *bulk sensing* or *homogeneous sensing* refers to another way of

sensitivity investigation where the refractive index change of cover and slot regions are detected. Detection of DNA sequencing by hybridization with the help of slot waveguide is investigated by surface sensing where both the SOI-based vertically and horizontally slot geometries were used.

14.3.1 Vertical Slot Waveguide

The novel vertical slot waveguide was designed by keeping two nanometers dimensioned Si cores close together that simultaneously forms a small nano-gap for light guiding. The schematic cross-section of the vertical slot waveguide is shown in Fig. 14.1. The refractive indices of silicon core, silica (SiO_2) substrate were considered as 3.4757 and 1.444, respectively. Cladding and the slot region is filled with deionized (DI) water-based stock solution having $RI = 1.31$. To immobilize the DNA strings, first, the waveguide is coated with a 1 nm ultra-thin receptor linker (silanes or ply-L-lysine) bio-layer (T_L). The detection process consists of sensing of complimentary DNA sequence, where a single stranded DNA (ssDNA) is subsequently combined with a double-stranded DNA (dsDNA). The thickness (T_D) of DNA probe layer was 8 nm, and it remains same after combining with complementary DNA strand. Only detectable change happens in probe layer refractive index, increased from 1.456 (ssDNA) to 1.53 (dsDNA).

The complete waveguide modeling and its performance analyses are carried out by using the **H**-field based FV-FEM. The one-fold symmetry of the waveguide structure is considered, in which more than 80,000 irregular triangular elements have been employed for domain discretization. The structure supports both fundamental quasi-TE and quasi-TM modes. Among all the field components, the E_x

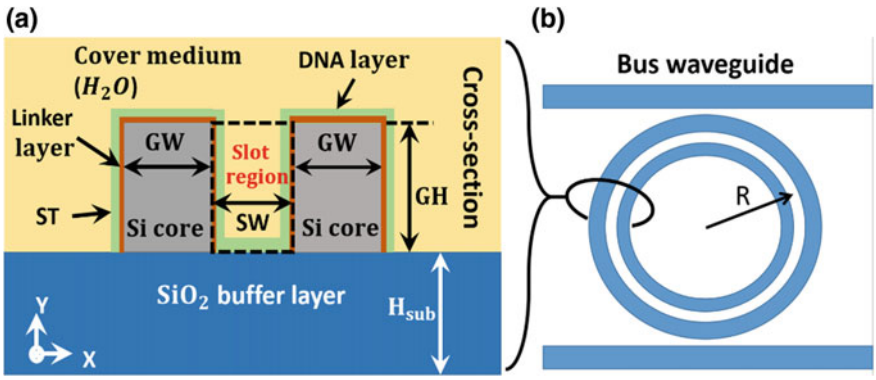

Fig. 14.1 **a** Depicts the schematic cross-section of silicon-on-insulator (SOI) based vertical slot waveguide for detection of DNA hybridization. The slot region is denoted by black dashed line where an enhanced light-matter interaction occurs. **b** Denotes a top-view of a ring resonator incorporated with SOI based vertically slot waveguide

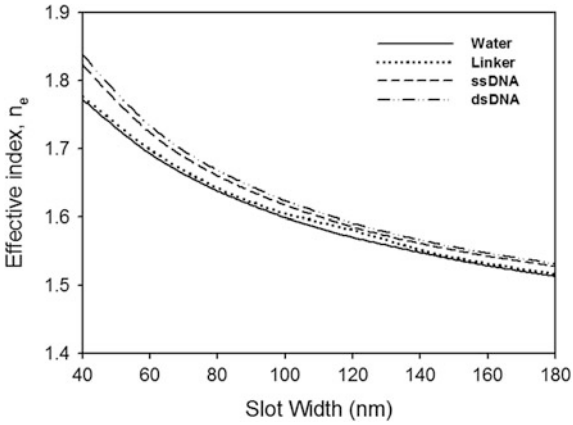

Fig. 14.2 Modal effective index (n_{eff}) variations with slot width (SW) for fixed Si core width, $GW = 180$ nm and height, $GH = 320$ nm. From [39]

field of fundamental H_y^{11} mode shows an enhanced discontinuity as the vertical slot is along y-direction. So, in vertical slot only quasi-TE mode shows enhanced confinement in slot region. Figure 14.2 depicts the effective index (n_{eff}) variations of the H_y^{11} mode with the slot width (SW) for different waveguiding conditions. Effective index is defined as the normalized propagation constant, $n_{eff} = \beta_0/k_0$ where β_0, k_0 and λ are the modal propagation constant, free-space wavenumber ($k_0 = 2\pi/\lambda$) and operating wavelength, respectively. Si core height (GH) and width (GW) are considered as 320 nm and 180 nm, respectively. The solid and dotted lines depict the n_{eff} variations for only DI water as cover medium and 1 nm linker layer and water as sensing medium, respectively. The dashed and dashed-dotted lines denote the same for 8 nm ssDNA and dsDNA with water as cover medium. Small slot width confines more power into the slot which enhance the light-analyte interactions. The n_{eff} increase with slot width in Fig. 14.2 also justify this fact. This in-turn also suggest that the change of effective index (Δn_{eff}) due to DNA hybridization waveguide sensitivity also increases with decrease of slot width. Optimizations of the waveguide design parameters are highly effective in order to improve the sensor design for high sensitivity. Measurement of waveguide sensitivity strongly depends on the optical power confinement in the targeted DNA probe layers. Power confinement in the DNA layers have been evaluated and plotted with the variation of the guide width keeping the slot width fixed at 60, 100 and 140 nm and guide height fixed at 320 nm, shown in Fig. 14.3. Although, the lower slot width (60 nm) shows maximum power confinement than followed by 100 and 140 nm slot width however, the 100 nm slot width, is considered for further device optimization and this will also be easy to fabricate compared to other smaller slot dimensions. Thus, a 100 nm slot width (SW) with 180 nm guide width (W) could be an ideal optimized parameters. It is also noticeable that the ssDNA confines more optical power compared with the dsDNA due to high index contrast of guiding. The waveguide sensitivity can be written as $S_{wg} = \Delta n_{eff}/RI$. Here RI is refractive index of DNA layers and Δn_{eff} is the effective index difference that

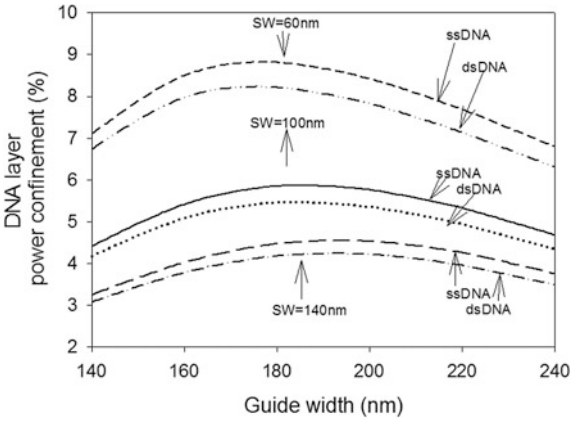

Fig. 14.3 Power confinement variations in the DNA layers with the Si core guide width (*GW*) for fixed slot widths, *SW* = 60, 100 and 140 nm. Si core height is fixed at *GH* = 320 nm for all the cases. From [39]

appears due to DNA hybridization. During modelling of DNA hybridization, the effective index difference is obtained by first simulating the ssDNA on top of bio-linker layer and then by considering the combination of the ssDNA with its complementary natured desired ssDNA which forms a layer of dsDNA. Now for the same waveguide structure (*GH* = 320 nm, *SW* = 60, 100 and 140 nm, and *GW* = variable) the waveguide sensitivity is determined. A greater change in Δn_{eff} makes the bio-sensor more sensitive. Figure 14.4 indicates that a greater Δn_{eff} and waveguide sensitivity for the *GW* in between 200 and 220 nm for all three slot widths. Both the Δn_{eff} and S_{wg} increase with the Si core height (*GH*) and for higher *GH*, most of the power would be started to confine in the Si cores. Thus, the waveguide sensitivity measurement parameters will show an almost saturated variation with high *GH* (not shown here). Therefore, for a compact slot waveguide sensor 320 and 340 nm guide heights are taken here as the desirable dimensions.

To calculate the Δn_{eff} accurately, a compact sensing device containing a slotted ring resonator with 5 μm bending radius is presented and analyzed. The schematic cross-sectional and top views of the device are presented in Fig. 14.1a, b, respectively. The device sensitivity only depends on its component waveguide sensitivity

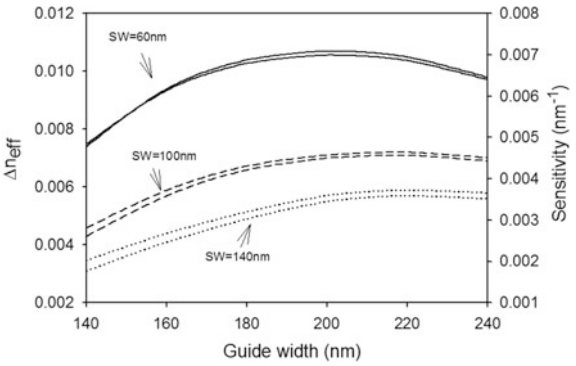

Fig. 14.4 Effective index difference (Δn_{eff}) and waveguide sensitivity (S_{wg}) variations with the guide width (*GW*). The solid, dashed, and dotted lines indicate three different slot widths, *SW* = 60, 100, and 140 nm, respectively. Si core height was fixed at *GH* = 320 nm. From [39]

regardless of the type of the devices. Transducing optical parameters are the only way to measure the device sensitivity. Thus, the relation between device sensitivity (S) and resonant wavelength shift ($\Delta\lambda$) can be expressed as

$$S = \frac{\Delta\lambda}{\Delta n} \tag{14.3.1}$$

$$\Delta\lambda = \frac{\Delta n_{eff}\,\Delta\lambda_{res}}{n_g} \tag{14.3.2}$$

Here Δn_{eff}, λ_{res} and n_g are the effective index change caused by the analyte bindings, resonating wavelength of the ring and waveguide group index, respectively. From Fig. 14.5a, the group index (n_g) is calculated as 1.81264 at the operating wavelength of 1550 nm for the optimized design parameters GW = 220 nm, GH = 320 nm and SW = 100 nm. For performance analysis, the waveguide was simulated once with ssDNA and then with dsDNA to obtain the $\Delta n_{eff} = n_{e,ssDNA} - n_{e,dsDNA}$. By using Eq. 14.3.2, the wavelength shift of the device is calculated and its variation with Si core width for three different slot widths (60, 100, and 140 nm) are shown in Fig. 14.5b. The slot waveguide with dimensions $GW = 220$ nm, $GH = 320$ nm and $SW = 100$ nm shows that the n_{eff} for ssDNA and dsDNA as a sensing layer were 1.80549 and 1.81264, respectively. A much higher resonance wavelength shift $\Delta\lambda = 6.12$ nm is achieved and this was calculated by using Eq. 14.3.2. Similarly, by using Eq. 14.3.1, the sensitivity of ring resonator is obtained as 856 nm/RIU.

Due to scattering, the propagation loss of a similar slot waveguide was reported as 12 dB/cm [40]. The absorption spectrum of water shows the absorption value as

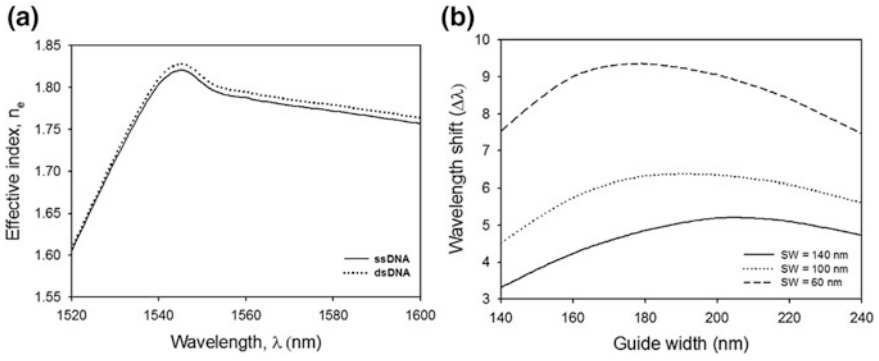

Fig. 14.5 **a** Shows the effective index (n_{eff}) variation of the slot waveguide against operating wavelength. The solid and dotted lines denote the n_{eff} variations due to ssDNA and dsDNA as a sensing layer, respectively; **b** shows the variation of resonating wavelength shift ($\Delta\lambda$) against the Si core guide width during DNA hybridization. The dashed, dotted, and solid lines indicate the variations for $SW = 60$, 100, and 140 nm, respectively. The Si core height is kept fixed at 320 nm. From [39]

47.5 dB/cm at the wavelength of 1550 nm. Our simulation shows around 30% power confinement in the cover medium that contains DI water. Thus, roughly the total propagation loss of our designed waveguide could be estimated as long as (12 dB/cm + 0.30 × 47.5 dB/cm) = 26.25 dB/cm. So, the total loss for few micron sensor would be very small.

14.3.2 Horizontal Slot Waveguide

Besides vertically slotted waveguide discussed earlier in the previous section, the light enhancement in void nanostructure is also true for a horizontal slot waveguide. A nano dimensioned low index channel along the horizontal x-axis is formed by keeping close two high index dielectric slabs. This geometry is easy to fabricate and often has smoother and regular interfaces exhibiting a much lower modal propagation loss. The fundamental mode supported by this waveguide shows a high discontinuity of E_y field (normal to the material interfaces) in the low index slot region. This would make higher power confinement in the slot region for a quasi-TM H_x^{11} mode. An effective horizontally slotted SOI-based sensor design that uses an enhanced optical power in the low index region, is proposed. Its design parameters optimization and performance analyses for detection of DNA hybridization (surface sensing) are investigated by the FV-FEM.

Such a horizontal slot can be fabricated on SOI substrate, where a low index slot channel is sandwiched by two high index polysilicon slabs. For applications towards bio-chemical or gas sensing, the slot region should be filled by the desired target analytes. Thus, the designed horizontal slot waveguide is connected with the tapered waveguides at both ends to maintain a nanogap by providing support to the suspended top poly-Si layer, as shown in Fig. 14.6a. Initially, a layer-by-layer fabrication on top of SiO_2 substrate is followed to fabricate a multi-layered nanowire, starting from poly-Si then followed by SiO_2 and poly-Si again. Next, a wet

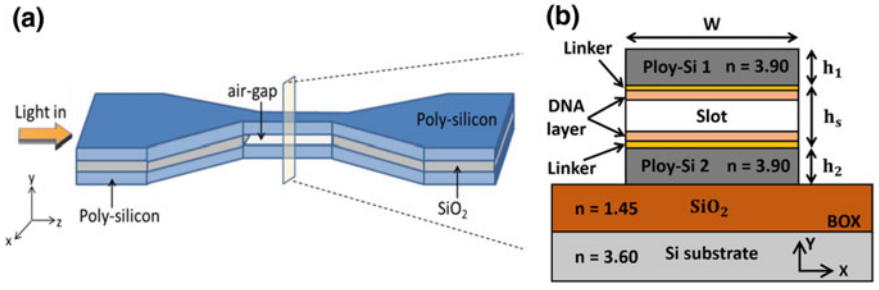

Fig. 14.6 Schematic diagram of the designed SOI based horizontally slotted waveguide for detection of DNA hybridization; **a** shows the 3D structure of the waveguide and **b** depicts a cross-sectional view of the waveguide geometry which is used for computational analysis by FV-FEM. From [41]

etching process using HCL can be followed to remove the middle oxide layer in the less wide slot region. Once the oxide under narrow waveguide region is removed when the etching process is stopped so that the ploy-Si layers can get mechanical support from the tapered section at both ends where the SiO_2 is only partially etched. For optimization and complete analyses of the waveguide as a bio-sensor, a cross-sectional geometry is considered as shown in Fig. 14.6b. The refractive indices and bio-layers thickness of linker layer, ssDNA and dsDNA are taken as same that are used for the previous application. The refractive indices of poly-Si layers, SiO_2 and cover DI water medium are taken as 3.9, 1.444 and 1.33 at the operating wavelength of 1550 nm. In this present work, the key optimization parameters are core width (w), top and bottom poly-Si core heights (h_1 and h_2) and slot height (h_s). For numerical computation, the one-fold symmetry of the geometry is exploited and used more than 34,000 triangular elements for half structured domain discretization. The field components of the fundamental quasi-TM mode are evaluated by mode solver. The E_y field shows the discontinuity at the high index contrast dielectric interface providing the strong field in the slot area. The propagating energy flux density termed as Poynting vector (S_z) is calculated from the **E** and **H** vector fields, is also presented in Fig. 14.7. The 1D line plot of S_z field also shown as an inset. It clearly shows that the optical power is mostly guided by the low index region of slot waveguide.

The power confinement and power density variations in the top and bottom DNA probe layers (8 nm for DNA layer and 1 nm for linker layer) with high indexed poly-Si core height are presented in Fig. 14.8. The power density is the average power confinement per unit area for both DNA probe layers, are shown by the solid lines and power confinement are shown by the dashed lines. Both the power confinement and power density exhibit similar trend with the core height. For smaller core height both the parameters show small values because initially it is closed to the cut-off. Thus, the smaller power confinement occurs due to most of the modal evanescent fields are spread over the substrate and the cladding regions. Modal power increases with the increase of core height, due to enlargement of the guided area, reaches the maximum confinement at a core height, $H = 0.15$ μm. With

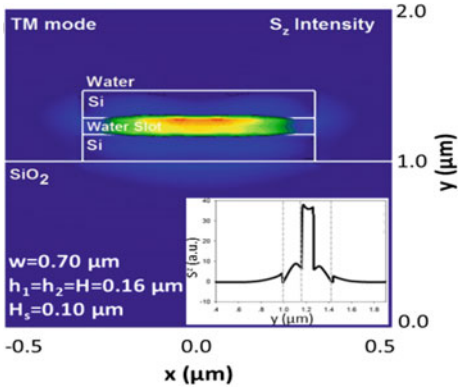

Fig. 14.7 The energy flux density (S_z) of the fundamental quasi-TM mode of the slot waveguide for width (w) = 0.7 μm, poly-Si core height, $h_1 = h_2 = 0.16$ μm and slot height (h_s) = 0.10 μm. From [41]

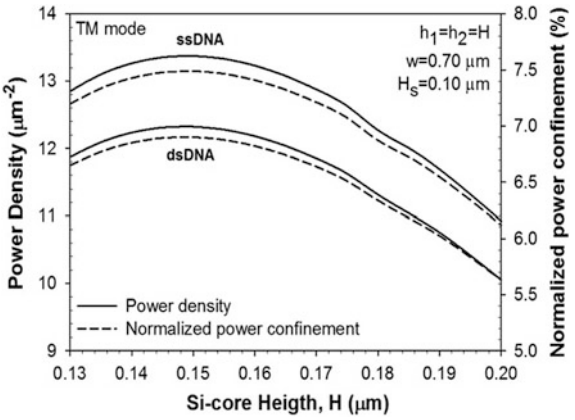

Fig. 14.8 Shows optical power density and power confinement variations in the top and bottom DNA probe layers with poly-Si core height ($h_1 = h_2 = H$) for fixed width, $w = 0.70$ μm and slot height, $h_s = 0.10$ nm. An 8 nm thick DNA probe layer and a 1 nm bio-linker layer ($n_a = 1.42$) are considered for simulations. From [41]

further increment of H, the power confinement decreases due to most of the light guided by the high index Si cores. The effective index change (Δn_{eff}) is one of the important parameter for the analyses of the bio-sensing waveguides, used to determine the sensitivity of the waveguide. The Δn_{eff} variation during DNA hybridization with core height (H) is shown in the Fig. 14.9. The solid and dashed lines denote the waveguide effective index variation (n_{eff}) and Δn_{eff}, respectively. The Δn_{eff} increases with core height until it reaches to the maximum value at height, $H = 0.17$ μm. Beyond this value, the optical power mostly guided by the core rather than the slot. This results reduction of the Δn_{eff} as well as the waveguide sensitivity. Individually, for both the DNA layers the waveguide n_{eff} increases with H because of stronger coupling. Poly-Si core height, $H = 0.15$ μm shows the maximum power confinement into DNA probe layer and $H = 0.17$ μm shows maximum the Δn_{eff} in Figs. 14.8 and 14.9, respectively. Therefore, the optimized poly-Si core height is taken as, $H = 0.16$ μm.

Similarly, the power confinement and power density variation in the sensing layer with the waveguide core width (w) are presented in Fig. 14.10 for a fixed height $H = 0.16$ μm. At smaller width, the power confinement in the sensing layer, shown by the dashed lines, were less due to smaller waveguide size. However, with the core width increment the power confinement slightly increased. Due to high refractive index contrast, the ssDNA shows higher confinement than the dsDNA. Besides, the power density variation shows an inversely proportional trend with w. At smaller width, the small guiding area results in higher power density. As the width increases, the power confinement per unit area reduces due to the larger guiding area. The results indicate that the change in the poly-Si core height (H) is much effective than the core width (w). Next, the dependencies of n_{eff} and Δn_{eff} due to DNA hybridization with the core width (w) are examined and presented in Fig. 14.11. It shows that the n_{eff} values due to both DNA layers, shown by two solid lines, increase with the increasing w. That indicates more light confinement and guidance by the larger waveguide geometry. On the other hand, the Δn_{eff},

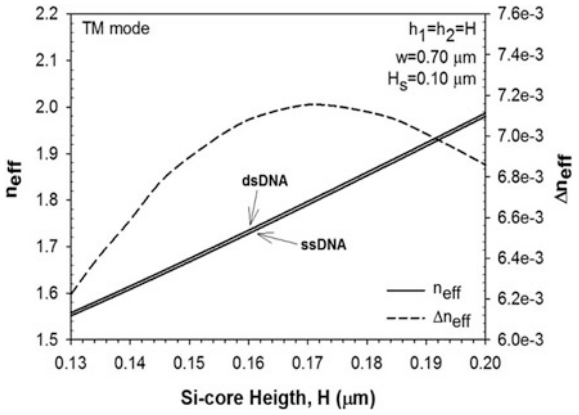

Fig. 14.9 Shows the variations of the effective index (n_{eff}) due to each sensing medium (ssDNA and dsDNA) and the effective index difference (Δn_{eff}) detected during DNA hybridization with Si core height (H). The DNA probe layer comprises of a 1 nm bio-linker layer ($n_a = 1.42$) and an 8 nm ssDNA ($n_b = 1.456$) or dsDNA ($n_b = 1.53$) layer. The core width (w) and slot height (h_s) are fixed at 0.7 and 0.1 μm, respectively. From [41]

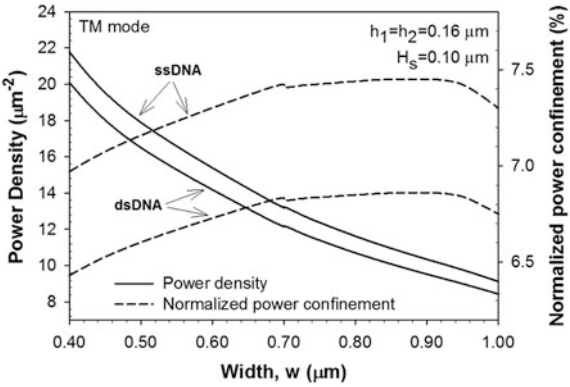

Fig. 14.10 Variation of the power density and power confinement in the DNA probe layer with the waveguide core width (w). The other parameters, such as waveguide core height and slot height are fixed at 0.16 μm and 0.10 μm, respectively. From [41]

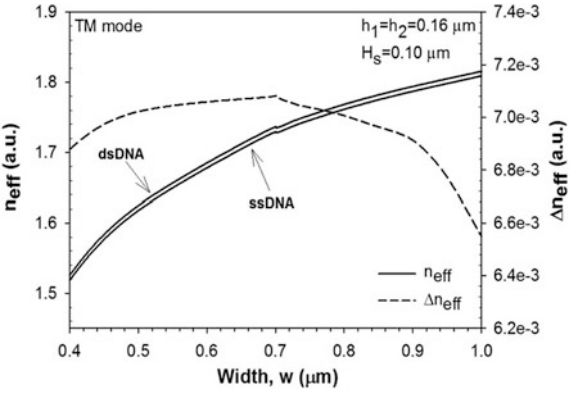

Fig. 14.11 The effective index (n_{eff}) due to individual ssDNA and dsDNA as sensing layer and change in effective index (Δn_{eff}) due to DNA hybridization variations with the core width (w) when the core height and slot height are fixed at 0.16 and 0.10 μm, respectively. From [41]

shown by the dashed line, initially increases with increment of w and reaches the maximum value at $w = 0.70$ μm. For $w > 0.70$ μm, the Δn_{eff} shows a decremental trend. Thus, the waveguide design parameters are optimized for the better performance and those can be listed as, $w = 0.70$ μm, $H = 0.16$ μm and $h_s = 0.10$ μm. Although a narrower slot provides a larger Δn_{eff}, but it would be difficult to fabricate a very small and uniform slot due to fabrication limitations. Thus, a 0.10 μm slot height is considered as an optimized value for this design. By looking at the results, it is also noted that the Δn_{eff} is more affected by the poly-Si core height (H) rather than the poly-Si core width (w) as the graph changes more rapidly with the core height.

To detect the Δn_{eff} due to DNA hybridization, this optimized horizontal slot waveguide is incorporated in the sensing arm of an integrated Mach-Zehnder interferometer (MZI) arrangement. The relative phase shift ($\Delta\phi$) depending on the effective index change can be obtained as

$$\Delta\phi = \frac{2\pi}{\lambda} \cdot L \cdot \Delta n_{eff} \tag{14.3.3}$$

where L is MZI arm length incorporated with slot waveguides. The destructive interference with minimum interference signal occurs when the relative phase difference is equal to π. Therefore, even a smaller effective index difference due to DNA sequencing can be measured with this efficient horizontal slot waveguide incorporated MZI transducing device of length 110 μm.

14.4 Cross-Slotted Bio-chemical Sensor

It was shown in Sects. 14.3.1 and 14.3.2 that vertical and horizontal slot guides can only be effective for the quasi-TE and quasi-TM modes, respectively. This signifies that both the designs are strongly polarization dependent. Thus, to overcome this difficulty a novel cross-slot waveguide for biochemical sensing which supports the much stronger field enhancement in the slot region for both quasi-TE and TM mode is designed and rigorously studied. The cross-slot structure is composed of both vertical and horizontal slot regions simultaneously, as shown in Fig. 14.12a.

This structure can be designed to connect via the tapered waveguides and can be fabricated on an SOI wafer with a 220 nm top-Si layer (or a thicker layer if necessary) on a 2 μm or similar thick buried oxide (BOX) layer. If necessary, the top waveguiding silicon layer can be thinned down to an optimized thickness. On top of this, SiO_2 can be deposited through plasma enhanced chemical vapor deposition (PECVD). Following that a low-loss hydrogenated amorphous silicon (a-Si) layer can be deposited followed by a thin SiO_2 layer deposition, which can act as a hard mask, by using PECVD [43]. If necessary these layers can be planarized by using chemical mechanical polishing (CMP), before the next layer deposition. A vertical slot waveguide can be defined by Deep UV (DUV) or

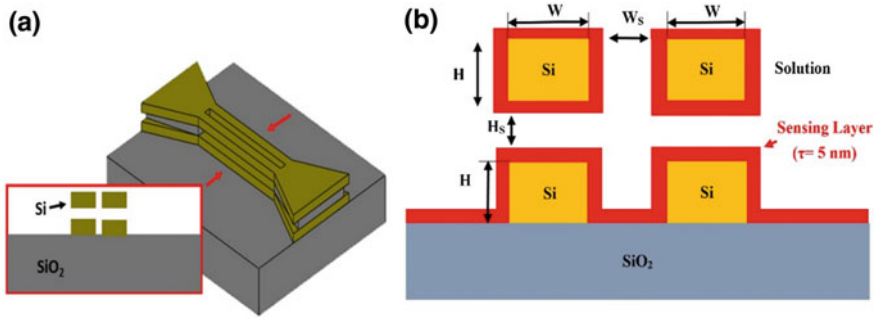

Fig. 14.12 **a** Schematic three-dimensional diagram of the SOI based cross-slot waveguide with hollow vertical and horizontal slots. **b** Cross-sectional view of the cross-slot waveguide used for bio-chemical sensing. A 5 nm bio-sensing layer of refractive index 1.45 is considered for waveguide surface sensing. From [42]

E-beam lithography and followed by dry etching of silicon and SiO_2 layer down to the BOX layer. Next, buffered hydrofluoric acid can be used to etch the SiO_2 layer in between the two horizontal silicon guiding layers to form the horizontal slot [44, 45]. Since the width of the two horizontal slots in between two silicon layers is smaller, hydrofluoric acid introduced through the vertical slot and outside will remove this SiO_2 layer earlier than the much wider SiO_2 layer beyond the vertical slot channel. Once the low-index oxide layer under the narrow waveguide region is removed the etching process is stopped so that two upper silicon layers are mechanically supported by the wider region at the two ends where silica was only partially removed. However, it should be noted that any CMOS compatible material, such as Si_3N_4 [46], can also be used to fabricate the initial slot regions, which later needs to be selectively removed to open the empty slot region. Previously, sensing arm of several microns long incorporating cantilever suspension from one end has been fabricated with negligible deformation [47]. However, since for the proposed structure only a short length of slot waveguide is suspended from both the ends, it is expected to be mechanically sturdier. After the cross-slot WG is formed, the several nm-thick sensing layers for biochemical sensing can be added to all the surface of the silicon cores [17, 25, 45, 48] such as silanized with 3-glycidyloxy propylitrimethoxy saline for label-free protein sensing [17], or dipped into aqueous glutaraldehyde for the study of label-free molecular binding reactions, as shown in Fig. 14.12b. Here the thickness of sensing layer is taken as 5 nm.

The 2D-FEM simulated E_x and E_y field profiles for the quasi-TE and TM modes are shown in Fig. 14.13a, b, respectively. For the quasi-TE mode, the power confinement factor in the total slot region (Γ_{T-Hy}) increases, reaches its peak value and then decreases with the increase of silicon core width (W). This peak value also increases with the increase of silicon core height (H). Similarly, the total-slot confinement factor (Γ_{T-Hx}) for quasi-TM mode shows a similar variation tendencies but with H and W. Thus, $\Gamma_{T-Hy}+\Gamma_{T-Hx}$ is taken as an optimization parameter

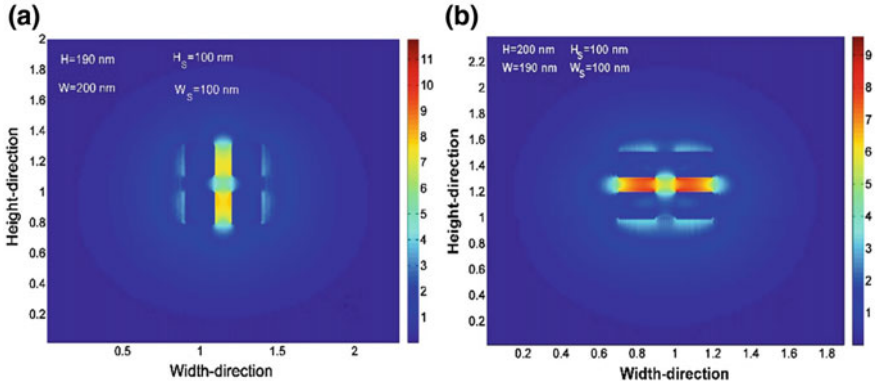

Fig. 14.13 Low index guided **E** field profile of the fundamental modes with different polarizations in the cross-slot waveguide. **a** E_x—field profile of the H_y^{11} mode, E_y-field profile of the H_x^{11} mode. All the field profiles are generated by using 2D-FEM. From [42]

to maximize the total-slot confinement. This parameter shows total 79% power confinement for silicon core width and height 205 nm and 220 nm, respectively. Besides, the ratio of the total-slot confinement factors for the H_y^{11} and H_x^{11} modes ($\Gamma_{T-Hy}/\Gamma_{T-Hx}$) is another important parameter for optimization to make the device polarization independent. Variations of $\Gamma_{T-Hy}/\Gamma_{T-Hx}$ with the width, W and height, H of silicon cores are shown in Fig. 14.14a, b, respectively. The ideal ratio of 1 is shown here by a black dashed line. It can be observed from Fig. 14.14a that for a given height, due to the parabolic variation tendency of Γ_{T-Hy} and the monotone-increasing variation tendency of Γ_{T-Hx} with the silicon core width, all the ratios increase initially and then decrease with the increase of the silicone core width. The red curve for $H = 250$ nm shows that the cross-slot WG can confine equal power in the whole slot region for both the polarizations, but total-slot confinement factor for each one is around 34%. On the other hand, for $H = 220$ nm, shown by a green line, total-slot confinement factor for each polarization can reach to the same value of 39.3%, when the silicon core width is taken as 212 nm. Again, for a given width, the confinement ratios decrease at first and then increase with the increase of the silicon core height, as shown in Fig. 14.14b. It is obvious that the ratio can reach 1 at several width and height combinations. To achieve a successful polarization-independent design, the sensitivities for the H_y^{11} and H_x^{11} modes should be not only nearly the same but also large enough, so the width and height of the silicon cores are optimized to be around 223 and 216 nm, with the total-slot confinement factor for each polarization of 39.4%. It can also be observed here that the performance would be remarkably stable even for a possible ±10 nm fabrication error of the silicon core dimensions.

Figure 14.15 gives the cross-slot dimension optimization based on surface sensitivity, $S = \Delta n_{eff}/\Delta\tau$. A bio-layer with completely saturated with analyte of

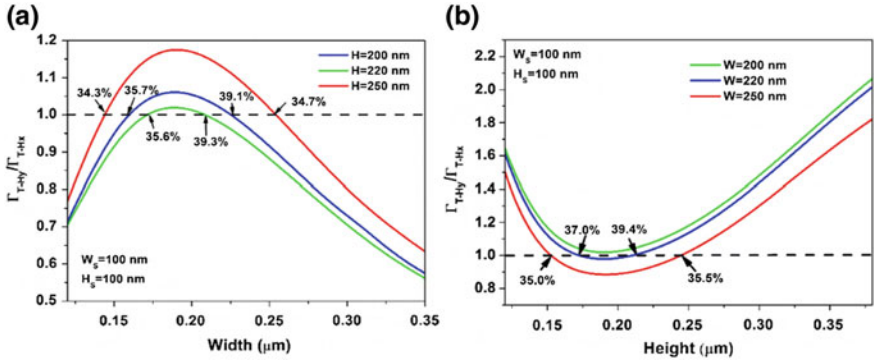

Fig. 14.14 Variations of the ratio $\Gamma_T - H_y/\Gamma_T - H_x$ with **a** the Si core width, W and **b** height, H. From [42]

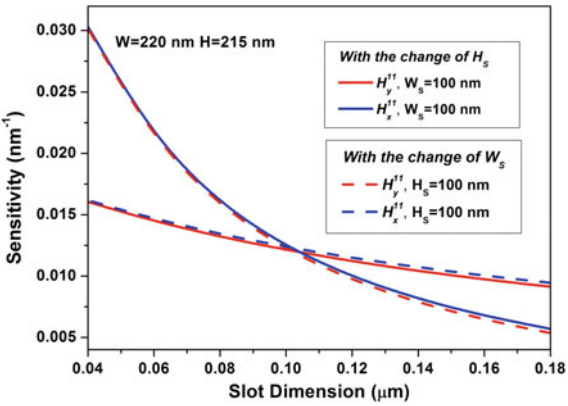

Fig. 14.15 Cross-slot waveguide sensitivities with the horizontal and vertical slot dimensions for different polarizations. The solid and dashed lines show the sensitivity variations with the horizontal slot height (H_s) and vertical slot width (W_s), respectively. From [42]

thickness $\Delta\tau = 5$ nm and refractive index of 1.45 is considered. It can be observed that with the decrease of the width or the height of cross-slot, the sensitivities for both the two polarization modes increase. However, the sensitivity for H_y^{11} mode increases more quickly when the cross-slot width decreases, while that for H_x^{11} mode increases more quickly with the decrease of slot height. When both the cross-slot width and height are set to 100 nm, the sensitivity value for each polarization mode is $0.012\ \text{nm}^{-1}$, which is twice the same of vertical-slot-waveguide or horizontal-slot-waveguide sensors with similar dimensions. Obviously, the sensitivities for both H_y^{11} and H_x^{11} modes can be improved synchronously by reducing the width and height of cross-slot simultaneously.

14.5 Straight Vertical Slotted Resonator

Slot waveguide is very attractive in sensing applications because of its enhanced light-matter interaction inside the low index slot region. So far, many refractometric sensing devices have been reported where a slot waveguide is incorporated in the ring resonators. However, a ring resonator also suffers from bending loss and coupling losses with the bus waveguides. Instead of a ring resonator with comparative larger device footprint, a nanometer-scaled straight vertically slotted resonator has been designed. The three-dimensional resonating device is shown in the Fig. 14.16. The main device of interest contains two high index straight silicon cores separated by a narrow slot channel. This resonating structure is coupled with the in and out bus waveguides. The tunable light from the laser travels through the bus waveguide and excites the slotted structure at a particular wavelength. During the resonance condition, the electromagnetic energy builds up in the slot cavity and allows to pass that particular light wavelength from input bus to output bus waveguide. Thus, the resonance wavelength (λ_{res}) can be detected by the photodetectors (not shown) at both facets of output bus waveguide (λ_{out1} and λ_{out2}) and at the opposite end of the input bus waveguide. The complete resonating structure is designed and its sensing ability is investigated at the widely-used telecommunication wavelength, $\lambda = 1550$ nm. The silicon slot guide is separated by a silicon dioxide (SiO_2) buffer layer from the silicon substrate. The silicon and silicon dioxide refractive indices are taken as $n_{Si} = 3.476$ and $n_{SiO_2} = 1.44$, respectively at the 1550 nm operating wavelength. The key advantages of this device can be explained in three steps. First, the nanometer dimension results high scale integration and ease of fabrication than other complex devices. Second, the dominant E_x field of the quasi-TE mode shows high magnitude inside the slot that results a in strong light-matter interaction. Third, a much-improved device sensitivity (S) and detection limit (DL) can be achieved with help of first two steps. For sensing applications, the slot and surrounding medium can be filled with any low index solution of one's interest.

The CMOS compatible fabrication process of this curve free device is simple compared to other photonic sensing devices. The two rails of Si core can easily be fabricated by the etching of unwanted Si into a commercially available SOI wafer. Besides, if required further increment of the Si core height can be achieved by precise control of Si layer growth with the help of plasma enhanced chemical vapor deposition (PECVD). A photoresist thin film is deposited on the Si layer for slot patterning. Then the reactive ion-etching (RIE) process can be followed to make Si core strips with a slot region in between them.

The 3D slotted resonator is shown in Fig. 14.16 is a short length straight vertical slot waveguide. Therefore, the rigorous investigation of the design parameters, calculation of dominant and non-dominant field components, profiles of for the fundamental quasi-TE and TM modes and power confinement into the different guiding region are done with the help of 2D FV-FEM. Throughout the 2D-FEM simulations, 1,280,000 first order triangular elements are used for computational

domain discretization. After completion of the device design, the 3D FV-FEM is used to determine the modal solutions and performance analyses of the 3D slotted resonator. Two different sensing mechanisms, both bulk and surface sensing have been considered here. A 5 nm ultra-thin sensing layer (T_s) is taken for bio-molecular detection, as shown in the bottom inset of the Fig. 14.16. The high sensitivity of the device strongly depends on the power confinement (Γ) in the region where the light and targeted analyte interaction occurs. Thus, optimization of the slot's cross-sectional design parameters, such as Si core width (W), height (H) and low index slot width (W_s) are much important. Both the total slot confinement ($\Gamma_{slot-total}$) and confinement into 5 nm sensing layer ($\Gamma_{slot\ sensing\ layer}$) increases with W, reach their maximum values and then decrease [49] for a fixed Si core height (H) and slot width (W_s). The maximum confinement into slot and sensing layer and corresponding W indicates the optimized value of Si core width (W). Now with a fixed W and W_s, the Si core height (H) variation shows that the $\Gamma_{slot-total}$ and $\Gamma_{slot\ sensing\ layer}$ continuously increase with H. However, the power density initially increases, reaches a maximum and then decrease with H [49]. Although, the variation of the effective index shift (Δn_{eff}) due to presence of 5 nm sensing layer shows an excellent correlation with the $\Gamma_{slot-total}$ variation. Although, in practice, a 220 nm Si height is widely used as it is the typical thickness of most commonly available Si in SOI wafer, however, in this case, the higher core height yields better sensors, so the optimized Si core height (H) is taken as 500 nm that can also be easily fabricable with modern technology [50]. Finally, a further investigation on slot width (W_s) shows a maximum confinement, $\Gamma_{slot-total} = 43.8\%$ could be achieved by the optimized slot waveguide design parameters as, Si core width (W) = 170 nm, Si core or slot height (H) = 500 nm and slot width (W_s) = 130 nm. The cover medium and the slot region are considered to be filled with aqueous solution of refractive index 1.33. By using 2D FV-FEM again, the effective index (n_{eff}) of the optimized slot structure is evaluated and it was 1.63827.

The vertical slotted cavity supports the longitudinal modes at the specific resonating wavelength (λ_{res}) and that can be defined as

$$\lambda_{res} = \frac{2L \cdot n_{eff}}{m} \tag{14.5.1}$$

Here $2L$ is the round-trip length of the longitudinal electromagnetic wave in the resonator and $m = 1, 2, 3\ldots$ denotes the order of supported longitudinal modes. Equation 14.5.1 indicates that the number of longitudinal modes strongly depends on the resonator length (L). As the fundamental mode is expected to be more stable and sensitive than the higher order modes, the slot resonator cavity length (L) has been calculated for a single ($m = 1$) longitudinal fundamental mode using Eq. 14.5.1. Finally, all the device design parameters can be summarized as, Si core width (W) = 170 nm, core or slot height (H) = 500 nm, slot width (W_s) = 130 nm and the device length (L) = 473 nm for a specific resonating wavelength, λ_{res} = 1550 nm.

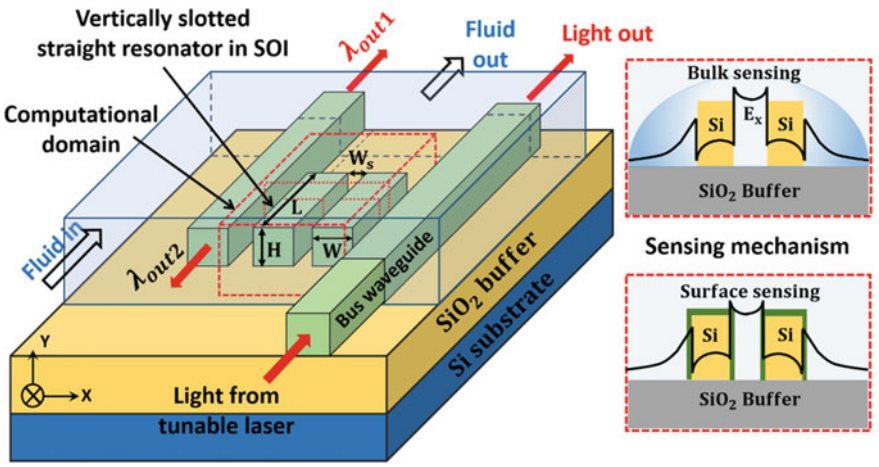

Fig. 14.16 Schematic diagram of the three dimensional (3D) vertically slotted straight resonator. The right sided insets bordered with red dashed lines show the sensing mechanisms considered for the refractometric sensing analyses. From [49]

In a resonating cavity, the self-consistent longitudinal field gets confined and oscillates at a particular wavelength. Thus, the further performance investigations require a complete three-dimensional analysis of the quasi-TE and TM modes inside the resonating structure. A dedicated rigorous and full vectorial **H**-field based three-dimensional finite element method (3D-FEM) is developed and used to solve the problem. All the field components of the resonating modes can be generated by the post-processing of the eigenvectors obtained from complete device simulation by the 3D FV-FEM. The 3D iso-surface profile of the dominant and most sensitive E_x field of the slotted resonator is simulated by the 3D-FEM shown in Fig. 14.17. During 3D-FEM simulations over 456817 first order tetrahedral elements are considered for the three-dimensional computational domain discretization of dimensions 1.47 μm (along x) × 0.473 μm (along y) × 1.5 μm (along z). Its performance analyses divided into two stages: (1) *surface sensing,* where an ultra-thin bio-molecular layer covers the sensing device surface (Fig. 14.16, **bottom inset**) and (2) *bulk sensing*, where refractometric changes of the homogeneous medium are considered (Fig. 14.16, **top inset**).

14.5.1 Surface Sensing

In case of surface sensing, a thick bio-layer (linker + bio-molecular layer) of refractive index 1.45 have considered on top of both Si strips and the slot region. The cover medium is filled with the aqueous solution (n_{water} = 1.33). The 3D-FEM computation measured a 5.2 nm resonating wavelength shift for a 5 nm sensing

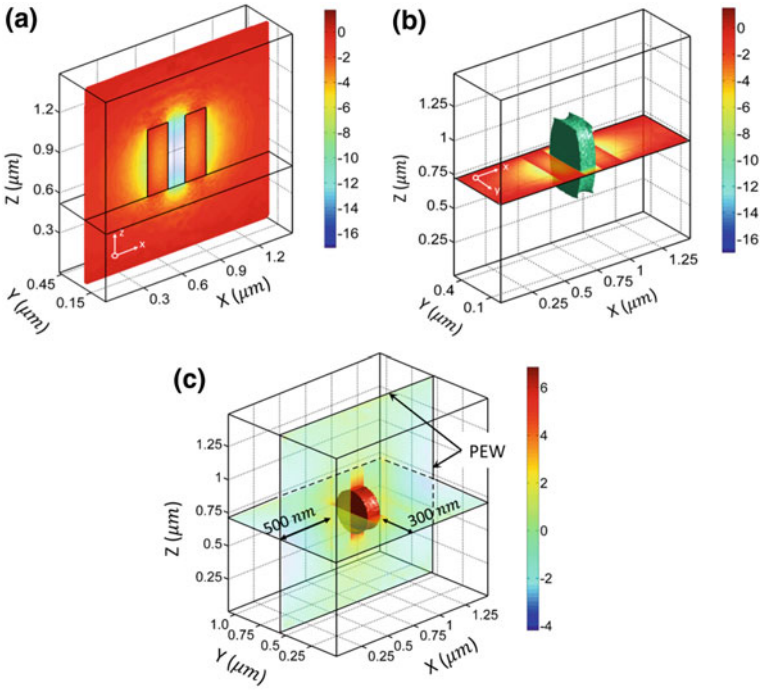

Fig. 14.17 2D and 3D profiles of the dominant E_x field confined into a straight single slotted resonator at the resonating wavelength, λ_{res} = 1550 nm; **a** shows the E_x field profile at the mid-sliced x-z plane of the slot resonator, **b** depicts the 3D iso-surface profile of the E_x field where boundary walls are considered to be placed at both end faces of the Si cores, **c** shows the 3D E_x field when the boundary walls are placed away from the both end faces and side faces of the Si strips. A 3D FV-FEM is used for complete resonating structure simulations. From [49]

layer of refractive index, $n = 1.45$. The device sensitivity has been investigated for different thickness of sensing layers ranging from 5 to 50 nm. The surface sensitivity of the device can be defined as

$$S_{surface} = \frac{\Delta\lambda_{res}}{\Delta t} \tag{14.5.2}$$

Here, $\Delta\lambda_{res}$ and Δt are the resonance wavelength shift and corresponding bio-layer thickness change. The $\Delta\lambda_{res}$ linearly increases with the thickness of sensing bio-layer shown by the red solid line in Fig. 14.18. Thus, $\Delta\lambda_{res}$ and bio-layer thickness change (Δt) shows a strong linear relationship. Similarly, the variation of the surface sensitivity of the device against different bio-layer thickness is shown by the green diamond markers, plotted using a high-resolution scale. Thus, the Fig. 14.18 shows a small reduction of $S_{surface}$ with an increase of bio-layer thickness.

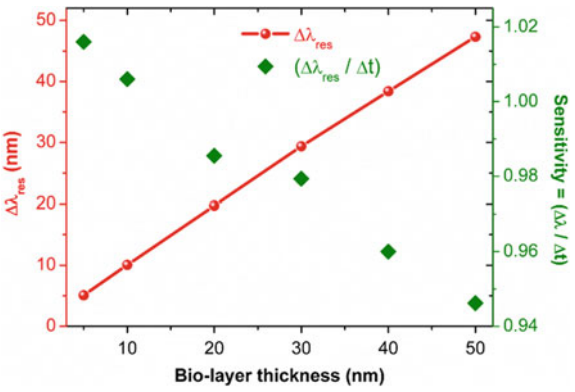

Fig. 14.18 Surface sensing of the designed device with optimized design parameters. The redline shows a linear response of wavelength shift ($\Delta\lambda_{res}$) for different bio-layer thickness of refractive index 1.45. The green diamond markers denote the surface sensitivity ($S_{surface}$) variation with bio-layer thickness ranging from 5 to 50 nm. From [49]

14.5.2 Bulk Sensing

The bulk sensing process follows the detection of the refractive index change of the homogeneous bulk medium in the cover and slot regions. For rigorous investigations, aqueous sucrose solutions with different concentrations are used over the sensing device. The refractive indices of sucrose solution for different sucrose concentration at ambient temperature (20 °C) are taken from the datasheet [51]. Similar to practical situations, two different cases have been investigated in the simulation process: (1) the cover and slot region are completely filled with the sensing fluid, and (2) only cover medium is filled with the fluid and the slot is filled with air bubbles.

The bulk refractometric sensitivity of the vertically slotted waveguide has been investigated by 2D-FEM. The low index guided E_x-field profile and its response to the homogeneous refractive index change are shown in Fig. 14.19. The variation of the normalized effective index change ($\Delta n_{eff}/n_{eff}$) with refractive index changes of the sucrose solution presents a linear relationship, shown by a red line. The bulk sensitivity of the waveguide structure can be determined from the slope of the curve as $S_{bulk} = \left(\Delta n_{eff}/n_{eff}\right)/RIU$ and its value was calculated as 1.025 per RIU. In case of the 3D resonating device, the bulk sensitivity can be defined as

$$S_{bulk} = \frac{\Delta\lambda_{res}}{RIU} \tag{14.5.3}$$

Here $\Delta\lambda_{res}$ and RIU denote the resonating wavelength shift of the device and the refractometric change due to different concentration of sucrose in the solution, respectively. The resonating wavelength change ($\Delta\lambda_{res}$) of the designed structure as a function of the sucrose solution refractive index are shown in Fig. 14.20. The solid and dashed lines show the device responses when the boundary electric walls are placed both ends of and far away from the Si strips, respectively. A strong linear shift is observed by the lines and its slope i.e. sensitivity (S_{bulk}) show the value of

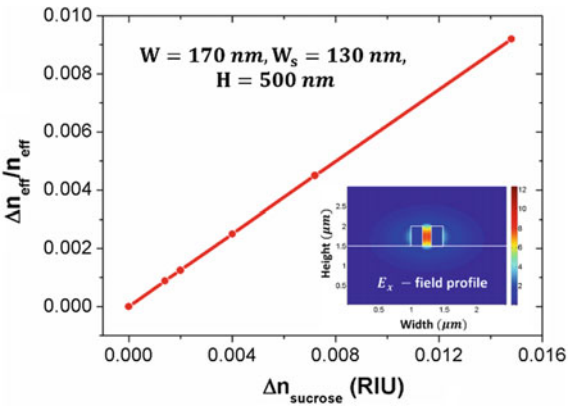

Fig. 14.19 Bulk refractometric sensitivity analysis of the vertically slotted waveguide with optimized design parameters, such as, $W = 170$ nm, $W_s = 130$ nm and $H = 500$ nm at 1550 nm operating wavelength. The curve slope denotes the sensitivity of the waveguide when the cover medium is fully covered with the sucrose solution. The inset shows the 2D-FEM simulated E_x-field profile that is essential for low index guiding sensing. From [49]

635 nm/RIU and 335 nm/RIU for the fully filled and empty slot cases. The empty slot condition may arise when the sensing liquid may not enter slot region due to the presence of air bubbles. A better response of the resonator device could be obtained when the boundary walls are placed away from the Si strip end faces. Fluid-Si contact at both ends increases in this case that also increases the device sensitivity, shown by the blue and green dashed lines in Fig. 14.20. The slope of the linear resonance wavelength shift indicates a much high device sensitivity of 820 nm/RIU and 683 nm/RIU for filled and empty slot cases, respectively. Besides the spectral shift the detection limit (*DL*) of the device can be estimated from the device sensitivity (S_{bulk}) and the sensor resolution (R) as, $DL = \mathrm{R}/S_{bulk}$. The device resolution strongly

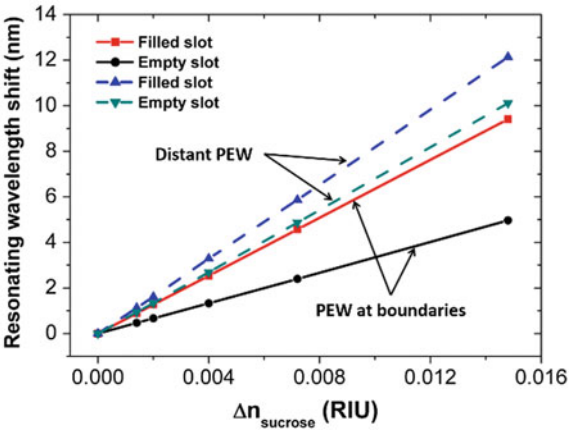

Fig. 14.20 Resonating wavelength shift of the proposed device versus refractive index variation ($\Delta n_{sucrose}$) of sucrose solution at ambient temperature (20 °C). The solid and dashed lines denote the device bulk sensitivity when the electric walls are kept at the end faces and away from the end faces from Si strips. The slope of each linear curve presents bulk sensitivity (S_{bulk}) for the filled and empty slot conditions. From [49]

depends on the wavelength resolution ($\lambda_{resolution}$) of the laser source. A laser source with wavelength resolution of 5 pm indicates that a minimal detectable refractive index of 7.9×10^{-6} RIU and 6.1×10^{-6} RIU could be achieved for the boundary walls touching the end facets and away from the Si strips, respectively.

A rigorous least-squares boundary residual (LSBR) [52] method is used to determine different coupling parameters of the coupled Si bus waveguides and the slotted resonating structure for different gaps. The junction interface between input guide and the resonator slot section shows some back reflections of the input signals. Those reflection coefficients (ρ_r) have been calculated as 0.024, 0.020, and 0.012 for three different separations 250, 300, and 450 nm, respectively. On the other hand, the coupling losses at the junction interface are calculated as 0.2886, 0.1956, and 0.0833 dB for all three mentioned separations. It shows that the 250 nm gap provides higher evanescent coupling the slot resonating structure but with higher coupling loss, whereas the 400 nm gap provides less evanescent coupling with higher coupling efficiency. Therefore, 250–400 nm could be considered as suitable separation range for this coupling between bus waveguide and slot resonating structure.

14.6 Plasmonic Gas Sensing by Al^{+3} Doped ZnO Coated Au Nanowire

Metal oxides have been extensively used in sensing devices. Among them, zinc oxide (ZnO) has attracted considerable interests for different areas, such as sensing [53], lasing [54], light harvesting [55] and detection [56]. Similarly, gold (Au) nanoparticles have also received much attention due to its plasmonic properties at visible wavelengths. In this section, an Au nanocore with an Al^{+3} doped ZnO (AZO) cladding layer has been designed and studied by using the **H**-field based full-vectorial finite element method (FV-FEM) for use as an optical gas sensor. In the numerical simulations, the wavelength dependent Au and ZnO refractive indices are taken from [57, 58], respectively. A small concentration of Al^{+3} doping in ZnO results in an effective replacement of Zn atoms by Al atoms which increase the conductivity of doped ZnO. This in turn also modify the plasmonic frequency of the AZO thin film that can be described by the Lorentz-Drude model [59] as follows

$$\varepsilon_\omega = \varepsilon_{ZnO} - \frac{\omega_p^2}{\omega_p^2 + j\gamma\omega} \tag{14.6.1}$$

Here ε_{ZnO} is the optical dielectric constant of ZnO and ω_p is the plasma frequency, defined by $\omega_p = Ne^2/\varepsilon_0 m^*$ with N as the carrier concentration in the range of 1×10^{17} to 1×10^{20} cm^{-3}. The γ denote the carrier damping constant given by $\gamma = e/\mu m^*$. Here the electron mobility μ has been considered as 24 cm^2/Vs for the

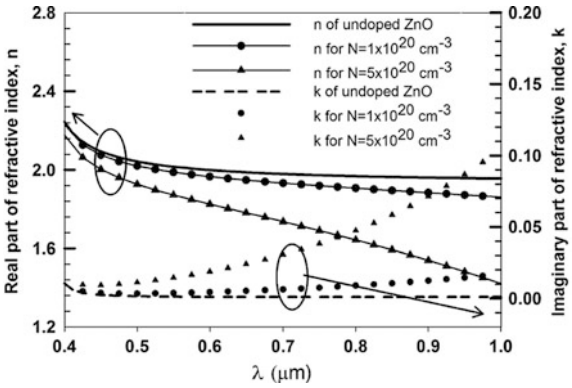

Fig. 14.21 Real and imaginary refractive index variations with the wavelength for ZnO and AZO. The Lorentz-Drude model is used for refractive index calculation. From [61]

target Al^+ of 2 w.% (weight ratio). m^* denotes the effective mass that has been taken as the 0.24 times of the electron mass. Figure 14.21 presents the real and imaginary parts of ZnO and AZO with the carrier concentration of $N = 1 \times 10^{20}$ cm^{-3} and 5×10^{20} cm^{-3}. The refractive index of ZnO is nearly 2.0 for visible wavelengths and tend to rise while reaching the UV direct band edge of ZnO at 3.3 eV. The figure illustrates that an increase in the carrier concentration reduces the AZO refractive index and this reduction is greater for longer wavelengths. Due to increased conductivity of AZO, the imaginary part of the refractive index also increases. Thus, the loss is higher for longer wavelengths and also for higher doping levels.

As a practical device, a finite dimension AZO coated Au nanowire with height, $h = 60$ nm and width, $w = 250$ nm is considered, as shown in the inset of Fig. 14.22. A 100 nm of AZO cladding around the metal core, which is also surrounded by the infinite air cladding is considered for computation analysis. In the simulation, it has been observed that the modal propagation length (L_p) of the waveguide is around 3 μm for an AZO cladding with lower carrier concentration, $N_L = 1 \times 10^{17}$ cm^{-3}. With the increase of carrier concentration, the refractive index of AZO reduces from its undoped ZnO value and as a result, the effective index of the quasi-TM mode decreases. Additionally, as N increases the material loss also increases due to increasing conductivity. Therefore, the change in effective index and differential loss could be the important parameters for sensing investigations.

$$\Delta n_{eff} = \left| n_{eff}(N_L) - n_{eff}(N) \right| \tag{14.6.2}$$

$$\Delta Loss = \left| Loss(N_L) - Loss(N) \right| \text{ in dB/mm} \tag{14.6.3}$$

Here N_L and N are the fixed (1×10^{17} cm^{-3}) and variable doping carrier concentration. The curves in Fig. 14.22 depict the variations of Δn_{eff} and $\Delta Loss$ with the carrier concentration, N. It can be seen that Δn_{eff} changes linearly with the carrier concentration. On the other hand, $\Delta Loss$ increases with N but tends to saturate at a high carrier concentration. This is due to the fact that as the N

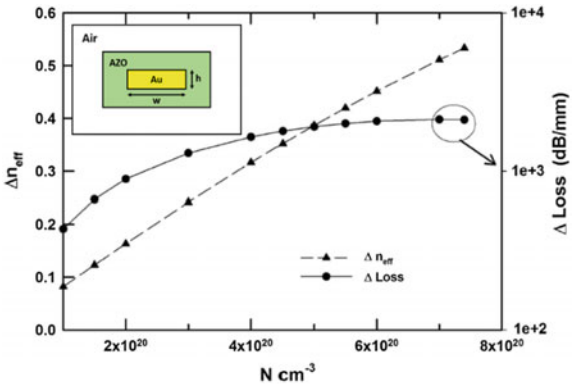

Fig. 14.22 Δn_{eff} and $\Delta Loss$ variations with the carrier concentration of AZO cladding at the operating wavelength, $\lambda = 750$ nm. The inset is showing the schematic cross-section of the plasmonic waveguide where a finite Au core is cladded with AZO layer. The dimension of the Au core is taken as, width (w) = 250 nm and height (h) = 60 nm. From [61]

increases, the refractive index of AZO decreases and simultaneously the modal power confinement in the AZO cladding reduces from a value of ~80% at $N_L = 1 \times 10^{17}$ cm^{-3} to a value ~55% at $N = 7.4 \times 10^{20}$ cm^{-3}. In the case of finite cladded Au nanowire, reducing the width of the core tends to reduce $\Delta Loss$ and Δn_{eff} as a large amount of power leaks into the surrounded air cladding. Thus, the width changes of the Au core and its effect has not been analysed rather a fixed core width, $w = 250$ nm has been considered for further investigations.

Electrons are the majority charge carrier in the AZO. Therefore, absorption of gas and vapor liquid on the AZO surface will deplete electrons, resulting in a decrease in conductivity. The Debye length is used to quantify the thickness of the space charge layer that has deficient carriers due to electron trapping by the chemisorbed oxidizing agent in the n-type semiconductor. The Debye length of the AZO layer is taken as 10 nm [60] for the carrier concentration of the order of 10^{17} cm^{-3}. Initially, the Au core dimension of $w = 250$ nm and $h = 60$ nm with $N = 7.4 \times 10^{20}$ cm^{-3} has been considered. It has also been assumed that the N in the depletion region is changing from $N_{D,L} = 7.4 \times 10^{20}$ cm^{-3} to a value of $N_{D,L} = 10^{17}$ cm^{-3} for a Debye depth equivalent to 10 nm. For simplicity, a uniform depletion of the carrier concentration also has been taken at the AZO boundaries. A large cladding thickness makes the core far away from the depletion layer. Thus, the quasi-TM mode do not get affected by the higher degree by the refractometric change in the depletion layer. When the cladding thickness is very small, a large portion of the modal power might spread into the outer air cladding region. Therefore, cladding thickness is considered as an important parameter for optimization. Figure 14.23 depicts the effective index change (Δn_{eff}) as a function of AZO thickness for three different operating wavelengths, such as 650, 700 and 750 nm. Above 90 nm thickness, the effective index change is larger for $\lambda =$ 750 nm, compared to that of $\lambda = 650$ nm. When the cladding thickness is larger, around 100 nm, the surface plasmon mode guided by the core has a spot size area that is two to three times larger than that of $\lambda = 650$ nm. This allows a higher proportion of the modal power in the depletion region, as shown by the Γ_D

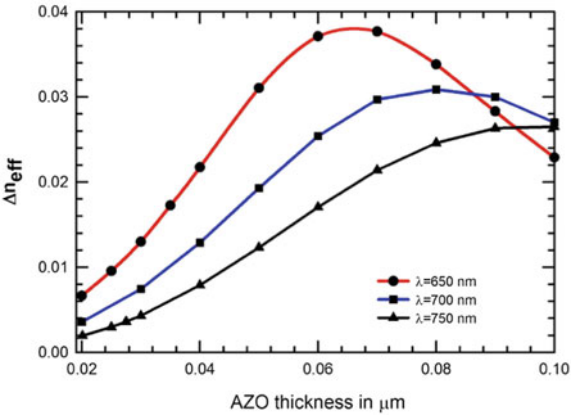

Fig. 14.23 Variation of real effective index change of the waveguide with the cladding thickness at three different operating wavelengths 650, 700, and 750 nm. From [61]

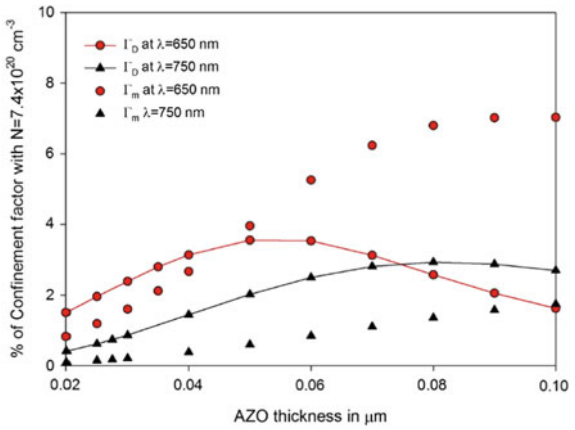

Fig. 14.24 Variation of power confinement (%) in the depletion (Γ_D) and metal core (Γ_m) with respect to the AZO cladding thickness. Two operating wavelengths, λ = 650 and 750 nm. From [61]

variations in the Fig. 14.24. Additionally, at 650 nm the metal core shows higher power confinement compared to that in the depletion region. Furthermore, the Δn_{eff} is larger for longer wavelengths. Due to these factors, for large AZO thickness ~100 nm, the Δn_{eff} is higher for longer wavelengths. It can be seen in the Fig. 14.23, for the lower thickness (<80 nm) the Δn_{eff} is higher at $\lambda = 650$ nm than that of λ = 750 nm. As the depletion region is closer to the metal core, the confinement in the depletion region (Γ_D) becomes larger for those operating wavelengths.

Figure 14.25 presents the percentage change of the modal propagation length, $L_p = 1/2\beta_i$ (β_i is the imaginary part of the propagation constant) with respect to the AZO cladding thickness. The percentage change of the modal propagation length ($\Delta L_p\%$) can be calculated as

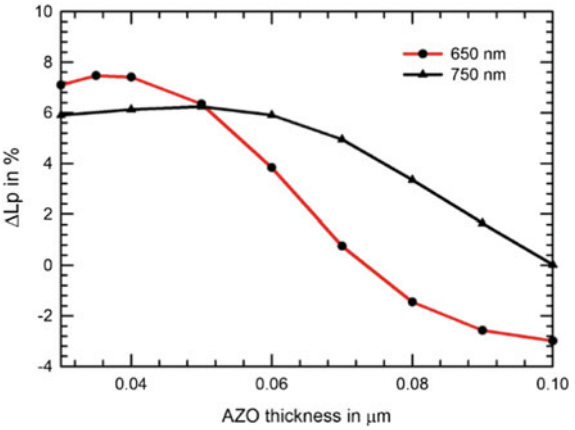

Fig. 14.25 Variations of the change in the propagation length (ΔL_p) as a function of AZO cladding layer thickness at two different wavelengths, λ = 650 nm and 750 nm shown by the red and black lines, respectively. From [61]

$$\Delta L_p\% = \left(1 - \frac{L_p(N_{D,L})}{L_P(N_{D,H})}\right) \times 100 \tag{14.6.4}$$

The red ($\lambda = 650$ nm) and black ($\lambda = 750$) nm) lines in Fig. 14.25 indicate that as the cladding thickness decreases, the modal propagation length change (ΔL_P) rises from its negative and reaches a maximum value. Further reduction of thickness starts leakage of a higher proportion of power in the air cladding and thus, the ΔL_p starts to decrease. For a larger thickness, the ΔL_p shows negative value whereas, for lower AZO thickness ΔL_p becomes positive. For a lower thickness of AZO cladding the confinement in both the depletion (Γ_D) and metal core (Γ_m) decrease. Furthermore, due the close position of the depletion and metal core influences the surface plasmonic mode such that the modal loss increases with the increasing refractive index in the depletion layer. With the help of these rigorous analyses, it has been shown that for finite AZO cladding thickness (20–100 nm), the depletion of carriers for a depth equivalent to Debye length can affect the modal effective index variation that is greater than 0.035 and a variation of the propagation length which is greater than 5%. These waveguide modal properties can be exploited by incorporating this plasmonic waveguide into a Mach-Zehnder based opto-chemical sensor.

14.7 Ethanol Vapor Sensor by Composite Plasmonic Waveguide

Now a day, ethanol (CH_3CH_2OH) is one of the most important constituents in daily life, from chemical and pharmaceutical products to heavy engineering and fuel industries. Mixing of excessive ethanol vapor with air may cause explosive fire with an easy ignition. Only 3.5% ethanol vapor in the air can causes fire explosions, and

this often called as *lower explosion limit* (LEL). On the other hand, the upper explosion limit (UEL) of ethanol is 19% [62]. Therefore, for accurate sensing of ethanol vapor in the industrial environment several sensing mechanisms can be considered, such as spectrometric sensing, electrochemical, sloid state semiconductor and microcontroller based devices. However, the dielectric waveguide based interferometric and resonating sensing devices are more convenient for its high precision sensitivity and compactness. Here a horizontal slotted composite plasmonic waveguide (CPWG) is designed and its performance has been rigorously investigated by incorporating it into a Mach-Zehnder interferometer (MZI) device. The novel CPWG is composed of lossy silver (Ag) layer, porous ZnO (P-ZnO), silicon (Si) and silica (SiO_2). The P-ZnO layer is sandwiched in between metal and high index Si, shown in Fig. 14.26a. This novel waveguide structure guides the light through its low index slot region as a supermode that is a coupled form of the surface plasmon (SP) mode and dielectric waveguide mode. Surface plasmon polaritons (SPPs) are the surface waves tightly confined at the metal-dielectric interfaces. The SP mode is TM-polarized in nature and that can be excited either by electrons or photons having same frequency and momentum. Here the CPWG is designed and optimized for the widely used telecommunication wavelength, $\lambda =$ 1550 nm. This waveguide supports both quasi-TE and TM modes. However, the plasmonic supermode which is quasi-TM polarized is concentrated in the low index region, whereas, the quasi-TE mode is guided by the high index Si core. The analytical and semi-analytical solutions to exploit the hybrid plasmonic mode is not so easy. Thus, a full-vectorial **H**-field based modified FEM is used as a computational tool for the device design and performance analyses. For accurate simulations, the one-fold symmetry of the CPWG is discretized with 1,280,000 triangular elements. A much higher mesh density is used near the metal-dielectric interfaces to resolve the sub-wavelength SP field confinements. The optical properties of the silver (Ag), Si and SiO_2 are taken as $n_{Ag} = 0.13880 + \mathrm{j}\ 11.310$ [63], $n_{Si} = 3.4757$ [64] and $n_{SiO_2} = 1.4440$ at the operating wavelength of 1550 nm. The electromagnetic boundary condition at the material interface demands the continuity of the normal component of electric flux density (**D**) at the interface that results in an enhanced E_y-field discontinuity at that interface. The FV-FEM simulated E_y and H_x field components of the fundamental quasi-TM mode are shown in the Fig. 14.26b, c, respectively.

The porous ZnO (P-ZnO) is used as a low index medium which shows a comparative lower index than that of bulk ZnO, as the P-ZnO contains air ($n_{air} = 1$) pores. To make the waveguide efficient for sensing, different types of P-ZnO layer templates can be used, such as porous flakes composed of ZnO spheres, P-ZnO nanosheets, and nanoplates. All these P-ZnO templates are mesoporous where the pore diameters are ranging from 2 to 50 nm. Different templates show its best response and selectivity at different operating temperatures. The P-ZnO sphere layer shows a great selective response to 100 ppm ethanol at 280 °C [65]. Similarly, the strong ethanol selectivity can be observed around 400–450 °C for nanosheets [66] and nanoplates [67], respectively. Thus, in terms of selectivity, all these P-ZnO

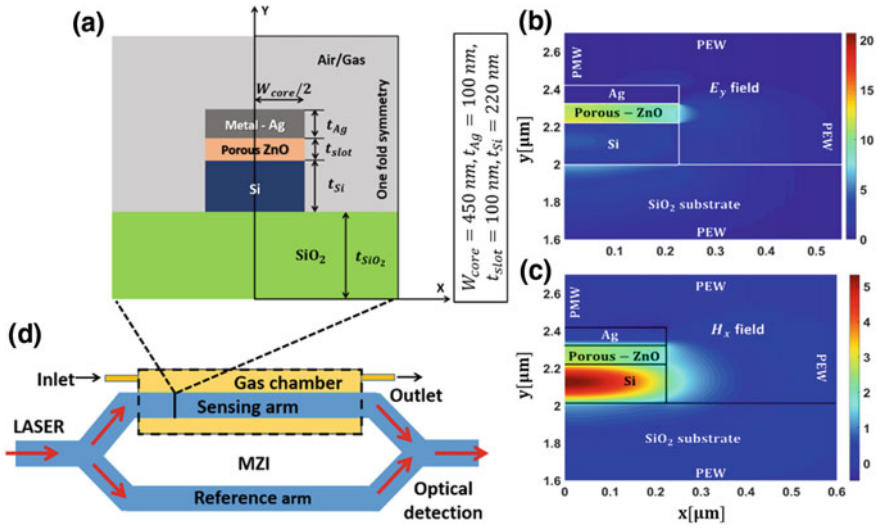

Fig. 14.26 Schematic diagram of a horizontal slotted CPWG and its simulated field distributions, **a** shows the waveguide cross-section. One-fold symmetry of the structure is used for FV-FEM simulations. **b** and **c** are the E_y and H_x field profiles of fundamental quasi-TM mode (H_x^{11}), respectively. **d** Shows a compact, integrated Mach-Zehnder set-up where the CPWG is used in the interferometer arms. From [70]

configurations show excellent ethanol selectivity compared to methanol, acetone, chlorobenzene, and methane at 280, 400 and ~450 °C. When the porous layer is placed in the target analyte vapor, the void pores are then filled with the condensed analyte ($n > 1$). Depending on different volume fraction of absorbed and condensed ethanol, the equivalent index as well as the dielectric constant of P-ZnO changes. To determine the effective refractive index of P-ZnO and the equivalent refractive index of ethanol absorbed P-ZnO, the Lorentz-Lorenz model [68] is used.

$$\frac{n_e^2-1}{n_e^2+2} = (1-P)\left(\frac{n_c^2-1}{n_c^2+2}\right) + (P-V)\left(\frac{n_a^2-1}{n_a^2+2}\right) + V\left(\frac{n_d^2-1}{n_d^2+2}\right) \tag{14.7.1}$$

Here P denotes the number of pores per unit volume, called *porosity* of the medium and V is the volume fraction of liquid after capillary condensation. n_a, n_c and n_d represent the refractive index of air ($n_a = 1$), homogeneous (bulk ZnO) and dispersed medium (condensed vapor), respectively. For the investigations, the P-ZnO layer of porosity $P = 30$, 40, 50 and 60% are considered. Corresponding refractive index variations ($n_{P-\mathrm{ZnO}}$) and equivalent refractive index of the P-ZnO with respect to the different volume fraction of ethanol are shown in Fig. 14.27. As expected, the $n_{P-\mathrm{ZnO}}$ decreases with the increasing porosity in the medium shown by the black solid line. Additionally, while the P-ZnO pores are replaced by the condensed ethanol the equivalent index of refraction increases for P-ZnO layers

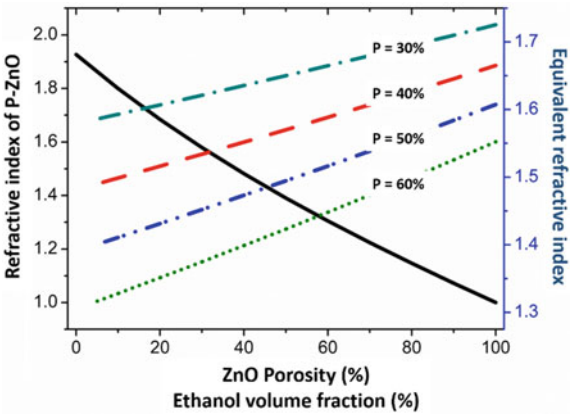

Fig. 14.27 Refractive index variation with ZnO porosity (P) and change of equivalent refractive index of P-ZnO layer with volume fraction (V) of condensed ethanol. From [70]

with P = 30, 40, 50 and 60%. The lower porosity (P = 30%) shows higher equivalent refractive index than the higher porosity (P = 60%). At ambient temperature (20 °C), the bulk ZnO refractive index is taken as 1.9267, derived from the dispersion formula in [69] and the condensed ethanol refractive index is derived by using the Sellmeier equation.

$$n^2(\lambda) - 1 = \frac{A_1\lambda^2}{\lambda^2 - B_1} + \frac{A_2\lambda^2}{\lambda^2 - B_2} \tag{14.7.2}$$

Here $A_{1,2}$ and $B_{1,2}$ denotes the material property parameters and absorption wavelengths. The constant values used for the analysis are, $A_1 = 0.83189$, $A_2 = -0.15582$, $B_1 = 0.00930\ \mu m^{-2}$ and $B_2 = -49.45200\ \mu m^{-2}$.

To obtain a high sensitive accurate CPWG, its design parameters, such as core width (W_{core}) and low index slot thickness (t_{slot}) are needed to be optimized carefully. For simplicity, fixed Si nanowire height and top Ag layer thickness have been considered as 220 nm and 100 nm, respectively. Figure 14.28 shows the power confinement variations of the fundamental quasi-TM and TE modes with slot thickness (t_{slot}) for three different CPWG core width, W_{core} = 350, 450, and 550 nm. For all three CPWG core widths the quasi-TM power confinements (Γ_{TMslot}), shown by solid lines, increase with t_{slot} increment, reach a maximum value of 41.79% at $t_{slot} = 70$ nm and then decrease gradually with further increment of t_{slot}. It can also be seen that the $W_{core} = 450$ nm, shown by the red solid line, confines higher optical power than other two core widths (350 and 550 nm). Additionally, the quasi-TE power confinement (Γ_{TEslot}), shown by dashed-dotted lines, increases with the increment of t_{slot}. But these values are much lower than the TM mode confinement. The curves for all three core widths intersect each other at 68 nm and exhibits only 3.56% power confinement. Thus, optimized t_{slot} value is taken as 70 nm with maximum power confinement in the slot region. Furthermore, the optimization of core width (W_{core}) has been carried out for two different t_{slot} = 70 and 100 nm and the results are presented in Fig. 14.29. As the W_{core} increase the

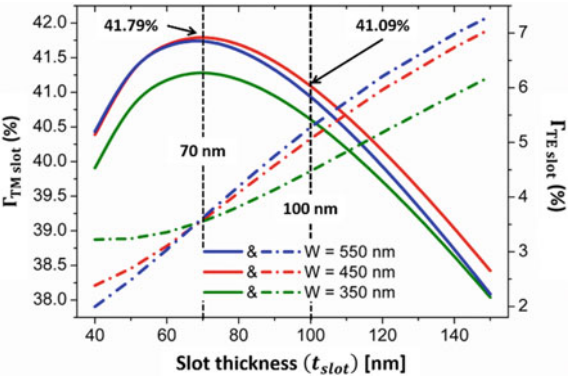

Fig. 14.28 Quasi-TM and TE slot confinement variations with slot thickness (t_{slot}). The TM and TE slot confinement for three different core widths, W_{core} = 350, 450 and 550 nm are denoted by solid and dashed-dotted green, red and blue lines, respectively. From [70]

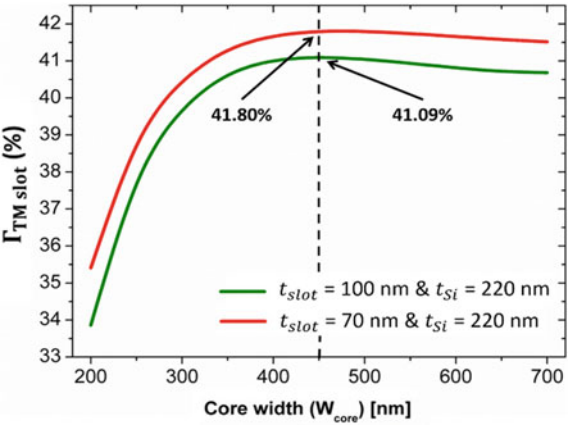

Fig. 14.29 Quasi-TM slot confinement (Γ_{TMslot}) with respect to the CPWG core width (W_{core}) for two different slot thicknesses. The red and green lines denote the same variations for t_{slot} = 70 nm and 100 nm, respectively. An over 41% power confinement is observed for W_{core} = 450 nm at t_{slot} = 70 nm and 100 nm. From [70]

Γ_{TMslot} grows and confines maximum 41.80% and 41.09% TM energy into 70 and 100 nm slots, respectively at W_{core} = 450 nm. From both the figures, it can be observed that a 100 nm slot can confine 41.09% power in the low index region. As the t_{slot} = 70 nm and 100 nm show a small difference in Γ_{TMslot} and a few nanometers extra wide may be convenient to accommodate more numbers of pores in mesoporous ZnO layer as well as be easier to fabricate. Thus, finally the optimized t_{slot} is considered as 100 nm.

Next, the efficiency of ethanol vapor detection with the help of CPWG is analyzed. The quasi-TM and TE real effective index difference ($\Delta Re(n_{eff})$) of the CPWG with the volume fraction of ethanol for different P-ZnO are shown in Fig. 14.30. The solid lines in the main figure and dashed lines in the inset represent the TM-$\Delta Re(n_{eff})$ and TE-$\Delta Re(n_{eff})$ variations, respectively. Both the effective index difference between TM and TE modes increase with the increment of the volume fraction of ethanol. The higher porosity (60%) shows better effective index difference than that of lower porosity (30%) P-ZnO. Furthermore, the $\Delta Re(n_{eff})$ for TM mode shows much higher values than that for the TE mode. This indicates that

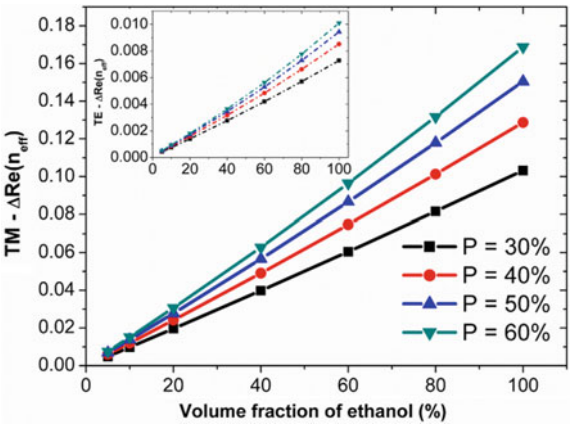

Fig. 14.30 Quasi-TM and TE effective index changes ($\Delta Re(n_{eff})$) against volume fraction of ethanol into P-ZnO layer. The black, red, blue and green solid and dashed lines in main and inset depict the TM and TE modal effective index change due to different volume fraction of ethanol into 30%, 40%, 50% and 60% porous P-ZnO layers, respectively. From [70]

the hybrid plasmonic quasi-TM mode is more sensitive in compare to the quasi-TE mode. Figure 14.31a, b depict the waveguide TM modal sensitivity variations for both real and imaginary effective index. The black, red, blue and cyan markers denote the real effective index sensitivity ($S_{Re(TM)} = \Delta Re(n_{eff})/\Delta n_{slot}$) and normalized attenuation sensitivity ($S_{Im(TM)} = \Delta Im(n_{eff})/\Delta n_{slot}$) of the fundamental quasi-TM mode for porosity, $P = 30\%$, 40%, 50% and 60%, respectively. For each P-ZnO layer the $S_{Re(TM)}$ and $S_{Im(TM)}$ initially decreases up to ~15% of ethanol absorption and then increases with the increase of volume fraction of ethanol. The sensitivity curves also indicate that the P-ZnO layer with lower porosity ($P = 30\%$) shows higher $S_{Re(TM)}$ and $S_{Im(TM)}$ than that of the higher porosity ($P = 60\%$). In case of waveguide based sensor, the $S_{Re(TM)}$ is much important than $S_{Im(TM)}$ and here a much higher $S_{Re(TM)}$ (≈0.71 per RIU) can be obtained with this novel design CPWG. Besides, the Fig. 14.31b depicts that the $S_{Im(TM)}$ is significantly less sensitive to slot refractometric changes.

Effective index change of the CPWG due to analyte's refractometric variation is the only detectable parameter for a waveguide-based sensor. Thus, for accurate measurement of this effective index change, a compact Mach-Zehnder interferometer (MZI) can be used as a transducer device. The MZI schematic diagram is shown in Fig. 14.26d where the designed and optimized CPWG is incorporated in MZI arms. One arm is passed through the ethanol vapor chamber to measure the volume fraction of ethanol, is called *sensing arm* and other is used as a *reference arm*. The phase difference between both arms can be derived from the detectable effective index change $\Delta Re(n_{eff})$ due to a different percentage of absorption of ethanol into P-ZnO.

$$\Delta\phi = \frac{2\pi}{\lambda} \cdot \Delta Re(n_{eff}) \cdot L \tag{14.7.3}$$

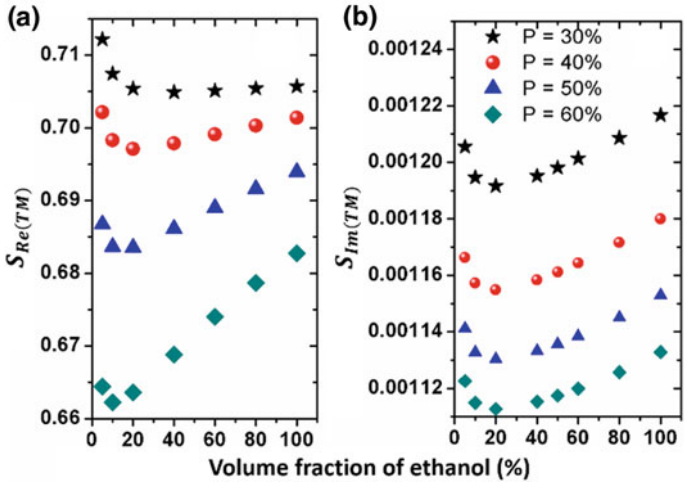

Fig. 14.31 **a** and **b** present the quasi-TM real effective index sensitivity ($S_{Re(TM)}$) and normalized attenuation sensitivity ($S_{Im(TM)}$) variations with volume fraction of ethanol, respectively. The black, red, blue and cyan markers on both figures denote the sensitivity variation with absorbed ethanol into low index P-ZnO slot with porosity, P = 30%, 40%, 50% and 60%, respectively. From [70]

Here L denotes the CPWG arm length. A π phase difference between reference and sensing arm makes a destructive interference with a zero MZI output. By using the fact in Eq. 14.7.3 the MZI arm lengths are calculated as 7.51, 6.02, 5.15 and 4.59 μm for each type of P-ZnO layer having porosity P = 30%, 40%, 50% and 60%, respectively. Thus, higher porosity gives higher Δn_{eff} that results in shorter MZI length (L). All these CPWG incorporated MZI arms show a much low propagation loss around 0.2 dB for each aforementioned arm lengths. It can also be seen that with and without ethanol vapor absorption the waveguide modal loss changes in PWG incorporated MZI arms are 0.045 dB for P = 30%, 40% and 50% and 0.047 dB for P = 60%, respectively. Often it is assumed that the attenuation (α) of the incorporated waveguide is same for both MZI waveguides. However, in case of the CPWG in sensing, both the sensing and reference arms may show different attenuations, $\alpha_{ref} = \alpha$ and $\alpha_{sen} = \alpha \pm \Delta\alpha_{sen}$, respectively. It is considered that the sensing waveguide arm attenuation is modified by a small change $\Delta\alpha_{sen}$ due to different absorption levels of ethanol vapor. Therefore, including this attenuation change, the normalized power output of the MZI can be expressed as [70]

$$P_{norm} = \frac{1}{2} e^{-2\alpha L} e^{-\Delta\alpha_{sen} L} cosh(\Delta\alpha_{sen} L)(1 + Fcos\Delta\phi) \qquad (14.7.4)$$

Here, the parameter F is defined as the interferometric fringe contrast and it can be defined as, $F = 1/\cosh(\Delta\alpha_{sen} L)$. Additionally, a part of the Eq. 14.7.4 could be

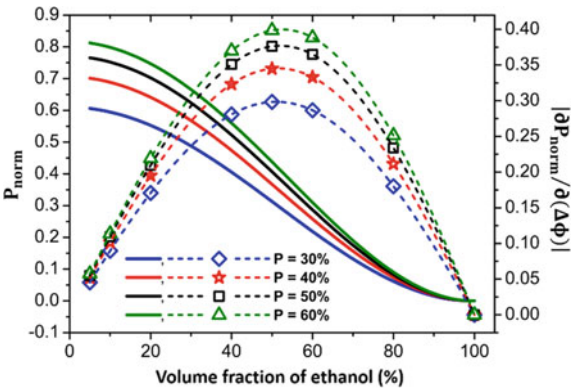

Fig. 14.32 Normalized power output (P_{norm}) and phase sensitivity ($|\partial P_{norm}/\partial(\Delta\phi)|$) variations of the MZI against volume fraction of ethanol absorbed into P-ZnO layer. The blue, red, black and green solid and dashed lines with markers denote the cosine natured P_{norm} and sinusoidal $|\partial P_{norm}/\partial(\Delta\phi)|$ variations for different porosity, $P = 30\%$, 40%, 50%, and 60%, respectively. From [49]

termed as *power fraction*, $PF = e^{-\Delta\alpha_{sen}L}cosh(\Delta\alpha_{sen}L)$. It denotes the sensing arm power increment or decrement compared to reference arm waveguide. The P_{norm} is the only measurable parameter of the MZI that changes with the resulting phase difference. Thus, the MZI phase sensitivity could be defined as

$$\frac{\partial P_{norm}}{\partial(\Delta\phi)} = -\frac{1}{2}e^{-(2\alpha+\Delta\alpha_{sen})L}cosh(\Delta\alpha_{sen}L)Fsin(\Delta\phi) \tag{14.7.5}$$

In this CPWG incorporated MZI, the balance between both arms may break due to different attenuations ($\alpha_{ref} \neq \alpha_{sen}$). Hence to make the device error free the attenuation in both arms should be controlled such that it does not interfere with the MZI balance. In this design, for all the volume fractions of ethanol into P-ZnO having porosity, $P = 30$, 40, 50, and 60%, the fringe contrast is ~0.99 and the power fraction (PF) is ~0.96 ($F \approx PF \approx 1$). Thus, the extra attenuation change in the sensing waveguide is very small to cause any noticeable effect in the MZI performance. The Fig. 14.32 depicts the normalized power (P_{norm}) and absolute value of the phase sensitivity ($|\partial P_{norm}/\partial(\Delta\phi)|$) variations with respect to the volume fraction of ethanol for different P-ZnO layers. The results indicate that 100% ethanol vapor absorption in sensing arm makes a π phase difference with zero output and a minimum 5% volume fraction of ethanol provides a minimum phase difference with maximum 60%, 70%, 76%, and 81% light output for 30%, 40%, 50%, and 60% P-ZnO, respectively. The high porosity in P-ZnO provides better light output. Blue, red, black and green markers with dashed lines show a sinusoidal variation of phase sensitivity for all four P-ZnO layers. The higher porosity ($P = 60\%$) shows better phase sensitivity than that of the lower porosity ($P = 30\%$). It can also be seen that for all P-ZnO layers with different porosity, $P = 30\%$, 40%, 50% and 60% exhibit maximum phase sensitivities of 0.30, 0.34, 0.38 and 0.40 when 51.57%, 52.05%, 52.59% and 53.16% of the P-ZnO pores are filled by the condensed ethanol, respectively when an exact $\pi/2$ phase difference is observed in between sensing and the reference arms. Thus, with the help of numerically

simulated investigation a label-free ethanol vapor or gas sensor using a coupled SPP and dielectric field confined in a low index horizontal slot is designed and demonstrated.

14.8 Conclusions

In this chapter, a range of compact micro and nano dimensioned integrated optical sensors are designed and optimized its performance for biochemical and gas sensing applications. The results suggest that the on-chip integrated dielectric, plasmonic and composite plasmonic waveguides and resonators have a great potential to be used for high precision sensing and detection technologies. Different numerical methods, such as 2D-FEM, 3D-FEM, and LSBR have been formulated and successfully used to analyse these photonic devices.

Recently published works on slot-waveguide based photonic devices have proved their advantages over conventional waveguides in many ways, such as enhanced and easy-accessible low index light confinement for sensing, trapping, manipulation of nanoparticles, biomolecules and opto-mechanical transducers. These exotic waveguides and resonators could be easily realized by CMOS compatible high index contrast materials and noble metals, such as Si/SiO_2, Si_3N_4/SiO_2, and SOI in combination with Au, and Ag metals. The reported applications in refractive index based liquid and gas detection, labeling-based and label-free biochemical detection, optical trapping, transport and manipulation bio-molecules lead us to a progressive improvement of nano-bio technology. However, standardization and commercialization of these devices require further attention on improved waveguiding design schemes, material engineering, modern sensing architectures, compatibility and assembly of photonic devices with electronic devices, and real-time signal processing.

References

1. E.A.J. Marcatili, Dielectric rectangular waveguide and directional coupler for integrated optics. Bell Syst. Tech. J. **48**, 2071–2102 (1969)
2. J.E.A. Goell, A circular-harmonic computer analysis of rectangular dielectric waveguides. Bell Syst. Tech. J. **48**, 2133–2160 (1969)
3. R.M. Knox, P.P. Toulios, Integrated circuits for the millimeter through the optical frequency range, in *Proceedings of the Symposium on Submillimeter Waves* (Poly Inst., Brooklyn, 1970), pp. 497–516
4. E.K. Sharma, A.K. Ghatak, I.C. Goyal, Matrix method for determining propagation characteristics of optical waveguides. IEEE J. Quantum Electron. **19**, 1231–1233 (1983)
5. N. Dagli, C.G. Fonstad, Analysis of rib dielectric waveguide. IEEE J. Quantum Electron. **21**, 315–321 (1985)
6. K.N. Bierwirth, M. Schulz, F. Arndt, Finite-difference analysis of rectangular dielectric waveguide structures. IEEE Microwave Theory Technol. **MTT-34**, 1104–1114

7. M.S. Stern, P.C. Kendall, P.W.A. Mcllroy, Analysis of the spectral index method for vector modes of rib waveguides. Proc IEEE J. Optoelectron. **137**, 21–26 (1990)
8. U. Rogge, R. Pregla, Method of lines for analysis of strip-loaded optical waveguides. J Opt. Soc. Am. B **8**, 459–463 (1991)
9. B.M.A. Rahman, J.B. Davies, Finite-element solution of integrated optical waveguides. J. Lightwave Technol. **2**, 682–688 (1984)
10. B.M.A. Rahman, J.B. Davies, Penalty function improvement of waveguide solution by finite-element. IEEE Trans. Microwave Theory Technol. **32**, 20–28 (1984)
11. P.P. Silvester, R.L. Ferrari, *Finite Elements for Electrical Engineers* (Cambridge University Press, 1990)
12. A.D. Berk, Variational principles for electromagnetic resonators and waveguides. IRE Trans. Antennas Propag. **4**, 104–111 (1956)
13. K.T.V. Grattan, T. Sun, Fiber optic sensor technology: an overview. Sens. Actuator A-Phys. **82**, 41–61 (2000)
14. L.S. Grattan, B.T. Meggitt (eds.), *Optical Fiber Sensor Technology: Fundamentals* (Springer, US, 2001)
15. Y. Saito, Y. Kanaya, A. Nomura, T. Kano, Experimental trial of a hollow-core waveguides used as an absorption cell for concentration measurement of NH_3 gas with a CO_2 laser. Opt. Lett. **18**, 2150–2152 (1993)
16. C.A. Barrios et al., Slot-waveguide biochemical sensor. Opt. Lett. **32**, 3080–3082 (2007)
17. C.A. Barrios et al., Label-free optical biosensing with slot-waveguides. Opt. Lett. **33**, 708–710 (2008)
18. V.M.N. Passaro et al., Efficient chemical sensing by coupled solt SOI waveguides. Sensors **9**, 1012–1032 (2009)
19. R.J. McCosker, G.E. Town, Optical chemical sensor using a multi-channel directional coupler with slot waveguides, in *International Conference on Photonics* (ICP) (2010), pp. 1–5
20. F. Dell`Olio, V.M.N. Passaro, Optical sensing by optimized silicon slot waveguides. Opt. Express **15**, 4977–4993 (2007)
21. L. Vivien et al., Vertical multiple-slot waveguide ring resonators in silicon nitride. Opt. Express **16**, 17237–17242 (2008)
22. X. Tu et al., Thermal independent Silicon-nitride slot waveguide biosensor with high sensitivity. Opt. Express **20**, 2640–2648 (2012)
23. A. Kargar, C.Y. Chao, Desigh and optimization of waveguide sensitivity in slot microring sensors. J. Opt. Am. A **28**, 596–602 (2011)
24. I. Khodadad et al., Optimization of multiple-slot waveguides for biochemical sensing. App. Opt. **53**, 5169–5178 (2014)
25. T. Claes et al., Label-free biosensing with a slot-waveguide-based ring resonator in silicon on insulator. IEEE Photonics J. **1**, 197–204 (2009)
26. J.I. Kou, F. Xu, Y. Lu, Loop-mirror-based slot waveguide refractive index sensor. AIP Adv. **2**, 042142-1–042142-6 (2012)
27. Q. Liu et al., Highly sensitive Mach-Zehnder interferometer biosensor based on silicon on nitride slot waveguide. Sens. Actuator B-Chem. **188**, 681–688 (2013)
28. Q. Liu et al., A refractive index sensor design based on grating-assisted coupling between a strip waveguide and a slot waveguide. Opt. Express **21**, 5897–5909 (2012)
29. G.D. Osowiecki et al., Vertically coupled plasmonic slot waveguide cavity for localized biosensing applications. Opt. Express **22**, 20871–20880 (2014)
30. X. Sun et al., High-sensitivity liquid refractive-index sensor based on a Mach-Zehnder interferometer with a double-slot hybrid plasmonic waveguide. Opt. Express **23**, 25688–25699 (2015)
31. X. Sun et al., Double-slot hybrid plasmonic ring resonator used for optical sensors and modulators. Photonics **2**, 1116–1130 (2015)
32. W. Zhou, Fully suspended slot waveguides for high refractive index sensitivity. Opt. Lett. **42**, 1245–1248 (2017)

33. L. Zhou, Miniature microring resonator sensor based on a hybrid plasmonic waveguide. Sensors **11**, 6856–6867 (2011)
34. X. Wang, C.K. Madsen, Highly sensitive compact refractive index sensor based on phase-shifted sidewall Bragg gratings in slot waveguide. App. Opt. **53**, 96–103 (2014)
35. J.T. Robinson, L. Chen, M. Lipson, On-chip gas detection in silicon optical microcavities. Opt. Express **16**, 4296–4301 (2008)
36. B. Kumari et al., Silicon-on-nitride slot waveguide: a promising platform as mid-IR trace gas sensor. Sens. Actuator B-Chem. **236**, 759–764 (2016)
37. B. Kumari, R.K. Varshney, B.P. Pal, Design of chip scale silicon rib slot waveguide for sub-ppm detection of N_2O gas at mid-IR band. Sens. Actuator B-Chem. **255**, 3409–3416 (2018)
38. V.R. Almeida et al., Guiding and confining light in void nanostructure. Opt. Lett. **29**, 1209–1211 (2004)
39. T. Dar, J. Homla, B.M.A. Rahman, M. Rajarajan, Label-free slot-waveguide biosensor for the detection of DNA hybridization. Appl. Opt. **51**, 8195–8202 (2012)
40. C. Koos et al., All-optical high-speed signal processing with silicon-organic hybrid slot waveguides. Nat. Photonics **3**, 216–219 (2009)
41. C. Viphavakit, M. Komodromos, C. Themistos et al., Optimization of a horizontal slot waveguide biosensor to detect DNA hybridization. Appl. Opt. **54**, 4881–4888 (2015)
42. C. Pan, B.M.A. Rahman, High-sensitivity polarization-independent biochemical sensor based on silicon-on-insulator cross-slot waveguide. IEEE J. Sel. Top. Quantum Electron. **23**, 64–71 (2017)
43. R. Sun et al., Horizontal single and multiple slot waveguides: optical transmission at $\lambda =$ 1550 nm. Opt. Express **15**, 17967–17972 (2007)
44. S. Lee et al., A silicon nitride microdisk resonator with a 40-nm-thin horizontal air slot. Opt. Express **18**, 11209–11215 (2010)
45. S. Lee et al., Label-free optical biosensing using a horizontal air-slot SiN_x microdisk resonator. Opt. Express **18**, 20638–20644 (2010)
46. J. Chee, S. Zhu, G.Q. Lo, CMOS compatible polarization splitter using hybrid plasmonic waveguide. Opt. Express **20**, 25345–25355 (2012)
47. A. Gupta, D. Akin, R. Bashir, Detection of bacteria cells and antibodies using surface micromachined thin silicon cantilever resonators. J. Vac. Sci. Technol. B **22**, 2785–2791 (2004)
48. K.D. Vos et al., SOI optical microring resonator with poly (ethylene glycol) polymer brush for label-free biosensor applications. Biosens. Bioelectron. **24**, 2528–2533 (2009)
49. S. Ghosh, B.M.A. Rahman, An innovative straight resonator incorporating a vertical slot as an efficient bio-chemical sensor. IEEE J. Sel. Top. Quantum Electron. **23**, 132–139 (2017)
50. S.H. Yang et al., Giant birefringence in multi-slotted silicon nanophotonic waveguides. Opt. Express **16**, 8306–8316 (2008)
51. Sucrose Conversion Table, File code 135-A-50, United States Department of Agriculture (USDA) (1981)
52. B.M.A. Rahman, J.B. Davies, Analysis of optical waveguide discontinuities. J. Lightwave Technol. **6**, 52–57 (1988)
53. S.A. Kumar, S.M. Chen, Nanostructured zinc oxide particles in chemically modified electrodes for biosensor applications. Anal. Lett. **41**, 141–158 (2008)
54. Z.K. Tang et al., Room-temperature ultraviolet laser emission from self-assembled ZnO microcrystallite thin films. Appl. Phys. Lett. **72**, 3270–3272 (1998)
55. M. Law et al., Nanowire dye-sensitized solar cells. Nat. Mater. **4**, 455–459 (2005)
56. A. Janotti, C.G. Van de Walle, Fundamentals of zinc oxide as a semiconductor. Rep. Prog. Phys. **72**, 126501 (2009)
57. P.G. Etchegoin, E.C. Le Ru, M. Meyer, An analytic model for the optical properties of gold. J. Chem. Phys. **125**, 164705 (2006)
58. G.E. Jellison, L.A. Boatner, Optical functions of uniaxial ZnO determined by generalized ellipsometry. Phys. Rev. B **58**, 3586–3589 (1998)

59. J. Han et al., Optical and dielectric properties of ZnO tetrapod structures at terahertz frequencies. Appl. Phys. Lett. **89**, 031107 (2006)
60. Y. Chen, C.L. Zhu, G. Xiao, Reduced-temperature ethanol sensing characteristics of flower-like ZnO nanorods synthesized by a sonochemical method. Nanotechnology **17**, 4537 (2006)
61. N.T. Kejalakshmy, K.T.V. Grattan, B.M.A. Rahman, Investigation of the optical model properties of Al^{+3} doped ZnO-coated Au waveguide for gas sensing applications using the finite element method. IEEE Sens. J. **16**, 1176–1181 (2015)
62. L. Gas, Lower and upper explosive limits for flammable gases and vapors. Matheson Gas Products (2013)
63. S. Babar, J.H. Weaver, Optical constants of Cu, Ag and Au revisited. Appl. Opt. **54**, 477–481 (2015)
64. H.H. Li, Refractive index of silicon and germanium and its wavelength and temperature derivatives. J. Phys. Chem. Ref. Data **9**, 561–658 (1980)
65. W. Wang, Ethanol sensing properties of porous ZnO spheres via hydrothermal route. J. Mater. Sci. **48**, 3232–3238 (2013)
66. L. Zhang et al., Facile synthesis and ultrahigh ethanol response of hierarchically porous ZnO nanoplates. Sens. Actuators B Chem. **54**, 3–15 (1999)
67. Z. Jiang, J. Zhan, Fabrication and gas-sensing properties of porous-ZnO nanoplates. Adv. Mater. **161**, 209–215 (2012)
68. A. Garahan, L. Pilon, J. Yin et al., Effective optical properties of absorbing nanoporous and nanocomposite thin films. J Appl. Phys. **101**, Art no 014320 (2007)
69. W.L. Bond, Measurement of the refractive indices of several crystals. J. Appl. Phys. **36**, 1674–1677 (1965)
70. S. Ghosh, B.M.A. Rahman, A compact Mach-Zehnder interferometer using composite plasmonic waveguide for ethanol vapor sensing. J. Lightwave Technol. **35**, 3003–3011 (2017)

Chapter 15
Silicon Ring Resonator-Based Biochips

S. Werquin, J.-W. Hoste, D. Martens, T. Claes and P. Bienstman

Abstract This chapter discusses the use of silicon photonics biochips incorporating ring resonator sensors. After an introduction to the ring sensor, we will discuss other aspects like peak splitting compensation, the exploitation of the Vernier effect for increased sensitivity, and the use of dual-polarization rings to determine conformational information.

Keywords Biosensors · Ring resonators · Silicon-on-insulator

15.1 Introduction

The emergence of silicon-on-insulator (SOI) optical biosensors is based on the possibility to manufacture at wafer scale and therefore at low-cost micrometer-sized waveguides and circuits on a silicon chip surface.

The application of SOI optical biosensors provides a number of advantages. The sensors can be made exceptionally small because of the large refractive index contrast of the material. This allows for the fabrication of dense and multiplexed label-free sensor arrays that provide real-time affinity information for the interaction between the analyte and the receptor molecules on the chip surface. By modifying the surface by the correct receptors, the sensor can respond selectively to a wide variety of target molecules. The high intensity of the optical mode at the waveguide surface explains the very high sensitivity of SOI biosensors. Reported applications range from nucleic acid detection, over proteins to the detection of entire pathogens like viruses.

Integrated photonic waveguide circuits have first been developed for the telecommunications industry. To benefit from the extensive experience from this field, the

S. Werquin · J.-W. Hoste · D. Martens · T. Claes · P. Bienstman (✉)
Ghent University-imec, Ghent, Belgium
e-mail: Peter.Bienstman@UGent.be

© Springer International Publishing AG, part of Springer Nature 2019

M. F. O. Hameed and S. Obayya (eds.), *Computational Photonic Sensors*, https://doi.org/10.1007/978-3-319-76556-3_15

first integrated optical biosensors also made use of infrared light from the telecom wavelength region around 1550 nm.

The rest of this chapter is structured as follows. First section introduces one of the main workhorses of biosensing in SOI: the microring resonator. The next sections will discuss a number of refinements, like peak splitting compensation, the exploitation of the Vernier effect for increased sensitivity, and the use of dual-polarization rings to determine conformational information.

15.2 Sensing with Microring Resonators

In this section, we will introduce the principles of guiding light in integrated waveguides. Evanescent field sensing with microring resonators is discussed, and some applications of microrings as label-free biosensors are provided.

15.2.1 Photonic Waveguides

Integrated silicon waveguides are much like the optical fibers used for data transfer, only smaller. An optical waveguide consists of a high refractive index core and a low refractive index cladding. Light is preferentially concentrated in the high index core, with a small fraction of its power extending into the cladding regions. For light with a wavelength of 1550 nm, the SOI material system shows an exceptionally high index contrast. The silicon waveguide core has a refractive index of 3.47, while the silica bottom cladding has an index of only 1.44. For most sensing applications, the top cladding will typically consist of aqueous solutions like serum- or water-based buffers with refractive indices around 1.31. Light that propagates through an invariant waveguide without changing its transversal shape is called a waveguide mode. Such a mode is characterized by an invariant transversal intensity profile and an effective index. The effective index of a mode is the ratio between the vacuum speed of light and the phase velocity of the propagating light. It represents how strongly the optical power is confined to the waveguide core. Optical modes with an effective index higher than the largest cladding index are guided modes. Modes with lower index are radiating, and the optical power will leak to the cladding regions. The waveguide dimensions determine which modes can exist. Most waveguides support modes of two independent polarizations, with either the major magnetic (quasi-TM) or electric (quasi-TE) field component along the transverse (horizontal) direction. For most biosensing applications, it is preferable that the waveguides operate in a single-mode regime for each polarization. This single-mode regime is obtained by reducing the waveguide dimensions until all but the fundamental waveguide modes become radiating. As an example, we have included an image of the cross section of a silicon wire waveguide with the corresponding distribution of the power of the fundamental optical mode in Fig. 15.1. For any waveguide geometry, part of the

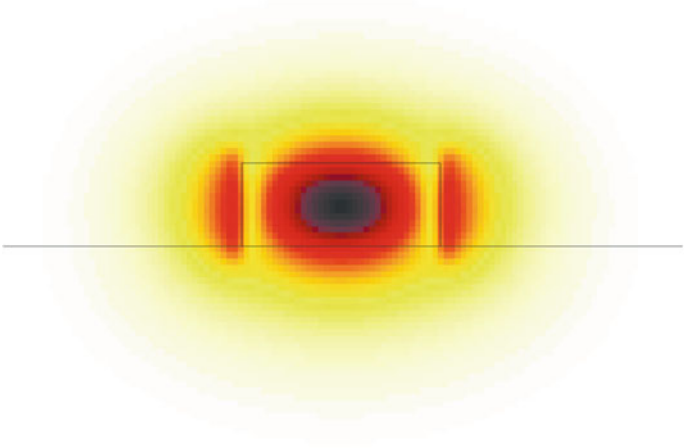

Fig. 15.1 Cross section of a silicon-on-insulator wire waveguide with the intensity distribution of the fundamental quasi-TE mode

optical mode power is confined to the silicon waveguide core. The remaining power is located in the cladding regions. For guided modes, the intensity in the cladding region decays exponentially with increasing distance to the core. It is this evanescent tail of the mode that can sense changes in the waveguide vicinity. The binding of biomolecules to the waveguide will locally change the surrounding refractive index which results in a changing effective index of the optical mode. To inspect the interaction between an optical mode and its environment, waveguides can be used in resonant structures with highly wavelength-dependent behavior.

15.2.2 Microring Resonators

The high index contrast of SOI waveguides allows the fabrication of micrometer size bends. The possibility to create very small ring resonators has made them one of the successful applications of silicon photonics. Because of their unprecedented small size and wide applicability, silicon microring resonators have been the subject of many scientific publications. In this section, we will discuss the characteristics of microring resonators that make them ideal candidates for biosensing transducers.

A microring resonator consists of a closed circular waveguide. A light wave propagating through a microring waveguide will interfere with itself after one roundtrip. When this interference is constructive, the light will start to resonate in the ring. The resonance condition for constructive interference is satisfied when the phase difference after one roundtrip amounts to an integer times 2π. This means the wavelength

of the optical mode has to fit an integer times in the roundtrip length of the ring. We can thus express the resonance condition as follows:

$$\lambda_{res} = \frac{n_{eff} L}{m}, m \in \mathbb{N} \tag{15.1}$$

A microring resonator will have an infinite number of resonances, one for every solution of the resonance condition. To address the resonator, connections to access waveguides are needed. Typically, these connections are made by including directional coupler sections. A directional coupler is a region where two waveguides are in close proximity. The evanescent tails of the fields in the waveguide will feel the presence of the other waveguide and coupling between both can occur. The strength of the coupling will depend on the overlap between both waveguide modes and the length of the coupler. Based on the number of access waveguides, we will consider two configurations of microring resonators that can be used for biosensing applications. If only a single access waveguide is present, the resonator is called an all-pass resonator. A microring with two access waveguides is an add-drop or channel-drop resonator. Both configurations are discussed in more detail in the next sections.

15.2.2.1 All-Pass Ring Resonators

A ring resonator with one access waveguide is in the all-pass configuration. A schematic representation is given in Fig. 15.2. A fraction k of the input field couples to the ring in the directional coupler. On resonance, the light in the ring interferes constructively and power in the resonator builds up. Light coupling back from the ring to the waveguide will then interfere destructively with the remainder of the input light that is transmitted by the directional coupler. For undercoupled microrings holds: the higher the losses in the resonator, the lower the transmitted power. Off resonance, the input light does not couple to the ring and the transmitted power is maximal. The power transmission of an all-pass microring is given by Eq. 15.2. Here a is the roundtrip amplitude reduction due to losses in the ring and r the amplitude self-coupling coefficient of the directional coupler. For a lossless coupler, r is related to the amplitude cross-coupling or coupling loss k as $r = \sqrt{1 + k^2}$. The transmission spectrum of an all-pass ring is plotted in Fig. 15.3.

$$T_{all-pass} = \frac{a^2 - 2ar\cos\phi + r^2}{1 - 2ar\cos\phi + (ar)^2}, \ \phi = \frac{2\pi}{\lambda} n_{eff} L \tag{15.2}$$

The spectrum is characterized by the full-width at half-maximum (FWHM) of the resonances, the on–off extinction ratio, and the free spectral range (FSR) between consecutive resonances. If the resonator losses and the coupling to the waveguide increase, the resonance broadens. The ring is undercoupled if the coupling loss is less than the roundtrip loss ($r > a$). The extinction ratio of the resonances becomes infinite for critical coupling, when the coupling loss balances the roundtrip loss of

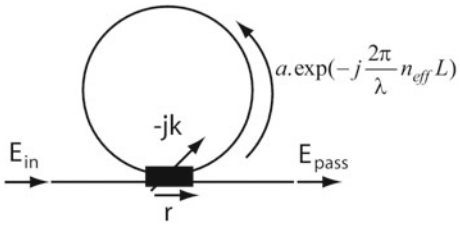

Fig. 15.2 Schematic representation of a microring in the all-pass configuration

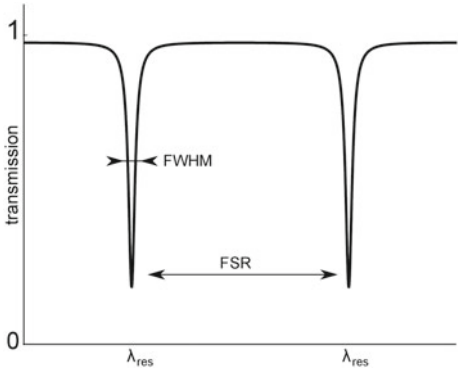

Fig. 15.3 Transmission spectrum of a microring in the all-pass configuration

the ring ($r = a$). If the coupling loss increases further ($r < a$), the ring becomes over-coupled. The resonances broaden and their extinction ratio is reduced.

15.2.2.2 Add-Drop Ring Resonators

An add-drop or channel-drop resonator has two access waveguides, as shown in Fig. 15.4. The second waveguide makes it possible to drop or add signals at the resonance wavelength to the signal in the input waveguide. Just like for the all-pass resonator, constructive interference builds up the power in the ring on resonance. Because a second waveguide is coupled to the microring, part of this power couples to this waveguide and light at the resonance wavelength is dropped to the drop port, hence the name. The drop port will show transmission peaks on the resonance wavelengths. The output of the access waveguide, the pass port, features a dip in transmitted power on resonance. Off resonance, the pass transmission is maximum and the drop port is dark. The add-drop resonator is described by two transmission functions: one for the pass port and one for the drop port that are given by Eq. 15.3. As an add-drop resonator has two directional coupler sections, two different amplitude self-coupling coefficients feature in the equations. r_1 represents the self-coupling of the input directional coupler, r_2 is the self-coupling coefficient of the directional coupler leading to the drop port. The transmission spectra are plotted in Fig. 15.5.

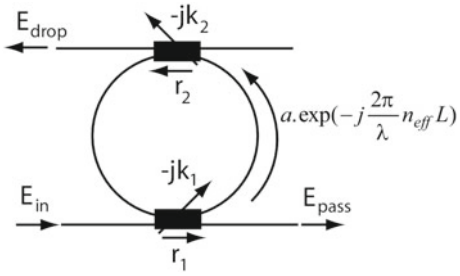

Fig. 15.4 Schematic representation of a microring in the add-drop configuration

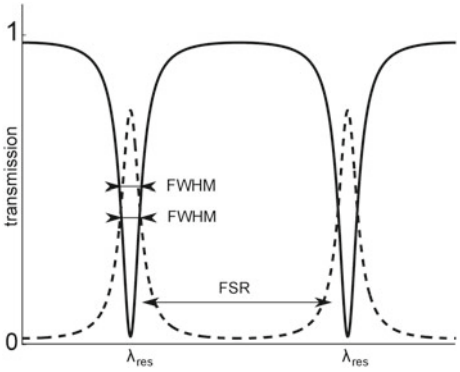

Fig. 15.5 Transmission spectrum of a microring in the add-drop configuration

$$
\begin{aligned}
T_{pass} &= \frac{a^2 r_2^2 - 2ar_1 r_2 \cos\phi + r_1^2}{1 - 2ar_1 r_2 \cos\phi + (ar_1 r_2)^2} \\
T_{drop} &= \frac{a(1 - r_1^2)(1 - r_2^2)}{1 - 2ar_1 r_2 \cos\phi + (ar_1 r_2)^2}, \text{ with } \phi = \frac{2\pi}{\lambda} n_{eff} L
\end{aligned}
\tag{15.3}
$$

When comparing the pass port transmission to that of an all-pass resonator, we see that the second coupler acts as an extra loss mechanism in the microring. The add-drop resonator is critically coupled if $r_1 = ar_2$.

15.2.3 Evanescent Field Sensing with Ring Resonators

A label-free microring resonator biosensor can directly measure selective affinity interactions between analyte molecules and receptor molecules on the ring waveguide surface. As most biological molecules have a higher refractive index than the surrounding aqueous environment, the binding of such a molecule to the waveguide will locally increase the refractive index. The evanescent tail of the optical field will sense this changing refractive index, and it will result in a change in effective index of the waveguide mode. As the ring resonance wavelength is directly proportional to the effective index, this change in effective index in the ring will induce a shift of

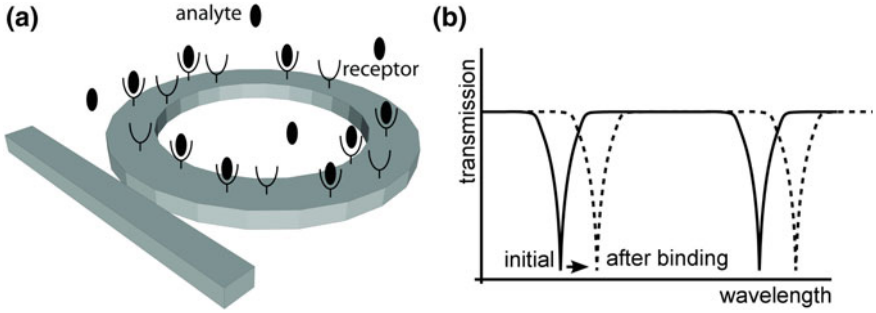

Fig. 15.6 Schematic representation of analyte molecules binding to the sensor receptors and the resulting wavelength shift in the transmitted signal

the resonance wavelength of the microring. For high index contrast material systems like SOI, the mode is strongly confined to the waveguide core. The high intensity at the waveguide edge explains the high sensitivity to index changes in the immediate vicinity of the chip surface. At the same time, the strong exponential decay of the evanescent field for increasing distance to the waveguide limits the effect of noise-inducing index changes in the bulk of the liquid. The binding of target molecules to an all-pass microring waveguide and resulting wavelength shift is displayed in Fig. 15.6. When more molecules bind to the ring surface, the total index change and wavelength shift will increase. This explains why continuous monitoring of a microring resonance wavelength allows one to create a binding curve of the reaction. Such a binding curve can provide information about, for example, the binding affinity between a target and the probe by considering the slope during binding. The total shift after an experiment represents the amount of molecules bound to the surface. The next section discusses some state-of-the-art applications using microring resonator biosensors.

15.2.4 Applications of Microring Resonators for Label-Free Biosensing

Multiplexed detection of different antibodies in complex serums using SOI microring resonator biosensor was reported by De Vos et al. [1]. In the reported sensing system, an array of microring sensors is used and the projected concentration detection limit is 3 ng/ml, which is lower than the detection limit for individual ring sensors previously reported by the same authors [2]. Advanced slot waveguide designs are investigated in [3–6]. It is shown that the sensitivity to protein binding is increased due to higher overlap between the optical mode and the detected proteins. The overall detection limit, however, is not reduced compared to simple microring sensors because of increased losses in the slot waveguides. As a microring resonator has a specific resonance wavelength determined by the ring circumference, waveguide

division multiplexing can be used for multiplexed assays by employing rings with different lengths. This is demonstrated by a multiplexed antibody assay in [7]. A fully integrated reader instrument with SOI microring sensor chips is reported by Densmore et al. [8]. This instrument is used with an optical microring array chip with up to 128 sensors for *E.coli* serotyping in [9]. A versatile SOI microring resonator sensing array in combination with high-speed scanning instrumentation is reported by [10]. The reported refractive index sensitivity is below 10^{-6} refractive index units. A streptavidin detection limit of 60 fM is established using biotin capture probes. Using two DNA oligonucleotide probes, multiplexed detection in complex media is demonstrated. A similar system is used for a variety of biosensing demonstrations in [11–16]. The detected molecules range from microRNA sequences to large protein biomarkers or entire viruses. By using the real-time microring response to study reaction dynamics, the identification of single-nucleotide polymorphism in hybridized DNA sequences is reported in [17]. Integration of microring sensors in different packaging configurations has been investigated by Arce et al. [18–20]. The successful integration of a microring on an optical fiber tip and the combination with digital microfluidics or Eppendorf tubes are reported.

15.3 Resonance Splitting in Microring Biosensors

15.3.1 Introduction

The high index contrast of the SOI-platform causes high confinement of the optical fields in the waveguides, which makes the microrings very sensitive to changes on the waveguide surface. This explains their very high sensitivity to biomaterials, but at the same time, waveguide roughness causes scattering of the guided light. This degrades the quality factor of the resonances and can ultimately lead to splitting of the resonance [21]. A lot of work has been done on using resonance splitting as a beneficial effect for sensing in non-integrated cavities with extreme quality factors, with very successful results [22]. However, in this chapter we will focus on the detrimental effects unexpected resonance splitting can have on the efficacy of microring biosensors integrated in a lab-on-a-chip context. In a biosensor device, the resonance wavelength will be tracked automatically by a fitting algorithm. This works fine for unsplit resonances, but unpredictable resonance splitting can introduce aliasing in the recorded binding curve signal. Since the resonance splitting in a microring sensor can easily amount to a measurable erroneous shift, unexpected resonance splitting can result in fitting errors and severely compromise a recorded binding curve. Jumps between both modes of a split resonance can lead to false positive or even false negative results when the sensor is implemented in a lab-on-a-chip setting, as demonstrated by Fig. 15.7. This section will discuss microring resonance splitting in detail. We present a simple theoretical description and an integrated interferometric approach to resolve the resonance splitting of a microring resonator on a single chip. We demonstrate experimentally how the resonance quality factor can be improved.

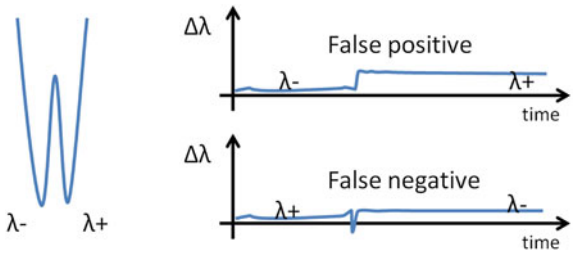

Fig. 15.7 Unexpected resonance splitting can lead to false positive or false negative results as a consequence of hopping between both modes of the split resonance. A false positive response occurs when the signal hops to the higher wavelength mode, and a false negative can occur when the signal hops to the lower wavelength mode during a binding event

15.3.2 Origin of Resonance Splitting

A perfectly symmetric microring resonator mode in the absence of a bus waveguide is twofold degenerate. Both clockwise (CW) and counterclockwise (CCW) propagation are possible in the microring, and both modes are uncoupled. This degeneracy is lifted when the CW-mode and CCW-mode become coupled, e.g., by surface roughness on the waveguide edges and by the proximity of bus waveguides. These deviations from circular symmetry cause forward propagating light to scatter back into the opposite direction, exciting a CCW-mode from a CW-mode and vice versa. Standing wave modes as a symmetric and antisymmetric superposition of the traveling waves can now be considered as the new eigenmodes of the system. They will, however, no longer be degenerate as a consequence of the symmetry breaking coupling [23]. If the linewidth of the resonance is small enough to distinguish both modes, the resonance splitting will be visible in the output signal. This occurs for high-quality resonances, when the backreflected power exceeds the coupling losses of the resonator. A critical relation between reflected power and microring coupling is derived in [24].

Using the simple coupled harmonic oscillator model described in [23], one can easily derive expressions for the CW- and CCW-modes of a microring resonator coupled to a waveguide in the all-pass configuration. The coupled mode system is described by Eq. 15.4:

$$\begin{aligned} \frac{da_{CW}}{dt} &= i\Delta\omega a_{CW} - \frac{1}{2\tau}a_{CW} + \frac{i}{2\gamma}a_{CCW} + \kappa s \\ \frac{da_{CCW}}{dt} &= i\Delta\omega a_{CCW} - \frac{1}{2\tau}a_{CCW} + \frac{i}{2\gamma}a_{CW} \end{aligned} \tag{15.4}$$

Here, a is the amplitude of the CW- and CCW-modes ($|a|^2$ is the energy stored in the CW- and CCW-modes, respectively) and s represents the field in the input waveguide ($|s|^2$ is the input power). The frequency of the lightwave is detuned by $\Delta\omega$ with respect to the resonance frequency of the resonator. τ is the lifetime of photons in the resonator and is determined by the total losses of the coupled microring resonator.

The photon lifetime is related to the quality factor (Q) of the microring as $Q = \omega\tau$. κ describes the coupling from the input wave to the resonator mode. By associating a lifetime $\kappa = \sqrt{1/\tau_{ext}}$ to the coupling coefficient, intrinsic resonator losses can be distinguished from coupling losses as $1/\tau = 1/\tau_{ext} + 1/\tau_0$. τ_0 is determined by material absorption and scattering losses in the microring waveguide. Losses in the bends and directional coupler also contribute to the intrinsic amplitude decay in the resonator. As explained in [25], the traditionally used power coupling coefficient K can be readily translated to the coupling coefficient κ used in this description. The coupling between CW- and CCW-mode is described by the scattering lifetime γ. The eigenmodes of the coupled system in Eq. 15.4 are a symmetric and antisymmetric superposition of the CW- and CCW-mode. The complex amplitudes of these new eigenmodes are given by Eq. 15.5:

$$\begin{aligned} a_+ &= \frac{1}{\sqrt{2}}\left(a_{CW} + a_{CCW}\right) = \frac{1}{\sqrt{2}}\frac{-\kappa s}{i\left(\Delta\omega + \frac{1}{2\gamma}\right) - \frac{1}{2\tau}} \\ a_- &= \frac{1}{\sqrt{2}}\left(a_{CW} - a_{CCW}\right) = \frac{1}{\sqrt{2}}\frac{-\kappa s}{i\left(\Delta\omega - \frac{1}{2\gamma}\right) - \frac{1}{2\tau}} \end{aligned} \tag{15.5}$$

From Eq. 15.5, it is clear that the eigenmodes are centered around the new eigenfrequencies $\omega = \omega_0 \pm 1/2\gamma$. They each have a linewidth of $1/\tau$, determined by the losses of the coupled microring. The results from Eq. 15.5 can be used to calculate both the CW- and CCW-mode as well as the transmitted and reflected fields for the microring coupled to an input waveguide by using the relations from Eq. 15.6:

$$t = s + \kappa a_{CW} \quad \text{and} \quad r = \kappa a_{CCW} \tag{15.6}$$

When comparing the theoretical transmission to the recorded transmission spectrum of an all-pass microring resonator, we obtain the results from Fig. 15.8. The resulting fitted parameter values indicate a quality factor of $Q = 20,850$ for the eigenmodes. The mode splitting amounts to $\Delta\lambda = 79\,\text{pm}$, and the power coupling ratio of the directional coupler is $K^2 = 0.0332$, which corresponds well to the projected design value for critical coupling. The width of the resonance splitting is of the same order of magnitude as the expected resonance shift in a complementary DNA binding curve. This indicates that the outcome of a detection experiment can indeed be severely compromised by unexpected mode hopping during DNA binding.

15.3.3 Integrated Interferometric Circuit

As demonstrated in [27], in the context of a fiber-based system, an interferometric approach can be used to retrieve the unsplit modes of the microring resonator in an output signal. However, such a fiber-based setup is difficult to stabilize and to integrate. Therefore, we have implemented this in an integrated circuit on a single SOI-chip. A layout of the circuit is provided in Fig. 15.9. Vertical grating couplers

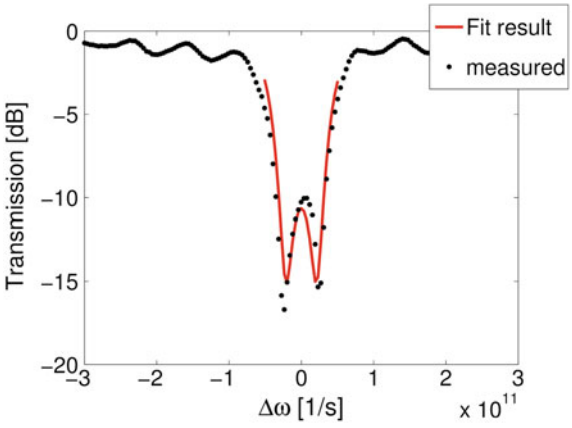

Fig. 15.8 Measured spectrum of all-pass microring with resonance splitting. The full line gives the theoretical transmission after fitting the model parameters. Reproduced from [26]

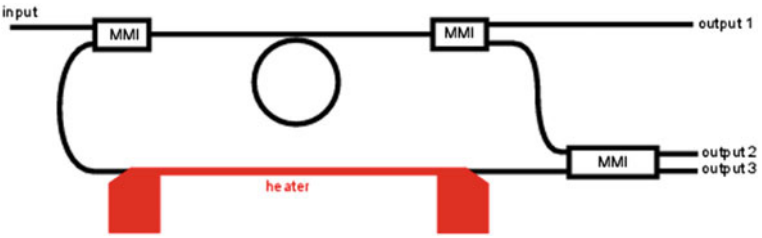

Fig. 15.9 Schematic representation of the integrated interferometric circuit. Reproduced from [26]

are used to couple light from a tunable laser light source into the circuit and collect the power at the output. The input light excites the CW-mode in the microring resonator, which in turn excites the CCW-mode as a consequence of mode coupling. The normal modes of the microring resonator are the symmetric and antisymmetric superposition of the CW- and CCW-mode, given by Eq. 15.5. If the coupling per unit time between the bus waveguide and the microring is represented by κ, the fields transmitted and reflected by the resonator are again given by Eq. 15.6. Here, $s = a_{in}/\sqrt{2}$ and $|a_{in}|^2$ is the total input power.

The input light is first passed through a 3 dB combiner before coupling into the microring. The CW propagating light will couple back to the waveguide to constitute the transmitted field. The CCW propagating light will form the reflected field when coupling back to the waveguide. The input combiner acts as a splitter for the reflected light which is guided through a feedback arm toward a 2×2 multimode interference (MMI) coupler. The transmitted light is passed to a 3dB MMI-splitter. It is split equally between output 1 and the 2×2 MMI coupler, where it is recombined with the reflected light. The signals from the 2×2 coupler are the result of

interference between the transmitted and reflected fields and are collected in output 2 and 3. For the case of a perfect 2×2 MMI coupler, the fields at the output ports for given input fields E_1 and E_2 are $1/\sqrt{2}\left(E_1 \pm iE_2\right)$. There is a quadrature phase relationship between both output signals. We can summarize the output fields of the interferometric circuit in Eq. 15.7:

$$\begin{aligned} out_1 &= \tfrac{1}{\sqrt{2}} t \\ out_2 &= \tfrac{1}{2}(\tfrac{1}{\sqrt{2}} a_{in} + \kappa a_{CW} + e^{i\phi}\kappa a_{CCW}) \\ out_3 &= \tfrac{1}{2}(\tfrac{1}{\sqrt{2}} a_{in} + \kappa a_{CW} - e^{i\phi}\kappa a_{CCW}) \end{aligned} \tag{15.7}$$

Here, ϕ is the phase difference between the interfering transmitted and reflected fields. We find that output 1 is always proportional to the pass signal of the microring resonator in the all-pass configuration. To obtain the required output signals in output 2 and 3, the phase difference ϕ between the transmitted and reflected wave has to be controlled carefully. In this case, this is done by processing a titanium–gold heater on the feedback waveguide. By setting the current through the heater, we can tune the phase difference to the required value. If it is a multiple of π, we see from Eq. 15.7 that the signals in output 2 and 3 are given by the sum of a constant and a signal proportional to the complex amplitudes of the normal modes of the resonator, given by Eq. 15.5. In other words, the spectral shape of the signals in output 2 and 3 will be identical to this of the complex amplitudes of the eigenmodes. This means we will have access to the unsplit, high-Q normal modes of the cavity. Since the detection limit of a biosensor is limited by the quality factor of the resonance [28]—higher resonator Q-factors give rise to lower detection limits—this provides a tool to improve the detection limit significantly. Even worse, fitting errors introduced by resonance splitting can cause jumps between both modes of a split resonance that lead to false positive or even false negative results when the sensor is implemented in a lab-on-a-chip setting.

15.3.4 Controlling Microring Resonance Splitting

The fabrication process for the optical chip with integrated interferometric circuit is described in detail in []. The experimental results are summarized in this section. Changing the phase difference between the reflected and transmitted fields gives us the ability to change the resonance state in the output signals from one normal mode, over the severely split intermediate state to the other normal mode.

The width and corresponding quality factors of the recorded eigenmode spectra compare favorably to those of the resonance signal in output 1, as can be seen from Fig. 15.10. When determined based on the fitted model of Eq. 15.5, we obtain a width of 50 pm for the unsplit eigenmodes and one of 130 pm for the split all-pass transmission. Since the limit of detection (LOD) scales with the square root of the

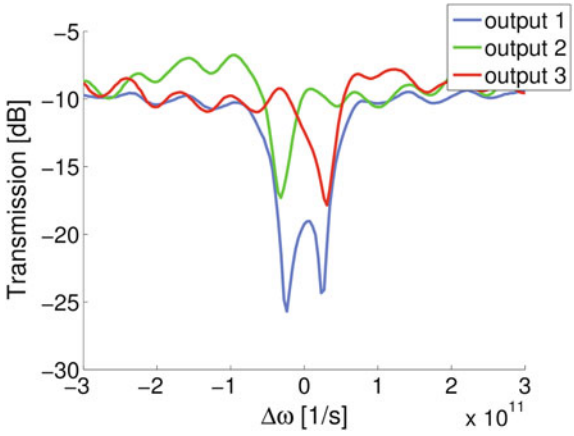

Fig. 15.10 Split all-pass transmission and interferometric output signals showing unsplit modes for a phase difference $\Delta\phi = 0$. Output power of output 1 has been scaled for clarity. Reproduced from [26]

resonance width, this technique provides a potential LOD improvement with a factor 1.6. One could argue that the total width of the transmission resonance is not a good measure for estimating detection limits. However, when the resonance splitting $\Delta\lambda$ is less than or equal to the width of the individual normal modes, splitting will be obscured while still causing significant broadening of the resonance dip. In that case, a fit to the more narrow unsplit mode revealed by this interferometric approach will always be more accurate and provide limit of detection improvements up to a factor $\sqrt{2}$, while at the same time eliminating the chance of false positive or negative detections due to intrinsic microring effects.

15.4 Vernier-Cascade Sensor

In this section, we will discuss the use of Vernier-cascade rings [29–31]. This setup consists of two rings which are put in series, in order to improve the sensitivity of the device, i.e., the resonance shift for a given excitation. The main advantage of this is that it allows for integration with on-chip spectrum analyzers, paving the way for the use of cheaper light sources than the tunable laser required for interrogation of the extremely small shifts of individual ring sensors.

15.4.1 Theoretical Analysis of the Vernier-Cascade Sensor

The Vernier-scale is a method to enhance the accuracy of measurement instruments. It consists of two scales with different periods, of which one slides along the other one. The overlap between lines on the two scales is used to perform the measure-

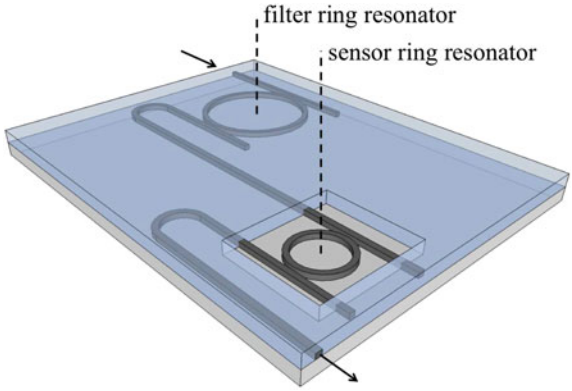

Fig. 15.11 Illustration of the concept of the photonic sensor consisting of two cascaded ring resonators. Two ring resonators with different optical roundtrip lengths are cascaded. The complete chip is covered with a thick cladding, with only an opening for one of the two resonators. This sensor ring resonator will be exposed to refractive index changes in its environment, while the other resonator, the filter ring resonator, is shielded from these refractive index changes by the cladding. Reproduced from [34]

ment. It is commonly used in calipers and barometers, and it has also been applied in photonic devices [32, 33].

In Fig. 15.11, it is illustrated how this concept can be applied to a ring resonator sensor. Two ring resonators with different optical roundtrip lengths are cascaded, so that the drop signal of the first ring resonator serves as the input of the second. Each individual ring resonator has a comb-like transmission spectrum with peaks at its resonance wavelengths. The spectral distance between these peaks, the free spectral range, is inversely proportional to the optical roundtrip of the resonator so that each resonator in the cascade will have a different free spectral range. As the transmission spectrum of the cascade of the two ring resonators is the product of the transmission spectra of the individual resonators, it will only exhibit peaks at wavelengths for which two resonance peaks of the respective ring resonators (partially) overlap, and the height of each of these peaks will be determined by the amount of overlap.

The complete chip is covered with a thick cladding, with only an opening for one of the two resonators. This sensor ring resonator will act as the sliding part of the Vernier-scale, as its evanescent field can interact with the refractive index in the environment of the sensor, where a change will cause a shift of the resonance wavelengths. The other resonator, the filter ring resonator, is shielded from these refractive index changes by the cladding and will act as the fixed part of the Vernier-scale. The cascade of both resonators can be designed such that a small shift of the resonance wavelengths of the sensor ring resonator will result in a much larger shift of the transmission spectrum of the cascade.

We can identify two regimes:

The first regime is illustrated in the left side of Fig. 15.12 and occurs when the free spectral range difference between the two resonators in the cascade is large

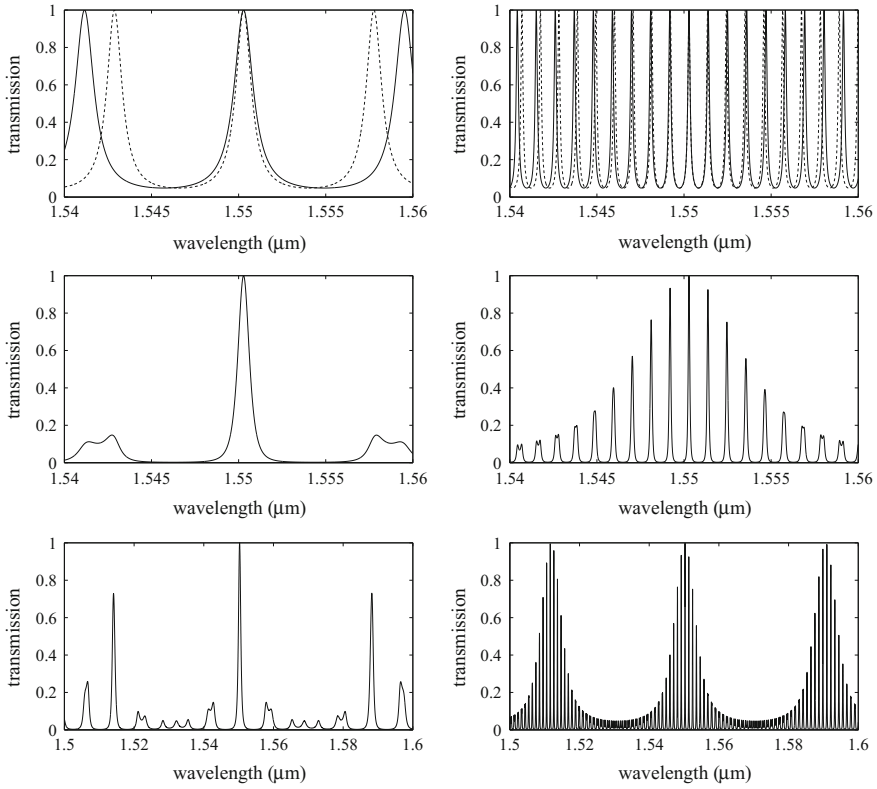

Fig. 15.12 Calculated transmission spectra that illustrate the operation of the cascade. The graphs on the left side illustrate a first regime that occurs when the free spectral range difference between the two resonators is large compared to the full-width at half-maximum of the resonance peaks of the individual resonators. The graphs on the right side illustrate a second regime that occurs when the free spectral range difference between the two resonators is small compared to the full-width at half-maximum of the resonance peaks of the individual resonators. Top: transmission spectra of the individual filter ring resonator (dashed line) and sensor ring resonator (normal line). Middle: transmission spectra of the cascade of these two resonators in the same wavelength range as the top image, illustrating only one clearly visible transmitted peak in the first regime (left), while in the second regime (right) an envelope signal is superposed on the constituent peaks. Bottom: transmission spectra of the cascade in a larger wavelength range. Reproduced from [34]

compared to the full-width at half-maximum of the resonance peaks of the individual resonators. The transmission spectrum of the cascade will then typically exhibit isolated peaks, of which the neighboring peaks are inhibited. The sensor will in this regime behave as a discrete sensor, of which the transmission peak will hop from one filter ring resonance wavelength to another for a changing refractive index. The smallest detectable shift of the transmission spectrum of this sensor is equal to the free spectral range of the filter ring resonator, which forms a limitation to the detection limit of the sensor. The sensor presented in [29] works in this regime.

A second regime occurs, however, when the free spectral range difference between the two resonators in the cascade is small compared to the full-width at half-maximum of the resonance peaks of the individual resonators. On the right side of Fig. 15.12, it is illustrated that in this regime a periodic envelope signal is superposed on the constituent transmission peaks. If we do not take dispersion into account, the envelope period is given by [34]

$$\frac{fsr_{sensor} \cdot fsr_{filter}}{\left| fsr_{sensor} - fsr_{filter} \right|} \tag{15.8}$$

where fsr_{sensor} and fsr_{filter} are the free spectral range values of the corresponding individual resonators. Note that in practice the envelope period can not be chosen larger than the available wavelength range of the measurement equipment, so that the second regime typically requires that the cascade consists of resonators with very large roundtrips. In the remainder of this article, we will work with sensors that work in this regime.

In this section, we will introduce an analytical formula for the envelope signal, and in Sect. 15.4.3, we will show that this formula can be fitted to experimental data, making it possible to continuously track the spectrum of the sensor, allowing a reduction of the detection limit.

As each peak in the transmission spectrum of the individual ring resonators is well approximated by a Lorentzian function, each of the constituent peaks in the transmission spectrum of the cascade can be described as the product of two Lorentzian functions that are shifted compared to each other:

$$T_{constituent}(\lambda) = \frac{t_{max,filter} \frac{fwhm_{filter}^2}{4}}{\frac{fwhm_{filter}^2}{4} + \left(\lambda - \lambda_0 - \frac{\Delta\lambda}{2}\right)^2} \cdot \frac{t_{max,sensor} \frac{fwhm_{sensor}^2}{4}}{\frac{fwhm_{sensor}^2}{4} + \left(\lambda - \lambda_0 + \frac{\Delta\lambda}{2}\right)^2} \tag{15.9}$$

where t_{max} and $fwhm$ are respectively the transmission at resonance and the full-width at half-maximum of the corresponding individual ring resonator, and where λ_0 and $\Delta\lambda$ are respectively the mean of and the difference between the two resonance wavelengths under consideration from both combs.

If we assume that both ring resonators have the same full-width at half-maximum $fwhm$, we can identify two different shapes of the constituent peaks, depending on their position in the envelope peak [34]:

If the difference between the resonance wavelengths is larger than the full-width at half-maximum of the individual resonances, $\Delta\lambda > fwhm$, the corresponding constituent peak has two maxima of which the transmission quickly converges to zero for increasing values of $\Delta\lambda$. This situation corresponds to the tails of the envelope, where the transmission is very low.

If, however, the difference between the resonance wavelengths is smaller or equal than the full-width at half-maximum of the individual resonators, $\Delta\lambda \leq fwhm$,

Eq. (15.9) has only one maximum. This situation corresponds to the constituent peaks in the center of the envelope peak, where the transmission is high. The envelope peak in the transmission of the cascade formed by these maxima is in good approximation given by [34]

$$T_{envelope}(\lambda) = \left(\frac{\sqrt{t_{max,filter} t_{max,sensor}} \left(\frac{FWHM}{2} \right)^2}{\left(\frac{FWHM}{2} \right)^2 + \left(\lambda - \lambda_{central} \right)^2} \right)^2 \tag{15.10}$$

with

$$FWHM = 2 \cdot \frac{fwhm \cdot min\left(fsr_{sensor}, fsr_{filter} \right)}{\left| fsr_{filter} - fsr_{sensor} \right|} \tag{15.11}$$

Here $\lambda_{central}$ is defined as the central wavelength of the envelope peak. Equation (15.10) shows that the envelope signal forms a peak described by the square of a Lorentzian function with full-width at half-maximum $FWHM$.

A change of the refractive index in the evanescent field of the sensor ring resonator will cause a shift of the resonance peaks in its transmission spectrum, which will be translated in a much larger shift of the central wavelength of the envelope peak in the transmission spectrum of the cascade. The sensitivity of the cascaded ring resonator sensor is given by [34]

$$\frac{\partial \lambda_{central}}{\partial n_{env}} = \frac{fsr_{filter}}{fsr_{filter} - fsr_{sensor}} \frac{\frac{\partial n_{eff,sensor}}{\partial n_{env}} \lambda}{n_{g,sensor}} \tag{15.12}$$

with $\frac{\partial n_{eff,sensor}}{\partial n_{env}}$ the change of the effective index of the sensor ring resonator waveguide due to a change of the refractive index in the environment of the sensor and $n_{g,sensor}$ the group index of the sensor ring resonator waveguide. The sensitivity of the cascaded ring resonator sensor is enhanced with a factor $\frac{fsr_{filter}}{fsr_{filter} - fsr_{sensor}}$ compared to the sensitivity of a single ring resonator sensor. As already stated earlier, in practice the period of the envelope signal of the cascade cannot be chosen larger than the available wavelength range of the measurement equipment. For a given envelope period, Eqs. (15.8) and (15.12) show that the sensitivity is in good approximation proportional to the optical roundtrip length of the resonators in the cascade. Note that for an increasing refractive index n_{env}, the resonance wavelength of a single ring resonator will always shift to larger wavelengths, while the central wavelength of the envelope peak in the transmission spectrum of the cascade will shift to smaller wavelengths if $fsr_{filter} < fsr_{sensor}$ and to larger wavelengths if $fsr_{filter} > fsr_{sensor}$.

15.4.2 Design and Fabrication

Our sensor was made in silicon-on-insulator with 2 µm buried oxide and 220 nm silicon top layer with CMOS-compatible 193 nm optical lithography and dry etching. An elaborate description of the fabrication process can be found in [35]. Figure 15.13 pictures the device.

Two ring resonators are cascaded similar to the concept explained in Sect. 15.4.1. In order to work in the second regime mentioned in that section and in order to have an envelope period smaller than the bandwidth of our grating couplers introduced in Sect. 15.4.3, the physical roundtrip length of the filter resonator and sensor resonator was respectively chosen to be 2528 and 2514 nm. By folding the cavity [36], their footprint was reduced to only 200 µm × 70 µm. The resonators consist of 450 nm-wide single-mode waveguides, and each one has two 6 µm-long directional couplers with a gap of 180 nm between the waveguides. The complete chip was covered with 500 nm silicon oxide by plasma deposition, and a window was etched to the second resonator in the cascade by consecutive dry and wet etching, so that only the evanescent field of this sensor ring resonator can interact with refractive index changes in the environment of the sensor. Note that this design is suboptimal and only serves as a proof-of-principle.

15.4.3 Experimental Performance

To allow controlled delivery of liquids to the sensor, a microfluidic channel with 600 µm × 50 µm cross section was made in PDMS by casting and directly bonded to the sensor chip at 135 °C after having applied a short oxygen plasma treatment to both surfaces [37]. The liquids were pumped through the channel over the sensor ring resonator with a syringe pump at a 5 µl/min flow rate. The chip was mounted on a temperature-stabilized chuck to avoid drifting of the sensor signal due to temperature

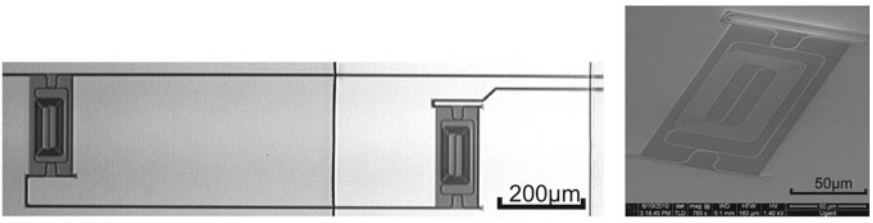

Fig. 15.13 Left: Optical microscope image of the device fabricated in silicon-on-insulator. Two ring resonators with 2.5 mm physical roundtrip length are cascaded, and their footprint is reduced by folding the cavity. The complete chip was covered with 500 nm silicon oxide, and an opening was etched to the second ring resonator. Right: Scanning electron microscope image of the second ring resonator with folded cavity. Reproduced from [34]

variations. A second-order diffractive grating, integrated on the input and output waveguides, is used to couple from a 10 μm-wide ridge waveguide to a vertically oriented, butt-coupled single-mode fiber. The grating has 10 periods of 630 nm with 50 nm etch depth. A linear, 150 μm-long taper is employed as a transition between the ridge waveguide and a 450 nm-wide photonic wire waveguide. A more detailed description of the grating couplers can be found in [38]. A polarization controller was used to tune the polarization of light from a tunable laser for maximum coupling to the quasi-TE mode of the waveguides, and the optical power transmitted by the sensor was measured with a photodetector.

In Fig. 15.14, the transmission spectrum of our sensor is plotted. Deionized water was flowing over the sensor. As predicted in Sect. 15.4.1, a periodic envelope signal is superposed on the sharp constituent peaks.

The detection limit of a refractive index sensor, the smallest change of the refractive index that can be detected, is often defined as the ratio between the smallest detectable spectral shift of its transmission spectrum and its sensitivity [39]. Next to having a sensor with a large sensitivity, it is thus equally important to be able to measure a small shift of the transmission spectrum. This smallest detectable shift is determined by the shape of the spectrum and the noise, but also the method that is adopted to analyze the spectrum has a large impact [40].

Here we will introduce a method to accurately determine the central wavelength of an envelope peak in the transmission spectrum of the cascaded ring resonator sensor, which is based on fitting the formulas derived in Sect. 15.4.1 to the measured spectrum. The fitting procedure is illustrated in Fig. 15.15

In first step, Eq. (15.9) is fitted to the highest constituent peaks in the transmission spectrum. In Fig. 15.15, a good correspondence can be observed between the fitted function and the experimental data, which was measured with 1 pm wavelength step. By taking the analytical maximum of the fitted function for each of these constituent peaks, the envelope signal is determined in a noise-resistant way.

In second step, Eq. (15.10) is fitted to the envelope signal that is formed by the output of previous step. In Fig. 15.15, this fit is shown by the dashed line. The position of the analytical maximum of this function is taken as the central wavelength of the measured envelope peak.

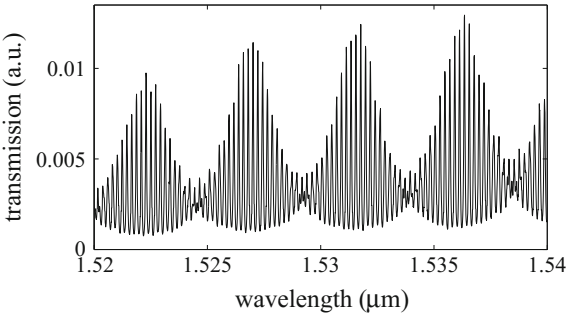

Fig. 15.14 Measured transmission spectrum of the device as deionized water is flowing over the sensor ring resonator. The height of the envelope peaks varies due to the wavelength-dependent coupling efficiency of the grating couplers. Reproduced from [34]

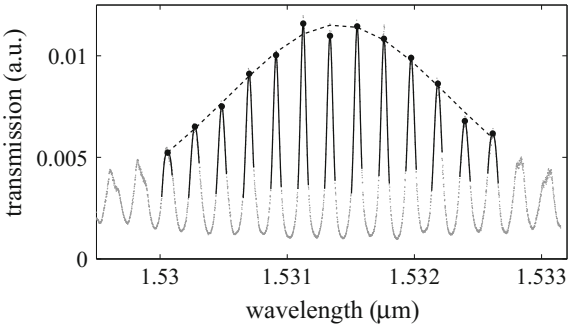

Fig. 15.15 Illustration of the fitting procedure. In gray, a measured transmission spectrum of our device is shown. In first step, Eq. (15.9) is fitted to the highest constituent peaks, shown by the solid lines. Then the analytical maxima of these fits are determined, shown by the dots. In second step, Eq. (15.10) is fitted to the envelope signal formed by these maxima, which is shown by the dashed line. The position of the analytical maximum of that last fit is taken as the central wavelength of the envelope peak. Reproduced from [34]

A good measure for the smallest detectable wavelength shift with this method is given by the standard deviation on the fitted central wavelength of the envelope peak. Based on the confidence interval of the fitting parameters returned by our standard fitting software, the smallest detectable wavelength shift was calculated to be 18 pm for the measured spectra of our sensor. Note that this value is an order of magnitude smaller than the distance between the peaks in the spectrum.

To measure the sensitivity of the sensor to changes in the bulk refractive index of its aqueous environment, it was measured how much the envelope peaks in the transmission spectrum shifted when changing between flowing deionized water and three aqueous solutions of NaCl with different concentrations. The refractive index

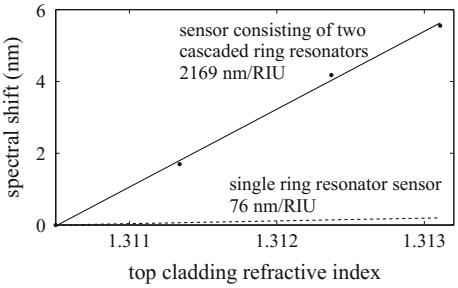

Fig. 15.16 Shift of the transmission spectrum of the sensor consisting of two cascaded ring resonators as a function of the bulk refractive index in its top cladding. The dots show the shift that was measured by changing the flow between deionized water and aqueous solutions of NaCl with different concentrations, and the solid line represents the linear fit to this experimental data, revealing a sensitivity of 2169 nm/RIU. For comparison, the dashed line shows the calculated resonance wavelength shift of a single ring resonator. Reproduced from [34]

of each of these solutions was calculated [41]. In Fig. 15.16, the dots indicate the measured shifts as a function of bulk refractive index. A linear function was fitted to the measured shifts, and its slope revealed a sensitivity of 2169 nm/RIU. This value corresponds well with the theoretical sensitivity of 2085 nm/RIU calculated with Eq. (15.12). The resonance wavelength shift of a single ring resonator comprised of a 450 nm-wide waveguide is calculated to be 76 nm/RIU, showing the large sensitivity improvement with the presented sensor. The calculation of both mentioned sensitivities is described in [34].

The resulting detection limit of our sensor is equal to the ratio of the smallest detectable wavelength shift and the sensitivity, that is, 18 pm/2169 nm/RIU = 8.3×10^{-6} RIU. Although the detection limit is currently not improved compared to that of a single ring resonator sensor [42], this first experimental result is promising for future optimized designs regarding the different levels of optimization of single ring resonator sensors and this new sensor.

15.4.4 Vernier-Cascade Sensor with On-chip Spectrometer

Here, we will show of the Vernier-cascade introduced earlier can be combined with cheap on-chip spectrometers in order to allow readout using a cheap broadband light source as opposed to an expensive tuneable laser.

We chose to integrate a Vernier-cascade sensor with a well-known and compact arrayed waveguide grating (AWG) [44], as depicted in Fig. 15.17. The Vernier-cascade can be made at least an order of magnitude more sensitive than

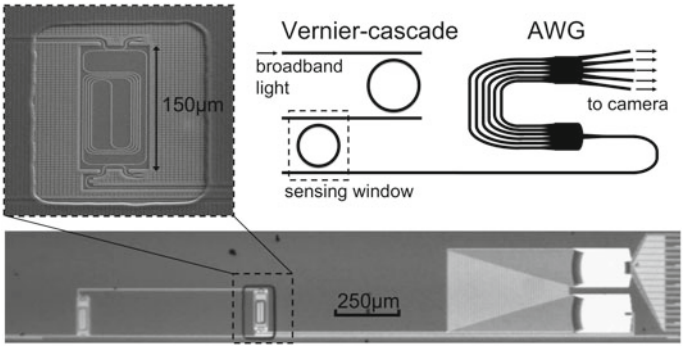

Fig. 15.17 Transmission spectrum of a Vernier-cascade sensor can be measured with a low-cost broadband light source by dividing it into different wavelength channels with an integrated arrayed waveguide grating (AWG) that distributes them to spatially separated output ports that can be monitored in parallel with a camera. The micrograph of the silicon-on-insulator chip shows the compact folded cavities of the ring resonators constituting the Vernier-cascade that is connected to a dense 16-channel AWG. The chip is covered with a polymer cladding except for a window to the second resonator to allow its evanescent field to interact with the fluid. Reproduced from [43]

a ring resonator sensor, with sensitivities as large as several thousands of nm/RIU. Moreover, it can be designed to have a transmission spectrum with an easy-to-resolve periodic envelope signal superposed on sharp constituent peaks, as we showed earlier.

The output of the AWG's ports can be monitored in parallel with an infrared camera, making this interrogation scheme compatible with the simultaneous readout of multiple sensors on the same chip.

Our implementation of the device consists of 450 nm-wide single-mode waveguides defined in the 220 nm high silicon top layer of a SOI wafer with 2 μm buried oxide using CMOS-compatible 193 nm optical lithography and dry etching. A 600 nm-thick cladding of a benzocyclobutene-based polymer with low water absorption covers the complete chip except for a window to the second resonator. The filter and sensor resonator roundtrip lengths were chosen respectively 1271 μm and 1257 μm so that the sensor would have a clearly visible envelope signal and would have a large sensitivity, while retaining acceptable roundtrip losses. Both resonator cavities were folded with a 6 μm bend radius to reduce their footprint to less than 7500 μm^2 (Fig. 15.17). The coupling of each resonator to its two access waveguides is matched to the roundtrip loss to have an optimal extinction and is achieved with directional couplers with 180 nm gap. The AWG has 16 channels with 1.6 nm spacing, so that its bandwidth is larger than the envelope period of the sensor (13 nm) to avoid it from limiting the sensor's dynamic range. The chosen channel spacing is the result of a trade-off between having a high resolution and having enough spectral averaging per channel to be able to disclose the envelope signal directly with a broadband light source.

To couple light from and to the device, the input and output waveguides were adiabatically tapered to a 10 μm-wide ridge waveguide in which a second-order grating was etched to diffract TE-polarized light out-of-plane. The relative power diffracted to free space by all output gratings, each corresponding with a channel of the AWG, was monitored in parallel using a near-infrared camera with a microscope objective at a distance of several centimeters from the chip. A standard single-mode optical fiber was butt-coupled to the input grating (Fig. 15.18).

An envelope peak superposed on the constituent peaks is visible in the transmission spectrum of the water-covered Vernier-cascade sensor filtered by the AWG to its different channels (Fig. 15.19), confirming the on-chip spectral filtering and

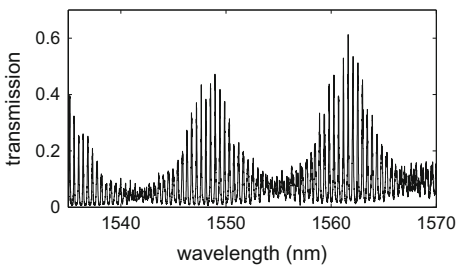

Fig. 15.18 Vernier-cascade's transmission spectrum exhibits a clearly visible envelope signal superposed on its constituent peaks with a period smaller than the bandwidth of the AWG in order not to limit the sensor's dynamic range

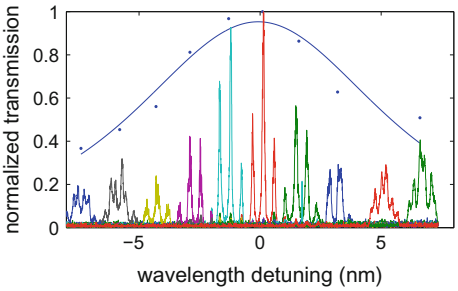

Fig. 15.19 Transmission spectrum of the Vernier-cascade through different channels of the AWG measured with a tunable laser (bottom, a color for each AWG-channel) shows the envelope peak superposed on the sharp constituent peaks. Approximately three constituent peaks are transmitted by each channel, providing enough power averaging per channel to also reveal the shape of the envelope peak when the transmission is measured with a broadband light source (blue dots). A squared Lorentzian function can be satisfactory fitted to the broadband transmission peak (blue line), allowing accurate determination of the peak position. Reproduced from [43]

parallel camera readout. The spectrum measured by stepping the wavelength of a tunable laser shows that approximately three constituent peaks are transmitted by each channel, providing enough power averaging to also reveal the envelope shape when the transmission spectrum is measured with a super-luminescent light emitting diode (LED) broadband light source with 1.55 μm central wavelength. A squared Lorentzian function is satisfactory fitted to this envelope peak [34], allowing accurate determination of the peak position.

The performance of our device as transducer for label-free biosensing was characterized by measuring the refractive index change of watery salt solutions in real time. To allow controlled delivery of the solutions to the sensor, a microfluidic channel with 600 μm × 50 μm cross section was made in polydimethylsiloxane (PDMS) by casting and directly bonded to the sensor chip. Using a syringe pump, the solutions were pumped at a 10 μl/min flow rate over both resonators of the Vernier-cascade to keep them both in thermal contact with the liquid. As the thermo-optic coefficient of the polymer cladding (-1.5×10^{-4}/K) is close to the thermo-optic coefficient of water (-8×10^{-5}/K), both resonators react similarly to changes in the liquid temperature. Hence, our device is very tolerant to temperature changes and no thermal control was needed for the experiment. While the flow was repeatedly switched between deionized water and three different concentrations of NaCl in water, the broadband transmission of the Vernier-cascade sensor through the different channels of the AWG was measured with a suboptimal 6 Hz resolution and the spectral position of the transmission peak was determined by fitting the squared Lorentzian function mentioned before. The refractive index of the salt solutions was calculated according to Ref. [41].

Our device allows to monitor refractive index changes fast and accurately (Fig. 15.20), despite the limited spectral resolution of the AWG and corresponding inaccuracy of the peak fitting. As the refractive index changes in label-free

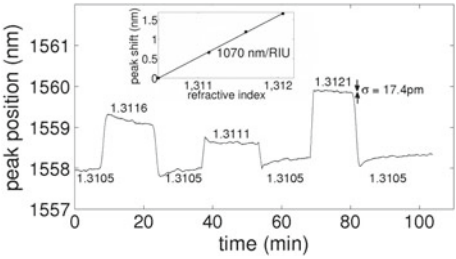

Fig. 15.20 Device can accurately monitor refractive index changes of watery NaCl solutions in real time while being interrogated with a low-cost broadband light source, making it very applicable in low-cost label-free biosensing. After smoothening the signal with a 1 min window, the standard deviation of the noise was only 17.4 pm. The sensor responded very linearly with 1070 nm/RIU sensitivity (inset). Reproduced from [43]

biosensing are typically slow compared to the period with which our spectra can be captured with a camera, the noise on the peak position signal can be reduced by smoothening the signal with a moving average over a time scale corresponding to the speed of the refractive index changes of interest. The central limit theorem in statistics predicts that the standard deviation on the signal will be reduced by the square root of the amount of spectra in the chosen window. We reduced the standard deviation of the noise on the signal to only 17.4 pm by smoothening with a 1 min window. The spectral position of the transmission peak shifts very linearly with the refractive index of the solution with a sensitivity as high as 1070 nm/RIU (inset Fig. 15.20). This brings the detection limit of this device to 17.4 pm/1070 nm/RIU $= 1.6 \times 10^{-5}$ RIU, which is in the same order as the detection limit we reported for a similar Vernier-sensor interrogated with a much more expensive tunable laser [34]. Moreover, it is expected to be an order of magnitude better than the interrogation with a broadband light source of the ring resonator sensor integrated with a photonic crystal spectral filter reported in [45], since our sensor is ten times more sensitive and can be resolved with a slightly better spectral resolution.

15.5 Dual-Polarization Biosensing

The optical microresonator biosensors discussed above have proven to be a valid tool to perform affinity analysis of a biological binding event. However, when a layer of biomolecules binds to these microrings which are excited by a single optical mode, the sensors cannot distinguish between a thin dense layer of biomolecules or a thick sparse layer. This means the sensor is "blind" to changes in shape of bound biomolecules. In this section, we introduce a novel technique to ascertain the conformation of bound molecules by determining the thickness and the density (or refractive index) of this layer simultaneously. By tracking the thickness change due to a binding event for instance, information can be gathered upon the folding or unfolding of the newly formed biomolecular system, which is interesting for drug discovery.

This technique is based on exciting the microring with two polarizations instead of one. Furthermore, a proof-of-concept is given by analyzing the conformational changes of Bovine Serum Albumin (BSA) proteins during adsorption to the silicon surface due to a change in pH of the buffer.

15.5.1 Introduction

The number of applications to the US Food and Drug Administration (FDA) for new drugs has decreased from 45 in 1996 to 23 in 2010 [46]. Combined with a more than twofold increase of the combined American and European investments in pharmaceutical R&D [47], it is clear that the ruling paradigm for drug research is no longer an efficient one. In the wake of these alarming conclusions, the FDA launched the FDA Critical Path Initiative in 2004 to address the increasing difficulty and unpredictability of medical product development [48]. In a 2011 *Nature Chemistry* Insight [49], the authors state that the reason for the high failure rate in drug development can be found in the lack of appropriate high-throughput tools to study molecular behavior at an analytical and biophysical level of the drug candidates we produce. This is in contrast to the current, more empirical screening of drug candidates. Specifically, cell metabolism and the failure thereof is often governed by subtle changes in the conformation (i.e., shape) of protagonist proteins or enzymes. Current degenerative diseases (Alzheimer, Huntington, Parkinson, etc.) that prove difficult to produce effective drugs for, often find their cause in this misfolding of crucial proteins [50].

To accommodate these needs of the pharmaceutical industry, we adapt the high-throughput sensor system based on multiple microring resonators such that it can detect conformational changes of proteins. An inherent limitation to all label-free optical sensing technologies that use a single optical mode is that they respond in a similar way to both to an increase in thickness and an increase in refractive index of a bound layer. In order to disentangle both contributions, we need to record the wavelength shifts of two optical modes at the same time. A more comprehensive treatment of this technique and applications is given in [51].

15.5.2 Working Principle

The two optical modes that are used to excite the microring are the fundamental quasi-TE and the fundamental quasi-TM mode. In the remainder of this text, we shall call these modes TE and TM modes for ease of notation. Due to birefringence, the field profile of these two modes is different. The response of this mode to the local geometry, including the bound biolayer, is translated to a scalar value by means of n_{eff} which in turn determines the resonance wavelength, causing the modes to resonate at different wavelengths. The capturing of biomolecules on the microring surface is reflected by an increase in n_{eff} and thus implies a shift in the resonance wavelength, which is governed by the following equation:

$$\Delta\lambda(n,t) = \frac{\Delta n_{eff}(n,t) \cdot \lambda}{n_g} \tag{15.13}$$

In this equation, $\Delta n_{eff}(n,t)$ represents the change in effective refractive index of a specific mode due to the presence of the protein layer, λ is the resonant wavelength, while $\Delta\lambda(n,t)$ is the shift of this wavelength due to the protein layer. The group index is represented by n_g and its inclusion ensures that first-order dispersive effects are taken into account. Figure 15.21 shows the sensitivity of both modes to a change in layer thickness, expressed as $\frac{\partial\lambda_{res}}{\partial t}$ as a function of the width of a waveguide, with t the thickness of the biolayer. The width of the microring waveguide should be such that only the fundamental TE and fundamental TM modes are guided. Figure 15.21 denotes this region of interest by W_1 and W_2. The figure shows that in this region of interest, the TM mode is more sensitive to changes in the thickness of the layer.

The temperature dependence of the TE and TM modes have been determined experimentally and amount to 63 pm/K for the TE and 34 pm/K for the TM mode. The sensitivity to bulk index variations and the penetration depths of both modes have been determined via simulations based on the calibrated waveguide dimensions used in the following BSA experiment. The sensitivity to bulk index variations for the TE mode amounts to 57 and 222 nm/RIU for the TM mode. The penetration depth is defined as the distance over which the energy density of the modes decrease by a factor 1/e and this amounts to 60 nm for the TE mode and 114 nm for the TM mode.

The measurement setup tracks λ_{TE} and λ_{TM} during the experiment. In order to extract (t,n) of the protein layer, we require a set of 2 equations linking the resonance wavelength shifts with these 2 biological parameters:

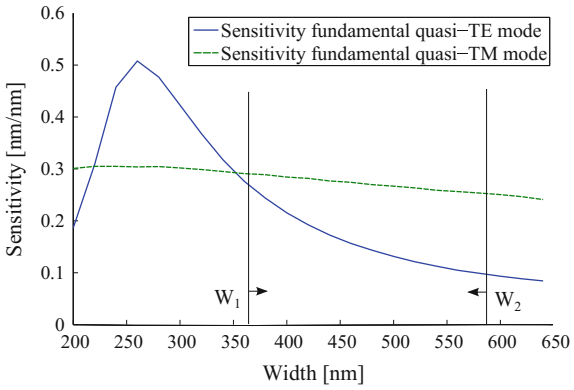

Fig. 15.21 Sensitivity of the microring resonator to binding of a thin biolayer in water for fundamental quasi-TE mode and fundamental quasi-TM mode, obtained with Fimmwave. The height of the waveguide is fixed at 220 nm, and the excitation wavelength is 1550 nm. The region of interest is denoted by W_1 and W_2, where only the fundamental TE and the TM mode are guided. Reproduced from [51]

$$\Delta\lambda_{TE} = f(n,t) \tag{15.14}$$

$$\Delta\lambda_{TM} = g(n,t) \tag{15.15}$$

In order to determine f and g, we perform a set of electromagnetic simulations using Fimmwave to calculate these shifts when sweeping over different values of n and t. We subsequently fit an analytical model to these sweeps, which is then used to numerically determine n and t from the measured shifts.

The blueprint of these functions f and g can be retrieved via derivations based on waveguide theory. Without going into details, we can say that there are 4 free parameters to determine per mode. In order to retrieve the free parameters, the wavelength shift of both modes is simulated for $t = 0$–$200\,\text{nm}$ and $\Delta n = 0$–$0.2\,\text{RIU}$ for a wire waveguide as depicted in Fig. 15.22a. We use refractive index unit (RIU) as a unit for the dimensionless refractive index throughout this text. These simulated shifts can then be fit to the model using a least square metric with physical constraints on the parameters. The results of this fit is shown in Fig. 15.22b. An R^2 goodness-of-fit of 0.9998 is obtained, confirming the validity of this model.

15.5.3 Influence of Noise on Measurement Accuracy

With this solving framework, we can make an estimate of the error of the system, arising due to noise on the determination of the resonance wavelength. There are various contributions to this wavelength noise from different elements in the measurement setup, such as temperature fluctuations, laser instability while sweeping the wavelength, thermal noise and shot noise from the camera capturing the light.

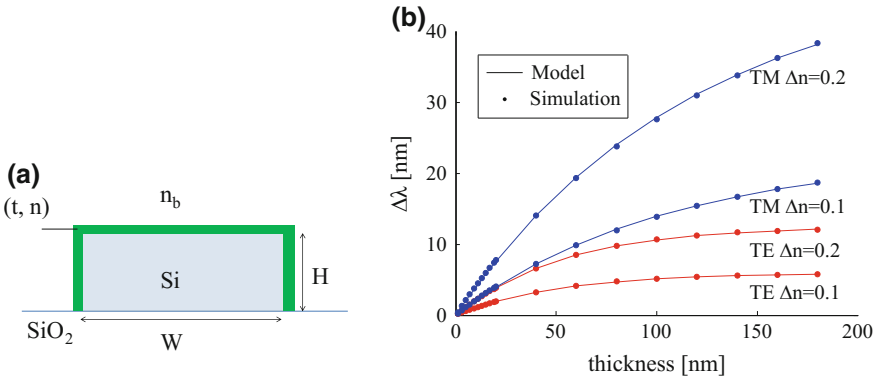

Fig. 15.22 **a** View of the cross section of the ring waveguide as it is used for simulations. **b** Simulations of the wavelength shifts for both modes in function of the thickness of the protein layer for various refractive indices of this layer. The fitting of this data to the model results in an R^2 value of 0.9998. Reproduced from [51]

To quantify the noise of our system, we have streamed phosphate-buffered saline (PBS) at 30 µl/min over the sensor array for 11 min, gathering 47 resonant wavelengths per mode. We have quantified the noise as the standard deviation on a linear curve through these measurements, to correct for time-dependent linear drift. We have experimentally obtained this noise as 220 fm for the TM mode and 246 fm for the TE mode. This is in good agreement with the noise determined in [10] for a TE mode, where a similar microring and lithographic fabrication process is used. The error in determining (t, n) is calculated as a function of the waveguide width, based on Gaussian wavelength noise with 220 fm standard deviation for both modes. These errors are determined for a protein layer with $n = 1.41 - 1.45$ RIU [52] and $t = 2$–9 nm. The average error for a specific waveguide width is depicted in Fig. 15.23.

Previously, we determined the region of interest for W as 361 nm $< W <$ 586 nm. However, for widths closer to 361 nm, the difference in n_{eff} between both modes decreases such that the mutual coupling increases in the bends of the microring [53]. The reduced width also causes the propagation losses to increase, which results in a decrease of the Q-factor of the cavity. These considerations lead to a choice of W between 460–560 nm. We can see in Fig. 15.23 that in this region, the average error does not differ much and amounts to 25–30 pm for t and 0.8×10^{-3} -1.0×10^{-3} RIU. for n. It has been shown that conformational changes of proteins can be measured with a similar resolution in [54].

15.5.4 Sensor Design

In order to excite both polarizations simultaneously, we take advantage of the vertical asymmetry of the waveguide. According to [55], the vertical mirror symmetry

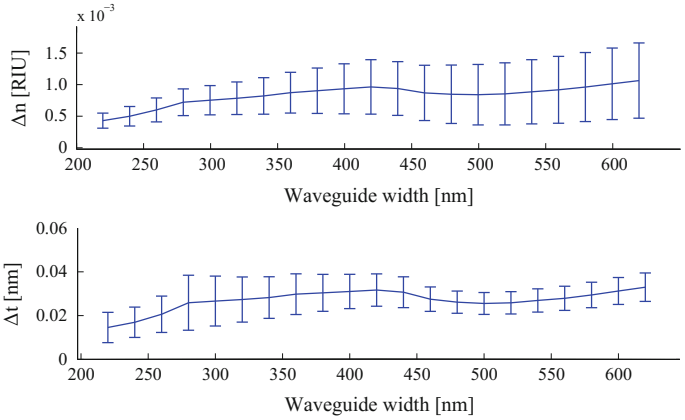

Fig. 15.23 Mean error on determination of t and n for various widths of the waveguide, with a fixed height of 220 nm. Reproduced from [51]

plane gives rise to two distinct polarizations: one with the electric field confined in this symmetry plane (TE polarization) and one with the electric field perpendicular to this plane (TM polarization). In [56], an asymmetrical directional coupler is suggested that can couple TE light to TM light in an adjacent waveguide by using two waveguides with different widths, such that $n_{eff,TE} \approx n_{eff,TM}$ and the modes are approximately phase-matched. A microring which has an asymmetrical coupling section has been examined in [57], where it was shown that a TE mode in the access waveguide can successfully excite a TM mode in the ring waveguide. However, if the gap in the coupling section is sufficiently small, the TE mode in the access waveguide can also excite the TE mode in the ring waveguide, even though they have a substantial phase mismatch. Indeed, the large modal overlap when the waveguides are very close can compensate for this phase mismatch.

To determine the optimal waveguide dimensions of the ring and the coupling section, we take into account the considerations of the previous section, where we determined that for a microring with a width 460 nm $< W <$ 550 nm we obtained a minimal error on (t, n). For the access waveguide, we need $W >$ 270 nm, such that the fundamental TE mode is still guided by the waveguide, as can be seen in Fig. 15.21. The waveguide of the microring was designed to have a width of 550 nm, such that with an access waveguide that is 290 nm wide, a small theoretical phase mismatch was achieved between the TE mode of the access waveguide and the TM mode of the ring waveguide of $\Delta n = 0.0481$. In Fig. 15.24a, this phase matching is illustrated.

Once the sensor was fabricated, fiber-to-fiber measurements were performed with water as cladding. The measured spectrum is shown in Fig. 15.24b where the two sets of resonances are visible, each with a different free spectral range (FSR). Figure 15.25 shows a SEM top view of the microring and a cross section of the coupling section. On the top view of the microring, we can see that the access waveguide quickly bends away after the coupling section, such that this section is only 1 µm long. This is done in order to reduce the influence of non-uniform protein binding on the microring behavior. The cross section shows that for a gap of 65 nm, the non-phase-matched coupling of the TE mode of the access waveguide to the TE mode of the ring waveguide can succeed. This gap has been achieved by designing the coupling section with a 120 nm gap on the lithographic mask. Due to optical proximity effects, the gap of the fabricated microring is smaller. Coupling sections with a gap greater than 65 nm have also shown to couple both modes efficiently.

15.5.5 Proof-of-Concept: BSA Experiment

A BSA molecule can be characterized as a prolate ellipsoid with dimensions 14 nm × 4 nm [58]. It is often used as a blocking agent in an immunoassay to prevent non-specific binding and adsorption to the surface [59]. The adsorption behavior of BSA on the silicon surface of the microring is thus crucial to avoid measuring false positives. It is a soft protein, meaning that it can easily change structure and shape

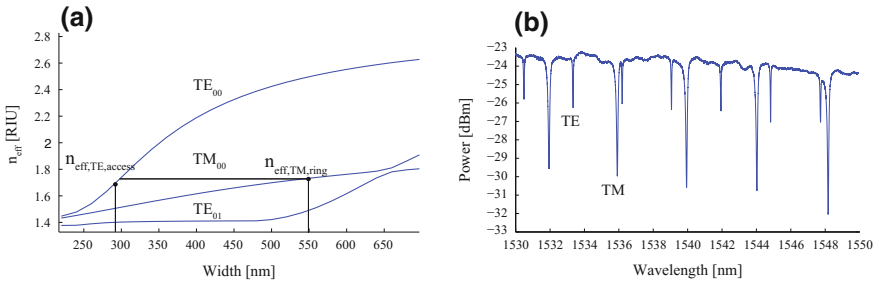

Fig. 15.24 **a** Effective index of the first three guided modes for a rectangular waveguide with a height of 220 nm and water cladding. The black lines show the slight phase mismatch for a 550 nm ring waveguide and a 290 nm access waveguide. **b** Measured fiber-to-fiber spectrum of the microring with water cladding. Both the TE and the TM resonances are visible. Reproduced from [51]

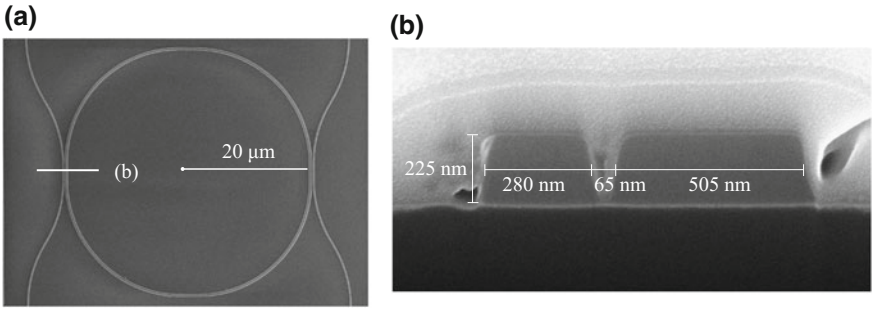

Fig. 15.25 SEM image of the microring with access waveguide and a square region where the ions bombarded the coupling section (**a**). After the ion bombardment, a SEM image of the cross section of the coupling section is taken (**b**), which shows the waveguide dimensions. Reproduced from [51]

depending on the chemical context. In [60], it is shown that it forms reversible conformational isomers in a bulk solution with changing pH. Previous experiments have studied this behavior in the context of adsorption on a silicon nitride surface [61]. They have shown that the adsorption is reduced at pH 3 with respect to pH 5 [61]. As a proof-of-concept, we record the (t,n) profile of a layer of BSA molecules during adsorption to the silicon surface, while changing the pH value of the buffer. This way, we show that the dual-polarization microring sensor is capable of recording conformational changes (Table 15.1).

The BSA molecules are dissolved in a PBS buffer with pH value 3 and 5. A sequence of water—BSA in PBS at pH 3, BSA in PBS at pH 5, BSA in PBS at pH 3—is streamed over the chip, and the captured resonance wavelengths of a TE and a TM mode are shown on Fig. 15.26a. A calibration protocol described in [51] is applied and used to calculate the thickness and the refractive index of the adsorbed BSA layer during the experiment, as shown in Fig. 15.27. With the commonly used

Table 15.1 The thickness, refractive index and adsorbed mass of the adsorbed BSA molecules for different pH values of the buffer. The values for pH 3 are those recorded during the first streaming of BSA in PBS at pH 3

	t pH 3	n pH 3	M pH 3	t pH 5	n pH 5	M pH 5
Microring	1.4 nm	1.433	1.70 ng/mm^2	3.0 nm	1.407	2.72 ng/mm^2

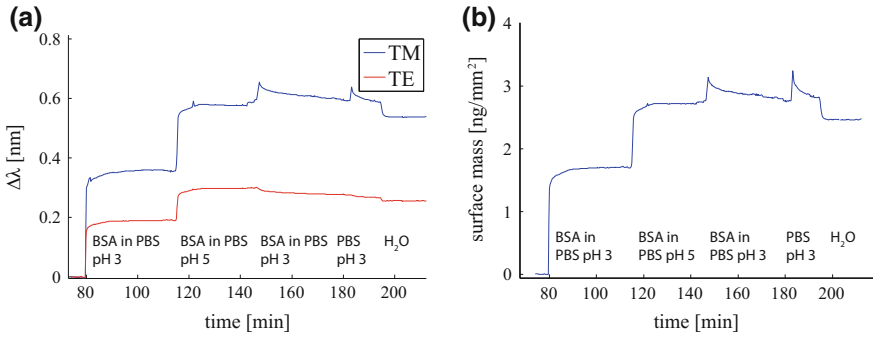

Fig. 15.26 **a** Resonance wavelength shift of the fundamental TE mode and fundamental TM mode of the BSA experiment in function of time. **b** Adsorbed mass ng/mm^2 of BSA molecules to the silicon surface. Reproduced from [51]

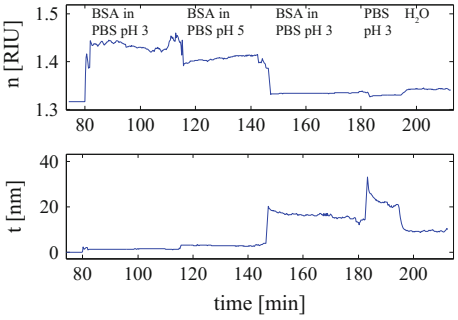

Fig. 15.27 Thickness and refractive index profile of the layer consisting of adsorbed BSA molecules. Reproduced from [51]

density of proteins of $\rho_{mol} = 1.35$ g/cm^3, the adsorbed mass can be obtained from n by using the following formula [62]:

$$\rho = \rho_{mol} \frac{n - n_B}{n_{mol} - n_B} \tag{15.16}$$

with n_B the refractive index of the buffer and n_{mol} the refractive index of the dry molecule, which is 1.45 for a wide class of proteins. The adsorbed mass, illustrated in Fig. 15.26b, can be calculated as

$$M = \rho\, t \tag{15.17}$$

The general trend of an increased adsorbed mass at pH 5 compared to pH 3 is confirmed. The increased adsorbed mass at pH 5 with respect to pH 3 can be explained by the fact that BSA molecules are close to their isoelectric point for pH 5, meaning that the molecules are almost free of charge such that they do not repel each other. This is in contrast to BSA molecules at pH 3, which have a positive charge. This also explains the slow contracting that is occurring during pH 5. This can be seen in Fig. 15.27, where the thickness decreases slightly during pH 5 and the refractive index, or density, rises with a similar small slope. At a pH value of 3, the BSA molecules are positively charged, while the silicon surface is negatively charged. The molecules tend to make as much contact as possible with the surface due to electrostatic attraction, forming a thin yet dense layer. When the pH value rises from 3 to 5, the BSA molecules become neutral and thus they lose this strong electrostatic attraction. They form a thicker layer which is albeit less dense due to the expansion of the molecules.

As a final observation, we note that when the fluid is switched back from pH 3 to pH 5, there is only a slight decrease in mass. This non-reversible behavior is clearly shown in Fig. 15.26b. This is explained in [63], where the authors describe the inability to wash off adsorbed BSA molecules on a hydrophilic surface. The surface of our chips is extremely hydrophilic, due to an oxygen plasma treatment. When the pH drop backs to 3, the BSA molecules become positively charged, such that they feel the electrostatic repulsion of neighboring molecules, yet they can not desorb easily. At this stage, we see a drop in refractive index to 1.335, accompanied by an increase in thickness to 19 nm, which saturates to 14 nm, which is exactly the long side of the BSA molecules in bulk solution. This suggests that the BSA molecules turn upright due to the increased repulsion, such that they are dangling in the buffer, explaining the very thick and sparse layer. Since the BSA molecules have a pronounced denaturation during adsorption to hydrophilic surfaces, they can be longer than in a bulk solution. The experimental observation of the inability to wash off the BSA molecules on a plasma-treated silicon surface under various conditions is important in an immunoassay as it prevents the blocking step to degrade in the washing steps of the immunoassay itself.

15.6 Conclusion

In this chapter, we discussed ring resonator sensors and showed how they can be a valuable tool for biosensing applications. Apart from the basic ring resonator sensors, we discussed mechanisms to eliminate resonance splitting, to improve sensitivity by using cascaded rings and to detect conformational changes by employing dual-polarization rings.

Acknowledgements Support from the EU is acknowledged through the projects FP7-Intopsens, FP7-CanDo, FP7 Pocket, and IMI-RAPPID.

References

1. K. De Vos, J. Girones, T. Claes, Y. De Koninck, S. Popelka, E. Schacht, R. Baets, P. Bienstman, Multiplexed antibody detection with an array of silicon-on-insulator microring resonators. IEEE Photonics J. **1**(4), 225–235 (2009)
2. K. De De Vos, I. Bartolozzi, E. Schacht, P. Bienstman, R. Baets, Silicon-on-Insulator microring resonator for sensitive and label-free biosensing. Opt. Express **15**(12), 7610–7615 (2007)
3. C.A. Barrios, K.B. Gylfason, B. Sánchez, A. Griol, H. Sohlström, M. Holgado, R. Casquel, Slot-waveguide biochemical sensor. Opt. Lett. **32**(21), 3080–3082 (2007)
4. M. Passaro, Optical sensing by optimized silicon slot waveguides. Opt. Express **15**(8), 4977–4993 (2007)
5. T. Claes, J.G. Molera, K. De Vos, E. Schacht, R. Baets, P. Bienstman, Label-free biosensing with a slot-waveguide-based ring resonator in silicon on insulator. IEEE Photonics J. **1**(3), 197–204 (2009)
6. K.B. Gylfason, C.F. Carlborg, A. Ka, F. Dortu, H. Sohlstr, L. Vivien, C.A. Barrios, W. Van Der Wijngaart, On-chip temperature compensation in an integrated slot-waveguide ring resonator refractive index sensor array Abstract. Optics express **18**(4), 3226–3237 (2010)
7. D.-X. Xu, M. Vachon, A. Densmore, R. Ma, A. Delâge, S. Janz, J. Lapointe, Y. Li, G. Lopinski, D. Zhang, Q.Y. Liu, P. Cheben, J.H. Schmid, Label-free biosensor array based on silicon-on-insulator ring resonators addressed using a WDM approach. Opt. Lett. **35**(16), 2771–3 (2010)
8. A. Densmore, D. Xu, N.A. Sabourin, H. Mcintosh, P. Cheben, J.H. Schmid, R. Ma, M. Vachon, A. Delâge, W. Sinclair, J. Lapointe, Y. Li, G. Lopinski, B. Lamontagne, S. Janz. A fully integrated silicon photonic wire sensor array chip and reader instrument. Opt. Express 350–352 (2011)
9. S. Janz, D. Xu, M. Vachon, N. Sabourin, P. Cheben, H. Mcintosh, H. Ding, S. Wang, J.H. Schmid, A. Delâge, J. Lapointe, A. Densmore, R. Ma, W. Sinclair, S.M. Logan, R. Mackenzie, Q.Y. Liu, D. Zhang, G. Lopinski, O. Mozenson, M. Gilmour, H. Tabor, Photonic wire biosensor microarray chip and instrumentation with application to serotyping of Escherichia coli isolates. Opt. Express **21**(4), 3243–3245 (2013)
10. M. Iqbal, M.A. Gleeson, B. Spaugh, F. Tybor, W.G. Gunn, M. Hochberg, T. Baehr-Jones, R.C. Bailey, L.C. Gunnm, Label-Free biosensor arrays based on silicon ring resonators and high-speed optical scanning instrumentation. IEEE J. Sel. Top. Quantum Electron. **16**(3), 654–661 (2010)
11. A.L. Washburn, L.C. Gunn, R.C. Bailey, Label-free quantitation of a cancer biomarker in complex media using silicon photonic microring resonators. Anal Chem. **81**(22), 9499–9506 (2010)
12. J.A. Qavi, R.C. Bailey, Multiplexed detection and label-free quantitation of microRNAs using arrays of silicon photonic microring resonators. Angew. Chem. (Int. ed. Engl.) **49**(27), 4608–4611 (2010)
13. M.S. Luchansky, A.L. Washburn, M.S. McClellan, R.C. Bailey, Sensitive on-chip detection of a protein biomarker in human serum and plasma over an extended dynamic range using silicon photonic microring resonators and sub-micron beads. Lab Chip **11**(12), 2042–2044 (2011)
14. A.J. Qavi, J.T. Kindt, M.A. Gleeson, R.C. Bailey, Anti-DNA:RNA antibodies and silicon photonic microring resonators: increased sensitivity for multiplexed microRNA detection. Anal. Chem. **83**(15), 5949–5956 (2011)
15. M.S. Luchansky, R.C. Bailey, Rapid, multiparameter profiling of cellular secretion using silicon photonic microring resonator arrays. J. Am. Chem. Soc. **133**(50), 20500–20506 (2011)
16. M.S. McClellan, L.L. Domier, R.C. Bailey, Label-free virus detection using silicon photonic microring resonators. Biosens. Bioelectron. **31**(1), 388–392 (2012)

17. A.J. Qavi, T.M. Mysz, R.C. Bailey, Isothermal discrimination of single-nucleotide polymorphisms via real-time kinetic desorption and label-free detection of DNA using silicon photonic microring resonator arrays. Anal. Chem. **83**(17), 6827–6833 (2011)
18. C.L. Arce, K. De Vos, T. Claes, K. Komorowska, D. Van Thourhout, P. Bienstman, Silicon-on-insulator microring resonator sensor integrated on an optical fiber facet. IEEE Photonics Technol. Lett. **23**(13), 890–892 (2011)
19. D. Witters, R. Puers, J. Lammertyn, P. Bienstman, Silicon photonic sensors incorporated in a digital microfluidic system. Anal. Bioanal. Chem. **404**(10), 2887–94 (2012)
20. C. Lerma Arce, S. Van Put, A. Goes, E. Hallynck, P. Dubruel, K. Komorowska, P. Bienstman, Reaction tubes: a new platform for silicon nanophotonic ring resonator sensors. J. Appl. Phys. **115**(4), 044702 (2014)
21. Wim Bogaerts, Peter De Heyn, Thomas Van Vaerenbergh, Katrien De Vos, Shankar Kumar, Tom Claes, Pieter Dumon, Peter Bienstman, Dries Van Thourhout, Roel Baets, Silicon microring resonators. Laser Photonics Rev. **6**(1), 47–73 (2011)
22. J. Zhu, S.K. Ozdemir, Y.-F. Xiao, L. Li, L. He, D.-R. Chen, L. Yang, On-chip single nanoparticle detection and sizing by mode splitting in an ultrahigh-Q microresonator, 4 (2009)
23. T.J. Kippenberg, S.M. Spillane, K.J. Vahala, Modal coupling in traveling-wave resonators. Opt. Lett. **27**(19), 1669–71 (2002)
24. B.E. Little, J.P. Laine, S.T. Chu, Surface-roughness-induced contradirectional coupling in ring and disk resonators. Opt. Lett. **22**(1), 4–6 (1997)
25. B.E. Little, S.T. Chu, H.A. Haus, J. Foresi, J.-P. Laine, Microring resonator channel dropping filters. J. Lightwave Technol. **15**(6), 998–1005 (1997)
26. S. Werquin, S. Verstuyft, P. Bienstman, Integrated interferometric approach to solve microring resonance splitting in biosensor applications. Opt. Express **21**(14), 16955–16963 (2013)
27. Joachim Knittel, Terry G. McRae, Kwan H. Lee, Warwick P. Bowen, Interferometric detection of mode splitting for whispering gallery mode biosensors. Applied Physics Letters **97**(12), 123704 (2010)
28. J. Hu, X. Sun, A. Agarwal, L.C. Kimerling, Biochem. Sens. **26**(5), 1032–1041 (2009)
29. D. Dai, Highly sensitive digital optical sensor based on cascaded high-q ring-resonators. Opt. Express **17**, 23817–23822 (2009)
30. M. La Notte, V.M. Passaro, Ultra high sensitivity chemical photonic sensing by Mach-Zehnder interferometer enhanced vernier-effect. Sens. Actuators B Chem. (2010). https://doi.org/10.1016/j.snb.2012.10.008
31. V. Zamora, P. Lutzow, M. Weiland, D. Pergande, A highly sensitive refractometric sensor based on cascaded SiN microring resonators. Sensors **13**(11), 1460110 (2013)
32. B. Liu, A. Shakouri, J. Bowers, Wide tunable double ring resonator coupled lasers. IEEE Photonics Technol. Lett. **14**, 600–602 (2002)
33. P. Rabiei, W. Steier, Tunable polymer double micro-ring filters. IEEE Photonics Technol. Lett. **15**, 1255–1257 (2003)
34. T. Claes, W. Bogaerts, P. Bienstman, Experimental characterization of a silicon photonic biosensor consisting of two cascaded ring resonators based on the Vernier-effect and introduction of a curve fitting method for an improved detection limit. Opt. Express **18**, 22747 (2010)
35. S.K. Selvaraja, P. Jaenen, W. Bogaerts, D.V. Thourhout, P. Dumon, R. Baets, Fabrication of photonic wire and crystal circuits in silicon-on-insulator using 193-nm optical lithography. IEEE J. Lightwave Technol. **27**, 4076–4083 (2009)
36. D.X. Xu, A. Densmore, A. Delâge, P. Waldron, R. McKinnon, S. Janz, J. Lapointe, G. Lopinski, T. Mischki, E. Post, P. Cheben, J.H. Schmid, Folded cavity soi microring sensors for high-sensitivity and real time measurement of biomolecular binding. Opt. Express **16**, 15137–15148 (2008)
37. S. Bhattacharya, A. Datta, J. Berg, S. Gangopadhyay, Studies on surface wettability of poly(dimethyl) siloxane (pdms) and glass under oxygen-plasma treatment and correlation with bond strength. IEEE J. Microelectromech. Syst. **14**, 590–597 (2005)

38. W. Bogaerts, D. Taillaert, B. Luyssaert, P. Dumon, J.V. Campenhout, P. Bienstman, D.V. Thourhout, R. Baets, V. Wiaux, S. Beckx, Basic structures for photonic integrated circuits in silicon-on-insulator. Opt. Express **12**, 1583–1591 (2004)
39. I.M. White, X. Fan, On the performance quantification of resonant refractive index sensors. Opt. Express **16**, 1020–1028 (2008)
40. J. Hu, X. Sun, A. Agarwal, L.C. Kimerling, Design guidelines for optical resonator biochemical sensors. J. Opt. Soc. Am. B **26**, 1032–1041 (2009)
41. H. Su, X.G. Huang, Fresnel-reflection-based fiber sensor for on-line measurement of solute concentration in solutions. Sens. Act. B **126**, 579–582 (2007)
42. M. Iqbal, M.A. Gleeson, B. Spaugh, F. Tybor, W.G. Gunn, M. Hochberg, T. Baehr-Jones, R.C. Bailey, L.C. Gunn, Label-free biosensor arrays based on silicon ring resonators and high-speed optical scanning instrumentation. IEEE J. Sel. Top. Quantum Electron. **16**, 654–661 (2010)
43. T. Claes, W. Bogaerts, P. Bienstman, Vernier-cascade label-free biosensor with integrated arrayed waveguide grating for wavelength interrogation with low-cost broadband source. Opt. Lett. **36**, 3320 (2011)
44. W. Bogaerts, S.K. Selvaraja, P. Dumon, J. Brouckaert, K. De Vos, D. Van Thourhout, R. Baets, Silicon-on-insulator spectral filters fabricated with CMOS technology. IEEE J. Sel. Topics Quantum Electron. **16**, 33 (2010)
45. Z. Xia, B. Momeni, M. Askari, M. Chamanzar, S. Yegnanarayanan, A.A. Eftekhar, A. Adibi, Silicon microring resonator sensor with integrated PC spectrometer for sharp spectral features detection. IEEE Photonics Annual Meeting **2010**, 329–330 (2010)
46. U.S. Department of Health and Human Services: Food and Drug Administration, Is it true FDA is approving fewer drugs lately? (2011), http://www.fda.gov/AboutFDA/Transparency/Basics/ucm247348.htm
47. European Federation of Pharmaceutical Industries and Associations, The pharmaceutical Industry in figures—Edition 2011 (2011), http://www.efpia.eu/pharmaceutical-industry-figures-edition-2011
48. U.S. Department of Health and Human Services: Food and Drug Administration, Innovation or stagnation: Challenge and opportunity on the critical path to new medical products (2004), http://www.fda.gov/ScienceResearch/SpecialTopics/CriticalPathInitiative/ucm076689.htm
49. P.R. Connelly, T.M. Vuong, M. Murcko, Getting physical to fix pharma. Nat. Chem. **3**, 692–695 (2011)
50. E. Reynaud, Protein misfolding and degenerative diseases. Nat. Educ. **3** (2010), http://www.nature.com/scitable/topicpage/protein-misfolding-and-degenerative-diseases-14434929
51. J.-W. Hoste, S. Werquin, T. Claes, P. Bienstman, Conformational analysis of proteins with a dual polarisation silicon microring. Opt. Express **22**, 2807–2820 (2014)
52. J. Voros, The density and refractive index of adsorbing protein layers. Biophys. J. **87**, 553–561 (2004)
53. F. Morichetti, A. Melloni, M. Martinelli, Effects of polarization rotation in optical ring-resonator-based devices. J. Lightwave Technol. **24**, 573–585 (2006)
54. K.E.D. Coan, M.J. Swann, J. Ottl, Measurement and differentiation of ligand-induced calmodulin conformations by dual polarization interferometry. Anal. Chem. **84**, 1586–1591 (2012)
55. J.D. Joannopoulos, S.G. Johnson, J.N. Winn, R.D. Meade, *Photonic Crystals: Molding the Flow of Light* (Princeton University Press, New Jersey, 2008)
56. L. Liu, Y. Ding, K. Yvind, J.M. Hvam, Silicon-on-insulator polarization splitting and rotating device for polarization diversity circuits. Opt. Express **19**, 12646–12651 (2011)
57. P. De Heyn, D. Vermeulen, D. Van Thourhout, G. Roelkens, Silicon-on-insulator all-pass microring resonators using a polarization rotating coupling section. IEEE Photonics Technol. Lett. **24**, 1176–1178 (2012)
58. T. Peters, Serum Albumin. Adv. Protein Chem. **37**, 161–245 (1985)
59. S.H. Brorson, Bovine serum albumin (BSA) as a reagent against non-specific immunogold labeling on LR-White and epoxy resin. Micron **28**, 189–195 (1997)
60. D.C. Carter, J.X. Ho, Structure of serum albumin. Adv. Protein Chem. **45**, 153–203 (1994)

61. N.J. Freeman, L.L. Peel, M.J. Swann, G.H. Cross, A. Reeves, S. Brand, J.R. Lu, Real time, high resolution studies of protein adsorption and structure at the solid-liquid interface using dual polarization interferometry. J. Phys. Condens. Matter **16**, 2493–2496 (2004)
62. B. Lillis, M. Manning, H. Berney, E. Hurley, A. Mathewson, M.M. Sheehan, Dual polarisation interferometry characterisation of DNA immobilisation and hybridisation detection on a silanised support. Biosens. Bioelectron. **21**, 1459–1467 (2006)
63. Y.L. Jeyachandran, E. Mielczarski, B. Rai, J.A. Mielczarski, Quantitative and qualitative evaluation of adsorption/desorption of bovine serum albumin on hydrophilic and hydrophobic surfaces. Langmuir **25**, 11614–11620 (2009)
64. X. Fan, I.M. White, S.I. Shopoua, H. Zhu, J.D. Suter, Y. Sun, Sensitive optical biosensors for unlabeled targets: a review. Anal. Chim. Acta **620**, 8–26 (2008)
65. A.J. Qavi, A.L. Washburn, J.-Y. Byeon, R.C. Bailey, Label-free technologies for quantitative multiparameter biological analysis. Anal. Bioanal. Chem. **394**, 121–135 (2009)
66. K. De Vos, J. Girones, T. Claes, Y. De Koninck, S. Popelka, E. Schacht, R. Baets, P. Bienstman, Multiplexed antibody detection with an array of silicon-on-insulator microring resonators. IEEE Photonics J. **1**, 225–235 (2009)
67. M. Lee, P.M. Fauchet, Two-dimensional silicon photonic crystal based biosensing platform for protein detection. Opt. Express **15**, 4530–4535 (2007)
68. T. Claes, J. Girones, K. De Vos, E. Schacht, R. Baets, P. Bienstman, Label-free biosensing with a slot-waveguide-based ring resonator in silicon on insulator. IEEE Photonics J. **1**, 197–204 (2009)
69. C.F. Carlborg, K.B. Gylfason, A. Kaźmierczak, F. Dortu, M.J. Bañuls, Polo, A. Maquieira Catala, G. M. Kresbach, H. Sohlström, T. Moh, L. Vivien, J. Popplewell, G. Ronan, C. A. Barrios, G. Stemme, W. Van der Wijngaart, A packaged optical slot-waveguide ring resonator sensor array for multiplex label-free assays in labs-on-chips. Lab Chip **10**, 281–90 (2010)
70. A. Densmore, M. Vachon, D.-X. Xu, S. Janz, R. Ma, Y.-H. Li, G. Lopinski, A. Delâge, J. Lapointe, C.C. Luebbert, Q.Y. Liu, P. Cheben, J.H. Schmid, Silicon photonic wire biosensor array for multiplexed real-time and label-free molecular detection. Opt. Lett. **34**, 3598–3600 (2009)
71. F. Blanco, M. Agirregabiria, J. Berganzo, K. Mayora, J. Elizalde, A. Calle, C. Dominguez, L. Lechuga, Microfluidic-optical integrated cmos compatible devices for label-free biochemical sensing. J. Micromech. Microeng. **16**, 1006–1016 (2006)
72. P. Dumon, W. Bogaerts, D. Van Thourhout, D. Taillaert, R. Baets, J. Wouters, S. Beckx, P. Jaenen, Compact wavelength router based on a silicon-on-insulator arrayed waveguide grating pigtailed to a fiber array. Opt. Express **14**, 664–669 (2006)
73. J. Brouckaert, W. Bogaerts, S. Selvaraja, P. Dumon, R. Baets, D. Van Thourhout, Planar concave grating demultiplexer with high reflective bragg reflector facets. IEEE Photonics Technol. Lett. **20**, 309–311 (2008)
74. D.X. Xu, M. Vachon, A. Densmore, R. Ma, A. Delage, S. Janz, J. Lapointe, Y. Li, G. Lopinski, D. Zhang, Q.Y. Liu, P. Cheben, J.H. Schmid, Label-free biosensor array based on silicon-on-insulator ring resonators addressed using a WDM approach. Opt. Lett. **35**, 2771 (2010)
75. P.S. Petrou, M. Kitsara, E. Makarona, I. Raptis, S.E. Kakabakos, R. Stoffer, G. Jobst, K. Misiakos, Monolithically Integrated Biosensors based on Frequency-Resolved Mach-Zehnder Interferometers for Multi-analyte determinations, in *Conference on Proceeding of the IEEE Engineering Medicine and Biology Society* (2010), p. 298
76. P.S. Petrou, M. Kitsara, E. Makarona, I. Raptis, S.E. Kakabakos, R. Stoffer, G. Jobst, K. Misiakos, Monolithically Integrated Biosensors based on Frequency-Resolved Mach-Zehnder Interferometers for Multi-analyte determinations, in Conference on Proceeding of the IEEE Engineering Medicine and Biology Society, p. 298 (2010)
77. L. Jin, M. Li, J.-J. He, Optical waveguide double-ring sensor using intensity interrogation with a low-cost broadband source. Opt. Lett. **36**, 1128 (2011)
78. L. Jin, M. Li, J.-J. He, Highly-sensitive silicon-on-insulator sensor based on two cascaded micro-ring resonators with vernier effect. Opt. Commun. **284**, 156 (2011)

79. N.J. Freeman, L.L. Peel, M.J. Swann, G.H. Cross, A. Reeves, S. Brand, J.R. Lu, Dual-polarisation interferometry: an analytical technique to measure changes in protein structure in real time, to determine the stoichiometry of binding events, and to differentiate between specific and nonspecific interactions. Anal. Biochem. **329**, 190–198 (2004)
80. S. Ricard-Blum, L.L. Peel, F. Ruggiero, N.J. Freeman, Dual polarisation interferometry characterization of carbohydrate-protein interactions. Anal. Biochem. **352**, 252–259 (2006)
81. F. Bahrami, M.Z. Alam, J.S. Aitchison, M. Mojahedi, Dual polarization measurements in the hybrid plasmonic biosensors. Plasmonics **8**, 465–473 (2013)
82. Y. Atsumi, D.-X. Xu, A. Delge, J.H. Schmid, M. Vachon, P. Cheben, S. Janz, N. Nishiyama, S. Arai, Simultaneous retrieval of fluidic refractive index and surface adsorbed molecular film thickness using silicon wire waveguide biosensors. Opt. Express **20**, 26969–26977 (2012)
83. S.K. Selvaraja, P. Jaenen, W. Bogaerts, D. Van Thourhout, P. Dumon, R. Baets, Fabrication of photonic wire and crystal circuits in silicon-on-insulator using 193 nm optical lithography. J. Lightwave Technol. 1–8 (2009)
84. J.T. Robinson, K. Preston, O. Painter, M. Lipson, First-principle derivation of gain in high-index-contrast waveguides. Opt. Express **16**, 16659–16669 (2008)
85. K. Okamoto, *Fundamentals of Optical Waveguides* (Academic Press, Burlington, 2008)
86. P.D. Coffey, M.J. Swann, T.A. Waigh, F. Schedin, J.R. Lu, Multiple path length dual polarization interferometry. Opt. Express **17**, 10959–10969 (2009)
87. K. De Vos, I. Bartolozzi, E. Schacht, P. Bienstman, R. Baets, Silicon-on-Insulator microring resonator for sensitive and label-free biosensing. Opt Express **15**, 7610–7615 (2007)
88. P. Schiebener, J. Straub, J.M.H. Levelt, Sengers, and J. S. Gallagher, "Refractive index of water and steam as function of wavelength, temperature and density,". J. Phys. Chem. Ref. Data **19**, 677–717 (1990)
89. S.B. Habib, E.G. Ii, R.F. Hicks, Atmospheric oxygen plasma activation of silicon (100) surfaces. J. Vac. Sci. Technol. A **28**, 476–485 (2013)

Chapter 16
SOI Waveguide-Based Biochemical Sensors

Ahmmed A. Rifat, Rajib Ahmed and Bishanka Brata Bhowmik

Abstract Silicon-on-insulator (SOI)-based nanophotonic is a well-matured technology which enables to fabricate a myriad of optical devices such as sensors, light-emitting diode (LED), organic-LED, photodetectors. The SOI-based biochemicals sensing overcomes the limitations of previous electrical and fiber-based sensing technologies. Here, theoretical framework, performance criteria, and recent progress on SOI-based waveguide and micro-ring resonator sensors are discussed. Finally, this chapter summarizes the SOI-based sensors design and optimizes the configurations for high-sensing performance. Furthermore, the main challenges in SOI-based sensors and possible solutions to these challenges are also outlined.

Keywords Silicon-on-insulator · Waveguide · Chemical sensors
Ring resonators · Optical sensing and sensors

16.1 Introduction

Recently, optical waveguide (WG)-based sensing has become an emerging technology. It allows real time, fast and precise sensing of different physical parameters like temperature, pressure, humidity, corrosion [1, 2]. The advancement of SOI technology has enabled the possibility to fabricate the miniaturized WG-based sensors. The optical WG sensors have shown the great advantages compared to the

A. A. Rifat (✉)
Nonlinear Physics Centre, Research School of Physics and Engineering,
Australian National University, Acton, ACT 2601, Australia
e-mail: RifatAhmmed.Aoni@anu.edu.au

R. Ahmed
Nanotechnology Laboratory, School of Engineering, University of Birmingham,
Birmingham B15 2TT, UK

B. B. Bhowmik
Electronics & Communication Engineering, Tripura University,
Suryamaninagar 799007, Tripura, India

© Springer International Publishing AG, part of Springer Nature 2019

M. F. O. Hameed and S. Obayya (eds.), *Computational Photonic Sensors*, https://doi.org/10.1007/978-3-319-76556-3_16

mechanical and electronic sensors such as quick response, high sensitivity, lower power consumption, free from electromagnetic interference, small footprint which make them promising in the sensing technology [3, 4].

In WG sensing, the advantages over electronic and mechanical sensors are that there is no electromagnetic interference, and having higher sensitivity, quick response, lower power consumption, higher multiplexed configuration, small footprint eliminates the necessity of fluorescent labelling process for biosensing and facilities the label-free configuration [5–7]. To date, several types of WG-based sensors such as long-period fiber grating [8], oligomer [9], MZI interferometer [10], prism-based surface plasmon resonance sensor [11], Bragg-grating sensor [12] have been reported. Among the reported sensing schemes, micro-ring resonator (MRR) is one of the key sensing techniques in WG platform which consist of a ring and one or two straight WGs. Moreover, CMOS compatible optical MRR technology has attracted the field of integrated photonic sensor due to its low cost and capability of mass production. Also using technology, monolithically integration of photonics and electronics can be done. Recent advancements and realization of photonics elements using silicon-on-insulator technology have been demonstrated in Refs. [10–13]. Different optical properties of MRR have been used to act as sensor. Some of the important sensing may be based on refractive index variation, light absorption capability, or Raman and fluorescence-based [13–15]. Moreover, sensing may be classified as a bulk and surface sensing. Therefore, sensing principle may be based on WG surface or surrounding volume refractive index (RI) variation. WG-based sensor is also classified as refractive index sensor. The sensing principle is based on shift in resonance frequency due to RI variation. WG-based bulk RI sensors have been used to sense liquid/gaseous analytes (chemicals, DNA, proteins, etc.). 2.8×10^{-8} RIU variation was measured efficiently with 0.01 μg/m L^{-1} protein variation [4, 16]. Moreover, liquid or gaseous phase analytes are also used for surface detection. For example, antibodies, immobilized DNA can be detected using RI-based surface sensing and sensitivity ~1.6 pg mm^{-2} can be achieved. DNA or antibodies detection can be used as a point-of-care diagnostic or clinical purpose. Nowadays, using photonics sensors, a small amount of sample in the range of nmol L^{-1} [17] or even less than 10 pmol L^{-1} [18] and accurate DNA detection is possible.

In this chapter, different WG structures, WG-based biochemical sensing principles, approaches, developments are discussed. Different WG-based MRRs and their applications in biochemical sensing are described. Sensing performance criteria, limitations, and future challenges are also outlined.

16.2 SOI-Based Optical Sensing

Generally, light is confined within the WG along the dimensions of 1D, 2D, or 3D. Based on the light confinement dimension, planar WG can be classified as planar WGs (1D), channel WGs (2D), and photonic crystals (3D), respectively.

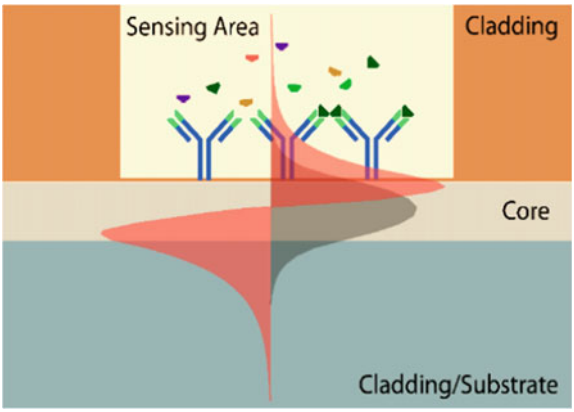

Fig. 16.1 Evanescent wave detection principle [19]

The working principle of the optical sensors is mainly based on the evanescent field detection principle [6, 7]. The light propagate through the SOI waveguide following the total internal reflection (TIR). In SOI waveguide, the light propagate through the core-medium and some of the light penetrates through the cladding region (See Fig. 16.1). By etching, the cladding surface sensing performance can be achieved and the behavior of the guided light in the core is directly related to the evanescent area over the surface.

16.2.1 Historical Sensing Approaches

The invention of laser technology has led the advancement of communication system. The WG technology shows the tremendous way to carrying the information and optical energy. Due to planar surface structure, WG shows great development in the optical sensing area. Until 1990s, the development of WG-based sensors was slow due to lack of advanced optical instrumentations and also prices of the components were high [1, 2, 8]. For example, a simple laser diode price was approximately $3000 (prototypes) in 1980s and it reduced to $3 (compact disk players) in 1990s.

Furthermore, the development of WG sensor was difficult for technological limitation and also its applications were limited. Due to high price and limited applications, WG was not widely applicable. However, nowadays, due to advancement to silicon photonics, it is possible to produce compact and cheaper price WGs, and as a result, WG has got great attention since last few decades. Optical fiber is one of the promising optical sensing schemes due to its efficient light propagating capabilities; however, nowadays, strip and dielectric WG structures are also capable of propagating light. As a result, WG structures are now widely used in the field of integrated optics with broad range of applications including sensing. The relationship between available components and the

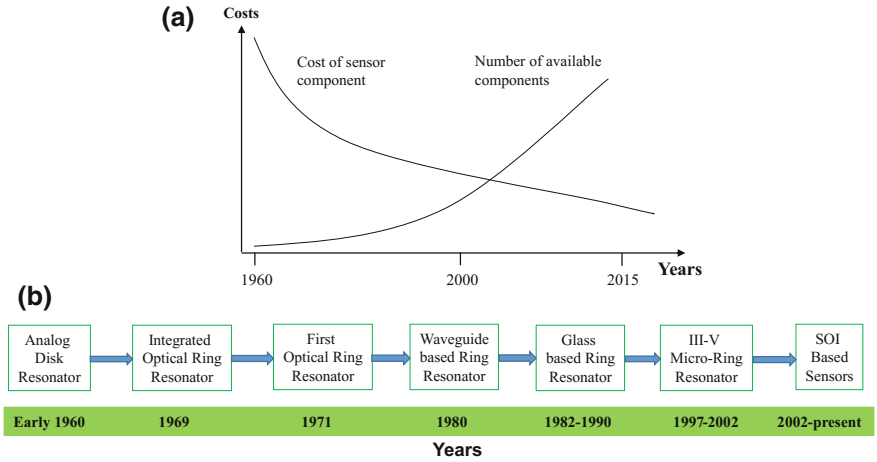

Fig. 16.2 **a** Relationship between cost and available components, and **b** milestones in WG resonators [7]

approximate costs in the years from 1960 to 2017 is shown in Fig. 16.2a. Moreover, the progress of waveguide-based sensors is also shown in Fig. 16.2b.

In 1893, Joseph John Thomson proposed the WG structure for the first time which has been implemented by Oliver Joseph Lodge in 1894 [20]. In 1897, Rayleigh theoretically developed the wave propagation through the metal-based WG structure and showed the transverse mode for the sound wave [21, 22]. Like the optical fiber, WG-based structures have gained the attention in 1920s, and initially, it focused the attention for communication applications [16].

Early 1960s, various types of WG structures such as disk and ring resonators have been introduced. Integrated ring resonator has been proposed by Bell Laboratories in 1969. In 1971, optical resonator has been proposed by Weber and Ulrich. Initially, optical fiber-based ring resonator has been proposed by Stokes et al. in 1982. However, the structure was bulky and large scale of integration was required. In 1997, Rafizadeh et al. have reported the GaAs-AlGaAs (III–V) material-based micro-ring resonator for the first time [4, 23–27].

16.2.2 Development, Materials, and Sensor Configurations

Nowadays, to advance the SOI WG technology, various materials are widely used such as silicon, silica, polymer, compound semiconductor, and glass. Among them, silica-based WG technology has shown great attention due to low propagation loss, inexpensive price, and fabrication simplicity [12, 18–20]. Moreover, each material has its own advantages and disadvantages, and a comparison chart between widely used materials is shown in Table 16.1. Different types of WG structures such as

Table 16.1 Comparison between widely used optical materials in SOI [27]

Materials	Advantages	Disadvantages
Semiconductors	• Well-developed fabrication process • Ultra-compact devices • High optical nonlinearity • Ease to integrate with existing CMOS technology	• Processing steps are complex • High cost • High propagation loss
Silica	• Easy fabrication process • Low propagation loss • Low cost	• Low optical nonlinearity • Limited photonic-circuit applications
Polymers	• Various fabrication techniques • Fabrication steps are straightforward • Low propagation loss • High optical nonlinearity	• Processing steps are not well mature

slotted WG, strip WG, single-slotted, double-slotted WG have been developed based on the applications with design feasibility. The basic WG structures are shown in Fig. 16.3.

The conventional strip WG and its electric field distribution are shown in Fig. 16.3a [28]. Due to large refractive index contrast between silicon and air, this kind of WG structure shows strong confinement. This kind of WG structure can be easily utilized as a sensor by simply flowing through or dripped the unknown analyte/sample top of the surface.

Due to the presence of sample with different refractive index, light will couple with the outside sensing medium; as a result, optical phenomena such as either transmission or intensity will change. Another silicon WG approach is shown in Fig. 16.3b, where the silicon WG is covered with the nonlinear materials. Due to thin WG strip, magnetic field can oscillate far into the external surface. Nowadays, another interesting WG sensing approach is the slotted WG structure where the WGs are divided into two or three slots. The slots not only individually guide the light but also enhance the intensity (Fig. 16.3c). Moreover, it also leads to the multi-analytes detection by using different materials/samples in different slots. Photonic crystal-based slot WG is another interesting approach (Fig. 16.3d). Photonic crystal leads to the selective liquid infiltration facility and also can be coated or filled with plasmonic materials such as gold, silver, copper, etc. which can enhance the sensing performance significantly.

Recently, Wei Ru et al. experimentally demonstrated a long-range surface plasmon-based WG sensor for the detection of dengue infection in blood plasma (Fig. 16.4) [29].

Due to planar surface, homogenous metal coating can be developed easily which is the key problem of photonic crystal fiber-based surface plasmon resonance sensors [30, 31]. The microscopic image of the long-range surface plasmon-based WG sensor is shown in Fig. 16.4a and the cross section of the functionalized WG and a CYTOP-embedded WG (a fluoropolymer having a refractive index close to

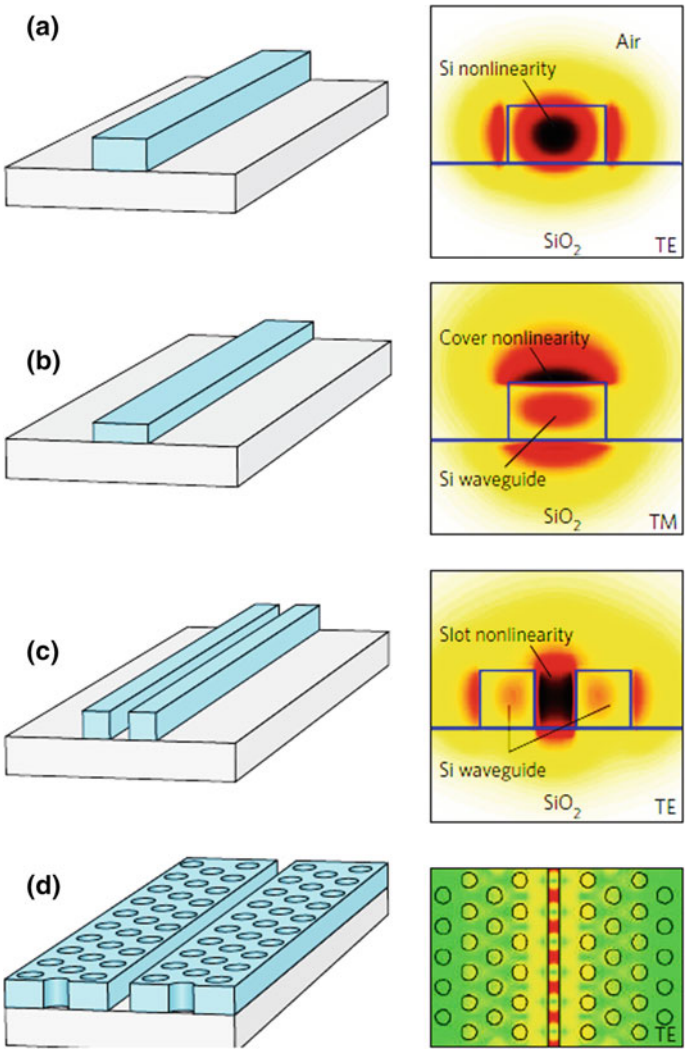

Fig. 16.3 SOI WG structure and corresponding electric field distributions. **a** Strip WG using silicon nonlinearity in core. **b** Strip WG using cover nonlinearities. **c** Slot WG using nonlinearities in the slot. **d** Slotted photonic crystal WG. Reprinted with permission from Macmillan Publishers Ltd. [28]

that of biologically compatible fluids) is shown in Fig. 16.4b. Recently, combining the Mach–Zehnder interferometer (MZI) and micro-ring resonator techniques, a highly sensitive WG sensor has been reported where optical phenomena show the Fano-resonance response (Fig. 16.5).

Polymer WG and substrate are used to fabricate the optical accelerometer. It could be realized by liftoff process. It shows the maximum sensitivity of

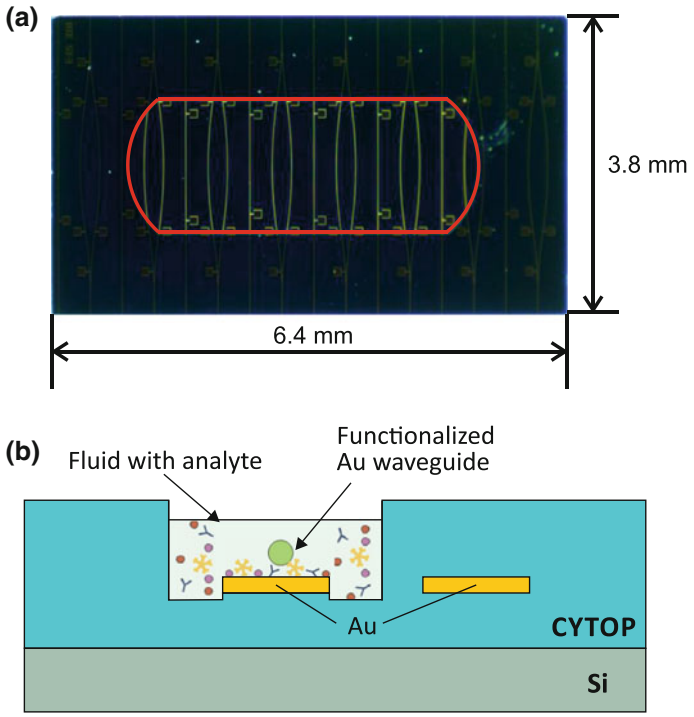

Fig. 16.4 Long-range surface plasmon (LRSPP)-based sensor: **a** SEM image of the LRSPP-based sensor. **b** Cross section functional view of the proposed sensor with a CYTOP-embedded WG. Reprinted with permission from American Chemical Society [29]

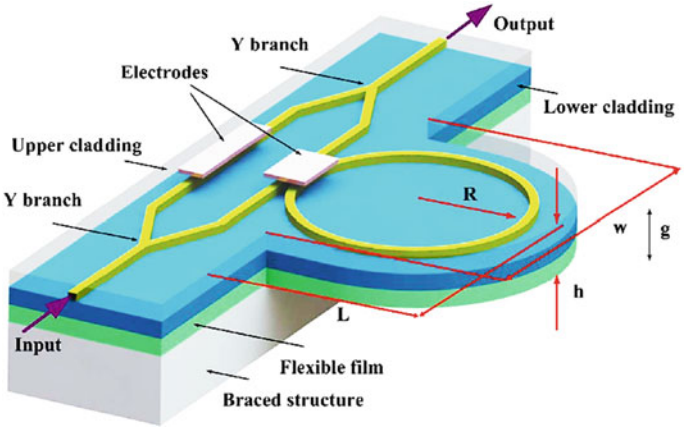

Fig. 16.5 Schematic diagram of the Mach–Zehnder interferometer-based optical WG sensor. Reprinted with permission from the Optical Society [32]

111.75 mW/g, which is 393-fold increase in sensitivity compared to the conventional MZI WG-based sensors [32]. Yipei et al. reported a plasmonic nano-sensor for refractive index sensing using Au-nanowire WG (Fig. 16.6a) [26]. To realize the phase-shift effect due to change of surrounding mediums refractive index, a plasmonic nanowire Mach–Zehnder interferometer has been used. It shows the maximum sensitivity as high as 5.5 π/(μm RIU), and the sensitivity can be enhanced by reducing the nanowire diameter. It is clearly visible in Fig. 16.6b that with the increasing of nanowire diameter sensor performance reduced significantly and maximum sensor performance has been achieved at nanowire diameter 10 nm. Also, it is notable that with the increase of sample concentration, propagation constant increases monotonically.

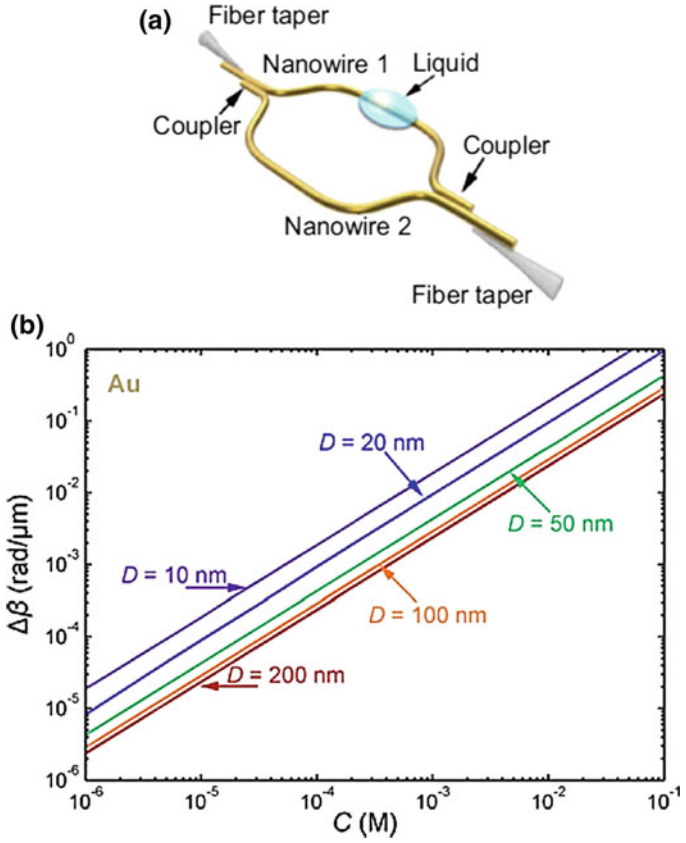

Fig. 16.6 **a** Schematic of the MZI-based WG sensor. **b** Propagation constant as a function of molecular concentration benzene [26]

16.3 WG-Based Sensing

WG-based sensing techniques can be generalized into two categories such as bulk sensing and surface sensing. The details of bulk and surface sensing schemes are described in the following sections.

16.3.1 Bulk Sensing

The upper cladding refractive index can be changed consistently as a result bulk refractive index will also change accordingly. The sensitivity which is measured by using the bulk refractive index changed is known as the bulk sensing [7, 13, 33].

$$\text{Bulk Sensitivity, } S_{\text{Bulk}}\,(\text{nm/RIU}) = \frac{\lambda^* \left(\frac{\partial n_{eff}}{\partial n}\right)}{n_g} \tag{16.1}$$

where group index is n_g, effective index is n_{eff}, and the central wavelength, λ_0.

Figure 16.7a, b show the mode profiles of 800 × 220 nm^2 WG for the TE_{00} and TM_{00} modes [33].

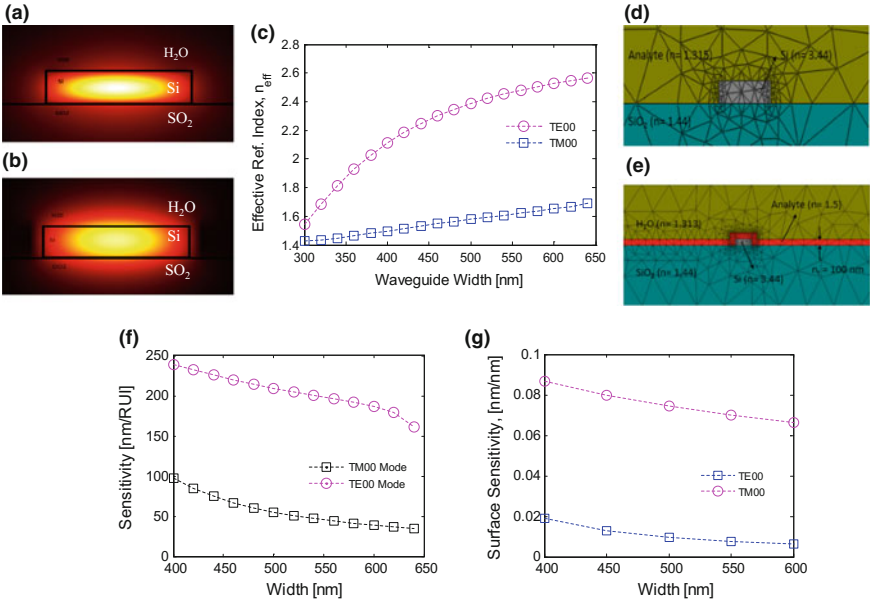

Fig. 16.7 Modeled WG-based sensing. **a** TE mode, **b** TM mode profile and **c** effective RI as a function of WG width for TE and TM mode. Optical modeling of **d** bulk and **e** surface sensing. **f** Bulk sensing and **g** surface sensitivity (nm/RIU) for TE and TM modes as a function of WG width (nm) [27]

Due to smaller height compared to the width, most of the magnetic field TM_{00} is confined outside the core, and only electric field TE_{00} is confined in the core. With the increase of WG width, refractive index of TE_{00}, and TM_{00} modes increases significantly and n_{eff} of electric field is high compared to the magnetic field (Fig. 16.7c). Figure 16.7d shows the cross section of bulk WG, and corresponding bulk sensitivity is shown in Fig. 16.7f. It is visible that maximum bulk sensitivity is achieved of 240 nm/RIU for the TE_{00} mode whereas 100 nm/RIU for TM_{00} mode.

16.3.2 Surface Sensing

In the surface sensing, surface thickness and analyte refractive index can be changed simultaneously. Surface sensing is advantageous if the electric field decays exponentially in the surface. By using the suitable adhesive layer, surface sensing can be enhanced as the different materials have analyte attraction capability due to their large surface area and surface to volume ratio [7, 34, 35]. The surface sensing depends on the change in n_i or n_t.

Therefore, the surface sensitivity can be

$$S_{Surface}[\text{nm/RIU}] = \frac{\lambda * \left(\frac{\partial n_{eff}}{\partial n_i}\right)}{n_g} \tag{16.2}$$

$$S_{Surface}[\text{nm /nm}] = \frac{\lambda * \left(\frac{\partial n_{eff}}{\partial n_t}\right)}{n_g} \tag{16.3}$$

The cross-sectional view of the surface WG sensor is shown in Fig. 16.7e, and bulk sensitivity of the sensor is shown in Fig. 16.7g. According to Fig. 16.7g, it is visible that magnetic mode intensity is high compared to the electric field which is opposite in the case of bulk sensitivity.

16.4 Mode Multiplex WG Sensing

Recently, multimode WG sensor based on semi-triangular resonator has been demonstrated by Rajib et al. [27]. It shows three different analytes detection capability using the matrix inversion method (MIM). The reported ring WG dimension is 800 × 200 nm^2, which helps to allow three different modes such as TE_{00}, TE_{01}, and TM_{00} modes (see Fig. 16.8). The access WG is either single (Coupler-1) or multi-mode (Coupler-2, 3). The important part of this sensor is coupler design which helps to couple between different modes and analytes. The field distribution of different modes is shown in Fig. 16.9. The effective index

method (EIM) has been used to investigate the performance. The parameters of the couplers are defined as WGs distance (d), coupling length (Lc), and coupler length (L).

It shows the different analytes (n_1, n_2, and n_3) detection capability with different modes such as TE_{00}, TE_{01}, and TM_{00} in the ring WG, whereas the bus WG contains only TE_{00} and TM_{00} modes. The odd–even index pairs have been used to optimize the parameters. For coupler-1, the optimized distance d = 200 nm and coupling length $L_c^{TE_{01}} = 130$ μm, and 3 dB coupler length $L^{TE_{01}} = 65$ μm. Similarly, d = 90 nm and $L_c^{TE_{00}} = 1038$ μm, and $L^{TE_{00}} = 519$ μm for coupler-2 and d = 150 nm, $L_c^{TM_{00}} = 36.55$ μm, and $L^{TM_{00}} = 18.27$ μm have been optimized for coupler-3, respectively. As a result, the total length of the ring is as follows:

$$L_R = L_1 + L_2 + L_3 + 3 \times \left(\frac{1}{3}\right) \times (2\pi r)$$
$$= (65 + 519.29 + 18.27)\,\mu m + (2\pi \times 5)\,\mu m = 633.98\,\mu m$$

Here, the radius of the ring is r = 5 μm and the attenuation is α = 3 dB/cm.

Generally, SOI WG-based structure shows high refractive index contrast (n_{eff} difference between core and cladding), and as a result, it exhibits the sharp bents.

Utilizing the optimized parameters, it showed that TM mode has high sensitivity compared to the TE mode in both surface and bulk sensitivity methods and this statement has well agreement with Ref. [36]. Moreover, it is evident that evanescent fields are situated near the surface; as a result, surface sensitivity is more suitable compare to the bulk sensing. Among the three different modes, TE01 mode shows the highest Q-factor of 41,728 and lower full width at half maxima (FWHM) of 57.56 and lower free spectral range (FSR) of 824.8. Minimum FWHM enhances the detection accuracy, and Q-factor has significant effects to enhance the sensor performance.

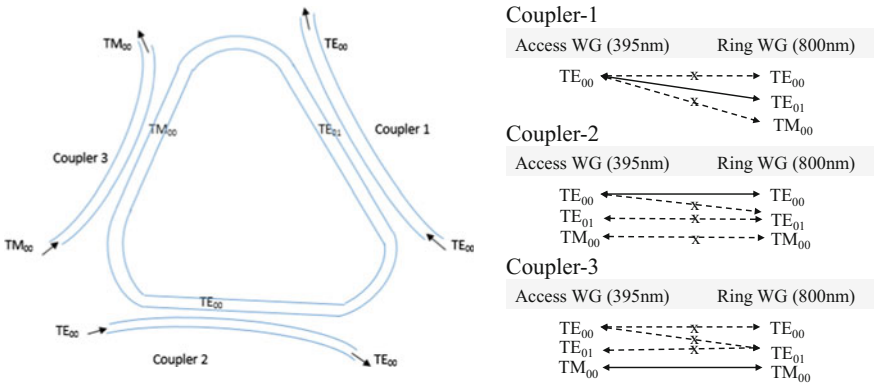

Fig. 16.8 Semi-triangular ring resonator sensor consisting of three couplers for TE_{00}, TE_{01}, and TM_{00} modes in the ring to sense three analyte layers [33]

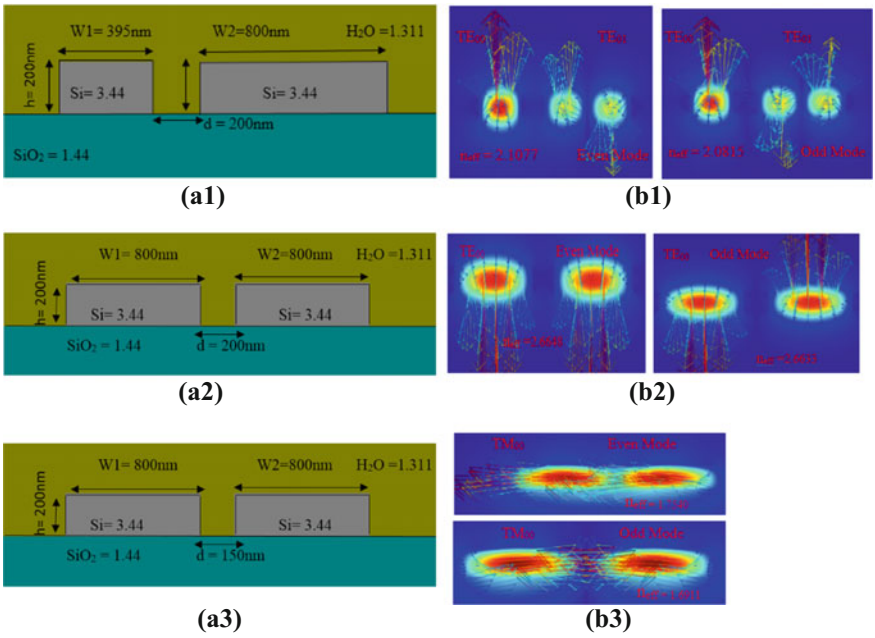

Fig. 16.9 Multi-mode WG sensor. (**a1–3**) Cross-sectional view of Coupler-1, 2, 3, and (**b1–3**) field distribution of odd and even modes [33]

16.5 Micro-ring Resonator-Based Sensing and Performance Criteria

Micro-ring resonator (MRR) is a device, which works following the principle of circulating light inside an optical cavity. It is a WG structure with a ring WG and one or two straight WGs (see Fig. 16.10). The MRR can be categorized into active and passive optical resonators based on the light-circulating medium and need of external energy. Active optical resonators are widely used for the modulators, phase shifter, producing lasers, etc. In 1969, Marcatili proposed the micro-ring resonator for the first time [37]. Based on the ring coupling with the WGs, micro-ring resonator is also divided into two categories such as all-pass ring resonator (when ring coupled with single WG) and add-drop ring resonator (when ring coupled with two WGs). All-pass ring resonator and its field distribution have been shown in Fig. 16.10a, b. Similarly, add-drop ring resonator and its corresponding field distribution have been shown in Fig. 16.10c, d.

In MRR, the ring resonator is placed close to the WGs so that propagating light through the WGs can couple with the ring resonator and vice versa [13, 38]. This mechanism is called directional coupling. There are few other methods also available such as multi-mode interference (MMI) coupler, effective mode interference (EMI) [39].

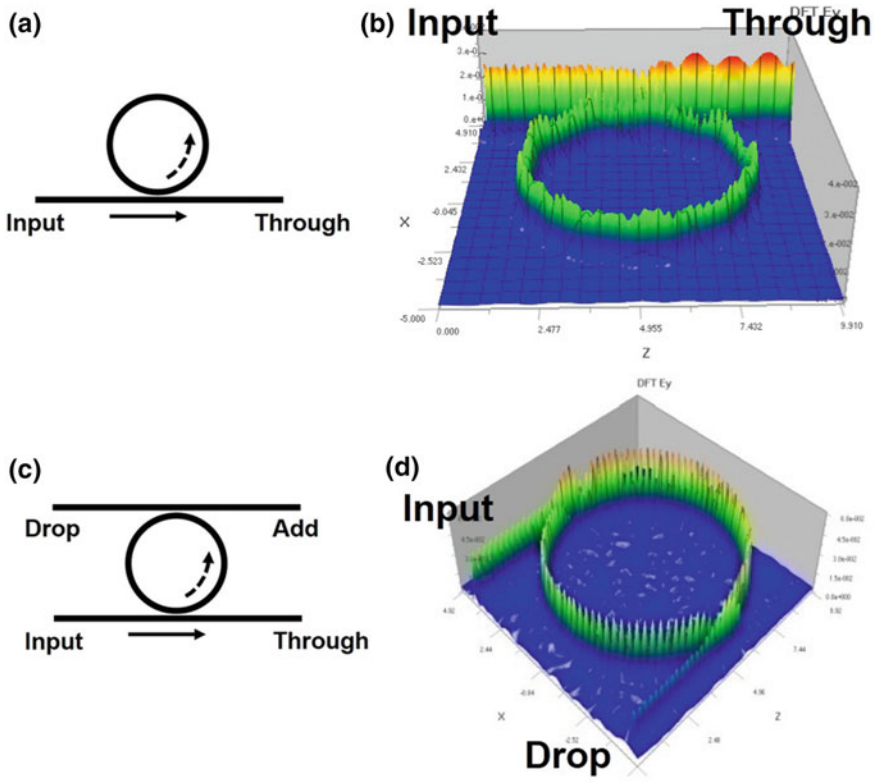

Fig. 16.10 **a** and **b** All-pass MRR configuration and E-field distribution, respectively. **c** and **b** Add-drop MRR configuration and E-field distribution, respectively

Like other optical sensing techniques such as optical grating, MZI, surface plasmon resonance, sensitivity of the ring resonator also depends on the shift of the resonance wavelength which occurs due to change of analyte refractive index. The sensitivity of a ring resonator can be calculated by the following equation [32]:

$$\Delta\lambda_{res} = \left(\frac{\Delta n_{eff} L}{m}\right), \quad m = 1, 2, 3 \ldots \tag{16.4}$$

where m is the resonance mode, L (= 2πr) is circumference of the ring WG, Δn_{eff} is the effective index variation of the WG influenced by the surrounding medium.

n_{eff} is the effective refractive index of WG influenced by the surrounding sensing medium. Due to the presence of the analytes (n_i), effective index (n_{eff}) will change; as a result, wavelength shift will occur:

$$\begin{aligned}
\Delta\lambda_{res} &= \frac{\left[\left(\frac{\partial n_{eff}}{\partial n_i}\right)\Delta n_i + \left(\frac{\partial n_{eff}}{\partial \lambda}\right)\lambda\right]}{m} \cdot L \\
\Rightarrow m \cdot \Delta\lambda_{res} &= \left[\left(\frac{\partial n_{eff}}{\partial n_i}\right)\Delta n_i + \left(\frac{\partial n_{eff}}{\partial \lambda}\right)\lambda\right] \cdot L \\
\Rightarrow \left(\frac{m}{L} - \frac{\partial n_{eff}}{\partial \lambda}\right) \cdot \Delta\lambda_{res} &= \frac{\partial n_{eff}}{\partial n_i} \cdot \Delta n_i \\
\Rightarrow \Delta\lambda_{res} &= \frac{\frac{\partial n_{eff}}{\partial n_i} \cdot \Delta n_i}{\frac{m}{L} - \frac{\partial n_{eff}}{\partial \lambda}} = \frac{\lambda \frac{\partial n_{eff}}{\partial n_i} \cdot \Delta n_i}{\lambda\left(\frac{m}{L} - \frac{\partial n_{eff}}{\partial \lambda}\right)}
\end{aligned} \tag{16.5}$$

Here, group index $n_g = \lambda\left(\frac{m}{L} - \frac{\partial n_{eff}}{\partial \lambda}\right) = n_{eff} - \lambda\frac{\partial n_{eff}}{\partial \lambda}$ (From Eq. 16.4)

$$\begin{aligned}
\Rightarrow \Delta\lambda_{res} &= \frac{\frac{\partial n_{eff}}{\partial n_i} \cdot \Delta n_i}{n_g} \\
\therefore S &= \frac{\Delta\lambda_{res}}{\Delta n_i} = \frac{\lambda \cdot \frac{\partial n_{eff}}{\partial n_i}}{n_g}
\end{aligned} \tag{16.6}$$

Here, sensitivity of ring is defined by S. Due to change of evanescent field, dielectric constant of the surrounding medium is change; as a result; device sensitivity also changes.

Micro-ring resonator is an optical module which can confine light by following the total internal reflection (TIR) and can be realized by micro-/nanofabrication techniques. In ring resonator, the dimensions of the ring and bus WG can vary based on symmetric or asymmetric coupling. A standard all-pass ring resonator is shown in Fig. 16.11, where the relationship between the input (P_0, Q_0) and output (P, Q) is as follows:

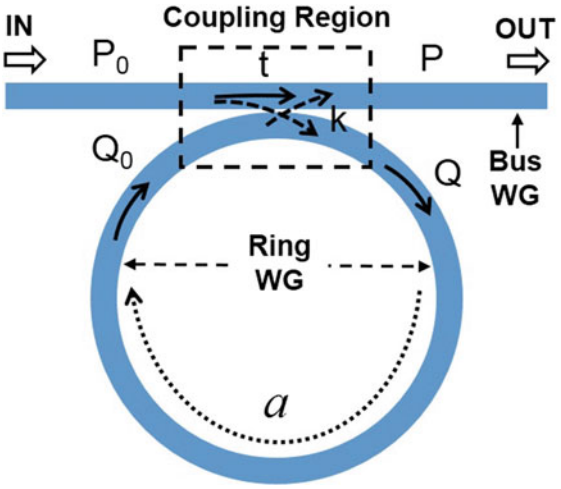

Fig. 16.11 All-pass ring resonator. Reprinted with permission from Royal Society of Chemistry [34]

$$\begin{pmatrix} P \\ Q \end{pmatrix} = \mathrm{R}\begin{pmatrix} P_0 \\ Q_0 \end{pmatrix}$$
$$\mathrm{P} = (1-\gamma)^{1/2}[\mathrm{P}_0 \cos(\kappa l) - \mathrm{jQ}_0 \sin(\kappa l)] \tag{16.7}$$
$$\mathrm{Q} = (1-\gamma)^{1/2}[\mathrm{P}_0 \cos(\kappa l) - \mathrm{jQ}_0 \sin(\kappa l)]$$
$$\mathrm{R} = \begin{pmatrix} t & jk \\ jk^* & t^* \end{pmatrix}$$

where κ, l, γ, and ρ are mode-coupling coefficient, coupling length, and loss coefficient.

The transmission and coupling coefficients have strong effects on the amplitude transmission and coupling. The transmission and coupling intensities as a function of wavelength are shown in below [40]:

$$T(\lambda) = (1-\gamma)\left[\frac{a^2 - 2at\cos(\lambda) + t^2}{1 - 2at\cos(\lambda) + (at)^2}\right] \tag{16.8}$$

$$C(\lambda) = 1 - (1-\gamma)\left[\frac{a^2 - 2at\cos(\lambda) + t^2}{1 - 2at\cos(\lambda) + (at)^2}\right] = 1 - T(\lambda) \tag{16.9}$$

where a is the single-round-trip amplitude transmission, t is the transmission coefficient, and for lossless case, $\mathrm{t}^2 + a^2 = 1$. Figure 16.10 shows transmission and coupled power as a function of wavelength. Transmission and coupled power varies with a and t variation. For the commercial software (Opti-FDTD or JCMwave), WGs dimensions (widths and length) were changed to vary propagation constants. Moreover, transmission or coupling power also depends on coupling length $L_c = \pi/2k$. In critical coupling $a = \mathrm{t}$ or $1 - a^2 = \mathrm{k}^2$, the transmitted power equals to the loss in the ring.

The resonance wavelength of the resonator is defined as

$$\lambda_{res} = \frac{n_{eff} L}{m} \quad \mathrm{m} = 1, 2, 3 \ldots . \tag{16.10}$$

The critical coupling is defined as the resonance condition in which the transmission at the output port is zero. That means $\mathrm{T}_{\min}$ drops to zero, $\mathrm{a} = \mathrm{t}$ or $1 - \mathrm{a}^2 = \mathrm{k}^2$, which indicate the transmitted power equals to the loss in the ring.

The full width half maximum (FWHM) is the 3 dB resonance width which can be defined as,

$$\mathrm{FWHM} = \frac{(1-at)\lambda_{res}^2}{\pi n_g L\sqrt{at}} \tag{16.11}$$

Here, n_g = group index of the WG and function of effective index and wavelength is defined as

$$n_g = n_{eff} - \lambda \frac{dn_{eff}}{d\lambda} \tag{16.12}$$

The on–off extinction ratio is defined as the ratio of T_{max} and T_{min}:

$$ER = \frac{T_{max}}{T_{min}} = \frac{(a+t)^2(1-at)^2}{(a-t)^2(1+at)^2} \tag{16.13}$$

The wavelength range between two resonances is known as free spectral range (FSR):

$$FSR = \frac{\lambda^2}{n_g L} \tag{16.14}$$

For 486 × 220 nm^2, SOI WG group index is found $n_g \approx 4.55$. FSR as a function of round-trip lengths is shown in Fig. 16.10.

Figure 16.12a, b shows the normalized transmission as a function of wavelength. In Fig. 16.12a, transmission coefficient t is varied with constant (a = 0.95)

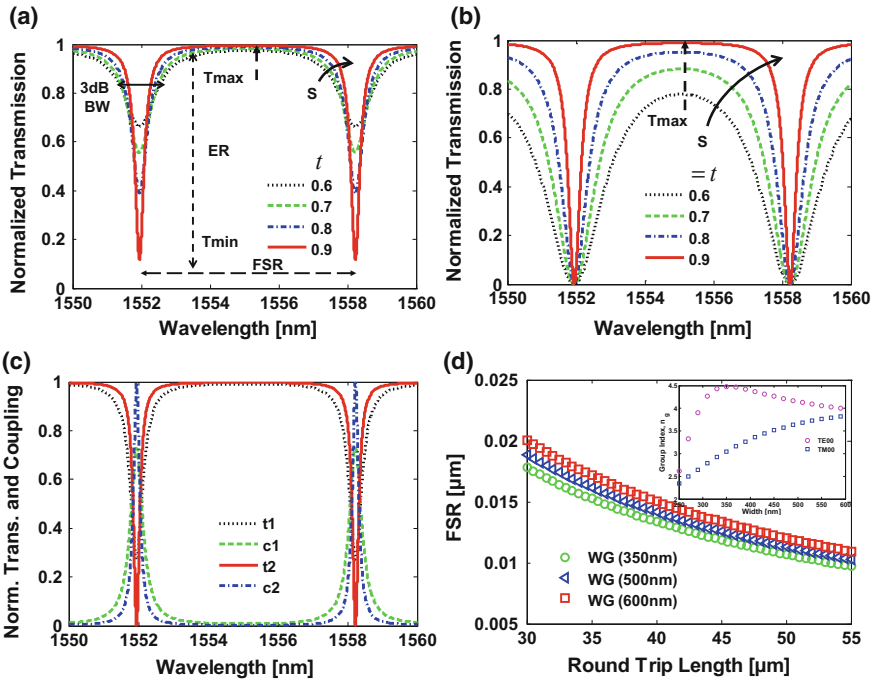

Fig. 16.12 **a–c** Transmission and coupling properties of MRR as a function of illumination wavelength. **d** FSR as a function of round-trip length at operation wavelength, λ = 1.55 nm [40]

round-trip amplitude transmission. As t increases, the extraction ratio ER (ratio between maximum T_{max} and minimum T_{min} transmission) decreases. The sharpness S of the transmission increases as t increases. Therefore, 3 dB bandwidth (BW) of the transmission curve decreased. Figure 16.12b shows normalized transmission in the critical coupling condition (a = t). As value (a = t) increased, T_{max}, S increased and 3 dB BW decreased, respectively. The ER is infinite in critical coupling condition as T_{min} is zero.

The finesses are defined as the ratio of FSR and resonance width:

$$\text{Finesse} = \frac{FSR}{FWFM} \tag{16.15}$$

The finesses indicate the sharpness of the resonance relative to their spacing. The Q-factor is measured as the sharpness relative to the central frequency:

$$\text{Q-factor} = \frac{\lambda_{res}}{FWHM} \tag{16.16}$$

It can be also defined as

$$\text{Q-factor} = \frac{\pi n_g L\sqrt{at}}{\lambda_{res}(1-at)} \tag{16.17}$$

The physical meaning of the Q-factor indicates the number of round-trip by the light through the ring WG before it loss to initial values. More specifically, at Q-value, energy lost is 1/e of the initial energy. To define the Q-factor, ring is excited to some energy level and considers the loss of energy with time. Therefore, to make high Q-factor reduction of loss due to coupler is important [33, 39, 40].

16.5.1 Materials and Configurations of Micro-ring Resonators

Micro-ring resonator is mainly developed based on WG structure. To date, different types of micro-ring resonators have be reported such as microsphere, ring, disk, capillary, microtoroid, opto-fluidic, micro-tube and micro- or nano-fiber based [4]. Also, due to advancement of optical materials, various materials such as silicon, silica, quartz, silicon-nitride, polymers, and also other hybrid materials have been widely used for MRR [6].

Recently, photonic crystal-based ring resonators have been reported which shows the high Q-factor [41, 42]. Q-factor is a quality indication of a device. Vollemer et al. proposed a microsphere ring resonator [34]. Microsphere ring resonator is inexpensive, and fabrication process is straightforward, and it can be achieved with various materials like liquid, fused silica, polymers [34, 43, 44].

Recently, tapered optical tip-based silica microsphere has been reported [45, 46]. Hybrid configuration also shows great performance in terms of sensing. However, hybrid structure shows the better sensing performance compared to the ring-based resonator but lower than the disk type [5].

16.5.2 Overview of MRR Sensors

Similar to the micro-ring resonator, micro-disk resonators are also made with the polymer, metal-capped, silicon, silica, etc., on a silica wafer [6]. Ciminelli et al. reported that micro-disk resonator made with SiO_2 showed better performance compared to the ring resonator having Q-factor 6×10^4 [47]. Propagation loss can be diminished using the disk-based resonator; as a result, disk resonator shows better sensing performance compared to the other ring resonator configurations [5]. However, the main drawback of the disk-based resonator is that it supports multi-mode which hamper the sensing performance.

Micro-ring resonators sensing performance depends on various parameters such as sensitivity, FSR, finesses, coupling efficiency, Q-factor, detection limit, full width at half maximum (FWHM) [40, 48]. Among the sensor quality measuring parameters, Q-factor is the key parameter. However, Q-factor also related to other sensing parameters like FWHM. Q-factor value indicates how large area of propagating light and analyte are coupled together. Furthermore, higher Q-factor value also indicates the high-sensing performance. To improve the Q-factor, several numbers of approaches have been reported following the all-pass ring resonator and add-drop ring resonator [40]. By increasing the air gap between the ring and WG, the Q-factor can be increased; however, large air gap will reduce the coupling efficiency as well. Lower coupling efficiency will diminish the excitation ratio which is very important for the sharp-resonant dips. The sharp resonance depth indicates the higher signal to noise ratio (SNR); as a result, detection accuracy also enhances. By increasing the cavity length, Q-factor also can be enhanced. However, increasing the length means increasing the overall size.

Recently, microsphere resonator has been demonstrated with Q-factor of $\sim 2\ 10^6$ [46]. Another, PDMS polymer-based microsphere has also been reported with Q-factor $\sim 10^5$. Hybrid silica-polymer microsphere has also been demonstrated and having Q-factor $\sim 10^7$ [44]. Due to fabrication limitation of microsphere structures, it is limited for the mass production and small-scale integration. Moreover, polymer-based ring resonators also show the limited Q-factor which indicates the limited sensor performance [4]. Recently, slotted WG-based ring resonator has sown great interest due to feasibility of placing the sample in the micro-fluidic slots. The maximum reported refractive index detection limit is 5×10^{-6} (RIU), and surface mass density detection limit is 0.9 pg mm^{-2} [49].

Microspheres resonators (Fig. 16.13a) are inexpensive, and the fabrication process is simple. However, the main drawback of microsphere resonators is the array-type fabrication which is important in terms of mass production [50, 51].

This array-type fabrication problem can be solved by using the ring, disk, and toroid-shaped resonators with SOI environment (Fig. 16.13b) [52].

By utilizing the advanced nano-micro fabrication facility ring, disk, or toroid-shaped resonators can be achieved easily. Slotted WG-based micro-ring resonator can pave the way of multi-analyte detection capabilities which fabrication process is also simple (Fig. 16.13c) [53]. Another interesting sensing scheme is the capillary-integrated ring resonators where capillary can be used to flow the sample (Fig. 16.13d) [4]. To achieve this kind of structure, two separate methods such as WG and fiber drawing are required. Resonator array-based ring resonator has also been reported recently (Fig. 16.13e) [54]. However, its fabrication is complex. Recently, utilizing the advantages of optical fiber fabrication microtoroid (Fig. 16.13f) [55], capillary-based (Fig. 16.13g) [56] and micro-fiber coil (Fig. 16.13h) [57]-based ring resonators have been reported. However, the integration of fiber with WG structure is not mature enough for the mass production. Recently, Chao et al. reported a highly sensitive sharp asymmetric biochemical sensor utilizing the fano-resonance optical property (see Fig. 16.14a) [58].

Kippenberg et al. have also been reported a cavity-based WG sensor which shows the high Q-factor around 1 million (see Fig. 16.14b) [60]. Niehusmann et al. reported the silicon WG-based micro-ring resonator which also shows the ultra-high Q-factor with the minimum propagation loss 1.96 ± 0.1 dB/cm (see Fig. 16.14c) [61]. Due to high Q-factor and minimal propagation loss, it is suitable for the biochemical sensing. Nowadays, another interesting sensing scheme is the photonic crystal-based WG sensor where photonic crystals are infiltrated with the various liquids and lead to the multi-analyte detections. Loncar et al. have reported photonic crystal lasers for the chemical detection (see Fig. 16.14d) [62]. It shows very little amount of analyte like femto-litter detection capability using the nanocavity laser.

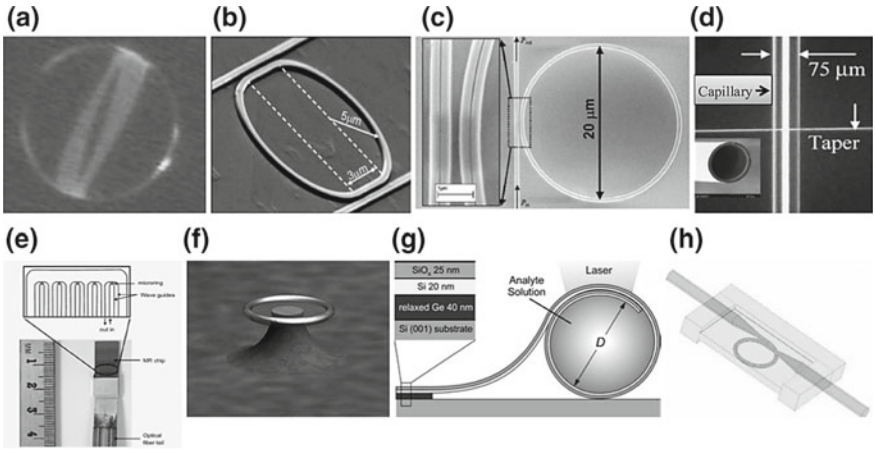

Fig. 16.13 Micro-ring resonators. **a** Microsphere, **b** Silicon-on-insulator (SOI), **c** slot WG, **d** capillary-based, **e** resonator array, **f** microtoroid, **g** capillary-based, and **h** micro-fiber coil-based ring resonator. Reprinted with permission from Springer [4]

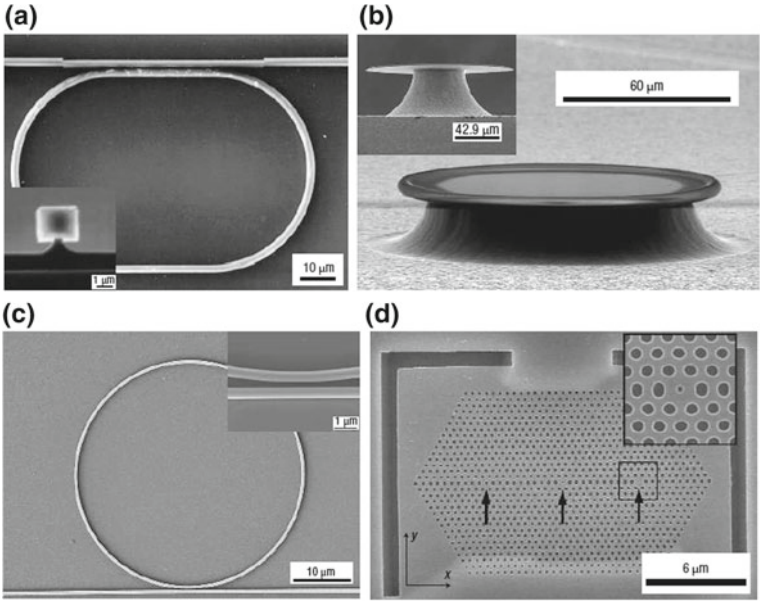

Fig. 16.14 Scanning electron micrographs (SEM) of various optical microcavities for biosensing. **a** Suspended polystyrene micro-ring. **b** Silica microtoroid WG structure. **c** Silicon on insulator micro-ring. **d** InGaAsP membrane-based planar photonic crystal WG. Reprinted with permission from Macmillan Publishers Ltd. [59]

16.5.3 Micro-ring Resonator-Based Corrosion Sensing

Corrosion sensor is a special type of sensor which able to detect the oxidation of a metal. Recently, Rajib et al. have been reported a micro-ring resonator-based corrosion sensor which showed the iron metal to iron-oxide detection mechanism [40]. The schematic of MRR-based corrosion sensor and experimental setup are shown in Fig. 16.15a and Fig. 16.15b, respectively. The iron nano-disks (NDs) are arranged periodically in the ring WG, and also, the number of NDs has effects on the sensor performance (see Fig. 16.15a). Due to change of iron NDs refractive index, it shows the resonance wavelength shift by which unknown sample could be detected. According to Fig. 16.15b, incident light will go through the bus WG and will couple with the ring WG, and finally, counter propagating wave will decouple to the bus WG. Optical analyzer/detector will receive the counter propagating wave which will pass through the bus WG. Light from the source is launched into the bus WG through an input port, coupled to the ring WG, and finally, counter propagating wave is decoupled to the bus WG. Generally, the wavelength tunable laser is used for the resonance shift measuring purpose. Figure 16.15c shows the transmission as a function of wavelength. It shows the resonance peak at 1707 nm wavelength in standard condition (without NDs), and with the presence of iron NDs, it exhibits the

blue shift and found the resonance peak at 1683 nm wavelength. As a result, normalized transmission also changed from −69 dB to −56 dB, respectively. Furthermore, in iron oxidation condition, WG effective index becomes lower compared to the ring WG with iron NDs. This condition also shows the blue shift and reduces the normalized transmission as well. By observing the resonance shift and also the transmission intensity, it will detect the oxidation condition of iron NDs. To investigate the sensor performance, linear fitting has been observed which shows the R^2 value of 0.90, which is a worthy indication of a good sensor (See Fig. 16.15d).

The micro-ring resonator-based corrosion sensor performance also depends on the number of nano-disks in the WG ring. According to Fig. 16.16a, it is visible that smaller number of nano-disks shows the large resonance wavelength shift that means with the presence of minimum number of iron NDs it shows maximum sensitivity and vice versa. The light interaction is increased by increasing the number of NDs; however, it leads to the lower resonant wavelength shift. Besides the number of NDs, radius of NDs has also notable effects on the sensing performance shown in Fig. 16.16b. Figure 16.16b shows that increase of NDs radius leads to the smaller resonant wavelength shift and vice versa. It shows the red

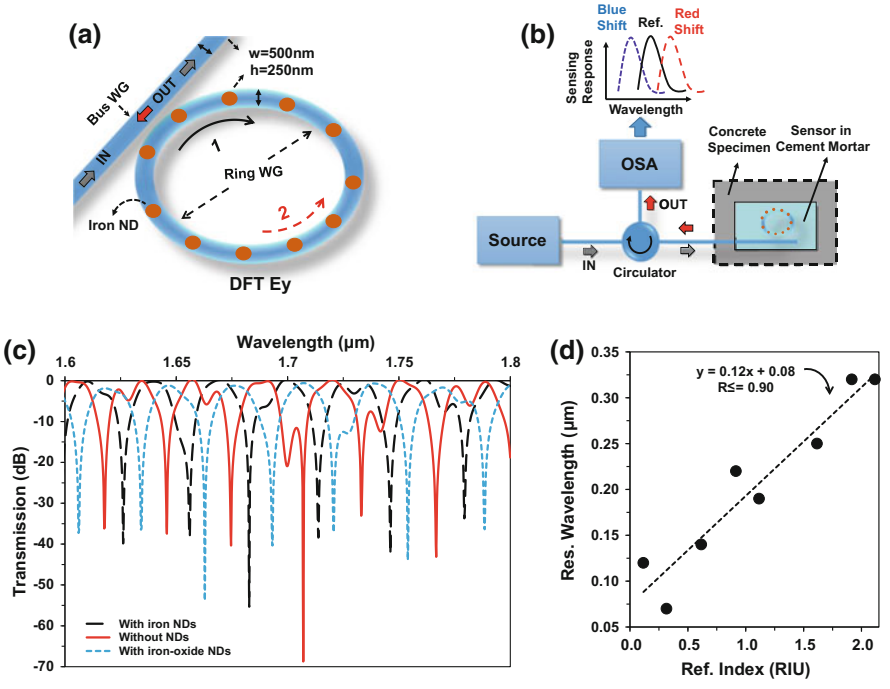

Fig. 16.15 Schematic of **a** ring resonator with periodic iron NDs, **b** experimental setup of the micro-ring resonator, **c** transmission spectra with varying NDs conditions, and **d** linear fit of resonant wavelength with refractive index variation of iron NDs [40]

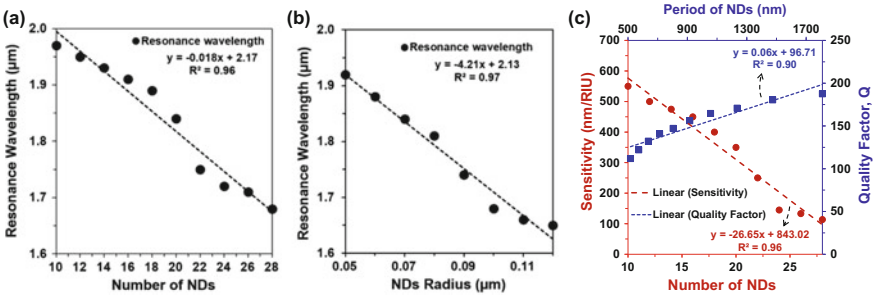

Fig. 16.16 Linear fit of the resonance wavelength with the variation of **a** number of iron NDs and **b** their radius in the ring WG. **c** Sensitivity and Q-factor as a function of number of iron NDs and its spacing [40]

resonant wavelength shift with the increase of NDs radius. So, by optimizing the number of NDs on the WG ring and also the radius of the NDs, sensor performance can significantly enhance. Figure 16.16c shows the important parameters such as Q-factor and sensitivity effects with the variation of number of disks and the period of the disks. It is clearly visible that with the increase in number of NDs, sensitivity of the sensor and the Q-factor decreases dramatically. Same observation is also found in terms of period. In the same size of ring WG, reducing the number of NDs means the increasing of period between the nano-disks, and it is found that with the increasing of period sensitivity of the sensor as well as the Q-factor also enhanced significantly. In summary, it can be said that WG-based ring resonator is a promising candidate for the corrosion or chemical sensing as it has more freedom to optimize the parameters to improve the sensor performance.

16.6 Present and Future Perspectives

SOI-based sensors have become very promising due to sharp resonance depth and high Q-factor. The SOI-based sensors are miniaturized, fast response and required very less power which makes SOI-based sensors more promising compared to the other optical sensors like available fluorescent-based sensor, optical fiber-based sensor [63–65]. Moreover, the multi-slots SOI structures are also open the way to detect the multi-analytes detections. Nowadays, micro-ring resonators integrated with SOI WG structures are one of the promising sensing candidates.

The existing and possible additional features which will make the SOI WG sensors more promising are listed below [4, 6, 7, 66],

- Multi-analyte detection: SOI WG-based multi-analyte detection technology is not well mature. By using the array type and slotted WGs configurations, multi-analyte system can be achieved easily.

- Mass production: SOI-based planar structures are capable of miniaturize the sensor architecture. Moreover, due to micro-nanoscale fabrication facility, mass production of sensor chips is feasible.
- Real-time detection: Real-time detection capability is one of key factors. Real-time detection capability can be achieved by parallel operation with ring array configuration. Following this method, multiple analyses can be done at the time instance; as a result, it will provide the higher throughput. Moreover, multiple analyte/sample also can be analyzed simultaneously; as a result, response time will be faster.
- Low-cost detection: By utilizing the on chip laser source technology, cost of the current sensor technology can be reduced (tuneable laser sources are widely used).
- Higher detection limit: Detection limit is one of the key parameters of a sensor. Using the upstream and downstream components, detection limit of the sensor can be improved.
- Small sample volume: Detection accuracy needs to improve for even a small size/volume of sample. Highly efficient system is required to detect the small amount of volume. Moreover, efficient integration with micro-fluidics and sample delivery components is required.

16.7 Conclusions

In this chapter, we have summarized the SOI-based WG structures with light propagation properties. A range of SOI-based WG sensors are analyzed with optimized parameters. Fabrication materials such as polymer, liquid environment, semiconductor, Si, SiO_2 have significant effects on the device fabrication and the sensor performance; as a result, optical properties of the currently using waveguide materials are discussed. Nowadays, MRR-based sensors are widely used for the commercial applications; as a result, we have covered the different types of MRR-based biochemical sensors in the SOI waveguide platform. Furthermore, performance criteria of the sensors are extensively studied. Finally, limitations and possible solutions of the currently available SOI waveguide-based sensors are discussed.

Contributions Ahmmed A. Rifat and Rajib Ahmed contribute to this chapter equally.

References

1. S.S. Yin, P. Ruffin, *Fiber Optic Sensors* (Wiley Online Library, 2002)
2. E. Udd, W.B. Spillman Jr, *Fiber Optic Sensors: an Introduction for Engineers and Scientists* (Wiley, 2011)

3. W. Chen, Ş.K. Özdemir, G. Zhao, J. Wiersig, L. Yang, Exceptional points enhance sensing in an optical microcavity. Nature **548**, 192–196 (2017)
4. Y. Sun, X. Fan, Optical ring resonators for biochemical and chemical sensing. Anal. Bioanal. Chem. **399**, 205–211 (2011)
5. C. Ciminelli, F. Dell'Olio, D. Conteduca, C. Campanella, M. Armenise, High performance SOI microring resonator for biochemical sensing. Opt. Laser Technol. **59**, 60–67 (2014)
6. M.S. Luchansky, R.C. Bailey, High-Q optical sensors for chemical and biological analysis. Anal. Chem. **84**, 793–821 (2011)
7. R. Ahmed, *Literature Review on Ring Resonator Based on Multi-mode Integrated Waveguide for Sensing Application* (Aston University, 2014)
8. Y. Rao, T. Zhu, A highly sensitive fiber-optic refractive index sensor based on an edge-written long-period fiber grating, in *Bragg Gratings, Photosensitivity, and Poling in Glass Waveguides* (2007), p. JWA53
9. K.E. Chong, H.W. Orton, I. Staude, M. Decker, A.E. Miroshnichenko, I. Brener et al., Refractive index sensing with Fano resonances in silicon oligomers. Philos. Trans. R. Soc. A **375**, 20160070 (2017)
10. Q. Wang, L. Kong, Y. Dang, F. Xia, Y. Zhang, Y. Zhao et al., High sensitivity refractive index sensor based on splicing points tapered SMF-PCF-SMF structure Mach-Zehnder mode interferometer. Sens. Actuators B Chem. **225**, 213–220 (2016)
11. L. Oliveira, C. Moreira, A. Lima, H. Neff, A prism-based polymeric surface plasmon resonance biochip for angular and spectral modes. Proced. Eng. **168**, 1350–1353 (2016)
12. A. Iadicicco, A. Cusano, A. Cutolo, R. Bernini, M. Giordano, Thinned fiber Bragg gratings as high sensitivity refractive index sensor. IEEE Photonics Technol. Lett. **16**, 1149–1151 (2004)
13. W. Bogaerts, P. De Heyn, T. Van Vaerenbergh, K. De Vos, S. Kumar Selvaraja, T. Claes et al., Silicon microring resonators. Laser Photonics Rev. **6**, 47–73 (2012)
14. A.L. Washburn, M.S. Luchansky, A.L. Bowman, R.C. Bailey, Quantitative, label-free detection of five protein biomarkers using multiplexed arrays of silicon photonic microring resonators. Anal. Chem. **82**, 69–72 (2009)
15. C.-Y. Chao, W. Fung, L.J. Guo, Polymer microring resonators for biochemical sensing applications. IEEE J. Sel. Top. Quantum Electron. **12**, 134–142 (2006)
16. H. Zhu, I.M. White, J.D. Suter, M. Zourob, X. Fan, Integrated refractive index optical ring resonator detector for capillary electrophoresis. Anal. Chem. **79**, 930–937 (2007)
17. J.D. Suter, D.J. Howard, H. Shi, C.W. Caldwell, X. Fan, Label-free DNA methylation analysis using opto-fluidic ring resonators. Biosens. Bioelectron. **26**, 1016–1020 (2010)
18. J.D. Suter, I.M. White, H. Zhu, H. Shi, C.W. Caldwell, X. Fan, Label-free quantitative DNA detection using the liquid core optical ring resonator. Biosens. Bioelectron. **23**, 1003–1009 (2008)
19. A. Fernández Gavela, D. Grajales García, J.C. Ramirez, L.M. Lechuga, Last advances in silicon-based optical biosensors. Sensors **16,** 285 (2016)
20. C. Susskind, Observations of electromagnetic-wave radiation before Hertz. Isis **55**, 32–42 (1964)
21. L. Rayleigh, V. On the incidence of aerial and electric waves upon small obstacles in the form of ellipsoids or elliptic cylinders, and on the passage of electric waves through a circular aperture in a conducting screen. Lon. Edinb. Dublin Philos. Mag. J. Sci. **44**, 28–52 (1897)
22. L. Rayleigh, CXII. The problem of the whispering gallery. Lon. Edinb. Dublin Philos. Mag. J. Sci. **20**, 1001–1004 (1910)
23. R. Grover, Indium phosphide based optical micro-ring resonators (2003)
24. A. Serpengüzel, G. Griffel, S. Arnold, Excitation of resonances of microspheres on an optical fiber. Opt. Lett. **20**, 654–656 (1995)
25. Z. Guo, H. Quan, Energy transfer to optical microcavities with waveguides. J. Heat Transfer **129**, 44–52 (2007)
26. Y. Sun, X. Fan, Analysis of ring resonators for chemical vapor sensor development. Opt. Express **16**, 10254–10268 (2008)

27. W.-Y. Chen, Benzocyclobutene microring resonators. University of Maryland, College Park (2007)
28. J. Leuthold, C. Koos, W. Freude, Nonlinear silicon photonics. Nat. Photonics **4**, 535–544 (2010)
29. W.R. Wong, O. Krupin, S.D. Sekaran, F.R. Mahamd Adikan, P. Berini, Serological diagnosis of dengue infection in blood plasma using long-range surface plasmon waveguides. Anal. Chem. **86**, 1735–1743 (2014)
30. A.A. Rifat, M.R. Hasan, R. Ahmed, H. Butt, Photonic crystal fiber-based plasmonic biosensor with external sensing approach. J. Nanophotonics **12**, 012503 (2017)
31. W.L. Ng, A.A. Rifat, W.R. Wong, G. Mahdiraji, F.M. Adikan, A novel diamond ring fiber-based surface plasmon resonance sensor. Plasmonics, 1–6 (2017)
32. F. Wan, G. Qian, R. Li, J. Tang, T. Zhang, High sensitivity optical waveguide accelerometer based on Fano resonance. Appl. Opt. **55**, 6644–6648 (2016)
33. R. Ahmed, A.A. Rifat, A.K. Yetisen, S.H. Yun, S. Khan, H. Butt, Mode-multiplexed waveguide sensor. J. ElEctromagn. Waves Appl. **30**, 444–455 (2016)
34. F. Vollmer, L. Yang, Review Label-free detection with high-Q microcavities: a review of biosensing mechanisms for integrated devices. Nanophotonics **1**, 267–291 (2012)
35. A.A. Rifat, R. Ahmed, A.K. Yetisen, H. Butt, A. Sabouri, G.A. Mahdiraji, et al., Photonic crystal fiber based plasmonic sensors. Sens. Actuators B Chem. (2016)
36. K. De Vos, *Label-Free Silicon Photonics Biosensor Platform with Microring Resonators* (Ghent University, 2010)
37. E. Marcatili, Bends in optical dielectric guides. Bell Labs Tech. J. **48**, 2103–2132 (1969)
38. S. Lin, E. Schonbrun, K. Crozier, Optical manipulation with planar silicon microring resonators. Nano Lett. **10**, 2408–2411 (2010)
39. R. Ahmed, A.A. Rifat, A. Sabouri, B. Al-Qattan, K. Essa, H. Butt, Multimode waveguide based directional coupler. Opt. Commun. **370**, 183–191 (2016)
40. R. Ahmed, A.A. Rifat, A.K. Yetisen, M.S. Salem, S.-H. Yun, H. Butt, Optical microring resonator based corrosion sensing. Rsc Adv. **6**, 56127–56133 (2016)
41. Z. Qiang, W. Zhou, R.A. Soref, Optical add-drop filters based on photonic crystal ring resonators. Opt. Express **15**, 1823–1831 (2007)
42. F.-L. Hsiao, C. Lee, Computational study of photonic crystals nano-ring resonator for biochemical sensing. IEEE Sens. J. **10**, 1185–1191 (2010)
43. N.M. Hanumegowda, I.M. White, H. Oveys, X. Fan, Label-free protease sensors based on optical microsphere resonators. Sens. Lett. **3**, 315–319 (2005)
44. M. Charlebois, A. Paquet, L. Verret, K. Boissinot, M. Boissinot, M. Bergeron et al., Toward automatic label-free whispering gallery modes biodetection with a quantum dot-coated microsphere population. Nanoscale Res. Lett. **5**, 524 (2010)
45. I.M. White, H. Zhu, J.D. Suter, N.M. Hanumegowda, H. Oveys, M. Zourob et al., Refractometric sensors for lab-on-a-chip based on optical ring resonators. IEEE Sens. J. **7**, 28–35 (2007)
46. D. Armani, T. Kippenberg, S. Spillane, K. Vahala, Ultra-high-Q toroid microcavity on a chip. Nature **421**, 925–928 (2003)
47. C. Ciminelli, C. Campanella, M. Armenise, Hybrid optical resonator for nanostructured virus detection and sizing, in *2011 IEEE International Workshop on Medical Measurements and Applications Proceedings (MeMeA)* (2011), pp. 555–558.
48. R. Ahmed, S.M. Ullah, Design & analysis on silicon based optical micro-ring resonator sensor device for biomedical applications at μm wavelength, in *CIOMP-OSA Summer Session: Lasers and their Applications* (2011), p. Tu3
49. C.F. Carlborg, K.B. Gylfason, A. Kaźmierczak, F. Dortu, M.B. Polo, A.M. Catala et al., A packaged optical slot-waveguide ring resonator sensor array for multiplex label-free assays in labs-on-chips. Lab Chip **10**, 281–290 (2010)
50. V. Roman, J. Popp, M. Fields, W. Kiefer, Species identification of multicomponent microdroplets by seeding stimulated Raman scattering. JOSA B **16**, 370–375 (1999)

51. F. Vollmer, D. Braun, A. Libchaber, M. Khoshsima, I. Teraoka, S. Arnold, Protein detection by optical shift of a resonant microcavity. Appl. Phys. Lett. **80**, 4057–4059 (2002)
52. N.A. Yebo, P. Lommens, Z. Hens, R. Baets, An integrated optic ethanol vapor sensor based on a silicon-on-insulator microring resonator coated with a porous ZnO film. Opt. Express **18**, 11859–11866 (2010)
53. Q. Xu, V.R. Almeida, R.R. Panepucci, M. Lipson, Experimental demonstration of guiding and confining light in nanometer-size low-refractive-index material. Opt. Lett. **29**, 1626–1628 (2004)
54. A. Ramachandran, S. Wang, J. Clarke, S. Ja, D. Goad, L. Wald et al., A universal biosensing platform based on optical micro-ring resonators. Biosens. Bioelectron. **23**, 939–944 (2008)
55. A.M. Armani, K.J. Vahala, Heavy water detection using ultra-high-Q microcavities. Opt. Lett. **31**, 1896–1898 (2006)
56. A. Bernardi, S. Kiravittaya, A. Rastelli, R. Songmuang, D. Thurmer, M. Benyoucef et al., On-chip Si/SiO x microtube refractometer. Appl. Phys. Lett. **93**, 094106 (2008)
57. F. Xu, V. Pruneri, V. Finazzi, G. Brambilla, An embedded optical nanowire loop resonator refractometric sensor. Opt. Express **16**, 1062–1067 (2008)
58. C.-Y. Chao, L.J. Guo, Biochemical sensors based on polymer microrings with sharp asymmetrical resonance. Appl. Phys. Lett. **83**, 1527–1529 (2003)
59. C. Monat, P. Domachuk, B. Eggleton, Integrated optofluidics: a new river of light. Nat. Photonics **1**, 106–114 (2007)
60. T. Kippenberg, S. Spillane, D. Armani, K. Vahala, Fabrication and coupling to planar high-Q silica disk microcavities. Appl. Phys. Lett. **83**, 797–799 (2003)
61. J. Niehusmann, A. Vörckel, P.H. Bolivar, T. Wahlbrink, W. Henschel, H. Kurz, Ultrahigh-quality-factor silicon-on-insulator microring resonator. Opt. Lett. **29**, 2861–2863 (2004)
62. M. Lončar, A. Scherer, Y. Qiu, Photonic crystal laser sources for chemical detection. Appl. Phys. Lett. **82**, 4648–4650 (2003)
63. T. Ling, S.-L. Chen, L.J. Guo, Fabrication and characterization of high Q polymer micro-ring resonator and its application as a sensitive ultrasonic detector. Opt. Express **19**, 861–869 (2011)
64. B. Diem, P. Rey, S. Renard, S.V. Bosson, H. Bono, F. Michel et al., SOI'SIMOX'; from bulk to surface micromachining, a new age for silicon sensors and actuators. Sens. Actuators, A **46**, 8–16 (1995)
65. D.-X. Xu, A. Densmore, A. Delâge, P. Waldron, R. McKinnon, S. Janz et al., Folded cavity SOI microring sensors for high sensitivity and real time measurement of biomolecular binding. Opt. Express **16**, 15137–15148 (2008)
66. S. Feng, T. Lei, H. Chen, H. Cai, X. Luo, A.W. Poon, Silicon photonics: from a microresonator perspective. Laser Photonics Rev. **6**, 145–177 (2012)

Index

© Springer International Publishing AG, part of Springer Nature 2019

M. F. O. Hameed and S. Obayya (eds.), *Computational Photonic Sensors*, https://doi.org/10.1007/978-3-319-76556-3